NANOSTRUCTURED CARBON NITRIDES FOR SUSTAINABLE ENERGY AND ENVIRONMENTAL APPLICATIONS

Edited by
Shamik Chowdhury
Mu. Naushad

ELSEVIER

Micro & Nano Technologies Series

NANOSTRUCTURED CARBON NITRIDES FOR SUSTAINABLE ENERGY AND ENVIRONMENTAL APPLICATIONS

Micro and Nano Technologies

NANOSTRUCTURED CARBON NITRIDES FOR SUSTAINABLE ENERGY AND ENVIRONMENTAL APPLICATIONS

Edited by

SHAMIK CHOWDHURY

Assistant Professor in the School of Environmental Science and Engineering, Indian Institute of Technology Kharagpur, West Bengal, India

MU. NAUSHAD

Full Professor in the Department of Chemistry, College of Science, King Saud University, Riyadh, Saudi Arabia

ELSEVIER

Elsevier
Radarweg 29, PO Box 211, 1000 AE Amsterdam, Netherlands
The Boulevard, Langford Lane, Kidlington, Oxford OX5 1GB, United Kingdom
50 Hampshire Street, 5th Floor, Cambridge, MA 02139, United States

ISBN 978-0-12-823961-2

For information on all Elsevier publications
visit our website at https://www.elsevier.com/books-and-journals

Publisher: Matthew Deans
Acquisitions Editor: Edward Payne
Editorial Project Manager: Clodagh Holland-Borosh
Production Project Manager: Nirmala Arumugam
Cover Designer: Miles Hitchen

Typeset by STRAIVE, India

Contents

Contributors

Behzad Ataie-Ashtiani
Department of Civil Engineering, Sharif University of Technology, Tehran, Iran

Raji Atchudan
Department of Chemical Engineering, Yeungnam University, Gyeongsan, Republic of Korea

Arabinda Baruah
Department of Chemistry, Gauhati University, Guwahati, Assam, India

Aman Bhardwaj
School of Physical Sciences, Jawaharlal Nehru University, New Delhi, India

Dhruba Chakrabortty
Department of Chemistry, B.N. College, Dhubri, Assam, India

Indrajit Chakraborty
Department of Civil Engineering, Indian Institute of Technology Kharagpur, Kharagpur, India

Konstantinos C. Christoforidis
Department of Environmental Engineering, Democritus University of Thrace, Xanthi, Greece; Institut de Chimie et Procédés Pour l'Energie, l'Environnement et la Santé (ICPEES), ECPM University of Strasbourg, Strasbourg, France

Pritam Deb
Advanced Functional Material Laboratory (AFML), Department of Physics, Tezpur University (Central University), Tezpur, India

Anil Dhanda
Department of Civil Engineering, Indian Institute of Technology Kharagpur, Kharagpur, India

M.M. Ghangrekar
Department of Civil Engineering, Indian Institute of Technology Kharagpur, Kharagpur, India

Priya Ghosh
Department of Applied Organic Chemistry, CSIR-NEIST, Jorhat, Assam, India

Ashish Guleria
Department of Applied Sciences, WIT Dehradun, Dehradun, Uttarakhand, India

Chanchal Gupta
Department of Chemistry, University of Delhi, New Delhi, India

Seiyed Mossa Hosseini
Physical Geography Department, University of Tehran, Tehran, Iran

Rama Kant
Department of Chemistry, University of Delhi, New Delhi, India

Mehdi Al Kausor
Department of Chemistry, Science College, Kokrajhar, Assam, India

Ali Khadir
Young Researcher and Elite Club, Yadegar-e-Imam Khomeini (RAH) Shahre Rey Branch, Islamic Azad University, Tehran, Iran

Hee-Je Kim
School of Electrical and Computer Engineering, Pusan National University, Busan, Republic of Korea

Santosh Kumar
Department of Chemical Engineering, Imperial College London, London, United Kingdom

Ritu Malik
Department of Mechanical Engineering, University of California, Berkeley, CA, United States

Afsaneh Mollahosseini
Research Laboratory of Spectroscopy & Micro and Nano Extraction, Department of Chemistry, Iran University of Science and Technology, Tehran, Iran

Mehrdad Negarestani
Department of Civil and Environmental Engineering, Iran University of Science and Technology, Tehran, Iran

Ebrahim Pakzad
Department of Civil and Environmental Engineering, Iran University of Science and Technology, Tehran, Iran

Satyabrata Patnaik
School of Physical Sciences, Jawaharlal Nehru University, New Delhi, India

Nirupamjit Sarmah
Department of Chemistry, Gauhati University, Guwahati, Assam, India

S.M. Sathe
Department of Civil Engineering, Indian Institute of Technology Kharagpur, Kharagpur, India

Ekta Sharma
Department of Chemistry, School of Basic and Applied Sciences, Maharaja Agrasen University, Baddi, Himachal Pradesh, India

Kulvinder Singh
Department of Chemistry, DAV College, Chandigarh, India

Shabnam Taghipour
Department of Civil Engineering, Sharif University of Technology, Tehran, Iran; Department of Chemical and Biological Engineering, The Hong Kong University of Science and Technology, Hong Kong

Meenakshi Talukdar
Advanced Functional Material Laboratory (AFML), Department of Physics, Tezpur University (Central University), Tezpur, India

Vijay K. Tomer
Department of Mechanical Engineering, University of California, Berkeley, CA, United States

Rajangam Vinodh
Department of Electronics Engineering, Pusan National University, Busan, Republic of Korea

King Lun Yeung
Department of Chemical and Biological Engineering; Division of Environment and Sustainability, The Hong Kong University of Science and Technology, Hong Kong

Moonsuk Yi
Department of Electronics Engineering, Pusan National University, Busan, Republic of Korea

Preface

With escalating world population, unsustainable consumption of fossil fuels, insatiable energy demand, rapid environmental degradation, and global climate change, energy and environmental issues are receiving considerable attention worldwide in the context of sustainable development. In order to address these interconnected challenges, the use of inexpensive, robust, and highly efficient energy conversion/storage devices and environmental remediation technologies based on advanced materials has intensified in recent years. In particular, carbon nitride, a new type of two-dimensional (2D) material, has stimulated great interest for fundamental scientific investigations and potential practical applications in a multitude of clean energy technologies (e.g., lithium-ion batteries, sodium-ion batteries, supercapacitors, fuel cells, microbial fuel cells, solar cells, photoelectrochemical water splitting devices, and hydrogen storage) and environmental remediation techniques (such as wastewater treatment, water purification, air pollution control, and climate change mitigation). This can be largely attributed to its excellent optoelectronic and physicochemical properties, including moderate band gap energy, adjustable energy band configuration, tailor-made surface functionalities, low cost, metal-free nature, remarkable thermochemical stability, and environmentally benign manufacturing protocol. Additionally, due to their polymeric structure, the surface chemistry of carbon nitrides can be easily tailored by means of surface engineering at the molecular level, leading to new material systems with novel functionalities. Indeed, in the last 5 years, over 1000 research articles have been published with a particular focus on fabricating high-performance nanostructured carbon nitrides for energy conversion and storage as well as environmental remediation applications. As such, a comprehensive and up-to-date account of carbon nitride-based 2D materials, explored for sustainable energy and environmental applications, is highly desirable as it would promote further advances in this rapidly evolving cross-disciplinary research field of current global interest. To this end, we believe that this book will help the global scientific community to gain deep insights into various aspects of carbon nitride materials from multidisciplinary perspectives and in applying these materials to tackle global energy and environmental challenges in a sustainable manner. Specifically, the book will have a great appeal to chemists, electrochemists, physical chemists, solid state physicists, chemical engineers, material scientists, environmental scientists and engineers, and energy specialists. Needless to say, this in turn will stimulate further advances in the development of multifunctional materials for clean energy-related applications and environmental remediation.

The book is systematically organized into 10 chapters. Chapter 1 narrates the unique set of optical, electronic, and chemical properties possessed by carbon nitrides, which make them particularly attractive for energy- and environment-related applications. It then collates the current state-of-the-art synthesis strategies available to realize carbon nitride nanostructures with superior physiochemical properties. The next nine chapters are divided into two sections. Section I focuses on sustainable energy applications (Chapters 2–5), while Section II deals with environmental remediation applications (Chapters 6–10).

Chapter 2 summarizes the recent advances in the design and development of exotic carbon nitride-based electrodes for the creation of supercapacitors with unprecedented performance. Chapter 3 highlights the recent progress in carbon nitride-based nanocatalysts with controllable size and shape for fuel cell applications. Chapter 4 presents a systematic, updated summary of the current status of the application of carbon nitride-based materials with high conductivity and biocompatibility in microbial fuel cells (MFCs) and discusses the key scientific and technological challenges in using them to improve the performance of MFCs. Chapter 5 provides a broad overview of the latest developments in carbon nitride-mediated solar energy harvesting for potential applications in sterilization of waste and seawater desalination.

Chapter 6 critically examines the recent progress in the development of novel carbon nitride-based nanostructures for fast and efficient removal of a variety of contaminants from water, with a special focus on interaction mechanisms with contaminant molecules. Chapters 7 and 8 collate the recent advances in the rational design of carbon nitride-based photocatalysts, with a special emphasis on graphitic carbon nitride, and highlight their applications in photocatalytic degradation of environmental contaminants. Chapter 9 provides a systematic overview of the latest progress in the development and application of carbon nitride-based photocatalysts for CO_2 reduction to solar fuels. Chapter 10 introduces the basic principles of sensor design and explores the application of carbon nitride-based sensors for the on-site detection of various heavy metal ions.

We are thankful to all the lead and contributing authors for sharing their valuable expertise in various aspects of carbon nitrides without which this book would not have been possible. We are also grateful to the Elsevier Editorial Project Manager, Cloe Holland-Borosh, for her constructive feedback, logistical support, and constant encouragement.

CHAPTER 1

Synthesis and properties of carbon nitride materials

Rajangam Vinodh[a], Raji Atchudan[b], Moonsuk Yi[a], and Hee-Je Kim[c]
[a]Department of Electronics Engineering, Pusan National University, Busan, Republic of Korea
[b]Department of Chemical Engineering, Yeungnam University, Gyeongsan, Republic of Korea
[c]School of Electrical and Computer Engineering, Pusan National University, Busan, Republic of Korea

Contents

1. Introduction

Carbon nitrides (C_3N_4), often referred to as g-C_3N_4, is a polymeric material containing carbon (C), nitrogen (N), and few contaminants such as hydrogen (H), which are bonded through tri-*s*-triazine-based patterns. The g-C_3N_4, one of the ancient polymers existing in the literature, has the molecular formula of $(C_3N_4H)_n$. The development history of g-C_3N_4 can be traced from 1834 [1]. In the 1990s, research work was inspired by the hypothetical prophecy that diamond-like C_3N_4 may possess the highest hardness [2]. The g-C_3N_4 was considered to be a more stable allotrope at room temperature. The g-C_3N_4 has a layered structure similar to graphite material, contains Van der Waals force layers, and every layer is made up of tri-*s*-triazine units linked to planar –NH_2 groups [3]. The ring structure of tri-*s*-triazine gives the polymer high thermal and chemical stability in alkaline and acidic conditions [4].

When compared to other materials, g-C_3N_4 possesses many advantages, such as (i) low cost, (ii) excellent CO_2 activation characteristics because of its nitrogen-rich

https://doi.org/10.1016/B978-0-12-823961-2.00008-2

configuration [5], (iii) photocatalytic CO_2 reduction, (iv) it can transfer electrons to surface chemical adsorption sites due to its two-dimensional (2D) layer structure, and (v) the structure/shape of g-C_3N_4 structure can be adjusted by optimizing the parameters like precursors of monomers, time, and temperature of the polymerization reaction; thus, a minor band off could be attained [6]. Furthermore, co-monomers can be made by adding combinations of monomer molecules preferred to precursors [7]. They can appreciably alter the capability of light absorption and electron transfer capabilities of g-C_3N_4 in organic compound degradation, and hydrogen manufacture and oxidation of NO_x (nitrogen oxides) can be improved by metal stimulants [8].

The semiconducting properties of g-C_3N_4 differ significantly from that of graphene sheets with a band gap of 2.7 eV for bulk g-C_3N_4; this makes it a normal band gap semiconductor. The g-C_3N_4 has an optical absorption peak of about 460 nm because of its yellow color. The g-C_3N_4 is one of the excellent materials for producing solar energy due to its remarkable chemical and thermal stability [9]. Furthermore, g-C_3N_4, also known as "melon," is a stable allotrope. Moreover, g-C_3N_4 is extracted from the Earth's crust, so it is cost-effective and reasonable for commercial utilizations in energy conversion and water splitting [10]. However, its electrical resistance has limited its electrocatalytic activity [11]. Until now, g-C_3N_4 is mostly used in its powder form, which prevents it from being reused for some applications. Therefore, the transformation of 2D construction modules into macroscopic 3D structural designs is critical for many applications [12].

In this chapter, we give an overview of the basic concepts and structure of g-C_3N_4, synthesis protocols, as well as the properties of g-C_3N_4. We firmly hope this will increase of the growth of g-C_3N_4. Novel physicochemical properties based on g-C_3N_4 nanostructures have not yet been discovered. We are at a crucial juncture to emphasize the development and offer high-quality evidence for this emerging research topic.

2. Structure of g-C_3N_4

Usually, g-C_3N_4 is prepared by the polycondensation of a melamine (MA) precursor, which is a low-cost nitrogen-containing monomer. Since the discovery of carbon nitride materials, many efforts have been carried out to conclude how different synthetic processes influence the material produced based on its morphology and reactivity.

2.1 Geometric structure

The exact building block of g-C_3N_4 contains two important units, tri-*s*-triazine (C_6N_7) and *s*-triazine (C_3N_4) rings, as shown in Fig. 1.1A and B [13]. Tri-*s*-triazine is recognized to be highly stable at room temperature [14]. The two major units of g-C_3N_4 also show that tri-*s*-triazine is thermodynamically more stable based on density functional theory

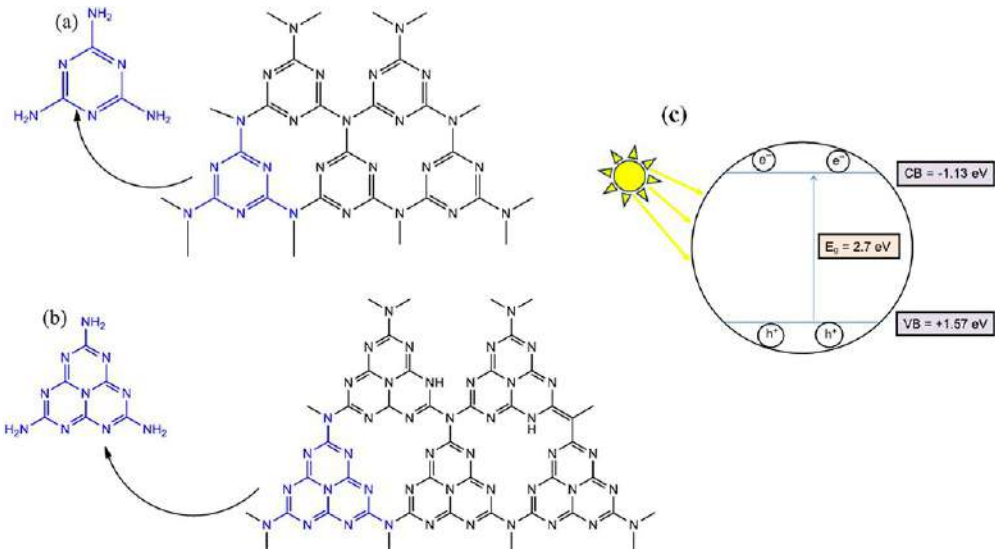

Fig. 1.1 g-C_3N_4 structures of (A) *s*-triazine and (B) tri-*s*-triazine. (C) A charge-transfer mechanism for typical g-C_3N_4. *((A) and (B) Reproduced with the permission from S. Zhang, P. Gu, R. Ma, C. Luo, T. Wen, G. Zhao, W. Cheng, X. Wang, Recent developments in fabrication and structure regulation of visible-light-driven g-C_3N_4-based photocatalysts towards water purification: a critical review, Catal. Today 335 (2019) 65–77, https://doi.org/10.1016/j.cattod.2018.09.013. (C) Reproduced with the permission from N. Rono, J.K. Kibet, B.S. Martincigh, V.O. Nyamori, A review of the current status of graphitic carbon nitride, Crit. Rev. Solid State Mater. Sci., https://doi.org/10.1080/10408436.2019.1709414.)*

(DFT) calculations [15]. Theoretically, it has been mentioned that the optimal surface area of a monolayer sheet can be enhanced to approximately 2500 m^2 g^{-1} [16,17]. It usually consists of a 2D sheet of sp^2 carbons [18], whereas g-C_3N_4 has p-conjugated graphitic planes produced by a sp^2 hybrid of C and N atoms [19]. Fina et al. [20] elucidated the 3D structure of g-C_3N_4 via powder X-ray diffraction (PXRD) and neutron diffraction techniques. They clearly revealed that the as-synthesized g-C_3N_4 shows a 3D arrangement with misalignment of tri-*s*-triazine-based layers. The layers were misaligned to evade the repulsive forces of p-electrons in adjacent layers.

2.2 Electronic structure

The g-C_3N_4 has become a center of debate due to its extraordinary electronic properties and prospective utilizations [21]. It consists of C and N, which is a sp^2 hybrid that forms the p-conjugated delocalized system. The lone pair of electrons from N causes a lone pair of valance bands to form, and therefore, creating the band structure [22]. It is important to note that the lone pair of nitrogen is important in the electronic configuration of g-C_3N_4 [23]. Theoretical approaches concerning DFT measurements predict that the valance band will have nitrogen P_z orbitals, whereas the conduction band will have carbon P_z orbitals; therefore, C atoms act as points where reduction occurs, and N atoms act as points where oxidation occurs [24]. As a photocatalyst, g-C_3N_4 tends to split the holes and electrons. The 2.7 eV of band gap allows it to absorb sunlight, which is used to purify water, produce hydrogen, and used for solar cell applications [25]. Fig. 1.1C represents a charge transfer in g-C_3N_4.

3. Preparation of g-C_3N_4

The g-C_3N_4 can be prepared by thermal polycondensation of nitrogen-containing precursors (triazine and heptazine derivatives), such as urea [26], MA ($C_3H_6N_6$) [27], dicyandiamide ($C_2N_3^-$) [28], cyanamide (CH_2N_2) [29], thiourea (CH_4N_2S) [30], guanidinium chloride ($CH_5N_3 \cdot HCl$) [31], guanidine thiocyanate ($C_2H_6N_4S$) [32], and thiourea oxide ($CH_4N_2O_2S$) [33]. The condensation routes from these C-N precursors are easy and prominent ways to build a g-C_3N_4-interpenetrating architecture [34]. Among them, MA is a common and straight monomer supply to synthesize C-N, whereas the high bonding energy of the chemical bond between $C_3H_6N_6$ units and $-NH_2$ groups of MA is inactivated at low temperatures, without the catalyst, and with no other reaction to form CN.

It has been argued that the physicochemical characteristics of the resulting g-C_3N_4 can be severely affected by a variety of precursors and treatments, including pore volume, surface area, photoluminescence (PL), C and N ratio, absorption, and nanostructures. Different functionalities and surface modifications have been used to get preferred morphology/structures such as 2D nanosheets (NSs), 3D bulks, 1D nanorods, 2D films, 1D nanowires, 1D nanotubes, and 0D quantum dots.

3.1 Chemical vapor deposition method

Urakami et al. [35] reported that g-C_3N_4 films were grown uniformly on the surface of different substrates by thermal chemical vapor deposition (CVD) method. The stoichiometric amount and nature of atomic bonds were characterized, and it was found to be equivalent to those of ideal g-C_3N_4. For a PL study, although electron excitation is to the sp^3 C-N conduction band, the sp^2 C-N conduction band was identified as the preferred electron injection from the PL intensity and the excitation-energy dependence of the PL peak shift. Also, Urakami et al. [36] discussed the growth of borane (B) atoms attached to the g-C_3N_4 films in c-plane sapphire substrates by thermal CVD at different augmentation temperatures (Fig. 1.2). Ammonium borane and MA were used as precursors. The incorporation of B is accomplished at 618°C of growth temperature. It was higher than the g-C_3N_4 thin film's ideal growth temperature to some extent. The signal peak for the B 1s core position due to the B—N bonds was noticed by XPS, which indicates the perception of B penetration into g-C_3N_4 films. When the growth temperature

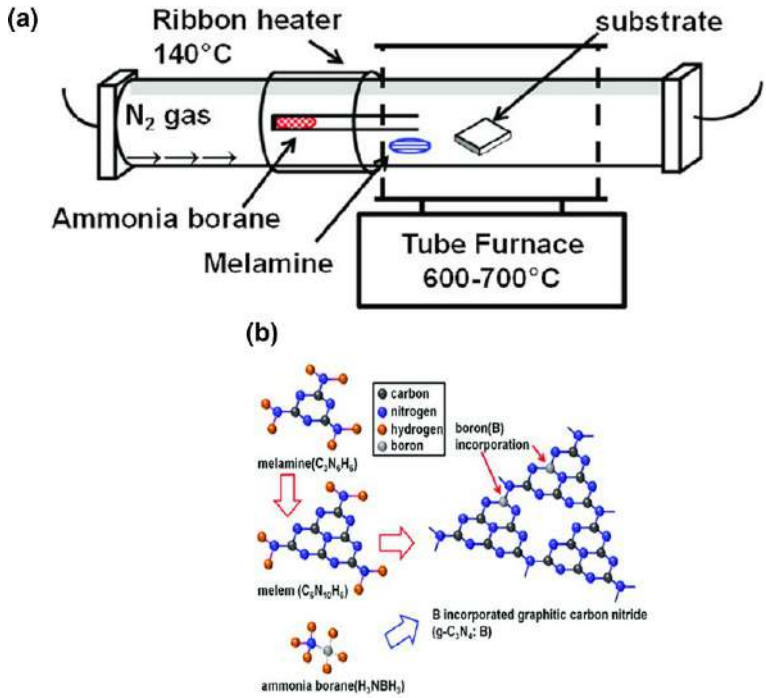

Fig. 1.2 (A) Sketch of in-house how-wall CVD equipment for B/g-C_3N_4 films; (B) pictorial representation of the B/g-C_3N_4 growth process using melamine as precursor and ammonia borane as borane molecular species. *(Reproduced with the permission from N. Urakami, M. Kosaka, Y. Hashimoto, Chemical vapor deposition of boron-incorporated graphitic carbon nitride film for carbon-based wide bandgap semiconductor materials, Phys. Status Solidi B 27(2) (2019) 1900375, https://doi.org/10.1002/pssb.201900375.)*

was increased to 650°C, a uniformly enhancing B composition and a declining graphite composition were noticed, indicating that B atoms are integrated into g-C_3N_4 as an alternative to the graphite sites. Wang et al. [37] prepared ordered cubic mesoporous (OCM) g-C_3N_4 by a simple CVD method using MA as the precursor and 3D OCM silica KIT-6 as the template. The synthesized OCM g-C_3N_4 could be seen to have a 3D cubic symmetry with a high surface area (129.8 m^2 g^{-1}) and regular pore size (3.5 nm). Due to these excellent properties, the OCM g-C_3N_4 showed improved photocatalytic activity to reduce CO_2 with water compared to flak-like g-C_3N_4. Yadav et al. [38] produced free-standing films with g-C_3N_4 nanolayers by the annealing of dicyandiamide (DCN) using a CVD method. The pyrolysis was carried out under low-pressure (approximately 3 Torr) at 600°C. Furthermore, excitation-dependent PL spectra of the prepared g-C_3N_4 film exhibited a stable, strong, and broad emission peak of 459 nm in the visible region. The free-standing g-C_3N_4 films showed a blue shift and band sharpening of the emission spectra (ES) compared to the g-C_3N_4 powder. Cui et al. [39] reported an easy and air-conditioned CVD process that would produce onion ring-like g-C_3N_4 (OR-g-C_3N_4) microstructures in a facile, ecofriendly, and consistent way. This technique uses approximately packed 350 nm SiO_2 microspheres as a rigid template and MA as a CVD precursor to form a thin layer of g-C_3N_4 in the narrow space between the SiO_2 microspheres. After dissolution of the SiO_2 microsphere hard template, the resulting g-C_3N_4 uniformly exhibits OR-like microstructures. A short description of the synthesis procedure is as follows: Typically, a few grams of MA precursor were taken in an alumina boat, and the few grams of SiO_2 microspheres were distributed uniformly on the MA powder surface. The alumina boat with a lid was annealed at 320°C for 2 h in a muffle furnace with a ramping rate of 10°C min^{-1}. Then, the muffle furnace temperature was further increased to 550°C and subjected into calcination for 3 h to form g-C_3N_4 phase. The resultant yellow-colored g-C_3N_4/SiO_2 solid sediment (top layer) was carefully separated and further subjected with ammonium bifluoride (4 M) for 12 h to isolate the SiO_2 microspheres. After thorough washing with water, centrifugation, and ultrasonication, a yellow powder of OR-g-C_3N_4 was procured. The determined band gap for OR-g-C_3N_4 was 2.58 eV, which was considerably shorter than that of 2.70 eV of bulk g-C_3N_4. Furthermore, the prepared OR-g-C_3N_4 facilitates charge separation, extends the lifespan of photoinduced carriers, and exhibits five times more photocatalytic hydrogen evolution than that of bulk g-C_3N_4.

3.2 Hydrothermal method

The hydrothermal (HT) process is essentially the least expensive and most common method of producing g-C_3N_4-based NSs. This is the easiest and most reliable method of producing g-C_3N_4-based ternary heterostructure, which can obtain high purity heterostructure NSs [40,41]. Zhang et al. [42] highlighted a HT method at low temperature to produce carbon-rich g-C_3N_4 NSs, which shows enhanced photocurrent and photocatalytic activity, because of its superior ability of electron transport and improved lifespan of photoexcited charge carriers. In a typical procedure, MA (5.5 mmol) and glucose powder (16.5 mmol) were placed in Teflon-lined autoclave (100 mL) and then filled with Millipore water up to 60% of the autoclave total volume. The reaction mixture in the autoclave was stirred for 12 h with the magnetic stirrer, then the autoclave was sealed with the nickel foam substrate and maintained at 180°C. After heating to the specified temperature, the autoclave was naturally cooled to ambient condition. The final material was thoroughly cleaned with Millipore H_2O and 92.1% ethanol to eliminate residual contaminants, and the resulting yellow powder was dried for 12 h at 60°C to get the ultimate product. The detailed schematic view is depicted in Fig. 1.3. Guo et al. [43] successfully synthesized a novel g-C_3N_4 and $BiVO_4$ (bismuth vanadate) composite (g-C_3N_4/$BiVO_4$) by a simple HT method for photocatalytic degradation reaction. The general reaction

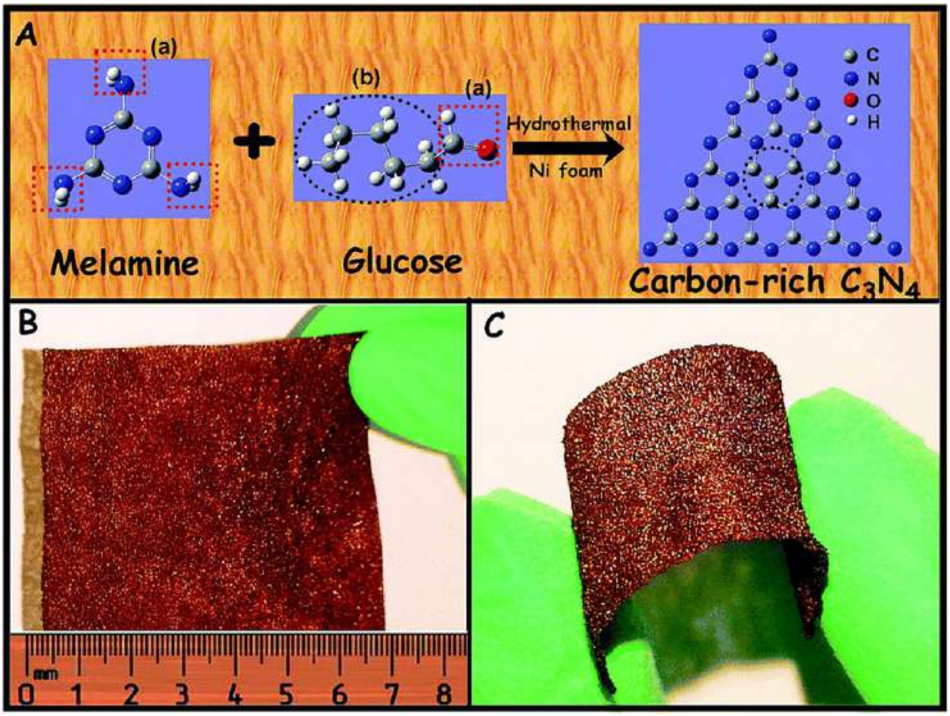

Fig. 1.3 (A) Thermal polycondensation of melamine precursor and glucose in water solution; (B) and (C) exhibition of the g-C_3N_4 on nickel foam. *(Reproduced with the permission from P. Zhang, X. Li, C. Shao, Y. Liu, Hydrothermal synthesis of carbon-rich graphitic carbon nitride nanosheets for photoredox catalysis, J. Mater. Chem. A 3 (2015) 3281–3284, https://doi.org/10.1039/C5TA00202H.)*

protocol is as follows: At first, the g-C_3N_4 was synthesized from MA monomer. Briefly, DCN (2 g) reactant was placed into an alumina jar with a lid, then annealed to reach a temperature of 550°C at a rate of 2.3 °C min^{-1} and then continued at 550°C for another 2 h. The yellow product was composed and grounded into fine particles for further use. Second, g-C_3N_4/$BiVO_4$ heterojunctions were prepared by a HT route. In a typical procedure, g-C_3N_4 (0.3 g) and NH_4VO_4 (0.1083 g) were placed in distilled water (30 mL) and stirred vigorously for 3 h followed by a homogeneous sedimentation. Simultaneously, $Bi(NO_3)_3 \cdot 5H_2O$ (0.449 g) was mixed in 3 mL of HNO_3 (1 mol L^{-1}) to attain a plain solution. The clear solution was quickly transferred to the sedimentation and immediately mixed well at room temperature for an extra 3 h. After altering the pH value (pH = 8) using sodium hydroxide solution, the reaction content was carefully moved into an autoclave, which was annealed in an oven for 20 h at 160°C. At last, the resulting g-C_3N_4/$BiVO_4$ was gathered and cleaned numerous times in ethanol and deionized water and desiccated for 2 h at 100°C. Tian et al. [44] coupled g-C_3N_4 by Bi_2WO_6 (g-C_3N_4/Bi_2WO_6) via a HT method. An interface was formed between g-C_3N_4 and

Bi_2WO_6 heterojunctions, which was confirmed by high-resolution transmission electron microscopy (HR-TEM). Further, more intensive absorption within the visible light region occurs in the composite than pristine Bi_2WO_6, which was attributed by UV-visible diffuse reflection (DRS UV-visible) spectra results. These outstanding structural and spectral characteristics provided the g-C_3N_4/Bi_2WO_6 heterojunctions with improved photocatalytic activities. Furthermore, it showed a greater strength and lifetime during six consecutive cycles. Zhuang et al. [45] developed an easy and ecofriendly HT methodology for the one-step preparation of g-C_3N_4 NS using sodium citrate ($Na_3C_6H_5O_7$) and MA ($C_3H_6N_6$) as the precursors. In brief, $Na_3C_6H_5O_7$ (0.075 g) was taken along with water (20 mL) and $C_3H_6N_6$ (0.22 g) in a 100-mL beaker. After 5 min of sonication, the content was moved into a Teflon-lined autoclave (50 mL) and annealed for 4 h at 200°C. After completion of the reaction, the brown-yellow-colored material was centrifuged at 12,000 rpm for 30 min. The attained material was then dialyzed beside deionized water to eliminate contaminants via cellulose dialysis membrane. The synthesized g-C_3N_4 NS released powerful fluorescence with a high percentage quantum yield (48.3%). Shi et al. [46] fabricated *n*-type g-C_3N_4 and modified with *p*-type $InVO_4$ (indium vanadate) to form a novel $InVO_4$/g-C_3N_4 *p-n* heterojunction photocatalyst for the competent photocatalytic degradation of Rh B (rhodamine B). In a classic preparation method, g-C_3N_4 was synthesized by polycondensation of an MA monomer. Briefly, a few grams of DCN powder was kept in a porcelain crucible with a stopper and then annealed to 550°C with a ramping rate of 2.3 °C min^{-1}, and then continued for 2 h. The obtained yellow product was gathered and ground into fine particles for future use. $InVO_4$/g-C_3N_4 heterojunctions were produced by HT methodology. In a classic protocol, g-C_3N_4 (0.54 g) and $NaVO_3 \cdot 2H_2O$ (1.58 g) were taken in 30 mL of deionized water and then stirred for 3 h for sedimentation. Simultaneously, 0.381 g of indium nitrate pentahydrate ($In(NO_3)_3 \cdot 5H_2O$) was mixed in dilute nitric acid (3 mL) to attain a plain sedimentation. The reactant was transferred quickly to the sedimentation and immediately well mixed at ambient temperature for extra 3 h. After tuning the pH value (pH = 4) with the help of 1 M sodium hydroxide solution, the combined solution was moved into an autoclave and pyrolyzed in a temperature-controlled oven for 24 h at 150°C. Finally, the synthesized $InVO_4$/g-C_3N_4 composite was gathered and cleaned numerous times with absolute ethanol and deionized water and desiccated for 2 h at 100°C.

3.3 Thermal exfoliation method

Generally, thermal exfoliation (TEXF) is achieved by subjecting bulk g-C_3N_4 to heat, which breaks the weak Van der Waals forces of attraction between the layers ensuing in exfoliation [47]. Supremely, while heating, H_2 anchored to the tri-*s*-triazine or *s*-triazine units reacts with O_2, and when this gas releases, it produces pores in the aggregate and forms sheets [48]. As a result, the g-C_3N_4 NSs are related with a higher surface area and pore sizes, thus increasing the porosity of the material. Xu et al. [49] studied g-C_3N_4 NSs with single atomic layer structure by a facile chemical exfoliation (CEXF) method. The as-synthesized g-C_3N_4 NSs exhibited 0.4 nm of single atomic thickness and micrometers of lateral size. The synthesis procedure involves two steps: First, g-C_3N_4 was synthesized by heating DCN for 4 h at 550°C in the muffle furnace and aerated at the same temperature for another 4 h. Secondly, single-layer g-C_3N_4 (SL g-C_3N_4) NSs were prepared by CEXF method. One gram of as-synthesized g-C_3N_4 was mixed with 98% of 10 mL sulfuric acid in a glass beaker and well-mixed at ambient temperature for 8 h. Subsequently, the reaction content was gently transferred into deionized water (100 mL) and ultrasonicated for exfoliation. The suspension temperature was increased quickly, and the color changed from yellow to pale yellow. The attained sediment was then centrifuged for 10 min at 3000 rpm to eliminate unreacted/unexfoliated g-C_3N_4 after thorough washing with ethanol and deionized water, and at last dried in air overnight at 80°C. To remove structural defects, the prepared pale-yellow powders (0.3 g) were placed into a glass round-bottom flask containing 150 mL of methanol and refluxed in a heating mantle for 6 h at 65°C. The g-C_3N_4 NSs were obtained after centrifugation and drying. When compared with bulk g-C_3N_4, SL g-C_3N_4 NSs exhibited superior enhancement in photogenerated charge carrier's transfer and separation. Consequently, the photocatalyst's hydrogen production, contaminant decomposition activities, and photocurrent generation of SL g-C_3N_4 NSs are far better than that of the bulk g-C_3N_4, illustrating that the SL g-C_3N_4 NSs was a powerful candidate for photosynthesis and photocatalysis.

The transformation and transportation of photogenerated carriers during the photocatalytic process of g-C_3N_4 were controlled by the efficacy of lower charge separation and inadequate surface-active site. As a top-down strategy, the exfoliation of layer-stacked bulk g-C_3N_4 into NSs was extensively acknowledged as a compatible pathway but is still challenging in terms of scalability and clean set of synthesis. This issue was overcome by Cui et al. [50] using a facile HT method in an NaClO solution, which combined the effect of alkaline metal ion intercalation and the oxidative exfoliation of bulk g-C_3N_4 (Fig. 1.4). Highly active g-C_3N_4 NSs were produced in the laboratory by a simple manner, and it could be immediately far-extended to a pilot scale (large-scale production). The HT method produced a vertically oriented pathway for direct electron transfer and resultant ultrathin g-C_3N_4 NSs with significant porosity (meso-, macro-, and micropores) and excellent hydrophilicity. The g-C_3N_4 NSs exhibited excellent surface area of 170.7 $m^2\ g^{-1}$, narrow band gap of 2.55 eV, high number of exposed edges, and outstanding electron transport capability. These g-C_3N_4 NSs have an average H_2 evolution rate nine times higher than that of bulk g-C_3N_4. Moreover, they concluded that this green, simple, and scalable method to prepare layered g-C_3N_4 NSs provides a new approach for designing and fabricating other functional 2D objects. In this work, Li et al. [51]

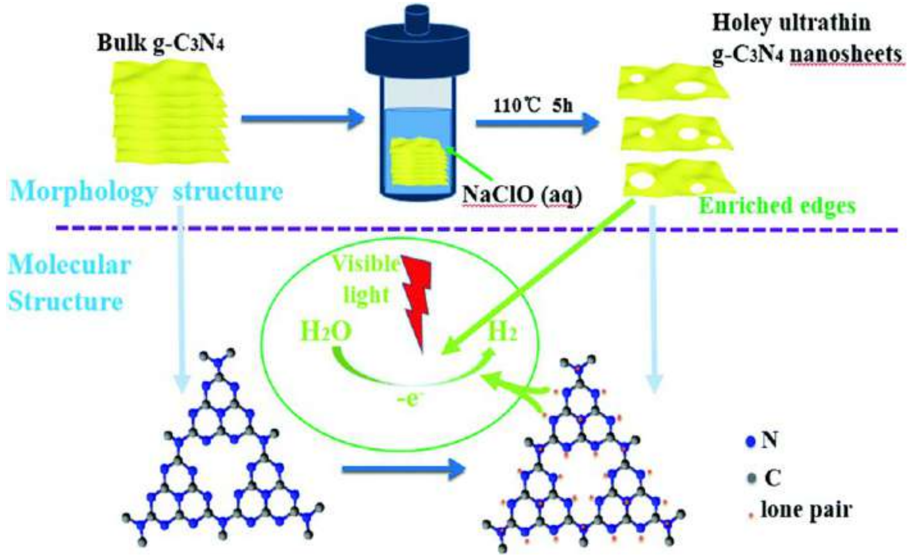

Fig. 1.4 Sketch of the aqueous NaClO HT exfoliation of bulk g-C_3N_4 into a SL, molecular structure models of bulk g-C_3N_4 (left) and exfoliated g-C_3N_4 (right), and anticipated mechanism for the photocatalytic hydrogen evolution. *Reproduced with the permission from L. Cui, Y. Liu, X. Fang, C. Yin, S. Li, D. Sun, S. Kang, Scalable and Clean Exfoliation of Graphitic Carbon Nitride in NaClO Solution: Enriched Surface Active Sites for Enhanced Photocatalytic H2 Evolution, Green Chem. 20 (2018) 1354-1361. https://doi.10.1039/C7GC03704J*

successfully prepared ultrathin graphene-like g-C_3N_4 NSs with rich nanoporous-enriched and superior hydrophilic properties by a facile and prominent TEXF of bulk g-C_3N_4. To understand the effect of TEXF conditions on the texture, surface state, and photocatalytic activity of the resulting g-C_3N_4, a series of exfoliated g-C_3N_4 NSs were synthesized by optimizing the TEXF parameters, such as time and temperature. The extensive physicochemical characterization results clearly revealed that the exfoliation temperature led to a greater number of nitrogen vacancies; the specific surface area also increased, as well as prolonged exfoliation time, increased degree of TEXF, higher carbon vacancies, and the expanded pore volume in the end materials. Furthermore, the degree of exfoliation and photocatalytic efficiency of the resultant products were improved by increasing TEXF time and temperature. Sun reported [52] g-C_3N_4 NSs with high photoactivity produced with the help of isopropanol (IPA) in the synthesis process. The g-C_3N_4 NSs were synthesized by the following two steps. First, bulk g-C_3N_4 was prepared from the polycondensation of precursor, MA. In brief, MA (3 g) was completely spread into IPA (30 mL) in a 50-mL porcelain crucible with a lid, and then the reactant was calcined at 550°C for 3 h in the muffle furnace at a heating rate of 5 °C min^{-1}. The material in the silica crucible was gathered after being naturally cooled down to ambient temperature and then was ground to a powder in a mortar and pestle. The prepared material was bulk g-C_3N_4. Second, g-C_3N_4 NSs were prepared by a TEXF process of bulk g-C_3N_4 in semiclosed surroundings. Bulk g-C_3N_4 (0.1 g) was taken with IPL (10 mL), and then the suspension was moved into a 30-mL crucible with a lid for TEXF process. The oxidation treatment was continued for 2 h after the furnace temperature was raised to 550°C with a ramping rate of 5 °C min^{-1}. The product finally collected was g-C_3N_4 NSs. The introduction of IPA causes very powerful oxidation in the exfoliation process, and the derived g-C_3N_4 NSs has its distinctive properties of a visible light with a wide absorption range, higher surface area, and uneven surface. As a result, the g-C_3N_4 NSs have good photocatalytic activity in the degradation of organic contaminants. Furthermore, the photocatalytic H_2 evolution rate of g-C_3N_4 NSs was three times that of g-C_3N_4 NSs, which is prepared without IPA using an identical method. Pattnaik [53] reported exfoliated g-C_3N_4 nanoparticles (NPs) by a green path. Degradation of an aqueous solution of ciprofloxacin (CPN) by exposure to solar radiation in the presence of g-C_3N_4 NPs was studied to evaluate the photocatalytic activities of a semiconductor photocatalyst. The photocatalytic activities of g-C_3N_4 NPs enhanced after its exfoliation. The improved behavior of photocatalysis of exfoliated g-C_3N_4 is the result of its efficient separation, low rearrangement of photogenerated charge carriers, and high specific surface area. As a whole, the exfoliation method delivers more advantages such as simple chemicals and equipment (low cost), no solvents, rapid and timely performance, good product yield, and produces valuable structural defects in the resultant NSs. However, this exfoliation method produces valuable structural defects in the resultant NSs. However, this exfoliation method produces a product with low crystallinity and comparatively smaller surface area.

3.4 Solvothermal method

Solvothermal (ST) technique is developed based on the HT method; the most important difference of ST process from the latter is that the preparative condition is organic solvent rather than water. Tian et al. [54] in-situ synthesized a new g-C_3N_4/Bi_2MoO_6 heterojunctions with varying content of Bi_2MoO_6 NSs by a facile ST method. A typical synthesis procedure of g-C_3N_4/Bi_2MoO_6 heterojunctions is as follows: A required quantity of sodium molybdate dihydrate was dissolved in ethylene glycol (10 mL) and ethanol (60 mL) mixture to form a clear solution. Subsequently, few grams of g-C_3N_4 powder was uniformly dispersed in this clear solution via ultrasonication for 5 min, and then a solution of ethylene glycol (10 mL) with a certain amount of bismuth nitrate pentahydrate was rapidly added. After vigorous stirring (30 min), the sediment was gently moved to an autoclave and kept for 24 h at 160°C. Finally, the suspension was gathered, washed numerous times with H_2O and ethanol, dried at 60°C in an oven, and grinded for future use. The obtained g-C_3N_4/Bi_2MoO_6 heterojunctions have improved absorption within the visible light range compared with virgin g-C_3N_4. Xu et al. [55] studied polymeric g-C_3N_4 (Pg-C_3N_4) prepared via a two-step method of low-temperature ST synthesis and postcalcination using DCN and $C_3Cl_3N_3$ (cyanuric chloride) mixture as precursors and acetonitrile (solvent). The microstructure, chemical states, band gap, charge migration, and photocatalytic performance of the Pg-C_3N_4 were comparatively enhanced with that of classic bulk g-C_3N_4. The Pg-C_3N_4 exhibited greatly prominent performance in both the RhB photodegradation and hydrogen evolution reaction (HER), advantageous from irregularly ordered hybrid plane configuration, which prevents photoelectron recombination and offers higher charge separation performance. Kojima and Ohfuji [56] carefully examined g-C_3N_4 obtained by the ST reaction between $C_3Cl_3N_3$ and $NaNH_2$ (sodium amide). The chemical measurements by the electron microprobe and combustion methods revealed that the $C_3N_5H_3$ composition contains a considerable amount of hydrogen. Furthermore, they made it clear that the present study eventually demonstrates that pristine g-C_3N_4 without hydrogen cannot be formed by the current ST reaction, as anticipated by the previous study. Lu et al. [57] self-assembled TiO_2-based nanorods (TNRs) on large g-C_3N_4 sheets via ST-assisted pathway. The results showed that the effective anchor of the TNRs was highly distributed to the surface of entire g-C_3N_4 sheets. The schematic sketch of the reaction protocol of TNRs/g-C_3N_4 is illustrated in Fig. 1.5. In a typical reaction procedure, initially TNRs (1 g) and a required amount of g-C_3N_4 (approximately 0–0.5 g) were dispersed into tertiary butyl alcohol (40 mL) followed by sonication

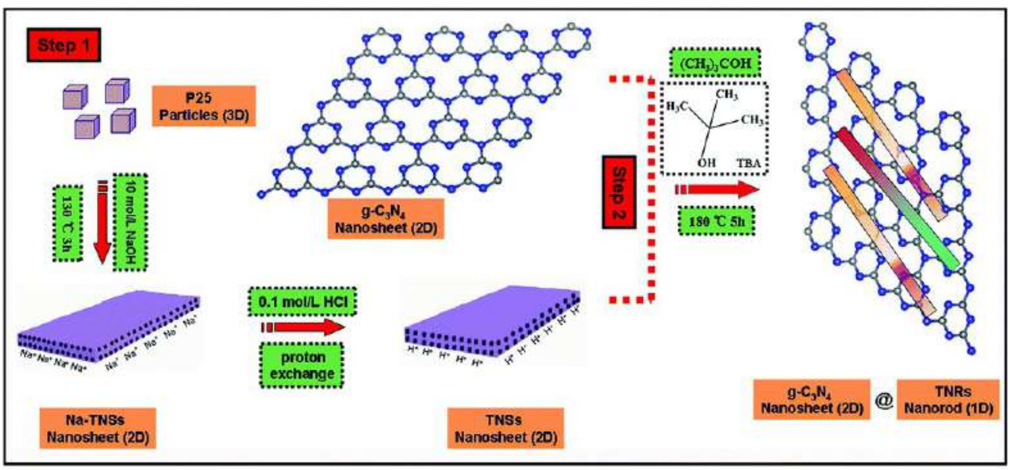

Fig. 1.5 Schematic representation of the TNRs/g-C_3N_4 photocatalyst synthesis. *(Reproduced with the permission from D. Lu, P. Fang, W. Wu, J. Ding, L. Jiang, X. Zhao, C. Li, M. Yang, Y. Li, Solvothermal-assisted synthesis for self-assembling TiO_2 nanorods on large graphitic carbon nitride sheets with their anti-recombination in photocatalytic removal of Cr(VI) and rhodamin B under visible light irradiation, Nanoscale 9 (2017) 3231–3245, https://doi.org/10.1039/C6NR09137G.)*

(30 min). Then the suspensions were gently transferred into a Teflon-lined autoclave and maintained at 180°C for 5 h and then allowed to attain ambient temperature. Using a membrane filter with pore size of 0.45 μm, the obtained material was filtered. The suspension was thoroughly washed with a copious amount of NaOH (0.1 M) solution and then with deionized water. Cao et al. [58] prepared crystalline C_3N_4 powder by a ST method from $C_3N_3Cl_3$ and lithium nitride (Li_3N) in benzene at 300–400°C and pressure of 5–7 MPa. The detailed experimental procedure is as follows: $C_3N_3Cl_3$ and Li_3N powder was placed into an autoclave (50 mL volume). Benzene was carefully added to pack the autoclave up to 70% of its total capacity. The temperature was maintained between 200°C and 500°C, and the pressure of the autoclave was 3–15 MPa. The experiment was continued for 12 h. The precipitate was filtered and cleaned with ethanol, dilute acid/alkali, and deionized water to eliminate the unreacted Li_3N, $C_3N_3Cl_3$ and the by-product (LiCl). Then, the obtained material was dried in a vacuum oven for 4 h at 100°C. Finally, a crystalline C_3N_4 product was obtained.

The use of ST method for g-C_3N_4 synthesis has better advantages, such as even and well-formed particles, smaller energy consumption, and higher economic viability as compared to the outdated thermal condensation methods. On the other hand, these methods have some drawbacks like tedious synthesis process to complete crystallization and particle formation.

3.5 Sol-gel method

Sol-gel (SG) method involves the formation of a solid product or nanomaterial from a solution after modification of the gel intermediate. In this preparation method, the reactants are mixed at the molecular level, which allows for faster reactions and leads to homogeneous products with larger surface area. Kailasam et al. [59] prepared mesoporous C_3N_4 (M-C_3N_4), silica (TEOS), and their composites by integrated SG thermal condensation approach. Cyanamide and TEOs, the precursors of carbon nitride and silica, respectively, were mixed and condensed together. After condensation and heat treatment, C_3N_4 and silica formed interpenetrating mesophases, which selectively removed a phase that then leads to the formation of M-C_3N_4 or silica. Notably, the M-C_3N_4 protects its graphitic stacking even in the spatial internment introduced by the surrounding silica part. Since both the starting materials are liquids, this approach allows for the comfortable creation of thin and dense films or monolayers of M-C_3N_4. Chunyong et al. [60] synthesized TiO_2/g-C_3N_4 by a simple two-step method, including SG and calcination process, MA as a N_2 source, and titanium (IV) butoxide as a titanium source. The following is the detailed experimental procedure. Titanium (IV) butoxide (30 mL) and MA (20 g) were mixed in 500 mL ethanol to obtain a reaction mixture that was stirred strongly at ambient temperature for 30 min. Then 40 mL of distilled water was transferred into the reaction content under stirring condition, and the SG was attained. The prepared SG was then kept in a drying oven for 24 h at 80°C under vacuum to offer a pale-yellow suspension of precursor of TiO_2/g-C_3N_4. The precursor TiO_2/g-C_3N_4 was then pyrolyzed in a closed muffle furnace for 2 h at 520°C with ramping rate of 2 °C min^{-1} to get the TiO_2/g-C_3N_4 photocatalyst. The obtained results suggested that TiO_2/g-C_3N_4 apparently improved visible light photocatalytic activity, and the degradation efficiency of methylene blue (MB) reaches 94.46% after irradiation for 1 h, which is higher than that of pure g-C_3N_4 and TiO_2. Liu et al. [61] prepared the g-C_3N_4/TiO_2 with controllable particle size as well as the interface contact by a general nonaqueous SG method for photocatalytic activity. In brief, cyanuric acid (6.45 g) was added to ethanol (100 mL) under stirring condition. Then, MA (6.3 g) was grinded and added to the reaction content, continuously mixed for 8 h, and then dried in an oven at 60°C. The attained white-colored solid was subsequently calcined for 4 h at 550°C under nitrogen condition with a ramping rate of 2.3 °C min^{-1} to yield the final g-C_3N_4 powder. The g-C_3N_4/TiO_2 composite was synthesized through the "benzyl alcohol route" on the prepared nanostructured g-C_3N_4. Firstly, xylol (10 mL) was spouted into a flask, and then titanium tetrachloride (0.69 mL) was dissolved in a magnetic stirrer. After few minutes, benzyl alcohol (66 mL) was carefully transferred into the reaction mixture. The desired quantity of the prepared g-C_3N_4 was grinded well and transferred to the titanium precursor solution after a few minutes of stirring. At last, the resulting composite, g-C_3N_4/TiO_2, was composed by centrifugation and washing with water and ethanol, dried at 100°C for 12 h.

3.6 Physical vapor deposition

It features reaction sputtering (RS), magnetron sputtering (MS), pulsed laser deposition (PLD), ion beam deposition (IBD), and more. RS is a basic method to produce composite materials. When this technique is used to produce g-C_3N_4, the mass fraction of N_2 is usually less than 40%. Conversely, to form –C_3N_4, the system must contain sufficient nitrogen and stoichiometric ratio must reach 57%. Sun et al. [62] fabricated g-C_3N_4 sheets with a band gap of 2.61 eV via physical vapor deposition (PVD) of g-C_3N_4. A sequence of gaseous products obtained from pristine g-C_3N_4 at 700°C condenses into g-C_3N_4 sheets at low temperature (less than 400°C) in the PVD process. Briefly, DCN (10 g) was placed in a quartz boat and calcined at 550°C with a ramping rate of 2.3 °C min^{-1} for 4 h under flowing nitrogen gas. After calcination, g-C_3N_4 was obtained. Then, g-C_3N_4 (300 mg) solid alone (without aluminum foil cover) was annealed for another 2 h at 700°C with a ramping rate of 10 °C min^{-1} under a nitrogen environment; the final material was g-C_3N_4 sheets.

4. Summary and outlook

In summary, this chapter culminates the current developments in the structure, preparation techniques, and properties of g-C_3N_4-based materials. Reasonably, g-C_3N_4 has proven to be one of the best adapters for planning and integrating innovative blends/composites for versatile applications in HER, photocatalysts, and adsorption studies. Therefore, it is unclear whether the massive improvement of g-C_3N_4 materials will be sustained in the future. With that in mind, further research is needed to make full use of the exceptional structure, composition, properties, and preparation techniques of g-C_3N_4 materials.

Two-dimensional polymeric g-C_3N_4 materials that are cheap, nonmetallic, and eco-friendly with an adequate band gap, good chemical activity, and excellent stability have only been studied for the past few years (from indigenous to pilot scale production). We firmly believe that the most promising features and applications of g-C_3N_4 are around the corner. Integrations between theoretical approaches and experimental research will greatly enhance the research progress of g-C_3N_4. As the investigation of g-C_3N_4 continues to grow, it will face a number of key challenges in the near future, including pore nanostructures for drug loading, memory device fabrication, solid state lights, wearable sensors, and energy conversion technologies.

Acknowledgment

The authors gratefully acknowledge the financial support from BK21 Plus Creative Human Resource Education and Research Programs for ICT Convergence in the 4th Industrial Revolution, Pusan National University, Busan, South Korea.

References

[1] J. Liebig, Uber einige stickstoff-verbindungen, Eur. J. Org. Chem. 10 (1) (1834) 1–47, https://doi.org/10.1002/jlac.18340100102.
[2] A.Y. Liu, M.L. Cohen, Prediction of new low compressibility solids, Science 245 (4920) (1989) 841–842, https://doi.org/10.1126/science.245.4920.841.
[3] F. Goettmann, A. Fischer, M. Antonietti, A. Thomas, Metal-free catalysis of sustainable Friedel–Crafts reactions: direct activation of benzene by carbon nitrides to avoid the use of metal chlorides and halogenated compounds, Chem. Commun. 43 (2006) 4530–4532, https://doi.org/10.1039/B608532F.
[4] D.M. Teter, R.J. Hemley, Low-compressibility carbon nitrides, Science 271 (5245) (1996) 53–55, https://doi.org/10.1126/science.271.5245.53.
[5] Z. Huang, F. Li, B. Chen, T. Lu, Y. Yuan, G. Yuan, Well-dispersed g-C_3N_4 nanophases in mesoporous silica channels and their catalytic activity for carbon dioxide activation and conversion, Appl. Catal. Environ. 136–137 (2013) 269–277, https://doi.org/10.1016/j.apcatb.2013.01.057.
[6] S. Cao, J. Low, J. Yu, M. Jaroniec, Polymeric photocatalysts based on graphitic carbon nitride, Adv. Mater. 27 (13) (2015) 2150–2176, https://doi.org/10.1002/adma.201500033.
[7] J. Zhang, G. Zhang, X. Chen, S. Lin, L. Mohlmann, G. Dołęga, G. Lipner, M. Antonietti, S. Blechert, X. Wang, Co-monomer control of carbon nitride semiconductors to optimize hydrogen evolution with visible light, Angew. Chem. Int. Ed. 124 (2012) 3237–3241, https://doi.org/10.1002/ange.201106656.
[8] A. Kumar, G. Sharma, M. Naushad, A.H. Al-Muhtaseb, A. Kumar, I. Hira, A.A. Ghfar, F.J. Stadler, Visible photodegradation of ibuprofen and 2,4-D in simulated waste water using sustainable metal free-hybrids based on carbon nitride and biochar, J. Environ. Manage. 231 (2019) 1164–1175, https://doi.org/10.1016/j.jenvman.2018.11.015.
[9] D.J. Li, J. Kang, H.J. Lee, D.S. Choi, S.H. Koo, B. Han, S.O. Kim, High activity hydrogen evolution catalysis by uniquely designed amorphous/metal interface of core–shell phosphosulfide/N-doped CNTs, Adv. Energy Mater. 8 (2018) 1702806, https://doi.org/10.1002/aenm.201702806.

[10] H. Zhou, R. Yan, D. Zhang, T. Fan, Challenges and perspectives in designing artificial photosynthetic systems, Chem. A Eur. J. 22 (29) (2016) 9870–9885, https://doi.org/10.1002/chem.201600289.

[11] H.Z. Zhong, Q. Zhang, J. Wang, X.B. Zhang, X.L. Wei, Z.J. Wu, K. Li, F.L. Meng, D. Bao, J.M. Yan, Engineering ultrathin C_3N_4 quantum dots on graphene as a metal-free water reduction electrocatalyst, ACS Catal. 8 (2018) 3965–3970, https://doi.org/10.1021/acscatal.8b00467.

[12] P. He, X. Tang, L. Chen, P. Xie, L. He, H. Zhou, D. Zhang, T. Fan, Patterned carbon nitride–based hybrid aerogel membranes via 3D printing for broadband solar wastewater remediation, Adv. Funct. Mater. 28 (2018) 1801121, https://doi.org/10.1002/adfm.201801121.

[13] S. Zhang, P. Gu, R. Ma, C. Luo, T. Wen, G. Zhao, W. Cheng, X. Wang, Recent developments in fabrication and structure regulation of visible-light-driven g-C_3N_4-based photocatalysts towards water purification: a critical review, Catal. Today 335 (2019) 65–77, https://doi.org/10.1016/j.cattod.2018.09.013.

[14] E. Kroke, M. Schwarz, E. Horath-Bordon, P. Kroll, B. Noll, A.D. Norman, Tri-S-triazine derivatives. Part I. From trichloro-tri-S-triazine to graphitic C_3N_4 structures, New J. Chem. 26 (2002) 508–512, https://doi.org/10.1039/b111062b.

[15] A. Wang, C. Wang, L. Fu, W. Wong-Ng, Y. Lan, Recent advances of graphitic carbon nitride-based structures and applications in catalyst, sensing, imaging, and leds, Nano-Micro Lett. 9 (2017) 47, https://doi.org/10.1007/s40820-017-0148-2.

[16] S. Cao, J. Yu, G-C_3N_4-based photocatalysts for hydrogen generation, J. Phys. Chem. Lett. 5 (2014) 2101–2107, https://doi.org/10.1021/jz500546b.

[17] X. Chen, Q. Liu, Q. Wu, P. Du, J. Zhu, S. Dai, S. Yang, Incorporating graphitic carbon nitride (GC_3N_4) quantum dots into bulk-heterojunction polymer solar cells leads to efficiency enhancement, Adv. Funct. Mater. 26 (2016) 1719–1728, https://doi.org/10.1002/adfm.201505321.

[18] H. Sun, S. Liu, G. Zhou, H.M. Ang, M.O. Tade, S. Wang, Reduced graphene oxide for catalytic oxidation of aqueous organic pollutants, ACS Appl. Mater. Interfaces 4 (2012) 5466–5471, https://doi.org/10.1021/am301372d.

[19] M. Wu, J. Zhang, C. Liu, Y. Gong, R. Wang, B. He, H. Wang, Rational design and fabrication of noble-metal-free Nixp cocatalyst embedded 3D $NTiO_2$/G-C_3n_4 heterojunctions with enhanced photocatalytic hydrogen evolution, ChemCatChem 10 (2018) 3069–3077, https://doi.org/10.1002/cctc.201800197.

[20] F. Fina, S.K. Callear, G.M. Carins, J.T. Irvine, Structural investigation of graphitic carbon nitride via XRD and neutron diffraction, Chem. Mater. 27 (2015) 2612–2618, https://doi.org/10.1021/acs.chemmater.5b00411.

[21] Y. Zheng, J. Liu, J. Liang, M. Jaroniec, S.Z. Qiao, Graphitic carbon nitride materials: controllable synthesis and applications in fuel cells and photocatalysis, Energy Environ. Sci. 5 (2012) 6717–6731, https://doi.org/10.1039/c2ee03479d.

[22] G. Liu, P. Niu, C. Sun, S.C. Smith, Z. Chen, G.Q. Lu, H.M. Cheng, Unique electronic structure induced high photoreactivity of sulfur-doped graphitic C3n4, J. Am. Chem. Soc. 132 (2010) 11642–11648, https://doi.org/10.1021/ja103798k.

[23] G. Dong, Y. Zhang, Q. Pan, J. Qiu, A fantastic graphitic carbon nitride (g-C_3N_4) material, electronic structure, photocatalytic and photoelectronic properties, J. Photochem. Photobiol. C Photochem. Rev. 20 (2014) 33–50, https://doi.org/10.1016/j.jphotochemrev.2014.04.002.

[24] M.Z. Rahman, K. Davey, C.B. Mullins, Tuning the intrinsic properties of carbon nitride for high quantum yield photocatalytic hydrogen production, Adv. Sci. 5 (2018) 1800820, https://doi.org/10.1002/advs.201800820.

[25] Y. Zhang, T. Mori, J. Ye, Polymeric carbon nitrides: semiconducting properties and emerging applications in photocatalysis and photoelectrochemical energy conversion, Sci. Adv. Mater. 4 (2012) 282–291, https://doi.org/10.1166/sam.2012.1283.

[26] J. Liu, W. Li, L. Duan, X. Li, L. Ji, Z. Geng, K. Huang, L. Lu, L. Zhou, Z. Liu, W. Chen, L. Liu, S. Feng, Y. Zhang, A graphene-like oxygenated carbon nitride material for improved cycle-life lithium/sulfur batteries, Nano Lett. 15 (8) (2015) 5137–5142, https://doi.org/10.1021/acs.nanolett.5b01919.

[27] G.S. Li, Z.C. Lian, W.C. Wang, D.Q. Zhang, H.X. Li, Nanotube-confinement induced size-controllable g-C_3N_4 quantum dots modified single-crystalline TiO_2 nanotube arrays for stable synergetic photoelectrocatalysis, Nano Energy 19 (2016) 446–454, https://doi.org/10.1016/j.nanoen.2015.10.011.

[28] G. Liu, T. Wang, H. Zhang, X. Meng, D. Hao, K. Chang, P. Li, T. Kako, J. Ye, Nature-inspired environmental phosphorylation boosts photocatalytic H_2 production over carbon nitride nanosheets under visible-light irradiation, Angew. Chem. Int. Ed. 127 (46) (2015) 13765–13769, https://doi.org/10.1002/ange.201505802.
[29] Y. Shiraishi, Y. Kofuji, H. Sakamoto, S. Tanaka, S. Ichikawa, T. Hirai, Effects of surface defects on photocatalytic H_2O_2 production by mesoporous graphitic carbon nitride under visible light irradiation, ACS Catal. 5 (5) (2015) 3058–3066, https://doi.org/10.1021/acscatal.5b00408.
[30] J. Xiao, Y. Xie, F. Nawaz, Y. Wang, P. Du, H. Cao, Dramatic coupling of visible light with ozone on honeycomb-like porous g-C_3N_4 towards superior oxidation of water pollutants, Appl. Catal. Environ. 183 (2016) 417–425, https://doi.org/10.1016/j.apcatb.2015.11.010.
[31] W. Shan, Y. Hu, Z. Bai, M. Zheng, C. Wei, In situ preparation of g-C_3N_4/bismuth-based oxide nanocomposites with enhanced photocatalytic activity, Appl. Catal. Environ. 188 (2016) 1–12, https://doi.org/10.1016/j.apcatb.2016.01.058.
[32] B.H. Long, J.L. Lin, X.C. Wang, Thermally-induced desulfurization and conversion of guanidine thiocyanate into graphitic carbon nitride catalysts for hydrogen photosynthesis, J. Mater. Chem. A 2 (9) (2014) 2942–2951, https://doi.org/10.1039/c3ta14339b.
[33] S. Yuan, Q. Zhang, B. Xu, S. Liu, J. Wang, J. Xie, M. Zhang, T. Ohno, A new precursor to synthesize g-C_3N_4 with superior visible light absorption for photocatalytic application, Catal. Sci. Technol. 7 (9) (2017) 1826–1830, https://doi.org/10.1039/c7cy00213k.
[34] A. Thomas, A. Fischer, F. Goettmann, M. Antonietti, J.-O. Muller, R. Schlogl, J.M. Carlsson, Graphitic carbon nitride materials: variation of structure and morphology and their use as metal-free catalysts, J. Mater. Chem. 18 (41) (2008) 4893–4908, https://doi.org/10.1039/b800274f.
[35] N. Urakami, M. Kosaka, Y. Hashimoto, Thermal chemical vapor deposition and luminescence property of graphitic carbon nitride film for carbon-based semiconductor systems, Jpn. J. Appl. Phys. 58 (2019), https://doi.org/10.7567/1347-4065/aaf225, 010907.
[36] N. Urakami, M. Kosaka, Y. Hashimoto, Chemical vapor deposition of boron-incorporated graphitic carbon nitride film for carbon-based wide bandgap semiconductor materials, Phys. Status Solidi B 27 (2) (2019) 1900375, https://doi.org/10.1002/pssb.201900375.
[37] Y. Wang, F. Wang, Y. Zuo, X. Zhang, L.F. Cui, Simple synthesis of ordered cubic mesoporous graphitic carbon nitride by chemical vapor deposition method using melamine, Mater. Lett. 136 (2014) 271–273, https://doi.org/10.1016/j.matlet.2014.08.078.
[38] R.M. Yadav, R. Kumar, A. Aliyand, P.S. Dobal, S. Biradarb, R. Vajtaib, D.P. Singh, A.A. Martíc, P.M. Ajayan, Facile synthesis of highly fluorescent free-standing films comprising of graphitic carbon nitride (g-C_3N_4) nanolayers, New J. Chem. 44 (2020) 2644–2651, https://doi.org/10.1039/C9NJ05108B.
[39] L. Cui, J. Song, A.F. McGuire, S. Kang, X. Fang, J. Wang, C. Yin, X. Li, Y. Wang, B. Cui, Constructing highly uniform onion-ring-like graphitic carbon nitride for efficient visible-light-driven photocatalytic hydrogen evolution, ACS Nano 12 (6) (2018) 5551–5558, https://doi.org/10.1021/acsnano.8b01271.
[40] J. Li, H. Yuan, Z. Zhu, Photoelectrochemical performance of g-C_3N_4/Au/$BiPO_4$ Z-scheme composites to improve the mineralization property under solar light, RSC Adv. 6 (2016) 70563–70572, https://doi.org/10.1039/C6RA13570F.
[41] B. Wang, J. Zhang, F. Huang, Enhanced visible light photocatalytic H_2 evolution of metal-free g-C_3N_4/SiC heterostructured photocatalysts, Appl. Surf. Sci. 391 (2017) 449–456, https://doi.org/10.1016/j.apsusc.2016.07.056.
[42] P. Zhang, X. Li, C. Shao, Y. Liu, Hydrothermal synthesis of carbon-rich graphitic carbon nitride nanosheets for photoredox catalysis, J. Mater. Chem. A 3 (2015) 3281–3284, https://doi.org/10.1039/C5TA00202H.
[43] F. Guo, W. Shi, X. Lin, G. Che, Hydrothermal synthesis of graphitic carbon nitride–$BiVO_4$ composites with enhanced visible light photocatalytic activities and the mechanism study, J. Phys. Chem. Solid 75 (2014) 1217–1222, https://doi.org/10.1016/j.jpcs.2014.05.011.
[44] Y. Tian, B. Chang, J. Lu, J. Fu, F. Xi, X. Dong, Hydrothermal synthesis of graphitic carbon nitride – -Bi_2WO_6 heterojunctions with enhanced visible light photocatalytic activities, ACS Appl. Mater. Interfaces 5 (2013) 7079–7085, https://doi.org/10.1021/am4013819.
[45] Q. Zhuang, L. Sun, Y. Ni, One-step synthesis of graphitic carbon nitride nanosheets with the help of melamine and its application for fluorescence detection of mercuric ions, Talanta 164 (2017) 458–462, https://doi.org/10.1016/j.talanta.2016.12.004.

[46] W. Shi, F. Guo, J. Chen, G. Che, X. Lin, Hydrothermal synthesis of $InVO_4$/graphitic carbon nitride heterojunctions and excellent visible-light-driven photocatalytic performance for rhodamine B, J. Alloys Compd. 612 (2014) 143–148, https://doi.org/10.1016/j.jallcom.2014.05.207.
[47] S. Challagulla, S. Payra, C. Chakraborty, S. Roy, Determination of band edges and their influences on photocatalytic reduction of nitrobenzene by bulk and exfoliated g-C_3N_4, Phys. Chem. Chem. Phys. 21 (2019) 3174–3183, https://doi.org/10.1039/C8CP06855K.
[48] G. Lei, Y. Cao, W. Zhao, Z. Dai, L. Shen, Y. Xiao, L. Jiang, Exfoliation of graphitic carbon nitride for enhanced oxidative desulfurization: a facile and general strategy, ACS Sustain. Chem. Eng. 7 (2019) 4941–4950, https://doi.org/10.1021/acssuschemeng.8b05553.
[49] J. Xu, L. Zhang, R. Shi, Y. Zhu, Chemical exfoliation of graphitic carbon nitride for efficient heterogeneous photocatalysis, J. Mater. Chem. A 1 (2013) 14766–14772, https://doi.org/10.1039/C3TA13188B.
[50] L. Cui, Y. Liu, X. Fang, C. Yin, S. Li, D. Sun, S. Kang, Scalable and clean exfoliation of graphitic carbon nitride in NaClO solution: enriched surface active sites for enhanced photocatalytic H_2 evolution, Green Chem. 20 (2018) 1354–1361, https://doi.org/10.1039/C7GC03704J.
[51] Y. Li, M. Wang, S. Bao, S. Lu, M. Xu, D. Long, S. Pu, Tuning and thermal exfoliation graphene-like carbon nitride nanosheets for superior photocatalytic activity, Ceram. Int. 42 (16) (2016) 18521–18528, https://doi.org/10.1016/j.ceramint.2016.08.190.
[52] H. Sun, X. Zhou, H. Zhang, W. Tu, An efficient exfoliation method to obtain graphitic carbon nitride nanosheets with superior visible-light photocatalytic activity, Int. J. Hydrogen Energy 42 (12) (2017) 7930–7937, https://doi.org/10.1016/j.ijhydene.2016.12.080.
[53] S.P. Pattnaik, A. Behera, S. Martha, R. Acharya, K. Parida, Facile synthesis of exfoliated graphitic carbon nitride for photocatalytic degradation of ciprofloxacin under solar irradiation, J. Mater. Sci. 54 (2019) 5726–5742, https://doi.org/10.1007/s10853-018-03266-x.
[54] Y. Tian, F. Cheng, X. Zhang, F. Yan, B. Zhou, Z. Chen, J. Liu, F. Xi, X. Dong, Solvothermal synthesis and enhanced visible light photocatalytic activity of novel graphitic carbon nitride–Bi_2MoO_6 heterojunctions, Powder Technol. 267 (2014) 126–133, https://doi.org/10.1016/j.powtec.2014.07.021.
[55] Y.-H. Xu, G. Xu, M.-Y. Sun, K. Wang, Low-temperature solvothermal–calcination preparation and enhanced photocatalytic performance of polymeric graphitic carbon nitride with disordered–ordered hybrid plane, Chem. Pap. 74 (2020) 4067–4074, https://doi.org/10.1007/s11696-020-01227-w.
[56] Y. Kojima, H. Ohfuji, Reexamination of solvothermal synthesis of layered carbon nitride, J. Mater. 2018 (2018), 6576457. 8 pp https://doi.org/10.1155/2018/6576457.
[57] D. Lu, P. Fang, W. Wu, J. Ding, L. Jiang, X. Zhao, C. Li, M. Yang, Y. Li, Solvothermal-assisted synthesis for self-assembling TiO_2 nanorods on large graphitic carbon nitride sheets with their anti-recombination in photocatalytic removal of Cr(VI) and rhodamin B under visible light irradiation, Nanoscale 9 (2017) 3231–3245, https://doi.org/10.1039/C6NR09137G.
[58] C.B. Cao, Q. Lv, H.-S. Zhu, Carbon nitride prepared by solvothermal method, Diamond Relat. Mater. 12 (2003) 1070–1074, https://doi.org/10.1016/S0925-9635(02)00309-6.
[59] K. Kailasam, J.D. Epping, A. Thomas, S. Losse, H. Junge, Mesoporous carbon nitride–silica composites by a combined sol–gel/thermal condensation approach and their application as photocatalysts, Energy Environ. Sci. 4 (2011) 4668–4674, https://doi.org/10.1039/C1EE02165F.
[60] Z. Chunyong, L. Mingshi, L. Mohong, Z. Guohua, Z. Chunzhi, W. Yingpin, C. Jiehong, Preparation of high activity TiO_2/g-C_3N_4 photocatalysts via a facile sol-gel method with $Ti(OBu)_4$ as Ti source and melamine as nitrogen source, Rare Metal Mater. Eng. 46 (2) (2017) 0322–0325, https://doi.org/10.1016/S1875-5372(17)30088-7.
[61] X. Liu, N. Chen, Y. Li, D. Deng, X. Xing, Y. Wang, A general nonaqueous sol-gel route to g-C_3N_4-coupling photocatalysts: the case of Z-scheme g-C_3N_4/TiO_2 with enhanced photodegradation toward RhB under visible-light, Sci. Rep. 6 (2016) 39531, https://doi.org/10.1038/srep39531.
[62] X. Sun, X. An, S. Zhang, Z. Li, J. Zhang, W. Wu, M. Wu, Physical vapor deposition (PVD): a method to fabricate modified g-C_3N_4 sheets, New J. Chem. 43 (2019) 6683–6687, https://doi.org/10.1039/c8nj06509h.

SECTION I

Sustainable energy applications

CHAPTER 2

Exploring smart graphitic carbon nitride material toward flexible energy storage supercapacitors

Meenakshi Talukdar and Pritam Deb
Advanced Functional Material Laboratory (AFML), Department of Physics, Tezpur University (Central University), Tezpur, India

Contents

1. Introduction

Our modern civilization is currently focused on the development of new equipment with ease of construction and flexibility, with added functionalities like lightweight, cost-effective, and renewable features to significantly enhance consumer demand [1–3]. Rigid energy storage devices result in poor performances, thus a myriad of studies on flexible devices has been investigated to sort out its need in industry and academia. High-cost traditional batteries used to store electricity have extant toxic components that overall hinders their use for wide adoption in modern tools [4]. Similarly, traditional capacitors are also unsuitable due to their very low tendency to store energy. Moreover, rechargeable Li ion batteries, which are used in portable and flexible devices, provide high energy density but suffers slow charging/discharging rates, which affects the cyclic capacity. Although high energy density electric batteries with improved performance are the most commonly used energy storage devices, they lack concert during their sluggish process in charging. One such type of energy storage system is the supercapacitor (SC), which has been espoused for years for energy conversion and storage [5]. SCs were created as an alternate to batteries with superior, long-duration working capacity without losing its performance, which links the gap between batteries and capacitors as shown

Nanostructured Carbon Nitrides for Sustainable Energy and Environmental Applications
https://doi.org/10.1016/B978-0-12-823961-2.00002-1

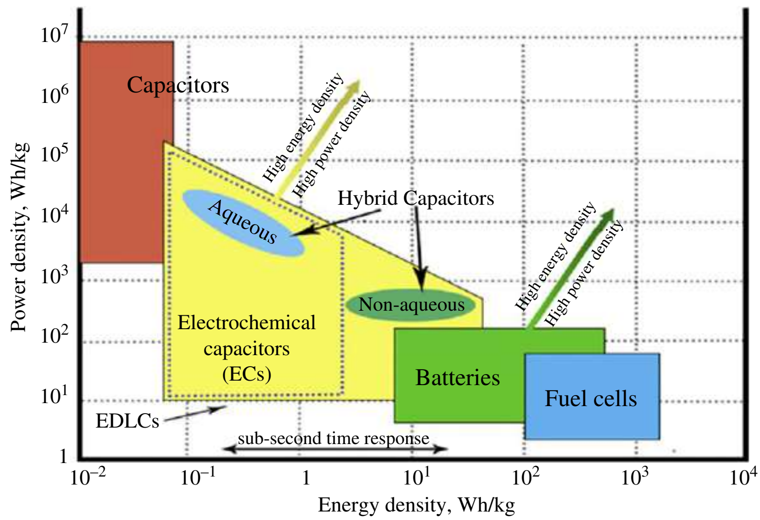

Fig. 2.1 Ragone plot showing performances of various energy storage devices. *(Reproduced with permission from A. Afif, S.M.H. Rahman, A.T. Azad, J. Zaini, Md. A. Islan, A.K. Azad, Advanced materials and technologies for hybrid supercapacitors for energy storage—a review, J. Energy Storage 25 (2019) 100852, https://doi.org/10.1016/j.est.2019.100852, Copyright 2020, Elsevier.)*

in Fig. 2.1. To meet the rising demand of flexible and portable devices, SCs with flexibility, are wearable, and with performance stability have been developed. The performance and efficiency of these systems are reliant on the functional properties of the materials used for constructing them. In recent years, several studies have been carried out to explore flexible energy storage devices, but developing flexible supercapacitors (FSC) has become critical because they attain greater energy density than those of conventional capacitors with greater power density than batteries [6,7]. Above all, a system with mechanical flexibility would have an added advantage. Looking into its smart power solution for upcoming applications, present research is focused on developing new SC electrode materials with superior results [8,9]. Numerous efforts have been made to design new materials and technologies for electrochemical SCs. With the advantages of long cycle life, high energy density, wide voltage range, and long operational life, SC devices—also known as electrical double-layer capacitors (EDLCs)—store the charge on the surface of the material by absorption of ions without any chemical reaction occurrences. Since no chemical redox reactions are required, they are highly reversible during operation, undergoing several charging and discharging cycles. However, due to limited confinement of the charges, the energy density is less compared to that of batteries [10].

Currently, there is a revolution in the convention of carbon nanomaterials for energy storage due to their novel properties, considering their electronic and other characteristics. Two-dimensional (2D) carbon-based systems have high surface area with advantageous electronic and mechanical properties, making them exceptional electrode materials for charge storage [11,12]. The storage mechanism is formed mainly between the electrode and electrolyte interface, and on surface area available for electrolyte ions. The storage performance of 2D carbon materials is also generated by their specific surface area, resulting in a high capability charge build-up at the electrode-electrolyte interface. Besides the surface area, pore dimension, presence of active sites, dimensionality, and morphologies also support in refining the capacitance of the individually developed system.

Even with an efficient surface area, pore size variation influences its electrochemical performances. Large pore volume can lead toward low conductivity, which hinders energy and power capacity [13]. Recently, a new type of carbon-based material known as graphitic carbon nitride (g-C_3N_4) has been explored owing to its unique properties [14]. Its structure is a sp^2 hybridized graphitic network where carbons are replaced by nitrogen atoms, making conjugation in the graphitic planes similar to that of graphite. Compared to graphene, the presence of one nitrogen lone pair in g-C_3N_4 accelerates its surface and electronic properties. This chapter comprehensively overviews recent advances of g-C_3N_4 based on its functional properties and preparation techniques. It also shows significant improvement when combined to form hybrid materials, particularly in energy storage FSC applications.

2. Functional properties of g-C_3N_4

g-C_3N_4 has a graphite-like structure with exceptional features such as thermal stability, smart electronic properties, and environment friendly nature, which have attracted significant consideration in many domains. High content of nitrogen enriches the system's characteristics, whose capacitances are much higher in comparison to traditional EDLCs without losing the fast charge/discharge kinetics [15,16]. In the case of bulk systems, its small surface area and low electronic conductivity hinder its application for electrochemical study. In many cases, a material's inadequacy can be overcome by finding different physical/chemical methods to modify the morphology and textures. Excellent physical, chemical, and mechanical properties of g-C_3N_4 attracted researchers to explore this system more. In general, N-rich functional groups (shown in Fig. 2.2) include oxidized pyridine-N (N-X), pyrrolic N (N-5), quaternary N (N-Q), and pyridinic/pyridone N (N-6). Pyrrolic N atoms and pyridinic N, which are always placed at the edge, are bonded to two carbon atoms, and therefore give rise to electron donor properties. Similarly, when pyridine is adjacent to a ring carbon-hydroxyl group, it donates an electron. Electron transfer and electrical conductivity of the material are significantly elevated by the N-Q atoms, which are located both within graphene layers and at the edges, bonded with three carbon atoms. Under mild electrochemical conditions and thermal treatment above 800°C, alternation of pyridinic N to quaternary N occurs. At temperatures above

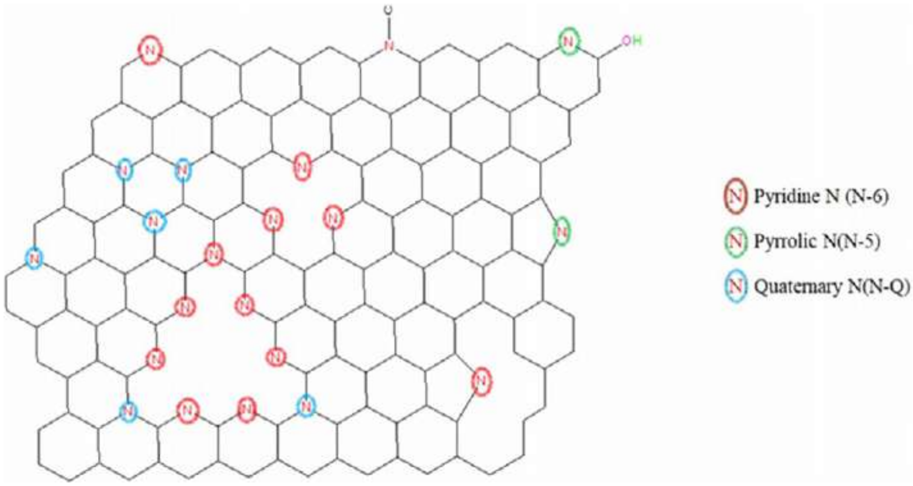

Fig. 2.2 Schematic representation of N-doping GCN. *(Reproduced with permission from M.G. Ashritha, K. Hareesh, A review on graphitic carbon nitride based binary nanocomposites as supercapacitors, J. Energy Storage 32 (2020) 101840, https://doi.org/10.1016/j.est.2020.101840, Copyright 2020, Elsevier.)*

600°C, pyrrolic N tends to change to pyridinic and quaternary N. Alternatively, conversion between pyridone nitrogen and N-6, or N-X and N-6 are achieved under collective electrochemical conditions. In the subsequent sections, we review the various routes for synthesis of g-C_3N_4.

2.1 Synthesis methods to produce g-C_3N_4

Compounds such as triazine and heptazine derivatives, which are nitrogen-rich and oxygen-free compounds, are found to be most unstable in nature; they are also difficult to process as they are highly explosive. Due to its low thermodynamic stability, it's a challenging task to develop single-phase carbon nitrides having sp^3- hybridized. Looking into its potential, various methods such as engineering hydrogen bonds, doping and copolymerization, chemical vapor deposition, hydrothermal, solvothermal, and other various techniques have been investigated to synthesize g-C_3N_4 [17–19]. Various compounds such as urea, melamine, thiourea, dicyandiamide, and cyanamide [20–24] were used as a precursor for the synthesis. Fig. 2.3 signifies development of g-C_3N_4 using a melamine precursor through a hydrothermal approach. However, preparing the same using urea has appeared to be a more suitable and easy approach due to its earth-abundance in nature. Wang et al. [25] using a cyanamide precursor reported the development of g-C_3N_4. At a preliminary stage of ~203–234°C, cyanamide molecule condenses to dicyanamide, which further turns into melamine. Later at a higher temperature of 335°C, melamine-based products form by removing ammonia at this temperature.

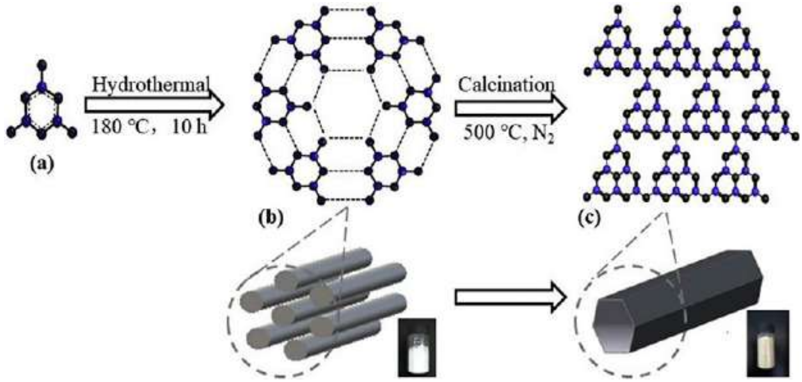

Fig. 2.3 Schematic representation of fabrication process of TGCN through hydrothermal pretreatment and thermal polymerization. *(Reproduced with permission from F. Li, Y. Dong, Q. Dai, T.T. Nguyen, M. Guo, Novel freestanding core-shell nanofibrillated cellulose/ polypyrrole/tubular graphitic carbon nitride composite film for supercapacitors electrodes, Vacuum 161 (2019) 283–290, https://doi.org/10.1016/j.vacuum.2018.12.046, Copyright 2020, Elsevier.)*

Beyond 335°C, i.e., at 390°C, the formation of tri-s-triazine units occurs by relocating melamine molecules, and polymeric g-C_3N_4 forms at 520°C. Moreover, further heating the sample may result in disappearance of g-C_3N_4.

With support to the experimental results, theoretical calculations using ab initio further confirms the reaction mechanism and formation of melamine, produced upon heating the cyanamide. While undergoing preparation using a thermal condensation approach, compounds with a prebonded C—N core arrangement with nitrogen-rich and oxygen-free atoms are mostly considered. Apart from cyanamide, urea, thiourea precursors, and other derivatives such as triazine and heptazine were also investigated for preparation of g-C_3N_4.

In this regard, Shen et al. [26] developed an activated carbon nitride (ACN) material for a SC application using KOH as the electrolyte. The research group studied the formation of a porous ACN material by pyrolysis of melamine and citric acid-derived precursor at different temperatures. Combining melamine with citric acid forms a porous framework through intermolecular hydrogen bonding, which results in a highly porous structure that helps in enhancing the performance of the system. Existence of a nitrogen element helps in increasing the capacity of the electrode by introducing pseudocapacitance, showing great potential in SCs. The research group investigated that, as the temperature of pyrolysis increased to 700°C, carbon nitride gradually decomposes and leads toward a decrease in mass ratio, justified by XPS. Also, in the case of XRD, the peak becomes less intensive and wider. The brilliant performance of the developed system originates mainly from introducing nitrogen-derived pseudocapacitance, which is related to a large surface area and surface oxygenation after KOH activation.

Tahir et al. [27] prepared a g-C_3N_4 nanofiber from melamine pretreated with HNO_3 in ethanol and heated at 450°C for 2h. The as-prepared system was tested as an electrode material for energy storage. The capacitances for both bulk and nanodimension were evaluated by taking Na_2So_4 as the electrolyte. The excellent performance of the electrode was mainly due to its large surface area and the presence of a high degree of nitrogen in the system. Also, they improved the capacitance of the system by improving surface wettability and providing various active sites where ions can intercalate within the surface and interface.

A further study was performed by the same group [28] changing the solvent from ethanol to ethylene glycol and tuning the morphology into a tubular-shaped g-C_3N_4. Tubular g-C_3N_4 formed from melamine precursor with high surface area (182.61 m^2/g) exhibited good specific capacitance of 233 $F g^{-1}$ at a current density 0.2 A/g. The tubular g-C_3N_4 was constructed mainly via breaking of a melamine ring and polymerization of ethylene glycol in the presence of HNO_3. The main phenomenon behind formation of a tubular structure was the controlled annealing temperature, during which ethylene glycol boosts the carbon content and stabilizes the structure formation. High surface area and specific tubular morphology are the main factors that enhance the capacitance.

2.2 g-C_3N_4 for flexible supercapacitor

A revolution in materials technology has led researchers to find new and efficient devices, changing the benchmark of their own or others. The latest development in the field of energy storage generates curiosity in researchers to search for unconventional materials, which can enhance the performances and mechanical properties. While developing new electrode materials, researchers came up with a new design called "Flexible Supercapacitors". The mechanism behind bending and folding of FSC is the smooth transport of ions under mechanical strain [29]. Apart from degradation, a short circuit may sometimes create a problem by hindering its efficient performances. To elevate the performances to a superior level, another possibility is to enhance the ion transport mechanism with 2D migration channels, which can travel a shorter distance, eliminating the need of a separator.

Surface functionalization plays a crucial role in energy storage applications. Aghazadeh et al. reported a composite using $Co(OH)_2$ nanosheets and oxygen-functionalized g-C_3N_4 (f-g-C_3N_4) through a one-step deposition process, without any binder as shown in Fig. 2.4 [30]. In the reported work, both $Co(OH)_2$ and oxygen-functionalized g-C_3N_4 are electrochemically co-embedded using an electrodeposition technique into a Ni-Foam substrate. Morphological analysis of the system confirms the growth of $Co(OH)_2$ nanosheets over g-C_3N_4 surfaces. Furthermore, composites are deposited on the surface of the Ni foam, forming a 3D porous network. g-C_3N_4 was prepared using

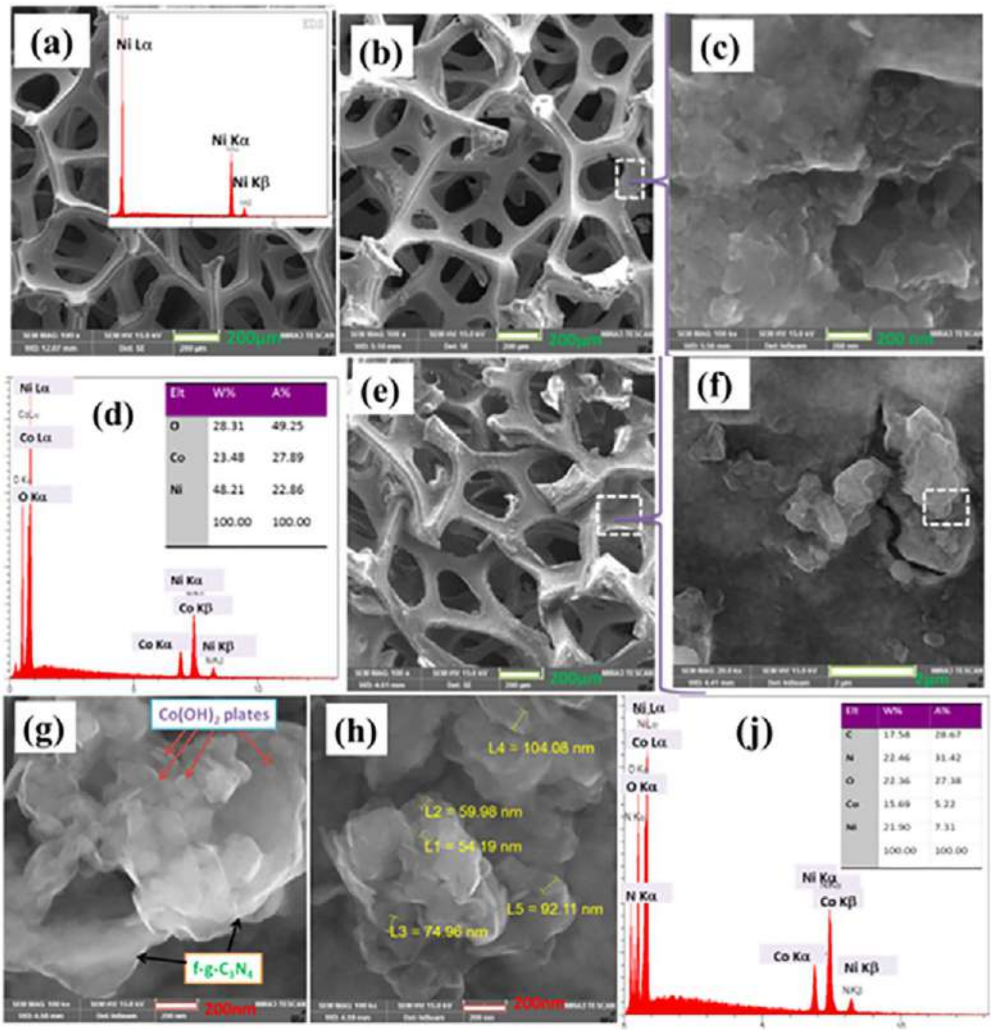

Fig. 2.4 Microstructural images along with their elemental composition the developed electrode. (A) Ni foam, the fabricated (B–D) pristine $Co(OH)_2$/Ni foam, and (E–J) $Co(OH)_2$@g-C_3N_4/Ni foam. *(Reproduced with permission from M. Aghazadeha, K. Yavari, H.F. Rad, K. Mohammadzadeh, Oxygen-functionalized graphitic carbon nitride nanosheets/co(OH)2 nanoplates anchored onto porous substrate as a novel high-performance binder-free electrode for supercapacitors, J. Energy Storage 32 (2020) 101743, https://doi.org/10.1016/j.est.2020.101743, Copyright 2020, Elsevier.)*

a melamine precursor, whereas f-g-C_3N_4 was prepared simply via an etching method in an acidic (H_2SO_4) solution. The specific capacitances were measured to be 1663 F g^{-1} at 1 A g^{-1} and 1064 F g^{-1} at 30 A g^{-1}, respectively, for the developed composite, which are more efficient compared to pristine electrodes. Presence of f-g-C_3N_4 further helps in increasing the capacitive retention and cycling capacity stability of the system. The improvements in the system were attributed to the synergistic effects between $Co(OH)_2$ nanosheets and f-g-C_3N_4, which assisted in enhancing the overall performances of the developed electrode. High interface area between the individual components showed a significant role in the electrochemical performance of the fabricated composite electrode. Addition of f-g-C_3N_4 into the pristine system increases the surface area of the composite due to the presence of an interstitial space between cobalt hydroxide and f-g-C_3N_4. Surface and interface further enhance the pore volume of the composite system. The mechanism behind charge storage performance occurred in pristine electrodes without the presence of f-g-C_3N_4, which was purely pseudocapacitance behavior rather than EDLC. Furthermore, the presence of EDLC behavior along with redox peak revealed in the composite system was due to the presence of f-g-C_3N_4. Existence of both EDLC and redox peak helps in enhancement of current-potential response and also facilitates better electrochemical performance of the system compared to pristine ones. Thus, the developed system leads toward a way for designing competitive electrode materials for energy applications.

Sharma et al. [31] reported a unique composite of g-C_3N_4 and $ZnCo_2O_4$ developed through a hydrothermal method for energy storage applications. Synergistic effect of individuals in g-C_3N_4@$ZnCo_2O_4$ hybrid composite shows significant enhancement in specific discharge capacity. Furthermore, a device was fabricated combining g-C_3N_4@$ZnCo_2O_4$//gel electrolyte//g-C_3N_4@$ZnCo_2O_4$ showing high energy density of 39 $Whkg^{-1}$ at a power density of 1478 Wkg^{-1} with good cyclic stability performance with an energy efficiency of 75% as shown in Fig. 2.5. Cyclic voltammetry (C—V) curve showed enhancement in specific capacitance of the system on further addition of g-C_3N_4 into the $ZnCo_2O_4$. Presence of g-C_3N_4 in the hybrid system marks the system mesoporous in nature, which provides easy access for the ions within a short diffusion path. Furthermore, SEM micrograph identifies clusters with fibrous distribution. Hence, high surface area of the system was due to the space between clusters, which provide a channel for the movement of electrolyte ions. The results suggest that the developed novel hybrid electrode marks an efficient system with excellent performances creating a solution toward upcoming energy storage devices. All these materials exhibit somewhat good specific or areal capacitance, but the cyclic stability and rate capability were low and unstable.

To advance the capacity retention and long-term stability of carbon-based materials, Talukdar et al. [32] investigated the development of an in-plane flexible micro-SCs combining both EDLC and faradaic material. 1D $FeNi_3$ nanoparticles were incorporated in 2D EDLC g-C_3N_4 nanosheets while developing the heterostructure system. Presence of g-C_3N_4 improves the transmission of ions and electrons by opening more active sites, whereas $FeNi_3$ prevented aggregation of the 2D sheets within the system. The developed micro-SCs with 19.21 $mFcm^{-2}$ areal capacitance show excellent quantum capacitance

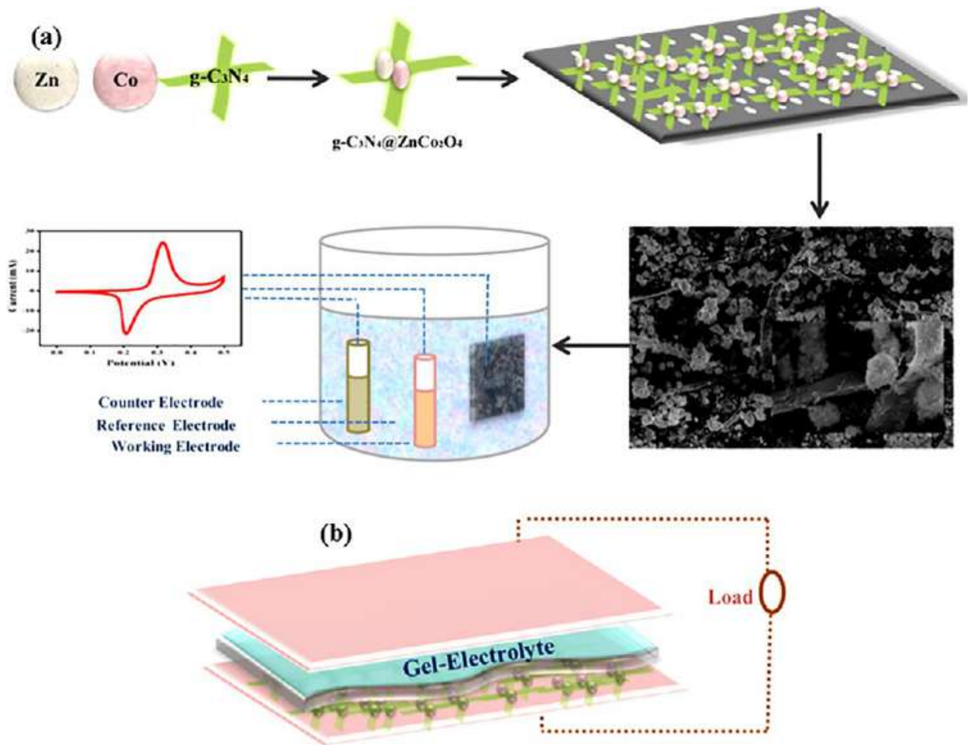

Fig. 2.5 (A) Schematic representation of mechanism occurred in the developed electrode. (B) Schematic illustration of the assembled supercapacitor device. *(Reproduced from M. Sharma, A. Gau, Designing of carbon nitride supported ZnCo2O4 hybrid electrode for high-performance energy storage applications, Sci. Rep. 10 (2020) 2035, https://doi.org/10.1038/s41598-020-58925-4 with permission from Scientific Reports.)*

over the presently reported works, which also have ~17 times higher power density to that of available SCs. Moreover, the system shows excellent flexibility with 94% capacitive retention stability as shown in Fig. 2.6. Such a device promises to meet positive potential requirements, having higher operating current and voltage within a short interval. An electrochemical study was carried out by taking three-electrode systems with varying electrolyte (KOH) concentrations. Presence of both EDLC and Faradic (pseudocapacitance) helps in better development of an ideal SC with quasi-rectangular curves, justified from C—V curves. A higher amount of nitrogen content in the 2D sheet improves conductivity, which eventually assists in charge transfer. Also, the polarity of 2D-layered material was enhanced due to the presence of $FeNi_3$. Hence, development of such flexibility within the system will help in achieving the due necessities of high working voltages and currents in the arena of in-plane micro-SCs.

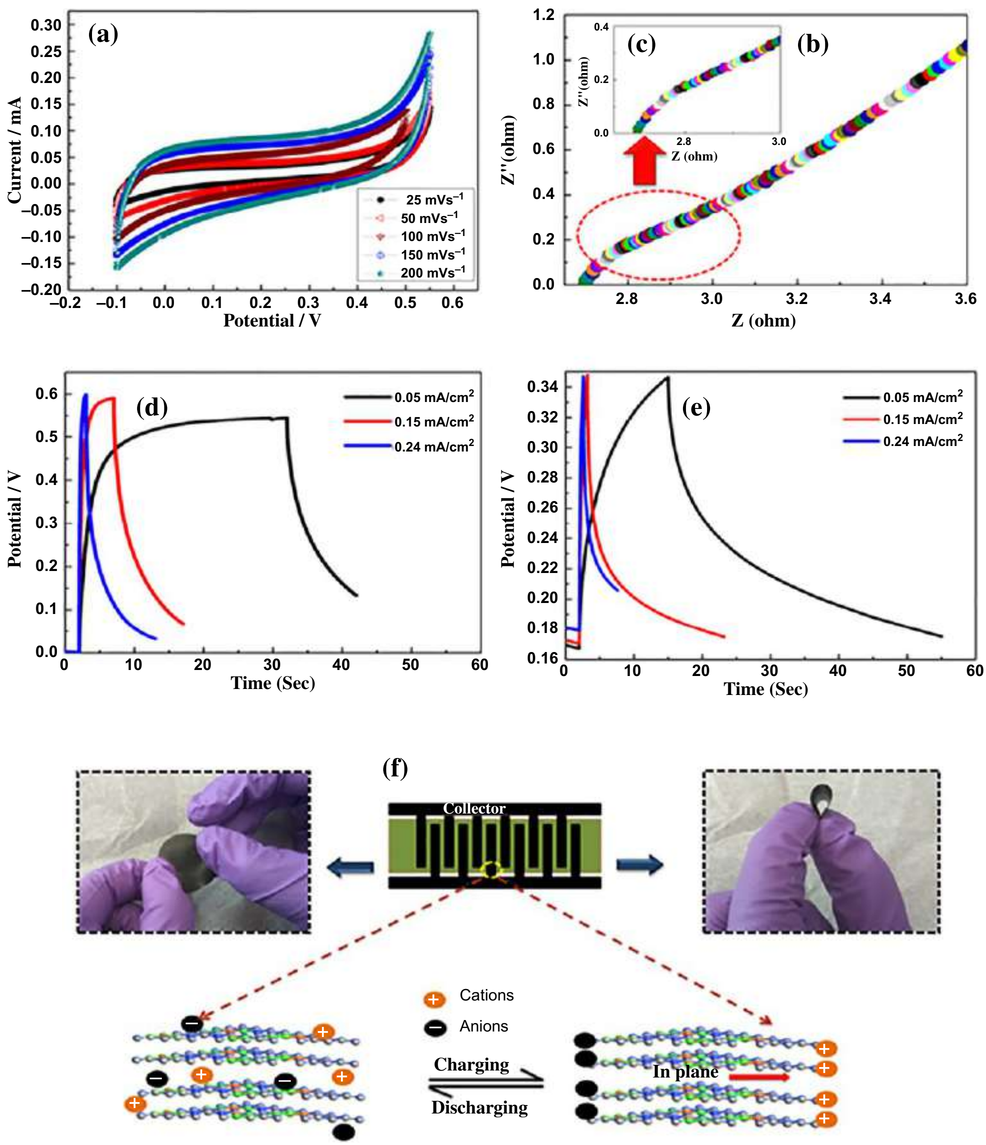

Fig. 2.6 (A–E) Represents the electrochemical characterization of the developed 2D g-C_3N_4-based heterostructure using three-electrode at various scan rates. (F) Real-time images showing the flexibility of the system. *(Reproduced from M. Talukdar, S.K. Behera, P. Deb, Graphitic carbon nitride decorated with FeNi3 nanoparticles for flexible planar micro-supercapacitor with ultrahigh energy density and quantum storage capacity, Dalton Trans. 48 (2019) 12137–12146, https://doi.org/10.1039/C9DT02423A.)*

2.3 Strategies to improve energy storage performance of g-C_3N_4 and fabrication of flexible transparent supercapacitor device

To overcome the disadvantages of pristine g-C_3N_4 in energy storage applications, approaches such as surface doping (metal or non-metal), surface engineering, building hybrid systems, creating heterojunctions, etc. have been carried out to successfully advance and boost its functionality [33–35]. Table 2.1 summarizes the different preparation techniques along with their advantages and disadvantages.

Although numerous efforts were made to boost the conductivity of pristine g-C3N4, a significant gap remains to achieve proficient outcomes. Proper precursors along with surface engineering expands its capacitive behavior, reducing the aforesaid efficiencies. A combination of mechanical properties along with excellent electrical conductivity in an electrode marks g-C_3N_4 as a favorable material for FSCs. Hou et al. [36] developed a hybrid system with an oxygen-vacancy-rich $NiCo_2O_4$ (Ov-$NiCo_2O_4$) and nitrogen-deficient g-C_3N_4 (ND-g-C_3N_4) using a one-plot approach for energy storage

Table 2.1 Summarizing various preparation approaches along with their advantages and disadvantages.

Different strategies used	Working principle	Benefits and drawbacks
Developing composite system with metal sulfide	Etching	*Advances the electrochemical mechanism resulting in efficient charge transfer* *Disadvantages: Acid used during preparation can be harmful to the environment*
Doping with single atom	Hydrothermal reaction	*Helps in capacitance enhancement compared to pristine form* *Disadvantages: Stability is low, Formation of other active species, Possibilities of getting aggregation*
Heterostructure composites	Solvothermal, CVD Hydrothermal method	*Enhancement in specific capacitance due to high surface area (face to face contact)* *Disadvantages: Difficulty during the growth process*
Combining with other carbon materials and other semiconductors	Hydrothermal route Sonication	*Improves specific capacitance, excellent stability, high cyclic concerts, and low self-aggregation* *Disadvantages: Low and uneven loading can affect the capacity and specific energy*

applications. Being a substrate, g-C_3N_4 enhances the conductivity of the overall system. Also, the presence of g-C_3N_4 with $NiCo_2O_4$ helped in the formation of Ov-$NiCo_2O_4$ and converted g-C_3N_4 into a nitrogen-deficient g-C_3N_4 (ND-g-C_3N_4). Electrochemical performance of the system was performed using the three-electrode system in an electrolyte solution made with 6M KOH. C—V analysis confirmed that capacitance behavior was mostly governed by Faradaic redox reactions. Furthermore, C—V curves as shown in Fig. 2.7 revealed storage performance with excellent rate capacity. Additionally, the device proved extraordinary stable with 95.22% retention despite testing for 5000 cycles. Thus, the effort focuses on development of pseudocapacitive materials for energy storage. Zhu et al. [37] further developed a CC@g-C_3N_4–900 electrode using carbon cloth (CC) as a flexible substrate. The developed electrode delivers a significant specific capacitance with enhanced rate capability and outstanding cyclic stability. The final product, CC@g-C_3N_4–900, was developed at 800°C. For comparison, the samples were also optimized by preparing under different calcination temperatures of 800–1000°C. It was conducted from Raman Spectra that the system developed at 900°C holds a high I_D/I_G value, which indicates more defects, favoring more active sites for energy storage behavior. Adding g-C_3N_4 onto a CC substrate further enhances the surface area of the system. Also, a high amount of N doping within the system accelerates the conductivity of the system. Presence of high specific area with suitable pore volume helps in creating more active sites, which improves the electrochemical performances by creating more ion penetration into the electrode. Furthermore, to identify the potential application of the electrode, a symmetric SC device was developed, which indicates good capacitance characteristics with superior rate cyclability as shown in Fig. 2.8 The synergistic effect of g-C_3N_4 with CC substrate helps in providing excellent electrochemical performance. Thus, the developed electrode structure signifies high stability with smaller charge transfer resistance, which can be used as an energy storage device in the future.

3. Future prospects

The domain of SCs has gained much attention throughout the world, focusing its studies on materials, their surfaces, and electrochemical reactions. There is no uncertainty that synergetic improvements have been achieved to handle and fabricate flexible energy storage capacitors with inimitable qualities in operation and handling. The current chapter revised recent advancements in their preparation, their functional properties (such as pore size, conductivity, flexibility, electrochemical, and mechanical properties), and mechanisms of charge storage within different g-C_3N_4 hybrid systems in the domain of energy storage devices. Although countless outcomes have been attained for carbon nitride-based materials such as FSCs, to conduct the experiments on a pilot scale,

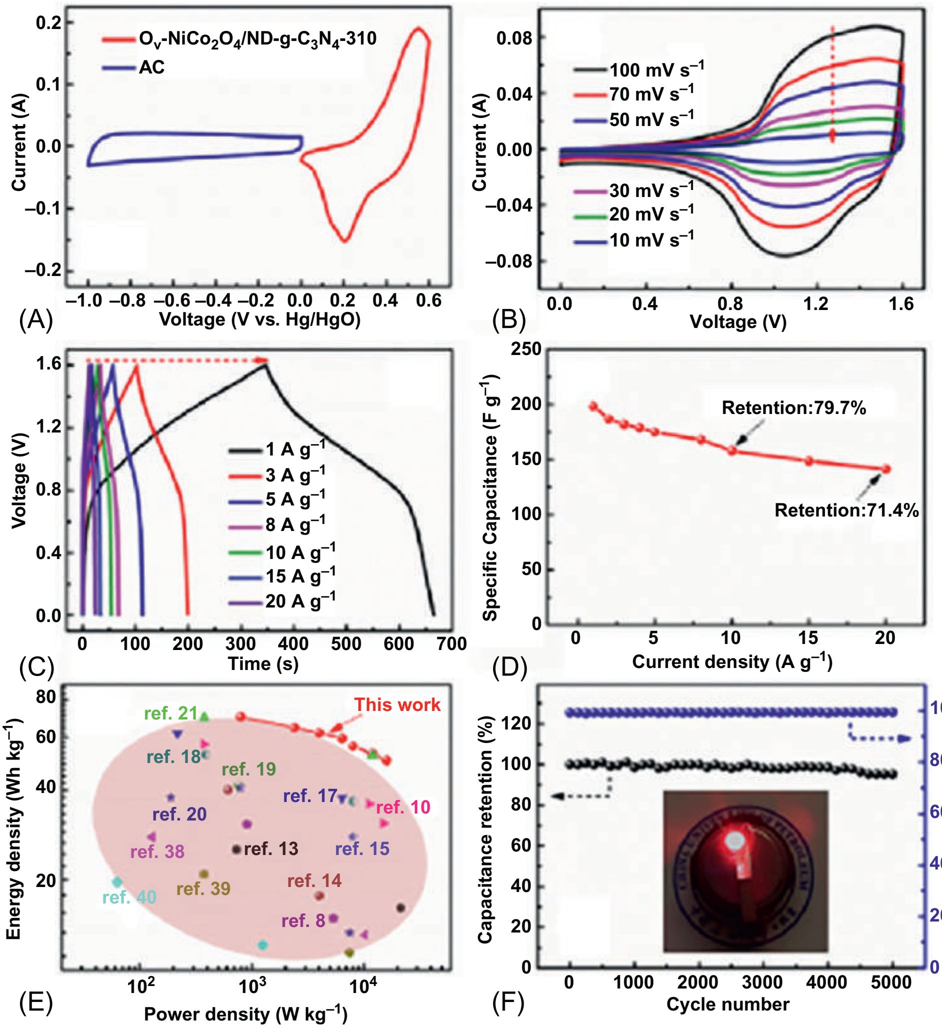

Fig. 2.7 (A–C) Electrochemical performances, (D) specific gravimetric capacitances as function of current densities, (E) Ragone plots, and (F) cyclic performance as well as Coulombic efficiency of the developed system. *(Figures are reproduced with permission from L. Hou, W. Yang, X. Xu, B. Deng, J. Tian, S. Wang, F. Yang, Y. Li, In-situ formation of oxygen-vacancy-rich NiCo2O4/nitrogen-deficient graphitic carbon nitride hybrids for high-performance supercapacitors, Electrochim. Acta 340 (2020), 135996, https://doi.org/10.1016/j.electacta.2020.135996 Copyright of Elsevier.)*

challenges still remain. Summary of some major challenges are as follows: (1) Varying the concentration of the electrolyte to improve the capacitive performances and understanding the mechanism with respect to it. (2) Designing electrode material with efficient surface area along with pore size and volume tunable for excellent mass transport. (3) Tunable pore volume by changing the preparation time and temperature can also be

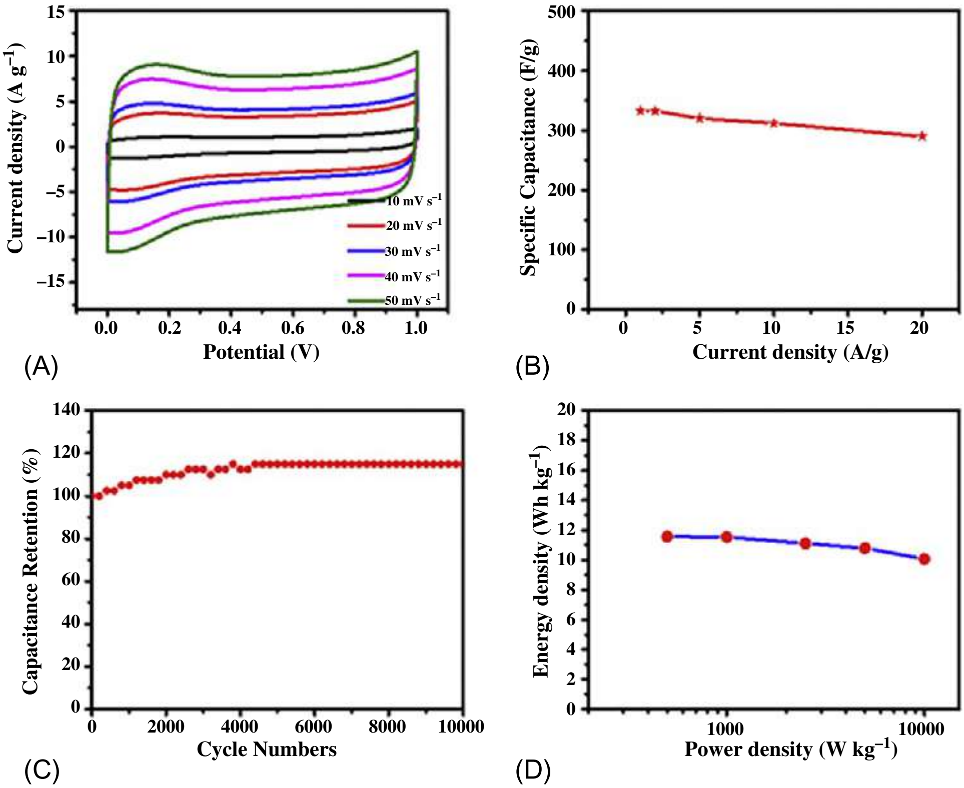

Fig. 2.8 Electrochemical performances: (A) C—V curves. (B) The specific capacitances at different scan rates and current densities. (C) Capacitance retention. (D) Ragone plot of the symmetric supercapacitor device. *(Figures are reproduced with permission from J. Zhu, L. Kong, X. Shen, G. Zhu, Z. Ji, K. Xu, H. Zhou, X. Yue, B. Li, Carbon cloth supported graphitic carbon nitride nanosheets as advanced binder-free electrodes for supercapacitors, J. Electroanal. Chem. 873 (2020), 114390, https://doi.org/10.1016/j.jelechem.2020.114390 Copyright of Elsevier.)*

studied. Although there is abundant literature that discuss the progress on designing FSCs, it's always a challenging task to develop a material with high power and energy density with excellent stability.

Proper functionalization of g-C_3N_4 will further expand its application possibilities in FSC. On the other hand, the previously mentioned drawbacks can be overcome by using various approaches such as considering and controlling the dimensionality of g-C_3N_4, precursors used, and also optimizing reaction time, temperature, and its surroundings. Moreover, comprehensive theoretical evidence justifying the experimental analysis is essential to recognize the in-depth fundamental phenomena, arising in active sites that accelerate better mass transfer over g-C_3N_4. The future outlook in this domain can be the improvement of g-C_3N_4 with optimized time, temperature, and maintaining different stoichiometric ratios of C and N. An out-of-the-box thought process is necessary to overcome the challenges and inventory of inbuilt flexible electrodes as a research hotspot.

4. Conclusion

The field of energy storage FSC has increased throughout the world with rigorous focus on g-C_3N_4, their surface, and their electrochemical properties. But, for better performances, the major phenomenon depends on the electrolyte, electrode materials, electrochemical properties, and factors governing voltage range. Despite this, most research studies are focused on developing environment-friendly material having low-cost energy storage systems, which can yield better performances. Research in modern science has been focused on g-C_3N_4, which has drawn attention in the field of FSC with its unique and potential features. Presence of nitrogen content in g-C_3N_4 creates many active sites that increase the mass transfer efficiency and surface polarity. Although it possesses excellent mechanical stability and flexibility, some features of pristine g-C_3N_4, with limited surface area and low conductivity, hinder its use in FSC. However, researchers are focusing to improve the properties by implementing many strategies to advance its electrical conductivity and enhance its electrochemical properties. One way to produce efficient electrode materials and improve its power and energy density is through combining g-C_3N_4 with other pseudocapacitive materials or by developing hybrid composite materials. Although FSC is a relatively new field of electrochemical energy storage, still there's plenty of room in the materials examining field for creating flexible and mechanically potent devices.

References

[1] Y. Fu, J. Zhu, C. Hu, X. Wu, X. Wang, Covalently coupled hybrid of graphitic carbon nitride with reduced graphene oxide as a superior performance lithium-ion battery anode, Nanoscale 6 (2014) 12555–12564, https://doi.org/10.1039/C4NR03145H.

[2] K. Liao, P. Mao, N. Li, M. Han, J. Yi, P. He, Y. Sun, H. Zhou, Stabilization of polysulfides via lithium bonds for Li–S batteries, J. Mater. Chem. A 4 (2016) 5406–5409, https://doi.org/10.1039/C6TA00054A.

[3] M. Winter, B. Barnett, K. Xu, Before Li Ion Batteries, Chem. Rev. 118 (23) (2018) 11433–11456, https://doi.org/10.1021/acs.chemrev.8b00422.

[4] D.P. Dubal, O. Ayyad, V. Ruiz, P. Gómez-Romero, Hybrid energy storage: the merging of battery and supercapacitor chemistries, Chem. Soc. Rev. 44 (2015) 1777–1790, https://doi.org/10.1039/C4CS00266K.

[5] P. Simon, Y. Gogotsi, B. Dunn, Where do batteries end and supercapacitors begin? Science 343 (2014) 1210–1211, https://doi.org/10.1126/science.1249625.

[6] M. Stoppa, A. Chiolerio, Wearable electronics and smart textiles: a critical review, Sensors 14 (2014) 11957, https://doi.org/10.3390/s140711957.

[7] W. Zeng, L. Shu, Q. Li, S. Chen, F. Wang, X.-.M. Tao, Fiber-based wearable electronics: a review of materials, fabrication, devices, and applications, Adv. Mater. 26 (2014) 5310–5336, https://doi.org/10.1002/adma.201400633.
[8] Y. Huang, M. Zhu, Y. Huang, Y. Huang, M. Zhu, Y. Huang, H. Li, Z. Pei, Q. Xue, Z. Liao, Z. Wang, C. Zhi, A modularization approach for linear-shaped functional supercapacitors, J. Mater. Chem. A 4 (2016) 4580–4586, https://doi.org/10.1039/C6TA00753H.
[9] S.T. Senthilkumar, Y. Wang, H. Huang, Advances and prospects of fiber supercapacitors, J. Mater. Chem. A 3 (2015) 20863–20879, https://doi.org/10.1039/C5TA04731E.
[10] G. Wang, L. Zhang, J. Zhang, A review of electrode materials for electrochemical supercapacitors, Chem. Soc. Rev. 41 (2012) 797–828, https://doi.org/10.1039/C1CS15060J.
[11] E. Frackowiak, Carbon materials for supercapacitor application, Phys. Chem. Chem. Phys. 9 (2007) 1774–1785, https://doi.org/10.1039/B618139M.
[12] L.L. Zhang, X.S. Zhao, Carbon-based materials as supercapacitor electrodes, Chem. Soc. Rev. 38 (2009) 2520–2531, https://doi.org/10.1039/B813846J.
[13] Z.S. Iro, A brief review on electrode materials for supercapacitor, Int. J. Electrochem. Sci. 11 (12) (2016) 10628–10643, https://doi.org/10.20964/2016.12.50.
[14] J. Safaei, N.A. Mohamed, M.F.M. Noh, M.F. Soh, N.A. Ludin, M.A. Ibrahim, W.N.R.W. Isahak, M.-A.M. Teridi, Graphitic carbon nitride (g-C3N4) electrodes for energy conversion and storage: a review on photoelectrochemical water splitting, solar cells and supercapacitors, J. Mater. Chem. A 6 (2018) 22346–22380, https://doi.org/10.1039/C8TA08001A.
[15] W.J.J. Ong, L.L.L. Tan, Y.H. Ng, S.T.T. Yong, S.P.P. Chai, Graphitic carbon nitride (g-C3N4)-based Photocatalysts for artificial photosynthesis and environmental remediation: are we a step closer to achieving sustainability? Chem. Rev. 116 (2016) 7159–7329, https://doi.org/10.1021/acs.chemrev.6b00075.
[16] T.S. Miller, A.B. Jorge, T.M. Suter, A. Sella, F. Cora, P.F. McMillan, Carbon nitrides: synthesis and characterization of a new class of functional materials, Phys. Chem. Chem. Phys. 19 (2017) 15613–15638, https://doi.org/10.1039/C7CP02711G.
[17] B. Xu, M.B. Ahmed, J.L. Zhou, A. Altaee, G. Xu, M. Wu, Graphitic carbon nitride based nanocomposites for the photocatalysis of organic contaminants under visible irradiation: Progress, limitations and future directions, Sci. Total Environ. 633 (2018) 546–559, https://doi.org/10.1016/j.scitotenv.2018.03.206.
[18] Y. Zheng, L. Lin, B. Wang, X. Wang, Graphitic carbon nitride polymers toward sustainable photoredox catalysis, Angew. Chem. Int. Ed. 54 (2015) 12868–12884, https://doi.org/10.1002/anie.201501788.
[19] A. Thomas, A. Fischer, F. Goettmann, M. Antonietti, J.O. Müller, R. Schlögl, et al., Graphitic carbon nitride materials: variation of structure and morphology and their use as metal-free catalysts, J. Mater. Chem. 18 (2018) 4893–4908, https://doi.org/10.1039/b800274f.
[20] M. Talukdar, S.K. Behera, K. Bhattacharya, P. Deb, Surface modified mesoporous g-C3N4@FeNi3 as prompt and proficient magnetic adsorbent for crude oil recovery, Appl. Surf. Sci. 473 (2019) 275–281, https://doi.org/10.1016/j.apsusc.2018.12.166.
[21] J. Cheng, X. Yan, Q. Mo, B. Liu, J. Wang, X. Yang, et al., Facile synthesis of g-C3N4/BiVO4 heterojunctions with enhanced visible light photocatalytic performance, Ceram. Int. 43 (2017) 301–307, https://doi.org/10.1016/j.ceramint.2016.09.156.
[22] Y. Zhang, H. Gong, G. Li, H. Zeng, L. Zhong, K. Liu, H. Cao, H. Yan, Synthesis of graphitic carbon nitride by heating mixture of urea and thiourea for enhanced photocatalytic H2 production from water under visible light, Int. J. Hydrog. Energy 42 (1) (2016), https://doi.org/10.1016/j.ijhydene.2016.11.040.
[23] W. Zhang, Q. Zhang, F. Dong, Z. Zhao, The multiple effects of precursors on the properties of polymeric carbon nitride, Int. J. Photoenergy 9 (2013), https://doi.org/10.1155/2013/685038, 685038.
[24] S. Hwang, S. Lee, J.S. Yu, Template-directed synthesis of highly ordered nanoporous graphitic carbon nitride through polymerization of cyanamide, Appl. Surf. Sci. 253 (13) (2007) 5656–5659, https://doi.org/10.1016/j.apsusc.2006.12.032.

[25] X. Wang, X. Chen, A. Thomas, X. Fu, M. Antonietti, Metal-containing carbon nitride compounds: a new functional organic-metal hybrid material, Adv. Mater. 21 (2009) 1609–1612, https://doi.org/10.1002/adma.200802627.
[26] C. Shen, R. Li, L. Yan, Y. Shi, H. Guo, J. Zhang, Y. Lin, Z. Zhang, Y. Gong, L. Niu, Rational design of activated carbon nitride materials for symmetric supercapacitor applications, Appl. Surf. Sci. 455 (2018) 841–848, https://doi.org/10.1016/j.apsusc.2018.06.065.
[27] M. Tahir, C. Cao, F.K. Butt, F. Idrees, N. Mahmood, Z. Ali, I. Aslam, M. Tanveer, M. Rizwan, T. Mahmood, Tubular graphitic-C3N4: a prospective material for energy storage and green photocatalysis, J. Mater. Chem. A 1 (2013) 13949, https://doi.org/10.1039/C3TA13291A.
[28] M. Tahir, C. Cao, N. Mahmood, F.K. Butt, A. Mahmood, F. Idrees, S. Hussain, M. Tanveer, Z. Ali, I. Aslam, Multifunctional g-C3N4 nanofibers: a template-free fabrication and enhanced optical, electrochemical, and photocatalyst properties, ACS Appl. Mater. Interfaces 6 (2014) 1258–1265, https://doi.org/10.1021/am405076b.
[29] Z. Tang, X. Zhang, L. Duan, A. Wu, W. Lü, Three-dimensional carbon nitride nanowire scaffold for flexible supercapacitors, Nanoscale Res. Lett. 14 (2019) 98, https://doi.org/10.1186/s11671-019-2932-z.
[30] M. Aghazadeha, K. Yavari, H.F. Rad, K. Mohammadzadeh, Oxygen-functionalized graphitic carbon nitride nanosheets/co(OH)2 nanoplates anchored onto porous substrate as a novel high-performance binder-free electrode for supercapacitors, J. Energy Storage 32 (2020), https://doi.org/10.1016/j.est.2020.101743, 101743.
[31] M. Sharma, A. Gau, Designing of carbon nitride supported ZnCo2O4 hybrid electrode for high-performance energy storage applications, Sci. Rep. 10 (2020) 2035, https://doi.org/10.1038/s41598-020-58925-4.
[32] M. Talukdar, S.K. Behera, P. Deb, Graphitic carbon nitride decorated with FeNi3 nanoparticles for flexible planar micro-supercapacitor with ultrahigh energy density and quantum storage capacity, Dalton Trans. 48 (2019) 12137–12146, https://doi.org/10.1039/C9DT02423A.
[33] B. Zhu, L. Zhang, J. Yu, Chapter 16—Surface modification of g-C3N4: first-principles study, Interface Sci. Technol. 31 (2020) 509–539, https://doi.org/10.1016/B978-0-08-102890-2.00016-6.
[34] W. Li, T. Shen, Y. Wang, F. Liu, W. Li, Photoelectrochemical in situ energy storage and the anticorrosion dual function system based on loose carbon nitride thick film electrodes, ACS Appl. Electron. Mater. 2 (7) (2020) 2180–2187, https://doi.org/10.1021/acsaelm.0c00377.
[35] P. Panigrahi, A. Kumar, A. Karton, R. Ahuja, T. Hussain, Remarkable improvement in hydrogen storage capacities of two-dimensional carbon nitride (g-C3N4) nanosheets under selected transition metal doping, Int. J. Hydrog. Energy 45 (4) (2020) 3035–3045, https://doi.org/10.1016/j.ijhydene.2019.11.184.
[36] L. Hou, W. Yang, X. Xu, B. Deng, J. Tian, S. Wang, F. Yang, Y. Li, In-situ formation of oxygen-vacancy-rich NiCo2O4/nitrogen-deficient graphitic carbon nitride hybrids for high-performance supercapacitors, Electrochim. Acta 340 (2020) 135996, https://doi.org/10.1016/j.electacta.2020.135996.
[37] J. Zhu, L. Kong, X. Shen, G. Zhu, Z. Ji, K. Xu, H. Zhou, X. Yue, B. Li, Carbon cloth supported graphitic carbon nitride nanosheets as advanced binder-free electrodes for supercapacitors, J. Electroanal. Chem. 873 (2020), https://doi.org/10.1016/j.jelechem.2020.114390, 114390.

CHAPTER 3

Carbon nitrides as catalyst support in fuel cells: Current scenario and future recommendation

Chanchal Gupta[a], Aman Bhardwaj[b], Rama Kant[a], and Satyabrata Patnaik[b]
[a]Department of Chemistry, University of Delhi, New Delhi, India
[b]School of Physical Sciences, Jawaharlal Nehru University, New Delhi, India

Contents

1. Introduction

The world's energy demands have been increasing continuously over the years and are anticipated to rise further in the near future. Most of these energy demands are currently met by fossil fuels which are nonrenewable, unsustainable in the long term, and are responsible for causing pollution, thus in turn correlated to global warming [1,2]. This growing demand of energy and sinking amount of fossil fuels have been a driving force for impetus to develop earth-abundant and eco-friendly energy technologies [3,4]. Among various "state-of-the-art" green energy technologies, fuel cell-based energy conversion systems have received much attention in recent years owing to their high efficiency and low emissions [5,6]. Fuel cell, therefore, will be a promising technology for distributed and mobile power applications in future. Fuel cells are electrochemical

Nanostructured Carbon Nitrides for Sustainable Energy and Environmental Applications
https://doi.org/10.1016/B978-0-12-823961-2.00004-5

devices which convert chemical energy of fuel directly into electrical energy. Hence, these are nearly two to three times more efficient than conventional internal combustion engines (ICEs) in converting fuel to electricity [7,8].

1.1 Working principle of fuel cells

Fuel cells are considered as highly efficient energy conversion electrochemical devices. Along with this, they also enable a clean and efficient production of heat and power from a diverse range of primary energy sources. The various fuel cell technologies differentiated according to the type of electrolyte they use include alkaline fuel cell (AFC), molten carbonate fuel cell (MCFC), direct methanol fuel cell (DMFC), polymer electrolyte membrane fuel cell (PEMFC), direct alcohol fuel cells (DAFC), and solid oxide fuel cells (SOFC). Each technology is suited toward a certain chemistry, operating temperature, and power density [8–11].

PEMFCs-based advanced power system is specifically applicable for mobile applications. PEMFCs have been of great interest because of their high power density, relatively quick start-up, rapid response to varying loading, and relatively low operating temperature, producing no environmental pollution at the point of operation, which make them an emerging technology for both stationary and mobile power applications [10,12–14].

In PEMFC, hydrogen flows on the anode side, a platinum catalyst facilitates the separation of the hydrogen gas into electrons and protons (hydrogen ions). The hydrogen ions pass through the electrolyte (polymeric membrane) and, again with the help of a platinum catalyst, combine with oxygen and electrons on the cathode side, producing water. The electrons, which cannot pass through the membrane, flow from the anode to the cathode through an external circuit containing a motor or other electric load, which consumes the power generated by the cell. The polymeric electrolyte based membrane consists of three regions: (i) fluorocarbon backbone which have repeating units of ($—CF_2—CF—CF_2—$), (ii) the side chains ($—O—CF_2—CF—O—CF_2—CF_2—$) that connect the molecular backbone, and (iii) the ion clusters containing sulfonic acid ions (SO_3^- H^+). The SO_3^- ions are eternally involved to the side chain hence immoveable. However, when the membrane becomes hydrated by captivating H_2O molecules, the H^+ ions become moveable. Because of this mechanism, the solid hydrated electrolyte is an excellent conductor of hydrogen ions. The electrochemical reactions that drive a PEMFC are significantly accelerated by the presence of an electrocatalyst, especially the oxygen reduction reaction (ORR) occurring at the cathode side of cell. Variety of precious metals and their alloys can be used as electrocatalysts but supported Pt and Pt alloys catalysts are considered as the most promising catalytic materials for fuel cells to meet the key requirements for high electrocatalytic activity and high fuel cell performance [10–12]. The electrocatalytic activity of Pt nanoparticles for fuel cell is determined by various factors, which involve the size and dispersion of particles [15], preparation method [16], supporting materials and their surface conditions [17]. To date, a great deal of research and development effort has been focused on the development of strategies to produce Pt-based catalysts with a high surface area for high catalytic activity and utilization efficiency [10].

1.2 Commercialization hindrance of fuel cells

The development of "state-of-the-art" fuel cell systems is largely dependent on Pt-based electrocatalyst which has low abundances in the earth's crust, also contributing as much as 40% of the total fuel cell cost [18,19]. Therefore, the economic feasibility of PEMFCs is directly linked to reducing the cost without sacrificing the efficiency of these catalysts. The cost of Pt-based electrocatalyst can be significantly reduced by increasing the mass specific activity of platinum catalyst (i.e., increasing the current density without increasing the mass of Pt), or finding an alternative nonnoble metal catalyst that can give an acceptable catalytic performance. Most of the presently used Pt-based catalysts are supported on porous conductive materials with a high specific surface area. The support materials are necessary to obtain a high dispersion and a narrow distribution of Pt and Pt-alloy NPs, which is the prerequisite to obtain a high catalytic performance of catalysts [20–22]. An ideal support material should have high crystallinity, high conductivity, high accessible surface area, and high porosity, should be resistant to corrosion, should have better stability to chemical attacks, stable under oxidizing and reducing atmospheres, manufactured by a low cost process, and have inherent hydrophobic nature [23–25].

1.3 Carbon-based electrocatalyst support materials

Among the various advanced support materials, carbon nanomaterials are most appealing with ample opportunity to improve the utilization of Pt catalyst and thereby enhance the efficiency of fuel cells [25–27]. They have several distinctive properties like good conductivity, easy processability, high surface area, high porosity, and stability under harsh conditions of acidic or basic environment [26,27]. Due to these extraordinary qualities, they can influence the performance of supported catalysts by shrinking the mass transport losses. Furthermore, they can improve the electronic conductivity, electrochemical active surface area and stability of catalyst layer [28].

A wide variety of carbon support materials like carbon black [29,30], ordered mesoporous carbons (OMCs) [31–33], carbon aerogels [34–37], carbon nanotubes (CNTs) [38–47], carbon nanohorns (CNHs) [48–51], carbon nanocoils (CNCs) [52,53], carbon nanofibers (CNFs) [54–57], graphene/reduced graphene oxide [58,59], and carbon nitrides [60–63] have attracted much interest as electrocatalyst support because of their good electrical and mechanical properties and their versatility in pore size and pore distribution tailoring. Recent studies have revealed that the physical properties of the carbon support material can greatly govern the electrochemical properties of the fuel cell catalyst

Table 3.1 Physicochemical characteristics of different carbon materials as support for metal particles.

Carbon material	Specific surface area (m^2/g)	Porosity	Electronic conductivity (S/cm)	Supported catalyst properties	References
VulcanXC-72R	254	Microporous	4.0	Good metal dispersion, low gas flow	[65,66]
OMC	400–1800	Mesoporous	0.3×10^{-2}–1.4	High metal dispersion	[31,32]
Carbon gels	400–900	Mesoporous	>1	High metal dispersion	[34–37]
CNT	200–400	Mesoporous	0.3, 3 (functionalized MWCNTs)	Low metal accessibility, high metal stability	[40–42,44,67]
CNF	10–300	Mesoporous	102–104	High metal dispersion	[56]
Graphene nanosheets/ flakes	2600	Nanoporous	$80–100 \times 10^2$	High metal dispersion, low stability	[58,59]
Carbon nitrides CNs	125	Nanoporous	0.72	High metal dispersion	[60–63]

[45,64]. Table 3.1 lists the properties of different carbon materials as support for metal particles. It has been reported that carbon materials with high surface area and good crystallinity can not only provide a high dispersion of Pt NPs, but also facilitate electron transfer, resulting in better device performance.

Generally, Pt nanoparticles supported on carbon black have been considered as suitable electrocatalyst support and used frequently in various commercial applications, but there is a major issue of oxidative corrosion associated with it [34,37]. Therefore, an alternative type of synthetic carbon that has started to be widely investigated for catalyst support, used in fuel cells, is ordered mesoporous carbons (OMCs) with tuneable pore sizes from 2 to 50 nm. It has been suggested that ordered mesopores offer better mass transport properties than the random range of mesopores shown by conventional carbon black [68,69]. However, due to its poor electrical conductivity and stability, mesoporous carbon has to be treated with high-temperature annealing and catalytic graphitization, which thereby, increases the synthesis cost [33]. Moreover, such treatment/strategies have to be implemented at the expense of the porosity and specific surface area, making it difficult to deposit metal nanoparticles. From past few decades, a wide variety of advanced carbon nanomaterials as support materials have been explored and several modifications including functionalization [70,71] or defect insertion, heat treatment [72,73], heteroatom (i.e., nitrogen, sulfur, boron, phosphorous) doping [74], etc. were adopted for enhancing the electrocatalytic activities. However, nitrogen doping of carbon materials is most fascinating and widely explored process as they astonishingly improves the durability and simultaneously increases the intrinsic catalytic activity of electrocatalysts. The additional lone pair of electron present on nitrogen can alter the electronic cloud and enhances the bonding of carbon with metal nanoparticles. Also captivation of nitrogen into carbon leads to a reduction in surface oxygen groups and thus provides enhanced tolerance toward oxidation of carbon support [75,76]. Generally N-doping is done *via* postsynthesis in which carbon material is treated with ammonia (NH_3) in N_2 atmosphere, which not only provides very less atomic percentage of nitrogen but also has less control over the functionalities. Therefore, researchers were searching a new class of carbon nanomaterials that inherently exhibit the nitrogen content. In this regard, carbon nitride materials are considered as potential candidate in the development of efficient electrocatalyst as they provide high percentage of nitrogen specific functionalities located at definite position. Carbon nitrides have unique properties like extreme hardness, resistance toward corrosion, chemically inertness, tuneable band gap, which make them most interesting carbon support material.

2. Carbon nitride as emerging materials for catalyst support

A class of polymeric compounds containing high concentration of N:C ratio mainly denoted by C_xN_y is known as carbon nitrides or simply CNs [77,78]. Berzelius was first person who reported a polymeric solid compound with high N:C ratios *via* using a nitrogen-rich molecules, which was further developed by group of researchers [79,80]. These materials have 2D crystalline graphene-like atomic structures along with semiconducting properties consisting C- and N-containing heterocycles with heptazine or triazine rings connected by sp^2-bonded N-atoms ($N(C)_3$ units) or —NH— groups. These are synthesized through carbon material *via* substituting nitrogen and vigorously investigated as potential next generation constituents for fuel cell electrocatalyst [60,81,82]. Their electronic, chemical, and optical properties are categorized on the nature of their structures and chemical composition of the constituent elements. As there are different classes of carbon nitride compounds based on their structural and chemical properties, they can be well suited for various applications which include charge storage, oxidation/reduction catalysis, and photocatalysis. Although, due to their variable crystallinity (i.e., ranging from amorphous to nanocrystalline) and tuneable composition of constituent element, creating an immense complication to establish structure-functionality relationships in between carbon nitride materials [60,82,83].

2.1 Types of carbon nitrides

From past two decades, two-dimensional carbon nitride C_xN_y or CNs-based nanomaterials have fascinated the researchers because of their graphene-like structure which have open band gap, large specific surface area, and good chemical stability. These unique features make carbon nitride-based nanomaterials ideal for ample applications ranging from electrocatalysis, electronics, photocatalysis, gas adsorption, and energy storage devices [82–86]. So far, various compounds of carbon nitride was discovered via altering the value of x and y in C_xN_y with different stoichiometric ratios between C and N. These compounds have been well recognized and reported in the literature with composition details as g-C_3N_4, CN, C_2N, C_3N, C_2N_2, C_2N_3,C_5N, and C_5N_2 [87]. The arrangement of C and N atoms in these C_xN_y compounds is identical to arrangement of C and H atoms in a benzene ring structure with similar sp^2 hydridization as shown in Fig. 3.1. Due to this, these compounds display different physicochemical properties with tuneable band gap and structural features. In the available carbon nitride compounds, g-C_3N_4, C_2N, and C_3N have fascinated much more attentions of the research community because of ease in fabrication, tuneable band gap, high absorption capacity toward visible light, make them potential candidate for catalysis applications including photocatalysis and electrocatalysis.

2.2 Graphitic carbon nitride (g-CNs)

g-CNs is the most stable and hardest form of carbon nitride. It has graphite-like planes with sp^2-hybridized C and N atoms. Incorporation of nitrogen atoms (i.e., *s*-triazine and tri-*s*-triazine) into g-CNs makes it most suitable for various applications including photocatalysis [88,89], energy storage [90], solar cells [91], and sensors [92]. They can also be applicable in removal of various organic and inorganic wastes from water. Several functional groups (like $-NH_2$, $>N-N<$, $=N-$, $-NH-$, $=C-N<$, etc.) present on the surface of g-CNs provides active sites for the adsorption or interaction with the organic or inorganic contaminants from effluent [93]. g-CNs are either linked through physical interactions (comprising electrostatic interactions, π–π conjugated interactions, and hydrophobic interactions) and/or chemical interactions (including complex

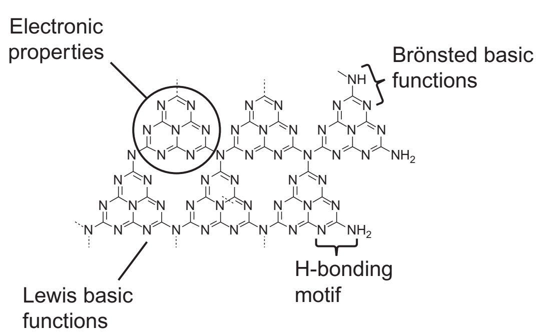

Fig. 3.1 Structure of g-CNs with multiple surface functionalities found on their surface.

formation or acid-base formation) with the impurities and thereby boosts their removal from waste water.

Graphitic carbon nitride is a general term that is in practice for compounds having different chemical and structural characteristics but containing graphitic planes with sp^2-hybridized C and N atoms. Recently, many publications set a tradition to use "g-C_3N_4" compounds instead of graphitic carbon nitride or g-CNs-based compounds. However, this is inappropriately referred to as "g-C_3N_4" compounds because it is very difficult to fabricate a compound having exactly 3:4 C:N ratio. These compounds always contain the considerable concentrations of H and O, although the word "graphitic" layers are probable to be far from complete, and the sheet-like domains are unlikely to be planar [94]. The g-CNs-based materials have been recognized in various distinct classes. The first type of class, commonly known as N-doped carbons, in which a graphitic carbon or graphene-like carbons or carbon nanotubes were synthesized and then incorporation of N was done that extends up to a few atomic percent [95,96]. They also contain some metallic properties [96,97]. These types of materials are termed as N-doped carbons rather than g-CNs and have been tremendously were used in electrocatalyst supports since 1980s [98,99]. They are prepared when carbonaceous materials are pyrolyzed along with nitrogen-containing precursors. Although they show good performance with less platinum loading but synthesis and durability issues limits their applicability as fuel cell catalyst. The performances of carbonaceous-based materials were further improved via various synthesis approaches including combination of various transition metal atoms [100–102]. In nitrogen-doped carbon materials, lone pair of electrons on nitrogen introduces/increases electron cloud which is localized on N-atom, whereas, in graphitic carbon nitrides contains several anchoring sites for Pt as well as adsorption sites for carbon monoxide (CO) like abundant Lewis acid and base sites (terminal and bridging NH— groups and lone pairs of N in triazine/heptazine rings, respectively).

3. Graphitic carbon nitrides as fuel cell electrocatalyst support material

Due to high nitrogen content, simplistic synthesis and tunability in polymeric structure of graphitic carbon nitride make them suitable candidate for fuel cell electrocatalyst support. They provide a worthy balance in three major commercialization hindrances of fuel cells, i.e., cost, performance and durability. g-CNs fascinated the researcher with their amazing steady chemical structure under high temperature and harsh condition of high acidic or basic mediums [103–105]. Owing to the presence of nitrogen atoms, they provide an appropriate synergistic bonding environment for anchoring metal nanoparticles. The triazine units can form efficient coordination complex with metal nanoparticles, thereby increasing the durability of electrocatalyst. This excellent feature makes them a promising durable candidate for fuel cell catalyst substrate. The 2D graphitic carbon nitrides can provide much higher specific surface area as compared to the bulk material and therefore exhibits outstanding electrocatalytic performance for oxygen reduction reaction. Many studies have been reported which shows the enhanced catalytic performance of these materials in basic medium. The poor conductivity is the major obstacle for application of these materials as an electrocatalytic support in acidic medium. Recently many novel approaches were adopted for increasing their specific surface area by integrating them with conductive carbon or metal nanoparticles [28,89,95]. These approaches have been successfully demonstrated by various research groups to increase the surface area to some level. First, Yu et al. exhibited the application of carbon nitride as catalyst support in direct methanol fuel cell (DMFC). They showed that PtRu supported on graphitic carbon nitride shows more than 75% of power density as compared to that on Vulcan XC-72 [106]. Earlier, it has been reported that Pt deposited on graphitic carbon nitride shows more stability as well as durability under acidic environment as compared to commercial Pt/Vulcan after 1000 scans and has superior methanol oxidation activity per electrochemical surface area [107]. Zheng et al. demonstrate that graphitic carbon nitride composite with carbon black shows comparable catalytic activity to that achieved by commercial Pt/C. Here, the metal-free carbon nitride-based electrocatalyst shows high durability as well as better tolerance toward carbon monoxide [108]. Recently, graphitic carbon nitrides are demonstrated as extremely durable Pt electrocatalyst support for fuel cells. Here, Pt deposited on three different graphitic carbon nitride materials (i.e., polymeric carbon nitride, crystalline poly(triazine) amide, and boron-doped graphitic carbon nitride) were synthesized and found to be more electrochemically stable as compared to conventional commercial Pt/Vulcan XC 72R elctrocatalyst. Fig. 3.2 displays the corrosion behavior for modified graphitic carbon nitride materials and Pt/Vulcan XC 72R. After 2000 cycles, all graphitic carbon nitride materials exhibit a higher degree of tolerance to cycling, compared to commercial carbon black (Vulcan XC72R) also, with boron doped graphitic carbon nitride showing the best tolerance toward methanol oxidation [109].

3.1 Electronic structure and physicochemical properties of g-CNs electrocatalyst

The lone pair of electron of nitrogen in graphitic carbon nitrides is primarily responsible for band structure and development of valence band. Moreover, in electronic structure, the valence and conduction bands are primarily formed by overlapping of 2*p* orbital of N and 2*p* orbital C atom. The 2D structure of g-CNs can be thought as N-substituted graphene planes in graphite with sp^2-hybridized C and N atoms in aromatic rings. The lone pair electron of N is considered to form valence band, which is stabilized by *p* electronic state and results in the formation of band gap of 2.7 eV. Generally, carbon nitride possesses graphitic-like structure. Still the ground state structure of g-CNs was not clear and much more clarification is needed. Thermal poly-condensation method is generally used to prepare g-CNs and the X-ray diffraction (XRD) patterns are applied to analyze

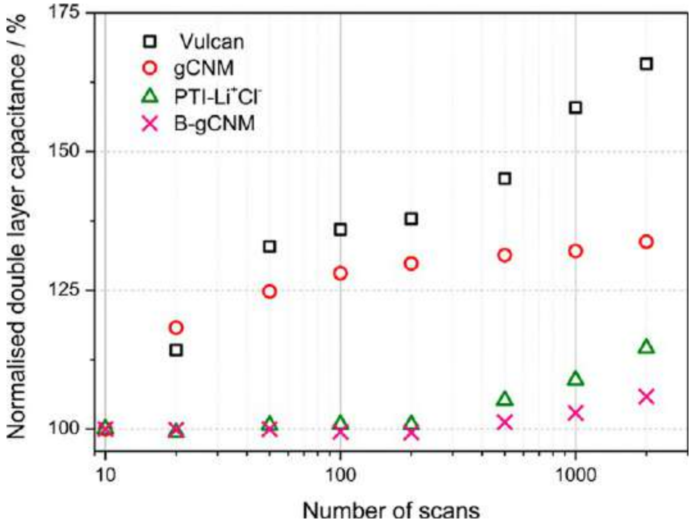

Fig. 3.2 Comparison of change in double-layer capacitance of the different support materials as a result of accelerated carbon corrosion cycling. Here, gCNM is polymeric carbon nitride; PTI/Li^+Cl^- is crystalline poly(triazine)imide; B-gCNM is B-doped graphitic carbon nitride; Vulcan XC 72R.

the crystal structure of g-CNs. Due to low crystallinity of g-CNs, XRD usually shows only two peaks at 13.04 degree and 27.25 degree. These peaks may correspond to in-plane ordering with repeated distance of about 6.788 Å and graphitic interlayer distance of 3.273 Å [110,111]. But due to synthetic restrictions, the precise stacking position of C and N atoms with respect to adjacent layers is not understandable.

The allotropes of g-CNs were generally synthesized by triazine (C_3N_4) and tri-*s*-triazine (or heptazine, C_6N_7) units. Among these phase of carbon nitride, heptazine-based g-CNs (or g-HCN) is believed as the most stable structure. g-CNH can exist in three different configurations, ranging from most stable configuration, stable distorted configuration, most stable planar configuration with specific band gap of 2.87, 3.14, and 2.27 eV, respectively. The g-CNH includes a range of "graphitic" or polymeric structures with compositions extending along tie-line between C_2N_3H and C_3N_4 in a ternary C—N—H phase diagram. They are readily synthesized by condensation reactions of dicyandiamide, melamine or urea at 500–700°C temperature range [112]. Whereas at lower temperatures poly-heptazines (PHs) formed with poorly organized ribbon-like structures terminated sideways by —NH— and —NH_2 groups. When the processing temperature is increased, the extent of condensation reaction increases with removal of NH_3 molecules and sheet-like graphitic structures initiated to form. Another class of g-CNs is formed when independent triazine (C_3N_3) rings linked together by —N= or —NH— groups to construct polytriazine imide (PTI) layers. These PTI layers were manufactured form chemical vapor deposition (CVD) techniques in nanocrystalline structure [113,114]. During the molten salt synthesis, a crystalline form of g-CN is produced, known as triazine-based g-CN or TGCN. These were deposited on the wall of the reaction vessel also at the molten phase surface [115]. TGCN layers consist of C_6N_6 voids, which are arranged according to the AB or ABC type stacking [115].

For enhancing the structural properties, incorporation of hetero atom such as H, Li, Br, and Cl has been done in PTI family. These were synthesized via implying molten salt like LiCl and KBr at high temperature or high pressure conditions [116,117]. They contain larger ring voids of $C_{12}N_{12}$ in between the layers along with hetero atoms ions such as H^+, Li^+, Br^-, and Cl^- exist in the interlayer spacing or in voids. Herein, the triazine units are connected with —NH— groups which attached along the interior of these void sites, whereas H^+ easily substitute the Li^+ cation. Moreover, Li^+ ions species may be exist in between the layers as shown in the Fig. 3.3 [116,117]. Fig. 3.3 displays the structural motifs found in graphitic carbon nitrides in which (a) shows the Liebig's melon ($[C_6N_7(NH_2)(NH)]_n$) with zig-zag chains of heptazine (or tri-*s*-triazine) units linked by bridging nitrogen and their edges are decorated by N—H groups; (b) shows the fully condensed C_3N_4 layer based on heptazine units; (c) shows the fully condensed C_3N_4 layer based on triazine units; (d) shows the PTI backbone based on triazine ring units, linked by N—H bridges; and (e) shows the side elevation of fully occupied PTI·LiCl.

3.2 Pristine graphitic carbon nitride applied as catalyst support for fuel cell

g-CNs are carbon materials with high N content along with extremely well chemical, mechanical, and thermal stability. Due to these properties, they are considered as better aptness for fuel cell electrocatalyst support [118,119]. Their structure contains high concentration of NH— functional group also, lone pair of electrons is present on nitrogen atoms of triazine or heptazine units. These sites provide improved environment for tethering metal nanoparticles with them. Owing to high N content, they provide intrinsic catalytic activity toward redox reactions. Studies reflect their better behavior toward corrosion as compared to commercially used carbon black support. Recently, Lyth et al. investigated the intrinsic catalytic activity for the ORR of g-CNH synthesized from cyanuric chloride [120]. They reported efficient catalytic properties of g-CNH as compared to carbon black. The pyridinic sites anchored within g-CNH not only provide better position for metal NP incorporation but also reduce the formation of aggregates and thereby increase the catalytic activity. Kim et al. reported more than 80% increment of PtRu supported on g-CNH as compared to PtRu supported carbon black [106]. Further, g-CNH and PTI materials exhibits enhanced electrochemical stability than carbon black during accelerated corrosion testing as reported by Mansor et al. [109]. Here,

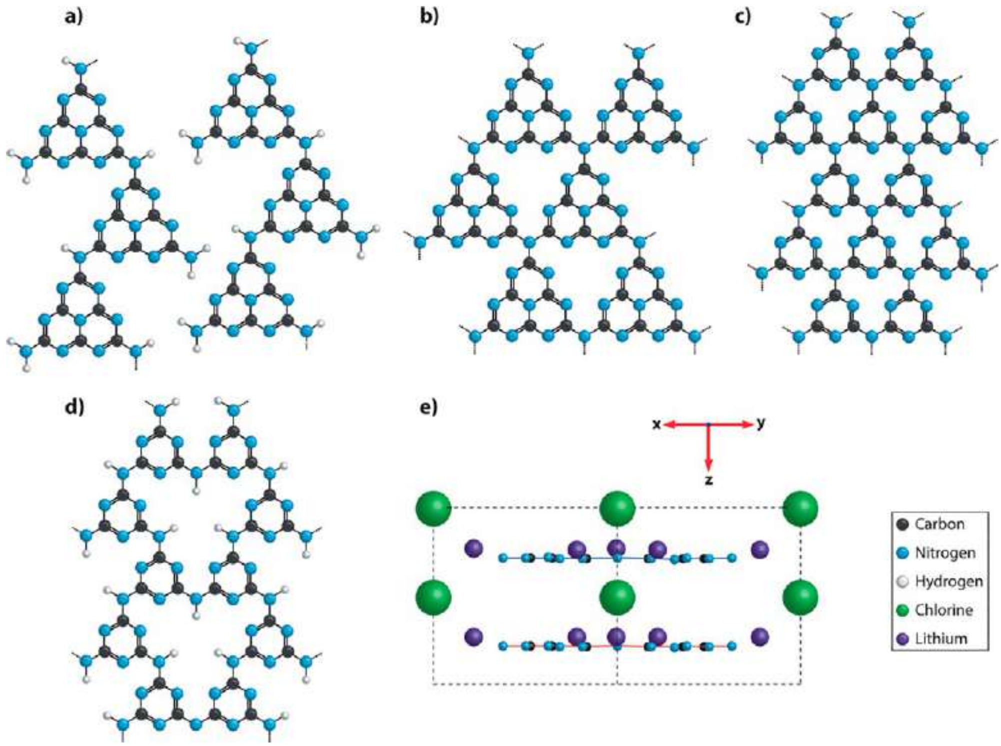

Fig. 3.3 Structural motifs found in graphitic carbon nitrides. (A) Liebig's melon model; (B) fully condensed C_3N_4 layer; (C) fully condensed C_3N_4; (D) PTI backbone based on triazine ring units, linked by N—H bridges; and (E) side elevation of fully occupied PTI·LiCl.

PTI·LiCl integrated material shows excellent durability, as defined by changes in the ECSA under potential cycling, and shows superior intrinsic methanol oxidation activity.

A major barrier toward the use of g-CNs as catalyst supports for metal NPs or as metal-free catalyst is their poor conductivity, because of their semiconducting nature. This not only limits their intrinsic electrical conductivity but also bound their practical application. Miller et al. illustrate that g-CNH-based Li-ion battery anodes have low conductivity or high resistivity which lowers its Li storage capacities [121]. On the other hand, when these materials are employed as an anodic catalyst support in fuel cells, they show fast reaction kinetics toward hydrogen evolution reaction (HOR). However, with sluggish kinetics of cathodic ORR, these materials show reduced performance. Kim et al. had reported that hybrid materials, in which g-CNs materials combined with high conductive carbon nanomaterials can overcome the issues of poor conductivity [106].

3.3 Hybrid g-CNs/carbon composite materials-based electrocatalysts and catalysts support

A theoretical study was conducted by using first principle employing pure melem units ($C_6N_{10}H_6$) as a base model for estimating the behavior of g-CNH. These materials shown decrease electron-transfer efficiency for the ORR and also favoring 2-electron over the direct 4-electron pathway which ultimately generating harmful intermediates like H_2O_2 [108]. As displayed in Fig. 3.4, the number of electrons accumulated on the melem surface is increasing by adding conductive substrate which takes part in the reaction, therefore, facilitating the direct 4-electron pathway in ORR process. Consequently, many studies have concentrated on analysis of the performance in g-CN/C composite materials as metal-free electrocatalysts and catalyst supports for fuel cell electrodes [122,123].

Graphene and grapheme-based materials like reduced graphene oxide (rGO) are most common and potential candidate for conducting substrate for g-CNH because of their high surface area and electrical conductivity [124–126]. Also, theoretical studies using

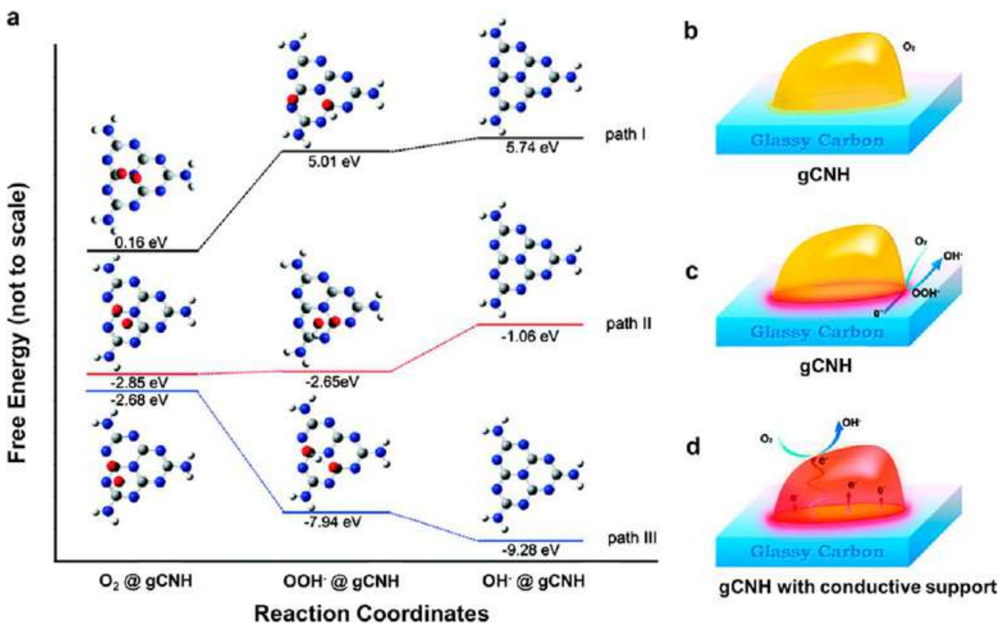

Fig. 3.4 (A) Free energy plots of ORR and optimized configurations of adsorbed species on the g-C_3N_4 surface with zero, two, and four-electron participation demonstrated as paths I, II, and III energy levels. Here, C, N, O, and H are represented by the balls and arranged according to the g-C_3N_4 structures. (B–D) Schemes of ORR's pathway on pristine g-C_3N_4 without electron participation, pristine g-C_3N_4 with $2e^-$ participation, and g-C_3N_4 and conductive support composite with $4e^-$ participation, respectively (*red* (*dark gray* in print version) areas represent the active sites facilitating ORR).

density functional theory (DFT) calculations in g-C_3N_4 material clearly shows a strong electronic coupling and charge transfer at the interface with graphene or rGO, which subsequently increase the electronic conductivity of the g-CNs [127]. As reported previously, experimentally observed results show that metal-free g-CNH-graphene composite-based electrocatalysts displayed an excellent ORR performance in alkaline electrolytes [122,128,129]. Also, electrocatalyst includes metals such as Pd and Pt-Ru supported on g-CNH/rGO demonstrated very high electrocatalytic activity with enhanced durability and alcohol tolerance [130]. All these research reports highlighted the prominence of optimizing the g-CN to graphene ratio in the composite materials to maintain the catalytic activity while improving the conductivity, simultaneously.

Another report displays a hybrid carbon nitride-reduced graphene oxide (g-CNH-rGO) composite materials were synthesized as an EC support for the ORR and HOR [131]. This g-CNH-rGO composite only contained ~30% graphene (rGO) with g-CNH as rest. The structure of the composite material is well integrated in which rGO layers closely associated with g-CNH to provide the conductive backbone. There Pt was subsequently deposited through modified $NaBH_4$-assisted ethylene glycol reduction method, which resulting an excellent dispersion of Pt nanoparticles (NPs) on the support. Although ECSA of Pt-supported gCNH/rGO is lower than commercial Pt/C, but it results three times enlarged value as compare to Pt on g-CNH alone, which clearly reveal that the incorporation of rGO enhances the electronic conductivity of the support and also enhances the electrical contact NPs to greater extent. The Pt-supported gCNH/rGO (Pt/gCNH-rGO) composite-based material has high ORR activity as compared to Pt/g-CNH or Pt/rGO. Whereas the addition of rGO into the composite resulted in an improvement in the electronic conductivity, but the layered structure of graphene restricted the number of active sites and mass transport access for reactants, which negatively affecting the ORR performance. The HOR performance of Pt/gCNH-rGO is comparable to commercial Pt/C because the HOR is a very fast reaction [132]; hence, the lowered ECSA has less impact on the catalytic performance here [103]. The fuel cell anodes frequently suffer from durability issues due to fuel cell operation, which ultimately results corrosion on electrode over time. Whereas Pt-supported gCNH/rGO (Pt/gCNH-rGO) composite-based material results long-term durability in comparison with commercial Pt/C. Hence, the hybrid Pt/gCNH-rGO composite is suitable substitute for anode catalyst support for PEM fuel cells [103].

3.4 Three-dimensional g-CN/carbon hybrid composite as electrocatalysts and catalysts support

Various methods were explore for synthesizing an ordered *three-dimensional (3D)* structure of g-CNH having a high surface area, abundant N active sites, porous structure along with high electrical conductivity. A report by Liang et al. showed a pathway to fabricate the 3D g-CNH materials via thermal poly-condensation of precursors deposited on a framework structure made from melamine sponge, which result a microporous structure having 3D interrelated network composed of 2D g-CNH nanosheets with hierarchical pores [133]. Other 3D frameworks were formed by incorporation of g-CNH, rGO, or carbon nanotubes (CNT) via hydrothermal synthesis, followed by freeze-drying/supercritical drying [134,135], or by chemical cross linking approaches [136]. Here, exfoliated g-CNH nanosheets were homogeneously dispersed in solution by mixing with GO and 3D network which was formed during the hydrothermal process, due to the partial removal of oxygen-containing groups from GO and restoration of van der Waals forces [135–137]. The exfoliated g-CNH nanosheets adhere onto the rGO surfaces, therefore, incorporated in the 3D porous network [135,137]. Huang et al. produced a 3D hybrid monolith with hierarchical pore distribution which has BET surface area $\sim 376\,m^2\,g^{-1}$ and homogeneous dispersion of ultrafine Pt NPs [134]. This interconnected and porous hybrid 3D catalyst system exhibited an excellent EC activity, high tolerance to poisoning, and reliable stability when used as anode ECs for DMFCs. One more 3D hybrid material was developed via using a highly crystalline PTI rather than an amorphous g-CNH. There Pt was deposited onto 3D material through ethylene glycol reduction which yielded NPs having average size ~5 nm. The rotating disk electrode results showed that the Pt/PTI-rGO hybrid composite revealed an enhanced ORR activity along with nearly 10 times higher current density than Pt on pristine PTI at 0.90 V (Fig. 3.5). This hybrid composite material also displayed a higher current density than Pt on rGO at 0.90 V that shows that this combination of PTI and rGO improving the overall performance. On the other hand, the current density of this composite was observed to be lower than that of commercial Pt/C. Further examination of routes to enhance the interaction between g-CNs and the conducting framework, the development of novel exfoliation ways for g-CNH and the enhancement of methods for improving the overall

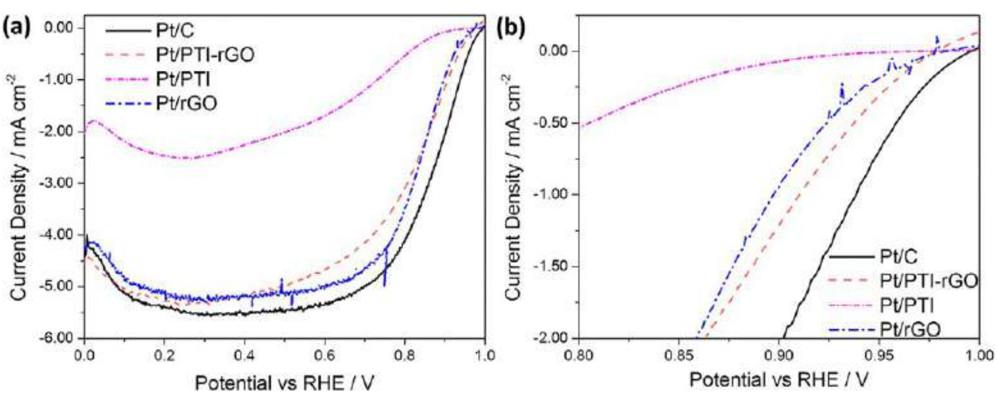

Fig. 3.5 Electrochemical (A) ORR polarization curves; (B) detailed highlighting the ORR overpotential region of PTI, and rGO, and PTI-rGO hybrid, in comparison to commercial Pt/C, at 1600 rpm in 0.1 M $HClO_4$.

surface area and therefore access to N-containing catalytic sites, will have considerable advantage in fuel cells applications.

3.5 Other type of hybrid g-CN/C composites electrocatalysts and catalyst supports

Various earth abundant nonnoble metals like Co and Fe with support on g-CNH mixed or hybrids-based composite was considered as suitable substitute for electrocatalysts for the ORR and HOR [138–140] in fuel cell applications. An excellent electrocatalyst was fabricated by Lie et al. via co-doping on g-CNH/graphene hybrid materials with high ORR activity and increased durability as compare to commercial Pt/C because of the formation of Co-N moieties which act as active sites to boost the quick charge transfer at the interface of Co-gCNH/graphene [139]. Afterward, Jin et al. synthesized a modified catalyst a novel core-shell structure in which CoO as core and Co-doped gCNH/graphene composite as shell. This modification leads to enhance the stability due to self-healing ability of CoO core that worked as a source of cobalt, deliberately liberating Co metal atoms or ions to heal the damaged active surface sites [140].

Some other elements like P and S also used for fabricating composite materials via doping with g-CNH which could as an EC supports. For instance, modified hybrid P-doped g-CNH grown on flexible carbon fiber paper (CFP) composite revealed an improved ORR activity as compared to its phosphorous-free composite and also comparable to Pt supported on carbon fiber paper (CFP) [141]. The EC-based composite material was also fabricated via using 2D nanohybrid structures based on graphene quantum dots decorated onto S-doped g-CNH. This S-gCNH-graphene quantum dots (or GQD) hybrid composite material was exhibited a high ORR activity which analogous to well-developed graphene and GQD-based catalysts [142]. Although, these heteroatom-doped g-CN hybrid composite materials aren't able to commercially available EC for fuel cell applications, but, however, they have the potential for fabricating new advanced types of g-CNH-based composite materials for commercial energy conversion technologies.

3.6 Integrated carbon nitrides-based electrocatalysts

The family of integrated carbon nitride-based electrocatalysts supports were composed of carbon-based matrix into which nitrogen atoms have been embedded [97]. They have comprises all of the N-doped carbons [143] which have structures ranging from N-doped carbon nanotubes [90] to N-doped mesoporous carbon [144]. They commonly have contained N contents of less than 5 atomic percent and exhibit significantly different catalytic behavior to the g-CN materials discussed above. CNs-based electrocatalysts are usually synthesized via one-pot synthesis in which solvated metal complexes and precursor molecules with large N content are adsorbed onto a carbon-based precursor and the subsequent obtained composite material is pyrolyzed to form the metal NPs and for the incorporation of nitrogen into the carbon matrix [98,99]. This methodology is used to fabricate bulk electrocatalysts [98] supports material but they are undefined structures and irreproducible that ultimately affects their overall performance and durability [97].

Another class of CNs-based ECs has fascinated the researcher, which have much more ordered and highly localized content of N atoms. These composites are fabricated via adopting devising strategies to intelligently incorporate catalyst precursors within carbon based matrices [145–147]. A report by Di Noto et al. showed that they were able to develop 3D cross linked inorganic-organic network in which metal ions have coordination with N-containing macromolecular ligands. They used soft pyrolysis technique than graphitized to form a foam-like conductive carbon based matrix in which NPs were held in stabilizing the "N co-ordination nests" [97,145,146]. Afterward, this method has been further modified via introduction of a core-shell approach [148,149] in which the metal and its surrounding N-containing matrix are constructed onto a conductive core. By employing this method, a standard Pt NPs could also be replaced with Pd in ORR ECs [91,150] or a bimetallic system [151], while attaining a decrease in ORR over potential as compare to commercial Pt/C [152]. Another report by Wu et al. had used a high Pt loading core-shell structures to increase the activity for methanol oxidation over Pt/C because of higher Pt loading a more rapid charge transfer is occur [87].

4. Summary and outlook

Over the past few decades, carbon nitrides have fascinated the researcher from their various advantageous properties which includes graphene-like structure, high nitrogen content, open band gap, large surface area, chemical steadiness toward oxidation/reduction environment and tuneable surface chemistry, etc. These properties enable them to be used in numerous applications including electronics, photocatalysis, energy storage devices, gas adsorption, electrocatalyst supports, etc. Among all these applications, fuel cell catalyst support is the most appealing field for green energy conversion technologies. As carbon nitrides contain high N atomic percentage, they can be used as promising cost effective and highly efficient futuristic fuel cell catalyst support. g-CN support has prospective to bind effectively with metal nanoparticles, and several N group present on its surface provides well-organized environment for synergic bonding. From the various results evaluated earlier, the improvement of catalyst dispersion, durability, reduced metal loading, and resistant nature toward oxidation demonstrate the improved catalyst performance of these materials. However, the development of g-CN as an emerging efficient fuel cell catalyst support has been done through systematic studies. The deeper understanding of g-CN support interaction with metal nanoparticles and their role in determining the fuel cell reactions kinetics is necessary. Apart from this, it is also important to improve the structure and chemistry of g-CN materials along with their interaction through other conductive carbonaceous materials in hybrid supports.

The development of new scientific approaches for 3D porous networks or materials based on g-CN is an attractive area for futuristic advancement toward commercialization of fuel cell technology. Here, the N-rich regions and metal nanoparticles are incorporated along with high conductive carbon material like graphene or carbon nanotubes. It will be significantly important to proceed with the identified and tested materials for efficient and inexpensive synthesis for large-scale production and thereby commercialization of fuel cell technology for variety of energy conversion applications.

Acknowledgment

The author AB and CG highly acknowledges UGC for Dr. DSK-PDF award (4-2/2006(BSR)/CH/18-19/0184) and UGC for Dr. DSK-PDF award (4-2/2006(BSR)/CH/17-18/0267) respectively.

References

[1] The Energy Outlook Report 2021, Brunel International N.V. John M. Keynesplein, Amsterdam, Netherlands.
[2] T. Ahmad, D. Zhang, A critical review of comparative global historical energy consumption and future demand: the story told so far, Energy Rep. 6 (2020) 1973–1991.
[3] International Energy Agency, Technology Roadmap – Hydrogen and Fuel Cells, IEA Publications, Paris, 2015.
[4] The European Commission High Level Group, EUR 20719 EN – Hydrogen Energy and Fuel Cells – A Vision of Our Future, European Commission, Brussels, 2003.
[5] Fuel Cells: Experiments, Activities and Useful Information, Prepared by H. T. Roman, presented in Charles Edison Fund Edison Innovation Foundation, 2008.
[6] Z. Li, Z. Zheng, L. Xu, X. Lu, A review of the applications of fuel cells in microgrids: opportunities and challenges, BMC Energy 1 (2019). Article number 8.
[7] G. Pearson, M. Leary, A. Subic, J. Wellnitz, Performance comparison of hydrogen fuel cell and hydrogen internal combustion engine racing cars, in: Proceedings of 3rd International Conference, 2011.
[8] J.B. Heywood, M.A. Weiss, A. Schafer, S.A. Bassene, V.K. Natarajan, The Performance of Future ICE and Fuel Cell Powered Vehicles and Their Potential Fleet Impact, Paper number 04P-254, Laboratory for the Energy and the Environmental, Massachusetts Institute of Technology, MA, USA, 2003.
[9] N. Sazali, W.N.W. Salleh, A.S. Jamaludin, M.N.M. Razali, New perspectives on fuel cell technology: a brief review, Membranes (Basel) 10 (5) (2020) 99.
[10] L.J.M.J. Blomen, M.N. Mugerwa, Fuel Cell Systems, A Division of Plenum Publishing Co-operation, 1993.
[11] Fuel Cells: A Better Energy Source for Earth and Space, Glenn Research Centre, NASA, 2005.
[12] World Energy Use Projected to Grow 49 Percent Between 2007 and 2035, U.S. Energy Information Administration, Washington, DC, 2010.
[13] Y. Wang, K.S. Chen, J. Mishler, S.C. Cho, X.C. Adroher, A review of polymer electrolyte membrane fuel cells: technology, applications and needs on fundamental research, Appl. Energy 88 (2011) 981.
[14] Y. Wang, D.F.R. Diaz, K.S. Chen, Z. Wang, X.C. Adroher, Materials, technological status, and fundamentals of PEM fuel cells – a review, Mater. Today 32 (2020) 178–203.

[15] Just the Basics: Fuel Cells, U.S. Department of Energy, Office of Energy Efficiency and Renewable Energy, 2003.
[16] M. Winter, R.J. Brodd, What are batteries, fuel cells, and supercapacitors? Chem. Rev. 104 (2004) 4245.
[17] C.E. Thomas, Fuel cell and battery electric vehicles compared, Int. J. Hydrog. Energy 34 (2009) 6005.
[18] J. Spendelow, J. Marcinkoski, DOE Fuel Cell Technologies Office Record 14012: Fuel Cell System Cost – 2013, Fuel Cell Technologies Office, 2013.
[19] U.S DRIVE Partnership, Fuel Cell Technical Team Roadmap, 2013.
[20] K. Kinoshita, Particle size effects for oxygen reduction on highly dispersed platinum in acid electrolytes, J. Electrochem. Soc. 137 (1990) 845.
[21] R.M. Rioux, H. Song, J.D. Hoefelmeyer, P. Yang, G.A. Somorjai, High-surface area catalyst design: synthesis, characterization, and reaction studies of platinum nanoparticles in mesoporous SBA-15 silica, J. Phys. Chem. B 109 (2005) 2192.
[22] I. Lee, R. Morales, M.A. Albiter, F. Zaera, Synthesis of heterogeneous catalysts with well shaped platinum particles to control reaction selectivity, Proc. Natl. Acad. Sci. 105 (2008) 15241.
[23] A. Chalgin, C. Song, P. Tao, W. Shang, T. Denga, J. Wu, Effect of supporting materials on the electrocatalytic activity, stability and selectivity of noble metal-based catalysts for oxygen reduction and hydrogen evolution reactions, Prog. Nat. Sci. Mater. Int. 30 (3) (2020) 289–297.
[24] H. Huang, X. Wang, Recent progress on carbon-based support materials for electrocatalysts of direct methanol fuel cells, J. Mater. Chem. A 2 (2014) 6266–6291.
[25] S. Samad, K.S. Loh, W.Y. Wong, T.K. Lee, J. Sunarso, S.T. Chong, W.R.W. Daud, Carbon and non-carbon support materials for platinum-based catalysts in fuel cells, Int. J. Hydrog. Energy 43 (16) (2018) 7823–7854.
[26] X.X. Wang, Z.H. Tan, M. Zeng, J.N. Wang, Carbon nanocages: a new support material for Pt catalyst with remarkably high durability, Sci. Rep. 4 (2014). Article number 4437.
[27] K. Yoshii, K. Yamaji, T. Tsuda, H. Matsumoto, T. Sato, R. Izumi, T. Torimoto, S. Kuwabata, Highly durable Pt nanoparticle-supported carbon catalysts for the oxygen reduction reaction tailored by using an ionic liquid thin layer, J. Mater. Chem. A 4 (2016) 12152–12157.
[28] B. Fang, N.K. Chaudhari, M.S. Kim, J.H. Kim, J.S. Yu, Homogeneous deposition of platinum nanoparticles on carbon black for proton exchange membrane fuel cell, J. Am. Chem. Soc. 131 (2009) 15330.
[29] K.E. Swider, D.R. Rolison, Catalytic desulfurization of carbon black on a platinum oxide electrode, Langmuir 15 (1999) 3302.
[30] S. Sharma, B.G. Pollet, Support materials for PEMFC and DMFC electrocatalysts—a review, J. Power Sources 208 (15) (2012) 96–119.
[31] G. Sevjidsuren, S. Zils, S. Kaserer, A. Wolz, F. Ettingshausen, D. Dixon, Effect of different support morphologies and pt particle sizes in electrocatalysts for fuel cell applications, J. Nanomater. 2010 (2010) 73.
[32] B. Kuppan, P. Selvam, Platinum-supported mesoporous carbon (Pt/CMK-3) as anodic catalyst for direct methanol fuel cell applications: the effect of preparation and deposition methods, Prog. Nat. Sci. Mater. Int. 22 (2012) 616.
[33] C. Liu, M. Chen, C. Du, J. Zhang, G. Yin, P. Shi, Durability of ordered mesoporous carbon supported Pt particles as catalysts for direct formic acid fuel cells, Int. J. Electrochem. Sci. 7 (2012) 10592.
[34] A. Smirnova, X. Dong, H. Hara, A. Vasiliev, N. Sammes, Novel carbon aerogel supported catalysts for PEM fuel cell application, Int. J. Hydrog. Energy 30 (2005) 149.
[35] J. Marie, S. Berthon-Fabry, P. Achard, M. Chatenet, A. Pradourat, E. Chainet, Highly dispersed platinum on carbon aerogels as supported catalysts for PEM fuel cell electrodes: comparison of two different synthesis paths, J. Non-Cryst. Solids 350 (2004) 88.
[36] E. Guilminot, F. Fischer, M. Chatenet, A. Rigacci, S. Berthon-Fabry, P. Achard, E. Chainet, Use of cellulose-based carbon aerogels as catalyst support for PEM fuel cell electrodes: electrochemical characterization, J. Power Sources 166 (2007) 104.
[37] A.L. Dicks, The role of carbon in fuel cells, J. Power Sources 156 (2006) 128.

[38] Z. Liu, X. Lin, J.Y. Lee, W. Zhang, M. Han, L.M. Gan, Preparation and characterization of platinum-based electrocatalysts on multiwalled carbon nanotubes for proton exchange membrane fuel cells, Langmuir 18 (2002) 4054.
[39] W. Li, C. Liang, J. Qiu, W. Zhou, H. Han, Z. Wei, Carbon nanotubes as support for cathode catalyst of a direct methanol fuel cell, Carbon 40 (2002) 791.
[40] C.T. Hsieh, W.M. Hung, W.Y. Chen, Electrochemical activity and stability of Pt catalysts on carbon nanotube/carbon paper composite electrodes, Int. J. Hydrog. Energy 35 (2010) 8425.
[41] W. Li, C. Liang, W. Zhou, J. Qiu, H. Li, G. Sun, Homogeneous and controllable Pt particles deposited on multi-wall carbon nanotubes as cathode catalyst for direct methanol fuel cells, Carbon 42 (2004) 436.
[42] N. Rajalakshmi, H. Ryu, M.M. Shaijumon, S. Ramaprabhu, Performance of polymer electrolyte membrane fuel cells with carbon nanotubes as oxygen reduction catalyst support material, J. Power Sources 140 (2005) 250.
[43] P. Divya, S. Ramaprabhu, Platinum-graphene hybrid nanostructure as anode and cathode electrocatalysts in proton exchange membrane fuel cells, J. Mater. Chem. A 2 (2014) 4912.
[44] W. Li, X. Wang, Z. Chen, M. Waje, Y. Yan, Carbon nanotube film by filtration as cathode catalyst support for proton-exchange membrane fuel cell, Langmuir 21 (2005) 9386.
[45] E. Antolini, Carbon supports for low-temperature fuel cell catalysts, Appl. Catal. B Environ. 88 (2009) 1.
[46] W. Zhang, P. Sherrell, A.I. Minett, J.M. Razal, J. Chen, Carbon nanotube architectures as catalyst supports for proton exchange membrane fuel cells, Energy Environ. Sci. 3 (2010) 1286.
[47] C. Gupta, P.H. Maheshwari, S. Sasikala, R.B. Mathur, Processing of pristine carbon nanotube supported platinum as catalyst for PEM fuel cell, Mater. Renew. Sustain. Energy 3 (2014) 1.
[48] T. Yoshitake, Y. Shimakawa, S. Kuroshima, H. Kimura, T. Ichihashi, Y. Kubo, D. Kasuya, K. Takahashi, F. Kokai, M. Yudasaka, S. Iijima, Preparation of fine platinum catalyst supported on single-wall carbon nanohorns for fuel cell application, Phys. B Condens. Matter 323 (2002) 124.
[49] C. Kim, Y.J. Kim, Y.A. Kim, T. Yanagisawa, K.C. Park, M. Endo, M.S. Dresselhaus, High performance of cup-stacked-type carbon nanotubes as a Pt–Ru catalyst support for fuel cell applications, J. Appl. Phys. 96 (2004) 5903.
[50] S. Zhu, G. Xu, Single-walled carbon nanohorns and their applications, Nanoscale 2 (2010) 2538.
[51] M. Kosaka, S. Kuroshima, K. Kobayashi, S. Sekino, T. Ichihashi, S. Nakamura, T. Yoshitake, Y. Kubo, Single-wall carbon nanohorns supporting Pt catalyst indirect methanol fuel cells, J. Phys. Chem. C 113 (2009) 8660.
[52] K.W. Park, Y.E. Sung, S. Han, Y. Yun, T. Hyeon, Origin of the enhanced catalytic activity of carbon nanocoil-supported PtRu alloy electrocatalysts, J. Phys. Chem. B 108 (2004) 939.
[53] T. Hyeon, S. Han, Y.E. Sung, K.W. Park, Y.W. Kim, High-performance direct methanol fuel cell electrodes using solid-phase-synthesized carbon nanocoils, Angew. Chem. 115 (2003) 4488.
[54] E.S. Steigerwalt, G.A. Deluga, D.E. Cliffel, C.M. Lukehart, A Pt-Ru/graphitic carbon nanofiber nanocomposite exhibiting high relative performance as a direct-methanol fuel cell anode catalyst, J. Phys. Chem. B 105 (2001) 8097.
[55] Y.L. Hsin, K.C. Hwang, C.T. Yeh, Poly (vinylpyrrolidone)-modified graphite carbon nanofibers as promising supports for PtRu catalysts in direct methanol fuel cells, J. Am. Chem. Soc. 129 (2007) 9999.
[56] J. Guo, G. Sun, Q. Wang, G. Wang, Z. Zhou, S. Tang, L. Jiang, B. Zhou, Q. Xin, Carbon nanofibers supported Pt–Ru electrocatalysts for direct methanol fuel cells, Carbon 44 (2006) 152.
[57] C.A. Bessel, K. Laubernds, N.M. Rodriguez, R.T.K. Baker, Graphite nanofibers as an electrode for fuel cell applications, J. Phys. Chem. B 105 (2001) 1115.
[58] H.-J. Choi, S.-M. Jung, J.-M. Seo, D.W. Chang, L. Dai, J.-B. Baek, Graphene for energy conversion and storage in fuel cells and supercapacitors, Nano Energy 1 (4) (2012) 534–551.
[59] J. Zhao, Z. Liu, H. Li, W. Hu, C. Zhao, P. Zhao, D. Shi, Development of a highly active electrocatalyst via ultrafine Pd nanoparticles dispersed on pristine graphene, Langmuir 31 (8) (2015) 2576–2583.

[60] J. Zhu, P. Xiao, H. Li, S.A.C. Carabineiro, Graphitic carbon nitride: synthesis, properties, and applications in catalysis, ACS Appl. Mater. Interfaces 6 (19) (2014) 16449–16465.

[61] M. Ismael, A review on graphitic carbon nitride (g-C_3N_4) based nanocomposites: synthesis, categories, and their application in photocatalysis, J. Alloys Compd. 846 (15) (2020), 156446.

[62] H.-X. Han, B.J. Feldman, Structural and optical properties of amorphous carbon nitride, Solid State Commun. 65 (9) (1988) 921–923.

[63] M. Deifallah, P.F. McMillan, F. Corà, Electronic and structural properties of two-dimensional carbon nitride graphenes, J. Phys. Chem. C 112 (14) (2008) 5447–5453.

[64] A.S. Arico, P. Bruce, B. Scrosati, J.M. Tarascon, W.V. Schalkwijk, Nanostructured materials for advanced energy conversion and storage devices, Nat. Mater. 4 (2005) 366.

[65] S. Mukerjee, Platinum Alloy Electrocatalyst With Enhanced Resistance to Anion Poisoning for Low and Medium Temperature Fuel Cells, U.S. Patent No. 8,912,114, 2014.

[66] D. Fofana, S.K. Natarajan, J. Hamelin, P. Benard, Low platinum, high limiting current density of the PEMFC (proton exchange membrane fuel cell) based on multilayer cathode catalyst approach, Energy 64 (2014) 398.

[67] P. Divya, S. Ramaprabhu, Platinum-graphene hybrid nanostructure as anode nd cathode electrocatalysts in proton exchange membrane fuel cells, J. Mater. Chem. A 2 (2014) 4912.

[68] B. Fang, J.H. Kim, M. Kim, M. Kim, J.S. Yu, Ordered hierarchical nanostructured carbon as a highly efficient cathode catalyst support in proton exchange membrane fuel cell, Chem. Mater. 21 (2009) 789.

[69] W. Zhang, J. Chen, A.I. Minett, G.F. Swiegers, C.O. Too, G.G. Wallace, Novel ACNT arrays based MEA structure-nano-Pt loaded ACNT/Nafion/ACNT for fuel cell applications, Chem. Commun. 46 (2010) 4824.

[70] V.D. Punetha, S. Rana, H.J. Yoo, A. Chaurasia, J.T. McLeskey Jr., M.S. Ramasamy, N.G. Sahoo, J.-W. Choc, Functionalization of carbon nanomaterials for advanced polymer nanocomposites: a comparison study between CNT and graphene, Prog. Polym. Sci. 67 (2017) 1–47.

[71] J.O. Medina, Z. Wang, R.C. Silva, A.M. Gomez, F. Wang, X.d. Yao, M. Terrones, M. Endo, Defect engineering and surface functionalization of nanocarbons for metal-free catalysis, Adv. Mater. 31 (13) (2019). 1805717.

[72] L. Dai, D.W. Chang, J.-B. Baek, W. Lu, Carbon nanomaterials for advanced energy conversion and storage, Small 8 (8) (2012) 1130–1166.

[73] Z. Li, L. Wang, Y. Li, Y. Feng, W. Feng, Carbon-based functional nanomaterials: preparation, properties and applications, Compos. Sci. Technol. 179 (28) (2019) 10–40.

[74] S. Miao, K. Liang, J. Zhu, B. Yang, D. Zhao, B. Kong, Hetero-atom-doped carbon dots: doping strategies, properties and applications, Nano Today 33 (2020), 100879.

[75] T.C. Nagaiah, A. Bordoloi, M.D. Snchez, M. Muhler, W. Schuhmann, Mesoporous nitrogen-rich carbon materials as catalysts for the oxygen reduction reaction in alkaline solution, ChemSusChem 5 (2012) 637–641.

[76] H. Zhang, Y. Zhou, C. Li, S. Chen, L. Liu, S. Liu, H. Yao, H. Hou, Porous nitrogen doped carbon foam with excellent resilience for self-supported oxygen reduction catalyst, Carbon 95 (2015) 388–395.

[77] M.L. Cohen, Calculation of bulk moduli of diamond and zinc blende solids, Phys. Rev. B 32 (1985) 7988–7991.

[78] A.Y. Liu, M.L. Cohen, Prediction of new low compressibility solids, Science 245 (1989) 841–842.

[79] J. Liebig, Uber einige Stickstoff-Verbindungen, Ann. Pharm. 10 (1834) 1–47.

[80] E.C. Franklin, The ammono carbonic acids, J. Am. Chem. Soc. 44 (1922) 486–509.

[81] V. Di Noto, E. Negro, S. Lavina, S. Gross, G. Pace, Pd-Co carbon-nitride electrocatalysts for polymer electrolyte fuel cells, Electrochim. Acta 53 (4) (2007) 1604–1617.

[82] N. Mansor, T.S. Miller, I. Dedigama, A.B. Jorge, J. Jia, V. Brázdová, C. Mattevi, C. Gibbs, D. Hodgson, P.R. Shearing, C.A. Howard, F. Corà, M. Shaffer, D.J.L. Brett, P.F. McMillan, Graphitic carbon nitride as a catalyst support in fuel cells and electrolyzers, Electrochim. Acta 222 (2016) 44–57.

[83] K. Qia, S.-y. Liu, A. Zada, Graphitic carbon nitride, a polymer photocatalyst, J. Taiwan Inst. Chem. Eng. 109 (2020) 111–123.
[84] Z. Zhao, Y. Sun, F. Dong, Graphitic carbon nitride based nanocomposites: a review, Nanoscale 7 (2015) 15–37.
[85] N. Rono, J.K. Kibet, B.S. Martincigh, V.O. Nyamoria, A review of the current status of graphitic carbon nitride, Crit. Rev. Solid State Mater. Sci. 46 (3) (2021) 189–217.
[86] T.S. Miller, A. Belen Jorge, T.M. Suter, A. Sella, F. Corà, P.F. McMillan, Carbon nitrides: synthesis and characterization of a new class of functional materials, Phys. Chem. Chem. Phys. 19 (2017) 15613.
[87] L. Tan, C. Nie, Z. Ao, H. Sun, T. An, S. Wang, Novel two-dimensional crystalline carbon nitrides beyond g-C_3N_4: structure and applications, J. Mater. Chem. A 9 (2021) 17.
[88] X. Wang, K. Maeda, A. Thomas, K. Takanabe, G. Xin, J.M. Carlsson, et al., A metal-free polymeric photocatalyst for hydrogen production from water under visible light, Nat. Mater. 8 (2009) 76.
[89] M. Groenewolt, M. Antonietti, Synthesis of g-C_3N_4 nanoparticles in mesoporous silica host matrices, Adv. Mater. 17 (2005) 1789–1792.
[90] S.J. Yang, J.H. Cho, G.H. Oh, K.S. Nahm, C.R. Park, Easy synthesis of highly nitrogen-enriched graphitic carbon with a high hydrogen storage capacity at room temperature, Carbon 47 (2009) 1585–1591.
[91] V. Di Noto, E. Negro, Development of nano-electrocatalysts based on carbon nitride supports for the ORR processes in PEM fuel cells, Electrochim. Acta 55 (2010), 756474.
[92] Y. Xu, W. Lei, J. Su, J. Hu, X. Yu, T. Zhou, et al., A high-performance electrochemical sensor based on g-C_3N_4-E-PEDOT for the determination of acetaminophen, Electrochim. Acta 259 (2018) 994–1003.
[93] E. Haque, J.W. Jun, S.N. Talapaneni, A. Vinu, S.H. Jhung, Superior adsorption capacity of mesoporous carbon nitride with basic CN framework for phenol, J. Mater. Chem. 20 (2010) 10801–10803.
[94] E. Kroke, M. Schwarz, Novel group 14 nitrides, Coord. Chem. Rev. 248 (2004) 493–532.
[95] H.Y. Du, C.H. Wang, H.C. Hsu, S.T. Chang, U.S. Chen, S.C. Yen, L.C. Chen, H.C. Shih, K.H. Chen, Controlled platinum nanoparticles uniformly dispersed on nitrogen-doped carbon nanotubes for methanol oxidation, Diam. Relat. Mater. 17 (2008) 535–541.
[96] J. Shui, M. Wang, F. Du, L. Dai, N-doped carbon nanomaterials are durable catalysts for oxygen reduction reaction in acidic fuel cells, Sci. Adv. 1 (2015) E1400129.
[97] V. Di Noto, E. Negro, K. Vezzù, F. Bertasi, G. Nawn, Origins, developments, and perspectives of carbon nitride-based electrocatalysts for application in low temperature FCs, Electrochem. Soc. Interface 24 (2015) 59–64.
[98] S. Gupta, D. Tryk, I. Bae, W. Aldred, E. Yeager, Heat-treated poly acrylo nitrile based catalysts for oxygen electro reduction, J. Appl. Electrochem. 19 (1989) 19–27.
[99] J.A.R. van Veen, J.F. van Baar, K.J. Kroese, Effect of heat treatment on the performance of carbon-supported transition-metal chelates in the electrochemical reduction of oxygen, J. Chem. Soc. Faraday Trans. 1 (77) (1981) 2827–2843.
[100] H. Wang, T. Maiyalagan, X. Wang, Review on recent progress in nitrogen doped graphene: synthesis, characterization, and its potential applications, ACS Catal. 2 (2012) 781–794.
[101] R. Czerw, M. Terrones, J.C. Charlier, X. Blase, B. Foley, R. Kamalakaran, N. Grobert, H. Terrones, D. Tekleab, P.M. Ajayan, W. Blau, M. Rühle, D.L. Carroll, Identification of electron donor states in N-doped carbon nanotubes, Nano Lett. 1 (2001) 457–460.
[102] K.N. Wood, R. O'Hayre, S. Pylypenko, Recent progress on nitrogen/carbon structures designed for use in energy and sustainability applications, Energy Environ. Sci. 7 (2014) 1212–1249.
[103] Y. Wang, J. Zhang, X. Wang, M. Antonietti, H. Li, Boron- and fluorine-containing mesoporous carbon nitride polymers: metal free catalysts for cyclohexane oxidation, Angew. Chem. Int. Ed. 49 (2010) 3356–3359.
[104] A.B. Jorge, D.J. Martin, M.T.S. Dhanoa, A.S. Rahman, N. Makwana, J. Tang, A. Sella, F. Cora, S. Firth, J.A. Darr, et al., H_2 and O_2 evolution from water half-splitting reactions by graphitic carbon nitride materials, J. Phys. Chem. C 117 (2013) 7178–7185.

[105] Y. Wang, X. Wang, M. Antonietti, Polymeric graphitic carbon nitride as a heterogeneous organocatalyst: from photochemistry to multipurpose catalysis to sustainable chemistry, Angew. Chem. Int. Ed. 51 (2012) 68–89.
[106] M. Kim, S. Hwang, J.-S. Yu, Novel ordered nanoporous graphitic C_3N_4 as a support for Pt–Ru anode catalyst in direct methanol fuel cell, J. Mater. Chem. 17 (2007) 1656–1659.
[107] N. Mansor, A. Belen Jorge, F. Cora, C. Gibbs, R. Jervis, P.F. McMillan, X. Wang, D.J.L. Brett, Development of graphitic carbon nitride materials as catalyst supports for polymer electrolyte fuel cells, ECS Trans. 58 (2013) 1767–1778.
[108] Y. Zheng, Y. Jiao, J. Chen, J. Liu, J. Liang, A. Du, W. Zhang, Z. Zhu, S.C. Smith, M. Jaroniec, et al., Nanoporous graphitic-C_3N_4@ carbon metal-free electrocatalysts for highly efficient oxygen reduction, J. Am. Chem. Soc. 133 (2011) 20116–20119.
[109] N. Mansor, A. Belen Jorge, F. Corà, C. Gibbs, R. Jervis, P.F. McMillan, X. Wang, D.J.L. Brett, Graphitic carbon nitride supported catalysts for polymer electrolyte fuel cells, J. Phys. Chem. C 118 (2014) 6831–6838.
[110] J. Wang, D. Hao, J. Ye, N. Umezawa, Determination of crystal structure of graphitic carbon nitride: ab initio evolutionary search and experimental validation, Chem. Mater. 29 (2017) 2694–2707.
[111] B.-w. Sun, H.-y. Yu, Y.-j. Yang, H.-j. Li, C.-y. Zhai, D.-J. Qian, M. Chen, New complete assignment of X-ray powder diffraction patterns in graphitic carbon nitride using discrete Fourier transform and direct experimental evidence, Phys. Chem. Chem. Phys. 19 (2017) 26072–26084.
[112] A. Schwarzer, T. Saplinova, E. Kroke, Tri-s-triazines (s-heptazines)—from a mystery molecule to industrially relevant carbon nitride materials, Chem. Rev. 257 (2013) 2032–2062.
[113] J. Kouvetakis, M. Todd, B. Wilkens, A. Bandari, N. Cave, Novel synthetic routes to carbon-nitrogen thin films, Chem. Mater. 6 (1994) 811–814.
[114] M. Todd, J. Kouvetakis, T.L. Groy, D. Chandrasekhar, D.J. Smith, P.W. Deal, Novel synthetic routes to carbon nitride, Chem. Mater. 7 (1995) 1422–1426.
[115] G. Algara-Siller, N. Severin, S.Y. Chong, T. Björkman, R.G. Palgrave, A. Laybourn, M. Antonietti, Y.Z. Khimyak, A.V. Krasheninnikov, J.P. Rabe, U. Kaiser, A.I. Cooper, A. Thomas, M.J. Bojdys, Triazine-based graphitic carbon nitride: a two-dimensional semiconductor, Angew. Chem. Int. Ed. 53 (2014) 7450–7455.
[116] E. Wirnhier, M. Döblinger, D. Gunzelmann, J. Senker, B.V. Lotsch, W. Schnick, Poly(triazine imide) with intercalation of lithium and chloride ions $[(C_3N_3)_2\ (NH_xLi_{1-x})_3\ LiCl]$: a crystalline 2D carbon nitride network, Chem. Eur. J. 17 (2011) 3213–3221.
[117] S.Y. Chong, J.T.A. Jones, Y.Z. Khimyak, A.I. Cooper, A. Thomas, M. Antonietti, M.J. Bojdys, Tuning of gallery heights in a crystalline 2D carbon nitride network, J. Mater. Chem. A 1 (2013) 1102–1107.
[118] X. Wang, K. Maeda, A. Thomas, K. Takanabe, G. Xin, J.M. Carlsson, K. Domen, M. Antonietti, A metal-free polymeric photocatalyst for hydrogen production from water under visible light, Nat. Mater. 8 (2009) 76–80.
[119] A. Thomas, A. Fischer, F. Goettmann, M. Antonietti, J.O. Muller, R. Schlogl, J.M. Carlsson, Graphitic carbon nitride materials: variation of structure and morphology and their use as metal-free catalysts, J. Mater. Chem. 18 (2008) 4893–4908.
[120] S.M. Lyth, Y. Nabae, S. Moriya, S. Kuroki, M. Kakimoto, J. Ozaki, S. Miyata, Carbon nitride as a nonprecious catalyst for electrochemical oxygen reduction, J. Phys. Chem. C 113 (2009) 20148–20151.
[121] T.S. Miller, A.B. Jorge, A. Sella, F. Corà, P.R. Shearing, D.J.L. Brett, P.F. McMillan, The use of graphitic carbon nitride based composite anodes for lithium-ion battery applications, Electroanalysis 27 (2015) 2614–2619.
[122] S. Yang, X. Feng, X. Wang, K. Müllen, Graphene-based carbon nitride nanosheets as efficient metal-free electrocatalysts for oxygen reduction reactions, Angew. Chem. Int. Ed. 50 (2011) 5339–5343.
[123] J. Liang, Y. Zheng, J. Chen, J. Liu, D. Hulicova-Jurcakova, M. Jaroniec, S.Z. Qiao, Facile oxygen reduction on a three-dimensionally ordered macroporous graphitic C_3N_4/carbon composite electrocatalyst, Angew. Chem. Int. Ed. 51 (2012) 3892–3896.

[124] C. Song, S. Kim, Preparation and electrochemical characterization of Pt supported flake-like graphitic carbon nitride on reduced graphene oxide as fuel cell catalysts, J. Electrochem. Soc. 162 (2015) F1181–F1190.
[125] C.Z. Li, Z.B. Wang, X.L. Sui, L.M. Zhang, D.M. Gu, Ultrathin graphitic carbon nitride nanosheets and graphene composite material as high-performance PtRu catalyst support for methanol electro-oxidation, Carbon 93 (2015) 105–115.
[126] C. Hu, Q. Han, F. Zhao, Z. Yuan, N. Chen, L. Qu, Graphitic C3N4-Pt nanohybrids supported on a graphene network for highly efficient methanol oxidation, Sci. China Mater. 58 (2015) 21–27.
[127] A. Du, S. Sanvito, Z. Li, D. Wang, Y. Jiao, T. Liao, Q. Sun, Y.H. Ng, Z. Zhu, R. Amal, S.C. Smith, Hybrid graphene and graphitic carbon nitride nanocomposite: gap opening, electron-hole puddle, interfacial charge transfer, and enhanced visible light response, J. Am. Chem. Soc. 134 (2012) 4393–4397.
[128] K. Qiu, Z.X. Guo, Hierarchically porous graphene sheets and graphitic carbon nitride intercalated composites for enhanced oxygen reduction reaction, J. Mater. Chem. A 2 (2014) 3209–3215.
[129] Y. Sun, C. Li, Y. Xu, H. Bai, Z. Yao, G. Shi, Chemically converted graphene as substrate for immobilizing and enhancing the activity of a polymeric catalyst, Chem. Commun. 46 (2010) 4740–4742.
[130] W. Zhang, H. Huang, F. Li, K. Deng, X. Wang, Palladium nanoparticles supported on graphitic carbon nitride-modified reduced graphene oxide as highly efficient catalysts for formic acid and methanol electrooxidation, J. Mater. Chem. A 2 (2014) 19084–19094.
[131] G. Peng, J. Qin, M. Volokh, C. Liu, M. Shalom, Graphene oxide in carbon nitride: from easily processed precursors to a composite material with enhanced photoelectrochemical activity and long-term stability, J. Mater. Chem. A 7 (2019) 11718–11723.
[132] W. Sheng, H.A. Gasteiger, Y. Shao-Horn, Hydrogen oxidation and evolution reaction kinetics on platinum: acid vs alkaline electrolytes, J. Electrochem. Soc. 157 (2010) B1529–B1536.
[133] Q. Liang, Z. Li, X. Yu, Z.H. Huang, F. Kang, Q.H. Yang, Macroscopic 3d porous graphitic carbon nitride monolith for enhanced photocatalytic hydrogen evolution, Adv. Mater. 27 (2015) 4634–4639.
[134] H. Huang, S. Yang, R. Vajtai, X. Wang, P.M. Ajayan, Pt-decorated 3D architectures built from graphene and graphitic carbon nitride nanosheets as efficient methanol oxidation catalysts, Adv. Mater. 26 (2014) 5160–5165.
[135] T.Y. Ma, S. Dai, M. Jaroniec, S.Z. Qiao, Graphitic carbon nitride nanosheet carbon nanotube three-dimensional porous composites as high performance oxygen evolution electrocatalysts, Angew. Chem. Int. Ed. 53 (2014) 7281–7285.
[136] M. De Marco, F. Markoulidis, R. Menzel, S.M. Bawaked, M. Mokhtar, S.A. AlThabaiti, S.N. Basahel, M.S.P. Shaffer, Cross-linked single-walled carbon nanotube aerogel electrodes via reductive coupling chemistry, J. Mater. Chem. A 4 (2016) 5385–5389.
[137] W.J. Ong, L.L. Tan, S.P. Chai, S.T. Yong, A.R. Mohamed, Surface charge modification via protonation of graphitic carbon nitride (g-C_3N_4) for electrostatic self-assembly construction of 2D/2D reduced graphene oxide (rGO)/g-C_3N_4 nanostructures toward enhanced photocatalytic reduction of carbon dioxide to methane, Nano Energy 13 (2015) 757–770.
[138] M.K. Kundu, T. Bhowmik, S. Barman, Gold aerogel supported on graphitic carbon nitride: an efficient electrocatalyst for oxygen reduction reaction and hydrogen evolution reaction, J. Mater. Chem. A 3 (2015) 23120–23135.
[139] Q. Liu, J. Zhang, Graphene supported Co-g-C_3N_4 as a novel metal–macrocyclic electrocatalyst for the oxygen reduction reaction in fuel cells, Langmuir 29 (2013) 3821–3828.
[140] J. Jin, X. Fu, Q. Liu, J. Zhang, A highly active and stable electrocatalyst for the oxygen reduction reaction based on a graphene-supported g-C_3N_4@cobalt oxide core-shell hybrid in alkaline solution, J. Mater. Chem. A 1 (2013) 10538–10545.
[141] T.Y. Ma, J. Ran, S. Dai, M. Jaroniec, S.Z. Qiao, Phosphorus-doped graphitic carbon nitrides grown in situ on carbon-fiber paper: flexible and reversible oxygen electrodes, Angew. Chem. Int. Ed. 54 (2015) 4646–4650.
[142] C. Xu, Q. Han, Y. Zhao, L. Wang, Y. Li, L. Qu, Sulfur-doped graphitic carbon nitride decorated with graphene quantum dots for an efficient metal-free electrocatalyst, J. Mater. Chem. A 3 (2015) 1841–1846.

[143] Y. Zhou, K. Neyerlin, T.S. Olson, S. Pylypenko, J. Bult, H.N. Dinh, T. Gennett, Z. Shao, R. O'Hayre, Enhancement of Pt and Pt-alloy fuel cell catalyst activity and durability via nitrogen-modified carbon supports, Energy Environ. Sci. 3 (2010) 1437–1446.
[144] Z. Lei, L. An, L. Dang, M. Zhao, J. Shi, S. Bai, Y. Cao, Highly dispersed platinum supported on nitrogen-containing ordered mesoporous carbon for methanol electrochemical oxidation, Microporous Mesoporous Mater. 119 (2009) 30–38.
[145] V. Di Noto, E. Negro, R. Gliubizzi, S. Gross, C. Maccato, G. Pace, Pt and Ni carbon nitride electrocatalysts for the oxygen reduction reaction, J. Electrochem. Soc. 154 (2007) B745–B756.
[146] V. Di Noto, A novel polymer electrolyte based on oligo(ethylene glycol) 600, K_2PdCl_4, and $K_3Fe(CN)_6$, J. Mater. Res. 12 (1997) 3393–3403.
[147] G. Wu, D. Li, C. Dai, D. Wang, N. Li, Well-dispersed high-loading Pt nanoparticles supported by shell-core nanostructured carbon for methanol electrooxidation, Langmuir 24 (2008) 3566–3575.
[148] E. Negro, K. Vezzu, F. Bertasi, P. Schiavuta, L. Toniolo, S. Polizzi, V. Di Noto, Interplay between nitrogen concentration, structure, morphology, and electrochemical performance of PdCoNi core-shell carbon nitride electrocatalysts for the oxygen reduction reaction, Chemelectrochem 1 (2014) 1359–1369.
[149] V. Di Noto, E. Negro, Pt-Fe and Pt-Ni carbon nitride-based 'core-shell' ORR electrocatalysts for polymer electrolyte membrane fuel cells, Fuel Cells 10 (2010) 234–244.
[150] V. Di Noto, E. Negro, Synthesis, characterization and electrochemical performance of tri-metal Pt-free carbon nitride electrocatalysts for the oxygen reduction reaction, Electrochim. Acta 55 (2010) 1407–1418.
[151] V. Di Noto, E. Negro, A new Pt–Rh carbon nitride electrocatalyst for the oxygen reduction reaction in polymer electrolyte membrane fuel cells: synthesis, characterization and single-cell performance, J. Power Sources 195 (2010) 638–648.
[152] V. Di Noto, E. Negro, G.A. Giffin, (Keynote lecture) multi-metal nanoelectrocatalysts based on carbon nitride supports for the ORR and for in PEM fuel cells, ECS Trans. 40 (2012) 3–10.

CHAPTER 4

Enhancing microbial fuel cell performance by carbon nitride-based nanocomposites

M.M. Ghangrekar, Anil Dhanda, S.M. Sathe, and Indrajit Chakraborty
Department of Civil Engineering, Indian Institute of Technology Kharagpur, Kharagpur, India

Contents

1. Introduction

The conventional aerobic wastewater treatment technologies are energy-intensive treatment processes. The major fraction of the energy utilized in aerobic treatments is associated with the use of aeration equipment required for the supply of oxygen. The cost of energy may vary up to 60% of the total cost associated with an operation of wastewater treatment plant [1]. However, considering the fact that energy present in wastewater is itself more than that required to treat it [2], the development of a wastewater treatment facility that can harvest this energy and utilize the harvested energy onsite is a sustainable proposition.

Microbial fuel cell (MFC) is an emerging technology for converting chemical energy stored in the organic substrate to electrical energy using microorganisms as biocatalysts, thus having the ability to offer effective wastewater treatment for removal of organic matter and nutrients. The substrate can be sourced from wastewater, sludge generated from biological processes, or the organic fraction of solid waste [3]. Similar to a conventional fuel cell, the MFC contains an anodic chamber where oxidation of organic pollutants present in the anolyte occurs, producing protons (H^+), electrons (e^-), and CO_2 (Fig. 4.1).

Nanostructured Carbon Nitrides for Sustainable Energy and Environmental Applications
https://doi.org/10.1016/B978-0-12-823961-2.00007-0

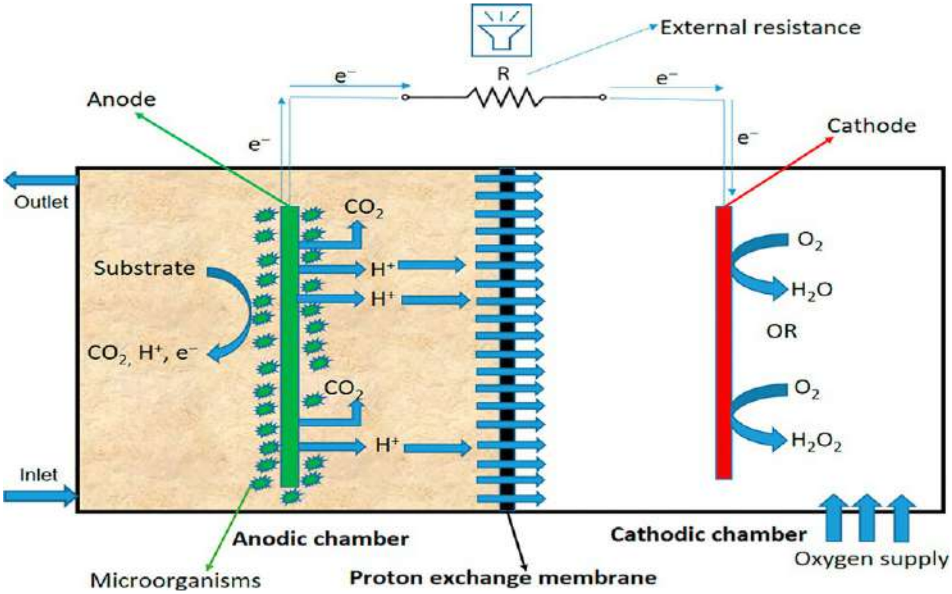

Fig. 4.1 Schematic and working of dual chamber microbial fuel cell. *No permission required*

The e^- generated in anolyte during oxidation of the organic matter travel to the cathodic chamber through an externally connected circuit, whereas H^+ travel from the proton exchange membrane (PEM) and ultimately both H^+ and e^- reach to the cathode where oxygen reduction reaction (ORR) occurs [4]. For reduction process to occur, a terminal electron acceptor, such as O_2, is necessary, which is accomplished by utilizing either aqueous dissolved oxygen or directly breathing oxygen from air depending upon the aqueous cathode or air cathode configuration used in MFC, respectively.

Apart from O_2, ferricyanide, permanganate, dichromate, and persulfate [5–8] can also be used as electron acceptors at cathode. However, nontoxic nature, ease of operation, and easy availability make O_2 the most suitable electron acceptor in MFC [9]. At the cathode of MFC, reduction of oxygen takes place either via accepting four electrons or two electrons. While accepting two electrons, hydrogen peroxide is produced, whereas the acceptance of four electrons in ORR results in water as the final product. Even though hydrogen peroxide works as a disinfecting agent, the energy generated from MFC following $2e^-$ oxygen reduction pathway is low and it may cause deterioration of the interior surface of the cathodic chamber due to its high oxidative power [10]. Owing to this, generally $4e^-$ reduction pathway is preferred and hence targeted in the cathodic chamber of MFC from the aspect of durability and electrochemical efficiency.

The MFC is considered as one of the upcoming wastewater treatment technologies and has been successfully applied for the treatment of domestic, distillery, brewery, bakery, dairy, hospital, landfill leachate, meat processing, paper recycling, and swine wastewaters [11]. The maximum power density using miniature MFC is reported to be $2.15\,kW\,m^{-3}$ [12]. A maximum power density of $26\,mW\,m^{-2}$ was reported simultaneously achieving a chemical oxygen demand (COD) removal of 80%, while both parameters were dependent on hydraulic retention time (HRT) in the anodic chamber of MFC [13]. The dairy wastewater has been treated successfully with power densities reported up to $27\,W\,m^{-3}$, coulombic efficiency of 36%, and up to 90% COD removal efficiency with a continuous mode operated MFC for 72 days [14].

In another case, a $20.2\,W\,m^{-3}$ of power density and 91% of COD removal efficiency was reported with a coulombic efficiency of 26.9% in a batch operated MFC for treatment of dairy wastewater [15]. In addition to low strength domestic wastewater, MFCs are capable of treating high-strength wastewaters such as brewery effluent as well. For instance, brewery wastewater with influent COD of $2240\,mg\,L^{-1}$ was treated in MFC to demonstrate 87% removal at an HRT of 94 h. The MFC produced a maximum power density of $5.1\,W\,m^{-3}$, thus showing the capability of handling a higher organic loading rate [16]. In another investigation on brewery wastewater treatment in MFC, a COD removal efficiency of 82.7%, energy recovery of $0.097\,kWh\,m^{-3}$, and coulombic efficiency of 8% were reported [17].

The bioelectricity recovery is considerably affected by various losses, which can be attributed to: (i) activation loss caused by slower reaction rate at the electrodes; (ii) ohmic loss due to restriction to the movement of protons and electrons; and (iii) mass transfer loss caused by inefficient supply of reactants to the catalytic sites in [9,18]. Although activation losses arise at both electrodes due to sluggish kinetics of the electrochemical reactions, nevertheless ORR kinetics at cathode is often the rate limiting factor due to requirement of higher activation energy to break bond between the oxygen atoms [19]. Theoretically, a redox potential of $E' = 0.805\,V$ (against standard hydrogen electrode (SHE), at pH 7 and $T = 298\,K$) is achieved for catalytic reduction of O_2 when H_2O is the final reaction product. Nevertheless, owing to the low diffusive rate of O_2, poor adsorption of O_2 over the electrode surface, and high activation energy requirement for cleavage of the O_2 molecule, the ORR occurs at a lower potential than the theoretical value [20]. This difference between the theoretical obtainable potential during ORR and the voltage obtained in real time when ORR occurs is termed as ORR overpotential. In order to reduce this ORR overpotential and increase the obtainable cell voltage, catalysts can be implemented to promote a faster $4e^-$ reduction of O_2.

Commonly Pt and Pt-based catalysts used on cathode are found to significantly reduce the overpotential and support $4e^-$ pathway of ORR, thus enhancing the electricity production [21]. Owing to the high cost associated with the use of Pt, several metal alloys and other metals, like cobalt, nickel, iron, etc., have been preferred as an inexpensive alternative to Pt for application as a cathode catalyst. Additionally, a few metal oxides, like lead oxide, manganese dioxide, vanadium oxide, perovskite oxide, zirconium oxide, cobalt oxide, etc., have also been used as a cathode catalyst in MFC [22,23].

As an alternative to metal and metal oxide electrocatalysts, carbon-based catalysts have also been developed by the researchers, which can be an economical option to conventional electrocatalysts. The use of carbonaceous materials, such as activated carbon, carbon black, carbon nanotubes, graphene, graphitic carbon, etc., have excellent electrocatalytic properties, which make it an attractive choice as a cathode catalyst in MFC [24]. Over the years of research outcome has witnessed modifications to plain carbon-based catalysts, of which nitrogen doping is one of the popular methods to enhance the ORR activity [25]. Similarly, application of graphitic carbon nitride as cathode catalyst in MFC has proved to have improved the ORR activity [26]. However, being a semiconductor, the electrocatalytic oxygen reduction activity of pure g-C_3N_4 is not up to the expected mark. Even then, g-C_3N_4 has an excellent electron collection and transmission ability and also deep negative conduction band; hence, its modification with other substances can enhance the cathodic electrochemical reactions in MFCs [27].

The shortcomings, such as less specific surface area, less electrocatalytic activity due to semiconductor nature, etc., of the sole g-C_3N_4 can be overcome via doping or composites with other compounds. In this regard, the aim of this chapter is to throw light on the different approaches used for improving the electrocatalytic properties of g-C_3N_4 and its composites to be used as cathode catalyst in MFC. Apart from this, the effects of the different modifications on the properties of g-C_3N_4 have also been discussed in detail.

2. Desirable properties of a cathode catalyst in MFC

A cathode catalyst should have high catalytic activity, extensive active sites, bridge mode interaction, ability to increase the distance of the O=O bond to 2.89 Å so that the activation energy barrier of O_2 is reduced by weakening the O=O bond, thus resulting in substantial improvement in ORR electrochemistry [28]. Additionally, the cathode catalyst should have good electrical conductivity and efficient electron acceptance capability to reduce the ohmic losses [29]. Whereas a catalyst should have enhanced surface area with porous structure, d-band core vacancies, and large positive atomic charge concentration to resolve mass transfer loss [24,28]. While from the view of scalability, the catalyst must be inexpensive, easily available/synthesizable for large-scale applications. The properties considered to be essential for catalysts are summarized in Fig. 4.2.

2.1 Properties of graphitic carbon nitride

Past researchers have demonstrated formation of two types of graphitic carbon nitride structural polymorphs by selecting appropriate precursor and related strategies. Among the two possible structures of the carbon nitride, one is based on s-triazine and the other on tri-s-triazine unit [30]. Graphitic carbon nitride has got excellent properties that include accessible crystalline pore walls, chemical stability [17] good catalytic activity

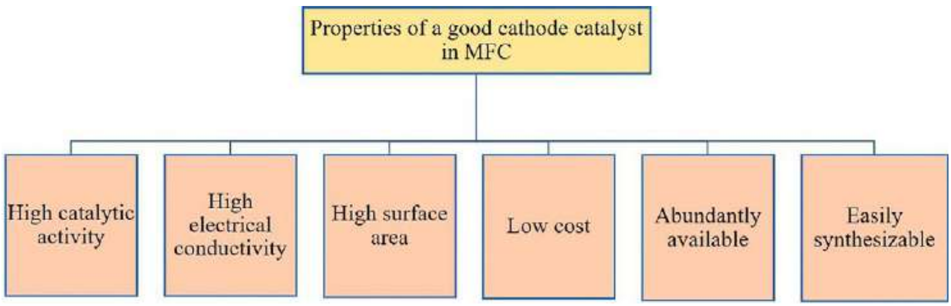

Fig. 4.2 Properties expected for a good cathode catalyst material to be used in MFC. *No permission required*

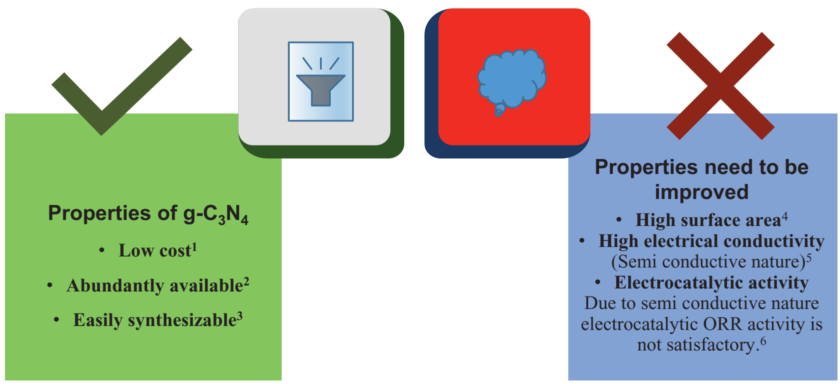

Fig. 4.3 Comparison of properties required for a cathode catalyst in MFC and properties of g- C_3N_4. *No permission required*

for various chemical reactions, like degradation of contaminants and photocatalytic hydrogen production, owing to its nitrogen active sites. In spite of this, g-C_3N_4 has poor electrocatalytic oxygen reduction activity [31]. A comparison of the inherent properties of g-C_3N_4 and intended properties for efficient cathode catalysts are summarized in Fig. 4.3 ([1,3]—[32], [2,4]—[33], [5,6]—[31]).

3. Application of graphitic carbon nitride as cathode catalyst in MFC

3.1 Sole graphitic carbon nitride

Synthesis of g-C_3N_4 is facile and being a highly active photocatalyst, it has been used in chemical reactions and for degradation of contaminants in water and wastewater treatment. The structure of g-C_3N_4 resembles graphene and the presence of nitrogen (almost 60%) in pyridinic position assists in improving its performance as an electrocatalyst [34].

The g-C_3N_4 polymer, with a structure similar to graphite, is a promising catalytic material for oxygen reduction reaction because of better thermal and chemical stability, suitable electronic structure, low-cost, and facile synthesis procedures [32,35].

Although g-C_3N_4 has some of the aforementioned useful properties, sole g-C_3N_4 cannot be used in MFC as cathode catalyst mainly due to inferior electrical conductivity. Because of the semiconductive nature, the electrocatalytic oxygen reduction activity of sole g-C_3N_4 is not satisfactory [31]. This was confirmed by the rotating disk electrode (RDE) test, which displayed an onset potential of +0.76 V for g-C_3N_4; compared to +0.91 V (reversible hydrogen electrode, RHE) for Pt/C, clearly stating that the ORR performance of sole g-C_3N_4 was less than that of Pt/C. The current density of sole g-C_3N_4 was nearly 7.6-folds lesser than Pt/C, which proves much lower ORR efficiency of g-C_3N_4 compared to Pt/C [36]. In addition, it prefers the $2e^-$ over the $4e^-$ pathway thereby leading to compromised electricity production [37]. This necessitates the requirement of modifying g-C_3N_4 with additional metal or elements in order to make it suitable to be used as a cathode catalyst that is following four-electron pathway for ORR in MFC.

3.2 Doped graphitic carbon nitride as a cathode catalyst

Doping of other metals or elements, such as nitrogen or carbon with pure g-C_3N_4, improves the electrocatalytic activity of the catalyst-C_3N_4. Early investigation for fuel cell application conducted by Lyth et al. [38] showed that the onset potential of g-C_3N_4 for oxygen reduction was 0.69 V vs Normal Hydrogen Electrode (NHE), which was improved to 0.76 V (vs NHE), when plain g-C_3N_4 was blended with carbon black. The onset potential for this particular work was defined as the voltage at which a current density of 2 μA cm^{-2} was recorded. Additionally, the modified electrode produced 2.42 times more current density (2.21 mA cm^{-2}) than carbon black electrode. This improved catalytic activity might be a result of carbon black doping that has high surface area that can boost the catalytic activity of g-C_3N_4. Although the prepared material was less efficient compared to Pt, however, the study confirmed that with further enhancement in the surface area of g-C_3N_4, it can become a material for use in MFC as well.

Graphene has a distinctive sp^2 hybridized structure with outstanding electron conductivity and benignity in the environment. Due to its superior electrical conductivity, excellent mechanical stability, and high surface area, it has vast application in electronic devices. Taking the benefit of these properties a novel catalyst, comprising of g-C_3N_4 polymer-doped cobalt species supported on graphene was synthesized for the application in fuel cell [13]. Graphitic carbon nitride can accommodate intermediate metals to create possible active sites, while graphene, with a similar bonding mechanism to g-C_3N_4, facilitates electron transfer by strong electronic bonding. The chemically doped

Co-g-C_3N_4 cathode catalyst delivered appreciable ORR activity and kinetics via a four-electron transfer mechanism ($n=3.86$), while possessing a good thermal stability and improved stability in the vicinity of methanol for prolonged test period of 10h in alkaline environment. Although the synthesized catalyst has not been used in MFC as a cathode catalyst, it can be proposed for use as a cathode catalyst in MFC.

In another investigation, iron and nitrogen-functionalized graphene (Fe-N-G) was synthesized via thermal treatment of Fe, g-C_3N_4, and chemically reduced graphene for application as a cathode catalyst in air-cathode MFC [39]. The maximum power density produced using Fe-N-G catalyst in MFC was 1149.8 $mW\,m^{-2}$, which was 2.1 times higher than that generated with the Pt/C-MFC (561.1 $mW\,m^{-2}$), while both MFCs adopted the same catalyst loading. Use of nitrogen-doped graphene (N-G) has proven to be beneficial in improving the electrocatalytic activity and conductivity of graphene [40,41]. The XPS analysis identified the presence of pyridinic N, pyrrolic N, and graphitic N in the Fe-N-G–doped g-C_3N_4, which are known for efficiently creating ORR active sites [42,43].

It has been indicated that carbon atoms present near the nitrogen dopant hold considerably high positive charge density to neutralize the strong electronic affinity possessed by nitrogen atom. The charge delocalization induced by nitrogen could also change the adsorption behavior of graphene toward oxygen that can elongate and weaken the bonding between oxygen atoms to assist the oxygen reduction reaction [42]. The electrocatalytic activity of Fe-N-G electrode was lower, when compared with Pt/C electrode, during the electrochemical analysis; however, it surpassed the latter when MFC performance was compared for maximum power density. This might have been a result of a restriction of the movement of proton or oxygen to the catalyst layer in the air-cathode in the Pt/C-MFC, which could be most likely due to platinum poisoning [44].

In another investigation, Zhang and Liu [27] prepared manganese dioxide/titanium dioxide/graphitic carbon nitride-coated granular-activated carbon (GAC) cathode (MnO_2/TiO_2/g-C_3N_4@GAC). Activated carbon is known to have a high specific surface area, diverse porous structure, and it has been widely used as a base material to support other electrocatalysts [45]. Manganese dioxide is a low-cost and environment friendly metal oxide, and it is extensively used as electrocatalyst in bioelectrochemical systems [46,47]. Titanium dioxide is a transition metal oxide that has strong photocatalytic degradation ability, chemical and biological stability, and similar to MnO_2 it has also been used as a cathode catalyst in MFC [48,49].

The MFC catalyzed with composite cathode catalyst (MnO_2/TiO_2/g-C_3N_4@GAC) achieved a maximum power density of 1176.47 $mW\,m^{-3}$, which was 1.65 times higher than MFC with sole GAC as a cathode material (711.76 $mW\,m^{-3}$). Simultaneously, the MFC achieved COD, $NH_4{}^{+}$-N, and $NO_3{}^{-}$-N removal of 98%, 99%, and 99%, respectively, during 12h of HRT with a COD removal rate of 17.77 kg COD $m^{-3}\,d^{-1}$ [27]. Electrochemical impedance spectroscopy (EIS) analysis also exhibited that ohmic, charge transfer (R_{ct}) and mass transfer resistance of the MnO_2/TiO_2/g-C_3N_4@GAC-catalyzed MFC were lower than the control MFC (sole GAC cathode). The decreased internal resistance (R_{int}) in the system contributing to the better energy production might have significantly minimized internal energy losses.

3.3 Graphitic carbon nitride composites as a cathode catalyst

Another method of improving the electrocatalytic performance of sole g-C_3N_4 is via composites, in which the properties of different materials are utilized simultaneously. Composite catalysts exhibit high performance as the heteroatom doping creates delocalization of charge and enhances the mobility of the electron cloud. Wang et al. prepared a composite catalyst consisting of g-C_3N_4-wrapped Co_3O_4 nanoparticles supported on nitrogen-doped graphene (NG) [50]. The Co_3O_4 is a low-cost material with abundant availability in nature and excellent durability in alkaline medium [51,52]. Because of their inadequate conductivity and limited surface areas, plain cobalt oxides show inadequate ORR electrocatalytic efficiency.

Instead, these above-mentioned shortcomings can be overcome by doping of g-C_3N_4, because Co_3O_4 activity sites can be protected by g-C_3N_4 to improve stability and NG as a conductive matrix can anchor Co_3O_4@g-C_3N_4 [53,54]. The synthesized catalyst surface features indicated that Co_3O_4@g-C_3N_4 was integrated into double sheet like the graphene framework. The RDE tests showed that the as-synthesized composite had an onset potential of 0.920 V vs RHE, which was comparable with Pt/C (0.917 V). Almost identical value of onset potential compared to Pt/C showed comparable activity of Co_3O_4@g-C_3N_4/NG, possibly due to the application of N to graphene, which can induce the reallocation of charge and facilitate the sorption of oxygen to increase the catalytic activity. The catalyst also demonstrated n value of 3.84–3.97, reflecting $4e^-$ pathway for ORR, which can directly enhance the power generation capability of the catalyst [55].

In work done by Yang et al. [36], nanocomposites based on cobalt oxide supported on nitrogen-doped carbon nanotubes (Co/N-CNT) were synthesized by controlled pyrolysis of g-C_3N_4 and cobalt acetate. The cobalt acetate was used as a precursor to cobalt and graphitic carbon nitride as a source of nitrogen as well as carbon. Graphitic carbon nitride was used as it consists of sp^2 hybridized carbon and nitrogen atoms in which the plentiful pyridine moieties of nitrogen can be used to coordinate transitional metal centers. Pyrolysis was performed for 2 h at 800°C resulting in Co, N-doped carbon nanotubes (Co/N-CNT). The Co/N-CNT nanocomposites displayed strong ORR electrocatalytic activity due to the greater ability of Co—N active sites, which aided the ORR kinetics. The number of electrons transferred at +0.6 V was 3.4 for Co/N-CNT, which suggested that ORR continued primarily through $4e^-$ pathway. With a charge-transfer resistance of 23.4 Ω, the maximum power density of the catalyze air cathode MFC was reported to be 1260 $mW\,m^{-2}$, which was 16.6% higher than that Pt/C-catalyzed MFC [36]. However, the Co/N-CNT catalyst loading used was four times greater than Pt/C catalyst. Poison tolerance of catalysts was assessed with S^{2-} as poisoning species. When 5 mM of S^{2-} was applied to the electrolyte, 93% of the current was maintained with Co/N-CNT, which confirmed the poison tolerance of as-synthesized catalyst [36].

In one of the recent investigations, a novel catalyst with isoreticular metal organic framework-3 (IRMOF-3) was modified with g-C_3N_4 and pyrolyzed at 850 °C [56,57]. In this investigation, effect of different weight ratios (0%, 25%, 50%, and 75%) of IRMOF-3 to g-C_3N_4 on the performance of MFC was evaluated and compared with commercial Pt/C. The half-wave potential revealed the ability of catalysts to suppress ORR overpotential [58]; which was 0.89 V vs RHE (with 50% IRMOF-3) compared to Pt/C (0.79 V vs RHE). The performance of IRMOF-3-catalyzed MFC (1402.8 $mW\,m^{-3}$) was higher than Pt-catalyzed MFC (1292.8 $mW\,m^{-3}$) in terms of maximum power density. The metal organic framework has organic compounds, metal ions with high specific surface area, porous structure, and excellent mass transfer and conductivity [59]. The use of g-C_3N_4 caused development of a porous nitrogen-doped carbon structure. The electrocatalytic efficiency of 50% for IRMOF-3 to g-C_3N_4 ratio was primarily due to the combined effect of hierarchically *meso*/microporous structures and abundant pyridine and quaternary nitrogen active sites. The porous structures provided a larger area for active sites and opened up the path for reactant to reach the active sites.

Feng et al. [16] implanted the nitrogen active sites to NG nanosheets (named as I-NG) with mesoporous g-C_3N_4 (mpg-C_3N_4). The MFC using this catalyst achieved a maximum power density of 1618 $mW\,m^{-2}$; whereas for Pt/C-MFC, it was 1423 $mW\,m^{-2}$ with similar loading adopted for both the catalysts. This enhanced power density might be a result of the reduced internal resistance of I-NG-MFC (75 Ω). The decrease in maximum power density in I-NG-catalyzed MFCs was approximately 4.8% after 80 days of operational duration, whereas the drop in Pt/C-MFCs was close to 16%, thus showing improved long-term stability of I-NG catalysts. The catalyst showed good metabolite crossover effect tolerance and proved its potential to be used in bioelectrochemical systems. The catalyst showed an excellent electrocatalytic activity and near to a $4e^-$ transfer pathway ($n = 3.7$). The enhanced activity of the catalyst might be attributed to two main reasons; one of them could be due to the use mpg-C_3N_4, which provided sufficient nitrogen content for NG nanosheets. The other reason might be due to improved electron transfer efficiency owning to the use of NG as the conductive support. This proves the ability of I-NG-MFCs as an excellent durable catalyst in MFC as an alternative to Pt.

The metal ions and organic compounds can be converted into possible active sites, and when used as a cathode catalyst in MFC, the addition of nitrogen source can greatly increase their catalytic activity [60–62]. Graphitic carbon nitride with abundant nitrogen dopants was suitably combined with Mn—Fe bimetallic MOFs nanoparticle to synthesize a highly conductive skeleton with a metal-based core shell structure to promote the ORR catalytic activity when used as catalyst [63]. The cathode catalyst was synthesized using Mn-doped g-C_3N_4 and Fe-based MOF termed as Mn–Fe@g-C_3N_4. The catalyst showed a power density of 413 mW m^{-2} when used in a 4e^- reduction pathway with an R_{ct} value of 5.44 Ω. The Mn–Fe@g-C_3N_4 as catalyst displayed a superior ORR performance with an onset potential of 0.197 V, which was more positive than the Pt/C (0.173 V). The enhanced ORR activity of Mn–Fe@g-C_3N_4 catalyst might be due to the addition of nitrogen that can boost oxygen adsorption to increase ORR kinetics. Additionally, Fe_3C nanocrystals may greatly improve the electrochemical efficiency of the conductive carbon layer and the adjacent Fe–N–C active sites. Overall, this investigation has shown that MOFs-induced catalysts with porous framework and active components can be used effectively in MFCs as cathode catalysts.

Chakraborty et al. [26] prepared two catalysts from exfoliated porous g-C_3N_4 and acetylene black (composite) and other with sole exfoliated porous g-C_3N_4. Exfoliation involves decrease of the overall layer thickness, thereby revealing increased specific surface area, active sites, and increasing the charge transfer conductance [64]. Acetylene black is used in the composite for the isolation and aggregation of electrons produced by the g-C_3N_4. For the prepared exfoliated catalyst, a peak current density of −0.228 mA cm^{-2} was reported, while for composite, a peak current density of −0.3 mA cm^{-2} was reported, which was close to Pt—C (−0.312 mA cm^{-2}). The EIS analysis showed R_{ct} value of ~138 for exfoliated g-C_3N_4 and 112 for the composite catalyst, both of which were slightly higher than Pt—C (94). The reduced R_{ct}, as compared to exfoliated g-C_3N_4, has reflected into higher maximum power density (14.74 ± 0.17 W m^{-3}) produced from exfoliated porous g-C_3N_4 and acetylene black composite–catalyzed MFC. The exfoliated catalyst showed a BET surface area of 21 m^2 g^{-1}, which is higher than plain g-C_3N_4 that ranges between 2 and 10 m^2 g^{-1} and demonstrated positive effect of exfoliation on enhancing the ORR than nonexfoliated g-C_3N_4.

It was also revealed in the cost analysis that the exfoliated porous g-C_3N_4 composite can be used as low-cost cathode catalysts in MFC owing to its 20-folds lower cost than Pt—C [26]. The performance of the composite might be attributed to presence of different N configurations (graphitic and pyridinic N), reduced thickness due to exfoliation, enhanced specific surface area as compared to plain g-C_3N_4, and presence of acetylene black that facilitated charge separation and transport from the g-C_3N_4 matrix. The presence of graphitic N provided a center for the oxygen reduction, which might improve the conductivity of the catalyst [65] while promoting 4e^- transfer mechanism of ORR. All these strategies discussed above are summarized in Table 4.1.

Table 4.1 Performance of microbial fuel cell catalyzed with g-C3N4-based cathode catalysts.

Sl. no.	Method used	Material used with graphitic carbon nitride	Max. power density (mW m^{-2})	COD Removal (%)	Resistance (Ω)	References
1	Doping	Fe, N, G	1149.8	–	–	[39]
2	Doping	MnO_2, TiO_2, GAC	1176.47 mW m^{-3}	98	91 ($R_{int.}$)	[27]
3	Composite	CO nanoparticles, nitrogen-doped CNT	1260	–	23.4 (R_{ct})	[36]
4	Composite	IRMOF-3	1402.8 mW m^{-3}	–	–	[66]
5	Composite	Nitrogen-doped graphene (NG) nanosheets	1618	–	75 ($R_{int.}$)	[67]
6	Composite	Mn-doped g-C_3N_4-assisted Fe-based Metal Organic Frameworks	413	–	5.44 (R_{ct})	[63]
7	Composite	Exfoliated porous g-C_3N_4 and acetylene black	14.74 W m^{-3}	83.3	112 (R_{ct})	[26]
8	Exfoliation	Exfoliated g-C_3N_4	12.47 W m^{-3}	78	138 (R_{ct})	[26]

4. Future scope

Graphitic carbon nitride is drawing attention nowadays to be used in MFC as a cathode catalyst because of its various useful properties like easy synthesis and abundant precursor availability at low cost. However, as mentioned previously, limitations like low specific surface area and limited electrocatalytic activity discourage the use of sole g-C_3N_4 as cathode catalyst in MFC. Based on the literature, it can be seen that introduction of metals via doping and composites can reduce the shortcomings of g-C_3N_4. However, further research is necessary to find easy and repeatable procedures to improve the surface area and electrocatalytic activity of the g-C_3N_4-based catalysts. Novel composite, doped or exfoliated g-C_3N_4 can also be prepared to investigate their performance so that rate of oxygen reduction can be enhanced further and the catalyst will be able to support large current density so that full-scale application of MFC can be possible.

It is well-known fact that bulk g-C_3N_4 exhibits $2e^-$ pathway leading to cathodic H_2O_2 production. Though the power generation of such system will be compromised, the produced H_2O_2 can be considered for disinfection of the treated anolyte. Thus, a complete system of secondary treatment followed by partial disinfection in the cathodic chamber can be explored using bulk g-C_3N_4 as cathode catalyst. In this regard, a combination of other electrocatalysts can be explored to enhance the H_2O_2 yield. Application of photo-electro-catalyst in MFC is gaining attention in the field of bioelectrochemical system. Graphitic carbon nitride being photocatalyst can be considered as cathode catalyst for application in photo-electro-catalyzed MFCs in presence of UV or suitable light source.

5. Conclusion

This chapter summarizes the application of g-C_3N_4-based cathode catalyst for the application in MFCs. Since pure g-C_3N_4 cannot be used as cathode catalyst, strategies such as doping, composites, and exfoliation techniques have been discussed in connection with the past investigations. Considering the current literature, it can be hypothesized that g-C_3N_4-based catalyst has the potential to efficiently work as a cathode catalyst in MFC. Nevertheless, there is still a wide scope of improvement, which needs to be addressed in the upcoming research to make it more practicable in the upcoming days.

Acknowledgment

The present research work is financially supported by Swachhta Action Plan (SAP), Ministry of Education, Government of India (File No. SAP17_IITKGP_05).

References

[1] R. Abbassi, A.K. Yadav, Introduction to Microbial Fuel Cells: Challenges and Opportunities, Elsevier BV, 2020, pp. 3–27, https://doi.org/10.1016/b978-0-12-817493-7.00001-1.

[2] R. Khiewwijit, H. Temmink, H. Rijnaarts, K.J. Keesman, Energy and nutrient recovery for municipal wastewater treatment: how to design a feasible plant layout? Environ. Model. Softw. 68 (2015) 156–165, https://doi.org/10.1016/j.envsoft.2015.02.011.

[3] Z. Du, H. Li, T. Gu, A state of the art review on microbial fuel cells: a promising technology for wastewater treatment and bioenergy, Biotechnol. Adv. 25 (5) (2007) 464–482, https://doi.org/10.1016/j.biotechadv.2007.05.004.

[4] A.J. Slate, K.A. Whitehead, D.A.C. Brownson, C.E. Banks, Microbial fuel cells: an overview of current technology, Renew. Sust. Energ. Rev. 101 (2019) 60–81, https://doi.org/10.1016/j.rser.2018.09.044.

[5] J. Li, Q. Fu, Q. Liao, X. Zhu, D.d. Ye, X. Tian, Persulfate: a self-activated cathodic electron acceptor for microbial fuel cells, J. Power Sources 194 (1) (2009) 269–274, https://doi.org/10.1016/j.jpowsour.2009.04.055.

[6] S.E. Oh, B.E. Logan, Proton exchange membrane and electrode surface areas as factors that affect power generation in microbial fuel cells, Appl. Microbiol. Biotechnol. 70 (2) (2006) 162–169, https://doi.org/10.1007/s00253-005-0066-y.

[7] S. Pandit, A. Sengupta, S. Kale, D. Das, Performance of electron acceptors in catholyte of a two-chambered microbial fuel cell using anion exchange membrane, Bioresour. Technol. 102 (3) (2011) 2736–2744, https://doi.org/10.1016/j.biortech.2010.11.038.

[8] S. You, Q. Zhao, J. Zhang, J. Jiang, S. Zhao, A microbial fuel cell using permanganate as the cathodic electron acceptor, J. Power Sources 162 (2) (2006) 1409–1415, https://doi.org/10.1016/j.jpowsour.2006.07.063.

[9] B.E. Logan, B. Hamelers, R. Rozendal, U. Schröder, J. Keller, S. Freguia, P. Aelterman, W. Verstraete, K. Rabaey, Microbial fuel cells: methodology and technology, Environ. Sci. Technol. 40 (17) (2006) 5181–5192, https://doi.org/10.1021/es0605016.

[10] J.M. Foley, R.A. Rozendal, C.K. Hertle, P.A. Lant, K. Rabaey, Life cycle assessment of high-rate anaerobic treatment, microbial fuel cells, and microbial electrolysis cells, Environ. Sci. Technol. 44 (9) (2010) 3629–3637, https://doi.org/10.1021/es100125h.

[11] V.G. Gude, Wastewater treatment in microbial fuel cells - an overview, J. Clean. Prod. 122 (2016) 287–307, https://doi.org/10.1016/j.jclepro.2016.02.022.

[12] K.P. Nevin, H. Richter, S.F. Covalla, J.P. Johnson, T.L. Woodard, A.L. Orloff, H. Jia, M. Zhang, D.R. Lovley, Power output and columbic efficiencies from biofilms of Geobacter sulfurreducens comparable to mixed community microbial fuel cells, Environ. Microbiol. 10 (10) (2008) 2505–2514, https://doi.org/10.1111/j.1462-2920.2008.01675.x.

[13] H. Liu, R. Ramnarayanan, B.E. Logan, Production of electricity during wastewater treatment using a single chamber microbial fuel cell, Environ. Sci. Technol. 38 (7) (2004) 2281–2285, https://doi.org/10.1021/es034923g.

[14] D. Cecconet, D. Molognoni, A. Callegari, A.G. Capodaglio, Agro-food industry wastewater treatment with microbial fuel cells: energetic recovery issues, Int. J. Hydrog. Energy 43 (1) (2018) 500–511, https://doi.org/10.1016/j.ijhydene.2017.07.231.

[15] M. Mahdi Mardanpour, M. Nasr Esfahany, T. Behzad, R. Sedaqatvand, Single chamber microbial fuel cell with spiral anode for dairy wastewater treatment, Biosens. Bioelectron. 38 (1) (2012) 264–269, https://doi.org/10.1016/j.bios.2012.05.046.

[16] Y. Feng, X. Wang, B.E. Logan, H. Lee, Brewery wastewater treatment using air-cathode microbial fuel cells, Appl. Microbiol. Biotechnol. 78 (5) (2008) 873–880, https://doi.org/10.1007/s00253-008-1360-2.

[17] Y. Dong, Y. Qu, W. He, Y. Du, J. Liu, X. Han, Y. Feng, A 90-liter stackable baffled microbial fuel cell for brewery wastewater treatment based on energy self-sufficient mode, Bioresour. Technol. 195 (2015) 66–72, https://doi.org/10.1016/j.biortech.2015.06.026.

[18] J. Park, J. Bae, Characterization of electrochemical reaction and thermo-fluid flow in metal-supported solid oxide fuel cell stacks with various manifold designs, Int. J. Hydrog. Energy 37 (2) (2012) 1717–1730, https://doi.org/10.1016/j.ijhydene.2011.10.040.

[19] Y. Fan, E. Sharbrough, H. Liu, Quantification of the internal resistance distribution of microbial fuel cells, Environ. Sci. Technol. 42 (21) (2008) 8101–8107, https://doi.org/10.1021/es801229j.

[20] A.A. Gewirth, M.S. Thorum, Electroreduction of dioxygen for fuel-cell applications: materials and challenges, Inorg. Chem. 49 (8) (2010) 3557–3566, https://doi.org/10.1021/ic9022486.
[21] P.N. Venkatesan, S. Dharmalingam, Synthesis and characterization of Pt, Pt–Fe/TiO2 cathode catalysts and its evaluation in microbial fuel cell, Mater. Renewable Sustain. Energy 5 (3) (2016), https://doi.org/10.1007/s40243-016-0074-0.
[22] P.J. Ferreira, G.J. la O', Y. Shao-Horn, D. Morgan, R. Makharia, S. Kocha, H.A. Gasteiger, Instability of Pt / C Electrocatalysts in proton exchange membrane fuel cells, J. Electrochem. Soc. 152 (11) (2005) A2256, https://doi.org/10.1149/1.2050347.
[23] B. Koo, S.P. Jung, Recent trends of oxygen reduction catalysts in microbial fuel cells: a review, J. Korean Soc. Environ. Eng. (2019) 657–675, https://doi.org/10.4491/ksee.2019.41.11.657.
[24] Z. Yang, H. Nie, X. Chen, X. Chen, S. Huang, Recent progress in doped carbon nanomaterials as effective cathode catalysts for fuel cell oxygen reduction reaction, J. Power Sources 236 (2013) 238–249, https://doi.org/10.1016/j.jpowsour.2013.02.057.
[25] L. Dai, Y. Xue, L. Qu, H.J. Choi, J.B. Baek, Metal-free catalysts for oxygen reduction reaction, Chem. Rev. 115 (11) (2015) 4823–4892, https://doi.org/10.1021/cr5003563.
[26] I. Chakraborty, N. Ghosh, D. Ghosh, B.K. Dubey, D. Pradhan, M.M. Ghangrekar, Application of synthesized porous graphitic carbon nitride and it's composite as excellent electrocatalysts in microbial fuel cell, Int. J. Hydrog. Energy 45 (55) (2020) 31056–31069, https://doi.org/10.1016/j.ijhydene.2020.08.118.
[27] Q. Zhang, L. Liu, A microbial fuel cell system with manganese dioxide/titanium dioxide/graphitic carbon nitride coated granular activated carbon cathode successfully treated organic acids industrial wastewater with residual nitric acid, Bioresour. Technol. 304 (2020), https://doi.org/10.1016/j.biortech.2020.122992.
[28] M.V. Kannan, Gnana kumar, G., Current status, key challenges and its solutions in the design and development of graphene based ORR catalysts for the microbial fuel cell applications, Biosens. Bioelectron. 77 (2016) 1208–1220, https://doi.org/10.1016/j.bios.2015.10.018.
[29] D.H. Lim, J. Wilcox, Mechanisms of the oxygen reduction reaction on defective graphene-supported Pt nanoparticles from first-principles, J. Phys. Chem. C 116 (5) (2012) 3653–3660, https://doi.org/10.1021/jp210796e.
[30] W.K. Darkwah, Y. Ao, Mini review on the structure and properties (photocatalysis), and preparation techniques of graphitic carbon nitride nano-based particle, and its applications, Nanoscale Res. Lett. 13 (2018), https://doi.org/10.1186/s11671-018-2702-3.
[31] Y. Zheng, Y. Jiao, M. Jaroniec, Y. Jin, S.Z. Qiao, Nanostructured metal-free electrochemical catalysts for highly efficient oxygen reduction, Small 8 (23) (2012) 3550–3566, https://doi.org/10.1002/smll.201200861.
[32] U. Ghosh, A. Pal, Fabrication of a novel Bi2O3 nanoparticle impregnated nitrogen vacant 2D g-C3N4 nanosheet Z scheme photocatalyst for improved degradation of methylene blue dye under LED light illumination, Appl. Surf. Sci. 507 (2020), https://doi.org/10.1016/j.apsusc.2019.144965.
[33] G. Mamba, A.K. Mishra, Graphitic carbon nitride (g-C3N4) nanocomposites: a new and exciting generation of visible light driven photocatalysts for environmental pollution remediation, Appl. Catal. B Environ. 198 (2016) 347–377, https://doi.org/10.1016/j.apcatb.2016.05.052.
[34] B. Jiang, A. Huang, T. Wang, Q. Shao, W. Zhu, F. Liao, Y. Cheng, M. Shao, Rhodium/graphitic-carbon-nitride composite electrocatalyst facilitates efficient hydrogen evolution in acidic and alkaline electrolytes, J. Colloid Interface Sci. 571 (2020) 30–37, https://doi.org/10.1016/j.jcis.2020.03.022.
[35] K. Kwon, Y.J. Sa, J.Y. Cheon, S.H. Joo, Ordered mesoporous carbon nitrides with graphitic frameworks as metal-free, highly durable, methanol-tolerant oxygen reduction catalysts in an acidic medium, Langmuir 28 (1) (2012) 991–996, https://doi.org/10.1021/la204130e.
[36] W. Yang, J.E. Lu, Y. Zhang, Y. Peng, R. Mercado, J. Li, X. Zhu, S. Chen, Cobalt oxides nanoparticles supported on nitrogen-doped carbon nanotubes as high-efficiency cathode catalysts for microbial fuel cells, Inorg. Chem. Commun. 105 (2019) 69–75, https://doi.org/10.1016/j.inoche.2019.04.036.
[37] Y. Zheng, Y. Jiao, J. Chen, J. Liu, J. Liang, A. Du, W. Zhang, Z. Zhu, S.C. Smith, M. Jaroniec, G.Q. Lu, S.Z. Qiao, Nanoporous graphitic-C 3N 4@carbon metal-free electrocatalysts for highly efficient oxygen reduction, J. Am. Chem. Soc. 133 (50) (2011) 20116–20119, https://doi.org/10.1021/ja209206c.

[38] S.M. Lyth, Y. Nabae, S. Moriya, S. Kuroki, M.A. Kakimoto, J.I. Ozaki, S. Miyata, Carbon nitride as a nonprecious catalyst for electrochemical oxygen reduction, J. Phys. Chem. C 113 (47) (2009) 20148–20151, https://doi.org/10.1021/jp907928j.

[39] S. Li, Y. Hu, Q. Xu, J. Sun, B. Hou, Y. Zhang, Iron- and nitrogen-functionalized graphene as a non-precious metal catalyst for enhanced oxygen reduction in an air-cathode microbial fuel cell, J. Power Sources 213 (2012) 265–269, https://doi.org/10.1016/j.jpowsour.2012.04.002.

[40] D. Geng, Y. Chen, Y. Chen, Y. Li, R. Li, X. Sun, S. Ye, S. Knights, High oxygen-reduction activity and durability of nitrogen-doped graphene, Energy Environ. Sci. 4 (3) (2011) 760, https://doi.org/10.1039/c0ee00326c.

[41] L. Qu, Y. Liu, J.B. Baek, L. Dai, Nitrogen-doped graphene as efficient metal-free electrocatalyst for oxygen reduction in fuel cells, ACS Nano 4 (3) (2010) 1321–1326, https://doi.org/10.1021/nn901850u.

[42] K. Gong, F. Du, Z. Xia, M. Durstock, L. Dai, Nitrogen-doped carbon nanotube arrays with high electrocatalytic activity for oxygen reduction, Science 323 (5915) (2009) 760–764, https://doi.org/10.1126/science.1168049.

[43] T.C. Nagaiah, S. Kundu, M. Bron, M. Muhler, W. Schuhmann, Nitrogen-doped carbon nanotubes as a cathode catalyst for the oxygen reduction reaction in alkaline medium, Electrochem. Commun. 12 (3) (2010) 338–341, https://doi.org/10.1016/j.elecom.2009.12.021.

[44] F. Zhao, R.C.T. Slade, J.R. Varcoe, Techniques for the study and development of microbial fuel cells: an electrochemical perspective, Chem. Soc. Rev. 38 (7) (2009) 1926–1939, https://doi.org/10.1039/b819866g.

[45] X. Zhang, K. Li, P. Yan, Z. Liu, L. Pu, N-type Cu2O doped activated carbon as catalyst for improving power generation of air cathode microbial fuel cells, Bioresour. Technol. 187 (2015) 299–304, https://doi.org/10.1016/j.biortech.2015.03.131.

[46] X. Li, B. Hu, S. Suib, Y. Lei, B. Li, Manganese dioxide as a new cathode catalyst in microbial fuel cells, J. Power Sources 195 (9) (2010) 2586–2591, https://doi.org/10.1016/j.jpowsour.2009.10.084.

[47] L. Zhang, C. Liu, L. Zhuang, W. Li, S. Zhou, J. Zhang, Manganese dioxide as an alternative cathodic catalyst to platinum in microbial fuel cells, Biosens. Bioelectron. 24 (9) (2009) 2825–2829, https://doi.org/10.1016/j.bios.2009.02.010.

[48] G.D. Bhowmick, I. Chakraborty, M.M. Ghangrekar, A. Mitra, TiO2/activated carbon photo cathode catalyst exposed to ultraviolet radiation to enhance the efficacy of integrated microbial fuel cell-membrane bioreactor, Bioresour. Technol. Rep. 7 (2019), https://doi.org/10.1016/j.biteb.2019.100303.

[49] J. Thomas, M. Yoon, Facile synthesis of pure TiO 2(B) nanofibers doped with gold nanoparticles and solar photocatalytic activities, Appl. Catal. B Environ. 111–112 (2012) 502–508, https://doi.org/10.1016/j.apcatb.2011.10.039.

[50] Y. Wang, X. Yin, H. Shen, H. Jiang, J. Yu, Y. Zhang, D. Li, W. Li, J. Li, Co3O4@g-C3N4 supported on N-doped graphene as effective electrocatalyst for oxygen reduction reaction, Int. J. Hydrog. Energy 43 (45) (2018) 20687–20695, https://doi.org/10.1016/j.ijhydene.2018.09.140.

[51] A. Muthurasu, S.V. Sheen Mers, V. Ganesh, Nitrogen doped graphene quantum dots (N-GQDs)/Co3O4 composite material as an efficient bi-functional electrocatalyst for oxygen evolution and oxygen reduction reactions, Int. J. Hydrog. Energy 43 (9) (2018) 4726–4737, https://doi.org/10.1016/j.ijhydene.2017.11.157.

[52] M.G. Park, D.U. Lee, M.H. Seo, Z.P. Cano, Z. Chen, 3D ordered mesoporous bifunctional oxygen catalyst for electrically rechargeable zinc-air batteries, Small 12 (20) (2016) 2707–2714, https://doi.org/10.1002/smll.201600051.

[53] Y. Li, C. Zhong, J. Liu, X. Zeng, S. Qu, X. Han, Y. Deng, W. Hu, J. Lu, Atomically thin mesoporous Co 3 O 4 layers strongly coupled with N-rGO nanosheets as high-performance bifunctional catalysts for 1D knittable zinc–air batteries, Adv. Mater. 30 (4) (2018) 1703657, https://doi.org/10.1002/adma.201703657.

[54] Y. Liang, Y. Li, H. Wang, J. Zhou, J. Wang, T. Regier, H. Dai, Co3O4 nanocrystals on graphene as a synergistic catalyst for oxygen reduction reaction, Nat. Mater. 10 (10) (2011) 780–786, https://doi.org/10.1038/nmat3087.

[55] C. Hu, L. Dai, Multifunctional carbon-based metal-free electrocatalysts for simultaneous oxygen reduction, oxygen evolution, and hydrogen evolution, Adv. Mater. 29 (9) (2017), https://doi.org/10.1002/adma.201604942.
[56] G. Dong, Y. Zhang, Q. Pan, J. Qiu, A fantastic graphitic carbon nitride (g-C3N4) material: electronic structure, photocatalytic and photoelectronic properties, J Photochem Photobiol C: Photochem Rev 20 (1) (2014) 33–50, https://doi.org/10.1016/j.jphotochemrev.2014.04.002.
[57] Y. Wang, X. Wang, M. Antonietti, Polymeric graphitic carbon nitride as a heterogeneous organocatalyst: from photochemistry to multipurpose catalysis to sustainable chemistry, Angew. Chem. Int. Ed. 51 (1) (2012) 68–89, https://doi.org/10.1002/anie.201101182.
[58] C. Wang, L. Ma, L. Liao, S. Bai, R. Long, M. Zuo, Y. Xiong, A unique platinum-graphene hybrid structure for high activity and durability in oxygen reduction reaction, Sci. Rep. 3 (2013), https://doi.org/10.1038/srep02580.
[59] L. Jiao, J.Y.R. Seow, W.S. Skinner, Z.U. Wang, H.L. Jiang, Metal–organic frameworks: structures and functional applications, Mater. Today 27 (2019) 43–68, https://doi.org/10.1016/j.mattod.2018.10.038.
[60] D. Guo, S. Han, J. Wang, Y. Zhu, MIL-100-Fe derived N-doped Fe/Fe 3 C@C electrocatalysts for efficient oxygen reduction reaction, Appl. Surf. Sci. 434 (2018) 1266–1273, https://doi.org/10.1016/j.apsusc.2017.11.230.
[61] L. Yang, X. Zeng, W. Wang, D. Cao, Recent Progress in MOF-derived, heteroatom-doped porous carbons as highly efficient electrocatalysts for oxygen reduction reaction in fuel cells, Adv. Funct. Mater. 28 (7) (2018), https://doi.org/10.1002/adfm.201704537.
[62] Y. Zhang, L. Liu, B. Van Der Bruggen, F. Yang, Nanocarbon based composite electrodes and their application in microbial fuel cells, J. Mater. Chem. A 5 (25) (2017) 12673–12698, https://doi.org/10.1039/c7ta01511a.
[63] K. Zhong, Y. Wang, Q. Wu, H. You, H. Zhang, M. Su, R. Liang, J. Zuo, S. Yang, J. Tang, Highly conductive skeleton graphitic-C3N4 assisted Fe-based metal-organic frameworks derived porous bimetallic carbon nanofiber for enhanced oxygen-reduction performance in microbial fuel cells, J. Power Sources 467 (2020), https://doi.org/10.1016/j.jpowsour.2020.228313.
[64] S.P. Pattnaik, A. Behera, R. Acharya, K. Parida, Green exfoliation of graphitic carbon nitride towards decolourization of Congo-red under solar irradiation, J. Environ. Chem. Eng. 7 (6) (2019), https://doi.org/10.1016/j.jece.2019.103456.
[65] L. Yang, Z. Cai, L. Hao, Z. Xing, Y. Dai, X. Xu, S. Pan, Y. Duan, J. Zou, Nano Ce2O2S with highly enriched oxygen-deficient Ce3+ sites supported by N and S dual-doped carbon as an active oxygen-supply catalyst for the oxygen reduction reaction, ACS Appl. Mater. Interfaces 9 (27) (2017) 22518–22529, https://doi.org/10.1021/acsami.7b04997.
[66] Y. Wang, K. Zhong, Z. Huang, L. Chen, Y. Dai, H. Zhang, M. Su, J. Yan, S. Yang, M. Li, T. Xu, J. Tang, Novel g-C3N4 assisted metal organic frameworks derived high efficiency oxygen reduction catalyst in microbial fuel cells, J. Power Sources 450 (2020), https://doi.org/10.1016/j.jpowsour.2019.227681, 227681.
[67] L. Feng, L. Yang, Z. Huang, J. Luo, M. Li, D. Wang, Y. Chen, Enhancing electrocatalytic oxygen reduction on nitrogen-doped graphene by active sites implantation, Sci. Rep. 3 (2013), https://doi.org/10.1038/srep03306.

Further reading

A.K. Geim, K.S. Novoselov, The rise of graphene, Nat. Mater. 6 (3) (2007) 183–191, https://doi.org/10.1038/nmat1849.
X. Li, J. Yu, J. Low, Y. Fang, J. Xiao, X. Chen, Engineering heterogeneous semiconductors for solar water splitting, J. Mater. Chem. A 3 (6) (2015) 2485–2534, https://doi.org/10.1039/c4ta04461d.
Q. Liu, J. Zhang, Graphene supported co-g-C3N4 as a novel metal-macrocyclic electrocatalyst for the oxygen reduction reaction in fuel cells, Langmuir 29 (11) (2013) 3821–3828, https://doi.org/10.1021/la400003h.

H.W. Park, D.U. Lee, P. Zamani, M.H. Seo, L.F. Nazar, Z. Chen, Electrospun porous nanorod perovskite oxide/nitrogen-doped graphene composite as a bi-functional catalyst for metal air batteries, Nano Energy 10 (2014) 192–200, https://doi.org/10.1016/j.nanoen.2014.09.009.

K. Rabé, L. Liu, N.A. Nahyoon, Y. Zhang, A.M. Idris, Enhanced rhodamine B and coking wastewater degradation and simultaneous electricity generation via anodic g-C 3 N 4/Fe 0 (1%)/TiO 2 and cathodic WO 3 in photocatalytic fuel cell system under visible light irradiation, Electrochim. Acta 298 (2019) 430–439, https://doi.org/10.1016/j.electacta.2018.12.121.

S.Y. Sawant, T.H. Han, M.H. Cho, Metal-free carbon-based materials: promising electrocatalysts for oxygen reduction reaction in microbial fuel cells, Int. J. Mol. Sci. 18 (1) (2017), https://doi.org/10.3390/ijms18010025.

X. Shen, T. Zhang, P. Xu, L. Zhang, J. Liu, Z. Chen, Growth of C3N4 nanosheets on carbon-fiber cloth as flexible and macroscale filter-membrane-shaped photocatalyst for degrading the flowing wastewater, Appl. Catal. B Environ. 219 (2017) 425–431, https://doi.org/10.1016/j.apcatb.2017.07.059.

S. Wang, P.K. Ang, Z. Wang, A.L.L. Tang, J.T.L. Thong, K.P. Loh, High mobility, printable, and solution-processed graphene electronics, Nano Lett. 10 (1) (2010) 92–98, https://doi.org/10.1021/nl9028736.

G. Yang, D. Chen, P. Lv, X. Kong, Y. Sun, Z. Wang, Z. Yuan, H. Liu, J. Yang, Core-shell Au-Pd nanoparticles as cathode catalysts for microbial fuel cell applications, Sci. Rep. 6 (2016), https://doi.org/10.1038/srep35252.

T. Yu, L. Liu, L. Li, F. Yang, A self-biased fuel cell with TiO2/g-C3N4 anode catalyzed alkaline pollutant degradation with light and without light - what is the degradation mechanism? Electrochim. Acta 210 (2016) 122–129, https://doi.org/10.1016/j.electacta.2016.05.162.

Y. Zheng, J. Liu, J. Liang, M. Jaroniec, S.Z. Qiao, Graphitic carbon nitride materials: controllable synthesis and applications in fuel cells and photocatalysis, Energy Environ. Sci. 5 (5) (2012) 6717–6731, https://doi.org/10.1039/c2ee03479d.

CHAPTER 5

Solar energy harvesting with carbon nitrides

Arabinda Baruah[a], Nirupamjit Sarmah[a], Santosh Kumar[b], Priya Ghosh[c], Ritu Malik[d], and Vijay K. Tomer[d]
[a]Department of Chemistry, Gauhati University, Guwahati, Assam, India
[b]Department of Chemical Engineering, Imperial College London, London, United Kingdom
[c]Department of Applied Organic Chemistry, CSIR-NEIST, Jorhat, Assam, India
[d]Department of Mechanical Engineering, University of California, Berkeley, CA, United States

Contents

1. Introduction

Semiconductor photocatalysis has emerged as a most promising new technology in the past few years for the production of clean energy and environmental remediation because the use of catalysts and solar energy is most economical [1–4]. A significantly efficient, stable, inexpensive, and easily separable semiconductor material that is capable of light harvesting is also essential for an economical use of catalysts [5]. Therefore, intense research activity has recently been focused on the development of an efficient semiconductor material with unique properties apart from TiO_2, which can directly split water or degrade environmental pollutants using solar energy [5–23]. It is an efficient technology for producing environmentally benign energy, in which one can use the sunlight as an energy source and it offers the possibility of accomplishing energy cycles without pollution of the environment and additional heating of the earth [3,24]. Unfortunately, most widely employed semiconductor photocatalysts are only active under UV-light irradiation, but photocatalysis using solar light could be highly economical compared to the process using an artificial UV-light source [4,25–27]. Therefore, development of efficient visible-light-driven photocatalysts is today's demand.

Nanostructured Carbon Nitrides for Sustainable Energy and Environmental Applications
https://doi.org/10.1016/B978-0-12-823961-2.00003-3

More recently, graphitic carbon nitride (g-C_3N_4) was found to be a typical metal-free polymeric semiconductor material with a suitable band gap to absorb visible-light radiation and unique properties [28–32]. Therefore, it is promising to consider graphitic carbon nitride as an alternative candidate for solar light harvesting and conversion because of its many interesting features, including visible-light adsorption ability and ease of large-scale preparation, which is always preferred for practical applications. Also, chemical functionalization or doping of g-C_3N_4 is easy because of its intrinsic organic nature, thus allowing its electronic band gap structure to be tuned, and contrary to many other organic semiconductors, graphitic carbon nitride has high thermal and chemical stability against oxidation reactions and is stable in atmosphere up to 500°C [33–42].

It possesses good photocatalytic potential for hydrogen production from water splitting and the photodegradation of organic pollutants under visible-light irradiation [43,44]. The metal-free g-C_3N_4 photocatalyst possesses a very high thermal and chemical stability, as well as electronic properties. However, the photocatalytic performance of g-C_3N_4 is still limited due to the high recombination rate of the photo-induced electron-hole pair. Therefore, making g-C_3N_4 a valuable material for visible-light-driven photocatalysts is important. Recently, several efforts have been made to improve the photocatalytic activity of g-C_3N_4 by employing different modifications, such as loading a cocatalyst onto the surface of g-C_3N_4, designing appropriate textural properties, doping and making composites with other semiconductor materials [29,45–48]. More recently Chengsi et al. reported a g-C_3N_4-$BiPO_4$ photocatalyst with a core-shell structure formed by a self-assembly process and its application in the photocatalytic degradation of methylene blue (MB). The results showed that the photocatalytic activity of such a composite material was dramatically improved [36].

To date, a large number of articles concerning the synthesis of g-C_3N_4 and its derivatives have been published. For example, loading some cocatalysts onto the surface of the catalyst and doping g-C_3N_4 with nonmetals such as B, C, and S can evidently promote the separation efficiency of photo-induced electron-hole pairs [36,49–51]. Another feasible strategy to improve its photocatalytic performance is to form a composite with a metal or another semiconductor by designing an appropriate textural porosity [39,52–54]. Unfortunately, the performance of the present g-C_3N_4-based photocatalysts does not meet the needs of practical applications because of the inconvenience of recycling these catalysts due to their highly dispersive nature, the fact that conventional separation techniques may lead to loss of catalyst, and the lack of a facile and environmentally friendly strategy to prepare g-C_3N_4-based photocatalysts with desired properties. Therefore, the development of a highly effective visible-light-driven photocatalyst for the production of clean energy and environmental remediation is still being sought.

A few visible-light photocatalysts, such as Ag-based photocatalysts, nanocomposite photocatalysts, and g-C_3N_4 photocatalysts have attracted much attention for the photo-degradation of organic pollutants and water splitting for environmentally clean energy in recent years [48,55–62]. However, a Ag_3PO_4 semiconductor has been reported as an active visible-light-driven photocatalyst for organic pollutants and hydrogen evolution from water splitting [63,64]. The photocatalytic performance of Ag_3PO_4 is significantly higher than that of currently known visible-light photocatalysts, such as g-C_3N_4, N-doped TiO_2, and $BiVO_4$ [65,66]. Unfortunately, this Ag_3PO_4 visible-light photocatalyst is photo-chemically unstable, since silver salts are well known to decompose on light irradiation [23]. In addition to this stability, silver usage and the particle size of the Ag_3PO_4 photocatalyst remains relatively large, hindering its performance in photocatalytic processes for large scale applications. Therefore, a challenging task associated with this visible-light photocatalyst is the synthesis of stable nano-sized Ag_3PO_4 particles with a high surface area. Thus, much attention has been employed to develop a simple and effective technology to reduce Ag consumption for a Ag_3PO_4 photocatalyst and to improve its stability and surface area for large scale applications.

On the other hand, Fe_3O_4 nanoparticles have attracted much interest because of their magnetic properties, which have led to their applications in drug delivery systems [67,68], lithium storage capacity [69], wastewater treatment [70], magnetic resonance imaging [71,72], and protein separation [73]. Interestingly, Fe_3O_4 can be considered as a conductor because its conductivity is as high as $1.9 \times 10^6\,S\,m^{-1}$, which is different from the other semiconductor characteristics of most metal oxide materials [74]. Heterostructured catalysts composed of magnetic components, including metal/Fe_3O_4, graphene/Fe_3O_4, WO_3/Fe_3O_4, and TiO_2/Fe_3O_4, have shown improved performance due to their unique properties and potential applications that could not be achieved solely with a single-component catalyst [75–77]. In this context, these studies initially intended to integrate superparamagnetic iron oxide nanoparticles and g-C_3N_4 sheets into a single hybrid nanocomposite as an efficient visible-light photocatalyst because the high conductivity of Fe_3O_4 and energy band structure matching ($E_{CB} = 1\,V$ vs NHE) makes it a good candidate for coupling with g-C_3N_4 and improving the photocatalytic performance by enhancing the photoinduced charge separation of electron-hole pairs and transport.

2. Magnetically separable g-C_3N_4-Fe_3O_4 as visible-light-driven photocatalyst

In a very interesting work reported by Kumar et al. [12], a facile and reproducible strategy for preparing g-C_3N_4-Fe_3O_4 hybrid nanocomposites has been reported. The results demonstrated that successful deposition of uniform monodispersed Fe_3O_4 nanoparticles onto the surface of g-C_3N_4 sheets allows the diffusion of light by multiple pathways to enhance light harvesting, and significantly enhanced photocatalytic activity was observed under visible-light irradiation. A possible mechanism for the enhancement of photocatalytic activity was also investigated. In addition, deposition of magnetic nanoparticles onto the surface of the photocatalysts proved to be an effective way to separate photocatalyst easily from the photocatalytic system with an external magnetic field, allowing them to be reused in multiple cycles. This approach prevented the agglomeration of the catalyst particles during recovery and can increase the durability of the catalysts. The goal of this work was to design more efficient g-C_3N_4-based photocatalysts by recycling and expanding the light absorption further into the visible range while still keeping a sufficient overpotential to carry out the desired reactions, making Fe_3O_4 a valuable photocatalytic material for its potential applications in environmental protection.

2.1 Synthetic methodology for the preparation of g-C_3N_4-Fe_3O_4

Adopted experimental procedure has been briefly discussed later. The g-C_3N_4 was prepared by direct heating of melamine to 550°C for 2h in a N_2 atmosphere. The g-C_3N_4-Fe_3O_4 nanocomposites were prepared by an in situ precipitation method. In a typical procedure, g-C_3N_4 (125mg) was dispersed in 500mL of ethanol/water (1:2) and ultrasonicated (PCI Analytics, 12mm probe, 33Hz, 150W) for 5h at ambient temperature. $FeCl_3 \cdot 6H_2O$ (1.838g, 0.0216mol) and $FeCl_2 \cdot 4H_2O$ (0.703g, 0.0108mol) were dissolved separately in 20mL of double-distilled water and added to the suspension of g-C_3N_4. The mixture was stirred at 80°C for 30min, and then 10mL of ammonia solution (NH_4OH) was quickly injected into the reaction mixture. The resulting mixture was stirred for another 30min, after which the reaction mixture was cooled and washed several times with double-distilled water and absolute alcohol. Finally, the as-obtained precipitate was dried in air at 80°C for further characterization. For comparison, free Fe_3O_4 nanoparticles were also synthesized using exactly the same procedure without adding g-C_3N_4. The as-prepared g-C_3N_4-Fe_3O_4 photocatalysts with 7.5, 15.2, and 23.0wt% Fe_3O_4 were named as CNFO-7.5, CNFO-15.2, and CNNFO-23.0, respectively. The pure g-C_3N_4 was named as CN, and Fe_3O_4 was named as FO. Rhodamine B (RhB), a widely used dye, was chosen as a model pollutant to examine the visible-light-driven photocatalytic activity of the samples. The photocatalytic activity of the samples was evaluated via degradation of RhB in an aqueous solution under visible-light irradiation. The visible-light source was a solar simulator 300W Xe lamp. The photocatalyst (0.025g) was added to an aqueous solution of RhB (100mL, $5\,mg\,L^{-1}$) in a beaker at room temperature under stirring at 250rpm throughout the test under visible-light irradiation. Prior to irradiation, the solution was stirred continuously for 30min in the dark to establish an adsorption-desorption equilibrium. During photocatalytic processes, the sample was periodically withdrawn, centrifuged to separate the photocatalyst from the solution, and used for the absorbance measurement. The concentration of RhB during the degradation process was monitored using a UV-vis spectrophotometer.

2.2 Results and discussion

Formation of g-C_3N_4-Fe_3O_4 nanocomposites

The in situ growth mechanism has been widely employed to synthesize a variety of carbon-based composites. A similar strategy was used for the preparation of the g-C_3N_4-Fe_3O_4 hybrid nanocomposites, as shown in Fig. 5.1. When iron salts were mixed with ultrasonically dispersed g-C_3N_4 sheets, the iron ions were deposited on the surface of g-C_3N_4 via chemical adsorption. Furthermore, iron ions were converted into Fe_3O_4 nanoparticles with controlled growth by using ammonia as a precipitating agent at room temperature. Thus, finely distributed and uniform Fe_3O_4 nanoparticles were successfully deposited on the surface of the g-C_3N_4 sheets. To minimize the surface energy, the as-prepared Fe_3O_4 nanoparticles led the heterojunction at the interface of the g-C_3N_4 and Fe_3O_4 in the resulting composite system. The size of the Fe_3O_4 nanoparticles in the hybrid nanocomposite was as small as 8 nm. The in situ growth mechanism also avoided the agglomeration of Fe_3O_4 nanoparticles.

Catalyst characterization

To calculate the content of Fe_3O_4 nanoparticles on g-C_3N_4 sheets, TGA was performed on g-C_3N_4-Fe_3O_4 nanocomposites under an air atmosphere from 50°C to 800°C. The decomposition of g-C_3N_4 starts at 550°C and is completed at ~720°C, which is attributed to the burning of g-C_3N_4. This weight loss region could be seen in the g-C_3N_4-Fe_3O_4 hybrid composite samples. The residual weight fractions of the different nanocomposites (CNFO-7.5, CNFO-15.2, and CNNFO-23.0) were found to be 7.5%, 15.2%, and 23.0%, which are considered to be the contents of Fe_3O_4 in the g-C_3N_4-Fe_3O_4 nanocomposites.

The XRD patterns of pure Fe_3O_4, pure g-C_3N_4, and the hybrid composites CNFO-7.5, CNFO-15.2, and CNFO-23.0, which were used to elucidate the phase and structural parameters. The observed diffraction peaks of pure Fe_3O_4 are in good agreement with

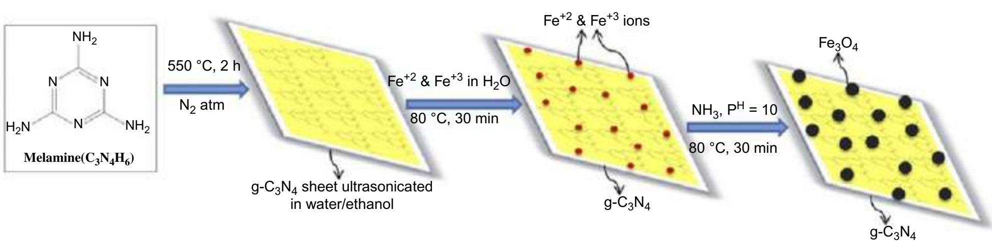

Fig. 5.1 Schematic representation of the in situ deposition of Fe_3O_4 nanoparticles on a g-C_3N_4 sheet. *(Adapted from S. Kumar, T. Surendar, B. Kumar, A. Baruah, V. Shanker, Synthesis of magnetically separable and recyclable g-C_3N_4-Fe_3O_4 hybrid nanocomposites with enhanced photocatalytic performance under visible-light irradiation, J. Phys. Chem. C 117(49) (2013) 26135–26143, https://doi.org/10.1021/jp409651g, American Chemical Society, Copyright 2013.)*

those reported in the literature for pure face-centered-cubic Fe_3O_4 [69,70]. For g-C_3N_4, a strong peak at $2\theta = 27.5°$ corresponding to the characteristic interplanar stacking peak (002) of an aromatic system was observed [78]. The diffraction peak (002) is a characteristic peak of g-C_3N_4 that was also present in pattern of the g-C_3N_4-Fe_3O_4 nanocomposite. It was also seen that the crystal phase of Fe_3O_4 did not change after hybridization with g-C_3N_4, but the diffraction peak positions for Fe_3O_4 were located at slightly lower angles than those for pure Fe_3O_4, suggesting a strong interaction between Fe_3O_4 and g-C_3N_4. Moreover, no other impurity phase was seen, indicating the g-C_3N_4-Fe_3O_4 to be a two-phase composite.

In the FT-IR spectra of pure Fe_3O_4, pure g-C_3N_4, and the g-C_3N_4-Fe_3O_4 hybrid nanocomposites, a broad Fe–O band in the region from 550 to 650 cm^{-1} was visible [72]. In the FT-IR spectrum of g-C_3N_4, the broad band around 3100 cm^{-1} is indicative of the N–H stretching vibration, and the peaks at 1243 and 1637 cm^{-1} correspond to C–N and C=N stretching vibrations, respectively. The peak at 808 cm^{-1} is related to the *s*-triazine ring vibrations. The characteristic peaks of g-C_3N_4 and Fe_3O_4 are retained in the g-C_3N_4-Fe_3O_4 hybrid nanocomposite samples. However, a broad band around 3300–3600 cm^{-1} and a band at 1658 cm^{-1} are observed, corresponding to OH stretching vibrations of adsorbed water molecules, and another peak at 1384 cm^{-1} corresponds to the H–O–H bending band of the adsorbed H_2O molecules on the surface of the products. The IR bands due to adsorbed water arise from water released as a decomposition product that later gets adsorbed during the measurement.

The UV-vis DRS spectra of g-C_3N_4-Fe_3O_4 hybrid nanocomposite showed absorption at 450 nm that corresponds to a band gap of 2.76 eV. It signifies its photocatalytic activity under visible-light irradiation. The enhanced light absorption of the g-C_3N_4-Fe_3O_4 nanocomposite led to the generation of more photoinduced electron-hole pairs under visible-light irradiation, which subsequently resulted in enhanced photocatalytic activity.

TEM analysis showed that the pure g-C_3N_4 consists of a sheet structure, whereas the pure Fe_3O_4 nanoparticles have sizes ranging from 50 to 200 nm. No distinctive morphological features appeared for Fe_3O_4 nanoparticles, and they were highly agglomerated. Fig. 5.2 shows TEM and high-resolution TEM (HRTEM) images of g-C_3N_4-Fe_3O_4 hybrid nanocomposites. The TEM image (Fig. 5.2A) reveals that Fe_3O_4 nanoparticles were successfully deposited on the surface of the g-C_3N_4 sheet by the in situ growth mechanism; almost no free Fe_3O_4 nanoparticles were found outside of the g-C_3N_4 sheet, which also prevented the agglomeration of Fe_3O_4 nanoparticles. The size of the Fe_3O_4 nanoparticles was found to be around 8 nm. The HRTEM image (Fig. 5.2B) confirms the heterostructure in the g-C_3N_4-Fe_3O_4 nanocomposite system, where the g-C_3N_4 sheet could serve as a support and surfactant to bind with Fe_3O_4 nanoparticles in the resulting composite system. As the content of Fe_3O_4 nanoparticles on the

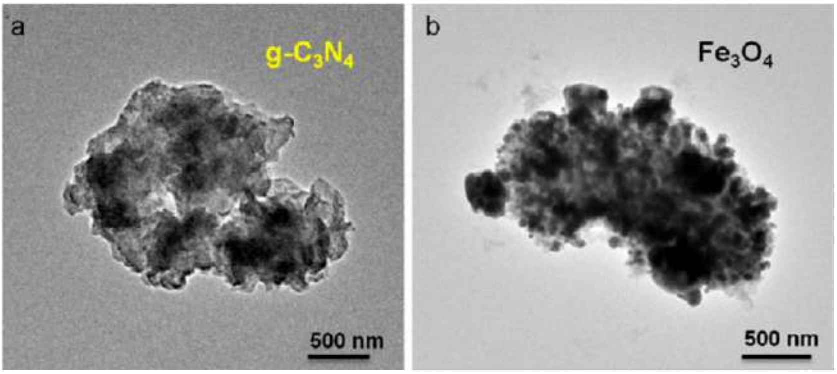

Fig. 5.2 Magnified (A) TEM and (B) HRTEM images of the as-prepared g-C_3N_4-Fe_3O_4 photocatalyst. *(Adapted from S. Kumar, T. Surendar, B. Kumar, A. Baruah, V. Shanker, Synthesis of magnetically separable and recyclable g-C_3N_4-Fe_3O_4 hybrid nanocomposites with enhanced photocatalytic performance under visible-light irradiation, J. Phys. Chem. C 117(49) (2013) 26135–26143, https://doi.org/10.1021/jp409651g, American Chemical Society, Copyright 2013.)*

surface of g-C_3N_4 sheet increased from 7.5 to 15.2 wt%, the density of Fe_3O_4 nanoparticles on the surface of g-C_3N_4 sheet increased.

Both the UV-vis DRS spectra and TEM results for the g-C_3N_4-Fe_3O_4 nanocomposites suggested the effective assembly of Fe_3O_4 nanoparticles on g-C_3N_4 sheets were successfully deposited on the surface of the g-C_3N_4 sheet by the in situ growth mechanism; almost no free Fe_3O_4 nanoparticles were found outside of the g-C_3N_4 sheet, which also prevented the agglomeration of Fe_3O_4 nanoparticles. The size of the Fe_3O_4 nanoparticles was found to be around 8 nm. The HRTEM image (Fig. 5.2B) confirms the heterostructure in the g-C_3N_4-Fe_3O_4 nanocomposite system, where the g-C_3N_4 sheet could serve as a support and surfactant to bind with Fe_3O_4 nanoparticles in the resulting composite system. As the content of Fe_3O_4 nanoparticles on the surface of g-C_3N_4 sheet increased from 7.5 to 15.2 wt%, the density of Fe_3O_4 nanoparticles on the surface of g-C_3N_4 sheet increased. Both the UV-vis DRS spectra and TEM results for the g-C_3N_4-Fe_3O_4 nanocomposites suggested the effective assembly of Fe_3O_4 nanoparticles on g-C_3N_4 sheets.

N_2 adsorption-desorption measurements were performed to investigate the Brunauer-Emmett-Teller (BET) specific surface area of pure g-C_3N_4, pure Fe_3O_4, and as-prepared CNFO-15.2. The BET surface area of CNFO-15.2 was found to be 72.73 $m^2\ g^{-1}$, which is much higher than the values for g-C_3N_4 (8.56 $m^2\ g^{-1}$) and bare Fe_3O_4 (6.81 $m^2\ g^{-1}$). Importantly, along with the apparent increment in surface area, an increase in the pore volume from 0.11 $cm^3\ g^{-1}$ for as-prepared g-C_3N_4 to 0.25 $cm^3\ g^{-1}$ for CNFO-15.2 was observed, which facilitated charge separation in the composite system.

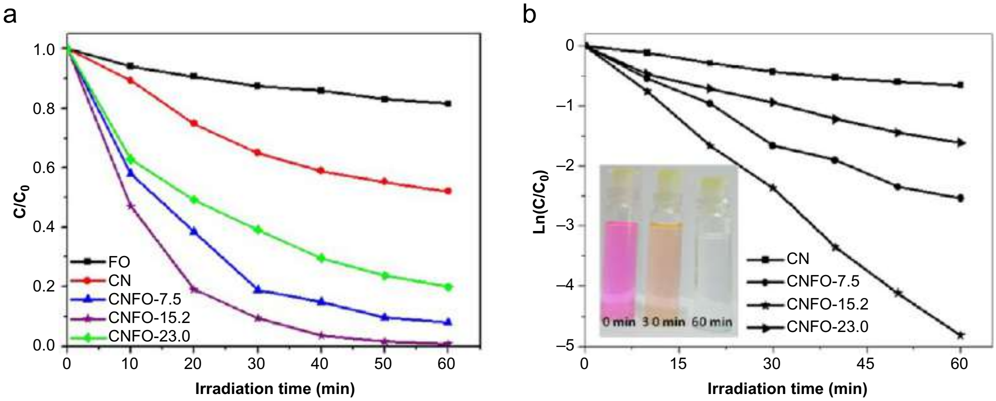

Fig. 5.3 (A) Photocatalytic degradation of RhB over pure g-C_3N_4, pure Fe_3O_4, and the as-prepared g-C_3N_4-Fe_3O_4 photocatalysts under visible-light irradiation. (B) Plots of ln(C/C_0) vs time. The inset is a photograph showing the degradation of RhB over the g-C_3N_4-Fe_3O_4 photocatalyst. *(From S. Kumar, T. Surendar, B. Kumar, A. Baruah, V. Shanker, Synthesis of magnetically separable and recyclable g-C_3N_4-Fe_3O_4 hybrid nanocomposites with enhanced photocatalytic performance under visible-light irradiation, J. Phys. Chem. C 117(49) (2013) 26135–26143, https://doi.org/10.1021/jp409651g.)*

Photocatalytic activity

The photocatalytic activity of the as-prepared nanocomposites for the degradation of RhB under visible-light irradiation was evaluated (Fig. 5.3). The initial concentration of the RhB suspension was measured and used as the initial concentration C_0. The Y axis is reported as C/C_0, where C is the actual concentration of RhB at the indicated reaction time. The decrease in the concentration of RhB is faster and more prominent with g-C_3N_4-Fe_3O_4 nanocomposites than with pure g-C_3N_4 or Fe_3O_4 under the same experimental conditions. Without the presence of a catalyst, the degradation of RhB was negligible under visible-light irradiation, indicating the high stability of RhB under visible-light irradiation. To disclose the adsorption effect of the catalyst on RhB, the suspension was stirred for 30 min in the dark to achieve adsorption-desorption equilibration before the photodegradation test. g-C_3N_4-Fe_3O_4 nanocomposite exhibited a much higher RhB adsorption capacity than pure g-C_3N_4. The results indicated that the presence of the catalyst and light is essential for the efficient degradation of RhB under visible-light irradiation. As shown in Fig. 5.3B, the plots of ln(C/C_0) versus irradiation time were linear, which indicates that the photodegradation of the RhB went through a pseudo-first-order kinetic reaction [75]. The optimum photocatalytic activity of g-C_3N_4-Fe_3O_4 at an Fe_3O_4 mass content of 15.2% under visible-light irradiation is almost seven times higher than that of pure g-C_3N_4. The enhanced photocatalytic performance of the g-C_3N_4-Fe_3O_4 nanocomposite may be attributed to the synergistic effect between the interface of Fe_3O_4 and g-C_3N_4.

Photoluminescence

In order to disclose the effect of Fe_3O_4 modification, PL spectral analysis was carried out to reveal the migration, transfer, and recombination processes of photoinduced electron-hole pairs in the composite system. The main emission peak is centered at about 435 nm for the pure g-C_3N_4 sample. The PL intensity of the g-C_3N_4-Fe_3O_4 nanocomposites is significantly decreased, which indicates that the composite has a much lower recombination rate of photoinduced electron-hole pairs.

EIS studies

In addition, EIS measurements were conducted to investigate the charge transfer resistance and the separation efficiency of the photoinduced charge carrier. The diameter of the Nyquist semicircle for CNFO-15.2 nanocomposite is smaller than those of g-C_3N_4 and Fe_3O_4, which indicates that the CNFO-15.2 nanocomposite has a lower resistance than g-C_3N_4 and Fe_3O_4. This result demonstrates that the introduction of Fe_3O_4 into g-C_3N_4 can enhance the separation and transfer efficiency of photoinduced electron-hole pairs, which is a favorable condition for improving the photocatalytic activity.

Reusability check

To study the stability of the as-prepared g-C_3N_4-Fe_3O_4 photocatalyst, the used g-C_3N_4-Fe_3O_4 was collected, and the reusability was further examined in six successive RhB degradation experiments. The g-C_3N_4-Fe_3O_4 retained over 90% of its original photocatalytic activity after six successive experimental runs, which is also very important from a practical application point of view. From PXRD analysis, it could be seen that no new peak appeared in the composite system. Therefore, the g-C_3N_4-Fe_3O_4 composite can be used efficiently in environmental protection.

Magnetic separation of the nanocomposite after the reaction

To collect and reuse the photocatalyst in multiple cycles, its preparation with good superparamagnetism is essential. The behavior of the g-C_3N_4-Fe_3O_4 hybrid nanocomposite dispersed in water in a magnetic field under neutral conditions was studied. The g-C_3N_4-Fe_3O_4 photocatalyst is strongly attracted to a permanent magnet. Therefore, the g-C_3N_4-Fe_3O_4 photocatalysts can be rapidly separated under an applied magnetic field.

Detection of reactive oxidative species

In general, reactive species including $^{\bullet}OH$ and $O_2^{\bullet-}$ are expected to be involved in the photocatalytic process. To investigate the role of these reactive species in the g-C_3N_4-Fe_3O_4 system, the effects of some radical scavengers and N_2 purging on the photodegradation of RhB were studied. When N_2 purging was conducted as an $O_2^{\bullet-}$

scavenger, a dramatic change in the photocatalytic activity was observed compared with the absence of scavenger, confirming that the dissolved O_2 has a clear effect on the photodegradation process under visible-light irradiation. Meanwhile, a similar change in the photocatalytic activity was observed upon the addition of tBuOH as an OH scavenger. However, no change in the photocatalytic activity was observed upon the addition of ammonium oxalate (AO) as a hole scavenger compared with no scavenger under similar conditions, indicating that the $O_2^{\bullet -}$ and $^{\bullet}OH$ are the main reactive species in the g-C_3N_4-Fe_3O_4 system. Moreover, PL spectra were used to disclose the formation of $^{\bullet}OH$. The PL emission peak of 2-hydroxyterephthalic acid was observed and gradually increased with the irradiation time, which indicates the formation of photoinduced $^{\bullet}OH$ under visible-light irradiation.

Mechanism of enhanced photocatalytic performance

A schematic drawing illustrating the synergistic effect in the photocatalytic degradation of RhB over the g-C_3N_4-Fe_3O_4 hybrid composite is shown in Fig. 5.4. Under visible-light irradiation, the photoinduced electrons can easily be transferred from the conduction band (CB) of g-C_3N_4 to the CB of Fe_3O_4 because the CB level of Fe_3O_4 is lower than that of g-C_3N_4 (i.e., energy matching band structure is observed in the g-C_3N_4-Fe_3O_4 hybrid composite system) [74,78]. Furthermore, because of the high conductivity of Fe_3O_4, the rate of electron transport is fast, which suppresses the direct recombination of photoinduced electron-hole pairs in the g-C_3N_4-Fe_3O_4 hybrid composite system.

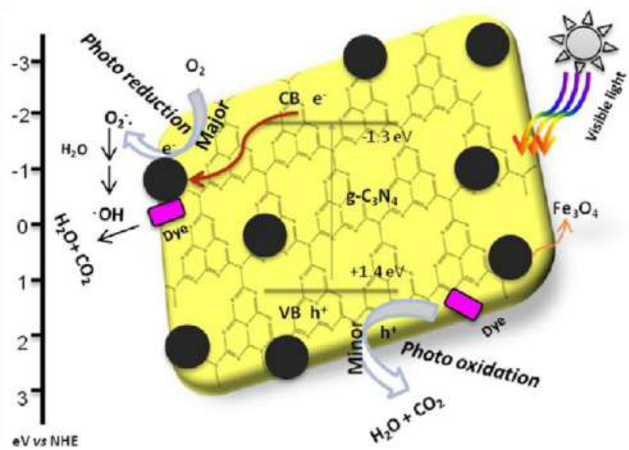

Fig. 5.4 Schematic illustration of the mechanism for photoinduced charge carrier transfers in the g-C_3N_4-Fe_3O_4 photocatalyst under visible-light irradiation. *(From S. Kumar, T. Surendar, B. Kumar, A. Baruah, V. Shanker, Synthesis of magnetically separable and recyclable g-C_3N_4-Fe_3O_4 hybrid nanocomposites with enhanced photocatalytic performance under visible-light irradiation, J. Phys. Chem. C 117(49) (2013) 26135–26143, https://doi.org/10.1021/jp409651g.)*

Thus, Fe_3O_4 acts as an acceptor of the photoinduced electrons from g-C_3N_4. Therefore, because of the presence of the g-C_3N_4-Fe_3O_4 interface, the chance of recombination of photoinduced electron-hole pairs is further successfully suppressed, leaving more charge carriers to form reactive species. The electrons in the CB of Fe_3O_4 are good reductants that could efficiently reduce the O_2 adsorbed onto the composite catalyst surface into various reactive species ($O_2^{\bullet-}$, $HO_2^{\bullet}$, H_2O_2), subsequently leading to the formation of $^{\bullet}OH$ and oxidation of RhB into CO_2, H_2O, etc. Therefore, the enhanced photocatalytic activity is achieved.

3. Solar energy harvesting using g-C_3N_4-Ag_3PO_4 hybrid nanocomposite

In another highly fascinating report by Kumar et al. [11], a facile and reproducible template free in situ precipitation method for the synthesis of Ag_3PO_4 nanoparticles on the surface of a g-C_3N_4 photocatalyst at room temperature has been discussed. The results demonstrated that after hybridization with g-C_3N_4, the stability of Ag_3PO_4 was enhanced under visible-light irradiation and more attractively a dramatic photocatalytic activity under visible-light irradiation was observed due to the introduction of g-C_3N_4 to Ag_3PO_4 which can effectively enhance the charge separation and photostability. The synergic effect between Ag_3PO_4 and g-C_3N_4, the possible mechanisms of photostability and enhancement of the photocatalytic activity via hybridization were also investigated. Therefore, the novel heterostructured photocatalyst, i.e., the combination of these two photocatalysts is of potential interest for overall water splitting via sunlight since g-C_3N_4 is a newly developed metal-free hydrogen evolution photocatalyst, whereas the Ag_3PO_4 is also a newly developed water oxidation photocatalyst. Moreover, the silver weight percentage of the photocatalyst decreases extensively, thereby reducing the cost of Ag_3PO_4-based photocatalysts. It has also made the g-C_3N_4 as a valuable photocatalytic material for its potential applications in environmental protection.

3.1 Synthesis of g-C_3N_4-Ag_3PO_4 photocatalysts

The preparation of the pure Ag_3PO_4 and g-C_3N_4-Ag_3PO_4 hybrid composites is shown by a schematic diagram (Fig. 5.5).

The g-C_3N_4 was prepared by direct heating of the melamine to 550°C for 2h in a N_2 atmosphere. Pure Ag_3PO_4 was prepared by using an ion exchange method. 0.1M aqueous solution of silver nitrate was added to a beaker and an aqueous solution of sodium phosphate dodecahydrate was added and stirred for 5h at room temperature. The solution was centrifuged and the solid product washed (three times) with water and ethanol and then dried in an oven for 2h at 100°C. For the preparation of the g-C_3N_4-Ag_3PO_4 photocatalysts, an appropriate amount of g-C_3N_4 was ultrasonicated in 50mL of water for 30min. To this, 0.42g of silver nitrate was added and stirred at room temperature for 1h. Further, 50mL of 0.1M Na_3PO_4 was added and stirred for 5h. The obtained solid

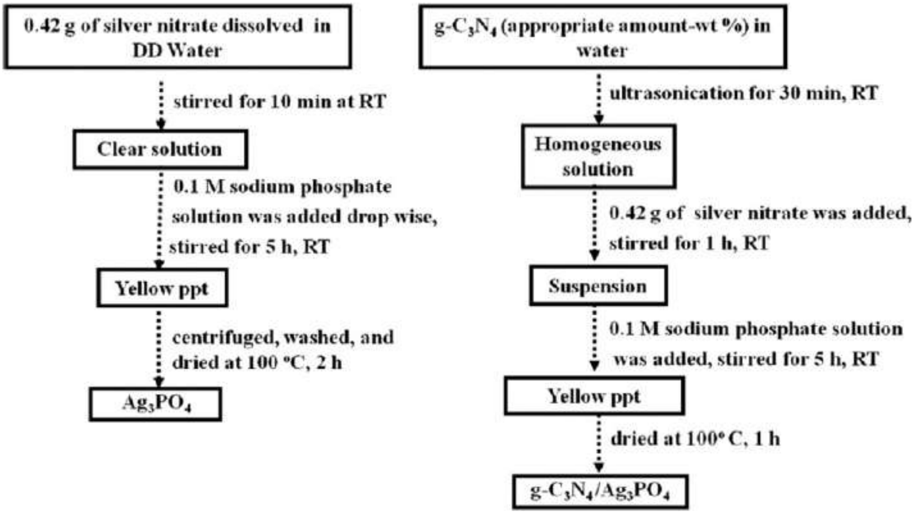

Fig. 5.5 Flow charts for the synthesis of pure Ag_3PO_4 and $g\text{-}C_3N_4/Ag_3PO_4$ photocatalysts. *(From S. Kumar, T. Surendar, A. Baruah, V. Shanker, J. Mater. Chem. A 1(17) (2013) 5333–5340, https://doi.org/10.1039/c3ta00186e.)*

product was centrifuged, washed and dried at 100°C for 1 h. The $g\text{-}C_3N_4\text{-}Ag_3PO_4$ photocatalysts with different weight ratios of $g\text{-}C_3N_4$, particularly 25% and 40% were synthesized and named as CNAGPO25, and CNAGPO40, respectively. The pure $g\text{-}C_3N_4$ was named as CN and Ag_3PO_4 was named as AGPO.

3.2 Results and discussion

Catalyst characterization

The XRD patterns of the Ag_3PO_4, $g\text{-}C_3N_4$, and $g\text{-}C_3N_4\text{-}Ag_3PO_4$ photocatalysts are shown in Fig. 5.6. The results indicate that the diffraction peaks corresponding to the body-centered cubic phase of Ag_3PO_4 (JCPDS#060505) are retained for the $g\text{-}C_3N_4\text{-}Ag_3PO_4$ hybrid composites. There are crystalline $g\text{-}C_3N_4$ peaks in the $g\text{-}C_3N_4\text{-}Ag_3PO_4$ hybrid composite photocatalysts, the peak intensities increased with the increase in $g\text{-}C_3N_4$ loading.

TGA was carried out for the $g\text{-}C_3N_4$ and $g\text{-}C_3N_4\text{-}Ag_3PO_4$ samples. The amount of loaded $g\text{-}C_3N_4$ was confirmed by TG analysis. For pure $g\text{-}C_3N_4$, a weight loss occurring from 550°C to 720°C could be attributed to the burning of $g\text{-}C_3N_4$. This weight loss region could be seen in all $g\text{-}C_3N_4\text{-}Ag_3PO_4$ hybrid composites. The amount of $g\text{-}C_3N_4$ in the hybrid composite was calculated from the corresponding weight loss. The $g\text{-}C_3N_4$ in the loaded compositions of 1:3 and 2:3 weight ratios of $g\text{-}C_3N_4\text{-}Ag_3PO_4$ was found to be 27 and 42 wt%, respectively. Therefore, the amount of $g\text{-}C_3N_4$ was nearly consistent to the dosage of $g\text{-}C_3N_4$ loaded.

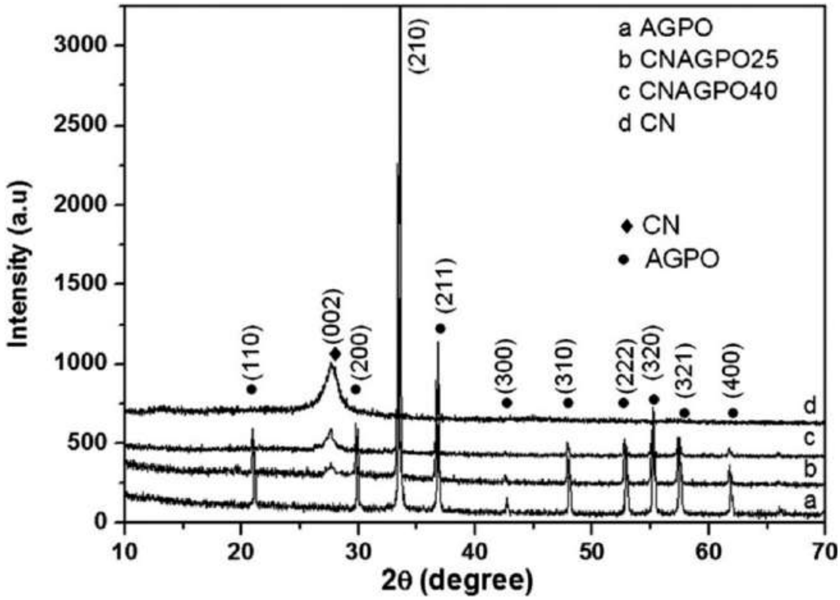

Fig. 5.6 XRD patterns of the as-synthesized g-C_3N_4-Ag_3PO_4 and g-C_3N_4-Ag_3PO_4 photocatalysts. *(From S. Kumar, T. Surendar, A. Baruah, V. Shanker, Synthesis of a novel and stable g-C_3N_4-Ag_3PO_4 hybrid nanocomposite photocatalyst and study of the photocatalytic activity under visible light irradiation, J. Mater. Chem. A 1(17) (2013) 5333–5340, https://doi.org/10.1039/c3ta00186e.)*

The FT-IR spectra of g-C_3N_4, Ag_3PO_4, and g-C_3N_4-Ag_3PO_4 photocatalysts. In the FT-IR spectrum of g-C_3N_4, the broad bands around 3100 cm^{-1} are indicative of N—H stretching vibrations, the peaks at 1243 and 1637 cm^{-1} correspond to the C—N and C=N stretching vibrations, respectively. The peak at 808 cm^{-1} is related to the *s*-triazine ring vibrations [79–81]. In the FT-IR spectrum of Ag_3PO_4, the broad absorption peaks were around 3300–3600 and 1658 cm^{-1} corresponding to OH stretching vibrations, and the peak at 1384 cm^{-1} is corresponding to the H—O—H bending band of the adsorbed H_2O molecules on the surface of the products. The two peaks at 1015 and 560 cm^{-1} are corresponding to the P—O stretching vibrations of PO_4^{3-} [82–84]. All the characteristic peaks of g-C_3N_4 and Ag_3PO_4 were observed in the g-C_3N_4-Ag_3PO_4 hybrid composite photocatalysts.

UV-vis diffuses reflectance measurements of g-C_3N_4, Ag_3PO_4, and g-C_3N_4-Ag_3PO_4 composites. In the g-C_3N_4-Ag_3PO_4 hybrid composite photocatalyst there is a small shift in the band edge positions to a higher wavelength as compared with pure g-C_3N_4 and pure Ag_3PO_4 suggesting that the recombination rate of the electron-hole pair was successfully reduced in the heterostructured g-C_3N_4-Ag_3PO_4 hybrid composite photocatalyst.

The pure g-C_3N_4 sample consists of submicrometer sheets with and Ag_3PO_4 particles ranging from 200 to 800 nm, respectively (Fig. 5.7). There is no distinctive morphological feature appearing for the Ag_3PO_4 particles. The size of Ag_3PO_4 nanoparticles was found to be around 12 nm. TEM studies confirm that g-C_3N_4 sheet could serve as a support and surfactant to bound Ag_3PO_4 particles in this composite system. Our results clearly indicate that in composite samples, Ag_3PO_4 nanoparticles were uniformly distributed on g-C_3N_4 sheet, no apparent aggregation of the Ag_3PO_4 nanoparticles was discerned which leads to the formation of interfaces between Ag_3PO_4 and g-C_3N_4. The specific surface area and pore size distribution of g-C_3N_4-Ag_3PO_4 were investigated by nitrogen adsorption-desorption analysis. The specific surface areas of the as-synthesized CNAGPO25 and CNAGPO40 were 11.24 and 12.38 $m^2\ g^{-1}$, respectively. The specific surface area of these composites is quite a bit higher than that of pure g-C_3N_4 (8 $m^2\ g^{-1}$),

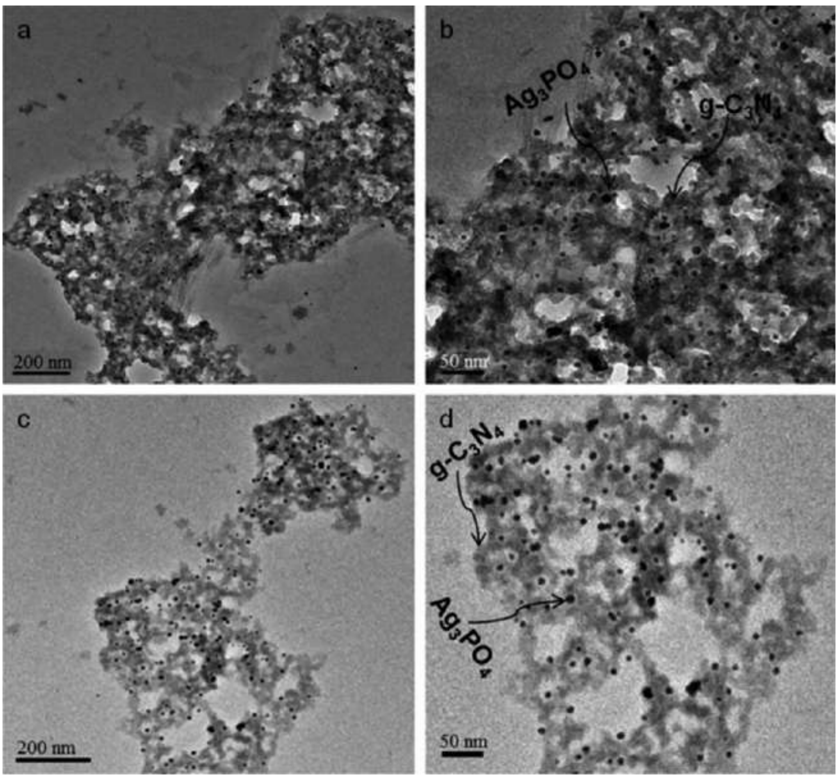

Fig. 5.7 TEM images of the as-synthesized g-C_3N_4-Ag_3PO_4: (A) CNAGPO25, (B) CNAGPO25 (magnified), (C) CNAGPO40, and (D) CNAGPO40 (magnified). *(From S. Kumar, T. Surendar, A. Baruah, V. Shanker, Synthesis of a novel and stable g-C_3N_4-Ag_3PO_4 hybrid nanocomposite photocatalyst and study of the photocatalytic activity under visible light irradiation, J. Mater. Chem. A 1(17) (2013) 5333–5340, https://doi.org/10.1039/c3ta00186e.)*

but it is much higher than that of pure Ag_3PO_4 (0.89 m^2 g^{-1}). This might be due to the Ag_3PO_4 nanoparticles being deposited on the g-C_3N_4 surface. A large specific surface area is useful for adsorption of organic compounds, and further enhances the efficiency of the photocatalytic process because the adsorption of organic compounds on the surface of the photocatalyst is the initial step of the photocatalytic oxidation of organic compounds. In addition to this, large surface area provides a higher number of reactive sites for the photocatalytic process. Therefore, uniformly distributed Ag_3PO_4 nanoparticles on g-C_3N_4 sheets with a high surface area can lead to a better interaction between g-C_3N_4 and Ag_3PO_4 improving the photocatalytic performance of hybrid composites under visible-light irradiation.

In situ growth strategy

Direct growth is widely used to prepare different kinds of composite such as graphene-based metal compounds such as graphene-metal oxide, and graphene-metal sulfides [85,86]. The precursor for Ag_3PO_4 is silver nitrate. Silver salt is mixed with an ultrasonically dispersed g-C_3N_4 sheet which is synthesized by direct heating of the melamine at 550°C for 2h. The Ag^+ ions from the silver salt can be bound to the surface of the g-C_3N_4 due to chemical adsorption and these Ag^+ ions were converted into Ag_3PO_4 nanoparticles due to ion exchange, with the addition of sodium phosphate dodecahydrate as a precipitating agent, under constant stirring at room temperature. Thus, finely distributed uniform Ag_3PO_4 nanoparticles were successfully deposited on the surface of the g-C_3N_4 sheet (Fig. 5.8). In the hybrid composite, the size of Ag_3PO_4 nanoparticles formed on g-C_3N_4 sheets were around 12nm. The in situ growth strategy could avoid the particle agglomeration of Ag_3PO_4 on the g-C_3N_4 sheet, resulting in a uniform distribution of Ag_3PO_4 nanoparticles on the g-C_3N_4 surface. This in situ precipitation

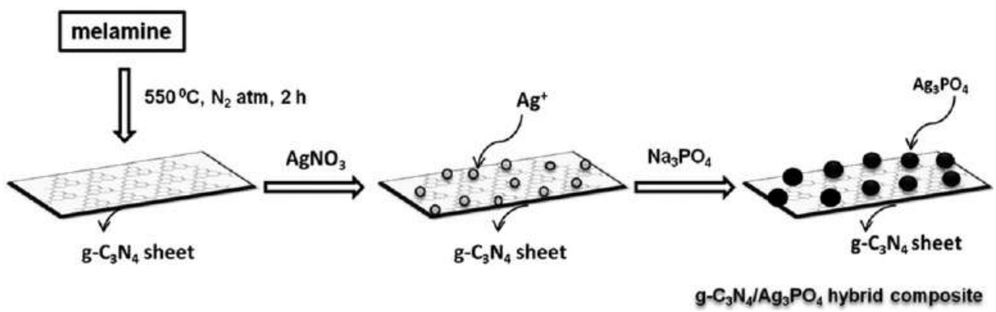

Fig. 5.8 Schematic representation for the in situ deposition of Ag_3PO_4 nanoparticles on g-C_3N_4 sheets. *(From S. Kumar, T. Surendar, A. Baruah, V. Shanker, Synthesis of a novel and stable g-C_3N_4-Ag_3PO_4 hybrid nanocomposite photocatalyst and study of the photocatalytic activity under visible light irradiation, J. Mater. Chem. A 1(17) (2013) 5333–5340, https://doi.org/10.1039/c3ta00186e.)*

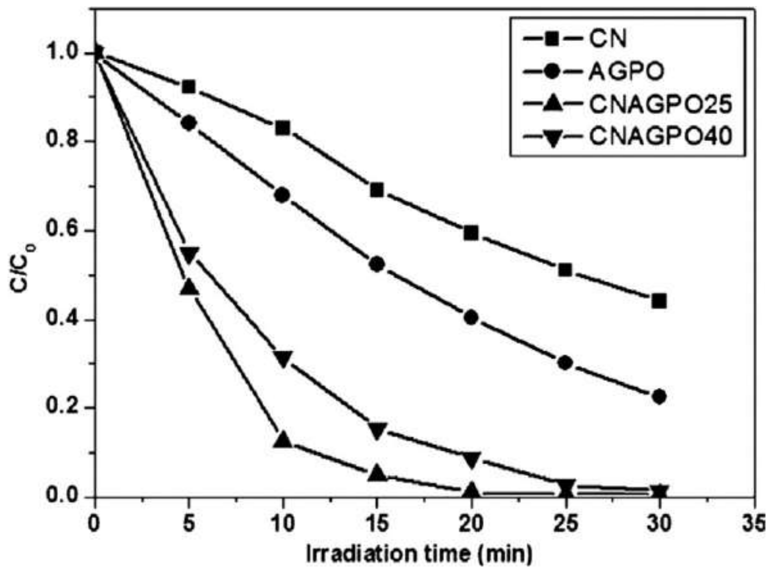

Fig. 5.9 Photocatalytic degradation of MO in aqueous solution over g-C_3N_4, Ag_3PO_4, and g-C_3N_4-Ag_3PO_4 photocatalysts. *(From S. Kumar, T. Surendar, A. Baruah, V. Shanker, Synthesis of a novel and stable g-C_3N_4-Ag_3PO_4 hybrid nanocomposite photocatalyst and study of the photocatalytic activity under visible light irradiation, J. Mater. Chem. A 1(17) (2013) 5333–5340, https://doi.org/10.1039/c3ta00186e.)*

method for the synthesis of a g-C_3N_4-Ag_3PO_4 hybrid composite photocatalyst can also be summarized as follows:

$$g-C_3N_4(s)+Ag^+(aq)\ g-C_3N_4-Ag^+(ad);pH=7$$

$$g-C_3N_4-Ag^+(ad)+PO_4^{3-}(aq)\ g-C_3N_4-Ag_3PO_4;pH=7$$

Photocatalytic performance

The photocatalytic activities of the as-synthesized samples were evaluated via the photodegradation of MO under visible-light irradiation, as shown in Fig. 5.9. The photolysis of MO was also studied for same duration under visible-light irradiation in the absence of catalyst which indicates that MO is stable under visible-light irradiation. The g-C_3N_4-Ag_3PO_4 photocatalysts showed much higher photocatalytic activities for the photodegradation of MO than pure g-C_3N_4 and Ag_3PO_4. Moreover, the photocatalytic activity of g-C_3N_4-Ag_3PO_4 photocatalyst with a 1:3 weight ratio was almost five times higher than that of pure g-C_3N_4 and 3.5 times higher than pure Ag_3PO_4. Our results clearly indicate that the g-C_3N_4-Ag_3PO_4 composite has better performance in the photodegradation of organic pollutant than the pure g-C_3N_4 and Ag_3PO_4 prepared under the same experimental conditions. However, when the g-C_3N_4 content increased from 25 to 40 wt% there was a slight decrease in photocatalytic activity, but it was much higher compared to the photocatalytic activity of pure g-C_3N_4 and Ag_3PO_4. The much higher content of g-C_3N_4 in the composite may make an unsuitable ratio between g-C_3N_4 and Ag_3PO_4, thereby lowering the electron transfer efficiency of the photoinduced electrons on Ag_3PO_4 nanoparticles to g-C_3N_4 surfaces, thus the activity goes down with much higher loading in the composite photocatalyst under visible-light irradiation. This result indicates that both g-C_3N_4 and Ag_3PO_4 play an important role in improving the photocatalytic activity, due to the significant synergistic effect between g-C_3N_4 and Ag_3PO_4 for the photodegradation of MO under visible-light irradiation.

Photoluminescence

Enhanced photocatalytic activity was observed for the synthesized g-C_3N_4-Ag_3PO_4 hybrid composites. This is because the Ag_3PO_4 and g-C_3N_4 have more closely contacted interfaces. This can be observed by the photoluminescence (PL) spectra, which are useful to explain the migration, transfer, and recombination processes of the photoinduced electron-hole pairs in the semiconductors [87,88]. Obviously, the pure g-C_3N_4 and Ag_3PO_4 have a strong and wide peak around 450 and 520 nm respectively in the PL spectrum. However, in the case of the g-C_3N_4-Ag_3PO_4 hybrid nanocomposite, the photoinduced electron-hole pair can migrate easily between g-C_3N_4 and Ag_3PO_4 due to their matching band potentials and therefore, the recombination of electrons and holes is greatly hindered. This result shows that the g-C_3N_4-Ag_3PO_4 composite is useful to reduce the recombination rate of the photoinduced electron-hole pair and improve the corresponding photocatalytic activity. So, no photoluminescence can be observed. This result shows good agreement with the other p-n heterojunction semiconductors [87]. Thus, the hybrid composites with matched energy band positions could be promising photocatalysts for environmental applications.

Reusability check

The stability of a photocatalyst is also very important from point of view of its practical application. However, it is well known that the pure Ag_3PO_4 would photochemically decompose if no sacrificial reagent was involved in the process. During the photocatalytic process, in the case of pure Ag_3PO_4, it is observed that the yellow color turned darker when the photocatalytic reaction was completed. This indicates the formation of Ag^o species due to the reduction of Ag^+ from Ag_3PO_4 by photoinduced electrons as Ag_3PO_4 is unstable under photo irradiation, which may reduce the structural and photochemical stabilities [89]. More importantly, the g-C_3N_4-Ag_3PO_4 hybrid composite photocatalysts were found to be more stable than pure Ag_3PO_4 under similar conditions. To study the stability of the g-C_3N_4-Ag_3PO_4 hybrid composite photocatalyst, the six successive photocatalytic experiments were carried out by adding used Ag_3PO_4 and g-C_3N_4-Ag_3PO_4 photocatalysts to fresh MO solutions with no change in the overall concentration of the catalyst (2–3 mg catalyst loss for each experimental run). The photocatalytic activity of g-C_3N_4-Ag_3PO_4 was retained at over 90% of its original activity after six successive experimental runs, which promotes the photocatalyst for its practical applications in environmental protection. The XRD studies were performed for Ag_3PO_4 and g-C_3N_4-Ag_3PO_4 after six successive experimental runs. For pure Ag_3PO_4, it is observed that a new peak corresponding to Ag^0 appeared together with the XRD peaks of Ag_3PO_4 after the six successive experimental runs, whereas no such peak was observed in the g-C_3N_4-Ag_3PO_4 hybrid composites. This indicates that the Ag_3PO_4 nanoparticles were tightly bound with the surface of the g-C_3N_4 sheet, which promotes the stability of the g-C_3N_4-Ag_3PO_4 composite photocatalysts due to the chemical adsorption between N—H groups or π-electrons in g-C_3N_4 and Ag^+ ions in Ag_3PO_4. Therefore, g-C_3N_4-Ag_3PO_4 composites can be used as high-performance and stable visible-light photocatalysts and their potential applications in environmental protection.

Mechanism for the improved photocatalytic activity and stability of the g-C_3N_4-Ag_3PO_4 composite

It is well known that an efficient charge separation, large surface area and high adsorption ability play an important role for the enhancement of photocatalytic activity. The g-C_3N_4 has been shown to be an effective electron transporter and acceptor in the systems of g-C_3N_4-TiO_2, g-C_3N_4-ZnO, and g-C_3N_4-$BiPO_4$. The g-C_3N_4 sheets could facilitate charge migration and reduce the recombination of electron-hole pairs of the g-C_3N_4-based photocatalysts. Our results also clearly indicate that reinforced charge migration might be achieved in the as-synthesized g-C_3N_4-Ag_3PO_4 hybrid composite. However, few reports have shown the partial reduction of Ag^+ ion into Ag metal, which could act as electron acceptors to make the photoexcited electrons migrate from Ag_3PO_4, and effectively protect Ag_3PO_4 from further photoreduction of the Ag^+ ion in Ag_3PO_4 [5,90].

On the basis of the above results, a proposed mechanism is discussed to explain that the enhanced photocatalytic activity and stability of the g-C_3N_4-Ag_3PO_4 photocatalysts is due to synergistic effects between the Ag_3PO_4 nanoparticles and the g-C_3N_4 sheet (Fig. 5.10). First, the deposition of Ag_3PO_4 nanoparticles on the surface of the insoluble g-C_3N_4 sheet of Ag_3PO_4 can effectively protect Ag_3PO_4 from dissolution in aqueous solution due to chemical adsorption between g-C_3N_4 and Ag_3PO_4, thus the structural stability of g-C_3N_4-Ag_3PO_4 can be greatly enhanced during the photocatalytic reaction. Second, the high separation efficiency may be due to the energy level match between g-C_3N_4 and Ag_3PO_4. According to the previous reports, the redox potential of both conduction band ($E_{CB} = -1.3$ eV vs NHE) and valence band ($E_{VB} = +1.4$ eV vs NHE) of g-C_3N_4 are more negative than those of the conduction band ($E_{CB} = +0.45$ eV vs NHE) and valence band ($E_{VB} = +2.9$ eV vs NHE) of Ag_3PO_4. A scheme for the separation and transport of photogenerated electron-hole pairs at the g-C_3N_4-Ag_3PO_4 interface. Under the visible-light irradiation a high energy photon excites an electron from the valence band (VB) to the

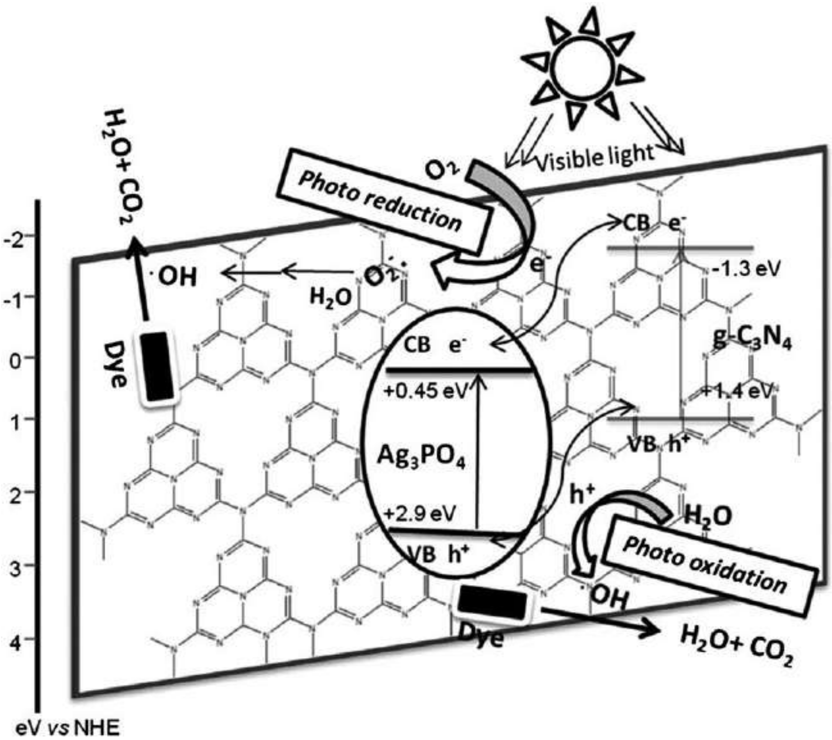

Fig. 5.10 Schematic diagram showing the process of the photocatalytic dye degradation over the g-C_3N_4-Ag_3PO_4 composite. *(From S. Kumar, T. Surendar, A. Baruah, V. Shanker, Synthesis of a novel and stable g-C_3N_4-Ag_3PO_4 hybrid nanocomposite photocatalyst and study of the photocatalytic activity under visible light irradiation, J. Mater. Chem. A 1(17) (2013) 5333–5340, https://doi.org/10.1039/c3ta00186e.)*

conduction band (CB) of Ag_3PO_4 and g-C_3N_4. The photoinduced electrons in g-C_3N_4 can move freely toward the surface of the Ag_3PO_4 while the holes can transfer to the VB of g-C_3N_4 conveniently and vice versa, since band edges of both g-C_3N_4 and Ag_3PO_4 lie in the visible region. Therefore, g-C_3N_4 can act as both an electron acceptor and donor. Hence, the electrons can easily migrate to the surface of Ag_3PO_4 and the redundant electrons on Ag_3PO_4 can also be transferred to g-C_3N_4. As a result, the photogenerated electrons and holes are efficiently separated between Ag_3PO_4 and g-C_3N_4 thereby enhances the photocatalytic activity.

Interestingly, the efficient electron migration from Ag_3PO_4 to g-C_3N_4 sheets also promotes the stability of the g-C_3N_4-Ag_3PO_4 composite by keeping electrons away from the Ag_3PO_4. This effective separation of photogenerated electron-hole pairs driven by band potentials between two semiconductors is also reported in other systems, such as g-C_3N_4-TaON [45,48]. Third, the g-C_3N_4 can act as an electron reservoir to trap electrons emitted from Ag_3PO_4 particles due to irradiation by visible light, thus protecting the electron-hole pair from recombination in the g-C_3N_4-Ag_3PO_4 hybrid composite photocatalysts. The electrons on g-C_3N_4 could also adsorb surface O_2 form various reactive oxygen species, thus could assist the degradation of organic MO effectively. Meanwhile, the photogenerated holes on Ag_3PO_4 could also oxidize polluted dyes. Fourth, monodispersed uniform Ag_3PO_4 nanoparticles with high surface area from its bulk counterpart were successfully deposited on the surface of g-C_3N_4 sheet and could also account for the enhanced photocatalytic activity in the hybrid composite. Fifth, the high adsorption ability of g-C_3N_4 toward the organic pollutant since the high level of Ag^+ ion release in hybrid composite increase adsorption capability of g-C_3N_4 to the organic pollutant. These above aspects together contributed to the enhanced photocatalytic activity and improved stability of this novel g-C_3N_4-Ag_3PO_4 hybrid composite photocatalyst compared to pure Ag_3PO_4 particles.

Detection of reactive oxidative species

The dramatic photocatalytic activity of the as-synthesized hybrid composite motivated us to further investigate the photocatalytic pathway of the degradation process. Generally, photoinduced reactive species including trapped holes, $^{\bullet}OH$ radicals, and $O_2^{\bullet -}$ are expected to be involved in the photocatalytic process. To examine the role of these reactive species, the effects of some radical scavengers and N_2 purging on the photodegradation of methyl orange were investigated to propose a reaction pathway. As the photoinduced electron-hole pair separated in the hybrid composite photocatalyst, the photoinduced holes could directly oxidize the adsorbed H_2O molecules to $^{\bullet}OH$ radicals on the surface of Ag_3PO_4 nanoparticles because the E_{VB} (Ag_3PO_4, +2.9 eV vs NHE) is higher than $E_{(OH/H_2O)}$ (+2.68 eV vs NHE). However, the ECB (Ag_3PO_4, +0.45 eV vs NHE) is also higher than $E_{(O_2/O_2^{\bullet -})}$ (+0.13 eV vs NHE), which cannot produce $O_2^{\bullet -}$ radicals from dissolved O_2 by photoinduced electrons in Ag_3PO_4, but the $E_{(CB)}$ (g-C_3N_4, −1.3 eV vs NHE) of g-C_3N_4 is lower than $E_{(O_2/O_2^{\bullet -})}$, so the radicals $O_2^{\bullet -}$ can still be produced in the g-C_3N_4-Ag_3PO_4 photocatalyst. When N_2 purging was conducted which acts as an $O_2^{\bullet -}$ radicals scavenger, no change was observed in the degradation of methyl orange compared with air-equilibrated conditions, i.e., in the absence of scavenger, which confirms that the dissolved O_2 has no effect on the photodegradation process under visible-light irradiation. A significant change was observed in the photocatalytic degradation of methyl orange by the addition methanol as the $^{\bullet}OH$ scavenger compared with no scavenger at the same conditions. However, the degradation rate was drastically inhibited by the addition of ammonium oxalate (AO) as a holes scavenger, indicating that the superoxide radicals are not the main active oxidative species of the g-C_3N_4-Ag_3PO_4 hybrid composite photocatalyst, but the holes and/or $^{\bullet}OH$ radicals can play an important role in the photodegradation of methyl orange under visible-light irradiation. Further, it was confirmed by $^{\bullet}OH$ trapping PL spectra of CNAGPO25 with TA solution under visible-light irradiation.

4. Conclusion and future outlook

Graphitic carbon nitride is a versatile material with variety of applications in the field of solar energy harvesting and environmental remediation. Its composite with metal oxides are known to exhibit highly fascinating optical and electronic properties. From the perspective of visible-light-driven photocatalysis via solar energy harvesting using carbon nitride-based hybrid materials, here, we have highlighted two extremely interesting works and discussed their synthesis as well as catalytic applications in complete details. The major findings from these two reports have been summarized later.

In the report by Kumar et al. [12] on magnetically separable g-C_3N_4-Fe_3O_4 nanocomposites for photocatalytic dye degradation, they have successfully prepared the nanomaterials by a facile, effective, and reproducible in situ growth mechanism. Monodispersed Fe_3O_4 nanoparticles with a size of about 8 nm are uniformly deposited on the g-C_3N_4 sheets, which effectively prevents the Fe_3O_4 nanoparticles from aggregating together. The g-C_3N_4-Fe_3O_4 nanocomposite exhibits enhanced photocatalytic activity for the degradation of RhB under visible-light irradiation. More importantly, g-C_3N_4-Fe_3O_4 photocatalyst could be recovered by an applied magnetic field and reused without loss of photocatalytic activity even after six successive cycles. Therefore, the g-C_3N_4-Fe_3O_4 nanocomposite is a promising photocatalytic material for environmental applications as well as water splitting. Another work that has been discussed here in this chapter is about the synthesis of a novel and stable g-C_3N_4-Ag_3PO_4 organic-inorganic hybrid composite photocatalyst by a facile and reproducible template free in situ precipitation method at room temperature. More attractively, the dramatic visible-light photocatalytic activity is generated due to the in situ deposition of monodispersed uniform Ag_3PO_4 nanoparticles on the surface of the g-C_3N_4 sheet.

Furthermore, the heterostructure improved the stability of the Ag_3PO_4 nanoparticles on the surface of the g-C_3N_4 sheet. On the basis of our analysis, it is assumed that the improved photocatalytic activity and stability of g-C_3N_4-Ag_3PO_4 hybrid composites under visible-light irradiation might be a synergistic effect, including the high charge separation efficiency of photoinduced electron-hole pair, high structural stability, the smaller particle size, relatively high surface area, and the energy band structure. The reactive oxidative species detection studies indicated that the photodegradation of methyl orange over the as-synthesized g-C_3N_4-Ag_3PO_4 under visible light is mainly via holes and hydroxyl radicals. Therefore, the facile and reproducible template free in situ precipitation method is expected to be extended for depositing other nanoparticles on the surface of the g-C_3N_4 sheets.

In this era of depleting fossil fuels and global environmental pollution, solar energy is the only most promising as well as viable solution. Therefore, indefatigable endeavors from the researchers are leading to the discovery of novel hybrid materials capable of harnessing greater percentage of energy from the available solar spectrum. However, current technological advancements are still inadequate to meet the global energy demand.

Owing to their limitless scopes and challenges in the domain of solar energy harvesting, research on carbon nitride and related materials is attracting larger audience in the recent years. This booming research hotspot has the potential to address and solve some of the major energy related issues in the coming years. On an optimistic note, it is highly anticipated that with the combined efforts from all the disciplines of researchers will lead us to the accomplishment of a clean environment via energy generation from the renewable resources. We expect that, in the coming years, green energy will no longer be a dream and, more importantly, these scientific advancements will lead us to a sustainable future.

References

[1] A. Baruah, V. Chaudhary, R. Malik, V.K. Tomer, 17—Nanotechnology based solutions for wastewater treatment, in: Nanotechnology in Water and Wastewater Treatment: Theory and Applications, Elsevier, 2018, pp. 337–368, https://doi.org/10.1016/B978-0-12-813,902-8.00017-4.

[2] X. Chen, S. Shen, L. Guo, S.S. Mao, Semiconductor-based photocatalytic hydrogen generation, Chem. Rev. 110 (11) (2010) 6503–6570, https://doi.org/10.1021/cr1001645.

[3] R. Malik, N. Joshi, V.K. Tomer, Advances in designs and mechanisms of MoO_3 nanostructures for gas sensors: a holistic review, Mater. Adv. 2 (2021) 4197–4227.

[4] R. Malik, V.K. Tomer, V. Chaudhary, M.S. Dahiya, S.P. Nehra, S. Duhan, K. Kailasam, A low temperature, highly sensitive and fast response toluene gas sensor based on In(III)-SnO_2 loaded cubic mesoporous graphitic carbon nitride, Sens. Actuators B: Chem. 255 (2018) 3564–3575.

[5] P.V. Kamar, Meeting the clean energy demand: nanostructure architectures for solar energy conversion, J. Phys. Chem. C 111 (7) (2007) 2834–2860.

[6] P.V. Adhyapak, S.P. Meshram, V. Tomar, D.P. Amalnerkar, I.S. Mulla, Effect of preparation parameters on the morphologically induced photocatalytic activities of hierarchical zinc oxide nanostructures, Ceram. Int. 39 (7) (2013) 7367–7378, https://doi.org/10.1016/j.ceramint.2013.02.076.

[7] A. Baruah, M. Jha, S. Kumar, A.K. Ganguli, Enhancement of photocatalytic efficiency using heterostructured SiO_2-Ta_2O_5 thin films, Mater. Res. Express 2 (5) (2015), https://doi.org/10.1088/2053-1591/2/5/056404.

[8] A. Baruah, A. Jindal, C. Acharya, B. Prakash, S. Basu, A.K. Ganguli, Microfluidic reactors for the morphology controlled synthesis and photocatalytic study of ZnO nanostructures, J. Micromech. Microeng. 27 (3) (2017), https://doi.org/10.1088/1361-6439/aa5bc4.

[9] A. Baruah, A. Singh, V. Sheoran, B. Prakash, A.K. Ganguli, Droplet-microfluidics for the controlled synthesis and efficient photocatalysis of TiO_2 nanoparticles, Mater. Res. Express 5 (7) (2018), https://doi.org/10.1088/2053-1591/aaafed.

[10] S. Kumar, A. Baruah, S. Tonda, B. Kumar, V. Shanker, B. Sreedhar, Cost-effective and eco-friendly synthesis of novel and stable N-doped ZnO/g-C_3N_4 core-shell nanoplates with excellent visible-light responsive photocatalysis, Nanoscale 6 (9) (2014) 4830–4842, https://doi.org/10.1039/c3nr05271k.

[11] S. Kumar, T. Surendar, A. Baruah, V. Shanker, Synthesis of a novel and stable g-C_3N_4-Ag_3PO_4 hybrid nanocomposite photocatalyst and study of the photocatalytic activity under visible light irradiation, J. Mater. Chem. A 1 (17) (2013) 5333–5340, https://doi.org/10.1039/c3ta00186e.

[12] S. Kumar, T. Surendar, B. Kumar, A. Baruah, V. Shanker, Synthesis of magnetically separable and recyclable g-C_3N_4-Fe_3O_4 hybrid nanocomposites with enhanced photocatalytic performance under

visible-light irradiation, J. Phys. Chem. C 117 (49) (2013) 26135–26143, https://doi.org/10.1021/jp409651g.
[13] S. Kumar, T. Surendar, B. Kumar, A. Baruah, V. Shanker, Synthesis of highly efficient and recyclable visible-light responsive mesoporous g-C_3N_4 photocatalyst via facile template-free sonochemical route, RSC Adv. 4 (16) (2014) 8132–8137, https://doi.org/10.1039/c3ra43942a.
[14] S. Kumar, S. Tonda, A. Baruah, B. Kumar, V. Shanker, Synthesis of novel and stable g-C_3N_4/N-doped $SrTiO_3$ hybrid nanocomposites with improved photocurrent and photocatalytic activity under visible light irradiation, Dalton Trans. 43 (42) (2014) 16105–16114, https://doi.org/10.1039/c4dt01076k.
[15] Y. Li, J. Wang, H. Yao, L. Dang, Z. Li, Efficient decomposition of organic compounds and reaction mechanism with BiOI photocatalyst under visible light irradiation, J. Mol. Catal. A Chem. 334 (1–2) (2011) 116–122, https://doi.org/10.1016/j.molcata.2010.11.005.
[16] R. Malik, V.K. Tomer, P.S. Rana, S.P. Nehra, S. Duhan, Surfactant assisted hydrothermal synthesis of porous 3-D hierarchical SnO_2 nanoflowers for photocatalytic degradation of Rose Bengal, Mater. Lett. 154 (2015) 124–127, https://doi.org/10.1016/j.matlet.2015.04.056.
[17] R.M. Mohamed, D.L. McKinney, W.M. Sigmund, Enhanced nanocatalysts, Mater. Sci. Eng. R. Rep. 73 (1) (2012) 1–13, https://doi.org/10.1016/j.mser.2011.09.001.
[18] S. Rehman, R. Ullah, A.M. Butt, N.D. Gohar, Strategies of making TiO_2 and ZnO visible light active, J. Hazard. Mater. 170 (2–3) (2009) 560–569, https://doi.org/10.1016/j.jhazmat.2009.05.064.
[19] M. Ritu, P.S. Rana, V.K. Tomer, V. Chaudhary, S.P. Nehra, S. Duhan, Nano gold supported on ordered mesoporous WO_3/SBA-15 hybrid nanocomposite for oxidative decolorization of azo dye, Microporous Mesoporous Mater. (2016) 245–254, https://doi.org/10.1016/j.micromeso.2015.12.013.
[20] M. Ritu, C. Vandna, V.K. Tomer, P.S. Rana, S.P. Nehra, S. Duhan, Visible light-driven mesoporous Au–TiO_2/SiO_2 photocatalysts for advanced oxidation process, Ceram. Int. (2016) 10892–10901, https://doi.org/10.1016/j.ceramint.2016.03.222.
[21] M. Sharma, D. Das, A. Baruah, A. Jain, A.K. Ganguli, Design of porous silica supported tantalum oxide hollow spheres showing enhanced photocatalytic activity, Langmuir 30 (11) (2014) 3199–3208, https://doi.org/10.1021/la500167a.
[22] A. Singh, A. Baruah, V. Katoch, K. Vaghasiya, B. Prakash, A.K. Ganguli, Continuous flow synthesis of Ag_3PO_4 nanoparticles with greater photostability and photocatalytic dye degradation efficiency, J. Photochem. Photobiol. A Chem. 364 (2018) 382–389, https://doi.org/10.1016/j.jphotochem.2018.05.017.
[23] Z. Yi, J. Ye, N. Kikugawa, T. Kako, S. Ouyang, H. Stuart-Williams, H. Yang, J. Cao, W. Luo, Z. Li, Y. Liu, R.L. Withers, An orthophosphate semiconductor with photooxidation properties under visible-light irradiation, Nat. Mater. 9 (7) (2010) 559–564, https://doi.org/10.1038/nmat2780.
[24] T.W. Yang, J.A. Scott, R. Amal, Progress in heterogeneous photocatalysis: from classical radical chemistry to engineering nanomaterials and solar reactors, J. Phys. Chem. Lett. (2012) 629–639, https://doi.org/10.1021/jz3000646.
[25] K. Anna, F.G. Marcos, C. Gerardo, Advanced nanoarchitectures for solar photocatalytic applications, Chem. Rev. 112 (2012) 1555–1614.
[26] R. Malik, V.K. Tomer, V. Chaudhary, M.S. Dahiya, P.S. Rana, S.P. Nehra, S. Duhan, Facile synthesis of hybridized mesoporous Au@TiO_2/SnO_2 as efficient photocatalyst and selective VOC sensor, ChemistrySelect 1 (12) (2016) 3247–3258, https://doi.org/10.1002/slct.201600634.
[27] R. Malik, V.K. Tomer, Y.K. Mishra, L. Lin, Functional gas sensing nanomaterials: a panoramic view, Appl. Phys. Rev. 7 (2) (2020), https://doi.org/10.1063/1.5123479.
[28] P. Mishra, M. Ritu, V.K. Tomer, J. Nirav, Hybridized graphitic carbon nitride (g-CN) as high performance VOCs sensor, Functional Nanomaterials: Advances in Gas Sensing Technologies, Springer, 2020, pp. 285–302.
[29] K. Maeda, X. Wang, Y. Nishihara, D. Lu, M. Antonietti, K. Domen, Photocatalytic activities of graphitic carbon nitride powder for water reduction and oxidation under visible light, J. Phys. Chem. C 113 (12) (2009) 4940–4947, https://doi.org/10.1021/jp809119m.
[30] R. Malik, V.K. Tomer, N. Joshi, T. Dankwort, L. Lin, L. Kienle, Au-TiO_2-loaded cubic g-C_3N_4 nanohybrids for photocatalytic and volatile organic amine sensing applications, ACS Appl. Mater. Interfaces 10 (40) (2018) 34087–34097, https://doi.org/10.1021/acsami.8b08091.

[31] D. Nepak, V.K. Tomer, K. Kailasam, Chapter 3: Carbon nitrides (g-C_3N_4) and covalent triazine frameworks (CTFs), RSC Catal. Ser. 2018 (31) (2018) 67–101. Royal Society of Chemistry https://doi.org/10.1039/9781788013116-00067.

[32] R. Malik, V.K. Tomer, State-of-the-art review of morphological advancements in graphitic carbon nitride (g-CN) for sustainable hydrogen production, Renew. Sustain. Energy Rev. (2021) 110235, https://doi.org/10.1016/j.rser.2020.110235.

[33] V.K. Tomer, T. Nishanthi, G. Sweta, K. Kamalakannan, Cubic mesoporous Ag@CN: a high performance humidity sensor, Nanoscale (2016) 19794–19803, https://doi.org/10.1039/C6NR08039A.

[34] R. Malik, V.K. Tomer, V. Chaudhary, M.S. Dahiya, A. Sharma, S.P. Nehra, S. Duhan, K. Kailasam, An excellent humidity sensor based on In-SnO_2 loaded mesoporous graphitic carbon nitride, J. Mater. Chem. A 5 (27) (2017) 14134–14143, https://doi.org/10.1039/c7ta02860a.

[35] R. Malik, V.K. Tomer, T. Dankwort, Y.K. Mishra, L. Kienle, Cubic mesoporous Pd-WO_3 loaded graphitic carbon nitride (g-CN) nanohybrids: highly sensitive and temperature dependent VOC sensors, J. Mater. Chem. A 6 (23) (2018) 10718–10730, https://doi.org/10.1039/c8ta02702a.

[36] C. Pan, J. Xu, Y. Wang, D. Li, Y. Zhu, Dramatic activity of $C_3N_4/BiPO_4$ photocatalyst with core/shell structure formed by self-assembly, Adv. Funct. Mater. 22 (7) (2012) 1518–1524, https://doi.org/10.1002/adfm.201102306.

[37] V.K. Tomer, R. Malik, K. Kailasam, Near room temperature ethanol detection using Ag-loaded mesoporous carbon nitrides, ACS Omega 2 (2017) 3658–3668.

[38] V.K. Tomer, R. Malik, V. Chaudhary, Y.K. Mishra, L. Kienle, R. Ahuja, L. Lin, Superior visible light photocatalysis and low-operating temperature VOCs sensor using cubic Ag(0)-MoS_2 loaded g-CN 3D porous hybrid, Appl. Mater. Today 16 (2019) 193–203, https://doi.org/10.1016/j.apmt.2019.05.010.

[39] X. Wang, S. Blechert, M. Antonietti, Polymeric graphitic carbon nitride for heterogeneous photocatalysis, ACS Catal. 2 (8) (2012) 1596–1606, https://doi.org/10.1021/cs300240x.

[40] Y. Wang, R. Shi, J. Lin, Y. Zhu, Enhancement of photocurrent and photocatalytic activity of ZnO hybridized with graphite-like C_3N_4, Energy Environ. Sci. 4 (8) (2011) 2922–2929, https://doi.org/10.1039/c0ee00825g.

[41] Y. Zhang, T. Mori, J. Ye, Polymeric carbon nitrides: semiconducting properties and emerging applications in photocatalysis and photoelectrochemical energy conversion, Sci. Adv. Mater. 4 (2) (2012) 282–291, https://doi.org/10.1166/sam.2012.1283.

[42] X. Zhou, B. Jin, R. Chen, F. Peng, Y. Fang, Synthesis of porous Fe_3O_4/g-C_3N_4 nanospheres as highly efficient and recyclable photocatalysts, Mater. Res. Bull. 48 (4) (2013) 1447–1452, https://doi.org/10.1016/j.materresbull.2012.12.038.

[43] J. Hu, W. Cheng, S. Huang, D. Wu, Z. Xie, First-principles modeling of nonlinear optical properties of C_3N_4 polymorphs, Appl. Phys. Lett. 89 (26) (2006), https://doi.org/10.1063/1.2402889.

[44] A. Thomas, A. Fischer, F. Goettmann, M. Antonietti, J.O. Müller, R. Schlögl, J.M. Carlsson, Graphitic carbon nitride materials: variation of structure and morphology and their use as metal-free catalysts, J. Mater. Chem. 18 (41) (2008) 4893–4908, https://doi.org/10.1039/b800274f.

[45] S.C. Yan, S.B. Lv, Z.S. Li, Z.G. Zou, Organic–inorganic composite photocatalyst of g-C_3N_4 and TaON with improved visible light photocatalytic activities, Dalton Trans. (2010) 1488–1491, https://doi.org/10.1039/B914110C.

[46] Y. Di, X. Wang, A. Thomas, M. Antonietti, Making metal-carbon nitride heterojunctions for improved photocatalytic hydrogen evolution with visible light, ChemSusChem 7 (2010) 834–837.

[47] Z. Ding, X. Chen, M. Antonietti, X. Wang, Synthesis of transition metal-modified carbon nitride polymers for selective hydrocarbon oxidation, ChemSusChem 4 (2) (2011) 274–281, https://doi.org/10.1002/cssc.201000149.

[48] S.C. Yan, Z.S. Li, Z.G. Zou, Photodegradation of rhodamine B and methyl orange over boron-doped g-C_3N_4 under visible light irradiation, Langmuir 26 (6) (2010) 3894–3901, https://doi.org/10.1021/la904023j.

[49] G. Dong, K. Zhao, L. Zhang, Carbon self-doping induced high electronic conductivity and photoreactivity of g-C_3N_4, Chem. Commun. 48 (49) (2012) 6178–6180, https://doi.org/10.1039/c2cc32181e.

[50] L. Ge, C. Han, J. Liu, Y. Li, Enhanced visible light photocatalytic activity of novel polymeric g-C_3N_4 loaded with Ag nanoparticles, Appl. Catal. Gen. 409–410 (2011) 215–222, https://doi.org/10.1016/j.apcata.2011.10.006.

[51] L. Ge, C. Han, X. Xiao, L. Guo, Y. Li, Enhanced visible light photocatalytic hydrogen evolution of sulfur-doped polymeric g-C_3N_4 photocatalysts, Mater. Res. Bull. 48 (10) (2013) 3919–3925, https://doi.org/10.1016/j.materresbull.2013.06.002.
[52] Y. He, J. Cai, T. Li, Y. Wu, H. Lin, L. Zhao, M. Luo, Efficient degradation of RhB over $GdVO_4$/g-C_3N_4 composites under visible-light irradiation, Chem. Eng. J. 215–216 (2013) 721–730, https://doi.org/10.1016/j.cej.2012.11.074.
[53] L. Huang, H. Xu, Y. Li, H. Li, X. Cheng, J. Xia, Y. Xu, G. Cai, Visible-light-induced WO_3/g-C_3N_4 composites with enhanced photocatalytic activity, Dalton Trans. 42 (24) (2013) 8606–8616, https://doi.org/10.1039/c3dt00115f.
[54] X. Lu, Q. Wang, D. Cui, Preparation and photocatalytic properties of g-C_3N_4/TiO_2 hybrid composite, Afr. J. Math. Sci. Technol. Educ. 26 (10) (2010) 925–930, https://doi.org/10.1016/S1005-0302(10)60149-1.
[55] S.C. Yan, Z.S. Li, Z.G. Zou, Photodegradation performance of g-C_3N_4 fabricated by directly heating melamine, Langmuir (2009) 10397–10401, https://doi.org/10.1021/la900923z.
[56] H. Cheng, B. Huang, P. Wang, Z. Wang, Z. Lou, J. Wang, X. Qin, X. Zhang, Y. Dai, In situ ion exchange synthesis of the novel Ag/AgBr/BiOBr hybrid with highly efficient decontamination of pollutants, Chem. Commun. 47 (25) (2011) 7054–7056, https://doi.org/10.1039/c1cc11525a.
[57] Q. Li, B. Yue, H. Iwai, T. Kako, J. Ye, Carbon nitride polymers sensitized with N-doped tantalic acid for visible light-induced photocatalytic hydrogen evolution, J. Phys. Chem. C 114 (9) (2010) 4100–4105, https://doi.org/10.1021/jp911803z.
[58] R.S. Mane, W.J. Lee, H.M. Pathan, S.H. Han, Nanocrystalline TiO_2/ZnO thin films: fabrication and application to dye-sensitized solar cells, J. Phys. Chem. B 109 (51) (2005) 24254–24259, https://doi.org/10.1021/jp0531560.
[59] J.X. Sun, Y.P. Yuan, L.G. Qiu, X. Jiang, A.J. Xie, Y.H. Shen, J.F. Zhu, Fabrication of composite photocatalyst g-C_3N_4-ZnO and enhancement of photocatalytic activity under visible light, Dalton Trans. 41 (22) (2012) 6756–6763, https://doi.org/10.1039/c2dt12474b.
[60] P. Wang, B. Huang, Y. Dai, M.H. Whangbo, Plasmonic photocatalysts: harvesting visible light with noble metal nanoparticles, Phys. Chem. Chem. Phys. 14 (28) (2012) 9813–9825, https://doi.org/10.1039/c2cp40823f.
[61] P. Wang, B. Huang, X. Zhang, X. Qin, H. Jin, Y. Dai, Z. Wang, J. Wei, J. Zhan, S. Wang, J. Wang, M.H. Whangbo, Highly efficient visible-light plasmonic photocatalyst Ag@AgBr, Chem. A Eur. J. 15 (8) (2009) 1821–1824, https://doi.org/10.1002/chem.200802327.
[62] W. Yao, B. Zhang, C. Huang, C. Ma, X. Song, Q. Xu, Synthesis and characterization of high efficiency and stable Ag_3PO_4/TiO_2 visible light photocatalyst for the degradation of methylene blue and rhodamine B solutions, J. Mater. Chem. 22 (9) (2012) 4050–4055, https://doi.org/10.1039/c2jm14410g.
[63] Y. Bi, S. Ouyang, N. Umezawa, J. Cao, J. Ye, Facet effect of single-crystalline Ag_3PO_4 sub-microcrystals on photocatalytic properties, J. Am. Chem. Soc. 133 (17) (2011) 6490–6492, https://doi.org/10.1021/ja2002132.
[64] C.T. Dinh, T.D. Nguyen, F. Kleitz, T.O. Do, Large-scale synthesis of uniform silver orthophosphate colloidal nanocrystals exhibiting high visible light photocatalytic activity, Chem. Commun. 47 (27) (2011) 7797–7799, https://doi.org/10.1039/c1cc12014j.
[65] R. Asahi, T. Morikawa, T. Ohwaki, K. Aoki, Y. Taga, Visible-light photocatalysis in nitrogen-doped titanium oxides, Science 293 (5528) (2001) 269–271, https://doi.org/10.1126/science.1061051.
[66] Y. Bi, S. Ouyang, J. Cao, J. Ye, Facile synthesis of rhombic dodecahedral AgX/Ag_3PO_4 (X = Cl, Br, I) heterocrystals with enhanced photocatalytic properties and stabilities, Phys. Chem. Chem. Phys. 13 (21) (2011) 10071–10075, https://doi.org/10.1039/c1cp20488b.
[67] X. Li, X. Huang, D. Liu, X. Wang, S. Song, L. Zhou, H. Zhang, Synthesis of 3D hierarchical Fe_3O_4/graphene composites with high lithium storage capacity and for controlled drug delivery, J. Phys. Chem. C 115 (44) (2011) 21567–21573, https://doi.org/10.1021/jp204502n.
[68] X. Yang, X. Zhang, Y. Ma, Y. Huang, Y. Wang, Y. Chen, Superparamagnetic graphene oxide – Fe_3O_4 nanoparticles hybrid for controlled targeted drug carriers, J. Mater. Chem. 17 (2009) 2710–2714.

[69] S. Jing, M. Cao, L. Ren, C. Hu, Fe_3O_4/graphene nanocomposites with improved lithium storage and magnetism properties, J. Phys. Chem. C 115 (30) (2011) 14469–14477.
[70] X. Piao, Z.G. Ming, H.D. Lian, F.C. Ling, H. Shuang, Z.M. Hua, L. Cui, W. Zhen, H. Chao, X.G. Xin, L.Z. Feng, Use of iron oxide nanomaterials in wastewater treatment: a review, Sci. Total Environ. (2012) 1–10, https://doi.org/10.1016/j.scitotenv.2012.02.023.
[71] W.J. Chen, P.J. Tsai, Y.C. Chen, Functional Fe_3O_4/TiO_2 core/shell magnetic nanoparticles as photokilling agents for pathogenic bacteria, Small 4 (4) (2008) 485–491, https://doi.org/10.1002/smll.200701164.
[72] J. Xie, K. Chen, H.Y. Lee, C. Xu, A.R. Hsu, S. Peng, X. Chen, S. Sun, Ultrasmall c(RGDyK)-coated Fe_3O_4 nanoparticles and their specific targeting to integrin αvβ3-rich tumor cells, J. Am. Chem. Soc. 130 (24) (2008) 7542–7543, https://doi.org/10.1021/ja802003h.
[73] L. Ren, S. Huang, W. Fan, T. Liu, One-step preparation of hierarchical superparamagnetic iron oxide/graphene composites via hydrothermal method, Appl. Surf. Sci. 258 (3) (2011) 1132–1138.
[74] G. Xi, B. Yue, J. Cao, J. Ye, Fe_3O_4/WO_3 hierarchical core-shell structure: high-performance and recyclable visible-light photocatalysis, Chem. A Eur. J. 17 (18) (2011) 5145–5154, https://doi.org/10.1002/chem.201002229.
[75] R. Chalasani, S. Vasudevan, Cyclodextrin-functionalized Fe_3O_4@TiO_2: reusable, magnetic nanoparticles for photocatalytic degradation of endocrine-disrupting chemicals in water supplies, ACS Nano 7 (5) (2013) 4093–4104, https://doi.org/10.1021/nn400287k.
[76] H. Liang, H. Niu, P. Li, Z. Tao, C. Mao, J. Song, S. Zhang, Multifunctional Fe_3O_4@C@Ag hybrid nanoparticles: aqueous solution preparation, characterization and photocatalytic activity, Mater. Res. Bull. 48 (7) (2013) 2415–2419, https://doi.org/10.1016/j.materresbull.2013.02.066.
[77] S. Xuan, W. Jiang, X. Gong, Y. Hu, Z. Chen, Magnetically separable Fe_3O_4/TiO_2 hollow spheres: fabrication and photocatalytic activity, J. Phys. Chem. C 113 (2) (2009) 553–558, https://doi.org/10.1021/jp8073859.
[78] W. Xinchen, M. Kazuhiko, T. Arne, T. Kazuhiro, X. Gang, J.M. Carlsson, D. Kazunari, A. Markus, A metal-free polymeric photocatalyst for hydrogen production from water under visible light, Nat. Mater. (2009) 76–80, https://doi.org/10.1038/nmat2317.
[79] M.J. Bojdys, J.O. Müller, M. Antonietti, A. Thomas, Ionothermal synthesis of crystalline, condensed, graphitic carbon nitride, Chem. A Eur. J. 14 (27) (2008) 8177–8182, https://doi.org/10.1002/chem.200800190.
[80] X. Li, J. Zhang, L. Shen, Y. Ma, W. Lei, Q. Cui, G. Zou, Preparation and characterization of graphitic carbon nitride through pyrolysis of melamine, Appl. Phys. Mater. Sci. Process. 94 (2) (2009) 387–392, https://doi.org/10.1007/s00339-008-4816-4.
[81] Y.C. Zhao, D.L. Yu, H.W. Zhou, Y.J. Tian, O. Yanagisawa, Turbostratic carbon nitride prepared by pyrolysis of melamine, J. Mater. Sci. 40 (9–10) (2005) 2645–2647, https://doi.org/10.1007/s10853-005-2096-3.
[82] L. Ge, X. Jing, J. Wang, J. Wang, S. Jamil, Q. Liu, F. Liu, M. Zhang, Trisodium citrate assisted synthesis of ZnO hollow spheres via a facile precipitation route and their application as gas sensor, J. Mater. Chem. 21 (29) (2011) 10750–10754, https://doi.org/10.1039/c0jm04405a.
[83] G. Huang, Y. Zhu, Enhanced photocatalytic activity of $ZnWO_4$ catalyst via fluorine doping, J. Phys. Chem. C 111 (32) (2007) 11952–11958, https://doi.org/10.1021/jp071987v.
[84] M. Thomas, S.K. Ghosh, K.C. George, Characterization of nanostructured silver orthophosphate, Mater. Lett. 56 (4) (2002) 386–392, https://doi.org/10.1016/S0167-577X(02)00496-2.
[85] N. Li, G. Liu, C. Zhen, F. Li, L. Zhang, H.M. Cheng, Battery performance and photocatalytic activity of mesoporous anatase TiO_2 nanospheres/graphene composites by template-free self-assembly, Adv. Funct. Mater. 21 (9) (2011) 1717–1722, https://doi.org/10.1002/adfm.201002295.
[86] J. Tang, Z. Zou, J. Ye, Photophysical and photocatalytic properties of $AgInW_2O_8$, J. Phys. Chem. B 107 (51) (2003) 14265–14269, https://doi.org/10.1021/jp0359891.
[87] J.S. Chen, Z. Wang, X.C. Dong, P. Chen, X.W. Lou, Graphene-wrapped TiO_2 hollow structures with enhanced lithium storage capabilities, Nanoscale 3 (5) (2011) 2158–2161, https://doi.org/10.1039/c1nr10162e.

[88] M. Long, W. Cai, J. Cai, B. Zhou, X. Chai, Y. Wu, Efficient photocatalytic degradation of phenol over $Co_3O_4/BiVO_4$ composite under visible light irradiation, J. Phys. Chem. B 110 (41) (2006) 20211–20216, https://doi.org/10.1021/jp063441z.
[89] H. Wang, Y. Bai, J. Yang, X. Lang, J. Li, L. Guo, A facile way to rejuvenate Ag_3PO_4 as a recyclable highly efficient photocatalyst, Chem. A Eur. J. 18 (18) (2012) 5524–5529, https://doi.org/10.1002/chem.201103189.
[90] K. Noriyoshi, G. Naoko, O. Hironobu, M. Takanori, Silver bromide as a photocatalyst for hydrogen generation from CH_3OH/H_2O solution, J. Phys. Chem. B. (1999) 5917–5919, https://doi.org/10.1021/jp990287q.

SECTION II

Environmental remediation applications

CHAPTER 6

Superior adsorption of environmental contaminants onto carbon nitride materials

Ali Khadir[a], Mehrdad Negarestani[b], Ebrahim Pakzad[b], and Afsaneh Mollahosseini[c]
[a]Young Researcher and Elite Club, Yadegar-e-Imam Khomeini (RAH) Shahre Rey Branch, Islamic Azad University, Tehran, Iran
[b]Department of Civil and Environmental Engineering, Iran University of Science and Technology, Tehran, Iran
[c]Research Laboratory of Spectroscopy & Micro and Nano Extraction, Department of Chemistry, Iran University of Science and Technology, Tehran, Iran

Contents

1. Introduction

Water scarcity has been a long-term issue in the modern world affecting almost 1.2 billion people. Although the Earth is mostly covered with water, water distribution is not homogenous throughout the world. Moreover, many water resources cannot be used as drinking water due to its salinity and poor management. Addressing water scarcity highlights the importance of water reuse that can thrive many sectors including agricultural, industrial, and domestic water sectors [1–3].

Contaminated water jeopardizes all living creatures as many contaminants tend to accumulate within organisms. Industrial revolution has taken its toll on the aquatic systems as many toxic pollutants are released to water media every year [4]. Among the various types of pollutants, heavy metals and dyes are of great importance as these contaminants are carcinogenic, toxic, and nonbiodegradable. Many studies have reported the adverse effects of heavy metals and dyes on both the flora and fauna as well as

Nanostructured Carbon Nitrides for Sustainable Energy and Environmental Applications
https://doi.org/10.1016/B978-0-12-823961-2.00006-9

suggesting ways for their removal [5–8]. Considering the fatal impacts of wastewater effluent on terrestrial and aquatic ecosystems, treating wastewater has become a top priority.

Many methods have been used for water decontamination, such as chemical precipitation, membrane separation, advanced oxidation, and bioremediation. Among all these methods, adsorption is by far an advantageous technique for water treatment due to its cost-efficiency, availability, easy handling, and high efficiency [9,10]. Although after adsorbing the pollutants, sorbents tend to lose their efficiency, there are many regeneration methods capable of reviving the sorbents. Using these methods or agricultural waste as green, low-cost adsorbent, adsorption could be named as an efficient method. Also, many studies have reported heavy metals, dyes, and pharmaceuticals removal using novel sorbents [4,5,10,11].

Graphitic carbon nitride (g-C_3N_4) is a green carbon-based material with tremendous adsorption potential. This novel sorbent has gained attention in recent years because of its high stability, high photoabsorption, and conductivity [12]. Graphitic carbon nitride is a great sorbent specially for adsorbing aromatic organic compounds due to its structure. This novel sorbent has been tested in many studies for the removal of aromatic hydrocarbons, organic solvents, oils, and heavy metals (such as lead, cadmium, and copper) from aqueous media [13–17].

The present chapter attempts to provide a systematic overview of the adsorptive abilities of carbon nitride-based composites. Accordingly, we first describe the different removal techniques (physical, chemical, and biological) that are currently available for the removal of dyes and heavy metals from wastewater. We then briefly summarize the fundamentals of adsorption-based separation. Thereafter, the removal of heavy metals by carbon nitride-based composites is highlighted. Finally, the removal of dyes by carbon nitride-based composites is discussed.

2. Pollutant removal techniques

In terms of water purification and decontamination, distinctive treatment techniques have been established based on several different assumptions and applications. Normally, treatment methods fall into three main domains: biological, chemical, and physical techniques (Fig. 6.1).

2.1 Biological treatments

Biological treatments (aerobic and anaerobic processes) use a variety of microbial communities such as algae, fungi, and bacteria to degrade organic matters into simple substances under the presence or/and absence of oxygen. In conventional wastewater treatment plants, bioprocesses are used for the treatment of influent wastewater and waste activated sludge. This technique requires low operational costs and has relatively desirable

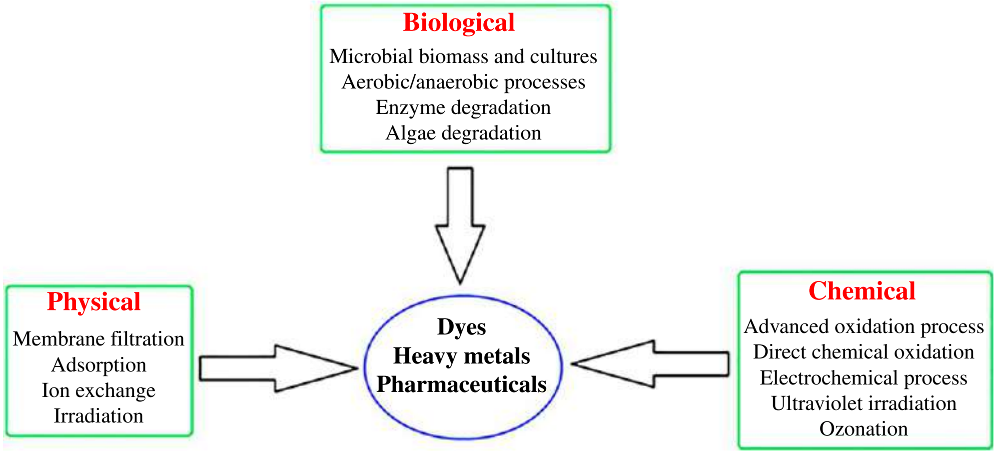

Fig. 6.1 Different techniques for contaminants removal.

performance with no use of special chemical substances. Moreover, it is considered that aerobic and anaerobic methods might be used together to eradicate organic substances and nutrients [18]. However, various factors such as long start-up, and sensitivity to working conditions such as pH, temperature, and nutrients might limit the applicability of this process.

2.2 Chemical treatments

In these methods, both chemicals and reagents are employed for the removal of contaminants from aqueous media. Although this method provides high removal efficiency in terms of pollutant removal, yet treatment cost and energy are often higher as compared to biological techniques [19]. Also, the disposal of chemical sludge seems to be difficult in some regions. In advanced oxidation processes, secondary pollutants are possibly generated that might peril human health [20]. Besides, electrocoagulation technique requires a high amount of electricity which could enhance the cost of the process [21].

2.3 Physical treatments

Physical treatment methods, including membrane filtration, adsorption, and ion exchange, separate a pollutant from water without any chemical or biological changes. As a matter of fact, the separated pollutant is not destroyed or blurred, it only moves from one media to another. Among the physical techniques, adsorption processes have drawn much attention lately as a suitable and facile technique. In the next section, the principles of adsorption are briefly described.

3. Fundamentals of adsorption

Adsorption technique for water and wastewater treatment has gained significant research attention over the past few years because of its efficiency and applicability toward different contaminants. This technique has been employed by myriads of researchers and industries for water depollution because of its plethora of advantages, which includes low-cost, less sludge generation, no risk of secondary pollutants, facile operation, simplicity of design, insensitivity to toxic pollutants, and virtually stable (as compared to biological processes) [22,23]. Adsorption method is the physical phase movement of the pollutants from the solution to a surface of a highly porous/functionalized material, named adsorbent. The adsorbent has a significant crucial impact on the performance of the adsorption process. Generally, removal via adsorption includes the following steps: (I) movement of the pollutants from the bulk liquid phase to the hydrodynamic boundary layer around the solid surface, (II) transfer of the pollutant's molecules to the outer layer of the adsorbent named as external diffusion, (III) occurrence of pore diffusion and surface diffusion by filling the pores and internal surface of the adsorbent, and (IV) formation of the physical or chemical bindings between the adsorbent empty sites and adsorbate molecules [24]. Fig. 6.2 illustrates these adsorption steps briefly. According to the interaction between the adsorbate and adsorbent, adsorption process is classified into two distinct groups: (I) physisorption or physical adsorption occurs when the interaction between the pollutant and the solid surface is controlled by hydrogen bonds, van der Waals, or dipole–dipole. In this case, desorption of the adsorbed pollutant and multilayer coverage of the adsorbents are possible in physical sorption energy. Unlike physisorption, in (II) chemisorption desorption is less likely to happen [25]. Chemisorption or chemical adsorption involves electron sharing between adsorbate and adsorbent to establish energetic chemical bonding. Hence, various properties of the adsorbent such as morphology, textural property, thermal stability, crystallinity, surface chemistry, hydrophilicity, elemental constituents, and physicochemical properties greatly influence the interactions and final performance of the treatment process.

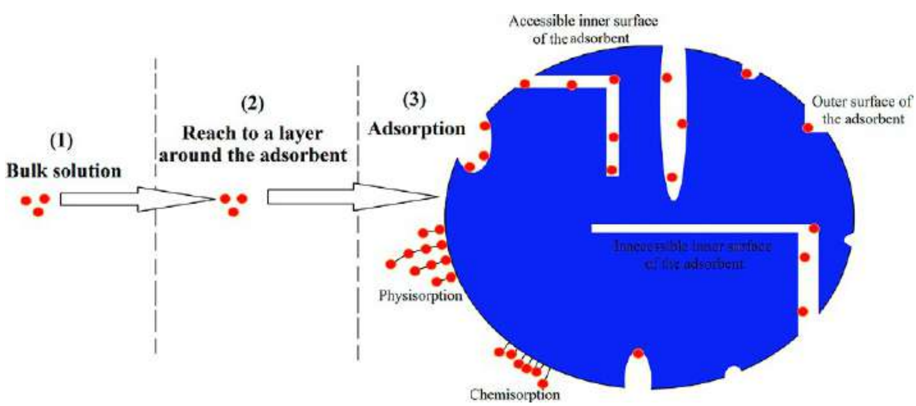

Fig. 6.2 The steps involved in the adsorption process to adsorb pollutant molecules.

4. Carbon nitride-based adsorbents for the removal of toxic metals/heavy metals

There is no doubt that heavy metals are among the most common contaminants in aqueous environment, and many studies have attempted to detect and remove them. The presence of heavy metals in aquatic media (surface water, drinking water, ground water, etc.) has been reported in many regions around the world, including Iran [26], China [27], Greece [28], India [29], Bangladesh [30], Pakistan [31], and Malaysia [32]. Although some heavy metals at controlled concentration are micronutrients and essential for human health, plants and microorganisms, excessive exposure to heavy metals could lead to severe health issues, such as high blood pressure, cancer, neurological disorder, hormonal issues, lung and renal diseases, and gastrointestinal bleeding [30]. Fig. 6.3 illustrates the different kinds and sources of heavy metals. It demonstrates that heavy metals have a strong propensity to enter the water media and environment through various available paths. Adsorbent-based materials have been introduced as an effective solution to decontaminate water containing heavy metals. In this regard, carbon nitride (C_3N_4) and its derivations have been searched as satisfactory adsorbents for the adsorption of heavy metal ions. Polymeric graphitic carbon nitride (g-C_3N_4) is the stable form of carbon nitride under ambient conditions that has a van der Waals layered structure, and is generally made by polymerization of cyanamide, dicyandiamide, or melamine [33,34]. The maximum adsorption capacity (mg/g), i.e., the amount of heavy metal ions taken up by the adsorbent (such as carbon nitride) per unit mass (or volume) of the adsorbent, is an essential parameter in adsorption systems to evaluate the performance of a material. Removal efficiency also may be used in some cases while adsorption capacity is not reported. In addition, isotherm and kinetics models are inevitable components of adsorption processes

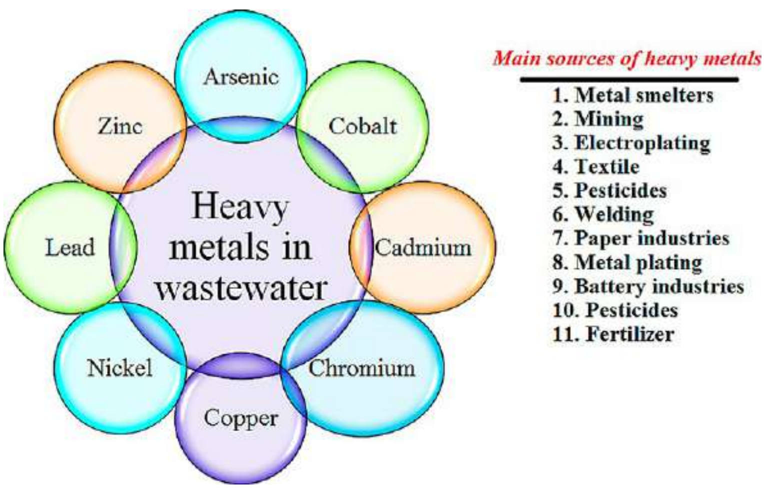

Fig. 6.3 Different kind of heavy metals and the main sources.

that expound the mechanisms involved in the adsorbate elimination. The maximum adsorption capacity and the best-fitting isotherm and kinetic models associated with heavy metals adsorption by carbon nitride-based materials are summarized in Table 6.1.

Zhu et al. [35], Li et al. [36], and Zou et al. [38] investigated the adsorption capacity of g-C_3N_4 toward Pb^{2+} ions, and found that the adsorption process reached the equilibrium at about 60, 350, and 12h, respectively, with the maximum adsorption capacity of 7.4, 31.25, and 71.1mg/g, respectively. The results also indicated that strong acidic media was not favorable for lead adsorption, and the optimum pH values were found to be 6 [35], 8–10 [36], and 9–12 [38], respectively. At low pH values, both hydrogen ions and the adsorbate compete for the active surface sites of g-C_3N_4, resulting in poor adsorption capacity. In addition, in acidic media, lead has the prime form of Pb^{2+} which is a bit difficult to interact with protonated g-C_3N_4 due to the electrostatic repulsion. In another investigation [40], green and low-cost g-C_3N_4 nanosheet was prepared for the removal of lead, and the obtained adsorption capacity (136.571mg/g) was far greater than the abovementioned studies [35,36,38]. One obvious reason may be attributed to BET surface area of g-C_3N_4 nanosheet (111.2m^2/g), which was higher than other prepared graphitic carbon nitride (32.1m^2/g [35] or 8.6m^2/g [36]). With the aim of improvement in lead removal, g-C_3N_4 was modified with β-cyclodextrin [38], alginate [39], or Fe_3O_4 [41] and found the adsorption capacities of 100.5, 383.4, and 137mg/g, respectively. This might be to the presence of new functional groups or even greater surface area of the g-C_3N_4 composite after the modification process. The authors believed that electrostatic attraction, surface complexation, and ion-exchange are the main mechanisms associated in Pb^{2+} elimination by g-C_3N_4 composite [38]. Among the mentioned g-C_3N_4 composite, alginate-modified g-C_3N_4 composite hydrogels exhibited the maximum adsorption capacity toward lead ions, and to evaluate its effectiveness with other adsorbents in terms of adsorption capacity, Fig. 6.4 was prepared. Accordingly, g-C_3N_4 might be a promising material for the removal of Pb^{2+} from aqueous solutions.

Su et al. [42] prepared oxygen-doped carbon nitride with molybdenum and sulfur hybridization for the removal of Cd^{2+}. The authors advocated the fact that g-C_3N_4 might be an appropriate engineered adsorbent; however, it lacks excellent surface area, so it is suggested to be modified for better usage. The combination of molybdenum, sulfur, and oxygen-doped g-C_3N_4 showed the maximum adsorption capacity of 293.8mg/g, which was 8.7 times superior to raw oxygen-doped g-C_3N_4. Qiu et al. proved that oxygen-doped g-C_3N_4 possessed increased surface area than pristine g-C_3N_4 [47]; therefore, oxygen-doped g-C_3N_4 provides an excellent media in order to be doped by molybdenum and sulfur. In addition, large surface area of oxygen-doped g-C_3N_4 (74.4m^2/g) prevented MoS_2 and MoO_3 nanoparticles agglomeration. After these nanoparticles reacted with Cd^{2+}, $CdMoO_4$ and CdS species are formed. Cadmium adsorption kinetic data followed pseudo second-order and intraparticle diffusion model assumptions, which are indicative of chemical interaction and particle diffusion process. In another study, Cai et al. [43] employed a 2D-g-C_3N_4 nanosheet for the remediation of Cd^{2+}. The influence of contact time and pH are illustrated in Fig. 6.5. The interaction of 2D-g-C_3N_4

Table 6.1 The maximum monolayer adsorption capacity and the best-fitting isotherm and kinetic models for the adsorption of heavy metals by $g-C_3N_4$-based adsorbents.

No.	Adsorbent	Heavy metal	Adsorption capacity (mg/g)	Removal efficiency (%)	Isotherm/ kinetics	References
1	$g-C_3N_4$	Pb (II)	7.4	98.5%	F/PSO	[35]
2	Individual $g-C_3N_4$	Pb (II)	31.25	–	L/PSO	[36]
3	Sulfur-doped $g-C_3N_4$ nanosheet	Pb (II)	52.63	–	L/PSO	
4	Mesoporous $g-C_3N_4$ functionalized with melamine-based dendrimeramine	Pb (II)	196.34	–	L/PSO	[37]
5	$g-C_3N_4$	Pb (II)	71.1	–	L, Sips/ PSO	[38]
6	β-Cyclodextrin/ $g-C_3N_4$	Pb (II)	100.5	–	L, Sips/ PSO	
7	Alginate modified $g-C_3N_4$ composite hydrogels	Pb (II)	383.4	–	L/PSO	[39]
8	green and low-cost $g-C_3N_4$ nanosheet	Pb (II)	136.571	–	F/PSO, Elovich	[40]
9	$g-C_3N_4/Fe_3O_4$	Pb (II)	137	–	F/PSO, IPM	[41]
10	$g-C_3N_4$	Cd (II)	123.205	–	–	[40]
11	Oxygen-doped $g-C_3N_4$	Cd (II)	33.9		Sips/PSO	[42]
12	Oxygen-doped $g-C_3N_4$ with molybdenum/ sulfur hybridization	Cd (II)	293.8	–	Sips/PSO	
13	A 2D- $g-C_3N_4$ nanosheet	Cd (II)	94.4	–	F/PSO	[43]
14	$g-C_3N_4$	Cr (VI)	9.96	–	–	[44]
15	$g-C_3N_4$/carbon layer		46.67	–	–	
16	$Fe_3O_4/g-C_3N_4$/carbon layer composite		50.09	–	L/PSO	
17	FeS@ graphite carbon nitride nanocomposites	Cr (VI)	61.8	100%	L/PSO	[45]
18	Oxidized $g-C_3N_4$/polyaniline nanofiber	Cr (VI)	178.58	–	L/PSO	[46]
19	Alginate/graphitic carbon nitride composite hydrogels	Ni (II) Cu (II)	306.3 168.2	– –	L/PSO L/PSO	[39]
20	Mesoporous $g-C_3N_4$ functionalized with melamine-based dendrimeramine	Cu (II)	199.75		L/PSO	[37]

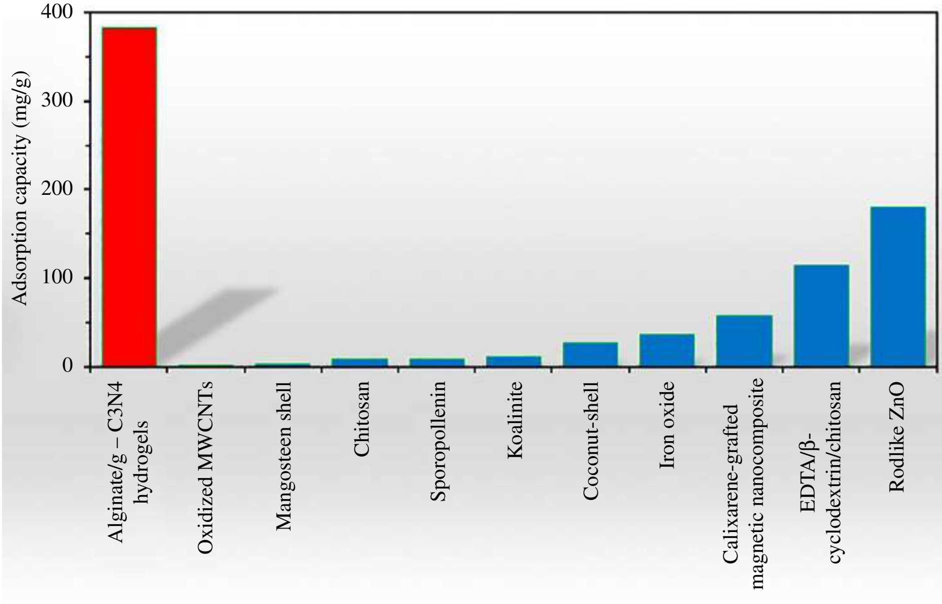

Fig. 6.4 Comparison of alginate-modified g-C_3N_4 composite hydrogels with other adsorbents in view of adsorption capacity.

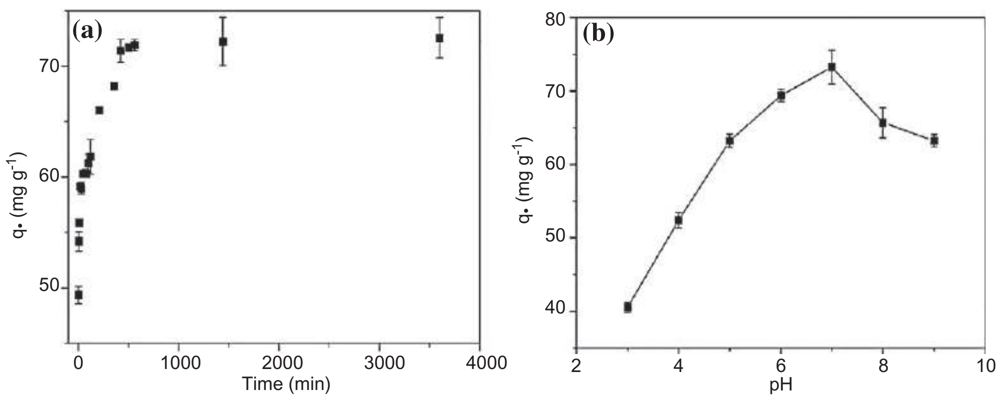

Fig. 6.5 The effect of contact time (A) and pH on Cd^{2+} adsorption by 2D-g-C_3N_4 nanosheet (B). The zeta potential curve of 2D- g-C_3N_4 nanosheet (C). *Reprinted with permission from X. Cai, J. He, L. Chen, K. Chen, Y. Li, K. Zhang, Z. Jin, J. Liu, C. Wang, X. Wang, L. Kong, J. Liu, A 2D-g-C3N4 nanosheet as an eco-friendly adsorbent for various environmental pollutants in water, Chemosphere 171 (2017) 192–201. https://doi.org/10.1016/j.chemosphere.2016.12.073.*

nanosheet and Cd^{2+} ions found the equilibrium state at approximately 300 min (Fig. 6.5A), with the adsorption capacity of higher than 70 mg/g. The rapid Cd^{2+} ions uptake at initial steps of the adsorption process is attributed to the presence of many vacant sites on the g-C_3N_4 nanosheet, which this high rate tends to slow down over time. Once the equilibrium is reached, the rate of Cd^{2+} ions adsorption and desorption from 2D-g-C_3N_4 nanosheet becomes equal. The pH results (Fig. 6.5B) showed that the maximum Cd^{2+} adsorption was at 7, while the minimum value was at pH 3. The key reason for this behavior might be the cadmium speciation at different pH and the surface charge of the adsorbent. According to Fig. 6.5C, at pH lower than 4, g-C_3N_4 is positively charged. At 7–8, cadmium is in negative state wherein electrostatic repulsion prevents its removal by negatively charged g-C_3N_4. Note that g-C_3N_4 has not only been employed for remediation of cadmium, but also it is potential to be used for detection of trace cadmium [48].

Chromium is a very common type of heavy metal, found in the effluent of metallurgy, electroplating, leather tanning, and printing industries. Toxicity of chromium is mainly related to Cr(VI) since Cr(III) presents less toxicity and lower mobility. Wang et al. [44] reported the utilization of Fe_3O_4/ g-C_3N_4/carbon layer composite for the removal of chromium. TEM images of the prepared materials are shown in Fig. 6.6. 2D layered structure of g-C_3N_4 can be figured out from Fig. 6.6A, and of course after loading C on g-C_3N_4, a dark surface area appeared in the TEM images (Fig. 6.6B). The magnetic nanoparticles are shown as sphere (diameter ~5 nm) which are spreading over the g-C_3N_4/carbon layer surface. The elemental mapping demonstrated the presence of C, Fe, O, and N, which are indicative of a successful adsorbent preparation. The BET surface area of g-C_3N_4 and Fe_3O_4/ g-C_3N_4/carbon layer composite was 69.6 and 40.4 m^2/g, respectively. This reduction is due to the low surface area of magnetic nanoparticles and C. The removal process reached equilibrium at 1440 min under optimum pH of 3. The adsorption capacity findings exhibited that Fe_3O_4/ g-C_3N_4/carbon layer composite had the maximum adsorption capacity of 50.09 mg/g which was greater than nano-Fe_3O_4-polymer (3.99 mg/g) [49], Fe_3O_4@SiO_2-NH_2 particles (27.2 mg/g) [50], Fe_3O_4@SiO_2 nanoparticles (3.8 mg/g) [51], and Fe_3O_4 /graphene oxide (32.33 mg/g) [52]. Ion exchange, reduction, and complexation were introduced as the processes for Cr (VI) removal. Other researchers, Su et al. [45] and Kumar et al. [46], suggested the use of FeS@ graphite carbon nitride and oxidized g-C_3N_4/polyaniline nanofiber for the removal of Cr (VI). In the first one, authors stated that FeS tends to agglomerate because of magnetic attraction and oxidation which impede its application. In the second one, oxidized g-C_3N_4 provides a great surface for polyaniline nanofiber, and due to its positive nature, it could greatly adsorb Cr (VI) ions. Fig. 6.7 shows the removal mechanism of Cr (VI) via FeS@ graphite carbon nitride and the changes in the Cr (VI) concentration during the process. It was found that the concentration of Cr (VI) decreased and reached to 2.6 mg/L; however, Cr (III) was simultaneously produced in the solution. This observation proved that Cr (VI) elimination involved chemical reduction along

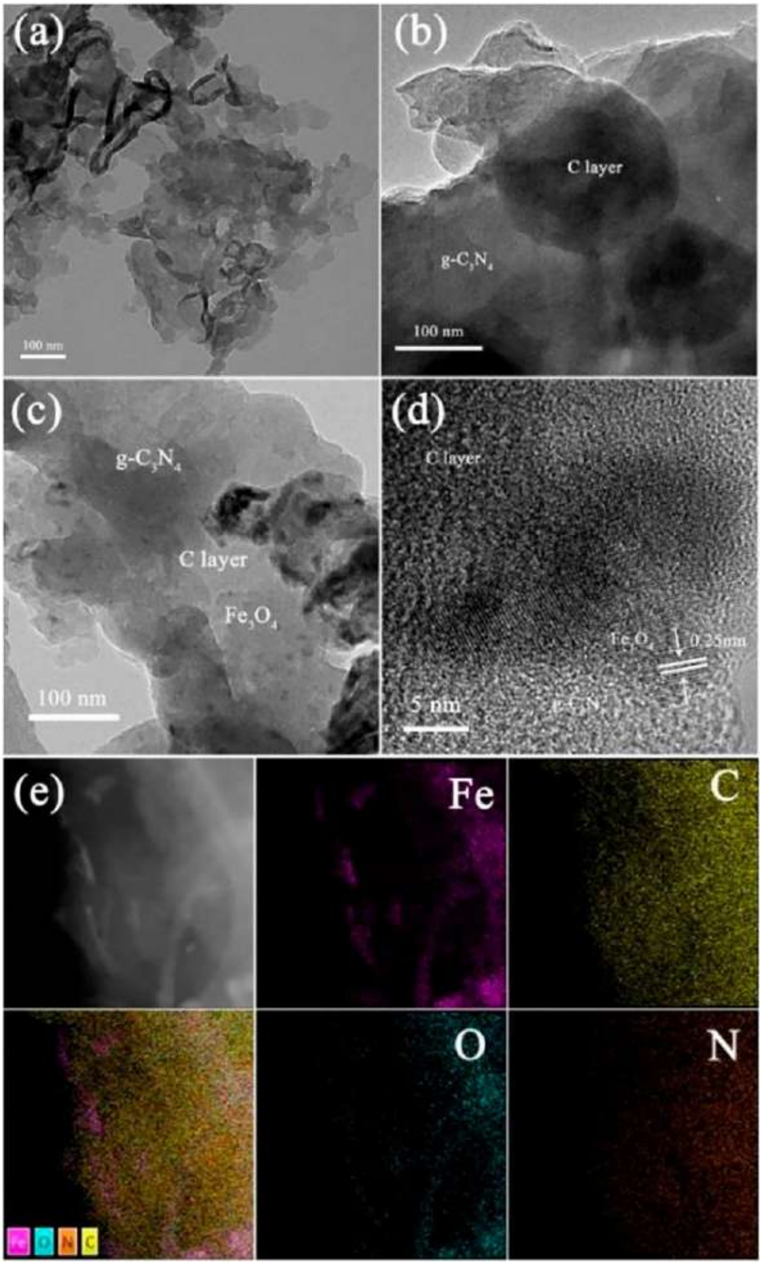

Fig. 6.6 TEM images of g-C_3N_4 (A), g-C_3N_4/ carbon layer (B) and Fe_3O_4/ g-C_3N_4/ carbon layer (C). HRTEM image of Fe_3O_4/g-C_3N_4/ carbon layer (D). Elemental mapping images of different elements (Fe, C, O, N) in Fe_3O_4/ g-C_3N_4/ carbon layer (E). *Reprinted with permission from T. Wang, L. Zheng, Y. Liu, W. Tang, T. Fang, B. Xing, A novel ternary magnetic Fe3O4/g-C3N4/carbon layer composite for efficient removal of Cr (VI): a combined approach using both batch experiments and theoretical calculation, Sci. Total Environ. 730 (2020) 138928.* https://doi.org/10.1016/j.scitotenv.2020.138928.

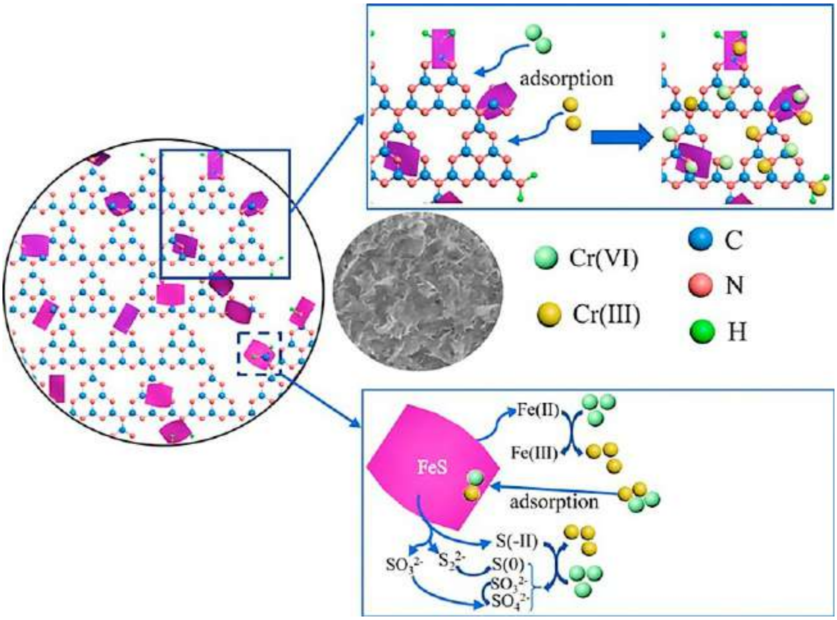

Fig. 6.7 The removal mechanism of Cr (VI) by FeS@ graphite carbon nitride and change of chromium concentration during the removal. *Reprinted with permission from ref. J. Su, H. Hao, X. Lv, X. Jin, Q. Yang, Properties and mechanism of hexavalent chromium removal by FeS@ graphite carbon nitride nanocomposites, Colloids Surf. A Physicochem. Eng. Asp. 597 (2020) 124751. https://doi.org/10.1016/j.colsurfa.2020.124751.*

with adsorption. Detection of Fe (II) in the working solution unveiled that FeS in graphite carbon nitride was dissolved by the following:

$$FeS + H^{+} \rightarrow Fe^{2+} + H\,S^{-} \tag{6.1}$$

For instance, the following reactions resulted in reduction of Cr (VI) (there are other complex steps):

$$Fe\,(II) + Cr\,(VI) \rightarrow 3Fe\,(III) + Cr\,(III) \tag{6.2}$$

$$3S\,(-II) + 2Cr\,(VI) \rightarrow 3S\,(0) + 2Cr\,(III) \tag{6.3}$$

Finally, the Cr(III)–Fe(III) oxides/hydroxides contributed to the elimination of chromium. The amino groups of FeS@ graphite carbon nitride composite could adsorb Cr (VI). It was confirmed that 73.1% and 269% of chromium removal was attributed to chemical reduction and adsorption, respectively [45]. In the oxidized g-C_3N_4/polyaniline nanofiber, the positive nature of the adsorbent and N/O-containing functional groups was responsible for Cr (III) removal [46].

Further studies were carried out for the removal of arsenic, nickel, and copper by means of graphite carbon nitride-based composites. Kim et al. [53] examined the removal of arsenic by iron-modified graphitic carbon nitride via simultaneous oxidation/adsorption. The prepared material was characterized by XRD, FTIR, TEM, SEM, EDS, TGA, and XPS. It was assumed that graphitic carbon nitride oxidizes As (III) to As (V) under light irradiation, and the produced ions were adsorbed by iron phase loaded on iron/$g\text{-}C_3N_4$ composite. This composite has oxidation and adsorption ability. It was confirmed that under visible light, the maximum arsenic reduction was occurred. These findings were also observed in [54]. In the case of Ni (II) and Cu (II), alginate/graphitic carbon nitride composite hydrogels represented the maximum adsorption capacity of 306.3 and 168.2 mg/g, respectively, and the obtained data for both heavy metals followed PSO and Langmuir assumptions [39].

In Table 6.1, the best fitted isotherm and kinetics were also summarized. Clearly, PSO was the best kinetics model among the others such as [35–37,39]. PSO is generally expressed to expound the presence of chemical adsorption or chemisorption between $g\text{-}C_3N_4$ composite and heavy metal ions. However, such deduction could not always be trusted only by results of simple kinetic models. Tran et al. [55] explained that this deduction must be supported by analytical techniques (mainly FTIR, XRD, EDS, NMR, XPD, etc.) plus the nature of the adsorbent and adsorbate. For isotherm models (Fig. 6.8), the first rank goes to Langmuir with 60% of the studies that were best fitted to Langmuir assumptions, and then to Freundlich (20%) and Sips (20%). Assuming that Langmuir assumptions are true for heavy metals adsorption by $g\text{-}C_3N_4$ composite, it can be suggested that $g\text{-}C_3N_4$ composite has a fixed number of surface sites that are actively equivalent along with monolayer surface coverage [56].

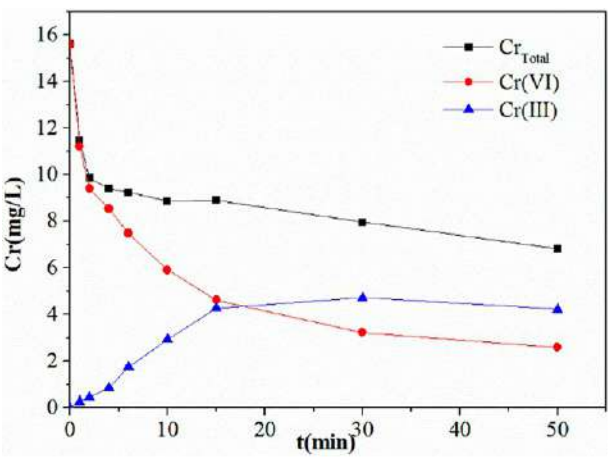

Fig. 6.8 The suitability of adsorption isotherms for $g\text{-}C_3N_4$ composite toward heavy metal ions.

5. Carbon nitride-based adsorbents for the removal of dyes

Dyes are regarded as important pollutants of environments that are used in many industrial activities, including cosmetics, leather, tannery, printing, paper, plastics and textile, etc. It is estimated that more than 7×10^5 tons of synthetic dyes are produced annually that have the potential of entering aquatic media. At the moment, there are more than 10^4 dyes in the market. Despite the fact that dyes have contributed to see a colorful world, they are often toxic, carcinogenic, mutagenic, nonbiodegradable, and stable. Even at dye concentration of 1 ppm, the transparency and gas solubility of water bodies can be affected [57]. Therefore, many researches have focused on the removal of dyes from waters. The maximum adsorption capacity and the best-fitting isotherm and kinetic models associated with dye adsorption by carbon nitride-based materials are summarized in Table 6.2.

The removal of methylene blue (MB) by g-C_3N_4-based composite has been extensively studied. Ren et al. [58] studied MB removal by carbon-doped g-C_3N_4. The authors believed that g-C_3N_4 does not have acceptable performance for aromatic compounds and its modification could increase its efficiency. Accordingly, carbon-doped g-C_3N_4 was prepared by using glucose and melamine. Based on Fig. 6.9, the adsorption capacity of the composite increased by increasing Ce value of MB until it reached a plateau and suggested a monolayer. Langmuir assumptions were better than Freundlich in describing the sorption process. Electrostatic attraction and π–π interactions are presumed to be the reasons for MB adsorption. The maximum adsorption capacity for Mb was found 57.87 mg/g which was superior to natural zeolite 29.18 mg/g [67] and activated carbon 9.81 mg/g [68]. Other researchers, Chegeni and Dehghan [59], also found that Langmuir (100 mg/g) was the best model for MB adsorption by phosphorus-doped g-C_3N_4. Gan et al. [60] conducted promising experiments by enhancing g-C_3N_4 by Polyoxoniobate to prepare a nanoporous material with high adsorption capacity toward MB dye. Polyoxoniobates is a branch of polyoxometalates that own high surface area and photocatalytic properties. Fig. 6.10 depicts the XRD of g-C_3N_4, NbO/g-C_3N_4, and NbO. 13.1° and 27.4° were characteristics peaks of pristine g-C_3N_4. According to XRD pattern of NbO and NbO/g-C_3N_4, it can be stated that the authors were successful in preparing the NbO/g-C_3N_4. The experimental results showed that at pH 11.25, MB removal occurred more satisfactorily in terms of adsorption capacity. The pHzpc of NbO/g-C_3N_4 was 6.93, indicating that at pH >6.93, the carbon nitride composite possessed negative charges on its surface which is beneficial for the adsorption of cationic MB. Enhancement in temperature and initial MB concentration resulted in higher adsorption capacity. The authors applied the kinetic data to intraparticle diffusion model by plotting the graph adsorption capacity vs time$^{0.5}$ (Fig. 6.11). As it is observed, this figure consisted of two regions; the first one is related to the MB molecules diffusion to the external surface of the adsorbent and the second region is for diffusion of the dye molecules into pores.

Table 6.2 The maximum monolayer adsorption capacity and the best-fitting isotherm and kinetic models for the adsorption of dyes by g-C_3N_4-based adsorbents.

No.	Adsorbent	Dye	Adsorption capacity (mg/g)	Removal efficiency (%)	Isotherm/ kinetics	References
1	2D-g-C_3N_4	MB	42.1	–	PSO	[43]
2	Carbon-doped g-C_3N_4	MB	57.87	–	L/PSO	[58]
3	Phosphorus-doped g-C_3N_4	MB	100	–	L/PSO	[59]
4	Polyoxoniobate/g-C_3N_4	MB	373.1	–	L/PSO	[60]
5	Boron-doped carbon nitride	MB	43.11	–	L/PSO	[61]
6	Pristine carbon nitride		13.05	–	–	
7	Graphene oxide/g-C_3N_4	MB	174.23	–	–	[62]
8	Graphene oxide/g-C_3N_4/Fe_3O_4	MB	187.36	–	L/PSO	
9	Ultra small gold nanoparticles/ carbon nitride sheets	RhB MB MR	400 250 130	–	Sips	[63]
10	Activated carbon (5%)/carbon nitride	RhB	13.57	–	F/PSO	[64]
11	g-C_3N_4		3.15	–	F/PSO	
12	COF@ g-C_3N_4	Eosin dye fluorescein	–	80%–97.5%	–	[65]
13	g-C_3N_4/graphene oxide	basic blue 26	3510	–	DR/PSO	[66]

MR—methyl red.

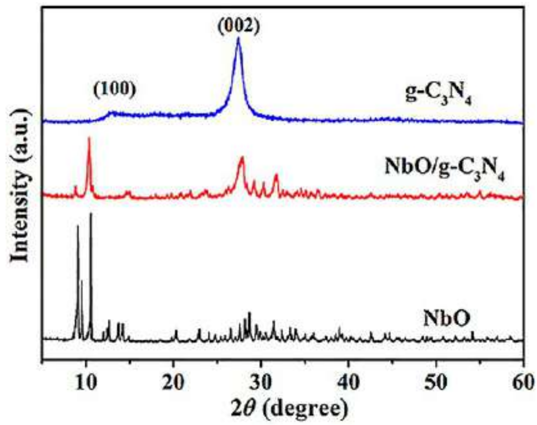

Fig. 6.9 Adsorption isotherm (A), Langmuir (B), and Freundlich (C) plot for MB adsorption by carbon-doped g-C_3N_4. *Reprinted with permission from B. Ren, Y. Xu, L. Zhang, Z. Liu, Carbon-doped graphitic carbon nitride as environment-benign adsorbent for methylene blue adsorption: kinetics, isotherm and thermodynamics study, J. Taiwan Inst. Chem. Eng. 88 (2018) 114–120. https://doi.org/10.1016/j.jtice.2018.03.041.*

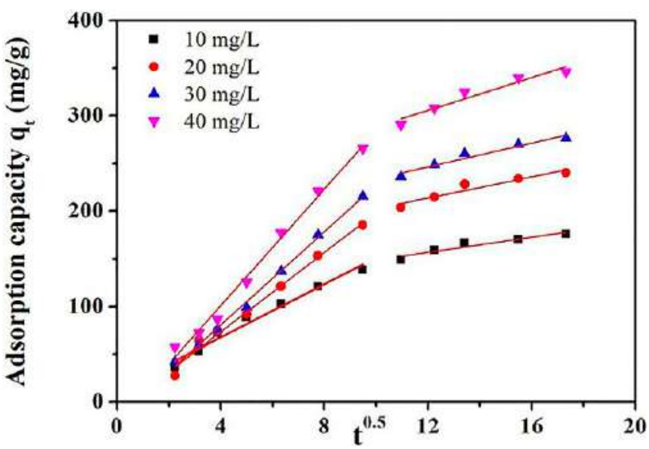

Fig. 6.10 XRD powder patterns of g-C_3N_4, NbO/g-C_3N_4, and NbO. *Reprinted with permission from Q. Gan, W. Shi, Y. Xing, Y. Hou, A Polyoxoniobate/g-C3N4 nanoporous material with high adsorption capacity of methylene blue from aqueous solution, Front. Chem. 6 (2018) 7. https://doi.org/10.3389/fchem.2018.00007.*

Magnetic nanoparticles are widely known as promising materials in adsorption studies. Many studies have proved the ability of these particles to eliminate pollutants from water media. Note that separation of the used adsorbent from solution might somehow be a complicated task that requires filtration, sedimentation, or even centrifugal. Magnetic-based composites are potential to be separated by applying an external

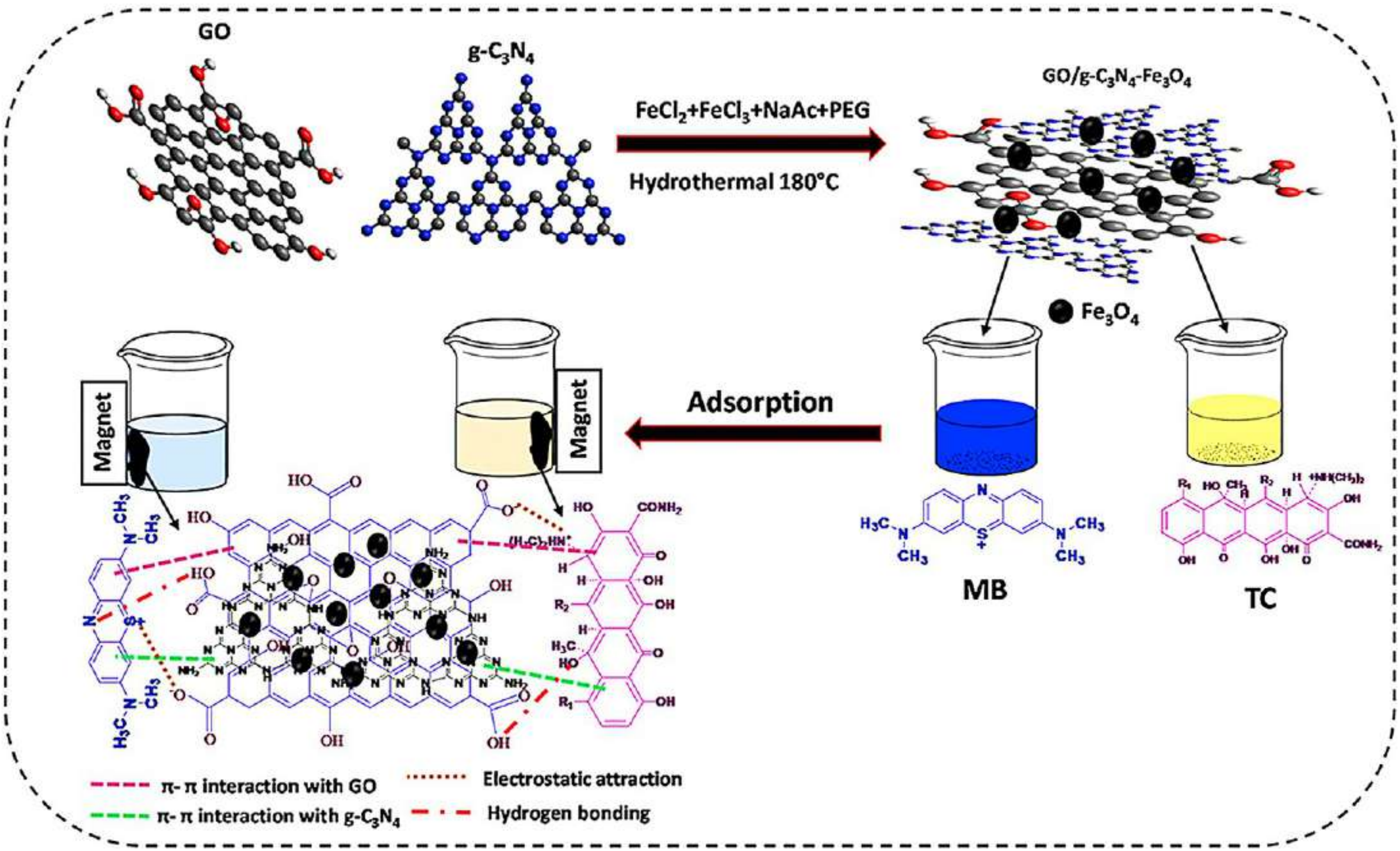

Fig. 6.11 Intraparticle diffusion model for adsorption of MB onto NbO/g-C3N4. *Reprinted with permission from Q. Gan, W. Shi, Y. Xing, Y. Hou, A Polyoxoniobate/g-C3N4 nanoporous material with high adsorption capacity of methylene blue from aqueous solution, Front. Chem. 6 (2018) 7. https://doi.org/10.3389/fchem.2018.00007.*

magnetic field which resolved the above-mentioned issues. In some cases, magnetic particles could increase the adsorbent surface area or even establish chemical bonds with pollutants molecules/ions that contribute to removal efficiency in addition to facile separation. Ku Sahoo et al. [62] reported the utilization of Fe_3O_4 nanoparticles functionalized graphene oxide/g-C_3N_4 nanocomposite for the removal of tetracycline antibiotic and MB dye (Fig. 6.12). π–π and hydrogen bonding interaction were introduced as the main mechanism of the removal. It was found that the whole process followed Langmuir and PSO model. In view of magnetic particles efficiency, graphene oxide/g-C_3N_4 nanocomposite showed the adsorption capacity of 174.23 mg/g; however, in combination with Fe_3O_4, it reached to 187.36 mg/g. The prepared material was also effective after 5 successive cycles, indicating that graphene oxide/g-C_3N_4/Fe_3O_4 is potential to be used for the adsorption of pollutants.

Rhodamine B (RhB) is another important dye belongs to cationic xanthene dye that causes carcinogenicity, neurotoxicity, and chronic toxicity (such as respiratory diseases and kidney failure) for the living environment [69]. Shi et al. [64] studied the adsorption-photocatalytic capability of activated carbon (AC)/g-C_3N_4 for the removal of RhB. The presence of AC in the composite could improve adsorption capacity and serve as a support for the removal process. According to Fig. 6.13, g-C_3N_4 peaks

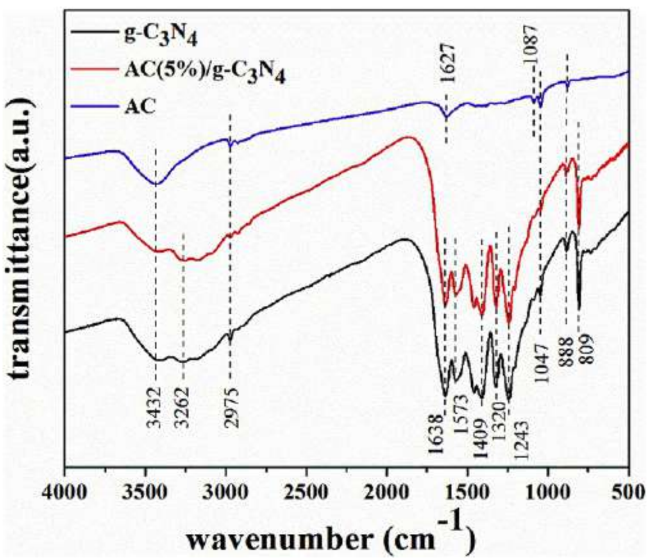

Fig. 6.12 Preparation and application of Fe_3O_4 nanoparticles functionalized graphene oxide/g-C_3N_4 nanocomposite for the removal of tetracycline antibiotic and MB dye. *Reprinted with permission from ref. S.K. Sahoo, S. Padhiari, S.K. Biswal, B.B. Panda, G. Hota, Fe3O4 nanoparticles functionalized GO/g-C3N4 nanocomposite: An efficient magnetic nanoadsorbent for adsorptive removal of organic pollutants, Mater. Chem. Phys. 244 (2020) 122710. https://doi.org/10.1016/j.matchemphys.2020.122710.*

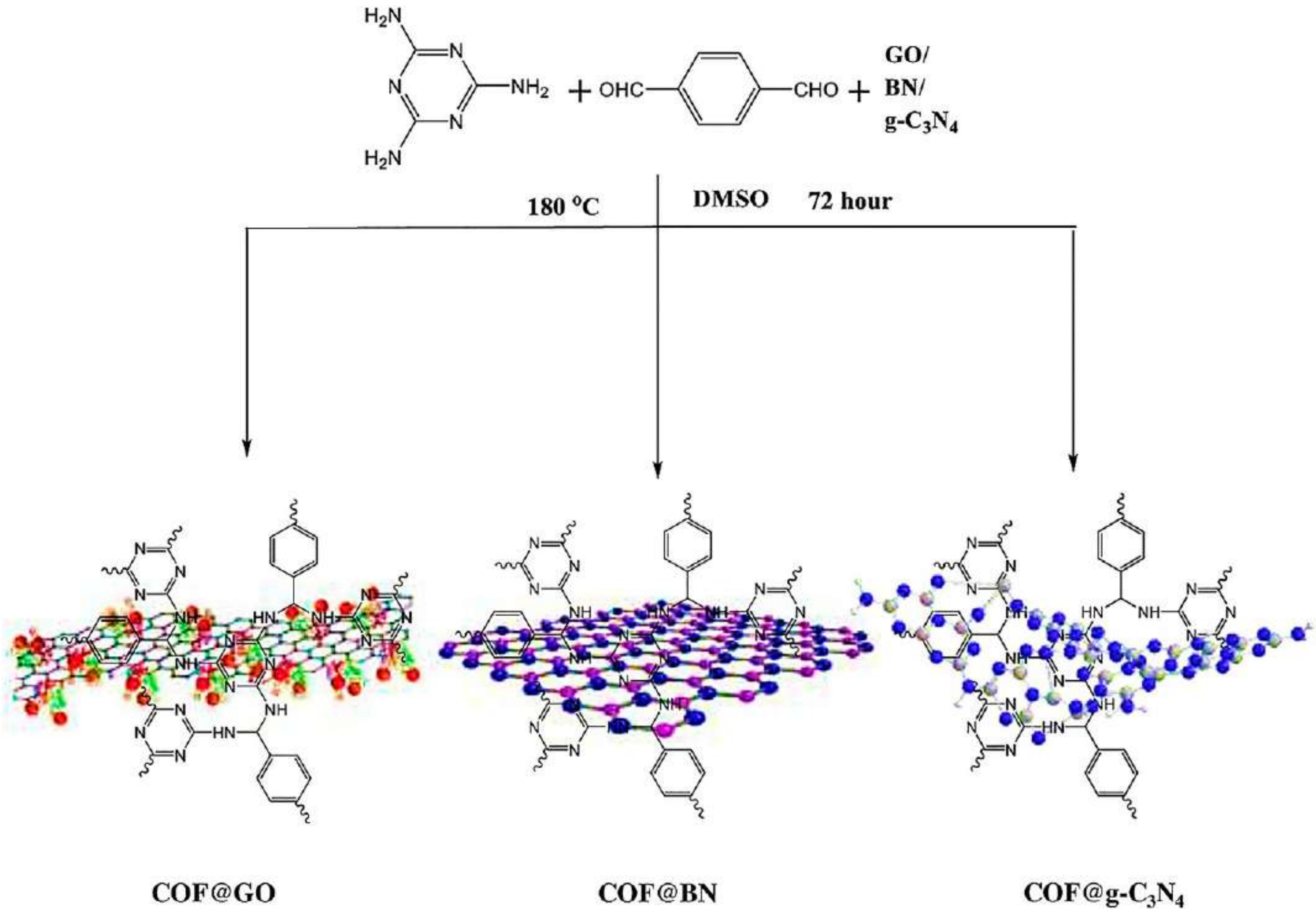

Fig. 6.13 FTIR spectra of g-C_3N_4, activated carbon, and activated carbon/g-C_3N_4. *Reprinted with permission from J. Shi, T. Chen, C. Guo, Z. Liu, S. Feng, Y. Li, J. Hu, The bifunctional composites of AC restrain the stack of g-C3N4 with the excellent adsorption-photocatalytic performance for the removal of RhB, Colloids Surf. A Physicochem. Eng. Asp. 580 (2019) 123701.* https://doi.org/10.1016/j.colsurfa.2019.123701.

were observed at 3262 cm^{-1} (uncondensed amine groups), 3432 cm^{-1} (water molecules), and 809 cm^{-1} (triazine units). g-C_3N_4 has also other peaks for stretching modes of CN heterocycles at 1638, 1573, 1409, 1320, and 1243 cm^{-1}. AC exhibited peaks of C=O, C–O, C–C, and C–N stretching vibrations at a wide range of 800–1700 cm^{-1}. AC/g-C_3N_4 characteristic absorption peaks were a combination of activated carbon and g-C_3N_4, indicating a satisfaction doping process. N_2 adsorption–desorption isotherms proved mesoporous structure of the modified adsorbent that had a surface area 457 m^2/g and pore volume 0.973 cm^3/g, and compared to g-C_3N_4 (21 m^2/g, 0.206 cm^3/g), a dramatic increment was happened. It is presumed that AC increased both surface area and active sites of g-C_3N_4. In terms of adsorption capacity, AC (5%)/g-C_3N_4 (13.57 mg/g) was 4.3 times higher than that of g-C_3N_4 (3.15 mg/g). Other scholars [63] reported the adsorption capacity of 400 mg/g for RhB dye by ultra-small gold nanoparticles/carbon nitride sheets. The authors pointed out that enough attention must be given to surface charges of the adsorbent and adsorbate. g-C_3N_4 itself is positively charged at neutral pH and since RhB is also a cationic dye, insignificant adsorption capacity was found. The ultra-small gold nanoparticles/g-C_3N_4 possessed the average zeta potential value of −45 mV which is appropriate for the removal of RhB cationic dye via electrostatic attraction. To sum up, these studies proved that by applying right modification, g-C_3N_4-based composites could also be effective for the removal of RhB as a cationic dye model.

Other studies have also been reported for the adsorptive performance of g-C_3N_4 for other dyes. Abdellah et al. [65] suggested the modification of covalent organic frameworks (COFs) by two-dimensional (2D) nanomaterials. Thermal/chemical stability, low density, regular porosity, large specific surface area, and porous structure are some of the properties of COFs that make them as brilliant adsorbents; however, they exhibited low diffusion rate for large molecules because of their mesoporous structure. Besides, COFs separation from solution is hard (because of the low density) [70]. Fig. 6.14 depicts the synthesis procedure for COF and its composites. COF@GO (graphene oxide), COF@BN (boron nitride), and cof@g-C3N4 had BET surface area and total pore volume of 42, 168, 509 m^2/g and 0.126, 0.779, 0.607 cm^3/g, respectively. By increasing the time, the intensity of absorbance tends to decrease which is a proof for the elimination of dye from the solution. The removal efficiency was 80%–97.5% at 170 min and 25°C. One-pot method synthesis, high surface area, no catalyst, and inexpensiveness were unique properties of the prepared composites. The removal of basic blue 26 as a cationic dye was studied by combining different mass ratio (30/70, 50/50, and 70/30) of CN and graphene oxide (GO) [66]. The cooperation of these adsorbents showed the best performance at 50/50 with the maximum adsorption capacity of 3510.68 mg/g at pH 2. The very significant adsorption capacity of this study was absolutely greater than some previous materials, including carbon/Ba/alginate beads 1.94 mg/g [71], activated carbon 76 mg/g [72], iron-doped titanium/silane 153.89 mg/g [73], zinc oxide nanoparticles

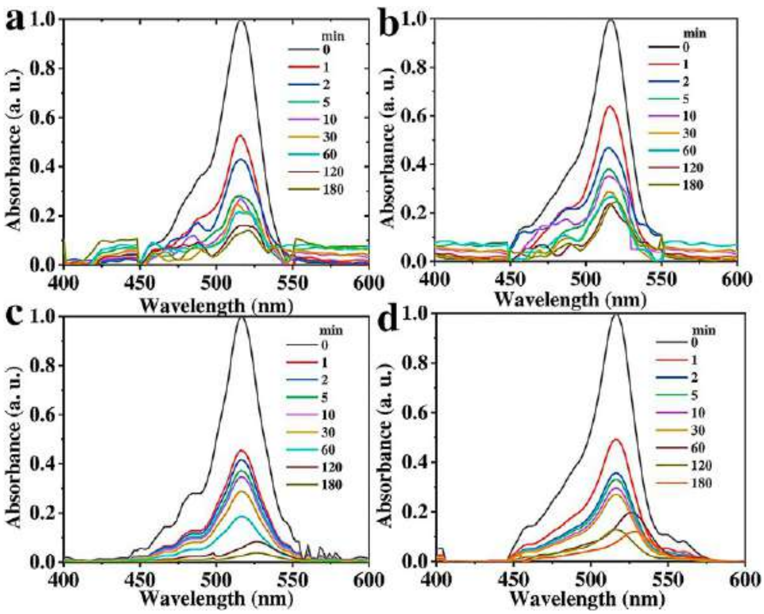

Fig. 6.14 The synthesis procedure for COF and its composites. *Reprinted with permission from A.R. Abdellah, H.N. Abdelhamid, A.-B.A.A.M. El-Adasy, A.A. Atalla, K.I. Aly, One-pot synthesis of hierarchical porous covalent organic frameworks and two-dimensional nanomaterials for selective removal of anionic dyes, J. Environ. Chem. Eng. 8 (2020) 104054. https://doi.org/10.1016/j.jece.2020.104054.*

163.93 mg/g [74], and H_3PO_4-activated carbons 51.11 mg/g [75]. Protonated amine groups of basic blue 26 were adsorbed by negatively charged CN–graphene oxide composite. Weak electrostatic and π–π interactions were introduced as the main removal forces.

6. Conclusion

Over the last few decades, overwhelming with water scarcity and water pollution, various physical chemical and biological remediation techniques for polluted water have been introduced. Among them, adsorption method has been extensively used for the treatment of water and wastewater. In this regard, to reach the maximum removal efficiency, many engineered nanomaterials have been suggested by scholars. CN has gained worldwide attention to its promising results in view of adsorbing pollutants from aqueous solutions. The discussion presented in this chapter along with literature data indicated considerable evidence for the potential ability of pristine CN and CN-based composites for the removal of heavy metals and dyes. The removal of important heavy metals, including Pb (II), Cd (II), Cr (IV), Ni (II), and Cu (II) were discussed. In view of dyes, it was found that CN-based composites were extensively applied for methylene blue removal which it may be attributed to its widespread existence in the waters. Note that pristine g-C_3N_4 exhibited an acceptable removal efficiency and adsorption capacity, especially for heavy metal ions. However, the results indicated that in some cases (dyes, for instance), pristine carbon nitride had poor removal. Many researchers suggested excellent composites based on g-C_3N_4 that could resolve the poor applicability of the basic material. It was found that electrostatic attraction was one of the main mechanisms involve in the interaction of heavy metals/dyes and g-C_3N_4-based composites. The comparison of g-C_3N_4-based composites with other sorbents demonstrated that carbon nitride might be superior to many former materials. In view of kinetics and isotherms, most studied were in a great agreement with the assumption of Langmuir and pseudo second-order models. Finally, from the above discussion, it can be concluded that g-C_3N_4-based composites have already exhibited their potential for application to the elimination of pollutants, and it is assumed that there are still so many modifications and functionalization that also could bring outstanding results in the field of carbon nitride.

References

[1] T. Oki, R.E. Quiocho, Economically challenged and water scarce: identification of global populations most vulnerable to water crises, Int. J. Water Resour. Dev. (2020), https://doi.org/10.1080/07900627.2019.1698413.

[2] D. Seckler, R. Barker, U. Amarasinghe, Water scarcity in the twenty-first century, Int. J. Water Resour. Dev. (1999), https://doi.org/10.1080/07900629948916.

[3] M. Kummu, J.H.A. Guillaume, H. De Moel, S. Eisner, M. Flörke, M. Porkka, S. Siebert, T.I.E. Veldkamp, P.J. Ward, The world's road to water scarcity: shortage and stress in the 20th century and pathways towards sustainability, Sci. Rep. (2016), https://doi.org/10.1038/srep38495.

[4] A. Khadir, M. Motamedi, M. Negarestani, M. Sillanpää, M. Sasani, Preparation of a nano bio-composite based on cellulosic biomass and conducting polymeric nanoparticles for ibuprofen removal: kinetics, isotherms, and energy site distribution, Int. J. Biol. Macromol. (2020), https://doi.org/10.1016/j.ijbiomac.2020.06.095.

[5] H. Pahlavanzadeh, M. Motamedi, Adsorption of nickel, Ni(II), in aqueous solution by modified zeolite as a cation-exchange adsorbent, J. Chem. Eng. Data 65 (2020) 185–197, https://doi.org/10.1021/acs.jced.9b00868.

[6] F. Piri, A. Mollahosseini, A. Khadir, M.M. Hosseini, Enhanced adsorption of dyes on microwave-assisted synthesized magnetic zeolite-hydroxyapatite nanocomposite, J. Environ. Chem. Eng. (2019), https://doi.org/10.1016/j.jece.2019.103338, 103338.

[7] H.N. Tran, S.-J. You, H.-P. Chao, Thermodynamic parameters of cadmium adsorption onto orange peel calculated from various methods: a comparison study, J. Environ. Chem. Eng. 4 (2016) 2671–2682, https://doi.org/10.1016/j.jece.2016.05.009.

[8] M. Abbas, M. Trari, Removal of methylene blue in aqueous solution by economic adsorbent derived from apricot stone activated carbon, Fibers Polym. 21 (2020) 810–820, https://doi.org/10.1007/s12221-020-8630-8.

[9] H. Panda, N. Tiadi, M. Mohanty, C.R. Mohanty, Studies on adsorption behavior of an industrial waste for removal of chromium from aqueous solution, S. Afr. J. Chem. Eng. (2017), https://doi.org/10.1016/j.sajce.2017.05.002.

[10] R.R. Elmorsi, S.T. El-Wakeel, W.A. Shehab El-Dein, H.R. Lotfy, W.E. Rashwan, M. Nagah, S.A. Shaaban, S.A. Sayed Ahmed, I.Y. El-Sherif, K.S. Abou-El-Sherbini, Adsorption of methylene blue and Pb 2+ by using acid-activated Posidonia oceanica waste, Sci. Rep. (2019), https://doi.org/10.1038/s41598-019-39945-1.

[11] C.E. Borba, R. Guirardello, E.A. Silva, M.T. Veit, C.R.G. Tavares, Removal of nickel(II) ions from aqueous solution by biosorption in a fixed bed column: experimental and theoretical breakthrough curves, Biochem. Eng. J. 30 (2006) 184–191, https://doi.org/10.1016/j.bej.2006.04.001.
[12] J. Wang, M. Yang, Two-dimensional nanomaterials in cancer theranostics, in: Theranostic Bionanomaterials, 2019, https://doi.org/10.1016/B978-0-12-815341-3.00011-0.
[13] K. Qiao, W. Tian, J. Bai, L. Wang, J. Zhao, Z. Du, X. Gong, Application of magnetic adsorbents based on iron oxide nanoparticles for oil spill remediation: a review, J. Taiwan Inst. Chem. Eng. 97 (2019) 227–236, https://doi.org/10.1016/j.jtice.2019.01.029.
[14] E. Marzi Khosrowshahi, H. Razmi, Application of sunflower stalk-carbon nitride nanosheets as a green sorbent in the solid-phase extraction of polycyclic aromatic hydrocarbons followed by high-performance liquid chromatography, J. Sep. Sci. (2018), https://doi.org/10.1002/jssc.201701248.
[15] Z. Feng, C. Huang, Y. Guo, W. Liu, L. Zhang, Graphitic carbon nitride derivative with large mesopores as sorbent for solid-phase microextraction of polycyclic aromatic hydrocarbons, Talanta (2020), https://doi.org/10.1016/j.talanta.2019.120541.
[16] P. Song, M. Wang, J. Di, J. Xiong, S. Zhao, Z. Li, Reusable graphitic carbon nitride nanosheet-based aerogels as sorbents for oils and organic solvents, ACS Appl. Nano Mater. (2020), https://doi.org/10.1021/acsanm.0c01592.
[17] B. Fahimirad, A. Asghari, M. Rajabi, Magnetic graphitic carbon nitride nanoparticles covalently modified with an ethylenediamine for dispersive solid-phase extraction of lead(II) and cadmium(II) prior to their quantitation by FAAS, Microchim. Acta (2017), https://doi.org/10.1007/s00604-017-2273-5.
[18] A. Aziz, F. Basheer, A. Sengar, S.U. Irfanullah, I.H.F. Khan, Biological wastewater treatment (anaerobic-aerobic) technologies for safe discharge of treated slaughterhouse and meat processing wastewater, Sci. Total Environ. 686 (2019) 681–708, https://doi.org/10.1016/j.scitotenv.2019.05.295.
[19] S. Mallakpour, S. Rashidimoghadam, 9 - Carbon nanotubes for dyes removal, in: G.Z. Kyzas, A.C.B. T.-C.N. Mitropoulos (Eds.), Composite Nanoadsorbents, Micro and Nano Technologies, Elsevier, 2019, pp. 211–243, https://doi.org/10.1016/B978-0-12-814132-8.00010-1.
[20] F. Beheshti, R.M.A. Tehrani, A. Khadir, Sulfamethoxazole removal by photocatalytic degradation utilizing TiO2 and WO3 nanoparticles as catalysts: analysis of various operational parameters, Int. J. Environ. Sci. Technol. (2019), https://doi.org/10.1007/s13762-019-02212-x.
[21] A. Mohammadi, A. Khadir, R.M.A. Tehrani, Optimization of nitrogen removal from an anaerobic digester effluent by electrocoagulation process, J. Environ. Chem. Eng. (2019), https://doi.org/10.1016/j.jece.2019.103195, 103195.
[22] E.I. Unuabonah, M.O. Omorogie, N.A. Oladoja, 5 - Modeling in adsorption: fundamentals and applications, in: G.Z. Kyzas, A.C.B.T.-C.N. Mitropoulos (Eds.), Composite Nanoadsorbents, Micro and Nano Technologies, Elsevier, 2019, pp. 85–118, https://doi.org/10.1016/B978-0-12-814132-8.00005-8.
[23] A. Mollahosseini, A. Khadir, J. Saeidian, Core–shell polypyrrole/Fe3O4 nanocomposite as sorbent for magnetic dispersive solid-phase extraction of Al+3 ions from solutions: investigation of the operational parameters, J. Water Process Eng. 29 (2019), https://doi.org/10.1016/j.jwpe.2019.100795, 100795.
[24] E. Worch, 5–Adsorption kinetics, in: Adsorption Technology in Water Treatment, 2012, pp. 123–168, https://doi.org/10.1515/9783110240238.123.
[25] J.S. Piccin, T.R.S. Cadaval, L.A.A. de Pinto, G.L. Dotto, in: A. Bonilla-Petriciolet, D.I. Mendoza-Castillo, H.E. Reynel-Ávila (Eds.), Adsorption Isotherms in Liquid Phase: Experimental, Modeling, and Interpretations BT - Adsorption Processes for Water Treatment and Purification, Springer International Publishing, Cham, 2017, pp. 19–51, https://doi.org/10.1007/978-3-319-58136-1_2.
[26] A. Rezaei, H. Hassani, S. Hassani, N. Jabbari, S.B. Fard Mousavi, S. Rezaei, Evaluation of groundwater quality and heavy metal pollution indices in Bazman basin, southeastern Iran, Groundw. Sustain. Dev. 9 (2019), https://doi.org/10.1016/j.gsd.2019.100245, 100245.
[27] C. Guo, Y. Chen, W. Xia, X. Qu, H. Yuan, S. Xie, L.-S. Lin, Eutrophication and heavy metal pollution patterns in the water suppling lakes of China's south-to-north water diversion project, Sci. Total Environ. 711 (2020), https://doi.org/10.1016/j.scitotenv.2019.134543, 134543.

[28] I. Karaouzas, N. Kapetanaki, A. Mentzafou, T.D. Kanellopoulos, N. Skoulikidis, Heavy metal contamination status in Greek surface waters: a review with application and evaluation of pollution indices, Chemosphere 263 (2021), https://doi.org/10.1016/j.chemosphere.2020.128192, 128192.
[29] R. Rajaram, A. Ganeshkumar, in: M. Ramkumar, R.A. James, D. Menier, K.B.T.-C.Z.M. Kumaraswamy (Eds.), Chapter 16 - Anthropogenic influence of heavy metal pollution on the southeast coast of India, Elsevier, 2019, pp. 381–399, https://doi.org/10.1016/B978-0-12-814350-6.00016-1.
[30] H.M. Zakir, S. Sharmin, A. Akter, M.S. Rahman, Assessment of health risk of heavy metals and water quality indices for irrigation and drinking suitability of waters: a case study of Jamalpur Sadar area, Bangladesh, Environ. Adv. 2 (2020), https://doi.org/10.1016/j.envadv.2020.100005, 100005.
[31] S. Muhammad, K. Ahmad, Heavy metal contamination in water and fish of the Hunza River and its tributaries in Gilgit–Baltistan: evaluation of potential risks and provenance, Environ. Technol. Innov. 20 (2020), https://doi.org/10.1016/j.eti.2020.101159, 101159.
[32] N.H. Ab Razak, S.M. Praveena, A.Z. Aris, Z. Hashim, Drinking water studies: a review on heavy metal, application of biomarker and health risk assessment (a special focus in Malaysia), J. Epidemiol. Glob. Health 5 (2015) 297–310, https://doi.org/10.1016/j.jegh.2015.04.003.
[33] M.F.R. Samsudin, N. Bacho, S. Sufian, Recent development of graphitic carbon nitride-based photocatalyst for environmental pollution remediation, in: Nanocatalysts, IntechOpen, 2018.
[34] K. Parvez, Chapter 1 - Two-dimensional nanomaterials: crystal structure and synthesis, in: M. Nurunnabi, J.R. McCarthy (Eds.), Biomedical Applications of Graphene and 2D Nanomaterials, Micro and Nano Technologies, Elsevier, 2019, pp. 1–25, https://doi.org/10.1016/B978-0-12-815889-0.00001-5.
[35] L. Zhu, L. You, Y. Wang, Z. Shi, The application of graphitic carbon nitride for the adsorption of Pb2+ ion from aqueous solution, Mater. Res. Express 4 (2017) 75606, https://doi.org/10.1088/2053-1591/aa7903.
[36] X. Li, J. Xing, C. Zhang, B. Han, Y. Zhang, R. Leng, Z. Jiang, Y. Ai, X. Wang, Adsorption of Lead on sulfur-doped graphitic carbon nitride nanosheets: experimental and theoretical calculation study, ACS Sustain. Chem. Eng. 6 (2018), https://doi.org/10.1021/acssuschemeng.8b01934.
[37] M. Anbia, M. Haqshenas, Adsorption studies of Pb(II) and cu(II) ions on mesoporous carbon nitride functionalized with melamine-based dendrimer amine, Int. J. Environ. Sci. Technol. 12 (2015) 2649–2664, https://doi.org/10.1007/s13762-015-0776-3.
[38] Y. Zou, X. Wang, Y. Ai, Y. Liu, Y. Ji, H. Wang, T. Hayat, A. Alsaedi, W. Hu, X. Wang, β-Cyclodextrin modified graphitic carbon nitride for the removal of pollutants from aqueous solution: experimental and theoretical calculation study, J. Mater. Chem. A 4 (2016) 14170–14179, https://doi.org/10.1039/C6TA05958A.
[39] W. Shen, Q.-D. An, Z.-Y. Xiao, S.-R. Zhai, J.-A. Hao, Y. Tong, Alginate modified graphitic carbon nitride composite hydrogels for efficient removal of Pb(II), Ni(II) and Cu(II) from water, Int. J. Biol. Macromol. 148 (2020) 1298–1306, https://doi.org/10.1016/j.ijbiomac.2019.10.105.
[40] G. Xiao, Y. Wang, S. Xu, P. Li, C. Yang, Y. Jin, Q. Sun, H. Su, Superior adsorption performance of graphitic carbon nitride nanosheets for both cationic and anionic heavy metals from wastewater, Chin. J. Chem. Eng. 27 (2019) 305–313.
[41] S. Guo, N. Duan, Z. Dan, G. Chen, F. Shi, W. Gao, G-C3N4 modified magnetic Fe3O4 adsorbent: preparation, characterization, and performance of Zn(II), Pb(II) and Cd(II) removal from aqueous solution, J. Mol. Liq. 258 (2018) 225–234, https://doi.org/10.1016/j.molliq.2018.03.029.
[42] J. Su, L. Bi, C. Wang, T. Lyu, G. Pan, Enhancement of cadmium removal by oxygen-doped carbon nitride with molybdenum and sulphur hybridization, J. Colloid Interface Sci. 556 (2019) 606–615, https://doi.org/10.1016/j.jcis.2019.08.104.
[43] X. Cai, J. He, L. Chen, K. Chen, Y. Li, K. Zhang, Z. Jin, J. Liu, C. Wang, X. Wang, L. Kong, J. Liu, A 2D-g-C3N4 nanosheet as an eco-friendly adsorbent for various environmental pollutants in water, Chemosphere 171 (2017) 192–201, https://doi.org/10.1016/j.chemosphere.2016.12.073.
[44] T. Wang, L. Zheng, Y. Liu, W. Tang, T. Fang, B. Xing, A novel ternary magnetic Fe3O4/g-C3N4/carbon layer composite for efficient removal of Cr (VI): a combined approach using both batch experiments and theoretical calculation, Sci. Total Environ. 730 (2020), https://doi.org/10.1016/j.scitotenv.2020.138928, 138928.

[45] J. Su, H. Hao, X. Lv, X. Jin, Q. Yang, Properties and mechanism of hexavalent chromium removal by FeS@ graphite carbon nitride nanocomposites, Colloids Surf. A Physicochem. Eng. Asp. 597 (2020), https://doi.org/10.1016/j.colsurfa.2020.124751, 124751.
[46] R. Kumar, M.A. Barakat, F.A. Alseroury, Oxidized g-C3N4/polyaniline nanofiber composite for the selective removal of hexavalent chromium, Sci. Rep. 7 (2017) 12850, https://doi.org/10.1038/s41598-017-12850-1.
[47] P. Qiu, C. Xu, H. Chen, F. Jiang, X. Wang, R. Lu, X. Zhang, One step synthesis of oxygen doped porous graphitic carbon nitride with remarkable improvement of photo-oxidation activity: role of oxygen on visible light photocatalytic activity, Appl. Catal. B Environ. 206 (2017) 319–327, https://doi.org/10.1016/j.apcatb.2017.01.058.
[48] M. Wang, R. Fu, C. Jin, Z. Li, J. Sun, P. Yu, M. You, The facile fabrication of g-C3N4 ultrathin nanosheets with higher specific surface areas for highly sensitive detection of trace cadmium, Measurement 140 (2019) 548–556, https://doi.org/10.1016/j.measurement.2019.03.067.
[49] Y.-G. Zhao, H.-Y. Shen, S.-D. Pan, M.-Q. Hu, Q.-H. Xia, Preparation and characterization of amino-functionalized nano-Fe3O4 magnetic polymer adsorbents for removal of chromium(VI) ions, J. Mater. Sci. 45 (2010) 5291–5301, https://doi.org/10.1007/s10853-010-4574-5.
[50] S. Shi, J. Yang, S. Liang, M. Li, Q. Gan, K. Xiao, J. Hu, Enhanced Cr(VI) removal from acidic solutions using biochar modified by Fe(3)O(4)@SiO(2)-NH(2) particles, Sci. Total Environ. 628–629 (2018) 499–508, https://doi.org/10.1016/j.scitotenv.2018.02.091.
[51] V. Srivastava, Y.C. Sharma, Synthesis and characterization of Fe3O4@n-SiO2 nanoparticles from an Agrowaste material and its application for the removal of Cr(VI) from aqueous solutions, Water Air Soil Pollut. 225 (2013) 1776, https://doi.org/10.1007/s11270-013-1776-x.
[52] M. Liu, T. Wen, X. Wu, C. Chen, J. Hu, J. Li, X. Wang, Synthesis of porous Fe 3 O 4 hollow microspheres/graphene oxide composite for Cr (VI) removal, Dalton Trans. 42 (2013) 14710–14717.
[53] J.-G. Kim, H.-B. Kim, J.-H. Choi, K. Baek, Bifunctional iron-modified graphitic carbon nitride (g-C3N4) for simultaneous oxidation and adsorption of arsenic, Environ. Res. 188 (2020), https://doi.org/10.1016/j.envres.2020.109832, 109832.
[54] J.-G. Kim, H.-B. Kim, G.-S. Yoon, S.-H. Kim, S.-J. Min, D.C.W. Tsang, K. Baek, Simultaneous oxidation and adsorption of arsenic by one-step fabrication of alum sludge and graphitic carbon nitride (g-C3N4), J. Hazard. Mater. 383 (2020), https://doi.org/10.1016/j.jhazmat.2019.121138, 121138.
[55] H.N. Tran, S.-J. You, A. Hosseini-Bandegharaei, H.-P. Chao, Mistakes and inconsistencies regarding adsorption of contaminants from aqueous solutions: a critical review, Water Res. 120 (2017) 88–116, https://doi.org/10.1016/j.watres.2017.04.014.
[56] A. Khadir, M. Motamedi, E. Pakzad, M. Sillanpää, S. Mahajan, The prospective utilization of Luffa fibres as a lignocellulosic bio-material for environmental remediation of aqueous media: a review, J. Environ. Chem. Eng. (2020), https://doi.org/10.1016/j.jece.2020.104691, 104691.
[57] A.G.B. Pereira, F.H.A. Rodrigues, A.T. Paulino, A.F. Martins, A.R. Fajardo, Recent advances on composite hydrogels designed for the remediation of dye-contaminated water and wastewater: a review, J. Clean. Prod. (2020), https://doi.org/10.1016/j.jclepro.2020.124703, 124703.
[58] B. Ren, Y. Xu, L. Zhang, Z. Liu, Carbon-doped graphitic carbon nitride as environment-benign adsorbent for methylene blue adsorption: kinetics, isotherm and thermodynamics study, J. Taiwan Inst. Chem. Eng. 88 (2018) 114–120, https://doi.org/10.1016/j.jtice.2018.03.041.
[59] M. Chegeni, N. Dehghan, Preparation of phosphorus doped graphitic carbon nitride using a simple method and its application for removing methylene blue, Phys. Chem. Res. 8 (2020) 31–44, https://doi.org/10.22036/pcr.2019.198012.1661.
[60] Q. Gan, W. Shi, Y. Xing, Y. Hou, A Polyoxoniobate/g-C3N4 nanoporous material with high adsorption capacity of methylene blue from aqueous solution, Front. Chem. 6 (2018) 7, https://doi.org/10.3389/fchem.2018.00007.
[61] X. Guo, L. Rao, P. Wang, L. Zhang, Y. Wang, Synthesis of porous boron-doped carbon nitride: adsorption capacity and photo-regeneration properties, Int. J. Environ. Res. Public Health 16 (2019) 581, https://doi.org/10.3390/ijerph16040581.
[62] S.K. Sahoo, S. Padhiari, S.K. Biswal, B.B. Panda, G. Hota, Fe3O4 nanoparticles functionalized GO/g-C3N4 nanocomposite: An efficient magnetic nanoadsorbent for adsorptive removal of organic pollutants, Mater. Chem. Phys. 244 (2020), https://doi.org/10.1016/j.matchemphys.2020.122710, 122710.

[63] T. Bhowmik, M.K. Kundu, S. Barman, Ultra small gold nanoparticles–graphitic carbon nitride composite: an efficient catalyst for ultrafast reduction of 4-nitrophenol and removal of organic dyes from water, RSC Adv. 5 (2015) 38760–38773, https://doi.org/10.1039/C5RA04913J.
[64] J. Shi, T. Chen, C. Guo, Z. Liu, S. Feng, Y. Li, J. Hu, The bifunctional composites of AC restrain the stack of g-C3N4 with the excellent adsorption-photocatalytic performance for the removal of RhB, Colloids Surf. A Physicochem. Eng. Asp. 580 (2019), https://doi.org/10.1016/j.colsurfa.2019.123701, 123701.
[65] A.R. Abdellah, H.N. Abdelhamid, A.-B.A.A.M. El-Adasy, A.A. Atalla, K.I. Aly, One-pot synthesis of hierarchical porous covalent organic frameworks and two-dimensional nanomaterials for selective removal of anionic dyes, J. Environ. Chem. Eng. 8 (2020), https://doi.org/10.1016/j.jece.2020.104054, 104054.
[66] J.T. Martins, C.H. Guimarães, P.M. Silva, R.L. Oliveira, P. Prediger, Enhanced removal of basic dye using carbon nitride/graphene oxide nanocomposites as adsorbents: high performance, recycling, and mechanism, Environ. Sci. Pollut. Res. (2020), https://doi.org/10.1007/s11356-020-10779-z.
[67] R. Han, J. Zhang, P. Han, Y. Wang, Z. Zhao, M. Tang, Study of equilibrium, kinetic and thermodynamic parameters about methylene blue adsorption onto natural zeolite, Chem. Eng. J. 145 (2009) 496–504, https://doi.org/10.1016/j.cej.2008.05.003.
[68] V.V.B. Rao, S.R.M. Rao, Adsorption studies on treatment of textile dyeing industrial effluent by flyash, Chem. Eng. J. 116 (2006) 77–84.
[69] H.-J. Cui, H.-Z. Huang, B. Yuan, M.-L. Fu, Decolorization of RhB dye by manganese oxides: effect of crystal type and solution pH, Geochem. Trans. 16 (2015) 10, https://doi.org/10.1186/s12932-015-0024-2.
[70] L. You, K. Xu, G. Ding, X. Shi, J. Li, S. Wang, J. Wang, Facile synthesis of Fe3O4@COF covalent organic frameworks for the adsorption of bisphenols from aqueous solution, J. Mol. Liq. 320 (2020), https://doi.org/10.1016/j.molliq.2020.114456, 114456.
[71] M. Kumar, R. Tamilarasan, V. Sivakumar, Adsorption of Victoria blue by carbon/Ba/alginate beads: kinetics, thermodynamics and isotherm studies, Carbohydr. Polym. 98 (2013) 505–513, https://doi.org/10.1016/j.carbpol.2013.05.078.
[72] T.N.V. de Souza, S.M.L. de Carvalho, M.G.A. Vieira, M.G.C. da Silva, D.D.S.B. Brasil, Adsorption of basic dyes onto activated carbon: experimental and theoretical investigation of chemical reactivity of basic dyes using DFT-based descriptors, Appl. Surf. Sci. 448 (2018) 662–670, https://doi.org/10.1016/j.apsusc.2018.04.087.
[73] T.S. Anirudhan, P.L. Divya, J. Nima, S. Sandeep, Synthesis and evaluation of Iron-doped titania/silane based hydrogel for the adsorptional photocatalytic degradation of Victoria blue under visible light, J. Colloid Interface Sci. 434 (2014) 48–58, https://doi.org/10.1016/j.jcis.2014.07.030.
[74] N. Kataria, V.K. Garg, M. Jain, K. Kadirvelu, Preparation, characterization and potential use of flower shaped zinc oxide nanoparticles (ZON) for the adsorption of Victoria blue B dye from aqueous solution, Adv. Powder Technol. 27 (2016) 1180–1188, https://doi.org/10.1016/j.apt.2016.04.001.
[75] T. Souza, M. Vieira, M. Silva, D. Brasil, S. Carvalho, H3PO4-activated carbons produced from açai stones and Brazil nut shells: removal of basic blue 26 dye from aqueous solutions by adsorption, Environ. Sci. Pollut. Res. 26 (2019), https://doi.org/10.1007/s11356-019-04215-0.

CHAPTER 7

Carbon nitride photocatalysts for water treatment and purification

Mehdi Al Kausor[a] and Dhruba Chakrabortty[b]
[a]Department of Chemistry, Science College, Kokrajhar, Assam, India
[b]Department of Chemistry, B.N. College, Dhubri, Assam, India

Contents

1. Introduction

A wide variety of organic pollutants are introduced into the freshwater system from various sources, such as industrial effluents, agricultural runoff, and chemical spills [1,2]. Their toxicity, stability to natural decomposition, and persistence in the environment have been the cause of much concern to societies and regulatory authorities around the world [3]. In particular, dye-containing effluents from textile industries and chemical manufacturing containing, methylene blue (MB), methyl orange (MO), rhodamine B (RhB), congo red (CR), acid orange 7 (AO7), etc., are becoming serious environmental problem because of their toxicity, unacceptable color, high chemical oxygen demand, and resistance to chemical, photochemical, and biological degradation [4]. Most of the

Nanostructured Carbon Nitrides for Sustainable Energy and Environmental Applications
https://doi.org/10.1016/B978-0-12-823961-2.00010-0

dyes are carcinogenic, mutagenic, and toxic to aquatic life as well as human health. Dyes may cause allergic problems, such as contact dermatitis, respiratory disease, irritation in eyes and respiratory tract, and may even cause cancer in kidney, urinary bladder, and liver. The highly toxic dyes may decrease the light penetration power through water, thereby decreasing the quality and transparency of water, as well as affect the photosynthetic activity of aquatic plants, which in turn may lead to oxygen deficiency in aquatic ecosystem. The treatment of such organic dyes in micropolluted water has always been paid attention by many researchers. Phenolic compounds are also a serious category of aqueous pollutants, which causes severe environmental problems [5]. Nitrophenols, chlorophenols, aminophenols, chlorocatechols, methylphenols, and other phenolic compounds have all been characterized as exerting toxic influence on humans [6]. Phenol is a kind of refractory organic compound, having carcinogeneic, teratogeneic, and mutagenic impact upon prolonged exposure [7]. Phenol and phenolic compounds, such as 2-Chlorophenol (2-CP), 4-chlorophenol (4-CP), 2,4,6-trichlorophenol (TCP), 2-nitrophenol (2-NP), 4-nitrophenol (4-NP), etc., are being released from different industrial activities, such as refineries, pesticides, insecticides, pharmaceutical, pulp and paper industries, etc. and are found along with other organic pollutants in water [8]. These compounds tend to persist in the environment over a long period of time, accumulate and exert toxic effects on humans and animals [9].

The traditional purification techniques have not been suitable to meet the existing water quality standards. The treatment of environmental pollutants in wastewater by using active semiconductor photocatalysts has recently attracted considerable attention due to its ability to completely degrade organic contaminants to carbon dioxide, water, and mineral acids [10–14]. Photocatalysis, based on semiconductor, is the most promising technology due to its potential applications in many aspects, mainly in degradation of organic pollutants [15,16]. The synthesis and application of semiconductor photocatalyst in environmental and energy applications has been a challenging area of research. There are numerous semiconductor materials, including TiO_2 [17], CuO [18], WO_3 [19], Ag_2O [20], ZnO [21], Bi_2WO_6 [22], FeO_3 [23], MoO_3 [24], Ag_2CO_3 [25], SnO_2 [26], CdS [27], CoO [28], Bi_2O_3 [29], Ag_3VO_4 [30], Ag_3PO_4 [31] among others. However, from the viewpoint of practical applications, there are some major challenges with these semiconductors, such as poor visible-light absorption, large band gap energy, and quick recombination of electron–hole pair, thereby limiting their photocatalytic activities. Therefore, the design and development of semiconductor nanocomposite materials has become an active area of research during recent years. In this context, various research groups are utilizing graphitic carbon nitride (g-C_3N_4) as a new type of metal-free polymeric-layered n-type semiconductor. The unique electronic, optical, structural, and physiochemical properties of g-C_3N_4, such as moderate band gap ($\sim$2.7 eV), appropriate electronic band structure, absorption of visible light, nontoxicity, low cost, and good stability [32,33] make g-C_3N_4 extremely promising in environmental and energy applications [34,35]. The tuneable band gaps and efficient intercalation of various compounds find profound use of this novel material in heterogeneous catalysis and support. The material can be readily utilized to fabricate some hybrid photocatalysts with controllable size and pore structures, size distributions, and morphologies [36]. Since the revolutionary photocatalytic water splitting studies by Wang and his research group [37], g-C_3N_4 has become a promising photocatalytic material. The number of citations per year for the Wang's ground-breaking paper published on "Nature Materials" in 2009 is significantly increasing day by day (Fig. 7.1). In 2021 itself, this article has already been cited over 351 times. This gives a clear indication that g-C_3N_4-based nanostructures are becoming promising material for various energy and environmental applications.

In this chapter, we discuss the research progress of semiconductor nanocomposite materials based on g-C_3N_4 in a chronological order. The fabrication process, characterization, and photocatalytic applications of g-C_3N_4-based materials in water treatment and purification from the purview of degradation of organic pollutants are discussed. In addition to this, we highlight the underlying mechanism, challenges, and scopes for further research on the photcatalytic activity of this material for widespread industrial applications.

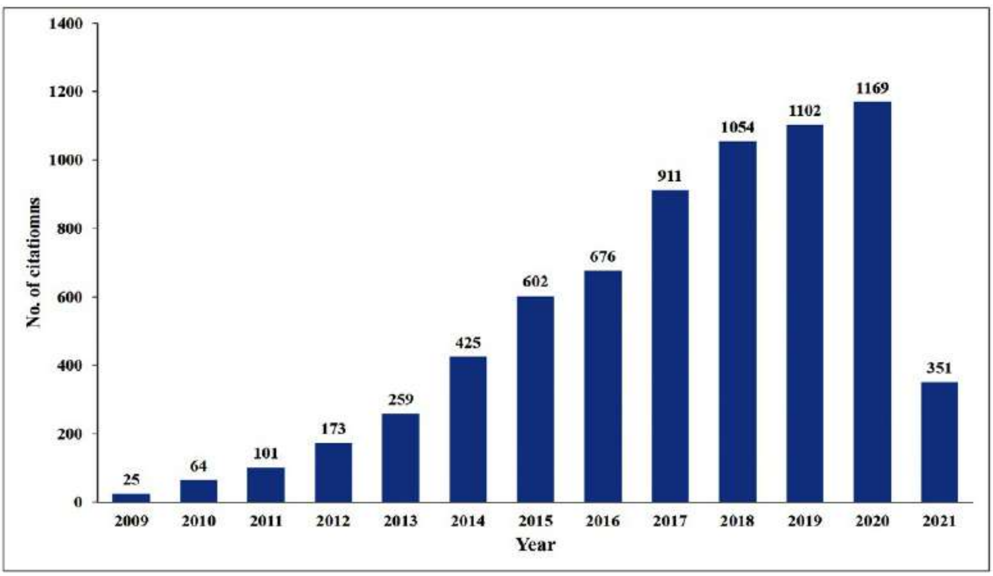

Fig. 7.1 The number of citations per year for Wang's pioneer work published in Nature Materials in 2009. (Using CrossRef, on 22nd February 2021). *(No permission required.)*

1.1 Structure and properties of g-C_3N_4

The electronic structures of pure monolayer g-C_3N_4 is shown in Fig. 7.2A. The monolayer structure of g-C_3N_4 is composed of a unit cell of bulk g-C_3N_4 along the (001) plane. The model structure contains 24C-atoms and 32 N-atoms. There exists a vacuum space of 15 Å in the z direction. The in-plane lattice constant of the g-C_3N_4 model is found to be 7.15 Å [38]. The previous computational data and experimental result revealed by X-ray diffraction pattern reveal similar observations [39,40]. From the symmetry of the tri-s-triazine structure of g-C_3N_4, it is found that there are three nonequivalent N-atoms and two nonequivalent C-atoms labeled as N1, N2, N3, C1, and C2, respectively [41]. The bond lengths of N1–C1, C1–N2, N2–C2, and C2–N3 are found to be 1.39, 1.33, 1.34, and 1.47 Å, respectively. Similar observations from DFT calculations were also obtained in previous studies [42]. The calculated band structure and corresponding density of states (DOS) of monolayer g-C_3N_4 are shown in Fig. 7.2B. The points G, F, Q, and Z represents highly symmetric points in the reciprocal space lattice while the short dashed line set at zero is assumed as the Fermi level. The material can be considered as an indirect band gap semiconductor having a band gap energy of 1.18 eV [38].

1.2 g-C_3N_4 as photocatalyst and its limitations

When visible light having higher energy (hυ) than the band gap energy (E_g) falls on the visible band (VB) of g-C_3N_4, the electrons get excited (e^-) to the conduction band (CB), leaving behind some positively charged holes (h^+), as shown in the Fig. 7.3. Eventually, the VB acquires positive charge and acts as an oxidizing center, while the CB acquires negative charge and acts as a reducing center [43]. The holes oxidize the OH^- ions to

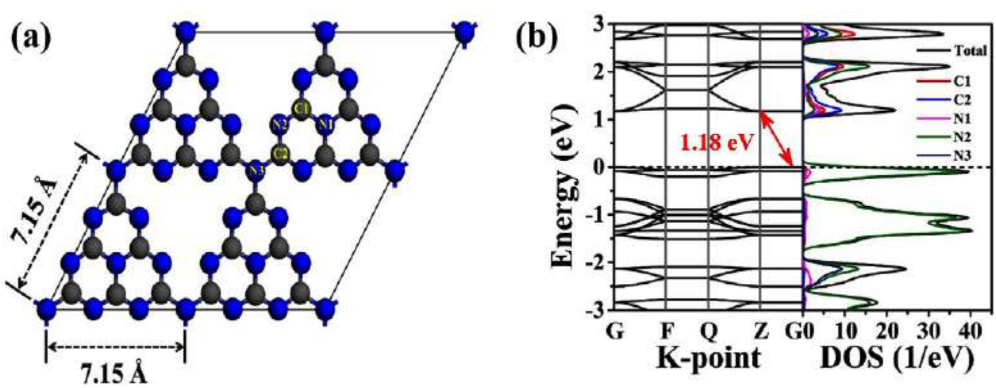

Fig. 7.2 (A) Monolayer g-C_3N_4 (B) Band structure and corresponding DOS of monolayer g-C_3N_4. *(From B. Zhu, J. Zhang, C. Jiang, B. Cheng, J. Yu, First principle investigation of halogen-doped monolayer g-C3N4 photocatalyst, Appl. Catal. Environ. 207 (2017) 27–34. https://doi.org/10.1016/j.apcatb.2017.02.020.)*

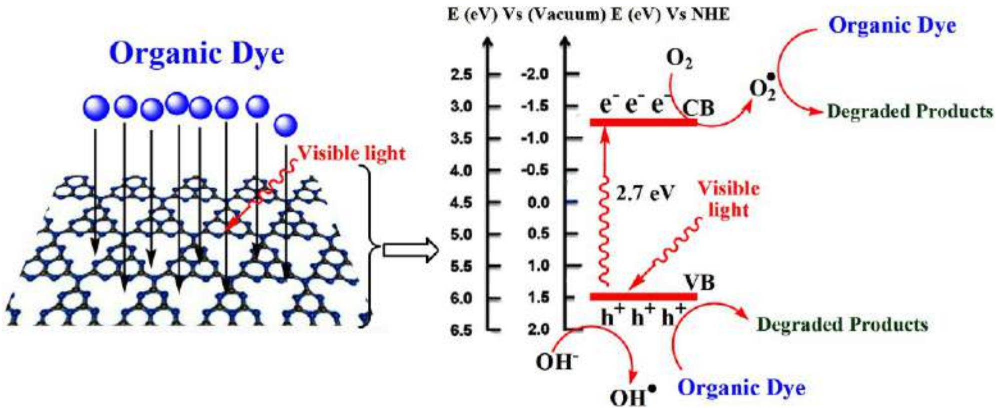

Fig. 7.3 Mechanism of organic dye degradation by g-C_3N_4 under visible light *(No permission required.)*

OH• radicals and simultaneously the organic dyes adsorbed on g-C_3N_4 sheets are degraded to CO_2 and H_2O. There is a probability that the O_2 from the solution in presence of the excited electrons undergo reduction to $O_2•^-$ radicals, which may further degrade the organic dyes into various byproducts. The OH• and $O_2•^-$ radicals also takes part in the degradation of the organic dyes into CO_2, H_2O, and inorganic ions. The process of capturing the electrons from the CB by O_2 to yield $O_2•^-$ radical is a very important step as it can suppress electron–hole (e^-–h^+) pair recombination [33]. However, the mechanism of the photocatalysis reveals every possibility that the photo-generated electrons (e^-) and holes (h^+) may recombine in the bulk of the photocatalyst and consequently diminish the photocatalytic activity of the material.

1.3 Synthesis of pristine g-C_3N_4

The graphitic carbon nitride is a polymeric-layered semiconductor material containing carbon and nitrogen. There are several methods of synthesizing g-C_3N_4 viz. thermal polycondensation [44], thermal exfoliation [45], thermal polymerization [46], solvothermal [28], chemical vapor deposition (CVD) [47], plasma sputtering reaction deposition [48], and sonochemical [49] methods. However, the choice of precursor and the mode of synthesis play an important role that affects the electronic band structures and morphology of the material. Some commonly used precursors include compounds containing prebonded C═N or C≡N core structure like cyanamide, dicyandiamide, trithiocyanuric acid, melamine, triazine, and heptazine derivatives, which are basically nitrogen-rich compounds [50–52].

A facile, economic, environmentally friendly, and large-scale method of synthesis of g-C_3N_4 was reported for the first time by Dong and his research group [53]. Their method involves direct heating of thiourea up to 550°C for 2 h. The research group used thiourea as the precursor, which is both inexpensive and commonly available, and thus can be used as a substitute of the other widely used toxic or unstable precursors. The as-prepared g-C_3N_4 using thiourea exhibits better photocatalytic activity under visible light for degradation of organic pollutant when compared with g-C_3N_4 prepared from dicyandiamide which is found to be toxic. In 2013, Dong and coworkers [54] also reported the synthesis of g-C_3N_4 by direct pyrolysis of cheap urea up to 550°C and observed the effect of pyrolysis time. In the typical synthesis, urea powder was taken in a silica crucible with a cover and then heated to 550°C in a muffle furnace for a certain time at a heating rate of 15°C per min. The resultant powder was collected and directly used without further treatment. The research group suggested that the surface areas of the photocatalyst can be increased remarkably by simply prolonging the pyrolysis time to 240 min under the temperature of 550°C. The g-C_3N_4 prepared from thiourea exhibits slightly smaller band gap energy compared with the g-C_3N_4 prepared from urea but it possesses much higher surface area than that prepared from melamine [55]. Fig. 7.4 presents a brief summarization about the synthetic processes of g-C_3N_4 by thermal polymerization of different precursors [56]. Thus, the easiest way to synthesize g-C_3N_4 is just to select an appropriate precursor and adopt a suitable method. However, the stress should be given on environmental, economical, and industrial aspects.

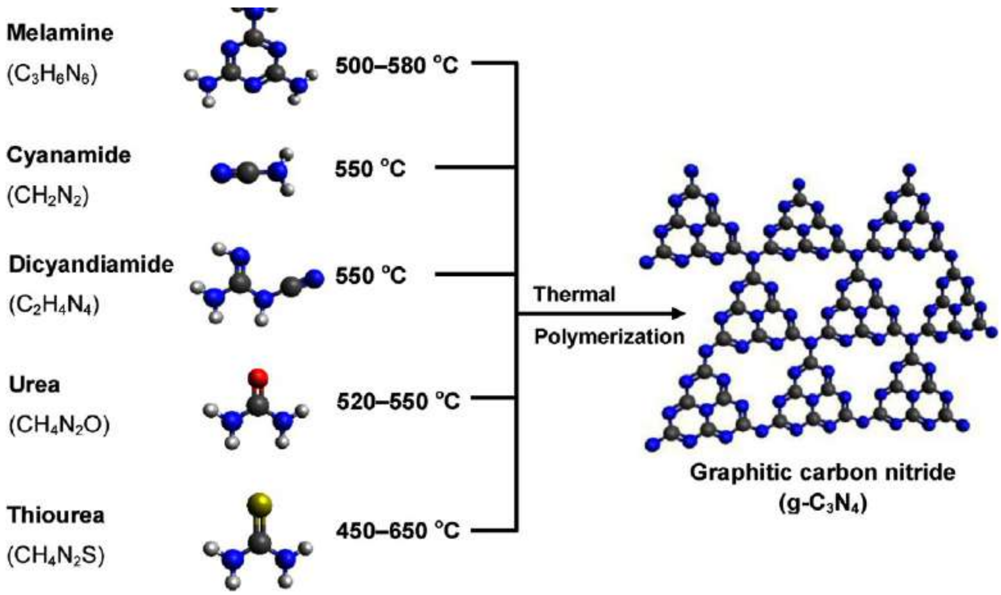

Fig. 7.4 Schematic illustration of the synthesis process from the possible precursors of g-C_3N_4. *(From W.J. Ong, L.L. Tan, Y.H. Ng, S.T. Yong, S.P. Chai, Graphitic carbon nitride (g-C_3N_4)-based photocatalysts for artificial photosynthesis and environmental remediation: are we a step closer to achieving sustainability? Chem. Rev. 116 (12) (2016) 7159–7329. https://doi.org/10.1021/acs.chemrev.6b00075.)*

2. Spectroscopic methods for characterization of g-C_3N_4 and g-C_3N_4-based materials

The g-C_3N_4 and g-C_3N_4-based materials are generally characterized by powder X-ray diffraction (XRD), X-ray photoelectron spectroscopy (XPS), scanning electron microscopy (SEM), transmission electron microscopy (TEM), Fourier transform infrared spectroscopy (FTIR), Raman spectroscopy, UV–vis diffuse reflectance spectroscopy (DRS), photoluminescenece (PL) spectroscopy, surface area and porosimetry analysis, and zeta potential measurement. The characterization by some of these methods is discussed as follows.

2.1 Powder X-ray diffraction studies

Analysis of g-C_3N_4 and g-C_3N_4-based heterostructure nanocomposites by powder XRD is an important technique in predicting the crystal structures and the dimensions of the spacing in the crystal structure. The powder XRD patterns can be taken using Cu K_α radiation ($\lambda = 0.15406$ nm) at 40 kV and 40 mA with 2θ ranging from 10° to 80° with various step size in a XRD instrument. A typical experimental XRD pattern (Fig. 7.5) of tubular g-C_3N_4 [57] exhibit a distinct peak at 17.4° (line a), which corresponds to an interplanar distance (d) of 0.49 nm. It indicates the formation of s-triazine units ($d = 0.47$ nm) [58] in g-C_3N_4. However, the bulky g-C_3N_4 powders display (Fig. 7.5) two distinct diffraction peaks obtained at $2\theta = 27.40°$ and 13.0° (line b), due to (002) and (100) diffraction planes of graphitic materials (JCPDS 87–1526) [37]. The XRD

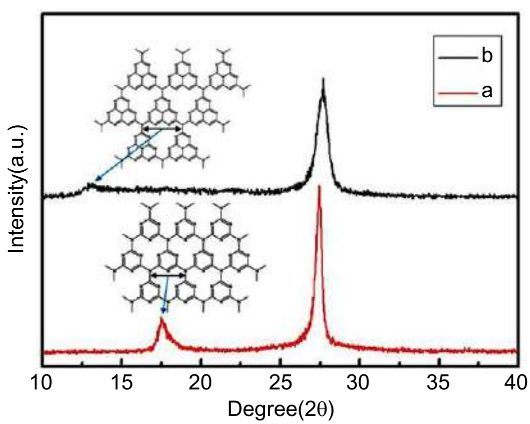

Fig. 7.5 Powder XRD patterns of (A) the tubular carbon nitride and (B) the bulky g-C_3N_4 synthesized by directly heating melamine at 520○C for 2 h. *(From B. Zhu, P. Xia, W. Ho, J. Yu, Isoelectric point and adsorption activity of porous g-C_3N_4, Appl. Surf. Sci. 344 (2015) 188–195. https://doi.org/10.1016/j.apsusc.2015.03.086.)*

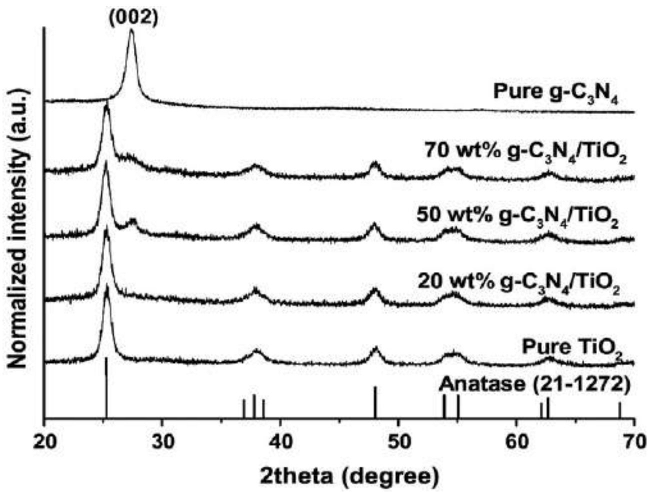

Fig. 7.6 XRD patterns of pure TiO_2, pure $g\text{-}C_3N_4$ and $g\text{-}C_3N_4/TiO_2$ composites. *(From N. Boonprakob, N. Wetchakun, S. Phanichphant, D. Waxler, P. Sherrell, A. Nattestad, J. Chen, B. Inceesungvorn, Enhanced visible-light photocatalytic activity of g-C3N4/TiO2 films, J. Colloid Interface Sci. 417. (2014) 402–409 https://doi.org/10.1016/j.jcis.2013.11.072.)*

pattern results reveal that the $g\text{-}C_3N_4$ exhibits flake-like structure with interplanar stacking distance of 0.325 nm revealed by (002) diffraction plane, which is similar to that of graphite with stacking distance of 0.34 nm [59]. The XRD patterns in Fig. 7.6 shows that the diffraction peak of pure $g\text{-}C_3N_4$ at 2θ of 27.4° is observed when the $g\text{-}C_3N_4$ content is higher than 50 wt% with a relative lower peak intensity which gradually improves on increasing the $g\text{-}C_3N_4$ content [60].

2.2 FESEM and TEM analysis

The morphology can be studied by field emission scanning electron microscopy (FE-SEM) and high-resolution transmission electron microscopy (TEM). FE-SEM is a type of electron microscope that generates the image by scanning the sample surface with a high energy electron beam focused onto the sample surface. TEM is a microscopic technique in which a focused beam of electron is transmitted through an ultrathin specimen. TEM provides most powerful magnification, potentially over a million times or more. This microscopic technique is able to provide information about the surface features, shape, size, and structure. TEM also provides information about the topography, morphology, composition and crystalinity of a material. Chen and his research group [61] reported the fabrication of a series of *Z*-scheme Ag_2CO_3/ $g\text{-}C_3N_4$ with different molar ratios of Ag/$g\text{-}C_3N_4$(0%, 1%, 2%, 3%, 4%, 5%, 6%,

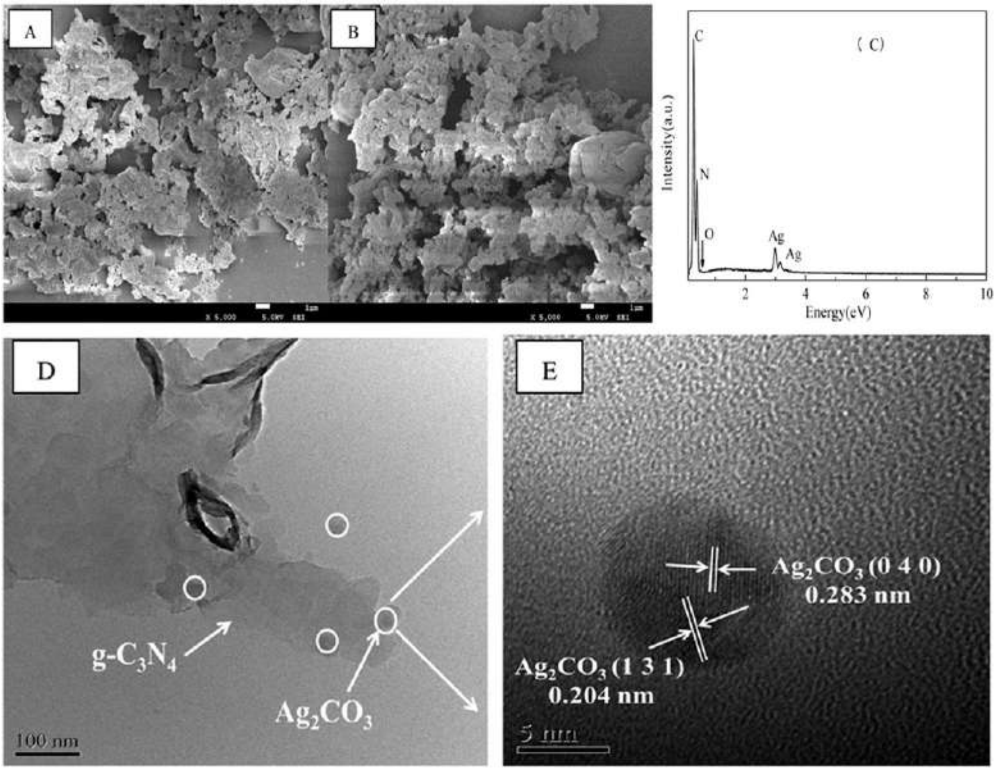

Fig. 7.7 SEM images of (A) bare g-C_3N_4 (B) 7% Ag_2CO_3/g-C_3N_4 (C) EDS pattern (D) TEM image and (E) HRTEM of 7% Ag_2CO_3/g-C_3N_4. *(From J. Chen, J. Zhong, J. Li, S. Huang, W. Hu, M. Li, Q. Du, Synthesis and characterization of novel Ag2CO3/g-C3N4 composite photocatalysts with excellent solar photocatalytic activity and mechanism insight, Mol. Catal. 435 (2017) 91–98, https://doi.org/10.1016/j.mcat.2017.03.026.)*

7%, 8%, and 9%). The morphology and microstructure of the samples thus synthesized were studied by SEM and TEM (Fig. 7.7) of g-C_3N_4 and the 7% Ag_2CO_3/g-C_3N_4 composite. In the SEM images, it was observed that both the 0% and 7% sample exhibit irregular lump and cotton-like shapes of g-C_3N_4. The results of energy dispersive X-ray (EDX) analysis demonstrated the presence of C, N, Ag, and O elements on the surface of 7% Ag_2CO_3/g-C_3N_4 composite. TEM image demonstrated that Ag_2CO_3 particles were deposited on the surface of g-C_3N_4. In the HRTEM image, lattice fringes of 0.238 and 0.204 nm corresponding to the (040) and (131) plane of the monoclinic Ag_2CO_3, respectively, were observed, which is in accordance with the JSPDS card (26–0339) [62]. The results of EDX and HRTEM confirmed the presence of Ag_2CO_3 and g-C_3N_4 in the composite.

2.3 X-ray photoelectron spectroscopy (XPS)

Photoelectron spectroscopy (PES) is an outstanding technique for the analysis of atomic and molecular energy levels. There are two types of PES, the X-ray PES (XPS), and UV–vis PES (UPES). g-C_3N_4 and g-C_3N_4-based materials are generally characterized by XPS. Fig. 7.8A displays a survey scan XPS spectrum of heterojunction photocatalyst Co_3O_4–g-C_3N_4 [63]. The research group had taken the XPS spectrum to determine the chemical states of the 0.2 wt% Co_3O_4–g-C_3N_4 and the valence states of various species present therein. The Fig. 7.8B displays the high-resolution deconvulated XPS spectra of C(1 s) with two peaks corresponding to 284.6 eV and 288.6 eV [64]. The key peak at 288.6 eV is attributed to C—C bonding in a pure carbon environment of g-C_3N_4, while the other peak at 288.6 eV is attributed to C-atoms bonded with three neighboring N-atom in its chemical backbone [65]. The XPS data gave an evidence for the existence of graphite-like sp^2-bonded structure in g-C_3N_4. The peak at 398.55 eV in the XPS spectrum of N(1 s) (Fig. 7.8C) corresponds to N-atoms [65]. The two peaks observed at 796.1 eV and 780.9 eV in the XPS spectrum of Co(2p) of the composite (Fig. 7.8D) corresponds to the Co($2p_{1/}2$) and Co($2p_{3/2}$) spin states. The presence of Co_3O_4 can be confirmed further by the O(1 s) XPS peak at 531.85 eV (Fig. 7.8), which corresponds to the O-atom lattice in the Co_3O_4. These results confirm the presence of Co_3O_4 in the g-C_3N_4 composite.

2.4 Infrared (IR) and Raman spectroscopy

IR spectroscopy is often used to identify structures because certain functional group gives rise to characteristic bands both in terms of intensity and position (frequency) regardless of the structure of the rest of the molecule. The chemical composition and information about the bonding of g-C_3N_4 can be identified by FTIR. Fig. 7.9 depicts a typical FTIR spectrum of g-C_3N_4 synthesized by heating melamine (MCN), thiourea (TCN), and urea (UCN) [55]. The characteristic peaks observed in the region around 900–1700 cm^{-1} were usually assigned to the stretching vibrations of aromatic heptazine-derived repeating units, including the typical sp^2-bonded C═N stretching modes and out-of-plane bending vibrations of the sp^3-bonded C—N stretching [66,67]. The sharp absorption peak centered around 810 cm^{-1} is attributed to the characteristic breathing mode of tri-s-triazine cycles [68]. The absorption peak at around 883 cm^{-1} is attributed to the deformation mode of N—H bond in amino groups [54]. The broad peaks observed between 3000 and 3500 cm^{-1} are attributed to the stretching vibration [54,67] of residual free N—H in the bridging C-NH-C units and O—H originated from physically adsorbed water molecules on the surface of g-C_3N_4.

The presence of some functional groups and C—N— networks can be further identified by Raman spectroscopy. Raman spectroscopy is a chemical analysis technique which can provide information about the chemical structure, phase, crystallinity, and

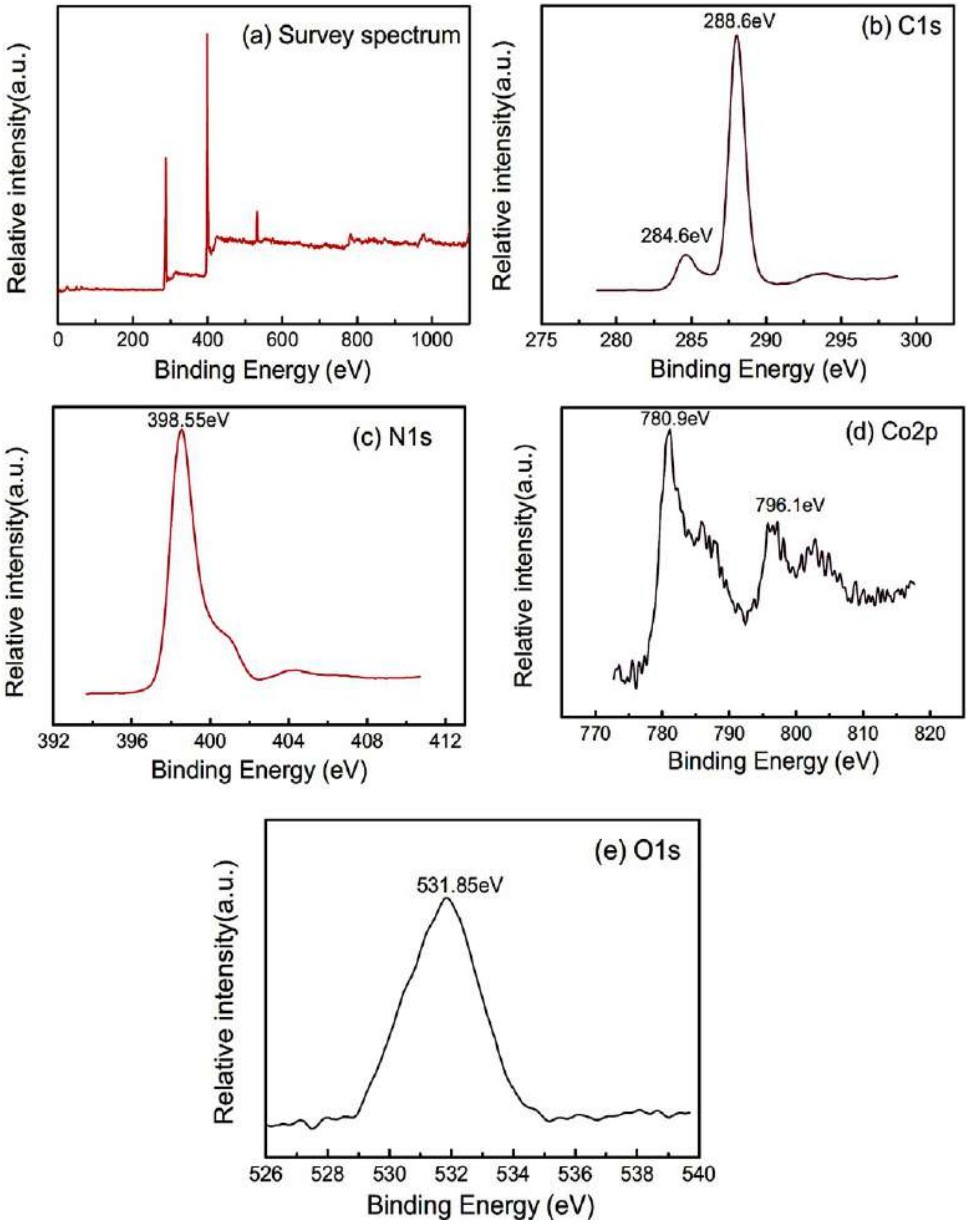

Fig. 7.8 XPS spectrum of the as-prepared 0.2 wt% Co_3O_4–g-C_3N_4 composite photocatalysts: (A) survey spectrum; (B) C(1 s), (C) N(1 s), (D) Co(2p), (E) O(1 s). *(From C. Han, L. Ge, C. Chen, Y. Li, X. Xiao, Y. Zhang, L. Guo, Novel visible light induced Co3O4-g-C3N4 heterojunction photocatalysts for efficient degradation of methyl orange, Appl. Catal. Environ. 147 (2014) 546–553, https://doi.org/10.1016/j.apcatb.2013.09.038.)*

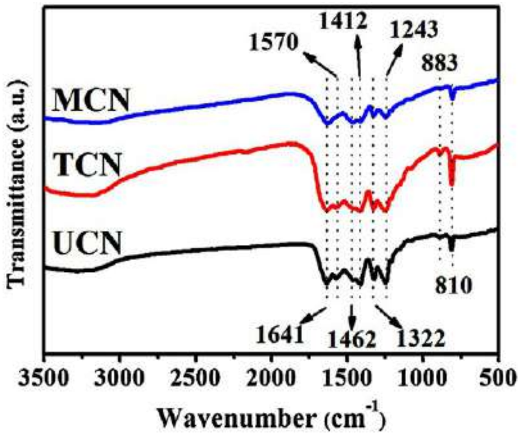

Fig. 7.9 FTIR spectra of g-C_3N_4 powders obtained by heating melamine (MCN), thiourea (TCN), and urea (UCN). *(From B. Zhu, P. Xia, Y. Lia, W. Ho, J. Yu, Fabrication and photocatalytic activity enhanced mechanism of directZ-scheme g-C3N4/Ag2WO4photocatalyst, Appl. Surf. Sci. 391 (2017) 175–183, https://doi.org/10.1016/j.apsusc.2015.08.149.)*

molecular interactions. It is based upon the interaction of light with the chemical bonds of a material. In the Raman spectra (Fig. 7.10), the characteristic peaks of g-C_3N_4 are observed at 1616, 1555, 1481, 1234, 751, 705, 543, and 479 cm^{-1} which confirms the vibration modes of CN heterocycles [70]. It is observed that the peak corresponding to 1234 cm^{-1} is attributed to the N=C (sp^2) bending vibration which exhibits a significant blue shift (1250 cm^{-1} for 1-layer g-C_3N_4), due to the phonon confinement and strong quantum confinement effect [70]. The ratio of peak heights of 751–705 cm^{-1} (I_{751}/I_{705}) and 543–479 cm^{-1} (I_{543}/I_{479}), corresponding to layer–layer deformation vibrations or the correlation vibrations, obviously increased with decreasing the number of layer in g-C_3N_4 [70].

2.5 Diffuse reflectance spectroscopy (DRS) and photoluminescence spectroscopy (PLS)

The DRS is a spectroscopic technique where the diffuse reflection of radiation in the ultraviolet to visible range (190–800 nm) of a sample is measured. This technique is used to characterize samples in solid (thin film) or in liquid form, where there is not much dispersion, and the angle of incidence is exactly equal to the angle of reflection, i.e., the reflection is specular. However, in the case of granular/powder or thin films of high surface roughness, the reflection is not specular and hence the transmitted intensity being too low cannot be measured to get the absorption of the sample. Therefore, for powdered samples or thin films of high surface roughness, the DRS is used. Boonprakob and his team [60] reported the synthesis of g-C_3N_4/TiO_2 composites by directly heating a mixture of melamine and presynthesized TiO_2 nanoparticles in Ar gas flow with varying

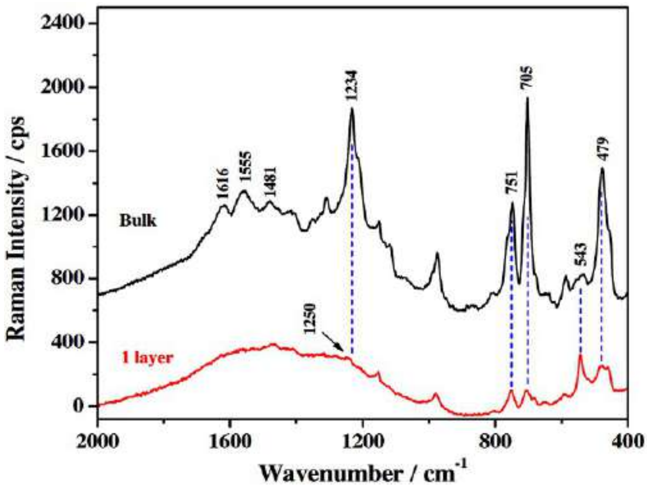

Fig. 7.10 Comparison between the Raman spectra of coplanar bulk and 1-layer g-C_3N_4 samples (780 nm laser) *(From J. Jiang, L. Ou-Yang, L. Zhu, A. Zheng, J. Zou, X. Yi, H. Tang, Dependence of electronic structure of g-C3N4 on the layer number of its nanosheets: a study by Raman spectroscopy coupled with first-principles calculations, Carbon 80(1) (2014) 213–221, https://doi.org/10.1016/j.carbon.2014.08.059.)*

contents of g-C_3N_4/TiO_2. The optical properties were investigated by UV–vis DRS study. As shown in Fig. 7.11, the composites exhibit higher absorbance in the visible region, and 50 wt% g-C_3N_4/TiO_2 composite has the highest absorbance. The corresponding band gap energy was calculated from $(\alpha h\upsilon)^{1/2}$ vs photon energy ($h\upsilon$) plot and are found to be 2.83 and 3.31 eV for g-C_3N_4 and TiO_2, respectively.

PLS is an extensively used technique for predicting the optical and electronic properties of heterogeneous semiconductor catalysts and other substances. A material that emits light is called luminescent material. The PLS (Fig. 7.12) exhibits that the g-C_3N_4/ZnO/AgCl composite has lower recombination probability of the photogenerated charge carriers compared with pure g-C_3N_4 and the binary composites g-C_3N_4/ZnO or g-C_3N_4/AgCl [71]. Thus, the ternary composite g-C_3N_4/ZnO/AgCl exhibited higher photocatalytic activity than the pure g-C_3N_4 and binary composites.

2.6 N_2 sorption studies and BET surface area analysis

The specific surface area of a sample including the pore size distribution of a solid or porous material can be measured by BET (Brunauer, Emmett, and Teller) surface area analysis method. The principle is based on the adsorption of an unreactive gas (e.g., N_2). The solid material under investigation is cooled by using a cryogenic liquid. By keeping the temperature constant, the pressure or concentration of the adsorbing gas is increased. As the relative pressure increases, more molecules are adsorbed on the

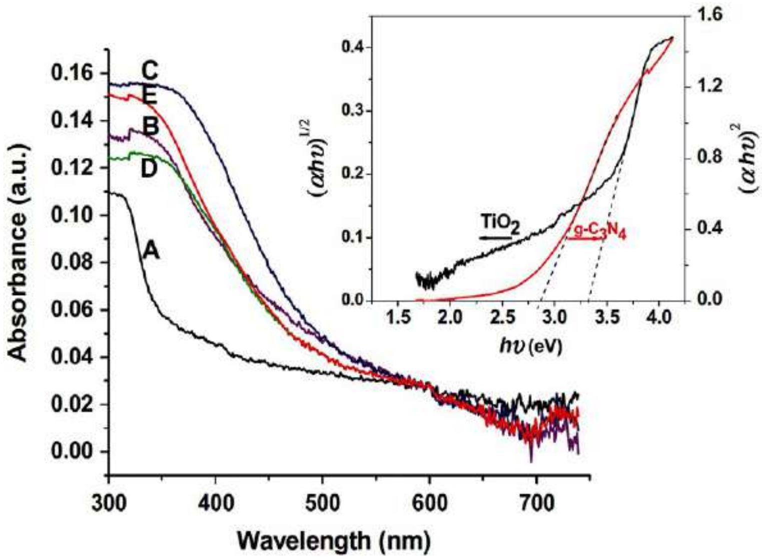

Fig. 7.11 UV–vis DRS of (A) pure TiO_2, (B) 20 wt% g-C_3N_4/TiO_2, (C) 50 wt% g-C_3N_4/TiO_2, (D) 70 wt% g-C_3N_4/TiO_2, and (E) pure g-C_3N_4 films. Inset is (αhυ)1/2 vs photon energy (hυ) plot of pure TiO_2 and g-C_3N_4 films, respectively. *(From N. Boonprakob, N. Wetchakun, S. Phanichphant, D. Waxler, P. Sherrell, A. Nattestad, J. Chen, B. Inceesungvorn, Enhanced visible-light photocatalytic activity of g-C3N4/TiO2 films, J. Colloid Interface Sci. 417 (2014) 402–409, https://doi.org/10.1016/j.jcis.2013.11.072.)*

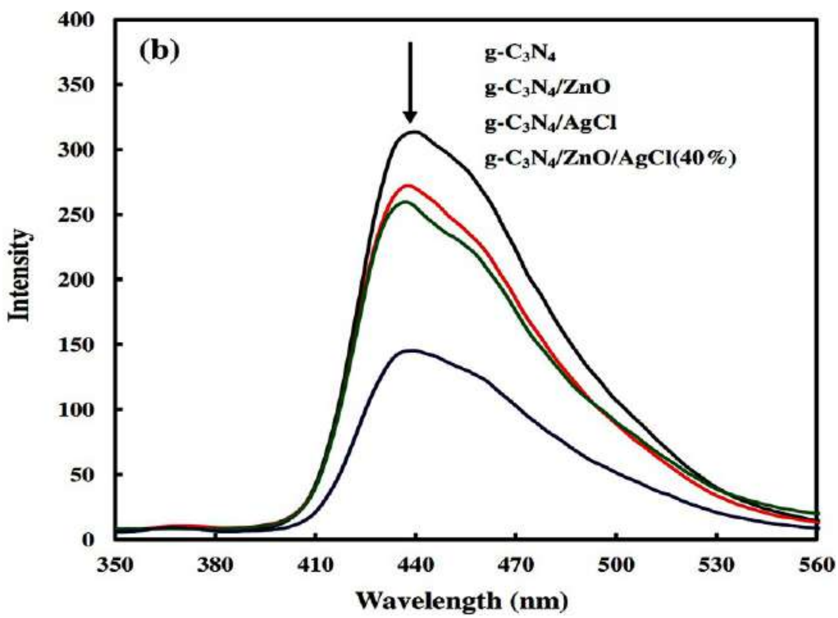

Fig. 7.12 PL spectra for the g-C_3N_4, g-C_3N_4/ZnO, g-C_3N_4/AgCl, and g-C_3N_4/ZnO/AgCl nanocomposite. *(From A. Akhundi, A. Habibi-Yangjeh, Ternary g-C 3N4/ZnO/AgCl nanocomposites: synergistic collaboration on visible-light-driven activity in photodegradation of an organic pollutant, Appl. Surf. Sci. 358 (2015) 261–269, https://doi.org/10.1016/j.apsusc.2015.08.149.)*

surface, resulting in the formation of a thin monolayer that covers the entire surface. By measuring the volume adsorbed, the number of gas molecules in the monolayer is recorded. As the area of cross-section of the adsorbate is known, the area of the accessible surface can be determined. The exact mathematical equation was developed by Brunauer, Emmett, and Teller [72].

$$\frac{1}{X[(P_0/P)-1]} = \frac{1}{X_m C} + \frac{C-1}{X_m C}\left(\frac{P}{P_0}\right)$$

The BET equation firmly describes a linear plot of $1/[X(P_0/P)-1]$ vs P/P_0 which is applicable for most of the solids, using nitrogen as the adsorbate. However, the plot is restricted to a P/P_0 range of 0.05–0.35. This equation describes the relationship between the number of gas molecules adsorbed (X) at a given relative pressure (P/P_0). The surface area can be calculated from the slope, intercept and the cross-sectional area (CSA) according to the following equation.

$$\text{Surface area} = \frac{1}{\text{Slope+ Intercept}} \cdot \text{CSA}$$

The liquid N_2 adsorption–desorption isotherms of g-C_3N_4 and the g-C_3N_4/Ag_2WO_4 composite synthesized by Zhu and coworkers [73] and the corresponding pore size distribution curves are displayed in Fig. 7.13. As per the Brunauer–Deming–Deming–Teller classification, the two isotherms are considered as type IV and they exhibit high adsorption in the high relative pressure (P/P_0) region. The results thus reveal the existence of mesopores and macropores in the composite [74]. The pore size distribution curves shown in the inset of Fig. 7.13 indicate a wide pore size distribution from 2 to 140 nm. The composite has some smaller mesopores with diameters of 2–15 nm due to the fact that some mesopores are sealed with Ag_2WO_4 particles. The BET surface areas

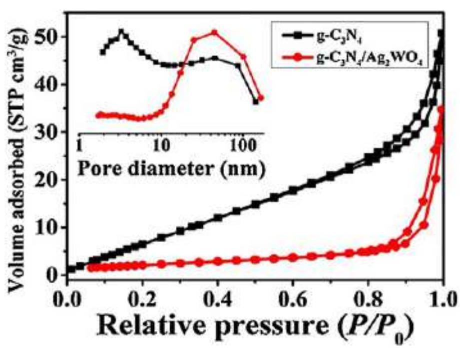

Fig. 7.13 N_2 adsorption–desorption isotherms and corresponding pore size distribution curves (inset) of g-C_3N_4 and the g-C_3N_4/Ag_2WO_4 composite. *(From B. Zhu, P. Xia, Y. Lia, W. Ho, J. Yu, Fabrication and photocatalytic activity enhanced mechanism of directZ-scheme g-C3N4/Ag2WO4photocatalyst, Appl. Surf. Sci. 391 (2017) 175–183, https://doi.org/10.1016/j.apsusc.2015.08.149.)*

Table 7.1 BET surface area and pore parameters of g-C_3N_4 and g-C_3N_4/Ag_2WO_4 [73].

Sample	S_{BET} (m^2/g)	V_{pore} (cm^3/g)	d_{pore} (nm)
g-C_3N_4	37	0.056	6
g-C_3N_4/Ag_2WO_4	8	0.054	27

and pore parameters are listed in Table 7.1. The g-C_3N_4/Ag_2WO_4 composite exhibits lower surface area because of the deposition of Ag_2WO_4 particles, which can block some mesopores and space of g-C_3N_4.

3. Photocatalytic degradation of organic pollutants by g-C_3N_4

Although g-C_3N_4 can be utilized as visible-light photocatalyst, it still has some limitations for practical applications due to small specific surface area ($<10\,m^2/g$) [69] and therefore poor adsorption, low efficiency of visible-light utilization, low electrical conductivity, and faster recombination rate of the photogenerated charge carriers [75].

3.1 Photocatalytic degradation of organic pollutants by doped g-C_3N_4

To address the limitations of g-C_3N_4 in photocatalytic applications, an attractive approach is to dope g-C_3N_4 with other materials. Previous studies established that doping with nonmetals like carbon, sulfur, oxygen, phosphorous, and boron and introduction of some halogen atoms like chlorine and bromine and metals like platinum, gold, palladium are some alternate ways to improve the electrical conductivity and reduce the recombination rate of the electron (e^-)–hole (h^+) pairs and thereby increase the photoactivity of g-C_3N_4. Ge and coworkers [76] reported for the first time about the facile synthesis of g-C_3N_4-doped with novel Ag metal with different weight ratios and discussed the effect of Ag loading on the photocatalytic performance on degradation of methyl orange (MO) under visible light. A significant increase in the absorption intensity is observed with Ag loading in the UV–vis DRS spectra. It is suggested that there may be a charge-transfer transition between the Ag species and the CB or VB of g-C_3N_4 due to which higher photocatalytic activity is observed. The characterization results revealed that the visible-light responses of these Ag/g-C_3N_4 composites are significantly improved by Ag doping, and there exist a separation of photogenerated electron–hole pairs in g-C_3N_4. Thus, the materials exhibit enhanced photocatalytic activities than the pure g-C_3N_4 samples. It was observed that 1.0 wt% Ag-g-C_3N_4 demonstrated the highest photocatalytic activity with a degradation rate of 1.00 (Fig. 7.14) as compared to the undoped g-C_3N_4. Thus, it can be concluded that the photocatalytic activity is dependent on the doping amount of Ag, and it was suggested that the Ag species actually covers the active sites of the g-C_3N_4 surface, which in turn reduces the charge separation.

The idea behind such doping involves the fact that the metals or nonmetals would strongly absorb visible light due to surface plasmon resonance, which will extensively

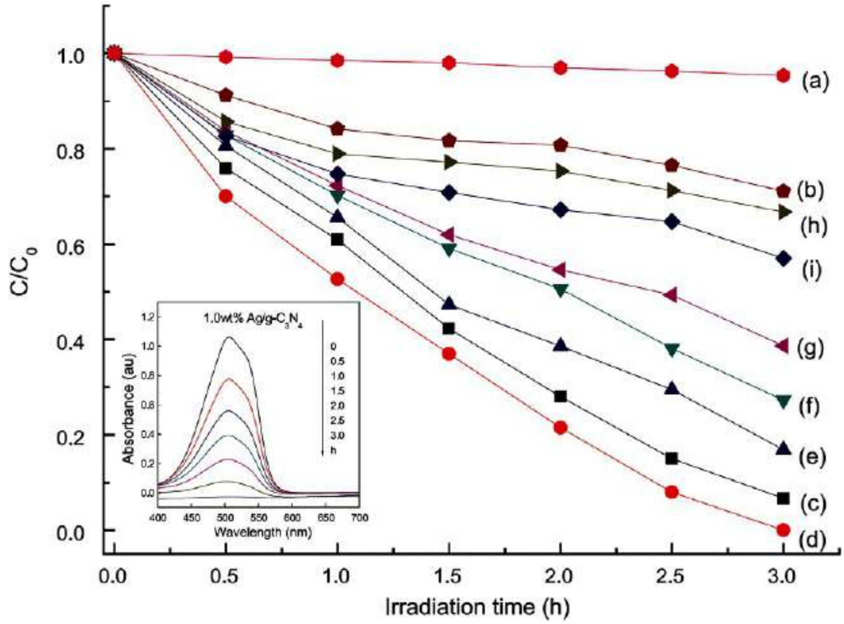

Fig. 7.14 (A) Photocatalytic performance in the presence of Ag/g-C_3N_4 samples, (a) blank, (b) pure g-C_3N_4, (c) 0.5 wt% Ag/g-C_3N_4, (d) 1.0 wt% Ag/g-C_3N_4, (e) 1.5 wt% Ag/g-C_3N_4, (f) 2.0 wt% Ag/g-C_3N_4, (g) 3.0 wt% Ag/g-C_3N_4, (h) 4.0 wt% Ag/g-C_3N_4, and (i) 5.0 wt% Ag/g-C_3N_4. *(From L. Ge, C. Han, J. Liu, Y. Li, Enhanced visible light photocatalytic activity of novel polymeric g-C 3N4 loaded with Ag nanoparticles, Appl. Catal. A. Gen. 409–410 (2011) 215–222, https://doi.org/10.1016/j.apcata.2011.10.006.)*

increase the absorbance of visible light [77]. The degradation performance in terms of the rate constants or % degradation value of various as-prepared doped g-C_3N_4 photocatalysts are shown in Table 7.2. However, it is observed that in most of the studies, the effect of amount of the doping substance on the photocatalytic performance and the possible mechanism of photocatalysis of g-C_3N_4 were not investigated properly.

3.2 Photodegradation of dye by g-C_3N_4-based binary composites

Besides the use of g-C_3N_4 and subsequent-doped g-C_3N_4 as photocatalysts, a wide variety of some other semiconductor photocatalysts are fabricated using the material g-C_3N_4. Such materials can be effectively used as visible-light-driven photocatalyst in wastewater treatment basically in organic pollutant degradation. A major advantage of g-C_3N_4 is that it can be used to facilitate electron transfer which consequently diminishes the probability of e^-–h^+ pair recombinations in such photocatalysts. Fabrication of such materials with g-C_3N_4 results in increase in the absorption of light as well as the surface area of the composites. Thus, the photocatalytic activity of the composite materials increases dramatically. Therefore, use of g-C_3N_4 as a supporting material along with various other semiconductors as stable, recyclable, and fully efficient photocatalyst has been found

Table 7.2 Photocatalytic degradation performance of various as-prepared doped g-C_3N_4 photocatalysts.

Doping element	Mode of synthesis	Band gap (eV)	Pollutant selected	Photocatalytic activity in terms of *k* or % degradation	Increment w.r.t. g-C_3N_4	Reference
B	Thermal condensation	2.66	RhB	$0.192\,min^{-1}$	3.6-fold	[78]
C	Polycondensation	2.65	RhB	$0.0362\,min^{-1}$	4.47-fold	[79]
P	Copolymerization	–	RhB	98% in 1 h	–	[80]
	Copolymerization	2.63	RhB	$0.0466\,min^{-1}$	4-fold	[81]
	Copolymerization	2.86	RhB	$0.0985\,min^{-1}$	2.7-fold	[82]
S	Thermal condensation	2.56	RhB	$0.0167\,min^{-1}$	12.8-fold	[83]
Na	Thermal polymerization	2.58	RhB	$0.0064\,min^{-1}$	3.6-fold	[84]
K	Annealing	2.57	RhB	$0.011\,min^{-1}$	26.9-fold	[85]
Fe	Impregnation	2.56	RhB	–	4.5-fold	[86]
	Calcination	–	MB	100% in 90 min	–	[87]
Cu	Thermal condensation	–	RhB	100% in 45 min	–	[88]
	Thermal condensation	2.25	MO	90.2% in 1 h	–	[89]
Eu	Thermal condensation	2.45	MB	$0.0121\,min^{-1}$	2.1-fold	[90]
Ce	Annealing	2.57	RhB	$0.0155\,min^{-1}$	2.1-fold	[91]
Mn	Calcination refluxing	2.62	RhB	$0.682 \times 10^{-2}\,min^{-1}$	2.3-fold	[92]
Fe	Thermal polymerization	2.5	Phenol	1000% in 50 min	–	[93]
Pd	Chemical reduction	–	BPA	100% in 360 min	Fivefold	[94]
Pt	Hydrothermal	–	PCP	98% in 420 min	–	[95]
Ag	Photodeposition	–	PNP	98% in 120 min	1.2-fold	[96]

to be a challenging area of research. Many research groups have reported the fabrication of some g-C_3N_4-based semiconductor materials to improve the photocatalytic activities to a significant extent to design some type-II heterojunctions or *Z*-scheme photocatalysts by coupling g-C_3N_4 with various materials such as ZnO, TiO_2, $SmVO_4$, SnO_2, Co_3O_4, Ag_3VO_4, Ag_3PO_4, $BiVO_4$, CdS, Ag_2CO_3, MoO_3, and many more.

The photocatalytic activities of g-C_3N_4/TiO_2 composites were investigated [60] by measuring the decolorization of MB under visible light. Fig. 7.15A clearly indicates that self-photolysis of MB is negligible and about 35% of the dye was degraded in presence of pure TiO_2 films within 3 h of irradiation. The photoactivity of the g-C_3N_4/TiO_2 composite was, however, much higher. The highest photoactivity of 68% was obtained in presence of 50 wt% g-C_3N_4/TiO_2 film. The improved photocatalytic activity observed from the g-C_3N_4/TiO_2 films may be due to the red-shift of the light absorption range and the strong light absorption intensity of the g-C_3N_4/TiO_2 composites as observed in the UV–vis DRS study and also due to an improved charge separation efficiency of photogenerated e^-–h^+ pairs due to the suitably matching CB and VB levels and the close interfacial connection between TiO_2 and g-C_3N_4 in the composite material [62] [97]. The recyclability of the material was tested with the best performing 50 wt% g-C_3N_4/TiO_2 composite. It is observed in the Fig. 7.15B that only about 5% deactivation of the material is observed after five consecutive cycles. The result revealed that the material has a very good stability and recyclability toward the photodegradation of MB dye.

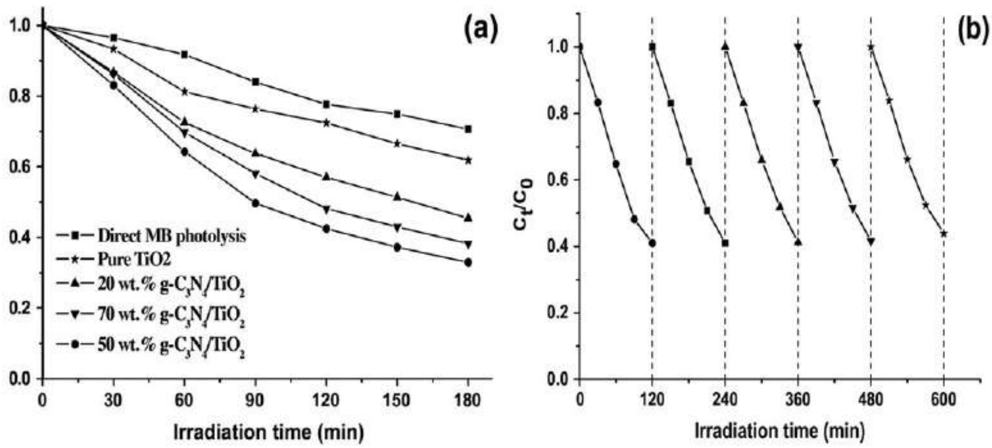

Fig. 7.15 (A) MB photolysis and photocatalytic degradation over pure TiO_2, pure g-C_3N_4 and g-C_3N_4/TiO_2 composite films and (B) cycling runs using 50 wt% g-C_3N_4/TiO_2 film (the initial MB concentration of 10.0 mg/L). *(From N. Boonprakob, N. Wetchakun, S. Phanichphant, D. Waxler, P. Sherrell, A. Nattestad, J. Chen, B. Inceesungvorn, Enhanced visible-light photocatalytic activity of g-C3N4/TiO2 films, J. Colloid Interface Sci. 417 (2014) 402–409, https://doi.org/10.1016/j.jcis.2013.11.072.)*

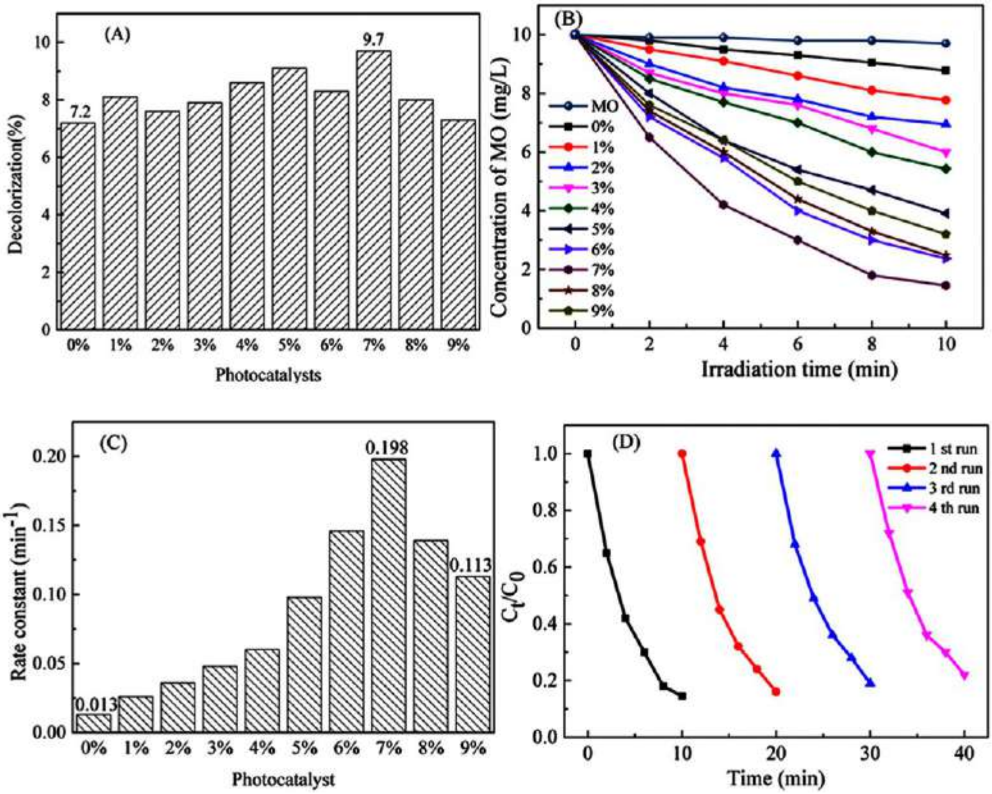

Fig. 7.16 (A) Adsorption of MO on the different photocatalysts after 3 h in dark; (B) Conversion of MO with the irradiation time; (C) Photocatalytic decolorization rate constants of MO over the samples; (D) Four consecutive cycles of degradation of MO using the 7% sample. *(From J. Chen, J. Zhong, J. Li, S. Huang, W. Hu, M. Li, Q. Du, Synthesis and characterization of novel Ag2CO3/g-C3N4 composite photocatalysts with excellent solar photocatalytic activity and mechanism insight, Mol. Catal. 435 (2017) 91–98, https://doi.org/10.1016/j.mcat.2017.03.026.)*

Chen and coworkers [61] reported the fabrication of a series of *Z*-scheme Ag_2CO_3/g-C_3N_4 with different molar ratios of Ag/g-C_3N_4 (0%, 1%, 2%, 3%, 4%, 5%, 6%, 7%, 8%, and 9%). The research group investigated the adsorption of MO (Fig. 7.16A) on photocatalysts thus synthesized and found that the dye is adsorbed onto the catalyst surface to an extent of mere 10% after 12 h in dark. This group also found that self-photolysis of MO is negligible and photocatalysis in presence of pure g-C_3N_4 is very slow. But, on coupling with Ag_2CO_3, the photoactivities of the composite are enhanced remarkably, and the 7% Ag_2CO_3/g-C_3N_4 composite exhibits the highest activity (Fig. 7.16B). The photodegradation of MO in presence of all the samples follows first-order kinetic equation as shown in Fig. 7.16C with the corresponding first-order rate constant values. It can be observed that the rate constant gradually increases with increase in Ag_2CO_3 loading, reaches a maximum $0.198\,min^{-1}$ in presence of 7% Ag_2CO_3/g-C_3N_4 composite, and then falls rapidly. It is observed that the first-order rate constant in presence of the 7% Ag_2CO_3/g-C_3N_4 composite is 15-fold higher than that in presence of the bare g-C_3N_4. From the recyclability study (Fig. 7.16D), it was found that the phocatalytic activity of 7% composite exhibit only a slight decrease in the phocatalytic activity after fourth cycle. Thus, the material possesses excellent photocatalytic stability.

On critical analysis, it was observed that the different heterostructure g-C_3N_4-based binary composite photocatalysts fabricated by various research groups are found to be efficient w.r.t. the photodegradation of organic dye as well as phenolic compound contaminated wastewater. The ease in the transfer of charge from the semiconductor material by the supporting g-C_3N_4, improved e^-–h^+ pair separation, band gap narrowing, enhanced visible-light absorption as well as higher stability are the deciding factor in this regard. As of now various binary composites containing g-C3N4 have been designed and developed with enhanced photocatalytic activities toward degradation organic pollutants. The degradation performance in terms of the rate constants or % degradation value of various as-prepared g-C_3N_4-based binary photocatalysts are shown in Table 7.3.

3.3 Photodegradation of dye by g-C_3N_4-based ternary composites

Many research groups are working toward fabrication of g-C_3N_4 with variety of other materials to improve the photocatalytic performance to a considerable extent. Research works are also underway for the fabrication of some highly efficient g-C_3N_4-based type-III dual channel *Z*-scheme heterostructure ternary composites by combining two metal oxides/sulfides with g-C_3N_4 or other materials like metal oxide/phosphate and metal halide with g-C_3N_4. Yuan and coworkers [118] synthesized a novel g-C_3N_4/CeO_2/ZnO ternary nanocomposite by decorating g-C_3N_4/CeO_2 binary nanosheets with ZnO nanoparticles. The research group at first synthesized binary g-C_3N_4/CeO_2 nanosheets by pyrolysis and subsequent exfoliation method followed by decoration with ZnO nanoparticles to construct the ternary nanocomposites. The as-prepared g-C_3N_4/CeO_2/ZnO ternary nanocomposites exhibit better photocatalytic activity, as compared to bare g-C_3N_4, ZnO, and g-C_3N_4/CeO_2 toward degradation of MB dye. The augmented photocatalytic activity of the material is attributed to the presence of numerous active sites of nanosheet shapes and the faster interfacial charge separation due to the formation of type-II band alignment with more than one heterointerface and the efficient three-level electron–hole transfer.

The research group investigated the photocatalytic activity of the material for the degradation of methylene blue (MB, 10 mg/L, 80 mL) with 30 mg of the photocatalysts under visible light. The photodegradation performance of MB dye over pure g-C_3N_4, ZnO, g-C_3N_4/CeO_2, and the g-C_3N_4/CeO_2/ZnO composite under

Table 7.3 Photocatalytic degradation performance of various g-C_3N_4-based binary photocatalysts.

Hetero structure	Method of synthesis	Pollutant	Experimental conditions: Initial dye conc. (C_0)	Experimental conditions: Catalyst dose	Experimental conditions: Illumination time	Rate constant (k_1)	% Degradation	Increment w. r.t. g-C_3N_4	Reference
ZnO/g-C_3N_4	Simple calcination	PNP	4 mg/L	3 g/L	300 min	0.0081 min^{-1}	100%	6.4-fold	[98]
g-C_3N_4/Bi_2WO_6	Ball Milling	2,4-DCP	0.02 g/L	1 g/L	300 min	–	92%	–	[99]
g-C_3N_4/$SmVO_4$	Mixing-Calcination	RhB	10 mg/L	1 g/L	–	2.07 h^{-1}	–	2.4-fold	[100]
ZnO/g-C_3N_4	Ball Milling	RhB	10 mg/L	2 g/L	150 min	0.0239 min^{-1}	97.60%	3.1-fold	[101]
g-C_3N_4/Ag_2O	Liquid-phase synthesis	MO	20 mg/L	0.4 g/L	30 min	–	90%	11-fold	[102]
		Phenol			180 min	–	82%	–	
Ag_3PO_4@g-C_3N_4	In situ deposition	4-CP	20 mg/L	1	180 min	18×10^{-3} min^{-1}	96.50%	5.5-fold	[103]
g-C_3N_4/SnO_2	Chemical synthesis	MO	10 mg/L	1 g/L	180 min	0.0078 min^{-1}	73%	6-fold	[104]
g-C_3N_4/$BiVO_4$	Hydrothermal	RhB	10 mg/L	1 g/L	40 min	0.0994 min^{-1}	99.70%	2.3-fold	[105]
g-C_3N_4/TiO_2	Direct heating	MB	10 mg/L	Thin film	180 min	–	68%	–	[60]
$AgVO_3$/g-C_3N_4	In situ hydrothermal	BPA	0.02 g/L	1 g/L	90 min	0.0552 min^{-1}	100%	10-fold	[106]
$Cd_{0.2}Zn_{0.8}S$/g-C_3N_4	Hydrothermal	Phenol	0.01 g/L	1 g/L	180 min	–	76.10%	4.2-fold	[107]
CeO_2/g-C_3N_4	In situ co-pyrolysis	Phenol	10 mg/L	1 g/L	300 min	–	55%	17.3-fold	[108]
Bi_2MoO_6/g-C_3N_4	Direct Coupling	MB	10 mg/L	1 g/L	40 min	0.0688 min^{-1}	90%	4.8-fold	[109]
Ag_2CrO_4/g-C_3N_4	Chemical precipitation	MO	10 mg/L	0.3 g/L	120 min	0.0068 min^{-1}	–	5.7-fold	[110]
g-C_3N_4/TiO_2 nanotube	Impregnation method	RhB	5 mg/L	2×2 cm^2 film/ 20 mL	300 min	354×10^{-5} min^{-1}	67%	1.4-fold	[111]

g-C_3N_4/ Ag_2WO_4	In situ precipitation	MO	10 mg/L	1 g/L	150 min		95%	2.3-fold	[55]
Ag_2CO_3/ g-C_3N_4	Facile precipitation	MO	10 mg/L	1 g/L	10 min	0.198 min^{-1}	80%	15-fold	[61]
ZnS/ g-C_3N_4	Atomic layer deposition	MB	6 mg/L	0.3 g/L	100 min	0.023 min^{-1}	90%	2.6-fold	[112]
Bi_2WO_6/g-C_3N_4	Calcination Hydrothermal	RhB	10 mg/L	1 g/L	120 min	–	80%	3.4-fold	[113]
CuS/ g-C_3N_4	In situ precipitation-hydrothermal	RhB	10 mg/L	0.3 g/L	120 min	1.722 min^{-1}	93%	3.5-fold	[114]
ZnO/ g-C_3N_4	Ball milling	RhB	10 mg/L	1 g/L	120 min	0.426 h^{-1}	51.30%	2.1-fold	[115]
MoS_2/ g-C_3N_4	Electrostatic self-assembly	Phenol	20 mg/L	1 g/L	120 min	–	95%	4.7-fold	[116]
g-C_3N_4/ WO_3	Hydrothermal	PNP	10 mg/L	1 g/L	60 min	0.0518	94%	5.8-fold	[117]

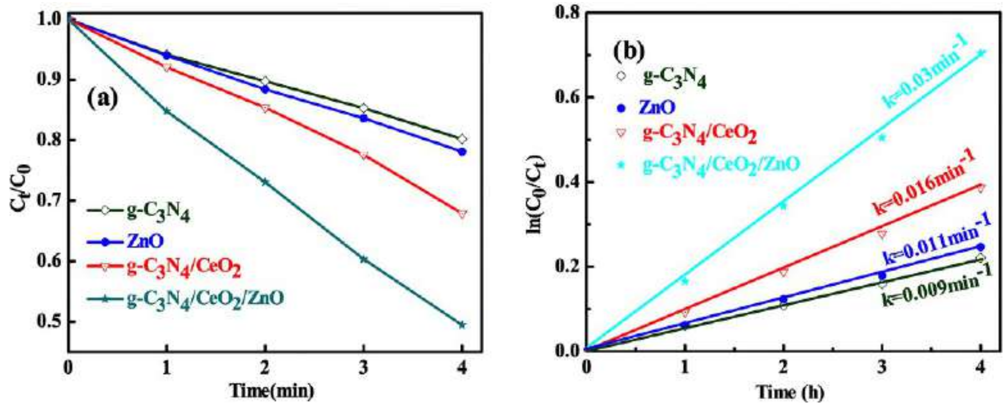

Fig. 7.17 The photocatalytic activity of the photocatalysts under visible light (A) and apparent rate constants for the photodegradation of MB (B). *(From Y. Yuan, G.F. Huang, W.Y. Hu, D.N. Xiong, B.X. Zhou, S. Chang, W.Q. Huang, Construction of g-C3N4/CeO2/ZnO ternary photocatalysts with enhanced photocatalytic performance, J. Phys. Chem. Solid. 106 (2017) 1–9,* https://doi.org/10.1016/j.jpcs.2017.02.015.*)*

visible-light illumination is displayed in Fig. 7.17A. It is observed that in presence of the photocatalysts, the concentration of the dye decreases steadily with increase in illumination time. Especially, the $g\text{-}C_3N_4/CeO_2/ZnO$ composite exhibits the highest photodegradation efficiency of 52.0% after 4 h. On the other hand, MB is photodegraded by only 22.0%, 20.0%, and 32.0% in the presence of ZnO, pure $g\text{-}C_3N_4$, and $g\text{-}C_3N_4/CeO_2$ binary composite, respectively. The first-order rate constant (*k*) of MB degradation as shown in Fig. 7.17B over the $g\text{-}C_3N_4/CeO_2/ZnO$ composite is found to be $0.03\,min^{-1}$ which is higher than that over pure ZnO ($0.011\,min^{-1}$), $g\text{-}C_3N_4$ ($0.009\,min^{-1}$), and $g\text{-}C_3N_4/CeO_2$ ($0.016\,min^{-1}$) by a factor of 2.7, 3.3, and 1.9, respectively. The results of this work suggest that the fabrication of type II multiheterostructures is highly efficient and reusable $g\text{-}C_3N_4$-based visible-light photocatalysts for environmental purification and energy conversion.

A ternary heterostructure nanocomposite, $Fe_3O_4/TiO_2/g\text{-}C_3N_4$, was prepared by Raza and his coworkers [119] by a facile and in situ growth process based on hydrothermal treatment using melamine, tetrabutyl titanate, and as-prepared Fe_3O_4 nanoparticles. The photocatalytic performance of the material was investigated for photodegradation of RhB (shown in Fig. 7.18) and MO (shown in Fig. 7.19) under visible-light irradiation. The as-prepared material exhibited about 96.4% and 90% of RhB and MO degradation in 80 min and 120 min, respectively. The pseudo first-order rate constants for RhB and MO degradation on the ternary $Fe_3O_4/TiO_2/g\text{-}C_3N_4$ nanocomposite were found to be

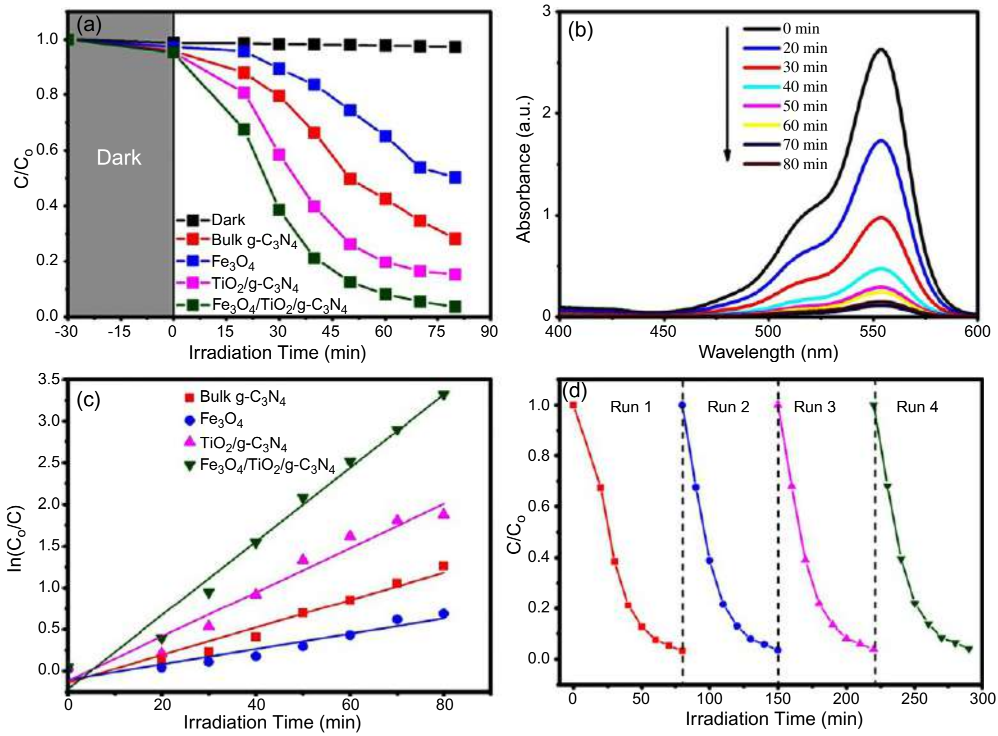

Fig. 7.18 (A) The photocatalytic degradation of RhB for bare g-C_3N_4, Fe_3O_4, TiO_2/g-C_3N_4, and Fe_3O_4/TiO_2/g-C_3N_4 nanocomposite; (B) Changes in absorption spectra of RhB solution with time; (C) Kinetic plots for the degradation of RhB; (D) Photostability for the RhB degradation in presence of Fe_3O_4/TiO_2/g-C_3N_4 nanocomposite. *(From A. Raza, H. Shen, A.A. Haidry, S. Cui, Hydrothermal synthesis of Fe3O4/TiO2/g-C3N4: advanced photocatalytic application, Appl. Surf. Sci. 488 (2019) 887–895, https://doi.org/10.1016/j.apsusc.2019.05.210.)*

0.0441 min^{-1} and 0.0186 min^{-1} which are about 3.73 and 2.74 times of the bare g-C_3N_4. The material also shows the high photocatalyst durability and good photocatalytic performance after four consecutive cycles. The results of the study reveal that the photocatalytic efficiency of g-C_3N_4-based material can be proficiently improved by coupling of anatase TiO_2 and Fe_3O_4. The enhanced photocatalytic performance is mainly attributed to the lager surface area and effective separation efficiency of the electron–hole pair's recombination (Fig. 7.18).

Till date, various ternary heterostructure nanocomposites have been designed and developed with enhanced photocatalytic activities toward degradation of organic pollutants. The degradation performance in terms of the rate constants or % degradation value of some as-prepared g-C_3N_4-based ternary composites is shown in Table 7.4.

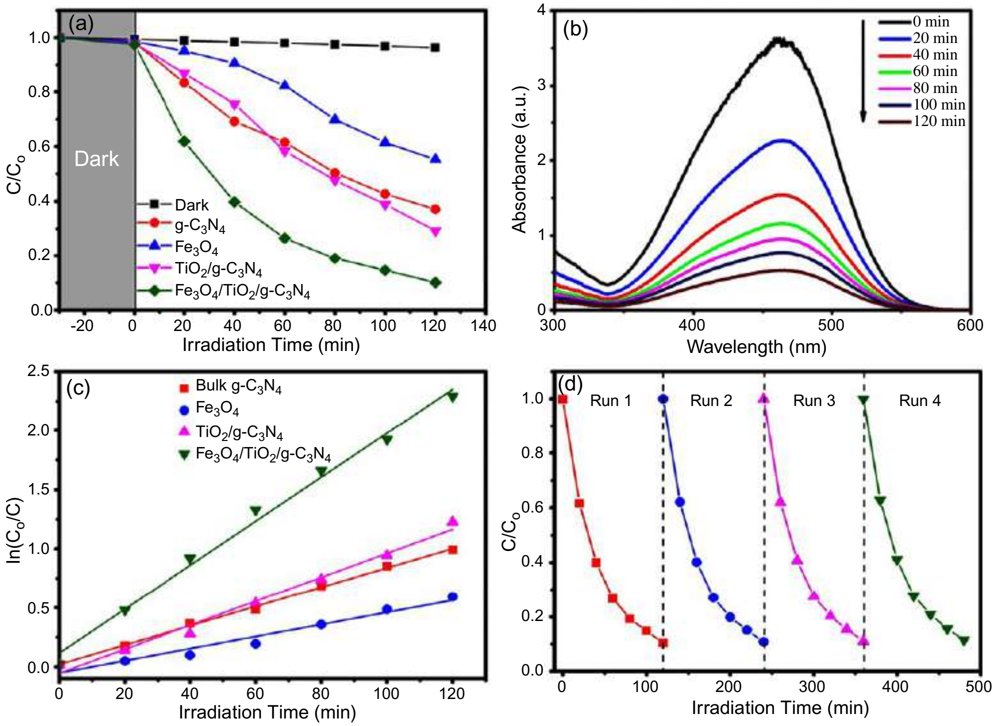

Fig. 7.19 (A) The photocatalytic degradation of MO for bare g-C_3N_4, Fe_3O_4, TiO_2/g-C_3N_4 and Fe_3O_4/TiO_2/g-C_3N_4 nanocomposite; (B) Changes in absorption spectra of MO solution with time; (C) Kinetic plots for the degradation of MO; (D) Photostability for the degradation of MO in presence of Fe_3O_4/TiO_2/g-C_3N_4 nanocomposite. *(From A. Raza, H. Shen, A.A. Haidry, S. Cui, Hydrothermal synthesis of Fe3O4/TiO2/g-C3N4: advanced photocatalytic application, Appl. Surf. Sci. 488 (2019) 887–895, https://doi.org/10.1016/j.apsusc.2019.05.210.)*

4. Mechanistic pathway of photodegradation by g-C_3N_4-based materials

There are many methods that have been developed to increase the visible-light absorption, inhibit the recombination of photogenerated electron–hole pairs, and also to facilitate charge transfer for augmentation of the photocatalytic efficiency of the material. The photocatalytic activity of g-C_3N_4 has been improved to a considerable extent by metal/nonmetal element doping and fabrication of g-C_3N_4 with some other semiconductor material(s) to design *Z*-scheme binary or ternary heterojunction photocatalytic systems. As shown in Fig. 7.20, the degradation mechanism proposed by Ge and coworkers [76] suggested that the doped Ag particles act as electron traps to facilitate the separation of

Table 7.4 Photocatalytic degradation performance of various g-C_3N_4-based ternary photocatalysts.

Heterostructure	Method of synthesis	Pollutant	Experimental conditions			Rate Constant (k_1)	% Degradation	Increment w.r.t. g-C_3N_4	Reference
			Initial dye conc. (C_0)	Catalyst dose	Illumination time				
g-C_3N_4/RGO/Bi_2WO_6	Hydrothermal	TCP	20 mg/L	1 g/L	120 min	30×10^{-2} min^{-1}	98%	–	[120]
RGO/g-C_3N_4/Ag-AgCl	Deposition-precipitation	MO	7 × 10–5 M	1.6 g/L	60 min	0.0271 min^{-1}	80%	9.34-fold	[121]
g-C_3N_4/Ag/Mo_2	Sol–gel-hydrothermal	RhB	20 mg/L	1 g/L	60 min	–	100%	–	[122]
g-C_3N_4/Fe_3O_4/$CuWO_4$	Refluxing-calcination	RhB	1×10^{-5} M	0.4 g/L	270 min	124.2×10^{-4} min^{-1}	100%	10.5-fold	[123]
g-C_3N_4/Ag_2CrO_4/AgI	Refluxing method	RhB	1×10^{-5} M	0.4 g/L	120 min	328×10^{-4} min^{-1}	99%	27.9-fold	[124]
g-C_3N_4/CNT/$BiVO_4$	Wet Impregnation	Phenol	10 mg/L	1 g/L	120 min	0.0102 min^{-1}	80.60%	5.2-fold	[125]
g-C_3N_4/ZnS/SnS_2	Hydrothermal	MB	8 mg/L	0.6 g/L	20 min	0.148 min^{-1}	95%	8.74-fold	[126]
CdS/CQDs/g-C_3N_4	Calcination-preparation	Phenol	10 mg/L	1 g/L	120 min	0.015 min^{-1}	58%	2.5-fold	[127]
		MB	10 mg/L	1 g/L	120 min	0.024 min^{-1}	98%	2.7-fold	
$CaTiO_3$/g-C_3N_4/AgBr	Hydrothermal assembly	RhB	5 mg/L	0.5 g/L	30 min	0.1907 min^{-1}	99.60%	19.9-fold	[128]
ZnO/g-C_3N_4/C-Xerogel	Sol–gel method	4-CP	10 mg/L	0.2 g/L	300 min	0.0051 min^{-1}	72%	10.2-fold	[129]
g-C_3N_4/WO_3/MoS_2	Facile co-calcination and hydrothermal	RhB	50 mg/L	1 g/L	10 min	0.097 min^{-1}	99.90%	3-fold	[130]
		MO	20 mg/L	1 g/L	60 min	0.023 min^{-1}	83.40%	2-fold	
		MB	20 mg/L	1 g/L	60 min	0.032 min^{-1}	91.80%	4-fold	
		AO-7	20 mg/L	1 g/L	60 min	0.055 min^{-1}	94.20%	5-fold	
rGO/g-C_3N_4/$CoFe_2O_4$	Hydrothermal	4-NP	20 mg/L	0.25 g/L	40 min	0.0802 min^{-1}	94%	15.7-fold	[131]
TiO_2/g-C_3N_4/Bi_2WO_6	Hydrothermal	Phenol	10 mg/L	1 g/L	210 min	–	64%	3.2-fold	[132]
AgBr/$BiPO_4$/g-C_3N_4	Hydrothermal	RB-9	20 mg/L	1 g/L	60 min	20.2×10^{-2} min^{-1}	80%	–	[133]

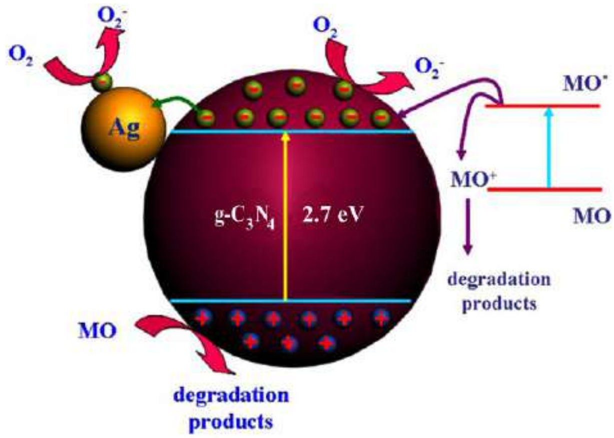

Fig. 7.20 Proposed mechanism of MO degradation over Ag/g-C_3N_4 composite photocatalyst. *(From L. Ge, C. Han, J. Liu, Y. Li, Enhanced visible light photocatalytic activity of novel polymeric g-C 3N4 loaded with Ag nanoparticles, Appl. Catal. A. Gen. 409–410 (2011) 215–222, https://doi.org/10.1016/j.apcata.2011.10.006.)*

photogenerated electron–hole pairs and promote interfacial electron transfer process. Under the influence of visible light, the electrons from the VB of g-C_3N_4 are excited to the CB leaving behind some holes (h^+) and react with O_2 molecules which are then reduced to superoxide radical anion $O_2•^-$. The electrons are then excited to the CB of g-C_3N_4 and are readily trapped by Ag nanoparticles due to its high Schottky barriers at the Ag/g-C_3N_4 interface. The reactive oxygen radicals and the photogenerated holes are responsible for the degradation of methyl orange dye.

A direct *Z*-scheme mechanism is proposed by Zhu and coworkers [55] which is illustrated in Fig. 7.21. The research group proposed that when the binary composite g-C_3N_4/Ag_2WO_4 is exposed to visible light, e^-s from the VB of both g-C_3N_4 and Ag_2WO_4 are excited to the higher energy CB leaving behind the holes. The e^-s from the CB of Ag_2WO_4 are then transferred to the VB of g-C_3N_4 due to strong electrostatic attractions. This process reduces the chance of recombination of e^- and h^+ within Ag_2WO_4 and g-C_3N_4 and consequently enhances the space separation of the charge carriers. The electrons in the CB of g-C_3N_4 are now trapped by O_2 to form $•O_2{}^-$ because the more negative (−1.12 eV) CB potential of g-C_3N_4 than the standard potential of $O_2/•O_2{}^-$ redox couple. Simultaneously, the holes in the VB of Ag_2WO_4 react with OH^- ions or H_2O molecules to produce •OH radicals because the more positive VB potential of Ag_2WO_4 than the standard potential of $•OH/OH^-$ redox couple. The $•O_2{}^-$ and •OH thus generated afterwards participate in the photodegradation of MO dye molecules.

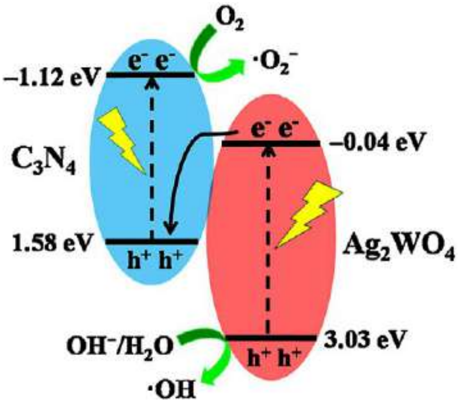

Fig. 7.21 Proposed mechanism for the direct Z-scheme g-C_3N_4/Ag_2WO_4 photocatalyst in dye degradation. *(From B. Zhu, P. Xia, Y. Lia, W. Ho, J. Yu, Fabrication and photocatalytic activity enhanced mechanism of directZ-scheme g-C3N4/Ag2WO4photocatalyst, Appl. Surf. Sci. 391 (2017) 175–183, https://doi.org/10.1016/j.apsusc.2015.08.149.)*

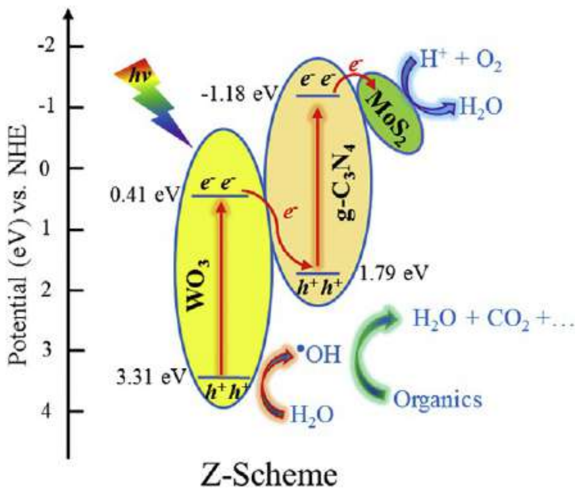

Fig. 7.22 Photocatalytic degradation and charge separation mechanisms in the g-C_3N_4/WO_3/MoS_2 heterojunction systems. *(From A. Beyhaqi, Q. Zeng, S. Chang, M. Wang, S.M. Taghi Azimi, C. Hu, Construction of g-C3N4/WO3/MoS2 ternary nanocomposite with enhanced charge separation and collection for efficient wastewater treatment under visible light, Chemosphere 247 (2020), https://doi.org/10.1016/j.chemosphere.2019.125784.)*

The possible charge-transfer processes and photocatalytic degradation mechanism proposed by Beyhaqi and coworkers [130] in the degradation of RhB dye by a Z-scheme ternary composite g-C_3N_4/WO_3/MoS_2 are illustrated in Fig. 7.22. Upon visible-light illumination, electrons (e^-) from the valence band (VB) of both g-C_3N_4 and WO_3 are excited to their respective higher energy conduction bands (CB) leaving behind the holes (h^+). The e^-s from the CB of WO_3 then migrate to the VB of g-C_3N_4 and combine with the holes of g-C_3N_4. This process reduces the chance of recombination of e^- and h^+ in both WO_3 and g-C_3N_4. The residual h^+s in WO_3 then oxidize H_2O to •OH radicals. At the same time, the e^-s in the g-C_3N_4 are trapped by MoS_2 and rapidly reduces O_2 to H_2O, since MoS_2 is an efficient catalyst material ion reaction [134,135]. This process also facilitates the separation of electron–hole pairs and the generation of •OH radicals. Consequently, the ternary composite g-C_3N_4/WO_3/MoS_2 exhibit higher photocatalytic activity compared to bare g-C_3N_4, WO_3, and the binary composites.

5. Conclusion and future scope

This chapter focuses on properties, fabrication, and potential application of g-C_3N_4-based composite photocatalysts in photocatalytic degradation of wastewater containing organic dyes and phenolic compounds. g-C_3N_4-based composite photocatalysts such as doped g-C_3N_4, binary or even ternary g-C_3N_4-based heterojunction photocatalysts exhibit superior photocatalytic performance. The enhanced photocatalytic activity is mostly owing to improved light absorption in the visible range, increased specific surface area, narrower band gap, faster charge transfer, and minimal electron–hole pair recombination Although considerable progress have been achieved in this regard, but the following challenges must be resolved in days to come.

The photoactivity of doped g-C_3N_4, binary or even ternary g-C_3N_4-based composites depend on proper choice of the material(s). The optimum weight % of the materials in the composite by which g-C_3N_4 is going to be fabricated should be determined so that maximum photocatalytic activity is achieved.

The accurate control on surface defects and facile scale preparation methods of g-C_3N_4 nanosheets are highly desired. Stress should be given on the development of low cost, environmental friendly, stable, and recyclable materials for large-scale industrial applications with considerable photocatalytic performance.

The optimization of the system parameters such as photocatalyst dose, initial dye concentration, solution pH, temperature, light intensity, presence of oxidizing agents/electron acceptors, and the presence of ionic components should be investigated properly and ensure that the optimum degradation efficiency is determined.

The photocatalytic performance of a material is dependent on the adsorption of the organic pollutants on the surface of the material. Therefore, it is extremely important to know the extent of adsorption of the pollutants by batch adsorption studies. The kinetics of adsorption should also be investigated by changing various system parameters applying various kinetic models to find the maximum adsorption capacity of the material.

The photodegradation of the g-C_3N_4-based heterojunction photocatalysts are tested by selecting some model pollutant such as RhB, MO or MB, phenol, 4-CP, 4-NP only.

However, a good number of cationic and anionic dyes as well as phenolic compounds are present in real effluents. Therefore, degradation of those pollutants should also be properly investigated. Furthermore, in real practice, the wastewater may contain a mixture of dyes and phenolic compounds. So, the study on the photocatalytic degradation of simultaneous coexisting wastewater containing dye and phenols should be included.

In summary, the authors believe that if the aforementioned issues and challenges are addressed properly, then in the near future, g-C_3N_4-based heterojunction photocatalysts will be an excellent material for large-scale industrial applications.

References

[1] S.Z. Cohen, C. Eiden, M.N. Lorber, in: W.Y. Gerne (Ed.), Evaluation of Pesticide in Ground Water, vol. 315, American Chemical Society, 1986, https://doi.org/10.1021/bk-1986-0315.ch010.
[2] L. Muszkat, D. Raucher, M. Magaritz, D. Ronen, in: U. Zoller (Ed.), Groundwater Contamination and Control, 1994, pp. 257–272.
[3] R.M. Dowd, M.P. Anderson, M.L. Johnson, Proc. 2nd Nat. Outdoor Action Conf. on Aquifer Restoration, Groundwater, Monitoring Geophysical Methods, 1998, pp. 1365–1379.
[4] K. Yanagisawa, J. Ovenstone, Crystallization of anatase from amorphous titania using the hydrothermal technique: effects of starting material and temperature, J. Phys. Chem. B 103 (37) (1999) 7781–7787, https://doi.org/10.1021/jp990521c.
[5] C.H. Chiou, C.Y. Wu, R.S. Juang, Influence of operating parameters on photocatalytic degradation of phenol in UV/TiO2 process, Chem. Eng. J. 139 (2) (2008) 322–329, https://doi.org/10.1016/j.cej.2007.08.002.
[6] N. Schweigert, R.W. Hunziker, B.I. Escher, R.I.L. Eggen, Acute toxicity of (chloro-)catechols and (chloro-)catechol-copper combinations in Escherichia coli corresponds to their membrane toxicity in vitro, Environ. Toxicol. Chem. 20 (2) (2001) 239–247, https://doi.org/10.1002/etc.5620200203.
[7] J. Matos, J. Laine, J.M. Herrmann, Synergy effect in the photocatalytic degradation of phenol on a suspended mixture of titania and activated carbon, Appl. Catal. Environ. 18 (3–4) (1998) 281–291, https://doi.org/10.1016/S0926-3373(98)00051-4.
[8] J. Michałowicz, W. Duda, Phenols—sources and toxicity, Pol. J. Environ. Stud. 16 (3) (2007) 347–362.
[9] R.M. Bruce, J. Santodonato, M.W. Neal, Summary review of the health effects associated with phenol, Toxicol. Ind. Health 3 (4) (1987) 535–568, https://doi.org/10.1177/074823378700300407.
[10] G. Li, D. Zhang, J.C. Yu, Ordered mesoporous $BiVO_4$ through nanocasting: a superior visible light-driven photocatalyst, Chem. Mater. 20 (12) (2008) 3983–3992, https://doi.org/10.1021/cm800236z.
[11] C. An, S. Peng, Y. Sun, Facile synthesis of sunlight-driven AgCl: Ag plasmonic nanophotocatalyst, Adv. Mater. 22 (23) (2010) 2570–2574, https://doi.org/10.1002/adma.200904116.
[12] Z. Liu, H. Bai, D. Sun, Facile fabrication of hierarchical porous TiO2 hollow microspheres with high photocatalytic activity for water purification, Appl. Catal. Environ. 104 (3–4) (2011) 234–238, https://doi.org/10.1016/j.apcatb.2011.03.027.
[13] S. Yuan, Y. Li, Q. Zhang, H. Wang, ZnO nanorods decorated calcined Mg-Al layered double hydroxides as photocatalysts with a high adsorptive capacity, Colloids Surf. A Physicochem. Eng. Asp. 348 (1–3) (2009) 76–81, https://doi.org/10.1016/j.colsurfa.2009.06.040.
[14] Q. Zhang, W. Fan, L. Gao, Anatase TiO2 nanoparticles immobilized on ZnO tetrapods as a highly efficient and easily recyclable photocatalyst, Appl. Catal. Environ. 76 (1–2) (2007) 168–173, https://doi.org/10.1016/j.apcatb.2007.05.024.
[15] S. Pasternak, Y. Paz, On the similarity and dissimilarity between photocatalytic water splitting and photocatalytic degradation of pollutants, ChemPhysChem 14 (10) (2013) 2059–2070, https://doi.org/10.1002/cphc.201300247.

[16] T. Wu, X. Zhou, H. Zhang, X. Zhong, Bi2S3 nanostructures: a new photocatalyst, Nano Res. 3 (5) (2010) 379–386, https://doi.org/10.1007/s12274-010-1042-0.
[17] F. Zhang, J. Zhao, T. Shen, H. Hidaka, E. Pelizzetti, N. Serpone, TiO2-assisted photodegradation of dye pollutants II. Adsorption and degradation kinetics of eosin in TiO2 dispersions under visible light irradiation, Appl. Catal. Environ. 15 (1–2) (1998) 147–156, https://doi.org/10.1016/S0926-3373(97)00043-X.
[18] J. Li, F. Sun, K. Gu, T. Wu, W. Zhai, W. Li, S. Huang, Preparation of spindly CuO micro-particles for photodegradation of dye pollutants under a halogen tungsten lamp, Appl. Catal. A. Gen. 406 (1–2) (2011) 51–58, https://doi.org/10.1016/j.apcata.2011.08.007.
[19] K. Hayat, M.A. Gondal, M.M. Khaled, Z.H. Yamani, S. Ahmed, Laser induced photocatalytic degradation of hazardous dye (safranin-O) using self synthesized nanocrystalline WO3, J. Hazard. Mater. 186 (2–3) (2011) 1226–1233, https://doi.org/10.1016/j.jhazmat.2010.11.133.
[20] X. Wang, S. Li, H. Yu, J. Yu, S. Liu, Ag2O as a new visible-light photocatalyst: self-stability and high photocatalytic activity, Chem. A Eur. J. 17 (28) (2011) 7777–7780, https://doi.org/10.1002/chem.201101032.
[21] C. Tian, Q. Zhang, A. Wu, M. Jiang, B. Jiang, H. Fu, Cost-effective large-scale synthesis of ZnO photocatalyst with excellent performance for dye photodegradation, Chem. Commun. 48 (23) (2012) 2858–2860, https://doi.org/10.1039/c2cc16434e.
[22] Y.H.B. Liao, J.X. Wang, J.S. Lin, W.H. Chung, W.Y. Lin, C.C. Chen, Synthesis, photocatalytic activities and degradation mechanism of Bi 2WO6 toward crystal violet dye, in: Catalysis Today, vol. 174, 2011, pp. 148–159, https://doi.org/10.1016/j.cattod.2011.03.048. issue 1.
[23] M.J. Pawar, A.D. Khajone, Photodegradation of malachite green dye over sol-gel synthesized nanocrystalline α-Fe2O3, J. Chem. Pharm. Res. 4 (2012) 1880–1884.
[24] M.B. Sreedhara, H.S.S.R. Matte, A. Govindaraj, C.N.R. Rao, Synthesis, characterization, and properties of few-layer moO3, Chem. Asian J. 8 (10) (2013) 2430–2435, https://doi.org/10.1002/asia.201300470.
[25] H. Dong, G. Chen, J. Sun, C. Li, Y. Yu, D. Chen, A novel high-efficiency visible-light sensitive Ag2CO3 photocatalyst with universal photodegradation performances: simple synthesis, reaction mechanism and first-principles study, Appl. Catal. Environ. 134–135 (2013) 46–54, https://doi.org/10.1016/j.apcatb.2012.12.041.
[26] S. Jana, B.C. Mitra, P. Bera, M. Sikdar, A. Mondal, Photocatalytic activity of galvanically synthesized nanostructure SnO 2 thin films, J. Alloys Compd. 602 (2014) 42–48, https://doi.org/10.1016/j.jallcom.2014.02.182.
[27] Z. Yu, B. Yin, F. Qu, X. Wu, Synthesis of self-assembled CdS nanospheres and their photocatalytic activities by photodegradation of organic dye molecules, Chem. Eng. J. 258 (2014) 203–209, https://doi.org/10.1016/j.cej.2014.07.041.
[28] C.R. Dhas, K. Venkateshkatachalam, A. Nithya, et al., Visible light driven photocatalytic degradation of Rhodamine B and Direct Red using cobalt oxide nanoparticles, Ceram. Int. 41 (8) (2015) 9301–9313, https://doi.org/10.1016/j.ceramint.2015.03.238.
[29] S. Sood, A. Umar, S. Kumar Mehta, S.K. Kansal, α-Bi2O3 nanorods: an efficient sunlight active photocatalyst for degradation of Rhodamine B and 2,4,6-trichlorophenol, Ceram. Int. 41 (3) (2015) 3355–3364, https://doi.org/10.1016/j.ceramint.2014.10.038.
[30] X. Zhao, J. Huang, L. Feng, L. Cao, J. Li, L. Zhou, Facile synthesis of α-Ag3VO4 hollow nanospheres with improved photocatalytic activities, J. Alloys Compd. 718 (2017) 7–14, https://doi.org/10.1016/j.jallcom.2017.05.107.
[31] M.A. Kausor, D. Chakrabortty, Optimization of system parameters and kinetic study of photocatalytic degradation of toxic acid blue 25 dye by Ag3PO4@RGO nanocomposite, J. Nanopart. Res. 22 (4) (2020), https://doi.org/10.1007/s11051-020-04829-3.
[32] S. Ye, R. Wang, M.Z. Wu, et al., A review on g-C_3N_4 for photocatalytic water splitting and CO_2 reduction, Appl. Surf. Sci. 358 (2015) 15–27, https://doi.org/10.1016/j.apsusc.2015.08.173.
[33] G. Mamba, A.K. Mishra, Graphitic carbon nitride (g-C_3N_4) nanocomposites: a new and exciting generation of visible light driven photocatalysts for environmental pollution remediation, Appl. Catal. B: Environ. 198 (2016) 347–377, https://doi.org/10.1016/j.apcatb.2016.05.052.

[34] J. Xu, T.J.K. Brenner, L. Chabanne, D. Neher, M. Antonietti, M. Shalom, Liquid-based growth of polymeric carbon nitride layers and their use in a mesostructured polymer solar cell with v oc exceeding 1 v, J. Am. Chem. Soc. 136 (39) (2014) 13486–13489, https://doi.org/10.1021/ja508329c.
[35] J. Xu, G. Wang, J. Fan, B. Liu, S. Cao, J. Yu, G-C3N4 modified TiO2 nanosheets with enhanced photoelectric conversion efficiency in dye-sensitized solar cells, J. Power Sources 274 (2015) 77–84, https://doi.org/10.1016/j.jpowsour.2014.10.033.
[36] J. Wen, J. Xie, X. Chen, X. Li, A review on g-C 3 N 4 -based photocatalysts, Appl. Surf. Sci. 391 (2017) 72–123, https://doi.org/10.1016/j.apsusc.2016.07.030.
[37] X. Wang, K. Maeda, A. Thomas, K. Takanabe, G. Xin, J.M. Carlsson, K. Domen, M. Antonietti, A metal-free polymeric photocatalyst for hydrogen production from water under visible light, Nat. Mater. 8 (1) (2009) 76–80, https://doi.org/10.1038/nmat2317.
[38] B. Zhu, J. Zhang, C. Jiang, B. Cheng, J. Yu, First principle investigation of halogen-doped monolayer g-C3N4 photocatalyst, Appl. Catal. Environ. 207 (2017) 27–34, https://doi.org/10.1016/j.apcatb.2017.02.020.
[39] S.M. Aspera, H. Kasai, H. Kawai, Density functional theory-based analysis on O 2 molecular interaction with the tri-s-triazine-based graphitic carbon nitride, Surf. Sci. 606 (11 – 12) (2012) 892–901, https://doi.org/10.1016/j.susc.2012.01.011.
[40] M.J. Bojdys, J.O. Müller, M. Antonietti, A. Thomas, Ionothermal synthesis of crystalline, condensed, graphitic carbon nitride, Chem. A Eur. J. 14 (27) (2008) 8177–8182, https://doi.org/10.1002/chem.200800190.
[41] J. Liu, Effect of phosphorus doping on electronic structure and photocatalytic performance of g-C3N4: insights from hybrid density functional calculation, J. Alloys Compd. 672 (2016) 271–276, https://doi.org/10.1016/j.jallcom.2016.02.094.
[42] S.M. Aspera, M. David, H. Kasai, First-principles study of the adsorption of water on tri-s-triazine-based graphitic carbon nitride, Jpn. J. Appl. Phys. 49 (11) (2010), https://doi.org/10.1143/JJAP.49.115703.
[43] R. Molinari, M. Borgese, E. Drioli, L. Palmisano, M. Schiavello, Hybrid processes coupling photocatalysis and membranes for degradation of organic pollutants in water, in: Catalysis Today, Vol. 75, 2002, pp. 77–85, https://doi.org/10.1016/S0920-5861(02)00047-0. Issues 1–4.
[44] M. Groenewolt, M. Antonietti, Synthesis of g-C3N4 nanoparticles in mesoporous silica host matrices, Adv. Mater. 17 (14) (2005) 1789–1792, https://doi.org/10.1002/adma.200401756.
[45] F. Dong, Y. Li, Z. Wang, W.K. Ho, Enhanced visible light photocatalytic activity and oxidation ability of porous graphene-like g-C 3 N 4 nanosheets via thermal exfoliation, in: Applied Surface Science, vol. 358, Elsevier B.V, 2015, pp. 393–403, https://doi.org/10.1016/j.apsusc.2015.04.034.
[46] W. Zhang, Z. Zhao, F. Dong, Y. Zhang, Solvent-assisted synthesis of porous g-C3N4 with efficient visible-light photocatalytic performance for NO removal, Chin. J. Catal. 38 (2) (2017) 372–378, https://doi.org/10.1016/S1872-2067(16)62585-8.
[47] Y. Cui, Y. Tang, X. Wang, Template-free synthesis of graphitic carbon nitride hollow spheres for photocatalytic degradation of organic pollutants, Mater. Lett. 161 (2015) 197–200, https://doi.org/10.1016/j.matlet.2015.08.106.
[48] Y. Wang, F. Wang, Y. Zhuo, et al., Simple synthesis of ordered cubic mesoporous graphitic carbon nitride by chemical vapor deposition method using melamine, Mater. Lett. 136 (2014) 271–273, https://doi.org/10.1016/j.matlet.2014.08.078.
[49] Z. Xu, L. Guan, H. Li, J. Sun, Z. Ying, J. Wu, N. Xu, Structure transition mechanism of single-crystalline silicon, g-C_3N_4, and diamond nanocone arrays synthesized by plasma sputtering reaction deposition, J. Phys. Chem. 119 (52) (2015) 29062–29070, https://doi.org/10.1021/acs.jpcc.5b10952.
[50] G.K. Dinesh, S. Chakma, Mechanistic investigation in degradation mechanism of 5-fluorouracil using graphitic carbon nitride, Ultrason. Sonochem. 50 (2019) 311–321, https://doi.org/10.1016/j.ultsonch.2018.09.032.
[51] Z.H. Sheng, L. Shao, J.J. Chen, W.J. Bao, F.B. Wang, X.H. Xia, Catalyst-free synthesis of nitrogen-doped graphene via thermal annealing graphite oxide with melamine and its excellent electrocatalysis, ACS Nano 5 (6) (2011) 4350–4358, https://doi.org/10.1021/nn103584t.

[52] J. Zhang, J. Sun, K. Maeda, K. Domen, P. Liu, M. Antonietti, X. Fu, X. Wang, Sulfur-mediated synthesis of carbon nitride: band-gap engineering and improved functions for photocatalysis, Energ. Environ. Sci. 4 (3) (2011) 675–678, https://doi.org/10.1039/c0ee00418a.
[53] F. Dong, Y. Sun, L. Wu, M. Fu, Z. Wu, Facile transformation of low cost thiourea into nitrogen-rich graphitic carbon nitride nanocatalyst with high visible light photocatalytic performance, Cat. Sci. Technol. 2 (7) (2012) 1332–1335, https://doi.org/10.1039/c2cy20049j.
[54] F. Dong, Z. Wang, Y. Sun, W.K. Ho, H. Zhang, Engineering the nanoarchitecture and texture of polymeric carbon nitride semiconductor for enhanced visible light photocatalytic activity, J. Colloid Interface Sci. 401 (2013) 70–79, https://doi.org/10.1016/j.jcis.2013.03.034.
[55] B. Zhu, P. Xia, W. Ho, J. Yu, Isoelectric point and adsorption activity of porous g-C_3N_4, Appl. Surf. Sci. 344 (2015) 188–195, https://doi.org/10.1016/j.apsusc.2015.03.086.
[56] W.J. Ong, L.L. Tan, Y.H. Ng, S.T. Yong, S.P. Chai, Graphitic carbon nitride (g-C_3N_4)-based photocatalysts for artificial photosynthesis and environmental remediation: are we a step closer to achieving sustainability? Chem. Rev. 116 (2016) 7159–7329, https://doi.org/10.1021/acs.chemrev.6b00075.
[57] J Gao, Y. Zhou, Z. Li, S. Yan, N. Wang, Z. Zou, High-yield synthesis of millimetre-long, semiconducting carbon nitride nanotubes with intense photoluminescence emission and reproducible photoconductivity, Nanoscale 4 (12) (2012) 3687–3692, https://doi.org/10.1039/C2NR30777D.
[58] D.M. Teter, R.J. Hemley, Low-compressibility carbon nitrides, Science 271 (5245) (1996) 53–55, https://doi.org/10.1126/science.271.5245.53.
[59] M.J. McAllister, J.L. Li, D Adamson H., H.C. Schniepp, A.A. Abdala, J. Liu, I.A. Aksay, Single sheet functionalized graphene by oxidation and thermal expansion of graphite, Chem. Mater. 19 (18) (2007) 4396–4404, https://doi.org/10.1021/cm0630800.
[60] N. Boonprakob, N. wetchakun, S. Phanichphant, D. Waxler, P. Sherrell, A. Nattestad, B. Inceesungvorn, Enhanced visible-light photocatalytic activity of g-C_3N_4/TiO_2 films, J. Colloid. Inter. Sci. 417 (2017) 402–409, https://doi.org/10.1016/j.jcis.2013.11.072.
[61] J. Chen, J. Zhong, J. Li, S. Huang, W. Hu, M. Li, Q. Du, Synthesis and characterization of novel Ag_2CO_3/g-C_3N_4 composite photocatalysts with excellent solar photocatalytic activity and mechanism insight, Mol. Catal. 435 (2017) 91–98, https://doi.org/10.1016/j.mcat.2017.03.026.
[62] S.C. Yan, S.B. Lv, Z.S. Li, Z.G. Zou, Organic–inorganic composite photocatalyst of g-C_3N_4 and TaON with improved visible light photocatalytic activities, Dalton Trans. 39 (6) (2010) 1488–1491, https://doi.org/10.1039/b914110c.
[63] C. Han, L. Ge, C. Chen, Y. Li, X. Xiao, Y. Zhang, L. Guo, Novel visible light induced Co_3O_4-g-C_3N_4 heterojunction photocatalysts for efficient degradation of methyl orange, Appl. Catal. B: Environ. 147 (2014) 546–553, https://doi.org/10.1016/j.apcatb.2013.09.038.
[64] X. Xie, Y. Li, Z.Q. Liu, M. Haruta, W. Shen, Low-temperature oxidation of CO catalysed by Co_3O_4 nanorods, Nature 458 (7239) (2009) 746–749, https://doi.org/10.1038/nature07877.
[65] X. Xh, T. Jp, Z. Yq, M. Yj, W. Xl, G. Cd, Z. Xb, Freestanding Co_3O_4 nanowire array for high performance supercapacitors, RSC Adv. 2 (5) (2012) 1835–1841, https://doi.org/10.1039/C1RA00771H.
[66] J. Zhang, G. Zhang, X. Chen, S. Lin, L. Mohlmann, G. Dolega, X. Wang, Co-monomer control of carbon nitride semiconductors to optimize hydrogen evolution with visible light, Ang. Chem. Int. Ed. 51 (13) (2012) 3183–3187, https://doi.org/10.1002/anie.201106656.
[67] Y. Chen, J. Li, Z. Hong, B. Shen, B. Lin, B. Gao, Origin of the enhanced visible-light photocatalytic activity of CNT modified g-C-$_3N_4$ for H_2 production, Phys. Chem. Chem. Phys. 16 (17) (2014) 8106–8113, https://doi.org/10.1039/C3CP55191A.
[68] J. Zhang, M. Zhang, G. Zhang, X. Wang, Synthesis of carbon nitride semiconductors in sulfur flux for water photoredox catalysis, ACS Catal. 2 (6) (2012) 940–948, https://doi.org/10.1021/cs300167b.
[69] S.C. Yan, Z.S. Li, Z.G. Zou, Photodegradation performance of g-C_3N_4 fabricated by directly heating melamine, Langmuir 25 (17) (2009) 10397–10401, https://doi.org/10.1021/la900923z.
[70] J. Jiang, L. Ou-yang, L. Zhu, A. Zheng, J. Zou, X. Yi, H. Tang, Dependence of electronic structure of g-C3N4 on the layer number of its nanosheets: a study by Raman spectroscopy coupled with first-principles calculations, Carbon 80 (2014) 213–221.

[71] A. Akhundi, A Habibi-Yangjeh, Ternary g-C_3N_4/ZnO/AgCl nanocomposites: synergistic collaboration on visible-light-driven activity in photodegradation of an organic pollutant, Appl. Surf. Sci. 358 (2015) 261–269, https://doi.org/10.1016/j.apsusc.2015.08.149.
[72] H.J. Lee, S.H. Eom, Y.K. Song, S.S. Cho, Effects of aluminium powder content and cold rolling on foaming behaviour of x Alp/$Al_5Si_4Cu_4Mg$/0.8TiH_2 composites, Mater. Sci. Technol. 19 (6) (2003) 819–825, https://doi.org/10.1179/026708303225002992.
[73] B. Zhu, P. Xia, Y. Li, W. Ho, J. Yu, Fabrication and photocatalytic activity enhanced mechanism of direct Z-scheme g-C_3N_4/Ag_2WO_4 photocatalyst, Pure Appl. Chem. 391 (2017) (2017) 175–183, https://doi.org/10.1016/j.apsusc.2016.07.104.
[74] J. Yu, S. Wang, B. Cheng, Z. Lin, F. Huang, Noble metal-free $Ni(OH)_2$–gC_3N_4 composite photocatalyst with enhanced visible-light photocatalytic H_2-production activity, Catal. Sci. Technol. 3 (7) (2013) 1782–1789, https://doi.org/10.1039/C3CY20878H.
[75] P. Niu, L. Zhang, G. Liu, H.M. Cheng, Graphene-like carbon nitride nanosheets for improved photocatalytic activities, Adv. Funct. Mater. 22 (22) (2012) 4763–4770, https://doi.org/10.1002/adfm.201200922.
[76] L. Ge, C. Han, J. Liu, Y. Li, Enhanced visible light photocatalytic activity of novel polymeric g-C_3N_4 loaded with Ag nanoparticles, Appl. Catal. A: Gen. 409 (2011) 215–222, https://doi.org/10.1016/j.apcata.2011.10.006.
[77] M.A. El-Sayed, Some interesting properties of metals confined in time and nanometer space of different shapes, Acc. Chem. Res. 34 (4) (2001) 257–264, https://doi.org/10.1021/ar960016n.
[78] S.C. Yan, Z.S. Li, Z.G. Zou, Photodegradation of rhodamine B and methyl orange over boron-doped g-C_3N_4 under visible light irradiation, Langmuir 26 (6) (2010) 3894–3901, https://doi.org/10.1021/la904023j.
[79] G. Dong, K. Zhao, L. Zhang, Carbon self-doping induced high electronic conductivity and photoreactivity of gC_3N_4, Chem. Commun. 488 (2012) 6178–6180, https://doi.org/10.1039/C2CC32181E.
[80] L. Zhang, X. Chen, J. Guan, Y. Jiang, T. Hou, X. Mu, Facile synthesis of phosphorus doped graphitic carbon nitride polymers with enhanced visible-light photocatalytic activity, Mater. Res. Bull. 48 (9) (2013) 3485–3491, https://doi.org/10.1016/j.materresbull.2013.05.040.
[81] S. Hu, L. Ma, J. You, F. Li, Z. Fan, F. Wang, J. Gui, A simple and efficient method to prepare a phosphorus modified g-C_3N_4 visible light photocatalyst, RSC Advances 4 (41) (2014) 21657–21663.
[82] B. Chai, J. Yan, C. Wang, Z. Ren, Y. Zhu, Enhanced visible light photocatalytic degradation of Rhodamine B over phosphorus doped graphitic carbon nitride, Applied Surface Science *391* (2017) 376–383.
[83] Q. Fan, J. Liu, Y. Yu, S. Zuo, B. Li, A simple fabrication for sulfur doped graphitic carbon nitride porous rods with excellent photocatalytic activity degrading RhB dye, Applied Surface Science 391 (2017) 360–368.
[84] J. Zhang, S. Hu, Y. Wang, A convenient method to prepare a novel alkali metal sodium doped carbon nitride photocatalyst with a tunable band structure, RSC advances 4 (108) (2014) 62912–62919.
[85] S. Hu, F. Li, Z. Fan, F. Wang, Y. Zhao, Z. Lv, Band gap-tunable potassium doped graphitic carbon nitride with enhanced mineralization ability, Dalton Transactions 44 (3) (2015) 1084–1092.
[86] S. Tonda, S. Kumar, S. Kandula, V. Shanker, Fe-doped and-mediated graphitic carbon nitride nanosheets for enhanced photocatalytic performance under natural sunlight, Journal of Materials Chemistry A 2 (19) (2014) 6772–6780.
[87] H.A. Bicalho, J.L. Lopez, I. Binatti, P.F.R. Batista, J.D. Ardisson, R.R. Resende, E. Lorençon, Facile synthesis of highly dispersed Fe (II)-doped g-C_3N_4 and its application in Fenton-like catalysis, Molecular Catalysis 435 (2017) 156–165.
[88] J. Gao, J. Wang, X. Qian, Y. Dong, H. Xu, R. Song, J. Yao, One-pot synthesis of copper-doped graphitic carbon nitride nanosheet by heating Cu–melamine supramolecular network and its enhanced visible-light-driven photocatalysis, Journal of Solid State Chemistry 228 (2015) 60–64.
[89] S. Le, T. Jiang, Q. Zhao, X. Liu, Y. Li, B. Fang, M. Gong, Cu-doped mesoporous graphitic carbon nitride for enhanced visible-light driven photocatalysis, RSC advances 6 (45) (2016) 38811–38819.
[90] X.U. Dongdong, L.I. Xiaoni, L.I.U. Juan, HUANG, L., Synthesis and photocatalytic performance of europium-doped graphitic carbon nitride, Journal of Rare Earths 31 (11) (2013) 1085–1091.

[91] R. Jin, S. Hu, J. Gui, D. Liu, A convenient method to prepare novel rare earth metal ce-doped carbon nitride with enhanced photocatalytic activity under visible light, Bulletin of the Korean Chemical Society 36 (1) (2015) 17–23.
[92] J.C. Wang, C.X. Cui, Y. Li, L. Liu, Y.P. Zhang, W. Shi, Porous Mn doped g-C_3N_4 photocatalysts for enhanced synergetic degradation under visible-light illumination, Journal of hazardous materials 339 (2017) 43–53.
[93] J. Hu, P. Zhang, W. An, L. Liu, Y. Liang, W. Cui, In-situ Fe-doped g-C_3N_4 heterogeneous catalyst via photocatalysis-Fenton reaction with enriched photocatalytic performance for removal of complex wastewater, Applied Catalysis B: Environmental 245 (2019) 130–142.
[94] C. Chang, Y. Fu, M. Hu, C. Wang, G. Shan, L. Zhu, Photodegradation of bisphenol A by highly stable palladium-doped mesoporous graphite carbon nitride (Pd/mpg-C_3N_4) under simulated solar light irradiation, Applied Catalysis B: Environmental 142 (2013) 553–560.
[95] K. Li, Z. Zeng, L. Yan, S. Luo, X. Luo, M. Huo, Y. Guo, Fabrication of platinum-deposited carbon nitride nanotubes by a one-step solvothermal treatment strategy and their efficient visible-light photocatalytic activity, Applied Catalysis B: Environmental 165 (2015) 428–437.
[96] Y. Yang, Y. Guo, F. Liu, X. Yuan, Y. Guo, S. Zhang, M. Huo, Preparation and enhanced visible-light photocatalytic activity of silver deposited graphitic carbon nitride plasmonic photocatalyst, Applied Catalysis B: Environmental 142 (2013) 828–837.
[97] Y. Wang, R. Shi, J. Lin, Y. Zhu, Enhancement of photocurrent and photocatalytic activity of ZnO hybridized with graphite-like C_3N_4, Energy & Environmental Science 4 (8) (2011) 2922–2929.
[98] J.X. Sun, Y.P. Yuan, L.G. Qiu, X. Jiang, A.J. Xie, Y.H. Shen, J.F. Zhu, Fabrication of composite photocatalyst g-C_3N_4–ZnO and enhancement of photocatalytic activity under visible light, Dalton Transactions 41 (22) (2012) 6756–6763.
[99] Y. Tian, B. Chang, J. Lu, J. Fu, F. Xi, X. Dong, Hydrothermal synthesis of graphitic carbon nitride–Bi_2WO_6 heterojunctions with enhanced visible light photocatalytic activities, ACS applied materials & interfaces 5 (15) (2013) 7079–7085.
[100] T. Li, L. Zhao, Y. He, J. Cai, M. Luo, J. Lin, Synthesis of g-C_3N_4/$SmVO_4$ composite photocatalyst with improved visible light photocatalytic activities in RhB degradation, Applied Catalysis B: Environmental 129 (2013) 255–263.
[101] W. Liu, M. Wang, C. Xu, S. Chen, X. Fu, Significantly enhanced visible-light photocatalytic activity of g-C_3N_4 via ZnO modification and the mechanism study, Journal of Molecular Catalysis A: Chemical 368 (2013) 9–15.
[102] M. Xu, L. Han, S. Dong, Facile fabrication of highly efficient g-C_3N_4/Ag_2O heterostructured photocatalysts with enhanced visible-light photocatalytic activity, ACS applied materials & interfaces 5 (23) (2013) 12533–12540.
[103] Y. Ren, Q. Zhao, X. Li, W. Xiong, M. Tade, L. Liu, 2D Porous graphitic C_3N_4 nanosheets/Ag_3PO_4 nanocomposites for enhanced visible-light photocatalytic degradation of 4-chlorophenol, Journal of nanoparticle research 16 (8) (2014) 1–8.
[104] Y. Zang, L. Li, X. Li, R. Lin, G. Li, Synergistic collaboration of g- C_3N_4/SnO_2 composites for enhanced visible-light photocatalytic activity, Chemical Engineering Journal 246 (2014) 277–286.
[105] Y. Ji, J. Cao, L. Jiang, Y. Zhang, Z. Yi, G– C_3N_4/$BiVO_4$ composites with enhanced and stable visible light photocatalytic activity, Journal of alloys and compounds 590 (2014) 9–14.
[106] W. Zhao, Z. Wei, H. He, J. Xu, J. Li, S. Yang, C. Sun, Supporting 1-D $AgVO_3$ nanoribbons on single layer 2-D graphitic carbon nitride ultrathin nanosheets and their excellent photocatalytic activities, Applied Catalysis A: General 501 (2015) 74–82.
[107] H. Liu, Z. Jin, Z. Xu, Hybridization of $Cd_{0.2}Zn_{0.8}S$ with gC_3N_4 nanosheets: a visible-light-driven photocatalyst for H 2 evolution from water and degradation of organic pollutants, Dalton Transactions 44 (32) (2015) 14368–14375.
[108] N. Tian, H. Huang, C. Liu, F. Dong, T. Zhang, X. Du, Y. Zhang, In situ co-pyrolysis fabrication of CeO_2/gC_3N_4 n–n type heterojunction for synchronously promoting photo-induced oxidation and reduction properties, Journal of Materials Chemistry A 3 (33) (2015) 17120–17129.
[109] J. Lv, K. Dai, J. Zhang, L. Geng, C. Liang, Q. Liu, C. Chen, Facile synthesis of Z-scheme graphitic-C_3N_4/Bi_2MoO_6 nanocomposite for enhanced visible photocatalytic properties, Applied Surface Science 358 (2015) 377–384.

[110] J. Luo, X. Zhou, L. Ma, X. Xu, Rational construction of Z-scheme Ag_2CrO_4/g-C_3N_4 composites with enhanced visible-light photocatalytic activity, Applied Surface Science 390 (2016) 357–367.
[111] D. Zhou, Z. Chen, Q. Yang, X. Dong, J. Zhang, L. Qin, In-situ construction of all-solid-state Z-scheme g-C_3N_4/TiO_2 nanotube arrays photocatalyst with enhanced visible-light-induced properties, Solar Energy Materials and Solar Cells 157 (2016) 399–405.
[112] W.J. Kim, E. Jang, T.J. Park, Enhanced visible-light photocatalytic activity of ZnS/g-C_3N_4 type-II heterojunction nanocomposites synthesized with atomic layer deposition, Applied Surface Science 419 (2017) 159–164.
[113] F. Chen, D. Li, B. Luo, M. Chen, W. Shi, Two-dimensional heterojunction photocatalysts constructed by graphite-like C_3N_4 and Bi_2WO_6 nanosheets: enhanced photocatalytic activities for water purification, Journal of Alloys and Compounds 694 (2017) 193–200.
[114] Z. Cai, Y. Zhou, S. Ma, S. Li, H. Yang, S. Zhao, W. Wu, Enhanced visible light photocatalytic performance of g-C_3N_4/CuS pn heterojunctions for degradation of organic dyes, Journal of Photochemistry and Photobiology A: Chemistry 348 (2017) 168–178.
[115] Q. Chen, H. Hou, D. Zhang, S. Hu, T. Min, B. Liu, J. Yang, Enhanced visible-light driven photocatalytic activity of hybrid ZnO/ g-C_3N_4 by high performance ball milling, Journal of Photochemistry and Photobiology A: Chemistry 350 (2018) 1–9.
[116] L. Shi, W. Ding, S. Yang, Z. He, S. Liu, Rationally designed MoS_2/protonated g-C_3N_4 nanosheet composites as photocatalysts with an excellent synergistic effect toward photocatalytic degradation of organic pollutants, Journal of hazardous materials 347 (2018) 431–441.
[117] X. Zhang, X. Wang, J. Meng, Y. Liu, M. Ren, Y. Guo, Y. Yang, Robust Z-scheme g-C_3N_4/WO_3 heterojunction photocatalysts with morphology control of WO3 for efficient degradation of phenolic pollutants, Separation and Purification Technology 255 (2021), 117693.
[118] Y. Yuan, G.F. Huang, W.Y. Hu, D.N. Xiong, B.X. Zhou, S. Chang, W.Q. Huang, Construction of g-C_3N_4/CeO_2/ZnO ternary photocatalysts with enhanced photocatalytic performance, Journal of Physics and Chemistry of Solids 106 (2017) 1–9.
[119] A. Raza, H. Shen, A.A. Haidry, S. Cui, Hydrothermal synthesis of Fe_3O_4/TiO_2/g-C_3N_4: Advanced photocatalytic application, Applied Surface Science 488 (2019) 887–895.
[120] D. Ma, J. Wu, M. Gao, Y. Xin, T. Ma, Y. Sun, Fabrication of Z-scheme g-C_3N_4/RGO/Bi_2WO_6 photocatalyst with enhanced visible-light photocatalytic activity, Chemical Engineering Journal 290 (2016) 136–146.
[121] T. Shen, D. Lang, F. Cheng, Q. Xiang, Ternary Reduced Graphene Oxide/ g-C_3N_4/Ag-AgCl Nanocomposites for Controlled Visible-Light Photocatalytic Selectivity, ChemistrySelect 1 (5) (2016) 1006–1015.
[122] D. Lu, H. Wang, X. Zhao, K.K. Kondamareddy, J. Ding, C. Li, P. Fang, Highly efficient visible-light-induced photoactivity of Z-scheme g-C_3N_4/Ag/MoS_2 ternary photocatalysts for organic pollutant degradation and production of hydrogen, ACS Sustainable Chemistry & Engineering 5 (2) (2017) 1436–1445.
[123] A. Habibi-Yangjeh, M. Mousavi, Deposition of $CuWO_4$ nanoparticles over g-C_3N_4/Fe_3O_4 nanocomposite: novel magnetic photocatalysts with drastically enhanced performance under visible-light, Advanced Powder Technology 29 (6) (2018) 1379–1392.
[124] J. Barzegar, A. Habibi-Yangjeh, M. Mousavi, Combination of Ag2CrO4 and AgI semiconductors with g-C_3N_4: Novel nanocomposites with substantially improved photocatalytic performance under visible light, Solid State Sciences 77 (2018) 62–73.
[125] M.F.R. Samsudin, N. Bacho, S. Sufian, Y.H. Ng, Photocatalytic degradation of phenol wastewater over Z-scheme g-C_3N_4/CNT/$BiVO_4$ heterostructure photocatalyst under solar light irradiation, Journal of Molecular Liquids 277 (2019) 977–988.
[126] K. Dai, J. Lv, J. Zhang, C. Liang, G. Zhu, Band structure engineering design of g-C_3N_4/ZnS/SnS_2 ternary heterojunction visible-light photocatalyst with ZnS as electron transport buffer material, Journal of Alloys and Compounds 778 (2019) 215–223.
[127] S. Feng, T. Chen, Z. Liu, J. Shi, X. Yue, Y. Li, Z-scheme CdS/CQDs/g-C3N4 composites with visible-near-infrared light response for efficient photocatalytic organic pollutant degradation, Science of The Total Environment 704 (2020), 135404.

[128] Y. Yan, H. Yang, Z. Yi, R. Li, T. Xian, Design of ternary $CaTiO_3$/g-C_3N_4/AgBr Z-scheme heterostructured photocatalysts and their application for dye photodegradation, Solid State Sciences 100 (2020), 106102.
[129] J.G.M. de Sousa, T.V.C. da Silva, N.P. de Moraes, M.L.C.P. da Silva, R. da Silva Rocha, R. Landers, L.A. Rodrigues, Visible light-driven ZnO/g-C_3N_4/carbon xerogel ternary photocatalyst with enhanced activity for 4-chlorophenol degradation, Materials Chemistry and Physics 256 (2020), 123651.
[130] A. Beyhaqi, Q. Zeng, S. Chang, M. Wang, S.M.T. Azimi, C. Hu, Construction of g-C_3N_4/WO_3/MoS_2 ternary nanocomposite with enhanced charge separation and collection for efficient wastewater treatment under visible light, Chemosphere 247 (2020), 125784.
[131] B. Palanivel, M. Lallimathi, B. Arjunkumar, M. Shkir, T. Alshahrani, K.S. Al-Namshah, M.S. Hamdy, S. Shanavas, M. Venkatachalam, G. Ramalingam, rGO supported g-C_3N_4/$CoFe_2O_4$ heterojunction: Visible-light-active photocatalyst for effective utilization of H2O2 to organic pollutant degradation and OH radicals production, Journal of Environmental Chemical Engineering 9 (1) (2021), 104698.
[132] G. Fang, M. Li, H. Shen, S. Yang, J. Israr, Enhanced photocatalytic characteristics and low selectivity of a novel Z-scheme TiO_2/g-C_3N_4/Bi_2WO_6 heterojunction under visible light, Materials Science in Semiconductor Processing 121 (2021), 105374.
[133] Y. Li, Z. Li, Y. Xia, H. Li, J. Shi, A. Zhang, L. Gao, Fabrication of ternary AgBr/$BiPO_4$/g-C_3N_4 heterostructure with dual Z-scheme and its visible light photocatalytic activity for Reactive Blue 19, Environmental Research 192 (2021), 110260.
[134] L. Zhang, P. Ghimire, J. Phuriragpitikhon, B. Jiang, A.A. Gonçalves, M. Jaroniec, Facile formation of metallic bismuth/bismuth oxide heterojunction on porous carbon with enhanced photocatalytic activity, Journal of colloid and interface science 513 (2018) 82–91.
[135] X. Lu, Y. Jin, X. Zhang, G. Xu, D. Wang, J. Lv, Y. Wu, Controllable synthesis of graphitic C 3 N 4/ultrathin MoS 2 nanosheet hybrid nanostructures with enhanced photocatalytic performance, Dalton Transactions 45 (39) (2016) 15406–15414.

CHAPTER 8

Graphitic carbon nitride-based composites for photocatalytic abatement of emerging pollutants

Shabnam Taghipour[a,b], Behzad Ataie-Ashtiani[a], Seiyed Mossa Hosseini[c], and King Lun Yeung[b,d]

[a]Department of Civil Engineering, Sharif University of Technology, Tehran, Iran
[b]Department of Chemical and Biological Engineering, The Hong Kong University of Science and Technology, Hong Kong
[c]Physical Geography Department, University of Tehran, Tehran, Iran
[d]Division of Environment and Sustainability, The Hong Kong University of Science and Technology, Hong Kong

Contents

1. Introduction

Today's modern society unavoidably relies on enormous energy consumption, which causes the gradual release of various contaminants from countless chemical industries to aquatic and terrestrial environmental and inevitably gives rise to environmental issues [1–9]. The produced wastewater is recognized as a precious resource for reuse after appropriate treatment, especially in water-scarce locations [10]. From 1900 to 1970, the primary goals of water treatment were confined to the following: (1) separation of suspended solids from wastewater, (2) removal of biodegradable compounds and biological oxygen demand (BOD), and (3) treatment of pathogens. Enhancing water quality first gained the attention of officials in the 1970s. From 1970 to 1990, the

Nanostructured Carbon Nitrides for Sustainable Energy and Environmental Applications
https://doi.org/10.1016/B978-0-12-823961-2.00001-X

treatment aims were concentrated on esthetic and environmental issues [11]. Waterborne disease outbreaks (arising from pathogens) endanger human health [12]. Over the past decades, countless scientific articles have reported the existence of unprecedented substances, namely "emerging pollutants," in aquatic environments [13]. Emerging pollutants (EPs) are natural or human-made chemicals that cannot be recognized commonly and are detectable by specific analytical techniques in low concentrations. EPs have raised significant concerns due to their long-term unknown or suspected negative environmental and/or human health consequences [14–16]. These nonregulated organic trace pollutants are continuously produced, consumed, and finally introduced into the environment.

Various physical, chemical, and biological technologies have been utilized for water decontamination. However, most of these methods are time-consuming with low efficiency in the treatment of hazardous pollutants [17–20]. Thus, rapid, sustainable, and cost-effective purification methods are necessary to address this issue as well as water scarcity. Conventional treatment methods suffer from drawbacks such as low removal efficiency, high power consumption, system obstruction and operation, and increment of toxicity level. In addition, considering the high land price, space shortage, and difficulties of chemical management, finding an appropriate method seems essential [21].

Among different water treatment technologies, advanced oxidation processes (AOPs) have exhibited outstanding results for purifying an extensive range of pollutants, e.g., to degrade different toxic compounds such as dyes, pesticides, pharmaceuticals, polycyclic aromatic hydrocarbons (PAHs), heavy metals, etc. [22,23]. This method has also been utilized as pretreatment for diminishing toxic organic compounds in aqueous solutions. Hitherto, several materials have been used in water treatment goals which cover a wide range of material types, including nanomaterials (NMs) from carbonaceous nanostructures (including fullerenes, carbon nanotubes, and graphene), nanoparticles (NPs) (e.g., metal oxides, oxyacids), and nanocomposites to biomaterials and polymeric materials [17,24–33]. Among these materials, carbon nitrides (C_3N_4) have gained great attention because they have turned carbon supplements (in the form of various allotropes with multiple characteristics) into a potential nominate for environmental applications [34].

Accordingly, the main focus of this study was in detail investigation of g-C_3N_4-based composites for photocatalytic degradation of EPs. Different properties of EPs and their adverse effects on human health and the environment are briefly presented. An in-depth description of g-C_3N_4-containing compounds, their origin, and characteristics, as well as adsorption and degradation mechanisms via photocatalytic reactions, are provided. Eventually, the results of several studies for decontamination of EP-containing water and wastewater are evaluated for possible cognizance of current knowledge gaps. So, this alternative water supply can be utilized without human health or environmental risks.

2. Emerging pollutants

The studies proved that dissemination of some EPs has likely occurred for the long term, but their presence has not been identified due to the lack of adequate detection methods. In some other cases, changes in application or discharge of the existing chemicals can cause the generation of new sources of EPs [35]. A major classification of well-known EPs is pharmaceuticals, veterinary products, disinfectants, pesticides, illicit drugs, personal care products (PCPs), surfactants and other industrial chemicals, food additives, water disinfection by-products, and biological toxins [36]. Another classification of EPs is based on their physical/chemical properties as following: (1) organic compounds including persistent bioaccumulative and toxic compounds and polar substances such as pesticides, industrial chemicals, pharmaceuticals, etc., (2) inorganic compounds such as metals, and (3) particulate pollutants (e.g., NPs and microplastics) [37].

Currently, comprehensive analysis and sampling procedures have not been presented by responsible institutions for most of the EP compounds. Therefore, by considering the hazardous threats of these substances, authorities must pay specific attention to industrial discharges and also the elimination of EPs from aquatics for population safety [38].

In general, particular EPs are detected by advanced ultrasensitive tools such as liquid chromatography-tandem mass spectrometry (LC-MS/MS), gas chromatography-mass spectrometry (GC-MS), and high-resolution accurate-mass spectrometry (HRAM) [39]. In different cases, mass analyzers, including time-of-flight (TOF), quadrupole, triple quadrupole (QqQ), ion traps mass spectrometry (ITMS) can be coupled to GC and/or LC. The involved factors in the application of these analyzers are resolution, the intended mass range, and available characteristics [40]. Utilization of such technologies can cause a simple sample preparation, the possibility of simultaneous assessment of manifold EP samples, and enhancement of detection limits. Despite the high price, these instruments provide a precise quantitative amount of EPs in the suspended matter, aqueous solution, and soil [14].

3. Photocatalytic reactions as advanced oxidation processes

The main aim of using AOPs is in-situ production of highly reactive oxygen species (ROS) and free radicals with at least one unpaired electron, such as hydroxyl radical ($^{\bullet}OH$, $E_0 = 2.80\,eV$), ozone (O_3, $E_0 = 2.08\,eV$), hydrogen peroxide (H_2O_2, $E_0 = 1.76\,eV$), hydroperoxyl radical ($^{\bullet}HO_2$, $E_0 = 1.44\,eV$ in weak acidic solution and $E_0 = 1.65\,eV$ in strong acidic solution), and superoxide anion radical ($^{\bullet}O_2^-$) for complete mineralization of contaminants to H_2O, CO_2, and inorganic ions or acids [41]. Owing to unique features including nonselective nature, high reactivity, and strong oxidation ability, hydroxyl radicals have attracted considerable attention among other oxidizing agents [42]. The $^{\bullet}OH$ radicals can attack and degrade a wide variety of organic pollutants in aqueous solutions with reaction rate constants in the range of 10^6–$10^9\,M^{-1}\,s^{-1}$ [43].

Studies reported that the reaction mechanisms of almost all AOPs for the participation of $^{\bullet}OH$ are similar [44]. Depending on the essence of the target substance, degradation by $^{\bullet}OH$ radicals can conform to one of the following three mechanisms:

1. If the target compound contains C—H bonds such as alkanes (R), the degradation mechanism will be based on the dehydrogenation or extraction of a hydrogen atom for the generation of the water molecule. The resultant radical $^{\bullet}R$ can contribute to the generation of peroxyl radical ($^{\bullet}ROO$) and subsequently mineralization of pollutants by oxidation reactions (Eqs. 8.1 and 8.2) [45]:

$$RH + {}^{\bullet}OH \rightarrow H_2O + {}^{\bullet}R \tag{8.1}$$

$$^{\bullet}R + O_2 \rightarrow {}^{\bullet}ROO \tag{8.2}$$

2. If the target compound contains aromatic or aliphatic compounds (Ar), the invasion of $^{\bullet}OH$ radicals will cause hydroxylation of target organic substances in the high electron-density zones and increase in the unsaturated bonds and onset of oxidation reactions (Eqs. 8.3–8.6) [46]:

$$^{\bullet}ROO + n({}^{\bullet}OH/O_2) \rightarrow xCO_2 + yH_2O \tag{8.3}$$

$$ArH + OH \rightarrow ArH(OH) \tag{8.4}$$

$$ArH(OH) + O_2 \rightarrow [ArH(OH)OO] \tag{8.5}$$

$$[ArH(OH)OO] \rightarrow ArH(OH) + HO_2 \tag{8.6}$$

3. Oxidation/reduction reactions which will cause charge transfer and consequently ionization of the target molecule (Eq. 8.7) [47]:

$$OH + RX \rightarrow {}^{\bullet}RX + OH^{-} \tag{8.7}$$

Based on the type of activation, AOPs are categorized into nonphotochemical (thermal) and photochemical processes. Nonphotochemical processes include Fenton, ozonation, electrochemical oxidation, ultrasound, and sonolysis, while photochemical processes include radiation, photo-Fenton, and photocatalysis [48]. Photocatalysis, as a feasible and green technology, attained growing attention after the early development of this technology by Fujishima and Honda for the application of TiO_2 in water splitting under solar light [49]. Later on, this technology found extensive application in numerous energy production and environmental purification due to easiness of operation and low time consumption [50].

In photocatalysis technology, photochemical reactions are speed up by utilization of an activated semiconductor by receiving energy equal to or more than its bandgap and absorption of photons [51,52]. If electron carriers recombine, no oxidation and/or reduction will occur on the surface or bulk of the catalyst causing aggravation in photodegradation efficiency [53]. A successful photocatalytic reaction consists of a few steps, including accumulation of contaminants near the surface of the photocatalyst, adsorption of contaminants on the surface of the photocatalyst, photoactivation and photodegradation of the adsorbed molecules, desorption of the reaction products, and elimination of the products from the surface [54].

In other words, electrons will migrate from the valence band (VB) to the conduction band (CB), and hole/electron (h^+/e^-) pairs will be generated on the surface of the semiconductor, which will participate in the degradation of pollutants (Eq. 8.8) [55]. The superoxide radical anion is the product of the reaction of an electron acceptor such as oxygen molecule and electron (e^-) (Eq. 8.9). On the other hand, hydroxyl radical is the product of the reaction of holes (h^+) and OH^- and H_2O (Eqs. 8.10 and 8.11, respectively) on the semiconductor's surface [56]. The produced hydroxyl radicals can contribute to the oxidization of organic substances to water, carbon dioxide, and inorganic ions (Eq. 8.12) [57].

$$\text{Semiconductor} + h\nu \rightarrow {e^-}_{CB} + {h^+}_{VB} \tag{8.8}$$

$${e^-}_{CB} + O_2 \rightarrow {}^{\bullet}{O_2}^- \tag{8.9}$$

$${h^+}_{VB} + OH^- \rightarrow {}^{\bullet}OH \tag{8.10}$$

$${h^+}_{VB} + H_2O \rightarrow H^+ + {}^{\bullet}OH \tag{8.11}$$

$$R - H + {}^{\bullet}OH \rightarrow {}^{\bullet}R' \rightarrow H_2O + CO_2 + \text{inorganic ions} \tag{8.12}$$

4. Graphitic-C_3N_4

The polymeric C_3N_4 is one of the oldest organic conjugated substances, and first discovered in 1834 by Berzelius and named "melon." The initial studies about C_3N_4 were concentrated on the synthesization of a stoichiometric C_3N_4 phase with an extremely stiff material by Liu and Cohen [58]. More attention was drawn to CNs after the prediction of β-C_3N_4 in 1989 [59]. Other anticipated phases of C_3N_4 are α-C_3N_4, cubic-C_3N_4, pseudocubic-C_3N_4, and graphitic-C_3N_4 (g-C_3N_4) [60]. g-C_3N_4 was first figured out in 1922 by the thermal decomposition of $Hg(SCN)_2$ by Franklin. As the most stable allotropes of CNs in ambient conditions, the polymeric g-C_3N_4 is attracting more and more attention of researchers to conduct a considerable number of studies about synthesization of g-C_3N_4-based composites for pollution abatement [61]. The statistical results of the publication trend about this material are presented in Fig. 8.1. People's Republic of China, India, United States, Germany, Australia, South Korea, Japan, Iran, Saudi Arabia, and England are the top 10 countries in studying photocatalytic applications of g-C_3N_4, respectively (Fig. 8.1A). As can be seen, the attention has drawn to this material so that only 25 publications in 2000 have exhibited a gradual increase and have reached 1863 in 2019 (Fig. 8.1B). Further, analyzing the context of reports revealed that these studies are mostly

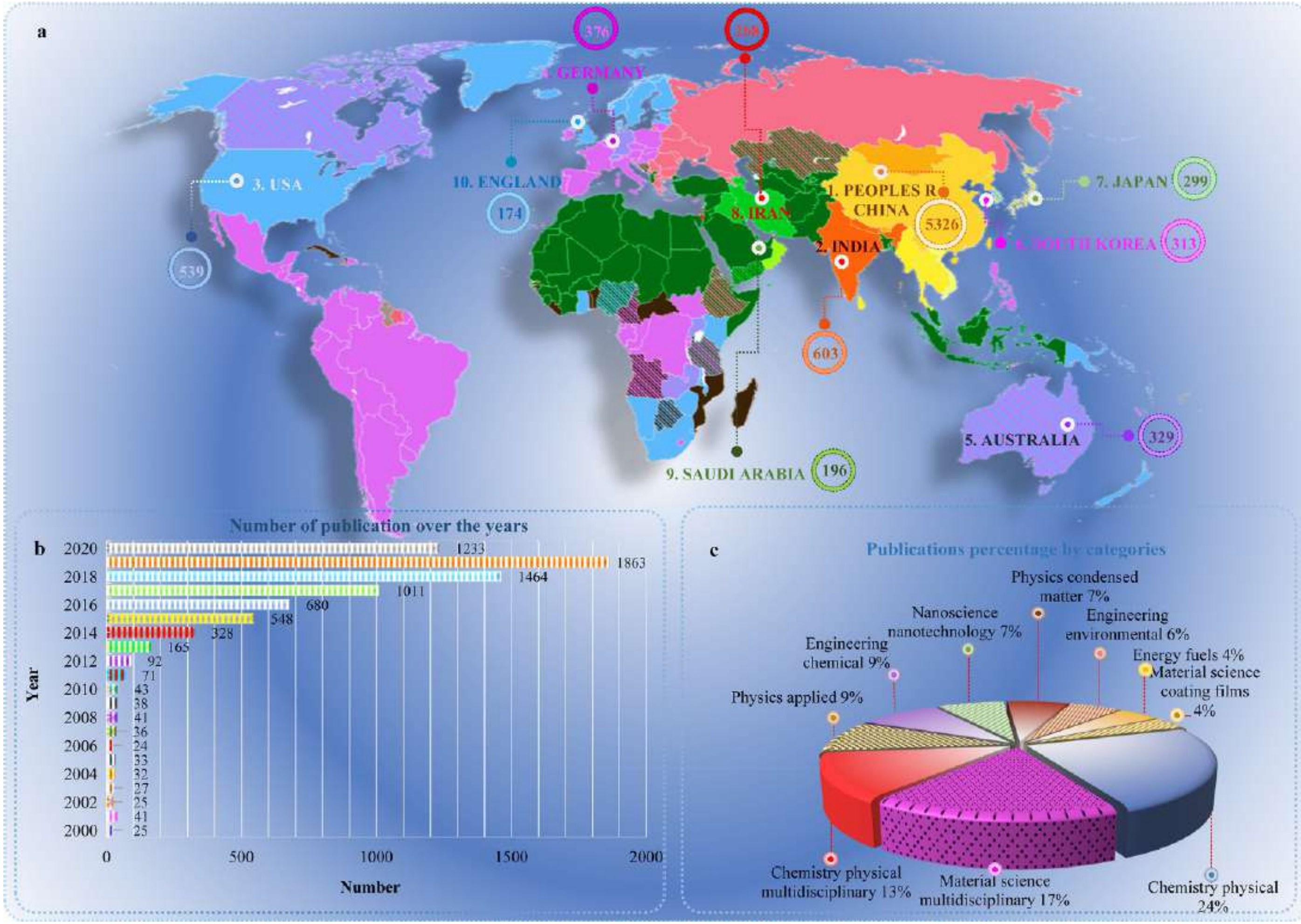

Fig. 8.1 Worldwide academic tendency to the photocatalytic application of g-C_3N_4 in case of selecting keywords: "g-C_3N_4," "graphitic carbon nitride," and "photocataly" in all databases of the Web of Science. (A) The top 10 paper publishing countries since 2000. The circles are related to the number of articles published by the country in the mentioned fields, (B) the gradual increase in publication trend of g-C_3N_4 in the world since 2000, and (C) the top 10 categories in the photocatalytic application of g-C_3N_4 and their contribution percentage compared to each other (July 25, 2020) [62–64].

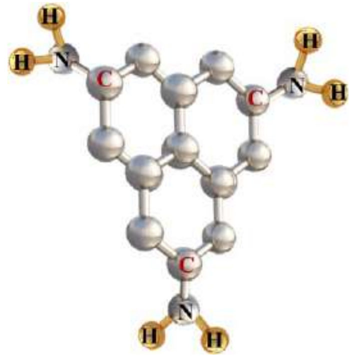

Fig. 8.2 Schematic diagram of g-C_3N_4.

in the following categories: chemistry, physics, material science, applied physics, chemical engineering, nanoscience and nanotechnology, condensed matter physics, environmental engineering, energy fuels, and material science coating films, respectively (Fig. 8.1C).

This novel metal-free semiconductor has a moderate bandgap of 2.7 eV. The monolayer π-conjugated structure of g-C_3N_4 has caused optical properties of this material, which has exhibited exemplary responsiveness to visible light due to the existence of nitrogen and sp^2-hybridized carbon at absorption edge around 460 nm [65,66]. A schematic structure of g-C_3N_4 is illustrated in Fig. 8.2. Nitrogen atoms are responsible for the π-π interaction among the neighbored layers and hamper electrons migration from one heptazine unit to another. As a result, the recombination rate of the bulk g-C_3N_4 can significantly reduce [67].

Due to considerable features such as proper and tunable conduction and valence band (1.1 and 1.6 eV vs the normal hydrogen electrode, respectively), high thermal and chemical tolerance, high stability in wide pH ranges, facile preparation, nontoxic and eco-friendly nature, biocompatibility, abundance, and low cost, g-C_3N_4 have been widely utilized in several applications such as water splitting, reducing CO_2, and contaminant degradation from aqueous solutions [12,50,68,69].

5. Different morphologies of g-C_3N_4

The dimension of g-C_3N_4 can be adjusted by differing the synthesis parameters. Researchers have conducted various modifications for the production of different dimensionalities of graphitic carbon nitride, including zero-dimensional quantum dot, one-dimensional micronanotube, micronanowire, and micronanorod, two-dimensional nanosheet (NS) and film, and three-dimensional bulk form (Fig. 8.3) [59]. 0D and 2D g-C_3N_4 can be transformed into 1D g-C_3N_4 via specific treatments. A brief description of these materials is provided in the following.

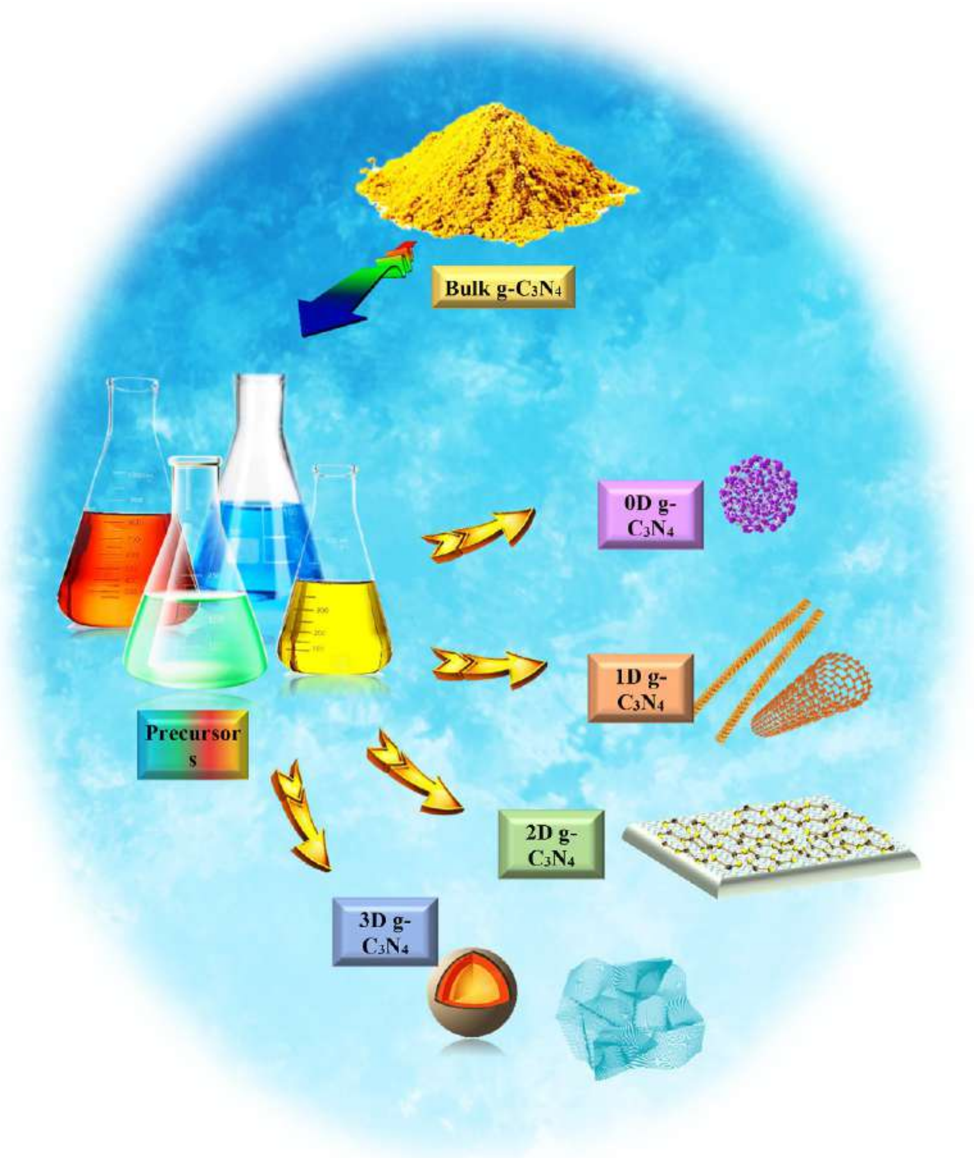

Fig. 8.3 Various dimensionalities of g-C_3N_4 which could be produced by utilizing diverse precursors and synthesization methods.

5.1 0D g-C_3N_4

In zero-dimensional g-C_3N_4 (also known as g-C_3N_4 quantum dots, CNQDs), electron/holes cannot move freely. Special attention has been drawn to this material due to owning significant properties, such as solubility in water, appropriate photoexcited electron transfer, inexpensiveness, nontoxicity, efficient upconversion features, size efficacy, and photochemical resistance [70].

Owing to these exemplary features, tremendous growth has occurred in the number of studies about photocatalytic application of CNQDs from 2014 to 2020 (Fig. 8.4). The statistical results obtained from Web of Science databases included "g-C_3N_4," "graphitic carbon nitride," and "g-C_3N_4 quantum dot" (or CNQD, g-C_3N_4/quantum dot, 0D g-C_3N_4, zero dimensional g-C_3N_4) as keywords.

CNQDs with an average size <10 nm have been fabricated by several methods such as solvothermal [72], hydrothermal [73], ultrasonic-assisted method [74], thermal polymerization [75], sol-gel [76], electrostatic self-assembly strategy [77], etc.

5.2 1D g-C_3N_4

As another morphology, one-dimensional g-C_3N_4 (1D g-C_3N_4) has gained considerable attention and prominence in academia for its remarkable optical and electrochemical properties (Fig. 8.5) [78]. These properties could be optimized for appropriate photoexcitation by adjusting parameters such as length, diameter, and aspect ratio (length: diameter) [79]. Compared to bulk g-C_3N_4, micronanorod C_3N_4 has shown higher photocatalytic efficiency. Utilization of physical approaches for their thermal, mechanical, ultrasonic, and high-pressure effects and chemical effects could result in compression of bulk g-C_3N_4 and fabrication of 1D structure [59]. One-dimensional g-C_3N_4 in which the electrons can be transferred in one direction have been synthesized by the template-

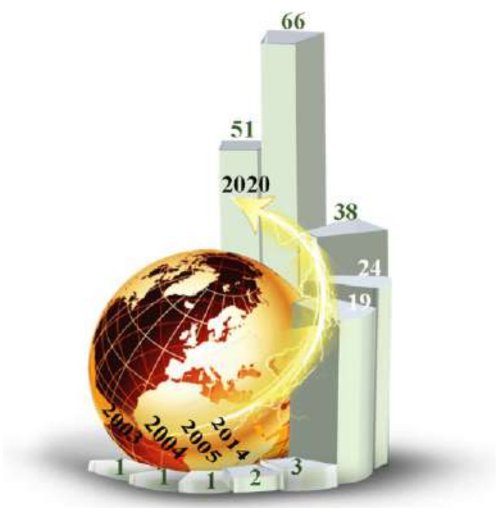

Fig. 8.4 Worldwide publication trend about g-C_3N_4 quantum dots from the first publication date so far (2003 – 20) in terms of the keywords including "g-C_3N_4," "graphitic carbon nitride," "photocataly," and "g-C_3N_4 quantum dot" (or CNQD, g-C_3N_4/quantum dot, 0D g-C_3N_4, zero dimensional g-C_3N_4) in all databases of the Web of Science (July 29, 2020) [71].

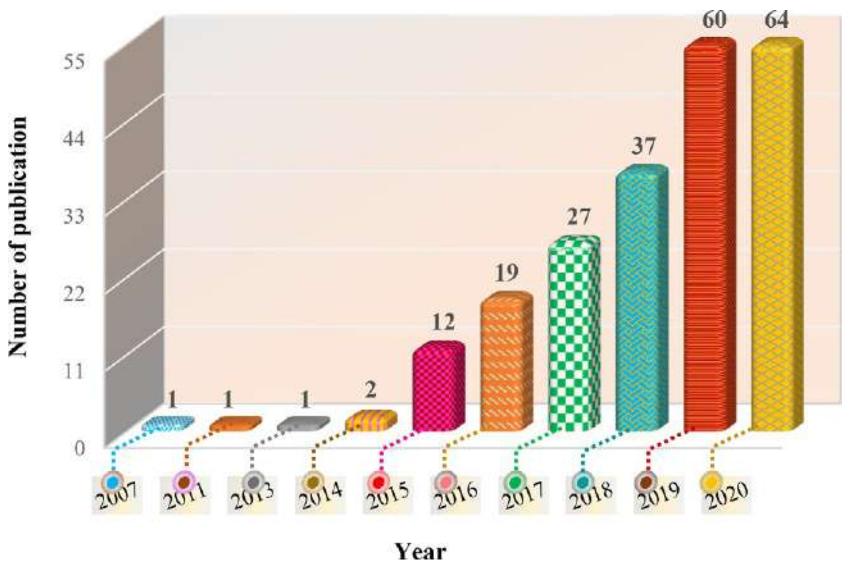

Fig. 8.5 Worldwide publication trend about 1D g-C_3N_4 in the case of the keywords: "g-C_3N_4," "graphitic carbon nitride," "photocataly," and "one dimensional g-C_3N_4" (or 1D g-C_3N_4, g-C_3N_4 wire, g-C_3N_4 rod, g-C_3N_4 tube) in all databases of the Web of Science (July 29, 2020) [85].

assisted method [80], CVD [81], thermal polymerization [82], ionic liquid promoted method [83], nanocasting technique [84], etc.

5.3 2D g-C_3N_4

Tremendous research effort has been dedicated to two-dimensional g-C_3N_4 nanosheets and films (Fig. 8.6) due to their excellent features such as great length to width, extensive surface area, ultrathin thickness, large surface anchoring groups for cocatalysts, and advanced pillared structure [86]. The interactions between 2D g-C_3N_4 NS and other coupled 2D semiconductors have superlative prominence in extending heterojunction interfaces to ease and prolong the lifetime of e^-/h^+ and finally lead to successful catalytic applications. Moreover, achieving an inexpensive and easily accessible metal-free 2D/2D g-C_3N_4-based photocatalyst will reduce costs for application on large scales [87]. Several methods such as calcination method [88], thermal vapor condensation [89], solvothermal route [90], spray coating [91], ultrasonication [92] are among the bottom-up approaches for NM fabrication. The utilization of bottom-up approaches for synthesization of g-C_3N_4 films can prevent aggregations and formation of cracks and consequently lead to the production of uniform structure, persistent coating, and well contact with the substrate [93].

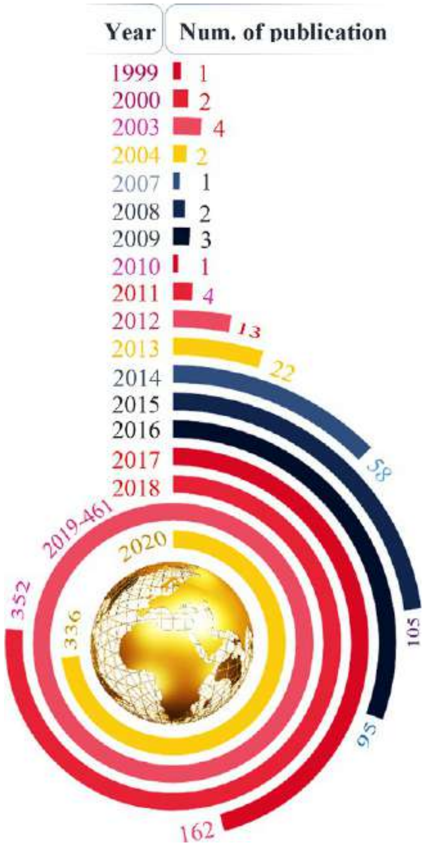

Fig. 8.6 Proceeding in publication number about 2D g-C_3N_4 since 2007 in the world considering the keywords: "g-C_3N_4," "graphitic carbon nitride," "photocataly," and "two dimensional g-C_3N_4" (or 2D g-C_3N_4, g-C_3N_4 film, g-C_3N_4 sheet) in all databases of the Web of Science (July 29, 2020) [94].

5.4 3D g-C_3N_4

Three-dimensional g-C_3N_4 (3D g-C_3N_4) benefits from higher Brunauer-Emmett-Teller (BET) surface area compared to other morphologies of g-C_3N_4, which can significantly enhance required active sites for surface reactions by light-harvesting and consequently more appropriate performance in adsorption [95]. In other words, 3D g-C_3N offers facile interfacial transport, straightforward diffusion path, and easily accessible dispersion of active sites with different dimensions [96]. These advantages have attracted the increasing attention of scientists over the years (Fig. 8.7) [97].

Fig. 8.7 Number of publication about 3D g-C_3N_4 in the world since the first publishing in terms of the keywords: "g-C_3N_4," "graphitic carbon nitride," "photocataly," and "three dimensional g-C_3N_4" (or 3D g-C_3N_4) in all databases of the Web of Science (July 29, 2020) [97].

6. Synthesis methods of g-C_3N_4 for water purification

Graphitic carbon nitride has been successfully fabricated by inexpensive N-rich feedstocks such as cyanamide (CH_2N_2) [98], urea (CH_4N_2O) [99], melamine ($C_3H_6N_6$) [100], thiourea (CH_4N_2S) [101], guanidinium chloride (CH_6ClN_3) [102], dicyandiamide ($C_2H_4N_4$), and so on [103,104]. Studies revealed that various feedstocks and treatment methods could strenuously affect the physical and chemical features of the obtained graphitic-C_3N_4, such as structure, porosity, surface area, absorption capacity, photoluminescence, and C/N ratio [65]. The presence of g-C_3N_4 is typically affirmed by instruments such as X-ray powder diffraction (XRD), Fourier transforms infrared spectroscopy (FTIR), X-ray photoelectron spectroscopy (XPS), UV-vis diffuse reflectance spectra (DRS/UV-vis), and high-resolution transmission electron microscopy (HRTEM) [105–107]. The VB and CB are usually identified by density function theory (DFT) calculations [108].

The effect of reaction parameters such as temperature, reaction time on physicochemical characterization of g-C_3N_4 is reported in several studies. For instance, Yan et al. reported an increase in C/N ratio from 0.721 to 0.742 after increasing calcination temperature from 500°C to 580°C, respectively. More investigations revealed a decrement in the band gap from 2.8 to 2.75 eV. The precursor in this study was melamine [109]. In another study, Hollmann et al. fabricated carbon nitride via sol-gel method using melamine as the precursor. Increasing the pyrolysis temperature from 450°C to 600°C resulted in facile charge separation, which was proved by the utilization of electron paramagnetic resonance (EPR) method [110]. To investigate the influence of pyrolysis duration on the physicochemical properties of the g-C_3N_4 (urea as the precursor) at constant temperature (550°C), Dong et al. extended reaction time from 0 to 240 min. They observed a significant increase in surface area from 31 to 288 m^2/g, which resulted from increased porosity and decreased layer thickness from 36 to 16 nm [111]. Mao et al. utilized urea and melamine as precursors to produce u-g-C_3N_4 and m-g-C_3N_4,respectively, at 580°C. After 3 h, surface studies demonstrated mesoporous flakes and nonporous flaky structures for u-g-C_3N_4 and m-g-C_3N_4, respectively. The u-g-C_3N_4 product exhibited more surface area (39.5 m^2/g) than m-g-C_3N_4 (3.7 m^2/g). In addition, u-g-C_3N_4 represented higher photoactivity (in terms of quantum efficiency) compared to m-g-C_3N_4 (0.18% vs 0.08%) for CO_2 reduction [112].

The low crystallinity and high disorder of typically prepared g-C_3N_4 are indescribable. The fabrication of g-C_3N_4 with high crystallinity is not simple [61]. These disorders operate as recombination zones and can enhance electrical conductivity, visible light absorption efficiency, and, consequently, expand this material's photocatalytic applications [113].

The synthesis method has a crucial effect on the physicochemical specifications and photocatalytic proficiency of the resultant photocatalyst. The most utilized synthesis methods for fabrication of g-C_3N_4 are sol-gel, thermal polycondensation, ultrasound, chemical vapor deposition (CVD), ionothermal, solvothermal reactions, and template-assisted methods [102,114,115]. These methods are briefly described in the following.

The sol-gel method (or chemical solution deposition) is a wet-chemical technology. The primary presentation of the sol-gel notion was by Ebelmen in 1845 [116]. In this method, a chemical solution (sol) operates as a precursor for an integrated network (gel) of separate particles or polymeric lattices and has extensively been engaged in the materials sciences field (especially for fabrication of metal oxides) [117]. The sol-gel technique is carried out in multiple stages, including (1) hydrolysis and condensation of precursor to generate a clear colloidal solution, (2) condensation of solution particles to form a 3D lattice product over time and after drying [118]. The thermal polycondensation is a typical polymer-formation process that connects monomers, which could lead to byproducts removal [119]. In ultrasound technique, the interaction of waves and gas bubbles inside the solution leads to the generation of chemical reactions and powerful physical force (namely acoustic cavitation) for appropriate conduction of chemical reactions via generation of extremely high pressure and temperature [120]. The resultants are the production of radicals, shock wave, shear force, turbulence, jets, and light emission-sonoluminescence, which could be utilized for water and wastewater treatment and the generation of protein bubbles for drug delivery [121]. Chemical vapor deposition (CVD) refers to the growth of solid material due to the reaction of gaseous source substances and resulting in the production of gaseous effluent [122]. Ionothermal method is defined as the fabrication of solids by simultaneous utilization of ionic liquids where the leading agents are the solvent and the template [123]. Solvothermal technique refers to the conduction of chemical reactions in a closed reaction vessel containing solvent and precursors with pressures more than 1 bar and temperature more than the solvent's boiling point [124]. Template assisted is a procedure for deposition of various materials in or on the templates to generate a multilayer structure. The application of a free-standing template enables the researchers to repeatedly utilize one template for several oxide systems regardless of their composition or preparation method of the solution in the beginning [125,126] (Table 8.1).

7. Defects of g-C_3N_4

The performance of g-C_3N_4 strongly depends on two principal parameters: (1) the surface condition including functional groups, defects, and doping, and (2) the structural condition including thickness, porosity, and morphology of g-C_3N_4 [65]. Besides, all preponderances, graphitic carbon nitride suffers from shortcomings such as high recombination rate due to poor van der Waals force among adjacent CN layers, narrow absorption at visible light region (beyond 470 nm), poor quantum yield, and low specific surface area [137]. These drawbacks significantly restrict extensive photocatalytic activity and also practical applications of pure g-C_3N_4. Thus, researchers have offered numerous strategies for enhancing the photoactivity of this material.

8. Methods to minimize defects

Diverse approaches have been applied to enhance the photocatalytic capability of g-C_3N_4. Nonmetal-ion and metal-ion doping, noble metal loading, passivation layer deposition, morphology control, fabrication of heterojunction compounds, application of suitable organic dyes as sensitizers, and metal-free hybridization are among the most applicated strategies [138]. The presence of nitrogen with six lone-pair electrons in the molecular structure of g-C_3N_4 predispose this material to metal acceptance (e.g., Co, Fe, Cu, and Pb), and as a result, electrons can be doped to g-C_3N_4 semiconductor [139]. Generation of impurity level (energy level) in the forbidden bandgap can effectively reduce the bandgap energy and recombination rate by creating traps for e^-/h^+ [140]. In the nonmetal-ion doping strategy, reduction of band gap energy occurs through upshifting the VB edge with less formation possibility of donor levels and recombination centers in the forbidden band [141]. So far several nonmetal ions such as bromine [142], boron and sulfur [143], phosphorus [144], fluorine [145], oxygen [146], nitrogen [147], and iodine [148] have been doped with g-C_3N_4. The usage of transition metals as dopants along with g-C_3N_4 leads to the generation of an acceptor level under the main CB or donor level beyond the main VB. Considering that noble metals have a smaller Fermi level than g-C_3N_4, the migration of the photoexcited e^- from CB to the deposited metal on the photocatalyst's surface will happen. This will occur while the work function of the metallic NPs has enough in accordance with the semiconductor's CB [149]. In the following, the generated h^+ will migrate to the surface of the photocatalyst. It is noteworthy that the surface plasmon resonance (SPR) of noble metals can sufficiently enhance solar energy absorption [150]. Various

Table 8.1 Synthesization method of various g-C_3N_4 contained composites, the reaction rate constant, and the associated species in photocatalytic degradation of emerging pollutants.

Composite	Synthesization method	Pollutant	Reactive species	Reaction rate constant	References
GO/g-C_3N_4/MoS_2	Solvothermal	Crystal violet	Holes (h^+)	$0.0123\ min^{-1}$	[127]
B@C_3N_4/$LiFePO_4$/$CuFe_2O_4$	In-situ deposition	Atenolol	$^{\bullet}O_2^-$ and $^{\bullet}OH$	$0.0712\ min^{-1}$	[128]
AgI/g-C_3N_4	Deposition-precipitation	Diclofenac	h^+ and $^{\bullet}O_2^-$	$0.561\ min^{-1}$	[129]
CdS/g-C_3N_4	Ultrasonication	Metronidazole	Holes (h^+)	–	[130]
N-doped carbon dots/ g-C_3N_4	Polymerization	Indomethacin	h^+ and $^{\bullet}O_2^-$	$0.0272\ min^{-1}$	[131]
g-C_3N_4/RGO/Bi_2WO_6	Hydrothermal	2,4,6-Trichlorophenol	Holes (h^+)	$0.003\ min^{-1}$	[132]
MoS_2/g-C_3N_4-PANI polymer	Sonochemical	Bisphenol-A	$^{\bullet}O_2^-$ and $^{\bullet}OH$	$0.0395\ min^{-1}$	[133]
Attapulgite/Cu_2O/Cu/ g-C_3N_4	One-pot redox strategy under anoxic calcination	Chloramphenicol	h^+ and $^{\bullet}OH$	–	[134]
g-C_3N_4/N-doped CeO_2	Thermal oxidation	Diuron	$^{\bullet}O_2^-$	$0.0047\ min^{-1}$	[135]
g-C_3N_4/TiO_2 (P25)	Hydrothermal-calcination	Clofibric acid	$^{\bullet}OH$	$(8.47 \pm 0.33) \times 10^9\ M^{-1}\ s^{-1}$	[136]

transition metals, including Fe, Ni [151], Co [152], Mn [153], Sc, V, Cr [154], Ag, Pt, and Au [155] are some of the doped metals along with g-C_3N_4.

Passivation layer deposition is another beneficial approach for efficacious charge transfer through the liquid and semiconductor interface. These narrow layers (<100 nm, mostly 1–2 nm) have several privileges such as diminishing recombination rate at surface state, lowering corrosion of the semiconductor, inclusion in NMs with high aspect ratio and surface areas, and enhancing the stability and oxidation reaction kinetics in aqueous solutions [156]. Therefore by passivation, layers become less affected by the surrounding environment. These kind of deposited layers can be constructed by atomic layer deposition [157,158], electron beam evaporation [159,160], spin-coating [161,162], electrochemical deposition [163,164], sputtering [165], dip-coating [166,167], and floating transfer [168,169].

Morphology control can improve the material's specific surface area and lead to the formation of ultra-thin NSs, hollow bubbles, and tubular nanostructures [170,171]. Designing reactions, controlling temperatures, selecting appropriate solvents, etc., are among the main activities in synthesizing materials with special shapes [172].

Fabrication of heterojunction semiconductors incorporates the stacking up of multiple semiconductors with distinct band gaps [173]. The precondition is the corrosion resistance and presence of these narrow and unequal band gaps in the visible region. Furthermore, by considering momentum, the direct bandgap (in which the greatest energy level of the VB equals the minimum energy level of the CB) is more favorable than the indirect bandgap [174].

The application of dyes as sensitizers on g-C_3N_4 is an advantageous strategy to capture energy at longer wavelengths [175]. For as much as organic dyes can be synthesized, they own proper CB and tunable absorption range. While the CB of g-C_3N_4 is lower and higher than the LUMO and HOMO value of dyes, respectively, the absorption region of the produced material will be remarkably enhanced [176]. As a result, the number of photoexcited electrons from the LUMO to the CB of g-C_3N_4 and consequently, the recombination rate of e^-/h^+ will be increased and decreased, respectively.

Metal-free hybridization refers to employment of carbonaceous structures (e.g., graphene oxide [177], graphene quantum dot [178], carbon spheres [179], etc.), polymeric materials (e.g., poly(indenofluorene) [180], polyaniline [181], poly(ethylene terephthalate) [182], poly(3-hexylthiophene) [183], etc.), and other metal free compounds (e.g., melem [184], g-C_3N_4 itself [185]) for modification of g-C_3N_4.

9. Photocatalytic applications of g-C_3N_4

Due to marvelous properties and capabilities, g-C_3N_4 is considered as a promising metal-free semiconductor photocatalyst, which could serve humanity and diminish the negative effects of environmental contaminants by the degradation of organic pollutants and reducing the CO_2 concentration by transformation to renewable fuels and other valuable substances [186,187]. Moreover, this valuable component has demonstrated a significant potential and flexibility in NO_x conversion [188], nitrogen fixation [189], water splitting, bacteria disinfection, reduction of heavy metals, and more important, in photodegradation of antibiotics and other emerging pollutants [190]. A detailed description of the applications of g-C_3N_4 in the photocatalytic abatement of emerging pollutants will be presented in the following section.

Polymeric g-C_3N_4 semiconductors are extensively utilized as catalysts due to their considerable chemical endurance and unique electronic band structure [191]. da Silva et al. [192] prepared g-C_3N_4/Nb_2O_5 semiconductor for photodegradation of 10 mg/L amiloride drug (AML) under visible-light irradiation (six 15 W fluorescent lamps). The g-C_3N_4 was prepared by urea feedstock, and the heterostructure was fabricated by a sonochemical process with different weight ratios of g-C_3N_4 and Nb_2O_5 (1:3, 1:1, and 3:1). To evaluate the adsorption/desorption equilibrium, the samples were kept in the darkness, and after 12 h, the adsorption capability of pollutants in all samples was less than 5%. Under direct photolysis (without any catalysts), no degradation was observed after 180 min. In the presence of 10 mg g-C_3N_4/Nb_2O_5, the 1CN:3Nb sample appropriated the highest photoactivity (Fig. 8.8), specific surface area (133.9 m^2/g), and apparent rate constant ($k_{app} = 13.7 \times 10^{-3}$ min^{-1}) which was ascribed to the generation of efficient heterojunction interfaces between g-C_3N_4 and Nb_2O_5 and the surface acidity difference of the semiconductor and AML. All samples with different weight ratios had

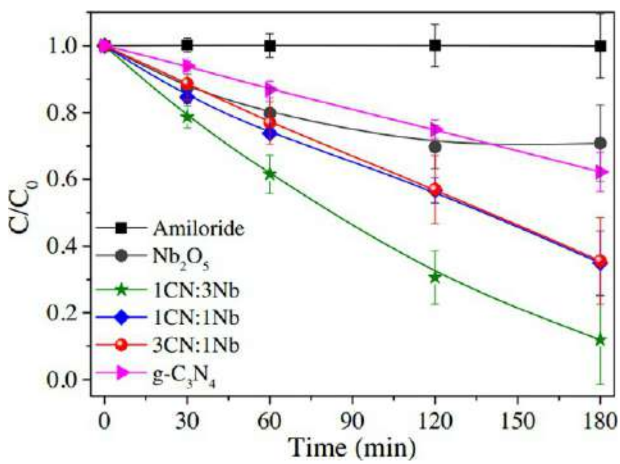

Fig. 8.8 Photodegradation of amiloride by various amount of g-C_3N_4/Nb_2O_5 (CAML = 10 mg/L, Cheterostructure = 500 mg/L). *(Adapted from G.T.S.T. da Silva, K.T.G. Carvalho, O.F. Lopes, C. Ribeiro, g-C_3N_4/Nb_2O_5 heterostructures tailored by sonochemical synthesis: enhanced photocatalytic performance in oxidation of emerging pollutants driven by visible radiation, Appl. Catal. B Environ. 216 (2017) 70–79, https://doi.org/10.1016/j.apcatb.2017.05.038.)*

the same bandgap value of g-C_3N_4 (2.8 eV), illustrating the optical conquest of g-C_3N_4 to Nb_2O_5 [192].

Dong et al. [193] investigated the purification of carbamazepine-contaminated water by 100 mg/L imidazole-modified g-C_3N_4-iron phthalocyanine ($FePcCl_{16}$) in the presence of peroxymonosulfate (PMS). Optimization was conducted by altering parameters such as the amount of $FePcCl_{16}$ (0%, 2%, 5%, and 8%), pH (3, 5, 7, and 9), presence of 10 mM of each of miscellaneous anions ($H_2PO_2^-$, HCO_3^-, SO_4^{2-}, NO_3^-), and effect of NaCl (0–30 mM). Increasing the Cl^- content from 0 to 30 mM (by adding NaCl) led to a doubling reaction rate constant (from 0.108 to 0.218) and complete degradation of carbamazepine (CBZ) by producing $Cl^{\bullet}$ radical and active chlorine species HOCl/Cl_2 (Fig. 8.9A). Adding 10 mM HCO_3^- and H_2PO_2 plays a preventive role in the

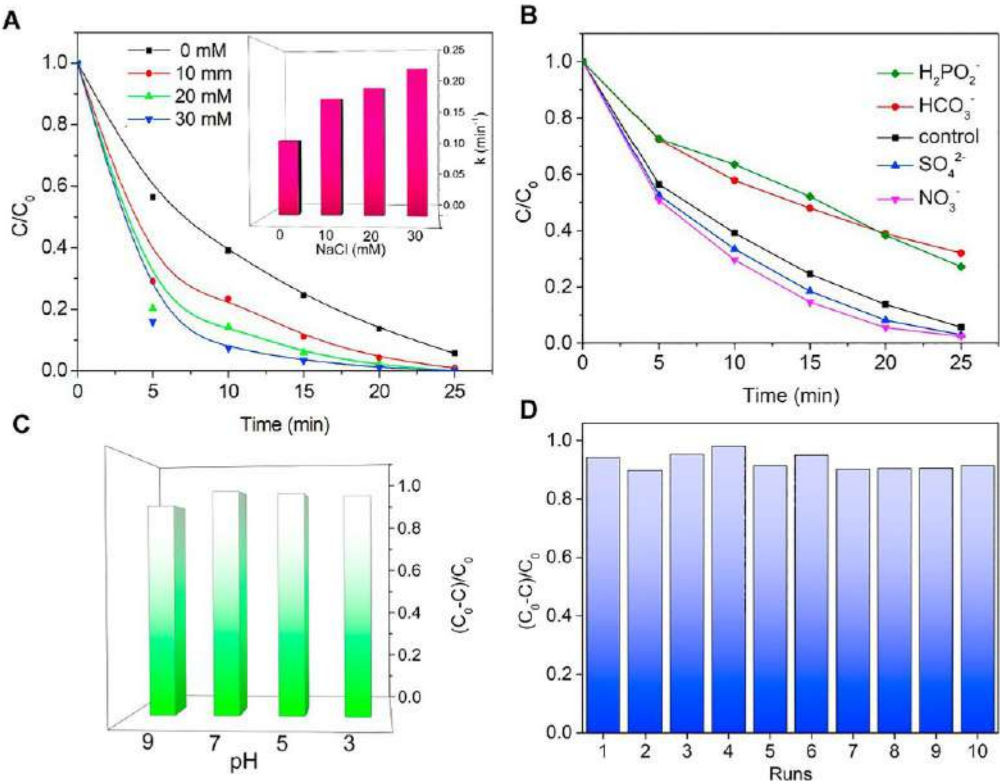

Fig. 8.9 The photocatalytic performance of g-C_3N_4-IMA-FePcCl16 visible light region in (A) the presence of various NaCl concentration, (B) the presence of miscellaneous anions (10 mM of each of which), (C) variation of pH, and (D) cyclic experiments (CCBZ = 25 μM, Cphotocatalyst = 100 mg/L, CPMS = 0.3 mM, $\lambda > 420$ nm, optimum pH = 7). *(Adapted from L. Dong, T. Xu, W. Chen, W. Lu, Synergistic multiple active species for the photocatalytic degradation of contaminants by imidazole-modified g-C_3N_4 coordination with iron phthalocyanine in the presence of peroxymonosulfate, Chem. Eng. J. 357 (2019) 198–208, doi:https://doi.org/10.1016/j.cej.2018.09.094.)*

degradation of CBZ due to their competition with PMS for adsorption of UV irradiation and reactive radicals (Fig. 8.9B). In contrast, SO_4^{2-} and NO_3^- positively affected the removal efficiency. The application of 0.3 mM PMS g-C_3N_4-IMA-$FePcCl_{16}$ illustrated superb photocatalytic degradation (~95% within 25 min) of 25 μM CBZ over a wide pH range (Fig. 8.9C). Cyclic experiments (up to 10-fold) proved that the material is reusable and applicable on large scales (Fig. 8.9D) [193].

Lakshmi Prabavathi et al. [194] synthesized $MnWO_4$@g-C_3N_4 nanocomposite by hydrothermal followed by ultrasonication method for photodegradation of ofloxacin (OFX). Several parameters, for instance, concentration of photocatalyst (10, 30, 50, and 70 mg/L), the dosage of OFX (10, 20, and 30 mg/L), and the existence of inorganic anions (e.g., 0.1 M of Cl^-, CO_3^{2-} and SO_4^{2-}) were evaluated in photocatalytic efficiency of the fabricated nanocomposite. The nanocomposite exhibited 3.5 and 4.8 times greater first-order reaction rate constant than that of pristine g-C_3N_4 (0.0095 min^{-1}) and $MnWO_4$ (0.0071 min^{-1}), respectively. By anchoring $MnWO_4$ nanorods on the g-C_3N_4 NSs, the computed energy band gaps of $MnWO_4$ (2.1 eV) and g-C_3N_4 (2.7 eV) changed to 2.58 eV, which clearly demonstrated narrower band gap and consequently enhancement in photoresponse in the visible region. At the optimum dosage of the nanocomposite and pollutant (50 and 10 mg/L, respectively) and among various contents of $MnWO_4$ and g-C_3N_4, the MnWO4@g-C_3N_4 (1:1) nanocomposite represented supreme performance (90.4%) in degradation of OFX. Results indicated that lower loading of g-C_3N_4 has led to a decrease in the removal efficiency which was ascribed to the insufficient formation of heterojunctions (Fig. 8.10). Further increase in the g-C_3N_4 ratio (>1) resulted in increase in the recombination rate of e^-/h^+ and reduction of light absorption by $MnWO_4$. CO_3^{2-} and SO_4^{2-} anions considerably reduced the degradation efficiency compared to Cl^- resulting from greater adsorption of divalent anions on the surface of photocatalyst and more prohibition of OFX removal [194].

In another study, Vigneshwaran et al. [195] investigated degradation of chlorpyrifos (CPFS) insecticide by chitosan-assisted g-C_3N_4 (CS/g-C_3N_4) under irradiation of visible light (using 300 W Xe lamp). In this study, the effects of parameters such as chlorpyrifos dosage (10–100 mg/L), composite dosage (10–70 mg), pH (1–12), and reaction time (10–60 min) were investigated for the purification of pesticide from aqueous solution at room temperature. The removal efficiency illustrated an uptrend with increase in CS/g-C_3N_4 dosage which was attributed to the addition of binding sites. The optimum composite dosage of 50 mg/L was chosen for the continuation of experiments. The maximum degradation efficiency (94%) was achieved at a pH range of 3–5 and an initial pollutant concentration of 10 mg/L. The reason was ascribed to the fact that at pH < 5.3, organophosphate is the prevailing anion and, as a donator of electron pairs, leads to higher adsorption by CS/g-C_3N_4. Investigation of contact time illustrated ascending trend and degradation reached the equilibrium after 50 min. Analysis of SEM images revealed a regular quasi-sheet (Fig. 8.11A) and typical stacked lamellar morphology (Fig. 8.11B) for pure g-C_3N_4 and synthesized CS/g-C_3N_4, respectively [195].

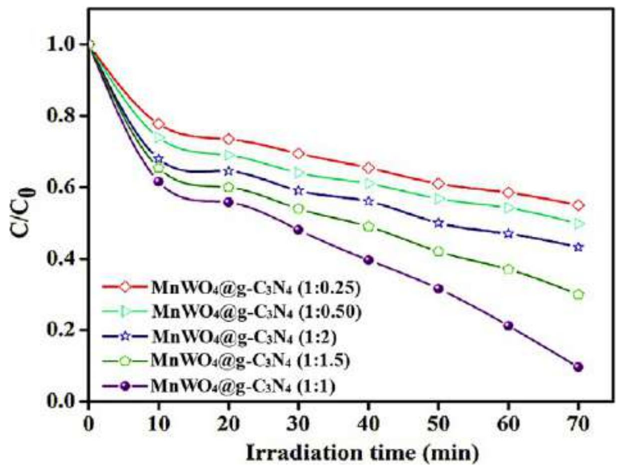

Fig. 8.10 Performance of different ratios of $MnWO_4$ and $g\text{-}C_3N_4$ in OFX removal (COFX = 10 mg/L, Cphotocatalyst = 50 mg/L). *(Reproduced from S. Lakshmi Prabavathi, K. Saravanakumar, G. Mamba, V. Muthuraj, 1D/2D $MnWO_4$ nanorods anchored on $g\text{-}C_3N_4$ nanosheets for enhanced photocatalytic degradation ofloxacin under visible light irradiation, Colloids Surfaces A Physicochem. Eng. Asp. (2019), doi:https://doi.org/10.1016/j.colsurfa.2019.123845.)*

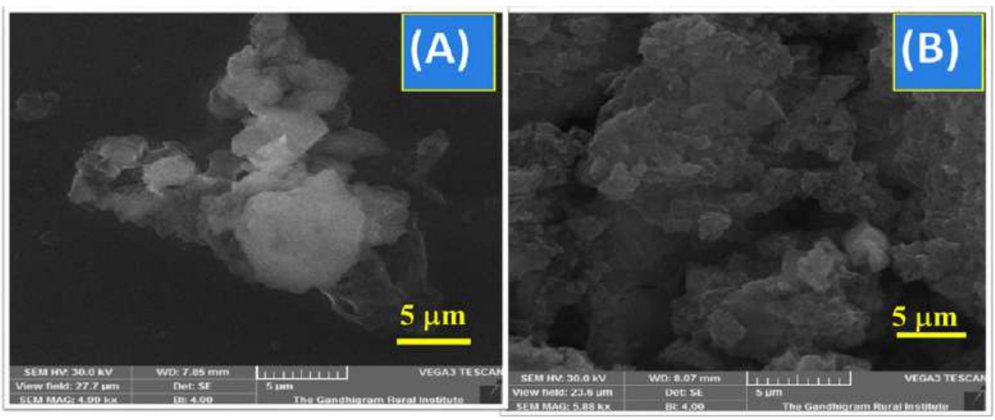

Fig. 8.11 Surface morphology of (A) pure $g\text{-}C_3N_4$, (B) $CS/g\text{-}C_3N_4$ composite. *(Adapted from S. Vigneshwaran, J. Preethi, S. Meenakshi, Removal of chlorpyrifos, an insecticide using metal free heterogeneous graphitic carbon nitride ($g\text{-}C_3N_4$) incorporated chitosan as catalyst: photocatalytic and adsorption studies, Int. J. Biol. Macromol. 132 (2019) 289–299, doi:https://doi.org/10.1016/j.ijbiomac.2019.03.071.)*

Diazinon is another emerging pollutant that was successfully eliminated by $g\text{-}C_3N_4/Fe_3O_4/Ag$ photocatalyst. Ghodsi et al. [196] synthesized this nanocomposite via a hydrothermal method and its photocatalytic performance under UV light irradiation was evaluated at various condition, including catalyst dosage (200, 500, 700, and 1000 mg/L), pH

(3, 5, 7, 9, 11), and diazinon concentration (5, 10, 20 mg/L). The complete removal efficiency was obtained at the optimum condition (60 min reaction, neutral pH, catalyst dosage of 500 mg/L, and pollutant concentration of 5 mg/L). The kinetic data best fitted with first-order model with the highest reaction rate constant ($k = 0.067$) and the linear correlation coefficient ($R^2 = 0.9982$). The utilization of different scavengers (e.g., ammonium oxalate, benzoquinone, and tert-butanol) was conducted for controlling holes, hydroxyl radical ($^{\bullet}O_2^-$), and superoxide radicals ($^{\bullet}OH$), respectively. In the presence of ammonium oxalate, benzoquinone, and tert-butanol, the complete removal efficiency of diazinon reduced to 95.22%, 89.9%, and 39.5%, respectively. The result implies that holes and hydroxyl radicals have played a vital role in the purification of diazinon by g-C_3N_4/Fe_3O_4/Ag [196].

Zhao et al. [197] constructed a multitasking membrane (GO/g-C_3N_4/Ag) for degradation and detection of organic contaminants (rhodamine 6G and paraoxon-ethyl pesticide, respectively) at low concentrations. The regularly arranged graphene oxide (GO) nanosheets were applicated for facile transportation and selectivity of small molecules. To enhance the self-cleaning and recyclability of the membrane, g-C_3N_4 photocatalyst was introduced. The noble metals, e.g., Ag were utilized due to their high surface plasmon resonance and enhancement of photoexcited charges transfer by the generation of heterojunctions. The preparation progress is demonstrated in Fig. 8.12. The bandgap energies of the g-C_3N_4 and GO/g-C_3N_4/Ag were 2.73 and 2.67 eV. After five cycles, a very low difference in signal intensities was observed. The water flux of GO and GO/g-C_3N_4/Ag membranes were 63.66 and 230.64 L/m^2 h MPa, respectively. The corresponded values of the rejection rate were 97.32% and 89.27%, respectively. The lowest detectable limit of paraoxon-ethyl was 10^{-9} M. Thanks to the production of more $^{\bullet}O_2^-$ and $^1O_2$ by GO/g-C_3N_4/Ag, 97.59% of rhodamine 6G was eliminated after 90 min irradiation of the visible light, which was approximately 1.4 times higher than that of solo g-C_3N_4 [197].

In another novel research, Moorthy et al. developed $ZnSeO_3$/g-C_3N_4 nanocomposite by an ultrasonic deposition method for removal of methyl parathion (MP, a toxic pesticide) and cefuroxime (CF, an antibiotic drug). Urea was utilized as the main feedstock for the fabrication of g-C_3N_4. By fabrication of $ZnSeO_3$/g-C_3N_4 nanocomposite, the bandgap energy of g-C_3N_4 reduced from 2.69 to 2.65 eV. Under visible-light irradiation, $^{\bullet}OH$ and $^{\bullet}O_2^-$ radicals were the main species in the reaction. The optimization studies were conducted by variation of several factors, including photocatalyst dosage (10, 25, 50, and 75 mg) and pollutant concentration (50, 75, and 100 μM). At the optimum condition (50 mg photocatalyst and 50 μM pollutant), the removal efficiency for both MP and CF was approximately 95% after 80 and 120 min, respectively. The reusability and stability studies illustrated supreme efficiency in the photocatalytic degradation of the input pollutants even after eight cycles (70%–75%) [198].

Aanchal et al. [199] developed layered and porous g-C_3N_4/H-ZSM-5 (zeolite) nanocomposite by calcination method for purification of organic endocrine disrupting

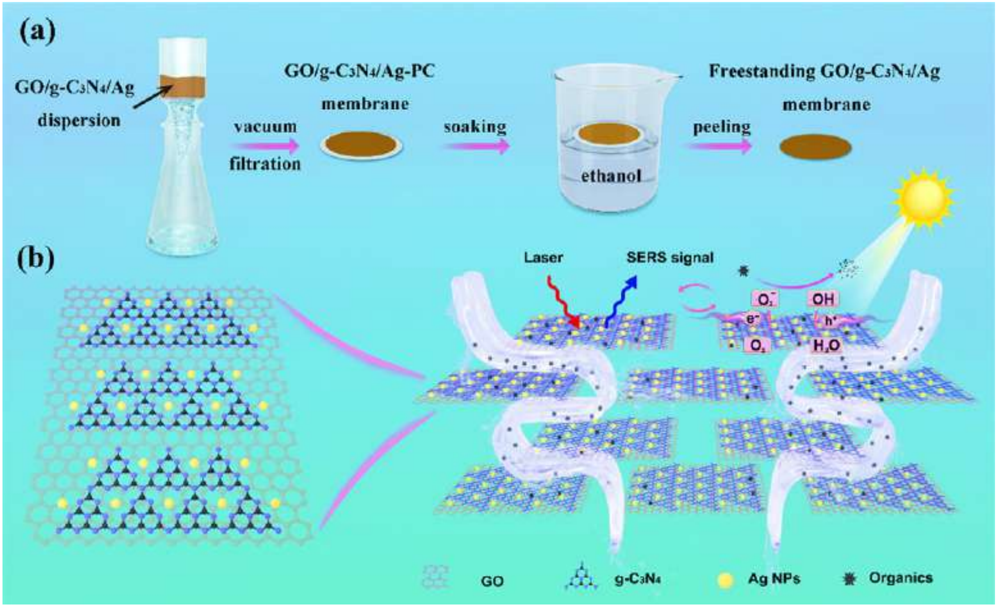

Fig. 8.12 (A) The preparation progress of the ultrathin GO/g-C_3N_4/Ag membrane, (B) the procedure of surface-enhanced Raman scattering (SERS) and photocatalytic degradation of organic pollutants by the membrane. *(Adapted from L. Zhao, C. Deng, S. Xue, H. Liu, L. Hao, M. Zhu, Multifunctional g-C_3N_4/Ag NPs intercalated GO composite membrane for SERS detection and photocatalytic degradation of paraoxon-ethyl, Chem. Eng. J. 402 (2020), doi:https://doi.org/10.1016/j.cej.2020.126223.)*

compounds (e.g., fipronil) from aqueous solutions. The moderate bandgap (2.63 eV) and high surface area (~175 m^2/g) of the nanocomposite offered abundant active sites for capturing photoinduced carriers, which caused high removal efficiency (~84%) and rate constant (0.00875 min^{-1}). The investigations on efficacy of parameters such as pH (1−11), photocatalyst concentration (40, 80, 120, and 160 mg/L), scavengers (10^{-3} M), and light sources (UV, visible, and sunlight) proved that after 140 min and at room temperature (25 ± 2°C), the degradation efficiency of 600 mg/L fipronil increased by increasing the photocatalyst dosage until a given amount (120 mg/L). Further increasing the catalyst led to saturation and opacity of the solution. The maximum degradation (89%) was obtained at pH 4 and under visible-light irradiation. Adding ascorbic acid (a scavenger for $^{\bullet}O_2^-$ radicals) significantly affects (~40% reduction) the elimination efficiency. The field emission scanning electron microscopy (FESEM) and high-resolution transmission electron microscopy (HRTEM) image of the nanocomposite indicated irregular plate-like shape of g-C_3N_4 with the crystalline structure of the H-ZSM-5 zeolite (Fig. 8.13) [199].

The ultrasonic synthesized g-C_3N_4/CdS composites by Ayodhya and Veerabhadram [200] exhibited superior performance toward purification of 15 mg/L monocrotophos

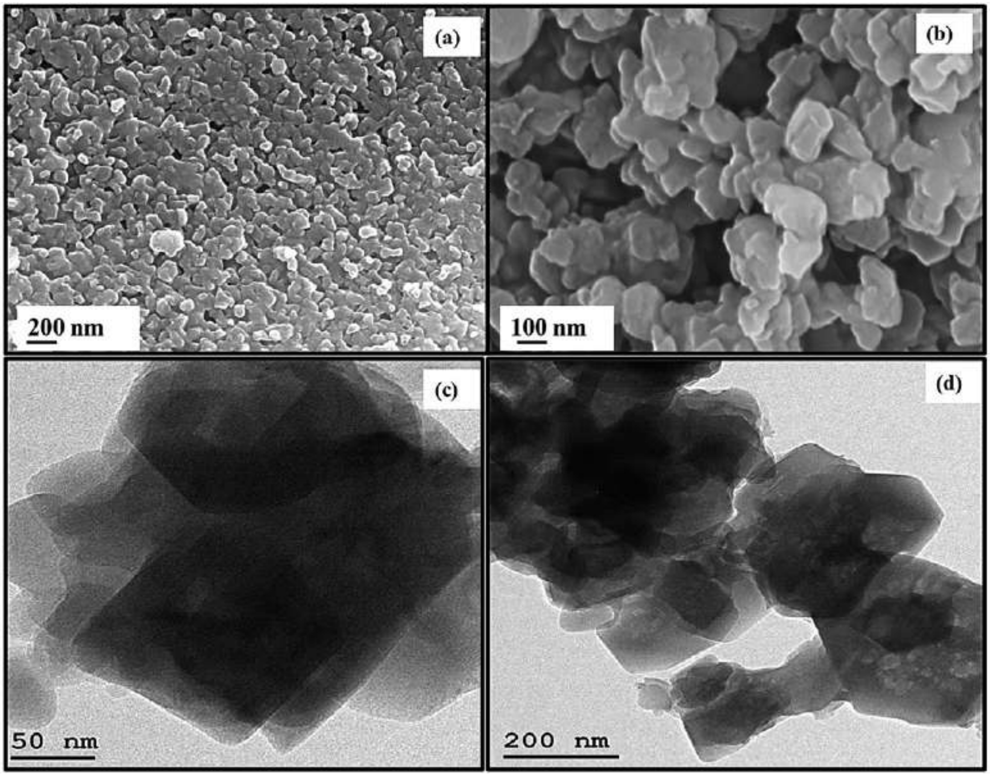

Fig. 8.13 (A, B) The FESEM images and (C, D) HRTEM image of the synthesized g-C_3N_4/H-ZSM-5 catalyst with a mean pore diameter of 4.25 nm. *(Adapted from Aanchal, S. Barman, S. Basu, Complete removal of endocrine disrupting compound and toxic dye by visible light active porous g-C_3N_4/H-ZSM-5 nanocomposite, Chemosphere 241 (2020), doi:https://doi.org/10.1016/j.chemosphere.2019.124981.)*

(MCP)-contaminated water. The bandgap energies of pure Cds, g-C_3N_4, and g-C_3N_4/CdS were estimated as 2.18, 2.18, and 2.51 eV. The surface area of the as-prepared composite was equal to 48.25 m^2/g. After 60 min sunlight irradiation and in the presence of 100 mg/L catalysts, 97.21% of MCP was successfully removed from polluted water, which was much higher than that of solo CdS and g-C_3N_4 (62.57% and 23.54%, respectively). The pseudo first-order reaction kinetics provided the best correlation of the experimental data. The catalyst demonstrated remarkable stability and recyclability after five cycles with (94.16% removal efficiency) [200].

Chen et al. [201] constructed a highly efficient ternary photocatalyst consisting of carbon dots (CDs), boron nitride (BN), and g-C_3N_4 via a facile calcination method and applied it for the elimination of 8 mg/L enrofloxacin antibiotic under blue LED irradiation (5.4 ± 0.2 mW/cm^2). Various g-C_3N_4/BN materials with different BN contents (0.5, 1.0, 1.5, 2.0, and 2.5 g) were prepared. Results proved that the compound with 1.5 g BN has had the highest photocatalytic efficiency. Later, diverse CDs/g-C_3N_4/BN with different CDs volume (0.01, 0.05, 0.1, 0.3, 0.5, 1.0 mL) was prepared. The most appropriate performance was obtained when the solution contained 0.1 mL CDs. Utilization of 1 g/L photocatalyst helped complete degradation of the enrofloxacin with high reaction rate constant (0.114 min^{-1}) within 40 min. The addition of extra CDs content generated competition for photon capture. The fabricated composite demonstrated fivefold higher activity than pristine g-C_3N_4 and considerable removal efficiency after five cycles (~91.8%). Application of CDs and BN caused improvement in the charge carriers transference and, consequently, higher production of reactive oxygen species (ROS) [201].

Sun et al. [202] developed novel Ag/g-C_3N_4/kaolinite composite by in situ calcination method followed by photodeposition process. Ibuprofen was used as the model sample, and dicyandiamide was utilized as feedstock for synthesis of g-C_3N_4. Using Ag (7% mass ratio) and under 5-h visible-light irradiation, the reaction rate constant of 1 g/L catalyst for complete degradation of 5 ppm pollutant was 0.0113 min^{-1}, which was 1.87 times more than that of the composite without kaolinite. The reason was ascribed to the provision of a more powerful adsorption propensity, proper charge separation, and wider photoresponse limit. Attachment of g-C_3N_4 on the kaolinite surface lessened the agglomeration possibility and supplied rather active sites for Ag adherence. In addition, the presence of Ag nanoparticles played a fundamental role as receivers of photoexcited electrons and gave rise to the number of accessible holes [202].

Zhao et al. [203] formed g-C_3N_4/carbon quantum dots (CQDs) by an adsorption-polymerization method for removal of CBZ by employing visible light as the irradiance source. The presence of CQDs made no difference in the bandgap energy of the g-C_3N_4 whereas considerably reduced the recombination rate and improved the removal kinetics over fivefold compared with solo g-C_3N_4 (1.36×10^{-2} min^{-1}). Radicals such as $^{\bullet}O_2^-$ and h^+ were the fundamental species in CBZ photodegradation. Within 60 min irradiation, at the neutral pH, and in the presence of 1 mg/L CBZ and 500 mg/L catalyst, the maximum removal efficiency reached to ~96%. The SEM images displayed tubular and rod-shaped frame (with 3–5 μm in diameter) for the synthesized g-C_3N_4. The tiny cavities were later observed on the surface of g-C_3N_4/CQDs. While sintering by polymerization procedure, the tubular CN and tubular g-C_3N_4/CQDs featured their porous structure which were due to amino and nitro groups loss [203].

Hong et al. [204] fabricated β-Bi_2O_3@g-C_3N_4 core/shell nanocomposite by a facile self-assembly strategy and examined its proficiency for purification of 10 mg/L tetracycline antibiotic under visible-light radiance. Among various mass ratios of g-C_3N_4 (1%, 3%, 5%, and 7%) in the nanocomposite, after 50 min contact time, 5 wt% loading of g-C_3N_4 demonstrated the highest reaction rate constant and removal efficiency values ($k = 0.0311$ min^{-1} and 80.2%, respectively). Increasing the g-C_3N_4 content from 1 to 5 wt% improved the photodegradation of the pollutant (from 58% to 80.2%). Further increment to 7 wt% reduced the efficiency to approximately 73%. In the presence of

500 mg/L catalyst, the synthesized nanocomposite illustrated remarkable stability and efficiency after five cycles (~75%) and exemplary photocatalytic performance due to the formation of *Z*-scheme heterojunction. At the same condition, the degradation efficiency of pristine g-C_3N_4 (E_g = 2.53 eV) and β-Bi_2O_3 (E_g = 2.42 eV) was 15.4% and 56.6%, respectively. Kinetic data best fitted to the pseudo first-order model. The proposed diagram of the photodegradation of tetracycline pollutants by researchers is presented in Fig. 8.14 [204].

Wang et al. [131] presented a novel N-doped carbon dot (NCDs)/g-C_3N_4 composite which was constructed by a facile polymerization method. The new-established composite possessed much higher photoactivity than that of g-C_3N_4 and CDs/g-C_3N_4 in the elimination of 4 mg/L nonsteroidal antiinflammatory drugs (NSAID-indomethacin) in such a way that the addition of even low NCDs loading (1 wt%) increased the reaction rate up to 13.6 times as compared with pristine g-C_3N_4 (0.0020 min^{-1}). After 90 min reaction, at neutral pH and in the presence of 1.0 g/L photocatalyst, 91.5% of the contaminant was degraded. The corresponding value obtained by application of pristine g-C_3N_4 was 16%. Just 5.3% of the indomethacin was absorbed by the composite in the dark condition [131].

In another investigation, Wang et al. [205] fabricated a ternary composite consisting of single atom-dispersed Ag and CQDs and loaded on ultrathin g-C_3N_4 (Ag-CQDs/UCN) and evaluated its photocatalytic performance for the purification of 4 mg/L

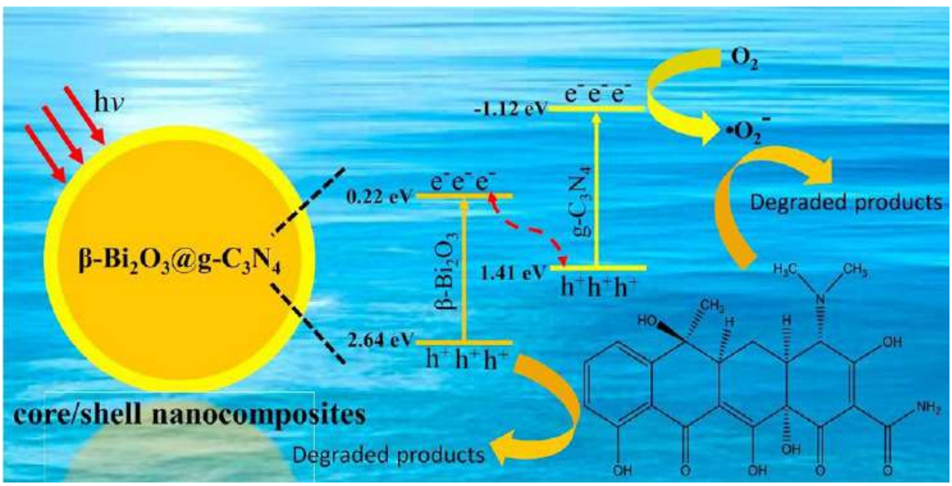

Fig. 8.14 The surface morphology of the as-prepared compounds: SEM images of (A) the precursor of tubular g-C_3N_4, (B) the precursor of g-C_3N_4/CQDs, (C) the porous structure of tubular g-C_3N_4 after sintering, and (D) the porous structure of g-C_3N_4/CQDs after sintering. *(Adapted from C. Zhao, Z. Liao, W. Liu, F. Liu, J. Ye, J. Liang, Y. Li, Carbon quantum dots modified tubular g-C_3N_4 with enhanced photocatalytic activity for carbamazepine elimination: mechanisms, degradation pathway and DFT calculation, J. Hazard. Mater. 381 (2020), doi:https://doi.org/10.1016/j.jhazmat.2019.120957.)*

NSAID, e.g., naproxen. The composite was synthesized by a facile thermo-polymerization method. It was reported that degradation of this component included two main steps: (1) decarboxylation and (2) naphthalene ring opening. Using Tauc equation, the bandgap energies of UCN, CQDs/UCN, and Ag-CQDs/UCN calculated as 2.62, 2.46, and 2.08 eV, respectively. Optimization was conducted by varying parameters such as CDs content (0.1, 0.25, 0.5, 1.0, and 2.0 wt%) and Ag amount (1, 3, 5, 10, and 20 wt%). Increasing CQD content from 0 to 1.0 wt% led to an increase in reaction rate constant from 0.0368 to 0.0883 min^{-1}, but further increment reduced the reaction rate constant due to competition of CQDs and UCN for photon capture. The existence of 3.0 wt% Ag increased the reaction rates up to 10 and 2.4 times greater than those of the UCN and CQDs/UCN, respectively. Using 1 g/L Ag-CQDs/UCN at the optimized condition (CDs = 1.0 wt% and Ag = 3.0 wt%), the efficiency reached the maximum value of 87.5% [205].

All these studies demonstrated the impressive performance of the g-C_3N_4 composites in the photodegradation of the emerging pollutants. Although there are countless carbon nitride-based composites, researchers in almost all studies emphasized the optimization of environmental and experimental parameters, which could strongly affect the synthesized catalysts' morphology and efficiency. A summary of some of these studies and their main key points are presented in Table 8.2.

10. Conclusion and future perspectives

This chapter reviewed the problems caused by EPs and the current state of the various g-C_3N_4-based composites utilized for abatement of these contaminants on the global platform. An in-depth overview of the characteristics of g-C_3N_4 and its different morphologies, diverse synthetic methods, and the significant achievements of the fabricated composites in treatment goals has been presented. The importance of this material in environmental issues was represented by the number of published researches and its upward trend from their first publication based on the selected keywords. Metal and nonmetal-ion doping, morphology control, developing heterojunction composites, and employment of sensitizers are among the strategies for reducing the available defects of pristine g-C_3N_4 and enhancing the removal efficiency. The advances in fabrication methods make it a cost-effective, efficient, time-saving material for in situ clean-up of contaminated aqueous solutions. This can be ascribed to the increment of surface area, charge carrier lifespan, and widening the absorbance wavelength range of the obtained composites compared to that of pristine g-C_3N_4.

This literature demonstrated that most of the prominent applications of g-C_3N_4-based composites for water or wastewater purification are in the small scales and laboratory phases. However, utilization in industrial scales requires to be profoundly analyzed. For instance, the operational costs, the fate of as-prepared composites, and health and

Table 8.2 Recent reports on g-C_3N_4-based composites in photocatalytic pollution abatement.

Catalysts composition	Feedstock of g-C_3N_4	Intended pollutant	Condition	Degradation efficiency (%)	References
Carbon-doped/g-C_3N_4	Urea	Atrazine	$C_{catalyst} = 1000$ mg/L Carbon = 0.07 wt% $C_{pollutant} = 100$ μM	86	[206]
g-C_3N_4/Ag_3PO_4/AgI	Dicyandiamide	Nitenpyram (insecticide)	$C_{pollutant} = 5$ ppm $C_{catalyst} = 0.5$ g/L	95	[207]
WO_3-TiO_2@g-C_3N_4	Melamine	Acetylsalicylate (pharmaceutical)	$TiO_2 = 2$ wt% g-$C_3N_4 = 1$ wt% $C_{pollutant} = 10$ mg/L $C_{catalyst} = 50$ mg/L	98	[208]
g-C_3N_4/CQDs/$CdIn_2S_4$	–	Ibuprofen (pharmaceutical)	CQDs = 0.075 g g-$C_3N_4 = 0.2115$ g $CdIn_2S_4 = 0.05$ g $C_{pollutant} = 80$ mg/L $C_{catalyst} = 100$ mg/L	91	[209]
0D/2D $Cu_{2-x}S$/g-C_3N_4	Dicyandiamide	Levofloxacin (pharmaceutical)	g-$C_3N_4 = 0.1$ g $Cu_{2-x}S = 0.8$ wt% $C_{pollutant} = 20$ mg/L $C_{catalyst} = 1000$ mg/L	100	[210]
Delaminated $Ti_3C_2T_x$/alkalized-C_3N_4	Urea	Tetracycline hydrochloride	Delaminated $Ti_3C_2T_x = 25$ mg $C_{pollutant} = 20$ mg/L $C_{catalyst} = 200$ mg/L	77	[211]
g-C_3N_4-shielding polyester fiber/TiO_2	Urea	Sulfaquinoxaline Thiamethoxam	$C_{pollutant} = 2 \times 10^{-5}$ mol/L Catalyst = 130 mg Reactor volume = 40 mL	97 ~100	[212]

environmental risks of these materials should be considered and evaluated with other conventional purification methods. Proper stability and separation of composites from aqueous solutions are serious subjects while studying the upscale application of these materials. In this way, researchers have utilized magnetic particles, which can finally diminish the total cost of treatment. These composites can benefit from privileges such as high selectivity and activity, large surface area, and prevention from aggregation.

Considering the fast-growth in synthesis of new g-C_3N_4-based composites and their wide application in water and/or wastewater treatment, especially in the degradation of emerging pollutants, uncontrollable release of these materials into the natural environments are reported. Hence, basic information about efficient utilization and fabrication of engineered composites are essential to make them more environmentally friendly.

References

[1] H. Ali, E. Khan, I. Ilahi, Environmental chemistry and ecotoxicology of hazardous heavy metals: environmental persistence, toxicity, and bioaccumulation, J. Chem. 2019 (2019), https://doi.org/10.1155/2019/6730305.

[2] M. Ahmadpur, I. Gokasar, Spatial analysis and evaluation of road traffic safety performance indexes across the provinces of Turkey from 2015 to 2019, Int. J. Injury Control Saf. Promot. 28 (3) (2021) 309–324, https://doi.org/10.1080/17457300.2021.1925923.

[3] M. Ahmadpur, I. Sen, I. Gokasar, Comparing the performance of machine learning algorithms for vehicle detection in highways, in: 14th International Congress on Advances in Civil Engineering, Istanbul-Turkey, vol. 1(1), 2021, 1329–1336, https://www.researchgate.net/profile/Morteza-Ahmadpur/publication/354445869_Comparing_the_Performance_of_Machine_Learning_Algorithms_for_Vehicle_Detection_in_Highways/links/6138af50349f12090ff00585/Comparing-the-Performance-of-Machine-Learning-Algorithms-for-Vehicle-Detection-in-Highways.pdf.

[4] S.A.A. Hosseini, F.F. Mojtahedi, H. Sadeghi, Optimisation of deep mixing technique by artificial neural network based on laboratory and field experiments, Georisk 14 (2) (2020) 142–157, https://doi.org/10.1080/17499518.2019.1612526.

[5] H. Sadeghi, A Micro-Structural Study on Hydro-Mechanical Behavior of Loess, Hong Kong University of Science and Technology, Sharif University of Technology, 2016. https://scholar.google.com/citations?view_op=view_citation&hl=en&user=Hoxz8ckAAAAJ&citation_for_view=Hoxz8ckAAAAJ:_FxGoFyzp5QC.

[6] A. Bazargan, H. Sadeghi, R. Garcia-Mayoral, G. McKay, An unsteady state retention model for fluid desorption from sorbents, J. Colloid Interface Sci. 450 (2015) 127–134, https://doi.org/10.1016/j.jcis.2015.02.036.

[7] H. Sadeghi, S.K.B. Hossen, A.C.F. Chiu, Q. Cheng, C.W.W. Ng, Water retention curves of intact and re-compacted loess at different net stresses, Jpn. Geotech. Soc. Spec. 2 (4) (2016) 221–225, https://doi.org/10.3208/jgssp.HKG-04.

[8] C.W.W. Ng, H. Sadeghi, F. Jafarzadeh, M. Sadeghi, C. Zhou, S. Baghbanrezvan, Effect of microstructure on shear strength and dilatancy of unsaturated loess at high suctions, Can. Geotech. J. 57 (2) (2020) 221–235, https://doi.org/10.1139/cgj-2018-0592.

[9] H. Sadeghi, C.W.W. Ng, Shear behaviour of a desiccated loess with three different microstructures, UNSAT2018 – The 7th International Conference on Unsaturated Soils, vol. 1 (401), The Hong Kong University of Science and Technology (HKUST), 2018, pp. 1–6. https://www.researchgate.net/profile/Hamed-Sadeghi-5/publication/331973542_Shear_behaviour_of_a_desiccated_loess_with_three_different_microstructures/links/5c97244f45851506d7275f8a/Shear-behaviour-of-a-desiccated-loess-with-three-different-microstructures.pdf.

[10] M.A. Salahat, M.I. Al-Qinna, R.A. Badran, Potential of treated wastewater usage for adaptation to climate change: Jordan as a success story, Water Resources in Arid Areas: The Way Forward, Springer, Cham, 2017, pp. 383–405.

[11] P. Rajasulochana, V. Preethy, Comparison on efficiency of various techniques in treatment of waste and sewage water—a comprehensive review, Resour. Technol. 2 (2016) 175–184, https://doi.org/10.1016/j.reffit.2016.09.004.

[12] H. Liu, S. Ma, L. Shao, H. Liu, Q. Gao, B. Li, H. Fu, S. Fu, H. Ye, F. Zhao, J. Zhou, Defective engineering in graphitic carbon nitride nanosheet for efficient photocatalytic pathogenic bacteria disinfection, Appl. Catal. Environ. 261 (2020), https://doi.org/10.1016/j.apcatb.2019.118201.

[13] T.T. Pham, S. Proulx, PCBs and PAHs in the Montreal urban community (Quebec, Canada) wastewater treatment plant and in the effluent plume in the St Lawrence river, Water Res. 31 (1997) 1887–1896, https://doi.org/10.1016/S0043-1354(97)00025-0.

[14] V. Geissen, H. Mol, E. Klumpp, G. Umlauf, M. Nadal, M. van der Ploeg, S.E.A.T.M. van de Zee, C.J. Ritsema, Emerging pollutants in the environment: a challenge for water resource management, Int. Soil Water Conserv. Res. 3 (2015) 57–65, https://doi.org/10.1016/j.iswcr.2015.03.002.

[15] A. Khadir, A.M. Ramezanali, S. Taghipour, K. Jafari, Insights of the removal of antibiotics from water and wastewater: a review on physical, chemical, and biological techniques, in: Applied Water Science: Remediation Technologies, 2, John Wiley & Sons, Inc, 2021, pp. 1–47. https://onlinelibrary.wiley.com/doi/abs/10.1002/9781119725282.ch1.

[16] S. Taghipour, A. Khadir, M. Taghipour, Carbon Nanotubes Composite Membrane for Water Desalination, Sustainable Materials and Systems for Water Desalination, Springer, Cham, 2021, pp. 163–184. https://link.springer.com/chapter/10.1007/978-3-030-72873-1_10.

[17] S. Taghipour, S.M. Hosseini, B. Ataie-Ashtiani, Engineering nanomaterials for water and wastewater treatment: review of classifications, properties and applications, New J. Chem. 43 (2019) 7902–7927, https://doi.org/10.1039/C9NJ00157C.

[18] S. Taghipour, B. Ayati, Cultivation of aerobic granules through synthetic petroleum wastewater treatment in a cyclic aerobic granular reactor, Desalin. Water Treat. 76 (2017) 134–142, https://doi.org/10.5004/dwt.2017.20779.

[19] S. Taghipour, B. Ayati, M. Razaei, Study of the SBAR performance in COD removal of petroleum and MTBE, Modares Civ. Eng. J. 17 (2017) 17–27. https://mcej.modares.ac.ir/article-16-7139-en.html.

[20] S. Taghipour, B. Ayati, Study of SBAR capability in petroleum wastewater treatment, J. Water Reuse 2 (2015) 119–128. https://scholar.google.com/scholar?hl=en&as_sdt=0,5&cluster=9833339585674475112.

[21] F. Tisa, A.A. Abdul Raman, W.M.A. Wan Daud, Applicability of fluidized bed reactor in recalcitrant compound degradation through advanced oxidation processes: a review, J. Environ. Manage. 146 (2014) 260–275, https://doi.org/10.1016/j.jenvman.2014.07.032.

[22] S.C. Ameta, Chapter 1—Introduction, in: Advanced Oxidation Processes for Waste Water Treatment: Emerging Green Chemical Technology, Academic Press, 2018.

[23] M. Seyyedi, B. Ayati, Treatment of petroleum wastewater using a sequential hybrid system of electro-Fenton and NZVI slurry reactors, future prospects for an emerging wastewater treatment technology, Int. J. Environ. Waste Manag. 28 (3) (2021) 328–348. https://www.inderscienceonline.com/doi/abs/10.1504/IJEWM.2021.118369.

[24] H. Khorsandi, M. Teymori, A.A. Aghapour, S.J. Jafari, S. Taghipour, R. Bargeshadi, Photodegradation of ceftriaxone in aqueous solution by using UVC and UVC/H_2O_2 oxidation processes, Appl. Water Sci. 9 (2019) 81, https://doi.org/10.1007/s13201-019-0964-2.

[25] X. Chen, M. Arruebo, K.L. Yeung, Flow-synthesis of mesoporous silicas and their use in the preparation of magnetic catalysts for Knoevenagel condensation reactions, Catal. Today 204 (2013) 140–147, https://doi.org/10.1016/j.cattod.2012.07.017.

[26] S.M. Hosseini, T. Tosco, B. Ataie-Ashtiani, C.T. Simmons, Non-pumping reactive wells filled with mixing nano and micro zero-valent iron for nitrate removal from groundwater: vertical, horizontal, and slanted wells, J. Contam. Hydrol. 210 (2018) 50–64, https://doi.org/10.1016/j.jconhyd.2018.02.006.

[27] S. Mossa Hosseini, B. Ataie-Ashtiani, M. Kholghi, Nitrate reduction by nano-Fe/Cu particles in packed column, Desalination 276 (2011) 214–221, https://doi.org/10.1016/j.desal.2011.03.051.

[28] S.M. Hosseini, B. Ataie-Ashtiani, M. Kholghi, Bench-scaled nano-Fe0 permeable reactive barrier for nitrate removal, Ground Water Monit. Remidiat. 31 (2011) 82–94, https://doi.org/10.1111/j.1745-6592.2011.01352.x.

[29] M. Jannesari, J. Varshosaz, M. Morshed, M. Zamani, Composite poly (vinyl alcohol)/poly (vinyl acetate) electrospun nanofibrous mats as a novel wound dressing matrix for controlled release of drugs, Int. J. Nanomed. 6 (2011) 993–1003, https://doi.org/10.2147/IJN.S17595.

[30] M. Zamani, M. Morshed, J. Varshosaz, M. Jannesari, Controlled release of metronidazole benzoate from poly ε-caprolactone electrospun nanofibers for periodontal diseases, Eur. J. Pharm. Biopharm. 75 (2) (2010) 179–185, https://doi.org/10.1016/j.ejpb.2010.02.002.

[31] O. Akhavan, M. Saadati, M. Jannesari, Graphene jet nanomotors in remote controllable self-propulsion swimmers in pure water, Nano Letters 16 (9) (2016) 5619–5630, https://doi.org/10.1021/acs.nanolett.6b02175.

[32] M. Jannesari, O. Akhavan, H.R. Madaah Hosseini, B. Bakhshi, Graphene/CuO^2 nanoshuttles with controllable release of oxygen nanobubbles promoting interruption of bacterial respiration, ACS Appl. Mater. Interfaces 12 (32) (2020) 35813–35825, https://doi.org/10.1021/acsami.0c05732.

[33] M. Jannesari, O. Akhavan, H.R. Madaah Hosseini, Graphene oxide in generation of nanobubbles using controllable microvortices of jet flows, Carbon 138 (2018) 8–17, https://doi.org/10.1016/j.carbon.2018.05.068.

[34] X. Wang, X. Chen, A. Thomas, X. Fu, M. Antonietti, Metal-containing carbon nitride compounds: a new functional organic-metal hybrid material, Adv. Mater. 21 (2009) 1609–1612, https://doi.org/10.1002/adma.200802627.

[35] L. Salihu, A.E. Adedayo, B.J. Olalekan, A.M. Afolabi, I.D. Mohammed, I.A. Oke, O.O. Adewale, Evaluation of selected reaeration models for water quality management, Effects of Emerging Chemical Contaminants on Water Resources and Environmental Health, IGI Global, 2020, pp. 214–241.

[36] G.F. Birch, D.S. Drage, K. Thompson, G. Eaglesham, J.F. Mueller, Emerging contaminants (pharmaceuticals, personal care products, a food additive and pesticides) in waters of Sydney estuary, Australia, Mar. Pollut. Bull. 97 (2015) 56–66, https://doi.org/10.1016/j.marpolbul.2015.06.038.

[37] M. Matthies, K. Solomon, M. Vighi, A. Gilman, J.V. Tarazona, The origin and evolution of assessment criteria for persistent, bioaccumulative and toxic (PBT) chemicals and persistent organic pollutants (POPs), Environ. Sci. Process Impacts 18 (2016) 1114–1128, https://doi.org/10.1039/c6em00311g.

[38] T. Deblonde, C. Cossu-Leguille, P. Hartemann, Emerging pollutants in wastewater: a review of the literature, Int. J. Hyg. Environ. Health 214 (2011) 442–448, https://doi.org/10.1016/j.ijheh.2011.08.002.

[39] X. Luo, L. Zhang, Z. Niu, X. Ye, Z. Tang, S. Xia, Liquid chromatography coupled to quadrupole-Orbitrap high resolution mass spectrometry based method for target analysis and suspect screening of non-ionic surfactants in textiles, J. Chromatogr. A 1530 (2017) 80–89, https://doi.org/10.1016/j.chroma.2017.11.001.

[40] M. Kemmerich, Technological developments in the determination of emerging contaminants in water, Effects of Emerging Chemical Contaminants on Water Resources and Environmental Health, IGI Global, 2020, pp. 81–108.

[41] D.B. Miklos, C. Remy, M. Jekel, K.G. Linden, J.E. Drewes, U. Hübner, Evaluation of advanced oxidation processes for water and wastewater treatment—a critical review, Water Res. (2018), https://doi.org/10.1016/j.watres.2018.03.042.

[42] H. Kaur, G. Hippargi, G.R. Pophali, A.K. Bansiwal, Treatment methods for removal of pharmaceuticals and personal care products from domestic wastewater, in: Pharmaceuticals and Personal Care Products: Waste Management and Treatment Technology, Butterworth-Heinemann, 2019, pp. 129–150.

[43] M.H. Dalhat, A. Ahmad, Removal of pesticides from water and wastewater by solar-driven photocatalysis, Development in Wastewater Treatment Research and Processes, Elsevier, 2022, pp. 435–458.

[44] M.A. Oturan, J.J. Aaron, Advanced oxidation processes in water/wastewater treatment: principles and applications. A review, Crit. Rev. Environ. Sci. Technol. 44 (2014) 2577–2641, https://doi.org/10.1080/10643389.2013.829765.
[45] E. Brillas, P.L. Cabot, J. Casado, Degradation of organic pollutants in aqueous media, Chemical Degradation Methods for Wastes and Pollutants: Environmental and Industrial Applications, CRC Press, 2003.
[46] E. Mousset, M. Zhou, Graphene-based nanostructured materials for advanced electrochemical water/wastewater treatment, in: Polymeric and Nanostructured Materials: Synthesis, Properties and Advanced Applications, Apple Academic Press, Waretown, 2017, pp. 321–358.
[47] E.M. Cuerda-Correa, M.F. Alexandre-Franco, C. Fernández-González, Advanced oxidation processes for the removal of antibiotics from water. An overview, Water (Switzerland) 12 (2020), https://doi.org/10.3390/w12010102.
[48] A.A. Oladipo, M. Gazi, A.O. Ifebajo, A.S. Oladipo, E.O. Ahaka, Photocatalytic degradation of toxic pesticides: mechanistic insights, in: Photocatalysts in Advanced Oxidation Processes for Wastewater Treatment, Wiley, 2020, pp. 93–138.
[49] G.L. Chiarello, E. Selli, Photocatalytic production of hydrogen, in: Advances in Hydrogen Production, Storage and Distribution, Woodhead Publishing, 2014, pp. 216–247.
[50] K. Qi, S.Y. Liu, A. Zada, Graphitic carbon nitride, a polymer photocatalyst, J. Taiwan Inst. Chem. Eng. 109 (2020) 111–123, https://doi.org/10.1016/j.jtice.2020.02.012.
[51] S.M. Hosseini, T. Tosco, Transport and retention of high concentrated nano-Fe/Cu particles through highly flow-rated packed sand column, Water Res. 47 (2013) 326–338, https://doi.org/10.1016/j.watres.2012.10.002.
[52] T. Tosco, S.M. Hosseini, Comparative assessment of injection strategies for highly concentrated nano Fe/Cu particles into sand columns, J. Environ. Eng. 141 (2015), https://doi.org/10.1061/(ASCE)EE.1943-7870.0000906.
[53] G. Theodorakopoulos, C. Athanasekou, G.E. Romanos, S.K. Papageorgiou, Current photocatalytic systems for intensified water purification applications, in: Handbook of Smart Photocatalytic Materials, Elsevier, 2020, pp. 231–264.
[54] J.J. Rueda-Marquez, I. Levchuk, P. Fernández Ibañez, M. Sillanpää, A critical review on application of photocatalysis for toxicity reduction of real wastewaters, J. Clean. Prod. 258 (2020), https://doi.org/10.1016/j.jclepro.2020.120694.
[55] J.L. White, M.F. Baruch, J.E. Pander, Y. Hu, I.C. Fortmeyer, J.E. Park, T. Zhang, K. Liao, J. Gu, Y. Yan, T.W. Shaw, E. Abelev, A.B. Bocarsly, Light-driven heterogeneous reduction of carbon dioxide: photocatalysts and photoelectrodes, Chem. Rev. 115 (2015) 12888–12935, https://doi.org/10.1021/acs.chemrev.5b00370.
[56] Z. Ahmad, R. Farooq, A.U. Khan, N. Hussain, A. Shafique, Bimodal UV-assisted nano-TiO_2 catalyst—crumb rubber device for treatment of contaminated water, in: Aquananotechnology: Global Prospects, CRC Press, 2014, pp. 26–39.
[57] E. Oturan, N. Oturan, M.A. Oturan, An unprecedented route of [rad]OH radical reactivity evidenced by an electrocatalytical process: ipso-substitution with perhalogenocarbon compounds, Appl. Catal. Environ. 226 (2018) 135–146, https://doi.org/10.1016/j.apcatb.2017.12.028.
[58] J. Lee, C. Chang, J. Kim, S.P. Lee, Properties of nanostructured carbon nitride films for semiconductor process applications, Nanostructured Materials and Nanotechnology II: Ceramic Engineering and Science Proceedings, 8th, 29, Wiley, 2008, pp. 107–116.
[59] Q. Hao, G. Jia, W. Wei, A. Vinu, Y. Wang, H. Arandiyan, B.J. Ni, Graphitic carbon nitride with different dimensionalities for energy and environmental applications, Nano Res. 13 (2020) 18–37, https://doi.org/10.1007/s12274-019-2589-z.
[60] S. Patnaik, G. Swain, K.M. Parida, Photo-/electro-catalytic applications of visible light-responsive porous graphitic carbon nitride toward environmental remediation and solar energy conversion, Green Photocatalysts for Energy and Environmental Process, Springer, Cham, 2020, pp. 211–246.
[61] W.J. Ong, L.L. Tan, Y.H. Ng, S.T. Yong, S.P. Chai, Graphitic carbon nitride ($g-C_3N_4$)-based photocatalysts for artificial photosynthesis and environmental remediation: are we a step closer to

achieving sustainability? Chem. Rev. 116 (2016) 7159–7329, https://doi.org/10.1021/acs.chemrev.6b00075.
[62] No Title (n.d.), http://wcs.webofknowledge.com/RA/analyze.do?product=WOS&SID=C2xkWKwJ7PDMlbazXWE&field=TASCA_JCRCategories_JCRCategories_en&yearSort=false.
[63] No Title (n.d.), http://apps.webofknowledge.com/RAMore.do?product=WOS&search_mode=GeneralSearch&SID=C2xkWKwJ7PDMlbazXWE&qid=5&ra_mode=more&ra_name=PublicationYear&colName=WOS&viewType=raMore.
[64] No Title (n.d.), http://wcs.webofknowledge.com/RA/analyze.do?product=WOS&SID=C2xkWKwJ7PDMlbazXWE&field=CU_CountryTerritory_CountryTerritory_en&yearSort=false.
[65] A. Wang, C. Wang, L. Fu, W. Wong-Ng, Y. Lan, Recent advances of graphitic carbon nitride-based structures and applications in catalyst, sensing, imaging, and LEDs, Nano-Micro Lett. 9 (2017), https://doi.org/10.1007/s40820-017-0148-2.
[66] R.M. Yadav, R. Kumar, A. Aliyan, P.S. Dobal, S. Biradar, R. Vajtai, D.P. Singh, A.A. Martí, P.M. Ajayan, Facile synthesis of highly fluorescent free-standing films comprising graphitic carbon nitride (g-C_3N_4) nanolayers, New J. Chem. 44 (2020) 2644–2651, https://doi.org/10.1039/c9nj05108b.
[67] R. You, H. Dou, L. Chen, S. Zheng, Y. Zhang, Graphitic carbon nitride with S and O codoping for enhanced visible light photocatalytic performance, RSC Adv. 7 (2017) 15842–15850, https://doi.org/10.1039/c7ra01036b.
[68] N. Tian, H. Huang, X. Du, F. Dong, Y. Zhang, Rational nanostructure design of graphitic carbon nitride for photocatalytic applications, J. Mater. Chem. A 7 (2019) 11584–11612, https://doi.org/10.1039/c9ta01819k.
[69] J. Yi, W. El-Alami, Y. Song, H. Li, P.M. Ajayan, H. Xu, Emerging surface strategies on graphitic carbon nitride for solar driven water splitting, Chem. Eng. J. 382 (2020), https://doi.org/10.1016/j.cej.2019.122812.
[70] T. Wang, C. Nie, Z. Ao, S. Wang, T. An, Recent progress in g-C_3N_4 quantum dots: synthesis, properties and applications in photocatalytic degradation of organic pollutants, J. Mater. Chem. A 8 (2020) 485–502, https://doi.org/10.1039/c9ta11368a.
[71] 0D g-C3N4 (n.d.), http://apps.webofknowledge.com/RAMore.do?product=WOS&search_mode=GeneralSearch&SID=C5AxdCr5yTdFVRsocYy&qid=22&ra_mode=more&ra_name=PublicationYear&colName=WOS&viewType=raMore.
[72] K. Li, F.Y. Su, W. De Zhang, Modification of g-C_3N_4 nanosheets by carbon quantum dots for highly efficient photocatalytic generation of hydrogen, Appl. Surf. Sci. 375 (2016) 110–117, https://doi.org/10.1016/j.apsusc.2016.03.025.
[73] Q. Liu, T. Chen, Y. Guo, Z. Zhang, X. Fang, Ultrathin g-C_3N_4 nanosheets coupled with carbon nanodots as 2D/0D composites for efficient photocatalytic H_2 evolution, Appl. Catal. Environ. 193 (2016) 248–258, https://doi.org/10.1016/j.apcatb.2016.04.034.
[74] W. Wang, Z. Zeng, G. Zeng, C. Zhang, R. Xiao, C. Zhou, W. Xiong, Y. Yang, L. Lei, Y. Liu, D. Huang, M. Cheng, Y. Yang, Y. Fu, H. Luo, Y. Zhou, Sulfur doped carbon quantum dots loaded hollow tubular g-C_3N_4 as novel photocatalyst for destruction of Escherichia coli and tetracycline degradation under visible light, Chem. Eng. J. 378 (2019), https://doi.org/10.1016/j.cej.2019.122132.
[75] Y. Wang, X. Liu, J. Liu, B. Han, X. Hu, F. Yang, Z. Xu, Y. Li, S. Jia, Z. Li, Y. Zhao, Carbon quantum dot implanted graphite carbon nitride nanotubes: excellent charge separation and enhanced photocatalytic hydrogen evolution, Angew. Chem. Int. Ed. 57 (2018) 5765–5771, https://doi.org/10.1002/anie.201802014.
[76] Z. Yao, X. Liu, H. Sui, H. Sun, Enhanced photocatalytic performance of dual Z-scheme BPQDs/g-C_3N_4/$BiFeO_3$ composites and mechanism insight, Mater. Lett. 275 (2020), https://doi.org/10.1016/j.matlet.2020.128007.
[77] X. Jian, X. Liu, H.M. Yang, J.G. Li, X.L. Song, H.Y. Dai, Z.H. Liang, Construction of carbon quantum dots/proton-functionalized graphitic carbon nitride nanocomposite via electrostatic self-assembly strategy and its application, Appl. Surf. Sci. 370 (2016) 514–521, https://doi.org/10.1016/j.apsusc.2016.02.119.

[78] M. Tahir, C. Cao, N. Mahmood, F.K. Butt, A. Mahmood, F. Idrees, S. Hussain, M. Tanveer, Z. Ali, I. Aslam, Multifunctional g-C_3N_4 nanofibers: a template-free fabrication and enhanced optical, electrochemical, and photocatalyst properties, ACS Appl. Mater. Interfaces 6 (2014) 1258–1265, https://doi.org/10.1021/am405076b.
[79] S. Kumar, S. Karthikeyan, A.F. Lee, g-C_3N_4-based nanomaterials for visible light-driven photocatalysis, Catalysts 8 (2018), https://doi.org/10.3390/catal8020074.
[80] L.W. Yin, Y. Bando, M. Sen Li, Y.X. Liu, Y.X. Qi, Unique single-crystalline beta carbon nitride nanorods, Adv. Mater. 15 (2003) 1840–1844, https://doi.org/10.1002/adma.200305307.
[81] L. Xiao, T. Liu, M. Zhang, Q. Li, J. Yang, Interfacial construction of zero-dimensional/one-dimensional g-C_3N_4 nanoparticles/TiO_2 nanotube arrays with Z-scheme heterostructure for improved photoelectrochemical water splitting, ACS Sustain. Chem. Eng. 7 (2019) 2483–2491, https://doi.org/10.1021/acssuschemeng.8b05392.
[82] X.H. Li, J. Zhang, X. Chen, A. Fischer, A. Thomas, M. Antonietti, X. Wang, Condensed graphitic carbon nitride nanorods by nanoconfinement: promotion of crystallinity on photocatalytic conversion, Chem. Mater. 23 (2011) 4344–4348, https://doi.org/10.1021/cm201688v.
[83] Z. Lin, X. Wang, Ionic liquid promoted synthesis of conjugated carbon nitride photocatalysts from urea, ChemSusChem 7 (2014) 1547–1550, https://doi.org/10.1002/cssc.201400016.
[84] Y. Zheng, L. Lin, X. Ye, F. Guo, X. Wang, Helical graphitic carbon nitrides with photocatalytic and optical activities, Angew. Chem. Int. Ed. 53 (2014) 11926–11930, https://doi.org/10.1002/anie.201407319.
[85] 1D g-C3N4 (n.d.), http://apps.webofknowledge.com/RAMore.do?product=WOS&search_mode=GeneralSearch&SID=C5AxdCr5yTdFVRsocYy&qid=18&ra_mode=more&ra_name=PublicationYear&colName=WOS&viewType=raMore.
[86] X. Dong, F. Cheng, Recent development in exfoliated two-dimensional g-C_3N_4 nanosheets for photocatalytic applications, J. Mater. Chem. A (2015), https://doi.org/10.1039/c5ta07374j.
[87] W.J. Ong, 2D/2D graphitic carbon nitride (g-C_3N_4) heterojunction nanocomposites for photocatalysis: why does face-to-face interface matter? Front. Mater. 4 (2017), https://doi.org/10.3389/fmats.2017.00011.
[88] H. He, J. Li, C. Yu, Z. Luo, Surface decoration of microdisk-like g-C_3N_4/diatomite with Ag/AgCl nanoparticles for application in Cr(VI) reduction, Sustain. Mater. Technol. 22 (2019), https://doi.org/10.1016/j.susmat.2019.e00127.
[89] X. Lv, M. Cao, W. Shi, M. Wang, Y. Shen, A new strategy of preparing uniform graphitic carbon nitride films for photoelectrochemical application, Carbon N. Y. 117 (2017) 343–350, https://doi.org/10.1016/j.carbon.2017.02.096.
[90] Q. Gu, X. Gong, Q. Jia, J. Liu, Z. Gao, X. Wang, J. Long, C. Xue, Compact carbon nitride based copolymer films with controllable thickness for photoelectrochemical water splitting, J. Mater. Chem. A 5 (2017) 19062–19071, https://doi.org/10.1039/c7ta06081e.
[91] M. Sima, E. Vasile, A. Sima, N. Preda, C. Logofatu, Graphitic carbon nitride based photoanodes prepared by spray coating method, Int. J. Hydrogen Energy 44 (2019) 24430–24440, https://doi.org/10.1016/j.ijhydene.2019.07.243.
[92] A. Kumar, M. Khan, X. Zeng, I.M.C. Lo, Development of g-C_3N_4/TiO_2/Fe_3O_4@SiO_2 heterojunction via sol-gel route: a magnetically recyclable direct contact Z-scheme nanophotocatalyst for enhanced photocatalytic removal of ibuprofen from real sewage effluent under visible light, Chem. Eng. J. 353 (2018) 645–656, https://doi.org/10.1016/j.cej.2018.07.153.
[93] L. Wang, Y. Tong, J. Feng, J. Hou, J. Li, X. Hou, J. Liang, G-C_3N_4-based films: a rising star for photoelectrochemical water splitting, Sustain. Mater. Technol. (2019), https://doi.org/10.1016/j.susmat.2018.e00089.
[94] 2D g-C3N4 (n.d.), http://apps.webofknowledge.com/RAMore.do?product=WOS&search_mode=GeneralSearch&SID=C5AxdCr5yTdFVRsocYy&qid=14&ra_mode=more&ra_name=PublicationYear&colName=WOS&viewType=raMore.
[95] Y. Sheng, Z. Wei, H. Miao, W. Yao, H. Li, Y. Zhu, Enhanced organic pollutant photodegradation via adsorption/photocatalysis synergy using a 3D g-C_3N_4/TiO_2 free-separation photocatalyst, Chem. Eng. J. 370 (2019) 287–294, https://doi.org/10.1016/j.cej.2019.03.197.

[96] H. Gao, R. Cao, S. Zhang, H. Yang, X. Xu, Three-dimensional hierarchical g-C_3N_4 architectures assembled by ultrathin self-doped nanosheets: extremely facile hexamethylenetetramine activation and superior photocatalytic hydrogen evolution, ACS Appl. Mater. Interfaces 11 (2019) 2050–2059, https://doi.org/10.1021/acsami.8b17757.
[97] A.J. Nathan, A. Scobell, How China sees America, Foreign Aff. 91 (2012) 1–224, https://doi.org/10.1017/CBO9781107415324.004.
[98] T.T. Pham, E.W. Shin, Influence of g-C_3N_4 precursors in g-C_3N_4/$NiTiO_3$ composites on photocatalytic behavior and the interconnection between g-C_3N_4 and $NiTiO_3$, Langmuir 34 (2018) 13144–13154, https://doi.org/10.1021/acs.langmuir.8b02596.
[99] J. Bai, C. Yin, H. Xu, G. Chen, Z. Ni, Z. Wang, Y. Li, S. Kang, Z. Zheng, X. Li, Facile urea-assisted precursor pre-treatment to fabricate porous g-C_3N_4 nanosheets for remarkably enhanced visible-light-driven hydrogen evolution, J. Colloid Interface Sci. 532 (2018) 280–286, https://doi.org/10.1016/j.jcis.2018.07.108.
[100] P. Wang, S. Sun, X. Zhang, X. Ge, W. Lü, Efficient degradation of organic pollutants and hydrogen evolution by g-C_3N_4 using melamine as the precursor and urea as the modifier, RSC Adv. 6 (2016) 33589–33598, https://doi.org/10.1039/c5ra26890g.
[101] M. Ismael, Y. Wu, D.H. Taffa, P. Bottke, M. Wark, Graphitic carbon nitride synthesized by simple pyrolysis: role of precursor in photocatalytic hydrogen production, New J. Chem. 43 (2019) 6909–6920, https://doi.org/10.1039/c9nj00859d.
[102] W.K. Darkwah, Y. Ao, Mini review on the structure and properties (photocatalysis), and preparation techniques of graphitic carbon nitride nano-based particle, and its applications, Nanoscale Res. Lett. 13 (2018), https://doi.org/10.1186/s11671-018-2702-3.
[103] I. Papailias, T. Giannakopoulou, N. Todorova, D. Demotikali, T. Vaimakis, C. Trapalis, Effect of processing temperature on structure and photocatalytic properties of g-C_3N_4, Appl. Surf. Sci. (2015), https://doi.org/10.1016/j.apsusc.2015.08.097.
[104] S.N. Talapaneni, G. Singh, I.Y. Kim, K. AlBahily, A.H. Al-Muhtaseb, A.S. Karakoti, E. Tavakkoli, A. Vinu, Nanostructured carbon nitrides for CO_2 capture and conversion, Adv. Mater. 32 (2020), https://doi.org/10.1002/adma.201904635.
[105] K. Saravanakumar, R. Karthik, S.M. Chen, J. Vinoth Kumar, K. Prakash, V. Muthuraj, Construction of novel Pd/CeO_2/g-C_3N_4 nanocomposites as efficient visible-light photocatalysts for hexavalent chromium detoxification, J. Colloid Interface Sci. 504 (2017) 514–526, https://doi.org/10.1016/j.jcis.2017.06.003.
[106] P. Praus, A. Smýkalová, K. Foniok, P. Velíšek, D. Cvejn, J. Žádný, J. Storch, Post-synthetic derivatization of graphitic carbon nitride with methanesulfonyl chloride: synthesis, characterization and photocatalysis, Nanomaterials 10 (2020), https://doi.org/10.3390/nano10020193.
[107] T. Suter, V. Brázdová, K. McColl, T.S. Miller, H. Nagashima, E. Salvadori, A. Sella, C.A. Howard, C.W.M. Kay, F. Corà, P.F. McMillan, Synthesis, structure and electronic properties of graphitic carbon nitride films, J. Phys. Chem. C 122 (2018) 25183–25194, https://doi.org/10.1021/acs.jpcc.8b07972.
[108] J. Liu, Origin of high photocatalytic efficiency in monolayer g-C_3N_4/CdS heterostructure: a hybrid DFT study, J. Phys. Chem. C 119 (2015) 28417–28423, https://doi.org/10.1021/acs.jpcc.5b09092.
[109] S.C. Yan, Z.S. Li, Z.G. Zou, Photodegradation performance of g-C_3N_4 fabricated by directly heating melamine, Langmuir 25 (2009) 10397–10401, https://doi.org/10.1021/la900923z.
[110] D. Hollmann, M. Karnahl, S. Tschierlei, K. Kailasam, M. Schneider, J. Radnik, K. Grabow, U. Bentrup, H. Junge, M. Beller, S. Lochbrunner, A. Thomas, A. Brückner, Structure-activity relationships in bulk polymeric and sol-gel-derived carbon nitrides during photocatalytic hydrogen production, Chem. Mater. 26 (2014) 1727–1733, https://doi.org/10.1021/cm500034p.
[111] F. Dong, Z. Wang, Y. Sun, W.K. Ho, H. Zhang, Engineering the nanoarchitecture and texture of polymeric carbon nitride semiconductor for enhanced visible light photocatalytic activity, J. Colloid Interface Sci. 401 (2013) 70–79, https://doi.org/10.1016/j.jcis.2013.03.034.
[112] J. Mao, T. Peng, X. Zhang, K. Li, L. Ye, L. Zan, Effect of graphitic carbon nitride microstructures on the activity and selectivity of photocatalytic CO_2 reduction under visible light, Catal. Sci. Technol. 3 (2013) 1253–1260, https://doi.org/10.1039/c3cy20822b.

[113] Y. He, J. Cai, T. Li, Y. Wu, H. Lin, L. Zhao, M. Luo, Efficient degradation of RhB over $GdVO_4$/g-C_3N_4 composites under visible-light irradiation, Chem. Eng. J. 215–216 (2013) 721–730, https://doi.org/10.1016/j.cej.2012.11.074.
[114] V. Hasija, P. Raizada, A. Sudhaik, K. Sharma, A. Kumar, P. Singh, S.B. Jonnalagadda, V.K. Thakur, Recent advances in noble metal free doped graphitic carbon nitride based nanohybrids for photocatalysis of organic contaminants in water: a review, Appl. Mater. Today 15 (2019) 494–524, https://doi.org/10.1016/j.apmt.2019.04.003.
[115] F. Dong, Y. Sun, L. Wu, M. Fu, Z. Wu, Facile transformation of low cost thiourea into nitrogen-rich graphitic carbon nitride nanocatalyst with high visible light photocatalytic performance, Catal. Sci. Technol. 2 (2012) 1332–1335, https://doi.org/10.1039/c2cy20049j.
[116] S.H. Soytaş, O. Oğuz, Y.Z. Menceloğlu, Polymer nanocomposites with decorated metal oxides, in: Polymer Composites with Functionalized Nanoparticles, Elsevier, 2019, pp. 287–323.
[117] T.K. Tseng, Y.S. Lin, Y.J. Chen, H. Chu, A review of photocatalysts prepared by sol-gel method for VOCs removal, Int. J. Mol. Sci. 11 (2010) 2336–2361, https://doi.org/10.3390/ijms11062336.
[118] D. Lončarević, Ž. Čupić, The perspective of using nanocatalysts in the environmental requirements and energy needs of industry, in: Industrial Applications of Nanomaterials, Elsevier, 2019, pp. 91–122.
[119] Y. Hu, W.A. Daoud, K.K.L. Cheuk, C.S.K. Lin, Newly developed techniques on polycondensation, ring-opening polymerization and polymer modification: focus on poly(lactic acid), Materials (Basel) 9 (2016), https://doi.org/10.3390/ma9030133.
[120] A. Gedanken, Ultrasonic processing to produce nanoparticles, in: Encyclopedia of Materials: Science and Technology, Elsevier, 2011, pp. 9450–9456.
[121] S.K. Bhangu, M. Ashokkumar, Theory of sonochemistry, Top. Curr. Chem. 374 (2016), https://doi.org/10.1007/s41061-016-0054-y.
[122] A. Rockett, The Materials Science of Semiconductors, Springer Science & Business Media, 2007.
[123] R.E. Morris, Ionothermal synthesis – ionic liquids as functional solvents in the preparation of crystalline materials, Chem. Commun. (2009) 2990–2998, https://doi.org/10.1039/b902611h.
[124] D. Nunes, A. Pimentel, L. Santos, P. Barquinha, L. Pereira, E. Fortunato, R. Martins, Synthesis, design, and morphology of metal oxide nanostructures, in: Metal Oxide Nanostructures, Elsevier, Amsterdam, The Netherlands, 2019, pp. 21–57.
[125] F. Zha, T. Wang, M. Luo, J. Guan, Tubular micro/nanomotors: propulsion mechanisms, fabrication techniques and applications, Micromachines 9 (2018), https://doi.org/10.3390/mi9020078.
[126] C. Anastasescu, S. Mihaiu, S. Preda, M. Zaharescu, 1D Oxide Nanostructures Obtained by Sol-Gel and Hydrothermal Methods, Springer, 2016, https://doi.org/10.1007/978-3-319-32988-8.
[127] M.H. Wu, L. Li, Y.C. Xue, G. Xu, L. Tang, N. Liu, W.Y. Huang, Fabrication of ternary GO/g-C_3N_4/MoS_2 flower-like heterojunctions with enhanced photocatalytic activity for water remediation, Appl. Catal. Environ. 228 (2018) 103–112, https://doi.org/10.1016/j.apcatb.2018.01.063.
[128] A. Kumar, A. Kumari, G. Sharma, M. Naushad, T. Ahamad, F.J. Stadler, Utilizing recycled $LiFePO_4$ from batteries in combination with B@C_3N_4 and $CuFe_2O_4$ as sustainable nano-junctions for high performance degradation of atenolol, Chemosphere 209 (2018) 457–469, https://doi.org/10.1016/j.chemosphere.2018.06.117.
[129] W. Zhang, L. Zhou, J. Shi, H. Deng, Fabrication of novel visible-light-driven AgI/g-C_3N_4 composites with enhanced visible-light photocatalytic activity for diclofenac degradation, J. Colloid Interface Sci. 496 (2017) 167–176, https://doi.org/10.1016/j.jcis.2017.02.022.
[130] Y. Xu, W. De Zhang, CdS/g-C_3N_4 hybrids with improved photostability and visible light photocatalytic activity, Eur. J. Inorg. Chem. 2015 (2015) 1744–1751, https://doi.org/10.1002/ejic.201403193.
[131] F. Wang, P. Chen, Y. Feng, Z. Xie, Y. Liu, Y. Su, Q. Zhang, Y. Wang, K. Yao, W. Lv, G. Liu, Facile synthesis of N-doped carbon dots/g-C_3N_4 photocatalyst with enhanced visible-light photocatalytic activity for the degradation of indomethacin, Appl. Catal. Environ. 207 (2017) 103–113, https://doi.org/10.1016/j.apcatb.2017.02.024.
[132] D. Ma, J. Wu, M. Gao, Y. Xin, T. Ma, Y. Sun, Fabrication of Z-scheme g-C_3N_4/RGO/Bi_2WO_6 photocatalyst with enhanced visible-light photocatalytic activity, Chem. Eng. J. 290 (2016) 136–146, https://doi.org/10.1016/j.cej.2016.01.031.

[133] T. Ahamad, M. Naushad, Y. Alzaharani, S.M. Alshehri, Photocatalytic degradation of bisphenol-A with g-C_3N_4/MoS_2-PANI nanocomposite: kinetics, main active species, intermediates and pathways, J. Mol. Liq. 311 (2020), https://doi.org/10.1016/j.molliq.2020.113339.
[134] S. Zuo, Y. Chen, W. Liu, C. Yao, X. Li, Z. Li, C. Ni, X. Liu, A facile and novel construction of attapulgite/Cu_2O/Cu/g-C_3N_4 with enhanced photocatalytic activity for antibiotic degradation, Ceram. Int. 43 (2017) 3324–3329, https://doi.org/10.1016/j.ceramint.2016.11.173.
[135] M.K. Kesarla, M.O. Fuentez-Torres, M.A. Alcudia-Ramos, F. Ortiz-Chi, C.G. Espinosa-González, M. Aleman, J.G. Torres-Torres, S. Godavarthi, Synthesis of g-C_3N_4/N-doped CeO_2 composite for photocatalytic degradation of an herbicide, J. Mater. Res. Technol. 8 (2019) 1628–1635, https://doi.org/10.1016/j.jmrt.2018.11.008.
[136] P. Chen, F. Wang, Q. Zhang, Y. Su, L. Shen, K. Yao, Z.F. Chen, Y. Liu, Z. Cai, W. Lv, G. Liu, Photocatalytic degradation of clofibric acid by g-C_3N_4/P25 composites under simulated sunlight irradiation: the significant effects of reactive species, Chemosphere 172 (2017) 193–200, https://doi.org/10.1016/j.chemosphere.2017.01.015.
[137] X. Liu, R. Ma, L. Zhuang, B. Hu, J. Chen, X. Liu, X. Wang, Recent developments of doped g-C_3N_4 photocatalysts for the degradation of organic pollutants, Crit. Rev. Environ. Sci. Technol. (2020), https://doi.org/10.1080/10643389.2020.1734433.
[138] M. Ismael, Y. Wu, A mini-review on the synthesis and structural modification of g-C_3N_4-based materials, and their applications in solar energy conversion and environmental remediation, Sustain. Energy Fuels 3 (2019) 2907–2925, https://doi.org/10.1039/c9se00422j.
[139] S. Ji, Y. Yang, X. Li, H. Liu, Z. Zhou, Facile production of a Fenton-like photocatalyst by two-step calcination with a broad PH adaptability, Nanomaterials 10 (2020), https://doi.org/10.3390/nano10040676.
[140] M. Khairy, W. Zakaria, Effect of metal-doping of TiO_2 nanoparticles on their photocatalytic activities toward removal of organic dyes, Egypt. J. Pet. 23 (2014) 419–426, https://doi.org/10.1016/j.ejpe.2014.09.010.
[141] X. Chen, S. Shen, L. Guo, S.S. Mao, Semiconductor-based photocatalytic hydrogen generation, Chem. Rev. 110 (2010) 6503–6570, https://doi.org/10.1021/cr1001645.
[142] Z.A. Lan, G. Zhang, X. Wang, A facile synthesis of Br-modified g-C_3N_4 semiconductors for photoredox water splitting, Appl. Catal. Environ. 192 (2016) 116–125, https://doi.org/10.1016/j.apcatb.2016.03.062.
[143] Q. Guo, Y. Zhang, J. Qiu, G. Dong, Engineering the electronic structure and optical properties of g-C_3N_4 by non-metal ion doping, J. Mater. Chem. C 4 (2016) 6839–6847, https://doi.org/10.1039/c6tc01831a.
[144] X. Ma, Y. Lv, J. Xu, Y. Liu, R. Zhang, Y. Zhu, A strategy of enhancing the photoactivity of g-C_3N_4 via doping of nonmetal elements: a first-principles study, J. Phys. Chem. C 116 (2012) 23485–23493, https://doi.org/10.1021/jp308334x.
[145] L. Zhang, Z. Jin, S. Huang, Y. Zhang, M. Zhang, Y.J. Zeng, S. Ruan, Ce-doped graphitic carbon nitride derived from metal organic frameworks as a visible light-responsive photocatalyst for H_2 production, Nanomaterials 9 (2019), https://doi.org/10.3390/nano9111539.
[146] X. She, L. Liu, H. Ji, Z. Mo, Y. Li, L. Huang, D. Du, H. Xu, H. Li, Template-free synthesis of 2D porous ultrathin nonmetal-doped g-C_3N_4 nanosheets with highly efficient photocatalytic H_2 evolution from water under visible light, Appl. Catal. Environ. 187 (2016) 144–153, https://doi.org/10.1016/j.apcatb.2015.12.046.
[147] J. Fang, H. Fan, M. Li, C. Long, Nitrogen self-doped graphitic carbon nitride as efficient visible light photocatalyst for hydrogen evolution, J. Mater. Chem. A 3 (2015) 13819–13826, https://doi.org/10.1039/c5ta02257f.
[148] Q. Han, C. Hu, F. Zhao, Z. Zhang, N. Chen, L. Qu, One-step preparation of iodine-doped graphitic carbon nitride nanosheets as efficient photocatalysts for visible light water splitting, J. Mater. Chem. A 3 (2015) 4612–4619, https://doi.org/10.1039/c4ta06093h.
[149] M. Wang, M. Ye, J. Iocozzia, C. Lin, Z. Lin, Plasmon-mediated solar energy conversion via photocatalysis in noble metal/semiconductor composites, Adv. Sci. 3 (2015), https://doi.org/10.1002/advs.201600024.

[150] J.G. Smith, J.A. Faucheaux, P.K. Jain, Plasmon resonances for solar energy harvesting: a mechanistic outlook, Nano Today 10 (2015) 67–80, https://doi.org/10.1016/j.nantod.2014.12.004.
[151] C. Ao, B. Feng, S. Qian, L. Wang, W. Zhao, Y. Zhai, L. Zhang, Theoretical study of transition metals supported on g-C_3N_4 as electrochemical catalysts for CO_2 reduction to CH_3OH and CH_4, J. CO_2 Util. 36 (2020) 116–123, https://doi.org/10.1016/j.jcou.2019.11.007.
[152] Y. Zheng, Y. Jiao, Y. Zhu, Q. Cai, A. Vasileff, L.H. Li, Y. Han, Y. Chen, S.Z. Qiao, Molecule-level g-C_3N_4 coordinated transition metals as a new class of electrocatalysts for oxygen electrode reactions, J. Am. Chem. Soc. 139 (2017) 3336–3339, https://doi.org/10.1021/jacs.6b13100.
[153] Q. Feng, Electronic, magnetic and optical properties of transition-metal and hydroxides doped monolayer g-C_3N_4: a first principles investigation, J. Phys. Condens. Matter 32 (44) (2020) 445602.
[154] S.L. Li, H. Yin, X. Kan, L.Y. Gan, U. Schwingenschlögl, Y. Zhao, Potential of transition metal atoms embedded in buckled monolayer g-C_3N_4 as single-atom catalysts, Phys. Chem. Chem. Phys. 19 (2017) 30069–30077, https://doi.org/10.1039/c7cp05195f.
[155] X. Chen, R. Hu, DFT-based study of single transition metal atom doped g-C_3N_4 as alternative oxygen reduction reaction catalysts, Int. J. Hydrogen Energy 44 (2019) 15409–15416, https://doi.org/10.1016/j.ijhydene.2019.04.057.
[156] K.R. Tolod, S. Hernández, E.A. Quadrelli, N. Russo, Visible light-driven catalysts for water oxidation: towards solar fuel biorefineries, Studies in Surface Science and Catalysis, 178, Elsevier, 2019, pp. 65–84.
[157] E. Jang, W.J. Kim, D.W. Kim, S.H. Hong, I. Ali, Y.M. Park, T.J. Park, Atomic layer deposition with rotary reactor for uniform hetero-junction photocatalyst, g-C_3N_4@TiO_2 core-shell structures, RSC Adv. 9 (2019) 33180–33186, https://doi.org/10.1039/c9ra05958j.
[158] Y. Zhang, J. Gao, J.M. Liu, X. Wang, G. Zhou, Fabrication and photoelectrochemical properties of silicon nanowires/g-C_3N_4 core/shell arrays, Appl. Surf. Sci. 396 (2017) 609–615, https://doi.org/10.1016/j.apsusc.2016.10.203.
[159] Y. Song, X. She, J. Yi, Z. Mo, L. Liu, H. Xu, H. Li, Single layer two-dimensional O-g-C_3N_4: an efficient photocatalyst for improved molecular oxygen activation ability, Phys. Status Solidi Appl. Mater. Sci. (2017), https://doi.org/10.1002/pssa.201600704.
[160] K. Striegler, Modified Graphitic Carbon Nitrides for Photocatalytic Hydrogen Evolution From Water: Copolymers, Sensitizers and Nanoparticles, Springer, 2015.
[161] N.A. Mohamed, J. Safaei, A.F. Ismail, M.F.A.M. Jailani, M.N. Khalid, M.F.M. Noh, A. Aadenan, S.-N.S. Nasir, J.S. Sagu, M.A.M. Teridi, The influences of post-annealing temperatures on fabrication graphitic carbon nitride, (g-C_3N_4) thin film, Appl. Surf. Sci. 489 (2019) 92–100, https://doi.org/10.1016/j.apsusc.2019.05.312.
[162] H. Fang, H. Ma, C. Zheng, S. Lennon, W. Wu, L. Wu, H. Wang, A high-performance transparent photodetector via building hierarchical g-C_3N_4 nanosheets/CNTs van der Waals heterojunctions by a facile and scalable approach, Appl. Surf. Sci. 529 (2020), https://doi.org/10.1016/j.apsusc.2020.147122.
[163] B. Ou, J. Wang, Y. Wu, S. Zhao, Z. Wang, Degradation of aniline by photoelectro-Fenton process using g-C_3N_4 based cathode, J. Electroanal. Chem. 848 (2019), https://doi.org/10.1016/j.jelechem.2019.113273.
[164] S. Zhang, J. Yan, S. Yang, Y. Xu, X. Cai, X. Li, X. Zhang, F. Peng, Y. Fang, Electrodeposition of Cu_2O/g-C_3N_4 heterojunction film on an FTO substrate for enhancing visible light photoelectrochemical water splitting, J. Catal. 38 (2017) 365–371, https://doi.org/10.1016/S1872-2067(16)62588-3.
[165] R. Tejasvi, S. Basu, Formation of C_3N_4 thin films through the stoichiometric transfer of the bulk synthesized gC_3N_4 using RFM sputtering, Vacuum 171 (2020), https://doi.org/10.1016/j.vacuum.2019.108937.
[166] B. Song, T. Wang, L. Wang, H. Liu, X. Mai, X. Wang, N. Wang, Y. Huang, Y. Ma, Y. Lu, E.K. Wujcik, Z. Guo, Interfacially reinforced carbon fiber/epoxy composite laminates via in-situ synthesized graphitic carbon nitride (g-C_3N_4), Compos. Part B Eng. 158 (2019) 259–268, https://doi.org/10.1016/j.compositesb.2018.09.081.

[167] S. Halevy, E. Korin, A. Bettelheim, Electropolymerization as a new route to g-C_3N_4 coatings on TiO_2 nanotubes for solar applications, RSC Adv. 6 (2016) 87314–87318, https://doi.org/10.1039/c6ra18855a.
[168] R. Liu, Z. Zheng, J. Spurgeon, X. Yang, Enhanced photoelectrochemical water-splitting performance of semiconductors by surface passivation layers, Energy Environ. Sci. 7 (2014) 2504–2517, https://doi.org/10.1039/c4ee00450g.
[169] L.F. Villalobos, M.T. Vahdat, M. Dakhchoune, Z. Nadizadeh, M. Mensi, E. Oveisi, D. Campi, N. Marzari, K.V. Agrawal, Large-scale synthesis of crystalline g-C_3N_4 nanosheets and high-temperature H_2 sieving from assembled films, Sci. Adv. 6 (2020), https://doi.org/10.1126/sciadv.aay9851.
[170] M. Shakeel, M. Arif, G. Yasin, B. Li, H.D. Khan, Layered by layered Ni-Mn-LDH/g-C_3N_4 nanohybrid for multi-purpose photo/electrocatalysis: morphology controlled strategy for effective charge carriers separation, Appl. Catal. Environ. 242 (2019) 485–498, https://doi.org/10.1016/j.apcatb.2018.10.005.
[171] Y. Wang, X. Zhang, Y. Liu, Y. Zhao, C. Xie, Y. Song, P. Yang, Crystallinity and phase controlling of g-C_3N_4/CdS heterostructures towards high efficient photocatalytic H_2 generation, Int. J. Hydrogen Energy 44 (2019) 30151–30159, https://doi.org/10.1016/j.ijhydene.2019.09.181.
[172] Y.T. Qian, Y.L. Gu, J. Lu, Solvothermal synthesis of non-oxide nanomaterials, in: The Chemistry of Nanomaterials, Wiley-VCH Verlag GmbH & Co. KGaA, 2004, pp. 170–207.
[173] P. Yadav, P.K. Dwivedi, S. Tonda, R. Boukherroub, M.V. Shelke, Metal and non-metal doped metal oxides and sulfides, Green Photocatalysts, Springer, Cham, 2020, pp. 89–132.
[174] Parul, K. Kaur, R. Badru, P.P. Singh, S. Kaushal, Photodegradation of organic pollutants using heterojunctions: a review, J. Environ. Chem. Eng. 8 (2020), https://doi.org/10.1016/j.jece.2020.103666, 103666.
[175] R. Jiang, H. Michaels, N. Vlachopoulos, M. Freitag, Beyond the limitations of dye-sensitized solar cells, in: Dye-Sensitized Solar Cells, Academic Press, 2019, pp. 285–323.
[176] A. Irfan, A.G. Al-Sehemi, S. Muhammad, Towards rational designing of efficient sensitizers based on thiophene and infrared dyes for dye-sensitized solar cells, J. Quantum Chem. 2014 (2014) 1–6, https://doi.org/10.1155/2014/796790.
[177] R. Zhang, A. Zhang, Y. Yang, Y. Cao, F. Dong, Y. Zhou, Surface modification to control the secondary pollution of photocatalytic nitric oxide removal over monolithic protonated g-C_3N_4/graphene oxide aerogel, J. Hazard. Mater. 397 (2020), https://doi.org/10.1016/j.jhazmat.2020.122822.
[178] R. Li, J. Huang, M. Cai, J. Huang, Z. Xie, Q. Zhang, Y. Liu, H. Liu, W. Lv, G. Liu, Activation of peroxymonosulfate by Fe doped g-C_3N_4/graphene under visible light irradiation for Trimethoprim degradation, J. Hazard. Mater. 384 (2020), https://doi.org/10.1016/j.jhazmat.2019.121435.
[179] Q. Song, J. Li, L. Wang, L. Pang, H. Liu, Controlling the chemical bonding of highly dispersed co atoms anchored on an ultrathin g-C_3N_4@carbon sphere for enhanced electrocatalytic activity of the oxygen evolution reaction, Inorg. Chem. 58 (2019) 10802–10811, https://doi.org/10.1021/acs.inorgchem.9b01089.
[180] W. Zhou, T. Jia, D. Zhang, Z. Zheng, W. Hong, X. Chen, The enhanced co-catalyst free photocatalytic hydrogen evolution and stability based on indenofluorene-containing donor-acceptor conjugated polymer dots/g-C_3N_4 nanosheets heterojunction, Appl. Catal. Environ. 259 (2019), https://doi.org/10.1016/j.apcatb.2019.118067.
[181] H.H. Wu, C.W. Chang, D. Lu, K. Maeda, C. Hu, Synergistic effect of hydrochloric acid and phytic acid doping on polyaniline-coupled g-C_3N_4 nanosheets for photocatalytic Cr(VI) reduction and dye degradation, ACS Appl. Mater. Interfaces 11 (2019) 35702–35712, https://doi.org/10.1021/acsami.9b10555.
[182] D. Qin, W. Lu, X. Wang, N. Li, X. Chen, Z. Zhu, W. Chen, Graphitic carbon nitride from burial to re-emergence on polyethylene terephthalate nanofibers as an easily recycled photocatalyst for degrading antibiotics under solar irradiation, ACS Appl. Mater. Interfaces 8 (2016) 25962–25970, https://doi.org/10.1021/acsami.6b07680.
[183] H. Yan, Y. Huang, Polymer composites of carbon nitride and poly(3-hexylthiophene) to achieve enhanced hydrogen production from water under visible light, Chem. Commun. 47 (2011) 4168–4170, https://doi.org/10.1039/c1cc10250h.

[184] S. Liu, H. Sun, K. O'Donnell, H.M. Ang, M.O. Tade, S. Wang, Metal-free melem/g-C_3N_4 hybrid photocatalysts for water treatment, J. Colloid Interface Sci. 464 (2016) 10–17, https://doi.org/10.1016/j.jcis.2015.11.003.
[185] X. Yang, F. Qian, G. Zou, M. Li, J. Lu, Y. Li, M. Bao, Facile fabrication of acidified g-C_3N_4/g-C_3N_4 hybrids with enhanced photocatalysis performance under visible light irradiation, Appl. Catal. Environ. 193 (2016) 22–35, https://doi.org/10.1016/j.apcatb.2016.03.060.
[186] S. Tonda, S. Kumar, M. Bhardwaj, P. Yadav, S. Ogale, G-C_3N_4/NiAl-LDH 2D/2D hybrid heterojunction for high-performance photocatalytic reduction of CO_2 into renewable fuels, ACS Appl. Mater. Interfaces 10 (2018) 2667–2678, https://doi.org/10.1021/acsami.7b18835.
[187] A. Akhundi, A. Habibi-Yangjeh, M. Abitorabi, S. Rahim Pouran, Review on photocatalytic conversion of carbon dioxide to value-added compounds and renewable fuels by graphitic carbon nitride-based photocatalysts, Catal. Rev. Sci. Eng. 61 (2019) 595–628, https://doi.org/10.1080/01614940.2019.1654224.
[188] Y. Sun, T. Xiong, Z. Ni, J. Liu, F. Dong, W. Zhang, Improving G-C_3N_4 photocatalysys for NOx removal by Ag nanoparticles decoration, Appl. Surf. Sci. 358 (2015) 356–362.
[189] G. Dong, W. Ho, C. Wang, Selective photocatalytic N_2 fixation dependent on g-C_3N_4 induced by nitrogen vacancies, J. Mater. Chem. A 3 (2015) 23435–23441, https://doi.org/10.1039/c5ta06540b.
[190] A. Mishra, A. Mehta, S. Basu, N.P. Shetti, K.R. Reddy, T.M. Aminabhavi, Graphitic carbon nitride (g–C_3N_4)–based metal-free photocatalysts for water splitting: a review, Carbon N. Y. 149 (2019) 693–721, https://doi.org/10.1016/j.carbon.2019.04.104.
[191] G. Dong, Y. Zhang, Q. Pan, J. Qiu, A fantastic graphitic carbon nitride (g-C_3N_4) material: electronic structure, photocatalytic and photoelectronic properties, J. Photochem. Photobiol. C Photchem. Rev. 20 (2014) 33–50, https://doi.org/10.1016/j.jphotochemrev.2014.04.002.
[192] G.T.S.T. da Silva, K.T.G. Carvalho, O.F. Lopes, C. Ribeiro, g-C_3N_4/Nb_2O_5 heterostructures tailored by sonochemical synthesis: enhanced photocatalytic performance in oxidation of emerging pollutants driven by visible radiation, Appl. Catal. Environ. 216 (2017) 70–79, https://doi.org/10.1016/j.apcatb.2017.05.038.
[193] L. Dong, T. Xu, W. Chen, W. Lu, Synergistic multiple active species for the photocatalytic degradation of contaminants by imidazole-modified g-C_3N_4 coordination with iron phthalocyanine in the presence of peroxymonosulfate, Chem. Eng. J. 357 (2019) 198–208, https://doi.org/10.1016/j.cej.2018.09.094.
[194] S.L. Prabavathi, K. Saravanakumar, G. Mamba, V. Muthuraj, 1D/2D $MnWO_4$ nanorods anchored on g-C_3N_4 nanosheets for enhanced photocatalytic degradation ofloxacin under visible light irradiation, Colloids Surf. A Physicochem. Eng. Asp. 581 (2019) 123845, https://doi.org/10.1016/j.colsurfa.2019.123845.
[195] S. Vigneshwaran, J. Preethi, S. Meenakshi, Removal of chlorpyrifos, an insecticide using metal free heterogeneous graphitic carbon nitride (g-C_3N_4) incorporated chitosan as catalyst: photocatalytic and adsorption studies, Int. J. Biol. Macromol. 132 (2019) 289–299, https://doi.org/10.1016/j.ijbiomac.2019.03.071.
[196] S. Ghodsi, A. Esrafili, R.R. Kalantary, M. Gholami, H.R. Sobhi, Synthesis and evaluation of the performance of g-C_3N_4/Fe_3O_4/Ag photocatalyst for the efficient removal of diazinon: kinetic studies, J. Photochem. Photobiol. A Chem. 389 (2020), https://doi.org/10.1016/j.jphotochem.2019.112279.
[197] L. Zhao, C. Deng, S. Xue, H. Liu, L. Hao, M. Zhu, Multifunctional g-C_3N_4/Ag NPs intercalated GO composite membrane for SERS detection and photocatalytic degradation of paraoxon-ethyl, Chem. Eng. J. 402 (2020), https://doi.org/10.1016/j.cej.2020.126223.
[198] S. Moorthy, G. Moorthy, K. Swaminathan, Fabrication of novel $ZnSeO_3$ anchored on g-C_3N_4 nanosheets: an outstanding photocatalyst for the mitigation of pesticides and pharmaceuticals, J. Inorg. Organomet. Polym. Mater. (2020), https://doi.org/10.1007/s10904-020-01615-5.
[199] Aanchal, S. Barman, S. Basu, Complete removal of endocrine disrupting compound and toxic dye by visible light active porous g-C_3N_4/H-ZSM-5 nanocomposite, Chemosphere 241 (2020), https://doi.org/10.1016/j.chemosphere.2019.124981.
[200] D. Ayodhya, G. Veerabhadram, Ultrasonic synthesis of g-C_3N_4/CdS composites and their photodegradation, catalytic reduction, antioxidant and antimicrobial studies, Mater. Res. Innov. 24 (2020) 210–228, https://doi.org/10.1080/14328917.2019.1634356.

[201] T. Chen, P. Chen, Q. Zhang, X. Zheng, Z. Xie, Y. Zeng, P. Chen, H. Liu, Y. Liu, W. Lv, G. Liu, Photocatalyst with a metal-free electron-hole pair double transfer mechanism for pharmaceutical and personal care product degradation, Environ. Sci.: Nano 6 (2019) 3292–3306, https://doi.org/10.1039/c9en00756c.
[202] Z. Sun, X. Zhang, X. Dong, X. Liu, Y. Tan, F. Yuan, S. Zheng, C. Li, Hierarchical assembly of highly efficient visible-light-driven Ag/g-C_3N_4/kaolinite composite photocatalyst for the degradation of ibuprofen, J. Mater. 6 (2020) 582–592, https://doi.org/10.1016/j.jmat.2020.04.008.
[203] C. Zhao, Z. Liao, W. Liu, F. Liu, J. Ye, J. Liang, Y. Li, Carbon quantum dots modified tubular g-C_3N_4 with enhanced photocatalytic activity for carbamazepine elimination: mechanisms, degradation pathway and DFT calculation, J. Hazard. Mater. 381 (2020), https://doi.org/10.1016/j.jhazmat.2019.120957.
[204] Y. Hong, C. Li, B. Yin, D. Li, Z. Zhang, B. Mao, W. Fan, W. Gu, W. Shi, Promoting visible-light-induced photocatalytic degradation of tetracycline by an efficient and stable beta-Bi_2O_3@g-C_3N_4 core/shell nanocomposite, Chem. Eng. J. 338 (2018) 137–146, https://doi.org/10.1016/j.cej.2017.12.108.
[205] F. Wang, Y. Wang, Y. Feng, Y. Zeng, Z. Xie, Q. Zhang, Y. Su, P. Chen, Y. Liu, K. Yao, W. Lv, G. Liu, Novel ternary photocatalyst of single atom-dispersed silver and carbon quantum dots co-loaded with ultrathin g-C_3N_4 for broad spectrum photocatalytic degradation of naproxen, Appl. Catal. B Environ. 221 (2018) 510–520, https://doi.org/10.1016/j.apcatb.2017.09.055.
[206] Q. Zheng, D.P. Durkin, J.E. Elenewski, Y. Sun, N.A. Banek, L. Hua, H. Chen, M.J. Wagner, W. Zhang, D. Shuai, Visible-light-responsive graphitic carbon nitride: rational design and photocatalytic applications for water treatment, Environ. Sci. Technol. 50 (2016) 12938–12948, https://doi.org/10.1021/acs.est.6b02579.
[207] M. Tang, Y. Ao, C. Wang, P. Wang, Facile synthesis of dual Z-scheme g-C_3N_4/Ag_3PO_4/AgI composite photocatalysts with enhanced performance for the degradation of a typical neonicotinoid pesticide, Appl. Catal. Environ. 268 (2020), https://doi.org/10.1016/j.apcatb.2019.118395.
[208] M.B. Tahir, M. Sagir, K. Shahzad, Removal of acetylsalicylate and methyl-theobromine from aqueous environment using nano-photocatalyst WO_3-TiO_2 @g-C_3N_4 composite, J. Hazard. Mater. 363 (2019) 205–213, https://doi.org/10.1016/j.jhazmat.2018.09.055.
[209] M. Liang, Z. Zhang, R. Long, Y. Wang, Y. Yu, Y. Pei, Design of a Z-scheme g-C_3N_4/CQDs/$CdIn_2S_4$ composite for efficient visible-light-driven photocatalytic degradation of ibuprofen, Environ. Pollut. 259 (2020), https://doi.org/10.1016/j.envpol.2019.113770.
[210] L. Zhou, Z. Liu, Z. Guan, B. Tian, L. Wang, Y. Zhou, Y. Zhou, J. Lei, J. Zhang, Y. Liu, 0D/2D plasmonic $Cu_{2-x}S$/g-C_3N_4 nanosheets harnessing UV-vis-NIR broad spectrum for photocatalytic degradation of antibiotic pollutant, Appl. Catal. Environ. 263 (2020), https://doi.org/10.1016/j.apcatb.2019.118326.
[211] X. Yi, J. Yuan, H. Tang, Y. Du, B. Hassan, K. Yin, Y. Chen, X. Liu, Embedding few-layer $Ti_3C_2T_x$ into alkalized g-C_3N_4 nanosheets for efficient photocatalytic degradation, J. Colloid Interface Sci. 571 (2020) 297–306, https://doi.org/10.1016/j.jcis.2020.03.061.
[212] Y. Chen, W. Lu, H. Shen, Y. Gu, T. Xu, Z. Zhu, G. Wang, W. Chen, Solar-driven efficient degradation of emerging contaminants by g-C_3N_4-shielding polyester fiber/TiO_2 composites, Appl. Catal. Environ. 258 (2019), https://doi.org/10.1016/j.apcatb.2019.117960.

CHAPTER 9

Artificial photosynthesis by carbon nitride-based composite photocatalysts

Konstantinos C. Christoforidis[a,b]
[a]Department of Environmental Engineering, Democritus University of Thrace, Xanthi, Greece
[b]Institut de Chimie et Procédés Pour l'Energie, l'Environnement et la Santé (ICPEES), ECPM University of Strasbourg, Strasbourg, France

Contents

The link between energy sources and development became clear even at the first steps of industrialization. Nowadays, it is evidenced that this is not enough and development must be realized with renewable energy sources produced through a sustainable process. There are two distinct reasons for this. First, the issue originates from the demand for energy that is globally rising rapidly and the progressive depletion of fossil fuels, i.e., currently the main source for energy production. Second, the sever environmental impact due to the use of traditional fossil fuels. This last issue is mostly linked with climate change and in particular global warming that has been evidenced in the last decades due to the production of greenhouse gas (GHGs). Among the different gases that contribute to global warming, carbon dioxide (CO_2) is listed among the top contributors. This is mainly due to its high production rates that results in increasing concentration. Although CO_2 has been in the atmosphere since the beginning of time, its negative effect originates from the destabilization of the natural carbon cycle. In this direction, man-kind activities are currently considered as major contributors of CO_2 emissions. Among the different CO_2 emission sectors, the energy sector occupies the vast majority of CO_2 emission in the atmosphere [1]. In this respect, "anthropogenic activities" and in particular activities related with the production of energy, is the only parameter that can be controlled by our site as a way to reestablish equilibrium in natural environment. Nature has established a cycle to maintain CO_2 at acceptable levels; however, this cycle is relatively slow and cannot manage the high amounts originating from anthropogenic activities. Based on the above-mentioned grounds, the search for alternative, renewable and clean energy

Nanostructured Carbon Nitrides for Sustainable Energy and Environmental Applications
https://doi.org/10.1016/B978-0-12-823961-2.00009-4

sources is an unavoidable step so that development will not be reached on the expense of natural environment and human health.

Even though sustainable clean energy production is a well-known issue for decades, it is still one of the major challenges man-kind is facing. Many different approaches have been proposed and explored including chemical, biological, thermally, and electrically triggered approaches. However, issues related with efficiency and the true environmental character of the process still remain. Among the proposed processes, the application of solid semiconductors as catalysts to perform photo-triggered reactions with the aid of solar energy has been emerged as promising approach that can deal both with clean energy production *via* a sustainable approach and environmental protection. The strategy of applying heterogeneous photocatalysis making use of a free, endless and renewable energy, e.g., solar energy, combined with the production of carbon-free fuels seems ideal for the development of a "carbon-neutral" society with zero CO_2 emissions during production and combustion of the fuel. One of the main advantages of photocatalysis is that it is a stand-alone process and does not require any external energy input. However, there are several shortcomings in this process that must be fixed in order to meet industrial needs.

Photocatalysis is based on a mechanism developed by nature, i.e., photosynthesis that makes use of solar energy as the only energy input to perform a specific reaction. Natural photosynthesis actually stores solar energy in chemical bonds through the synthesis of carbohydrates and oxygen using as feedstocks CO_2 and water. This directs a way to produce sustainable and clean energy. Based on this approach, the application of photocatalysis and proper choice of the substrate that will be converted seems suitable to deal with the issue of energy production *via* a sustainable and environmental friendly process. On our way to mimic natural photosynthesis, a chemical process named *artificial photosynthesis* has been developed. This term includes any reaction that is triggered by light (ideally solar light) and converts solar energy into chemical energy. In order for this process to be considered sustainable, suitable substrates must be used. Photocatalytic water splitting converts water into hydrogen (H_2) and O_2. H_2 is considered as the fuel of the future. It is a carbon-free fuel since when combined with O_2 (fuel cell technology), the energy stored is released with the concomitant production of only water. It must be pointed that currently natural gas is mostly used for the production of H_2 (steam reforming process). However, this process cannot be considered sustainable due to two issues: (i) it makes use of a fossil fuel that will inevitably deplete and (ii) produces CO_2. Photocatalytic CO_2 reduction into valuable chemicals including fuels is a process that mimics natural carbon fixation performed *via* photosynthesis. Although hydrocarbons are developed through this approach, the use of CO_2 before entering into the atmosphere results in a carbon neutral technology. Therefore, both H_2O and CO_2 could be used as cheap and largely available feedstocks for the production of clean energy and in particular fuels through artificial photosynthesis. This process is a fascinating and simple method to obtain energy reach chemicals. It should be highlighted that currently clean fuel production must be our primary target since large-scale energy storage using batteries is still expensive, although significant improvements have been achieved in this field in the last years.

Despite the tremendous efforts that have been devoted over the last years and the major improvements performed in the field of photocatalytic fuel production, efficiency still remains as the main drawback for large-scale applications, domestic or industrial. To this end, it is clear that the properties of the photocatalyst used plays essential role. As a limiting rule, the fundamental electronic properties (see in the next section) must be obeyed so that a semiconductor can be applied either for H_2 evolution or CO_2 reduction. Many different photocatalysts have been developed and tested (metal oxides, sulfides, and hydroxides) [2,3]. Among them, inorganic semiconductors have been mostly developed and optimized. TiO_2 is certainly the most used material for any photocatalytic reaction. Some inorganic photocatalysts present impressive photoactivity in hydrogen production, e.g., $Cd_xZn_{1-x}S$ presents ~93% quantum yield of H_2 production from aqueous S_2^-/SO_3^{2-} solution [4]. However, the main limitation of using inorganic materials is the difficulty to finetune important parameters such as the electronic and optical properties. In addition, toxicity issues may arise (i.e., dissolution and release of toxic Cd^{2+}). To add to the complexity of the optimization process, synthesis protocols must be usually performed under milled and perfectly controllable conditions. This is not the case for most of the inorganic semiconductors developed so far.

Although carbon based photocatalysts present advantages compared with inorganic semiconductors in several aspects, the development and application of organic photocatalysts is significantly less studied. In 2009, the photocatalytic properties of a new type of carbon-based semiconductor (graphitic like carbon nitride or polymeric carbon nitride (CN)) was demonstrated in the water splitting process [5]. CN, a conjugated polymer, is metal-free semiconductor made solely of earth abundant elements: carbon, nitrogen, and hydrogen. In CN structure, tri-*s*-triazine/heptazine or *s*-triazine unites are covalently connected via tertiary amines forming 2D sheets. The 2D sheets are stacked through weak van der Waals forces forming the bulk CN structure [5]. The photocatalytic properties of Cn originate from its π-conjugated electronic structure. Its chemical composition, structure and fasil synthesis process provides interesting properties such as chemical and thermal stability under working conditions, nontoxicity, interesting electronic properties and reasonable fabrication cost. One of the main advantages of CN as photocatalyst is that it absorbs light in the visible region of light ($\lambda < 460$ nm, i.e., relatively narrow band gap SC), a critical parameter in photocatalytic applications. This makes it suitable for applications using solar light irradiation. In this type of materials, the actual chemical composition, the structure as well as the morphology of the material plays crucial on the final chemical, optical, and electronic properties. Among the most interesting properties of CN is its polymeric nature that allows easy and permanent modification in contrast with traditional inorganic semiconductors. This gives a plethora of opportunities for chemical modification as a way to tune the chemical, textural, and optoelectronic properties. These advantages have emerged CN-based materials into promising candidates for many important applications. Among other, these include its application as photocatalyst for energy production and in particular solar fuels, since it possesses suitable band structure for both H_2 production and CO_2 reduction. Nevertheless, despite the many privileges mentioned earlier, bare bulk CN materials suffer from fast charge recombination rates, a phenomenon that diminish its application. As will be discussed in the following in detail, several different approaches have been studied to minimize this issue. Among these, CN-based composite materials cover a big class of materials that has been developed as a way to overcome the limitations of the bare bulk CN.

In this chapter, we will discuss the recent developments on CN-based composite materials applied as photocatalysts in artificial photosynthesis. Nevertheless, since a solid understanding of the principles of the photocatalytic process as well as the synthesis of CN materials are essential for the development of efficient catalysts for solar fuel production, an introduction on the basic principles of photocatalysis, the drawbacks and limitations followed by a brief discussion on the synthesis protocols of CN will be given before moving to the CN-based materials development section.

1. Elementary steps in photocatalytic processes

The photocatalytic process is a catalytic reaction that is initiated by light irradiation and performs redox (reduction and oxidation) reactions through the formation of photogenerated charges, electrons and hole pairs (e^-/h^+). Therefore, the first step in such reactions is the formation of photogenerated e^- and h^+. Photocatalytic reactions may be divided into two main classes, homogeneous and heterogeneous reactions. Obviously heterogeneous catalysis that makes use of semiconductors (SCs) offers advantages due to the easy separation of the catalyst from the reaction mixture. When SCs are exposed to light of energy greater than the energy difference between the bottom level of the conduction band (CB) and the top level of the valence band (VB), e^- are excited from the VB to the CB living behind an empty state at the VB, i.e., h^+. In other words, the energy of the light must be higher than the band gap (E_g) energy of the SCs. In SCs, the e^-/h^+ pairs should ideally be generated by solar light, and in particular by visible-light irradiation in order to make use as much as possible of the light reaching the surface of earth. This adds the first important limitation on the search of efficient photoactive materials, i.e., photocatalysts must make use the visible region of solar light as much as possible in order to ensure a better exploration of the environmental character of the process. Once the e^-/h^+ pairs are formed, several steps must follow so that a reaction on the surface of the catalyst to occur. Following formation, the photogenerated charges must be separated and transferred to the surface of the catalyst in order to perform redox reactions. Therefore, recombination phenomena at the bulk and the surface of the material must be avoided. Different approaches have been applied to minimize charge recombination including chemical/compositional and morphological modification including the size and the shape of the SC. A schematic illustration of the basic steps in a photocatalytic reaction

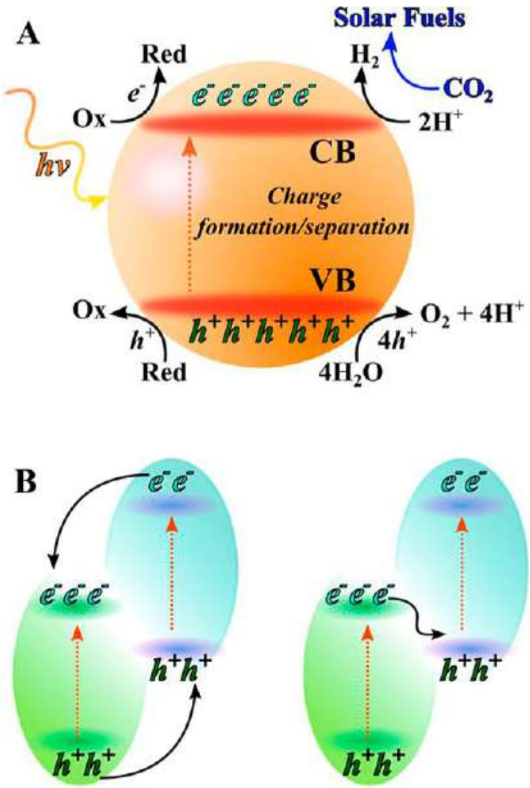

Fig. 9.1 (A) Charge formation in SCs and redox reactions performed on the surface of the SC. (B) Charge transfer mechanism in heterojunctions of Type-II (left panel) and Z-scheme heterojunction (right panel). *(Reprinted from K.C. Christoforidis, P. Fornasiero, Photocatalysis for hydrogen production and CO_2 reduction: the case of copper-catalysts, ChemCatChem 11 (2019) 368–382, with permission from Wiley.)*

together with the reactions describing water splitting process and CO_2 reduction is given in Fig. 9.1A.

The photoactivity of a SC is controlled by many different parameters such as the specific surface area since reactions are performed on the surface of the catalyst, charge recombination rates, light absorption (preferentially in the visible region of light), stability under working conditions to name a few. It is clear, therefore, that the choice of the SC will define activity. However, the property that allows the realization of a specific reaction is the actual band structure of the catalyst and in particular the energy of the CB and VB level. In order for a reduction reaction to occur, the CB level must by more negative than the specific redox couple's normal potential. The same stands for the VB h^+, i.e. VB h^+ must be more positive than the specific redox couple's normal potential. Therefore, the electronic properties related with E_g and the actual level of the CB and VB are the main parameters that direct the utilization of a photocatalyst in specific application.

2. Fundamentals of photocatalytic water splitting and CO_2 reduction

We should start by highlighting that photocatalytic H_2 production from the water splitting process and CO_2 reduction are competing reactions since both make use of CB electrons. They were both demonstrated for the first time in the same period [6,7] but H_2 evolution reaction is significantly more studied than CO_2 reduction due to the inherent difficulties of the later. In both processes, an electron donor must be supplied to consume the VB h^+. The choice of the reductant will define sustainability. Ideally, a largely available substance with no environmental impact should be used. Water fulfills these requirements. However, water oxidation is a highly demanding 4-electron reaction and practically is the bottleneck of the water splitting process.

Two half reactions consist the water splitting process. The first is the proton reduction into H_2 and the second water oxidation producing O_2 and H^+. Other inorganic and organic substrates have been also used as h^+ scavengers in the photocatalytic H_2 evolution reaction, mainly due to the easier oxidation process compared with water. In the case of organic oxygenates, the process is named photoreforming [8].

In the case of CO_2 reduction, the process is more difficult and complicated. First to mention is that the one-electron reduction reaction of CO_2 has high standard electrochemical potential (−1.9 eV vs SHE at pH 7). There is no photocatalyst with that high CB level and at the same time able to oxidize water. In addition, more than one product is usually formed during CO_2 reduction. This raises the question of selectivity toward one specific reaction product, making more difficult products detection and would require complicated separation processes. Compared with the direct CO_2 reduction process, the proton-assisted multielectron CO_2 reduction process is energetically less demanding reaction since it has lower redox potentials. However, besides thermodynamic and kinetic barriers due to the multielectron transfer process, the CO_2 reduction process requires C-C coupling and hydrogenation reactions. To add to the complexity of the CO_2 reduction reaction, one should mention the low solubility of CO_2 in water. This drawback can be bypassed by performing the reaction in organic solvents or in the presence of chemicals with high CO_2 affinity. However, this adds environmental issues to the overall process that cannot be overlooked. All these barriers resulted in the domination of the water splitting process over CO_2 reduction in the field of solar fuels production. The standard reduction potentials *vs* SHE of several common reactions for CO_2 reduction are listed in Table 9.1 together with the standard potentials for the two half reactions in the water splitting process. As it can be seen, the proton assisted multielectron reduction process of CO_2 possesses occur at similar potentials as the proton reduction in the H_2 evolution process.

Table 9.1 Redox potential of the two half reactions in the water splitting process and selected reactions in the CO_2 photocatalytic reduction [1,9].

Reaction	E_0 (SHE, pH 7)
$2H_2O + 4h^+ \rightarrow 4H^+ + 2O_2 + 4e^-$	+0.81
$2H^+ 2e^- \rightarrow H_2$	−0.42
$CO_2 + e^- \rightarrow CO_2^-$	−1.90
$CO_2 + 2H^+ + 2e^- \rightarrow HCOOH$	−0.61
$CO_2 + 2H^+ + 2e^- \rightarrow CO + H_2O$	−0.53
$CO_2 + 4H^+ + 4e^- \rightarrow HCHO + H_2O$	−0.48
$CO_2 + 6H^+ + 6e^- \rightarrow CH_3OH + H_2O$	−0.38
$CO_2 + 8H^+ + 8e^- \rightarrow CH_4 + 2H_2O$	−0.24

3. Composite photoactive materials—General remarks

As stated earlier, photoactivity depends on many different parameters. Usually, the fine-tuning of one parameter affects other critical parameters as well. For example, the doping process has been widely applied to improve the light absorption properties of SCs. However, the presence of dopants at interstitial or substitutional positions in the lattice many also introduce charge recombination centers in the material [10,11]. It is clear, therefore, that modification processes of the bare SC must be performed under perfectly controlled conditions. In this direction, the coupling of different materials for the formation of composites offers advantages, since the synthesis of each material can be tuned before the coupling. In addition, the plethora of photoactive nanomaterials presented in the literature offers the possibility of many different combinations as a way to improve more than one parameter in parallel. The restriction in this process is that the coupled materials should present a chemical interaction since simple physical mixtures do not offer the desired interaction.

Composite materials through the coupling of either bare CN or modified versions of CN with other materials including SCs correspond to a large class of CN-based materials applied as photocatalysts in many different applications. This is an efficient approach used to expand the properties of many SCs and improve photo activity [3,12]. Usually, the developed composite materials target on the improvement of light absorption, charge formation and separation, to introduce morphological restrictions to the one part [13] and selectivity. There is no restriction on the number of the coupled materials but, obviously, one must be photoactive. It should be emphasized though that multicomponent systems such as ternary [3] and quaternary materials increase the difficulty of the synthesis step and requires in depth analysis to elucidate the role of each part in the final composite.

In the specific case where two SCs are coupled, the resulted material is a heterojunction. However, coupling of a SC with insulators, conductive materials and metallic nanoparticles has been also applied to improve several material's properties [3,14–17]. In the case of heterojunctions, different types of heterojunctions can be developed depending on relative position of their CB and VB levels. Therefore, care must be given in the actual band structure of the coupled materials, so that charge separation will occur. In coupled SCs, photogenerated charges are spontaneously transferred to levels of lower energy. This, if certain criteria are fulfilled, allow efficient charge separation as well as sensitization of wide band-gap SCs. Fig. 9.1B presents a schematic representation of the charge transfer mechanism in Type-II and Z-scheme heterojunctions. In Type-II heterojunctions, coupled SCs with correctly aligned band structures allow the transfer of photogenerated e^- and h^+ in opposite parts of the composite. This reduces significantly charge recombination rates and increases their abundance and stability. This particular type may also be used to sensitize SCs with large E_g through the coupling with narrow E_g SCs. Despite the advantages in charge separation, Type-II heterojunctions present a significant shortcoming. The energy of the photogenerated charges is reduced since they are transferred to lower laying energy levels, reducing the driving force to perform a specific reaction. On the contrary, Z-scheme heterojunctions (right panel in Fig. 9.1B), that mimic the natural photosynthetic centers, allow charge separation not at the expense of the energy.

Special attention must be also given in the coupling of a SC with metallic nanoparticles. In the case of H_2 evolution reaction, noble metals have been widely used to increase activity. This is mostly attributed to the charge separation. The difference in the Fermi level between the metallic nanoparticles and the SC allows the formation of a Schottky barrier, allowing the migration of the photogenerated e^- to the metal center. In this class of materials special attention has been also given on the coupling of SCs with plasmonic metal particles, a direction that mimics the dye sensitization approach by increasing light absorption and injecting electrons to the SC. The presence of plasmons on the surface of the SC induces charge formation at or near the surface of the SC, increasing the abundance of such species by reducing their migration distance.

4. CN synthesis

The fasil development process of CN is one of its main advantages. However, the actual synthesis conditions applied including the precursor used (melamine, cyanamide, dicyanamide, urea, thiourea), the thermal conditions etc. play essential role on the properties of the final material. A variety of synthesis protocols have been developed for the preparation of bulk CN as well as to add dimensional, morphological, and compositional constrains or to posttreat bulk CN. Two general directions have been applied. The bottom-up approach involves the assembly via thermal polycondensation of nitrogen reach organic precursors while the top-down approach includes the treatment of preformed CN. Processes that have been applied for the development of CN-based materials include solvothermal/hydrothermal conditions (at moderate temperatures and high pressure) [18], electrochemical deposition [19], solid-state synthesis [20] but the process that

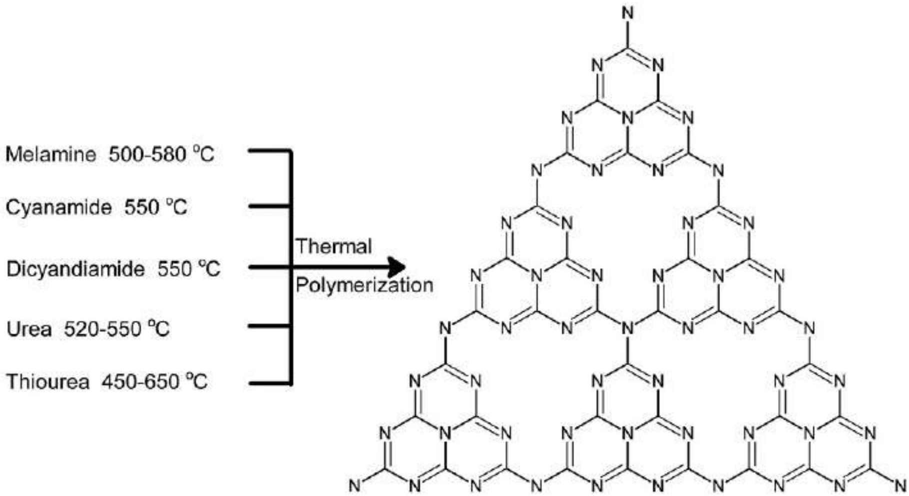

Fig. 9.2 Thermal polymerization process of different precursors for the synthesis of CN. *(Adapted from W.J. Ong, L.L. Tan, Y.H. Ng, S.T. Yong, S.P. Chai, Graphitic carbon nitride (g-C_3N_4)-based photocatalysts for artificial photosynthesis and environmental remediation: are we a step closer to achieving sustainability?, Chem. Rev. 116 (2016) 7159–7329.)*

has been mostly applied is a direct thermal treatment of an N-containing organic precursor, mainly due to the simplicity of the process. In this last case, at approximately 390–400°C the rearrangement of melamine molecules forms *s*-triazine units and with further hitting (>520°C) condensation of the *s*-triazine units results in the formation of polymeric CN. A schematic representation of the synthesis procedure using different precursors is given in Fig. 9.2. The temperature of the thermal treatment for the polycondensation of the organic precursor should be above 500°C. It is highlighted that even small alterations in the synthesis protocol may significantly affect the properties of CN. Different conditions have been applied in this step to optimize the synthesis process such as the use of different precursors, treatment of the precursors before the thermal treatment, variations of the actual thermal treatment (temperature, ramp, atmosphere) [21–23], etc.

One of the two main drawbacks of CN synthesized through the direct thermal polycondensation process is the low surface area due to the layered structure of the formed bulk material. As expected, variations have been reported in the literature depending on the actual thermal conditions applied as well as the precursor used. Low surface area is detrimental to photoactivity. In this direction, the application of the templating technique (hard and soft) has been reported to be useful in controlling primarily the surface area (i.e., formation of porous structures) but the morphology as well. All textural properties as well as morphology can be tubed using proper templates. SiO_2 particles including mesoporous silica templates (i.e., SBA-15) are typical examples of substrates in the hard-templating method [24] while ionic liquids and surfactants have been reported in the soft-templating process [25]. Self-templating processes, i.e., preassembling and formation of supramolecular structures (self-templating methods), by using different molecules/structures as precursors is another interesting approach to control key textural properties [26]. The obvious advantage of this process is that there is no need for an external template, a factor that diminishes the extra posttreatment step of removing the template that usually requires hazardous agents. Template-free methods have been also developed for controlling the morphology such as simple reflux of preformed CN in the presence of specific solvent mixtures [27]. Exfoliation of the bulk CN structure and the formation of CN nanosheets (NS) even single-layer CN is also a highly applied process to improve in parallel the textural properties and charge recombination phenomena. Many different processes have been applied for the formation of CN NS, of which the modification of the thermal treatment is one of the most used processes. For example, the presence of lithium chloride ions and the stepwise thermal polycondensation of dicyandiamide that was used as the CN precursor resulted in the formation of porous CN NS nanostructures with significantly improved specific surface area than the bulk CN [28]. The exact thermal conditions, besides optimization of the textural properties may induce changes in the electronic properties related with the actual band structure, i.e., the E_g and the energy level of the CB. This was very nicely demonstrated by Niu et al. that applied a thermal oxidation etching of bulk CN for the development of CN NS [29]. The authors controlled the thickness of CN NS by varying the temperature of the thermal treatment (Fig. 9.3). In general, posttreated bulk CN under high temperatures present higher surface area and improve the charge handling properties (higher electron mobility), prolonging the lifetime of charge carriers and enhancing significantly the photocatalytic activity [29,30]. In addition, by prolonging the pyrolysis step small CN layers may be produced [31]. Soft silk-like nanostructures were observed at 240 min pyrolysis period at 550°C, while large CN layers were detected at very short pyrolysis steps (Fig. 9.4). This

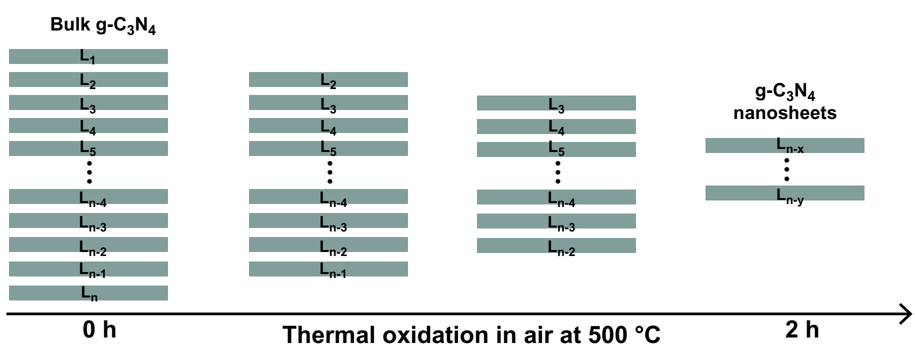

Fig. 9.3 Schematic of the formation process of the g-C_3N_4 nanosheets by thermal oxidation etching of bulk g-C_3N_4 at 500°C in air. *(Reproduced with permission from P. Niu, L. Zhang, G. Liu, H.-M. Cheng, Graphene-like carbon nitride nanosheets for improved photocatalytic activities, Adv. Funct. Mater. 22 (2012) 4763–4770, Copyright 2012, Wiley-VCH.)*

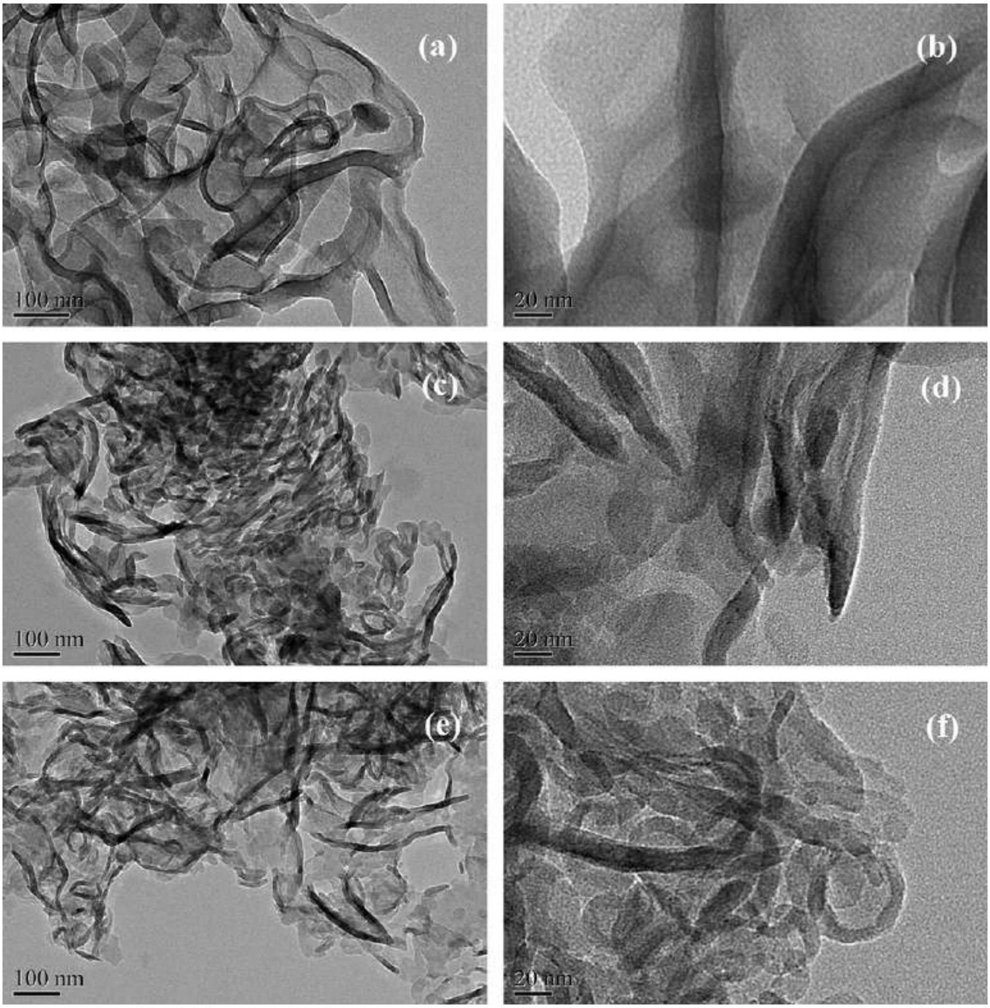

Fig. 9.4 TEM images of CN materials prepared by varying the pyrolysis period of urea at 550°C. *(Reprinted from F. Dong, Z. Wang, Y. Sun, W.K. Ho, H. Zhang, Engineering the nanoarchitecture and texture of polymeric carbon nitride semiconductor for enhanced visible light photocatalytic activity, J. Colloid Interface Sci. 401 (2013) 70–79, with permission from Elsevier.)*

was critical in controlling surface area. However, an increase in the E_g is usually observed in the modified catalysts without losing the visible-light activity (Fig. 9.5) [32].

The second main limitation of bulk CN materials is the fast recombination rate of photogenerated structures that hinders activity. In this case, besides control of the CN morphology, several other approaches have been applied to improve the electronic properties related with the abundance and stability of e^-/h^+ pairs. The doping technique is a well-known method applied extensively as a modification process of SCs. Doping of CN

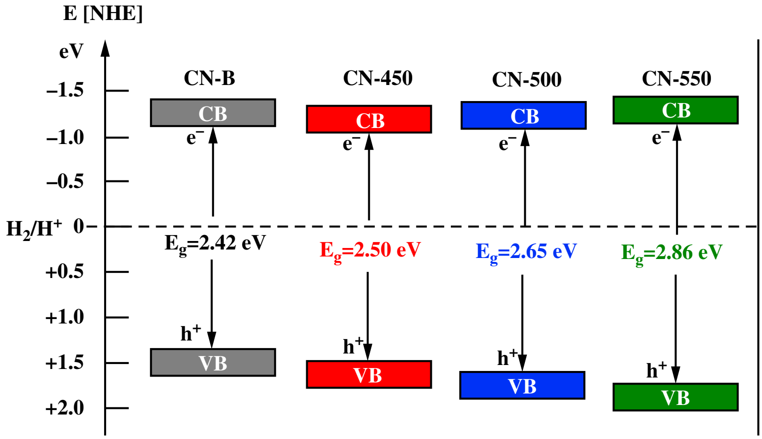

Fig. 9.5 Electronic band structure of CN posttreated at different temperatures. *(Reprinted from F. Dong, Y. Li, Z. Wang, W.-K. Ho, Enhanced visible light photocatalytic activity and oxidation ability of porous graphene-like g-C_3N_4 nanosheets via thermal exfoliation, Appl. Surf. Sci. 358 (2015) 393–403, with permission from Elsevier.)*

with heteroatoms has been also applied and besides improvements in light absorption, charge separation efficiency has been also improved [8]. Usually, the method adopted for the doping of CN is the in-situ process where the dopant precursor (metal salts or organics) is mixed with the CN precursor prior to the thermal treatment. As in all cases where impurities are introduced into the structure of the catalyst as a way to improve a specific parameter, the amount the dopant plays essential role. First to mention is that the heteroatom must occupy a small fraction of the catalyst in order to be considered as a dopant. Usually, photoactivity presents a "volcano" type relationship with the amount of the dopant used [2], presenting an increase up to a critical point after which begins to decrease with increasing dopant amount [33]. As mentioned earlier, the morphology of the CN material may also improve the charge availability and, therefore, activity. Liang et al. reported a simple thermal treatment for the development of CN NS with abundant structural defects and vacancies to modify light absorption properties and the band structure as well as to minimize recombination phenomena [34]. The structural defects formed together with the NS morphology were the main reasons for the nearly 20-fold increase of the H_2 production compared with the bulk CN.

CN-based composite materials and especially CN coupled with other SCs for the development of heterojunctions are a large class of materials that have been developed to eliminate the limitations of CN as photocatalyst. In this particular case, composites are formed in order to couple the properties of the different parts and also to develop properties unpresented in the individual counterparts, e.g., synergistic effect. The advantage of this process is that it offers the possibility to fine tune the properties of the final material under mild and perfectly controlled conditions and improve in parallel many different material properties. In the next section, the advantages in the field of CN-based composite materials applied as photocatalysts in the water splitting process and CO_2 reduction will be discussed.

5. CN-based composite materials for artificial photosynthesis

Due to the urgent need for the sustainable production of carbon-free fuels, it is not surprising that the photocatalytic properties of CN were first demonstrated in the water splitting process [5]. As a general remark in photocatalytic H_2 production, a cocatalyst is frequently required to improve photoactivity while usually a sacrificial reagent is used. The reason behind the use of a cocatalyst is to improve the availability of photogenerated electrons. In this direction, a noble metal with high work function can trap easily the e^-. It is generally accepted that between a SC and a metal nanoparticle the formation of a Schottky barrier takes place due to the difference in the Fermi levels of the coupled systems, allowing the transfer of e^- from the CB of the SC into the metal [35,36]. On the contrary, the promotional effect of the latter case, i.e., use of a sacrificial reagent, is based on the easier consumption of the h^+, i.e. lower redox potential required. However, even with these adjustments, the low efficiency of bulk CN against H_2 photocatalytic production still remains, a reason that dictated the need for modification of the bare catalyst. In this direction, many composite materials were developed mainly through the coupling of CN with other SC as well as other nanostructures. A variety metal oxides [2,37] and sulfides [38,39], metals [40,41], or even carbon nanostructures [14,42,43] were effectively coupled with CN toward enhancing activity.

Coupling of CN with metal nanoparticles may result in significant improvement in charge separation through the fast migration of e^- from the CB of CN to the metal to align the Fermi energy levels at the interface. Therefore, metal nanoparticles can act as electron traps and in this way the recombination phenomena are reduced. Based on this, noble metals have been widely applied due to their large work function. Metals with higher work function would perform better. This was very nicely shown in a series of metal nanoparticles/CN coupled systems where Pt/CN presented superior photoactivity due to the largest work function of Pt nanoparticles [44]. Of course, one should mention that many other parameters of the metal nanoparticle such as particle size that is also related with the dispersion of the nanoparticles on CN, light absorption properties including SPR effects, the content of the metal nanoparticle play vital role in activity. Therefore, care must be given on the characterization of the final material that should include as much as possible all effects. It should be pointed out that CN catalysts without the presence of a cocatalyst are practically inactive in the water splitting process. Traditionally, Pt nanoparticles played the role of the cocatalyst due to the easy preparation process (in-situ photodeposition is usually applied) and the large work function.

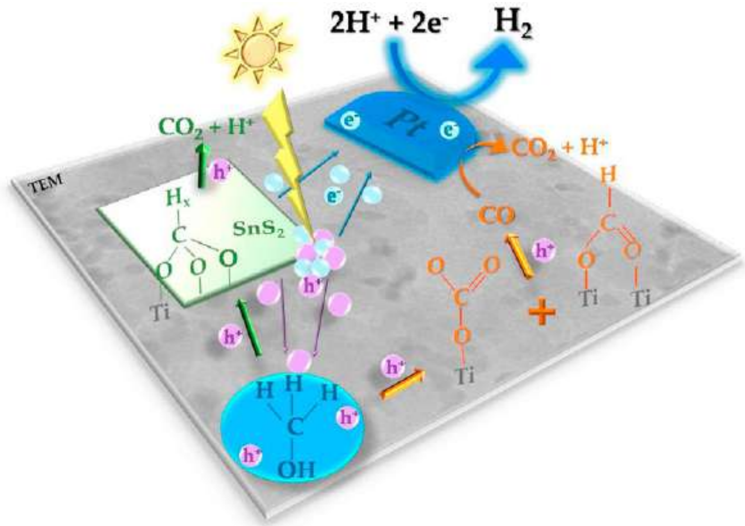

Fig. 9.6 Photochemical processes for H_2 photocatalytic production in Pt-TiO_2 system in the presence (*green*, *dark gray* in print version) and in the absence (*orange*, *light gray* in print version) of SnS_2. *(Reprinted from I. Barba-Nieto, K.C. Christoforidis, M. Fernández-García, A. Kubacka, Promoting H_2 photoproduction of TiO_2-based materials by surface decoration with Pt nanoparticles and SnS_2 nanoplatelets, Appl. Catal. B Environ. 277 (2020) 119246, with permission from Elsevier.)*

Improvements in photoactivity have been also shown for Pt loaded CN composite materials. For example, the presence of Pt nanoparticles enhanced H_2 evolution in CeO_x/CN composites [45]. This has been also documented for other types of heterojunctions, i.e., oxide/sulfide heterojunctions [3]. In these ternary systems, besides optimization of the content of all parts in the composite, care must be given in the order of the deposition. This may have a significant impact on the control of the interaction of the different parts in the composite. We have very recently demonstrated that in TiO_2-based materials decorated on the surface with SnS_2 nanoplatelets and Pt nanoparticles (i.e., ternary systems), Pt nanoparticles must have a strong interaction with both TiO_2 and SnS_2 phases, acting as e^- sink for both photoactive TiO_2 and SnS_2 (Fig. 9.6). This was controlled by the order of the deposition on TiO_2 particles. Even if the coupled SCs improve charge separation, the presence of Pt nanoparticles further improves the availability of the charges and, hence, activity. This observation can easily be expanded to other SCs and metal nanoparticles. However, it must be emphasized that the increase of the number of the phases in a composite increases the complexity of the system and full characterization with high resolution techniques able to discriminate changes at subnanometer level is essential to resolve the underlying mechanism.

As in all coupled systems, the interaction between CN and the metal plays essential role. This was very nicely demonstrated by Shiraishi et al. where they applied two different approaches to deposit Pt nanoparticles on CN [46]. The high temperature reduction process applied for the deposition of Pt nanoparticles on CN lead to stronger interaction between the Pt and CN and resulted in a significant enhancement in H_2 production. However, photodeposition of Pt nanoparticles on a SC is usually reported as the best deposition process since it allows the development of Pt nanoparticles close to the active surface centers of the catalyst. This highlights the complexity of the process for the development of efficient photocatalysts.

Noble metals have been widely applied as cocatalyst especially for the photocatalytic H_2 production reaction. Pt is the most used metal nanoparticle as cocatalyst. However, the use of noble metals should be avoided due to the high cost. In this direction, the development of bimetallic nanoparticles (i.e., alloy cocatalysts) has been introduced as an alternative. Besides lowering the cost, the development of alloys offers the possibility to control important parameters by varying the content of the different phases as well as the structure. For example, PtCo alloy nanoparticles deposited on 2D CN NS using an in-situ chemical method were identified as suitable cocatalyst for H_2 evolution under pure visible-light irradiation [47]. If fact, the optimum PtCo/CN catalyst was more active than the corresponding monometallic Pt/CN system, $960\,\mu mol\,h^{-1}\,g^{-1}$ vs $330\,\mu mol\,h^{-1}\,g^{-1}$, respectively. The Fermi energy level of the bimetallic PtCo nanoparticles was lower than the CB of CN, allowing efficient charge separation. More importantly, the driving force for e^- transfer from the CB of CN to the metal nanoparticle is higher in the PtCo case than the Pt due to the change of the Fermi energy level. This originated from the presence of Co that increased the surface defects in the bimetallic system. Nevertheless, the presence of Co decreased the adsorption of H^+. Therefore, care must be given in the molar ratio of the coupled metals in multiphase nanoparticles. Coupling of CN with Pd nanoparticles has been also utilized for H_2 evolution but Pd presents stronger adsorption of H_2 [48]. However, precise engineering has been applied by Cao et al. for the development of Pd/CN materials that presented superior photocatalytic H_2 production than the Pt/CN benchmark photocatalyst [49]. By applying a multistep process, atomic Pd was intercalated into the gap between the layers of CN framework and the simultaneous decoration of CN surface with single atomic Pd. The intercalated Pd acted as vertical channels and directed charge transport from the bulk through the different CN layers improving charge separation, a mechanism that is not easy to be accomplished in bare CN due to the weak van der Waals forces between the different layers. On the other hand, surface Pd atoms acted as reactive sites (Fig. 9.7). Single Pd atoms on CN were also found more active than CN functionalized with Pd nanoparticles [48].

No-noble metal nanoparticles on CN have been also utilized in the photocatalytic H_2 production reaction [16,50]. Ni nanoparticles were deposited on CN via a facile reduction of Ni(II) using the photogenerated e^- from CN [50]. The amount of Ni was optimized and the photocatalyst presented significant H_2 evolution rates under natural sunlight ($4000\,\mu mol\,g^{-1}\,h^{-1}$) without significant deactivation. The high production rates were ascribed to the efficient charge separation.

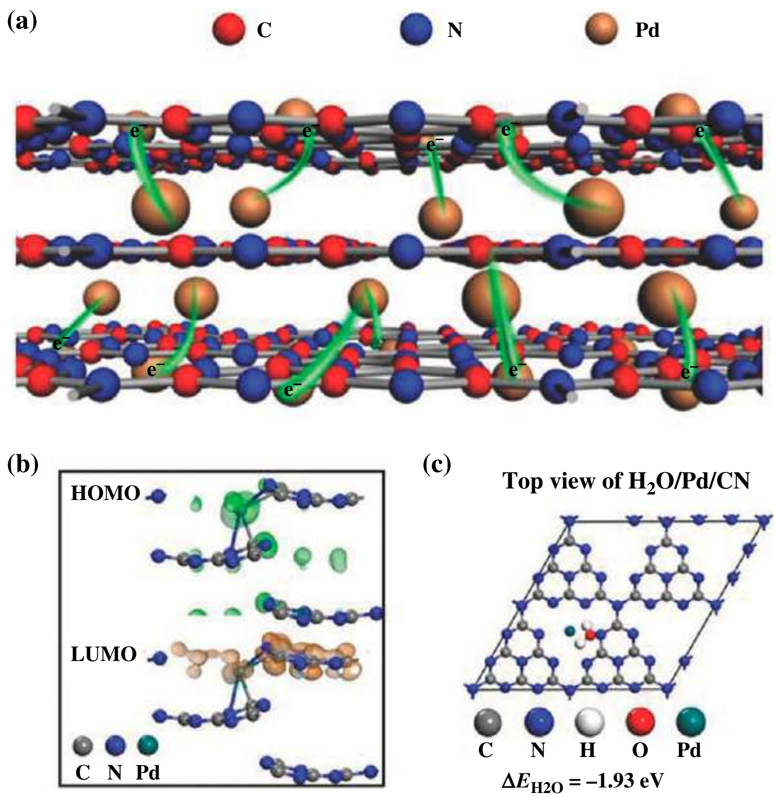

Fig. 9.7 (A) Schematic illustration of interlayered into CN and surface anchored of Pd on CN. (B) HOMO and LUMO of Pd/CN. (C) Adsorption energy of H_2O on the Pd/CN. *(Reproduced with permission from S. Cao, H. Li, T. Tong, H.-C. Chen, A. Yu, J. Yu, H.M. Chen, Single-atom engineering of directional charge transfer channels and active sites for photocatalytic hydrogen evolution, Adv. Funct. Mater. 28 (2018) 1802169, Copyright 2018, Wiley-VCH.)*

Besides coupling of the bare CN with other nanostructures, the combined modification of bare CN and the formation of a composite have been also shown beneficial to further improve photoactivity. The combined functionalization of CN with amines and Au nanoparticles developed under a single process presented (Fig. 9.8) enhanced photocatalytic CO_2 reduction compared with the reference materials under pure visible-light irradiation [51]. The enhanced photocatalytic activity was attributed to the improvement of the available e^- and the presence of NH_2 groups that increased CO_2 adsorption capacity. The structure of the metal nanoparticle may also affect significantly photoactivity and selectivity. This was documented in Pd/CN composites where the morphology (surface facets) of the Pd nanoparticle was controlled [52]. A solution-phase process using different facet-selective capping agents was adopted for the

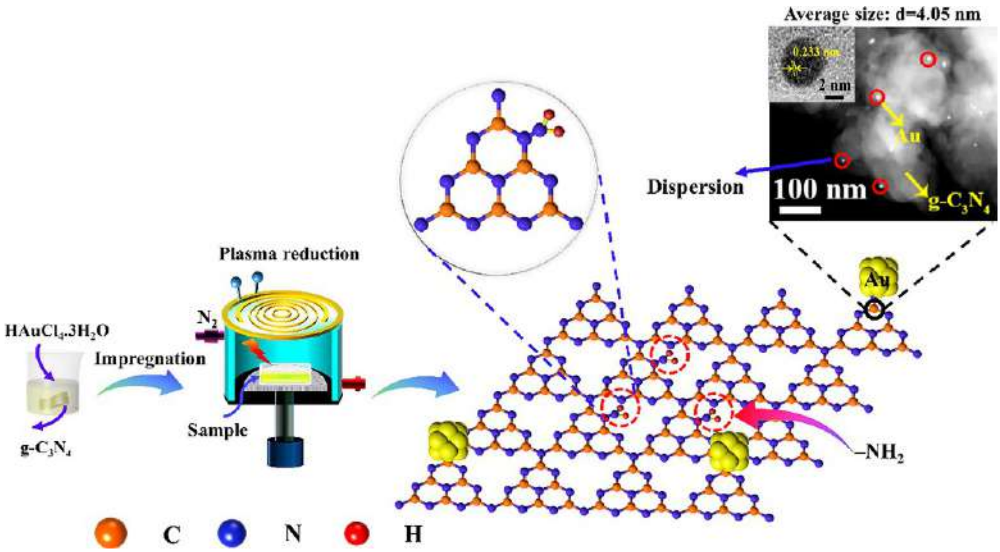

Fig. 9.8 Schematic illustration of the synthesis of NH_2-functionalized CN coupled with Au nanoparticles. *(Reprinted with from F. Li, H. Zhou, J. Fan, Q. Xiang, Amine-functionalized graphitic carbon nitride decorated with small-sized Au nanoparticles for photocatalytic CO_2 reduction, J. Colloid Interface Sci. 570 (2020) 11–19, with permission from Elsevier.)*

development of single-faceted Pd particles on the CN. The Pd [111] facets were selective for CO_2 reduction while the selectivity for H_2 evolution was higher on Pd [100] facets.

An additional advantage in the metal nanoparticles CN composites is that specific metal nanostructures can absorb strongly light in the visible region due to their surface plasmon resonance effect [35,36,53]. The use of transition metals for the development of binary metal nanoparticles such as CuPt alloys may be used not only to improve the economics of the process but also the light absorption properties [54]. Cu nanoparticles promoted light absorption to the visible region and improved the charge handling properties in Cu/CN composites improving significantly photoactivity [16]. Recently, the conditions applied for the synthesis of CN and the coupling with Au nanoparticles were evaluated for the H_2 evolution reaction [55]. It was shown that photoactivity is greatly affected by the properties of the CN and not only by the presence of plasmonic Au particles. This study once again highlighted that the possibilities to optimize the catalytic properties of composite materials are greatly enhanced compared to single phase materials. Nevertheless, although plasmonic nanoparticles offer obvious improvements in specific properties, research should focus on abundant metal. In this direction, Cu nanoparticles are promising candidates both for CO_2 reduction and H_2 evolution reaction.

Molecular doping through the introduction of organic functional into the framework of CN and the development of modified structures is also considered as a strategy to develop CN-based composites [56]. This is usually achieved in-situ through the copolymerization approach or via postsynthetic modification of CN through covalent functionalization. Different heteromolecules have been incorporated into the CN framework. Many examples in this family of materials have demonstrated that extended π-delocalization improves light absorption [57]. The introduction of barbituric acid did not alter the morphology of CN but affected significantly the electronic properties [58]. The amount of barbituric acid played also vital role in H_2 production. High amounts had detrimental effects in photoactivity under UV-vis irradiation while low amounts improved performance compared with the bare CN reference. The introduction of strong electron donor groups taking into account the aromaticity in order to match the structure of CN such as thiophene moieties [59] can be used to control the band structure. In the specific case of incorporating thiophene, charge separation was also improved [59]. Molecular complexes have been also used to functionalize CN. This approach resembles the molecular incorporation in the CN framework but molecular complexes offer the additional advantage to act as catalysts for a specific reaction. Recently, Pan et al. combined CN with bipyridine cobalt molecular catalyst by covalent bond and verified the importance of forming a surface molecular junction for improving H_2 evolution and CO_2 reduction [60]. The covalent assembly of $Co(bpy)_3^{2+}$ and CN presented significant improvement of charge separation due to the interfacial e^- transfer from CN to the CO molecular catalyst. Biisonicotinic acid was used as the covalent linker. Efficient charge transfer is not possible in physical mixtures (Fig. 9.9). The covalent functionalization of CN with $Co(bpy)_3^{2+}$ presented orders of magnitude superior photocatalytic activity for H_2 production and CO_2 reduction compared with $CN/Co(bpy)_3^{2+}$ physical mixtures (Fig. 9.10). Ruthenium binuclear complex coupled with CN where proven highly selective and robust catalysts for the reduction of CO_2 into HCOOH under pure visible-light irradiation [61]. In this system, the incorporation of Ag nanoparticles and the development of Ru/Au/CN ternary catalyst further improved photocatalytic activity. An impressive selectivity up to 99% toward the synthesis of HCOOH was demonstrated. The binuclear Ru/Ru′/Au/CN catalyst follows a Z-scheme charge transfer mechanism that resembles photosystem II. In such systems, many parameters affect efficiency and stability including the chemical moieties used to anchor the molecular catalyst [62,63].

Undoubtedly, the vast majority of CN-based composites applied in artificial photosynthesis concerns the coupling of CN with SCs for the synthesis of heterojunctions. In this case as well, the primary aim is to improve the charge separation efficiency and increase their availability. However, other important aspects such as the increase of the interaction of the catalyst with the substrate (i.e., CO_2) may be also improved. This last argument is based on the low solubility of CO_2 in water (i.e., the solvent of choice for

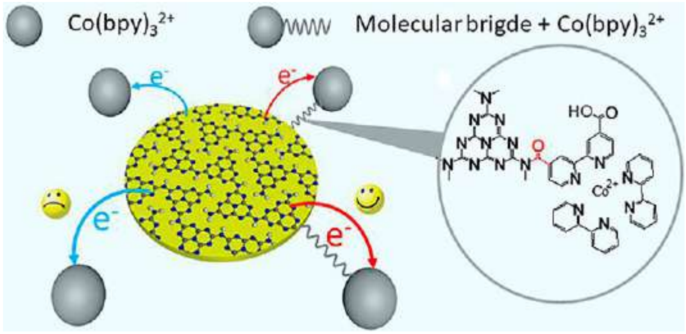

Fig. 9.9 Electron transfer in physical mixture and covalently linked CN and $Co(bpy)_3^{2+}$. *(Reproduced with permission from Z. Pan, P. Niu, M. Liu, G. Zhang, Z. Zhu, X. Wang, Molecular junctions on polymeric carbon nitrides with enhanced photocatalytic performance, ChemSusChem 13 (2020) 888–892, Copyright 2020, Wiley-VCH.)*

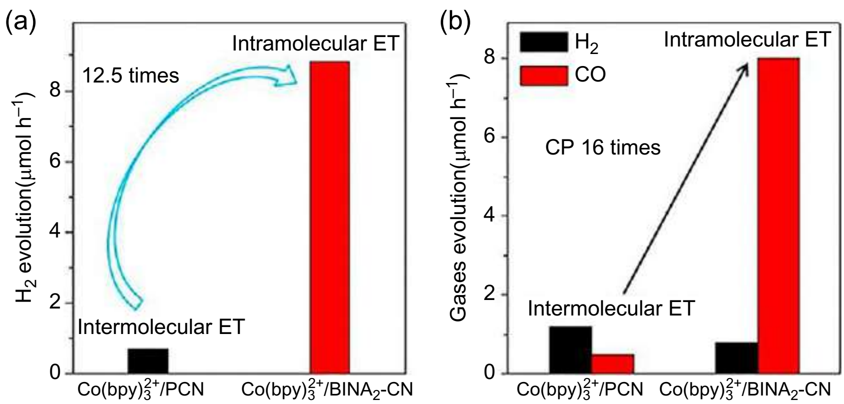

Fig. 9.10 Photocatalytic H_2 production rates (A) and CO_2 reduction (B) by CN/$Co(bpy)_3^{2+}$ physical mixture and covalently linked CN/$Co(bpy)_3^{2+}$. *(Reproduced with permission from Z. Pan, P. Niu, M. Liu, G. Zhang, Z. Zhu, X. Wang, Molecular junctions on polymeric carbon nitrides with enhanced photocatalytic performance, ChemSusChem 13 (2020) 888–892, Copyright 2020, Wiley-VCH.)*

a true environmental friendly technology) and the low specific surface area of traditional photocatalysts. Due to the huge number of SCs studied, different couplings have been tested. In this class of materials, of particular importance is the development of isotype CN heterojunctions where nonidentical CN structures are coupled, known also as crystal-phase heterojunctions. This is similar to the P25 TiO_2 case that contains both anatase and rutile TiO_2 structures and allows charge separation. Typical examples include the combined polymerization of different CN precursors [64,65]. Formation of a Type-II heterojunction was developed by the thermal polycondensation of both urea and thiourea [64]. A heterojunction was formed that allowed charge migration via the interphase

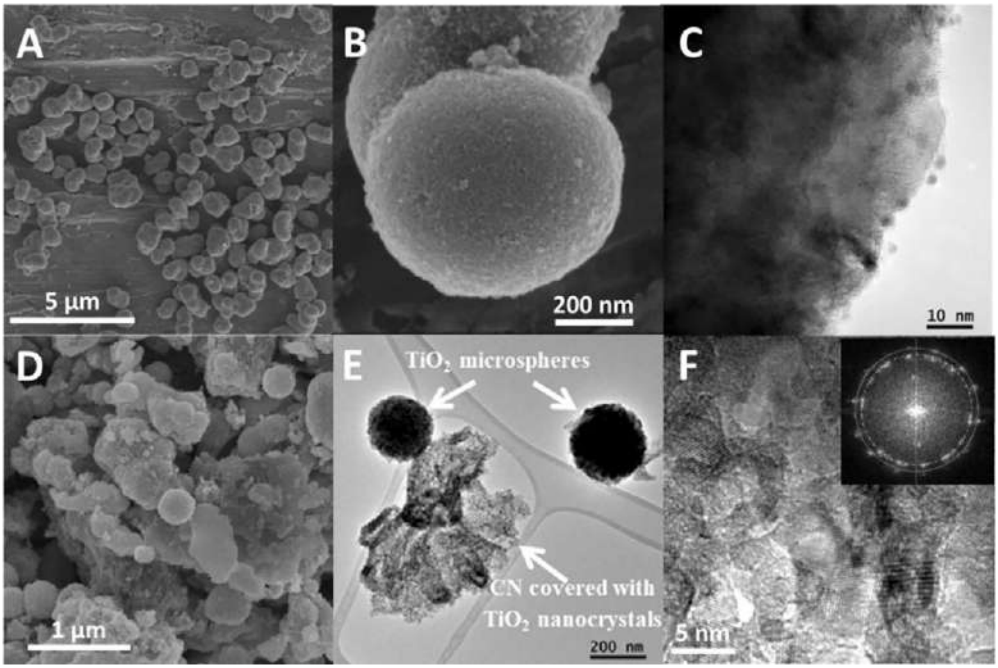

Fig. 9.11 SEM and HRTEM images of pure TiO_2 (A)–(C) and CN/B-doped TiO_2 composite (D)–(F). *(Reproduced with permission from K.C. Christoforidis, T. Montini, M. Fittipaldi, J.J.D. Jaén, P. Fornasiero, Photocatalytic hydrogen production by boron modified TiO_2/carbon nitride heterojunctions, ChemCatChem 11 (2019) 6408–6416, Copyright 2019, Wiley-VCH.)*

improving charge separation. Similarly, post formation process of the heterojunction can be also applied on preformed CN. Using dicyandiamide and trithiocyanuric acid, Zhang et al. developed CN isotype heterojunction in a two-step process [65]. The improved photocatalytic activity in H_2 production was ascribed to the improved charge separation via the interface of the CN parts developed from the different precursors.

CN-based heterojunctions have been also developed using other SCs. CN/TiO_2 heterojunctions have been widely applied in many different reactions [66–68]. In this type of materials, bare as well as modified version of the two parts was used. Coupling of CN NS with bare as well as B-doped CN resulted in improved photocatalytic H_2 production under artificial solar light irradiation and using Pt 1 wt% as cocatalyst (Fig. 9.11) [2]. A tight interaction of TiO_2 and CN was observed using EPR spectroscopy verified through the interaction of Ti^{3+} centers with the nuclear spin of N ($I=1$). This strong interaction allowed the photogenerated charges to migrate to opposite directions in the composite, e^- on TiO_2 and h^+ on CN. Besides chemical modification, studies have also shown that the morphology of TiO_2 crystals affect also activity in TiO_2/CN composites [69]. This is related with the reactivity of the specific TiO_2 plane [69]

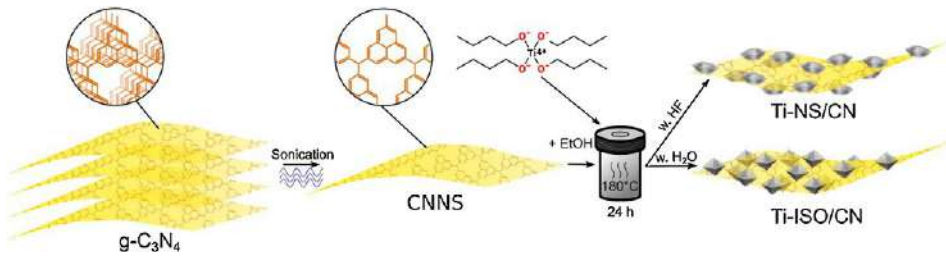

Fig. 9.12 Schematic representation of the TiO_2/CN NS composites synthesis controlling the morphology of TiO_2 particles. *(Reprinted from A. Crake, K.C. Christoforidis, R. Godin, B. Moss, A. Kafizas, S. Zafeiratos, J.R. Durrant, C. Petit, Titanium dioxide/carbon nitride nanosheet nanocomposites for gas phase CO_2 photoreduction under UV-visible irradiation, Appl. Catal. B Environ. 242 (2019) 369–378, with permission from Elsevier.)*

or even with the interaction with the CN [66]. Besides charge separation, CN coupled with TiO_2 may result in alteration of the specific surface area, improve the light absorption properties and affect the crystal size [70], all important parameters in controlling catalytic efficiency.

We have recently highlighted the crucial effect of morphology of TiO_2 nanoparticles on the efficiency of the photocatalytic CO_2 reduction reaction using TiO_2/CN NS heterojunctions [66]. TiO_2 NS nanocrystals with predominant |001} facets as well as nonshaped TiO_2 nanoparticles with |101} exposed facets were coupled with CN NS (Fig. 9.12). Although the bare TiO_2 NS showed lower activity compared with the isotropic shape TiO_2, when they were coupled with the CN NS the TiO_2 NS/CN NS heterojunction presented superior activity than the corresponding heterojunction containing nonshaped TiO_2 nanoparticles. By applying advanced transient absorption spectroscopy, we have shown that in the heterojunction with 2D/2D morphology charge separation via the interface was significantly improved. This was ascribed to the enhanced contact between the two phases of the composite. As is it obvious, in order for charge separation to take place in multiphase materials, an interface must be formed. If fact, more efficient charge transfer is anticipated for larger contact area. Comparing the different size interface based on the morphology at the nanoscale of the used counterparts in a composite (i.e., 0D, 1D, 2D, and 3D), the coupling of 2D materials offers the higher contact area [71]. 2D/2D van der Waals heterojunctions made of $Bi_xO_yS_z$ nanoplates and atomically thin CN NS have been synthesized and tested in CO_2 reduction [72]. Formation of CH_4 and CH_3OH was ascribed to the strong adsorption of CO* on the BiOS part.

Other oxides have been also used for the development of CN-based composites. Recently, Co_3O_4 has been effectively coupled with CN [73]. CN acted as platform, retarded the growth of Co_3O_4 and prevented active components from leaching. Cu_2O/CN composites presented also superior photocatalytic H_2 production under visible-light irradiation [74]. Due to the significantly more negative potential of

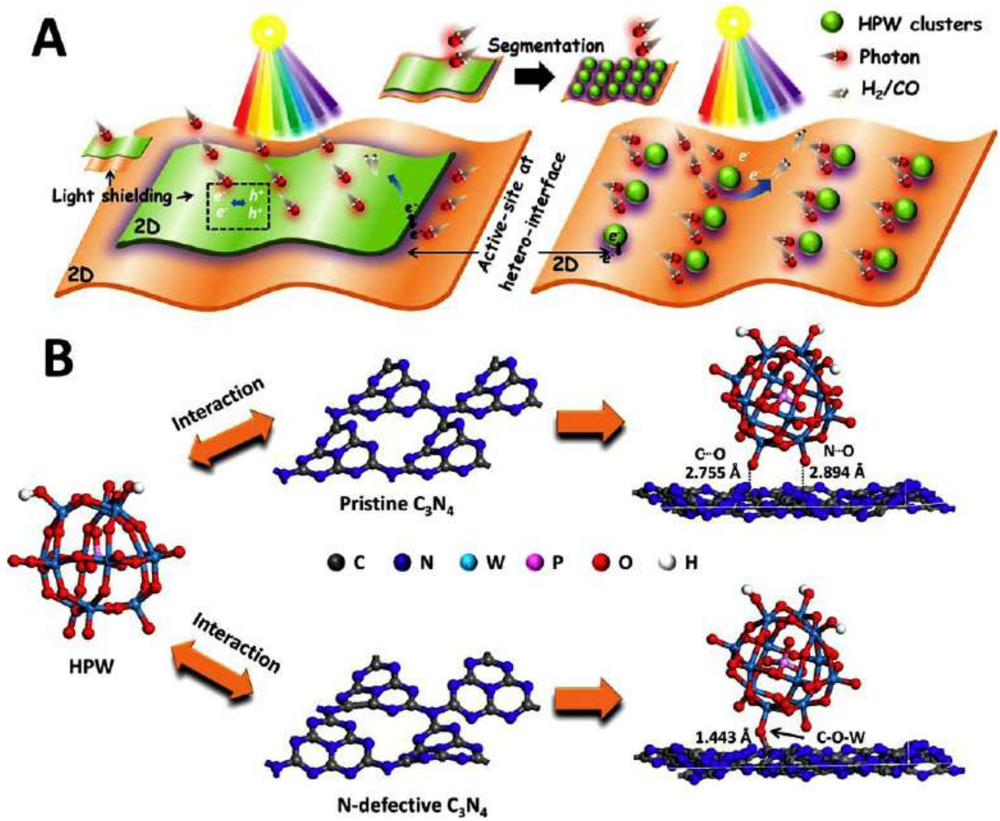

Fig. 9.13 (A) Surface active-sites at the 2D/2D and 0D/2D hetero-interface regions; (B) interaction between N-deficient and pristine CN NS with phosphotungstic acid. *(Reprinted from X. Jiang, Z. Zhang, M. Sun, W. Liu, J. Huang, H. Xu, Self-assembly of highly-dispersed phosphotungstic acid clusters onto graphitic carbon nitride nanosheets as fascinating molecular-scale Z-scheme heterojunctions for photocatalytic solar-to-fuels conversion, Appl. Catal. B Environ. 281 (2021) 119473, with permission from Elsevier.)*

Cu_2O CB, photogenerated e^- were transferred on CN, while h^+ followed the opposite direction increasing the availability of charges. Ultra-small phosphotungstic acid have been deposited on CN NS through a facile self-assembly method (Fig. 9.13) [75]. The heterojunction presented a Z-scheme charge transfer and H_2 production and CO_2 reduction was significantly increased compared with the reference CN material. Besides oxides, metal sulfides have been also coupled with CN. The development of metal sulfides usually includes the solvothermal/hydrothermal process and composites are formed in the presence of preformed CN. The coupling of hard templating method for the development of hollow CN structure and the further development of a heterojunction via the introduction of MoS_2 has been shown beneficial for the photocatalytic

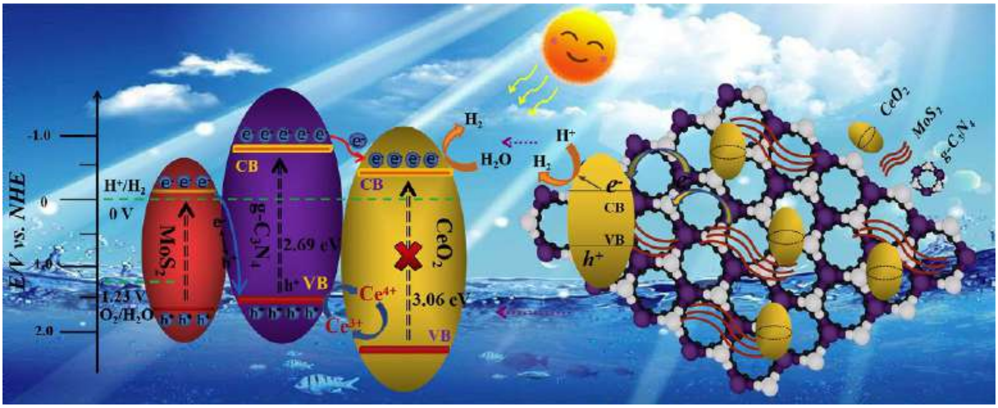

Fig. 9.14 Proposed multistep charge-transfer processes in CeO_2@MoS_2/CN composites. *(Reprinted from C. Zhu, Y. Wang, Z. Jiang, F. Xu, Q. Xian, C. Sun, Q. Tong, W. Zou, X. Duan, S. Wang, CeO_2 nanocrystal-modified layered MoS_2/g-C_3N_4 as 0D/2D ternary composite for visible-light photocatalytic hydrogen evolution: interfacial consecutive multi-step electron transfer and enhanced H_2O reactant adsorption, Appl. Catal. B Environ. 259 (2019) 118072, with permission from Elsevier.)*

production of H_2 [76]. A ternary system where 2D layered MoS_2/CN hybrid composite was functionalized with 0D CeO_2 nanoparticles promoted significantly H_2 production from water splitting [77]. The enhanced activity was ascribed to the efficient charge separation from the multistep charge transfer processes (Fig. 9.14). In addition, the developed ternary system presented more active sites and presented higher adsorption capacity for H_2O molecules, reducing further the energy barriers. A Z-scheme heterojunction was developed by coupling $Zn_xCd_{1-x}S$ with Au@CN where Au acted as electron mediator [78]. The significant higher production of CH_3OH from CO_2 reduction was ascribed to the efficient charge separation. Synergistic effects to increase activity have been documented for other multicomponent systems including oxides and sulfides, such as TiO_2/WO_3/CN [79] and CdS/CN/CuS [80]. In such systems, care should be given on the order of the interacting parts.

Finally, special attention must be given on the coupling of CN with carbon nanostructures (CNSs). Many contributions have shown that CNSs/CN composite materials improve important parameters such as light absorption and charge separation [14,42,43,81–83]. The content as well as the type and the structure at the nanoscale of the chosen CNS plays crucial role in photoactivity. We have highlighted recently the importance of the letter parameter in composites made through the coupling of CN with carbon nanotubes (CNTs) of different wall number [14]. The presence of CNTs modified the electronic properties of the final photoactive composite material. Besides the well-known effect of charge separation due to the conductivity of the CNSs and the improvements in light absorption, the actual structure at the nanoscale played vital role. As depicted in Fig. 9.15, when single-wall CNTs were coupled with CN

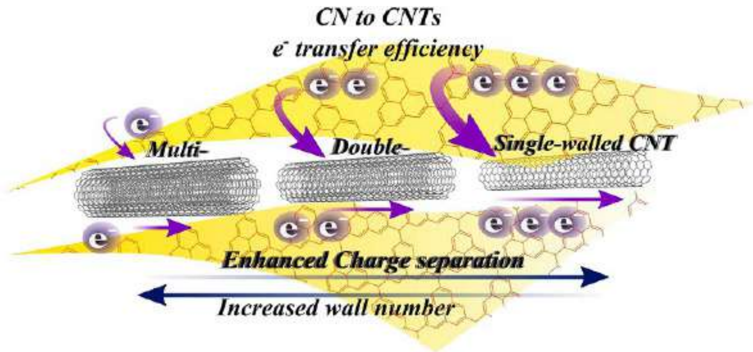

Fig. 9.15 Schematic representation of the electron transfer ability in composites made of CN and CNTs of different wall number. *(Reprinted from K.C. Christoforidis, Z. Syrgiannis, V.L. Parola, T. Montini, C. Petit, E. Stathatose, R. Godin, J.R. Durrant, M. Prato, P. Fornasiero, Metal-free dual-phase full organic carbon nanotubes/g-C_3N_4 heteroarchitectures for photocatalytic hydrogen production, Nano Energy 50 (2018) 468–478, with permission from Elsevier.)*

(SW-CN composites), the charge transfer of the photogenerated electrons from the CN part to the CNTs was significantly higher than all the other tested cases (i.e., double- and multiwall CNTs). This was experimentally evidenced by coupling advanced electron paramagnetic resonance and transient absorption spectroscopy to monitor both the photogenerated charges as well as their dynamics. This allowed more efficient charge separation and therefore, higher H_2 production from water splitting under both simulated solar light and pure visible-light irradiation.

6. Concluding remarks and directions

Converting solar energy into chemical energy via artificial photosynthesis is currently considered as a research field at the frond font of science. Based on the indigenous properties of CN and considering the resent advantages of CN materials development, CN-based composites are expected to play leading role in the field. However, improvements are still needed in terms of efficiency and selectivity for large-scale applications. Nevertheless, over the last years significant progress has been documented in both directions due to the advanced materials synthesis that allowed control of the composition, structure, morphology, size, and electronic properties. These all apply also in multicomponent architectures.

In the H_2 production process, work should focus on improving activity since selectivity is not an issue here. Future works should focus on improving the electronic properties in terms of both light absorptions, since bare CN absorbs only a small portion of solar energy, as well as charge separation. These two parameters will allow improvements in both formation and stability of photogenerated electrons. The situation is more complicated in the CO_2 photocatalytic reduction reaction. In this case, besides improvements in the electronic properties, the selectivity is a major issue. Different products have been detected, a factor that adds an extra separation step that will be required for practical applications. Therefore, materials with high selectivity toward the development of a specific product are urgently needed. In addition, research should focus on the development of high added value products and especially those that currently are synthesized using a process with high environmental impact, i.e., high CO_2 production during the process.

Ideally, in both H_2 production and CO_2 reduction, catalytic reactions should be performed under solar light irradiation since the ultimate goal is the utilization of sunlight. There is no point to develop materials that absorb in the whole region of solar spectrum if their performance is lower than materials possessing lower ability in light absorption. This will provide a platform of data to compare different systems. Furthermore, the use of expensive raw materials should be avoided. Regarding this point, it should be emphasized that current research is on the right direction since there are many examples of catalysts made of abundant raw materials presenting high efficiency. Furthermore, complete materials characterization of the catalyst is essential and will allow identifying the properties of the material that control activity. This requires the application of a multimethodology characterization process including structural, morphological, textural, electronic, and compositional characterization. Especially for multicomponent systems, high-resolution techniques able to discriminate changes at subnanometer scale are necessary as well as in-situ methodologies to study catalysts under real catalytic condition. The outcome of this approach will provide critical information that, unavoidably, will lead on the development of more advanced photocatalytic systems. As a final point, the ideal candidate for should be able to perform the desired reaction under environmental conditions. Pressure and temperature are controllable parameters; however, all current contributions have used anoxic conditions. Although this seems far from the present, our aim should be not only to mimic but to exceed the performance of natural photosynthesis.

References

[1] K.C. Christoforidis, P. Fornasiero, Photocatalysis for hydrogen production and CO_2 reduction: the case of copper-catalysts, ChemCatChem 11 (2019) 368–382.

[2] K.C. Christoforidis, T. Montini, M. Fittipaldi, J.J.D. Jaén, P. Fornasiero, Photocatalytic hydrogen production by boron modified TiO_2/carbon nitride heterojunctions, ChemCatChem 11 (2019) 6408–6416.

[3] I. Barba-Nieto, K.C. Christoforidis, M. Fernández-García, A. Kubacka, Promoting H_2 photoproduction of TiO_2-based materials by surface decoration with Pt nanoparticles and SnS_2 nanoplatelets, Appl. Catal. B Environ. 277 (2020), 119246.

[4] M. Liu, Y. Chen, J. Su, J. Shi, X. Wang, L. Guo, Photocatalytic hydrogen production using twinned nanocrystals and an unanchored NiSx co-catalyst, Nat. Energy 1 (2016) 16151.

[5] X. Wang, K. Maeda, A. Thomas, K. Takanabe, G. Xin, J.M. Carlsson, K. Domen, M. Antonietti, A metal-free polymeric photocatalyst for hydrogen production from water under visible light, Nat. Mater. 8 (2009) 76–80.

[6] A. Fujishima, K. Honda, Electrochemical photolysis of water at a semiconductor electrode, Nature 238 (1972) 37–38.
[7] T. Inoue, A. Fujishima, S. Konishi, K. Honda, Photoelectrocatalytic reduction of carbon dioxide in aqueous suspensions of semiconductor powders, Nature 277 (1979) 637–638.
[8] K.C. Christoforidis, P. Fornasiero, Photocatalytic hydrogen production: a rift into the future energy supply, ChemCatChem 9 (2017) 1523–1544.
[9] A.J. Morris, G.J. Meyer, E. Fujita, Molecular approaches to the photocatalytic reduction of carbon dioxide for solar fuels, Acc. Chem. Res. 42 (2009) 1983–1994.
[10] K.C. Christoforidis, A. Iglesias-Juez, S.J.A. Figuero, M.D. Michiel, M.A. Newton, M. Fernandez-Garcia, Structure and activity of iron-doped TiO_2-anatase nanomaterials for gas-phase toluene photo-oxidation, Catal. Sci. Technol. 3 (2013) 626–634.
[11] K.C. Christoforidis, M. Fernandez-Garcia, Photoactivity and charge trapping sites in copper and vanadium doped anatase TiO_2 nano-materials, Catal. Sci. Technol. 6 (2016) 1094–1105.
[12] K.C. Christoforidis, A. Sengele, V. Keller, N. Keller, Single-step synthesis of SnS(2) nanosheet-decorated TiO(2) anatase nanofibers as efficient photocatalysts for the degradation of gas-phase diethylsulfide, ACS Appl. Mater. Interfaces 7 (2015) 19324–19334.
[13] K.C. Christoforidis, T. Montini, E. Bontempi, S. Zafeiratos, J.J.D. Jaén, P. Fornasiero, Synthesis and photocatalytic application of visible-light active b-Fe_2O_3/g-C_3N_4 hybrid nanocomposites, Appl. Catal. B Environ. 187 (2016) 171–180.
[14] K.C. Christoforidis, Z. Syrgiannis, V.L. Parola, T. Montini, C. Petit, E. Stathatose, R. Godin, J.R. Durrant, M. Prato, P. Fornasiero, Metal-free dual-phase full organic carbon nanotubes/g-C_3N_4 heteroarchitectures for photocatalytic hydrogen production, Nano Energy 50 (2018) 468–478.
[15] K.C. Christoforidis, M. Melchionna, T. Montini, D. Papoulis, E. Stathatos, S. Zafeiratos, E. Kordouli, P. Fornasiero, Solar and visible light photocatalytic enhancement of halloysite nanotubes/g-C_3N_4 heteroarchitectures, RSC Adv. 6 (2016) 86617–86626.
[16] M. Fan, C. Song, T. Chen, X. Yan, D. Xu, W. Gu, W. Shi, L. Xiao, Visible-light-drived high photocatalytic activities of Cu/g-C_3N_4 photocatalysts for hydrogen production, RSC Adv. 6 (2016) 34633–34640.
[17] B. Tian, Y. Wu, G. Lu, Metal-free plasmonic boron phosphide/graphitic carbon nitride with core-shell structure photocatalysts for overall water splitting, Appl. Catal. B Environ. 280 (2021), 119410.
[18] Q. Guo, Y. Xie, X. Wang, S. Zhang, T. Hou, S. Lv, Synthesis of carbon nitride nanotubes with the C (3)N(4) stoichiometry via a benzene-thermal process at low temperatures, Chem. Commun. (2004) 26–27.
[19] Q. Fu, C.-B. Cao, H.-S. Zhu, Preparation of carbon nitride films with high nitrogen content by electrodeposition from an organic solution, J. Mater. Sci. Lett. 18 (1999) 1485–1488.
[20] J. Kouvetakis, M. Todd, B. Wilkens, A. Bandari, N. Cave, Novel synthetic routes to carbon-nitrogen thin films, Chem. Mater. 6 (1994) 811–814.
[21] A. Thomas, A. Fischer, F. Goettmann, M. Antonietti, J.-O. Müller, R. Schlögl, J.M. Carlsson, Graphitic carbon nitride materials: variation of structure and morphology and their use as metal-free catalysts, J. Mater. Chem. 18 (2008) 4893.
[22] D.J. Martin, K. Qiu, S.A. Shevlin, A.D. Handoko, X. Chen, Z. Guo, J. Tang, Highly efficient photocatalytic H(2) evolution from water using visible light and structure-controlled graphitic carbon nitride, Angew. Chem. 53 (2014) 9240–9245.
[23] D.J. Martin, K. Qiu, S.A. Shevlin, A.D. Handoko, X. Chen, Z. Guo, J. Tang, Highly efficient photocatalytic H_2 evolution from water using visible light and structure-controlled graphitic carbon nitride, Angew. Chem. 126 (2014) 9394–9399.
[24] K. Kailasam, J.D. Epping, A. Thomas, S. Losse, H. Junge, Mesoporous carbon nitride–silica composites by a combined sol–gel/thermal condensation approach and their application as photocatalysts, Energy Environ. Sci. 4 (2011) 4668.
[25] Y. Wang, X. Wang, M. Antonietti, Y. Zhang, Facile one-pot synthesis of nanoporous carbon nitride solids by using soft templates, ChemSusChem 3 (2010) 435–439.
[26] M.K. Bhunia, K. Yamauchi, K. Takanabe, Harvesting solar light with crystalline carbon nitrides for efficient photocatalytic hydrogen evolution, Angew. Chem. 126 (2014) 11181–11185.

[27] X. Bai, L. Wang, R. Zong, Y. Zhu, Photocatalytic activity enhanced via g-C_3N_4 nanoplates to nanorods, J. Phys. Chem. C 117 (2013) 9952–9961.
[28] L. Ma, H. Fan, J. Wang, Y. Zhao, H. Tian, G. Dong, Water-assisted ions in situ intercalation for porous polymeric graphitic carbon nitride nanosheets with superior photocatalytic hydrogen evolution performance, Appl. Catal. B Environ. 190 (2016) 93–102.
[29] P. Niu, L. Zhang, G. Liu, H.-M. Cheng, Graphene-like carbon nitride nanosheets for improved photocatalytic activities, Adv. Funct. Mater. 22 (2012) 4763–4770.
[30] E.M. Dias, K.C. Christoforidis, L. Francas, C. Petit, Tuning thermally treated graphitic carbon nitride for H_2 evolution and CO_2 photoreduction: the effects of material properties and mid-gap states, ACS Appl. Energy Mater. 1 (2018) 6524–6534.
[31] F. Dong, Z. Wang, Y. Sun, W.K. Ho, H. Zhang, Engineering the nanoarchitecture and texture of polymeric carbon nitride semiconductor for enhanced visible light photocatalytic activity, J. Colloid Interface Sci. 401 (2013) 70–79.
[32] F. Dong, Y. Li, Z. Wang, W.-K. Ho, Enhanced visible light photocatalytic activity and oxidation ability of porous graphene-like g-C_3N_4 nanosheets via thermal exfoliation, Appl. Surf. Sci. 358 (2015) 393–403.
[33] Z.-A. Lan, G. Zhang, X. Wang, A facile synthesis of Br-modified g-C_3N_4 semiconductors for photoredox water splitting, Appl. Catal. B Environ. 192 (2016) 116–125.
[34] Q. Liang, Z. Li, Z.-H. Huang, F. Kang, Q.-H. Yang, Holey graphitic carbon nitride nanosheets with carbon vacancies for highly improved photocatalytic hydrogen production, Adv. Funct. Mater. 25 (2015) 6885–6892.
[35] A.L. Linsebigler, G. Lu, J.T. Yates, Photocatalysis on TiO_2 surfaces: principles, mechanisms, and selected results, Chem. Rev. 95 (1995) 735–758.
[36] Y. Li, T. Kong, S. Shen, Artificial photosynthesis with polymeric carbon nitride: when meeting metal nanoparticles, single atoms, and molecular complexes, Small 15 (2019), e1900772.
[37] B. Chai, T. Peng, J. Mao, K. Li, L. Zan, Graphitic carbon nitride (g-C_3N_4)-Pt-TiO_2 nanocomposite as an efficient photocatalyst for hydrogen production under visible light irradiation, Phys. Chem. Chem. Phys. 14 (2012) 16745–16752.
[38] J. Hong, Y. Wang, Y. Wang, W. Zhang, R. Xu, Noble-metal-free NiS/C_3N_4 for efficient photocatalytic hydrogen evolution from water, ChemSusChem 6 (2013) 2263–2268.
[39] Z. Jiang, K. Qian, C. Zhu, H. Sun, W. Wan, J. Xie, H. Li, P.K. Wong, S. Yuan, Carbon nitride coupled with CdS-TiO_2 nanodots as 2D/0D ternary composite with enhanced photocatalytic H_2 evolution: a novel efficient three-level electron transfer process, Appl. Catal. B Environ. 210 (2017) 194–204.
[40] J. Liu, Y. Zhang, L. Lu, G. Wu, W. Chen, Self-regenerated solar-driven photocatalytic water-splitting by urea derived graphitic carbon nitride with platinum nanoparticles, Chem. Commun. 48 (2012) 8826–8828.
[41] S.M. Lang, T.M. Bernhardt, Gas phase metal cluster model systems for heterogeneous catalysis, Phys. Chem. Chem. Phys. 14 (2012) 9255–9269.
[42] Q. Xiang, J. Yu, M. Jaroniec, Preparation and enhanced visible-light photocatalytic H_2-production activity of graphene/C_3N_4 composites, J. Phys. Chem. C 115 (2011) 7355–7363.
[43] J. Liu, Y. Liu, N. Liu, Y. Han, X. Zhang, H. Huang, Y. Lifshitz, S.T. Lee, J. Zhong, Z. Kang, Water splitting. Metal-free efficient photocatalyst for stable visible water splitting via a two-electron pathway, Science 347 (2015) 970–974.
[44] Y. Guo, J. Chen, Photo-induced reduction of biomass-derived 5-hydroxymethylfurfural using graphitic carbon nitride supported metal catalysts, RSC Adv. 6 (2016) 101968–101973.
[45] J. Chen, S. Shen, P. Wu, L. Guo, Nitrogen-doped CeOx nanoparticles modified graphitic carbon nitride for enhanced photocatalytic hydrogen production, Green Chem. 17 (2015) 509–517.
[46] Y. Shiraishi, Y. Kofuji, S. Kanazawa, H. Sakamoto, S. Ichikawa, S. Tanaka, T. Hirai, Platinum nanoparticles strongly associated with graphitic carbon nitride as efficient co-catalysts for photocatalytic hydrogen evolution under visible light, Chem. Commun. 50 (2014) 15255–15258.
[47] C. Han, Y. Lu, J. Zhang, L. Ge, Y. Li, C. Chen, Y. Xin, L. Wu, S. Fang, Novel PtCo alloy nanoparticle decorated 2D g-C_3N_4 nanosheets with enhanced photocatalytic activity for H_2 evolution under visible light irradiation, J. Mater. Chem. A 3 (2015) 23274–23282.

[48] L. Liu, X. Wu, L. Wang, X. Xu, L. Gan, Z. Si, J. Li, Q. Zhang, Y. Liu, Y. Zhao, R. Ran, X. Wu, D. Weng, F. Kang, Atomic palladium on graphitic carbon nitride as a hydrogen evolution catalyst under visible light irradiation, Commun. Chem. 2 (2019) 18.
[49] S. Cao, H. Li, T. Tong, H.-C. Chen, A. Yu, J. Yu, H.M. Chen, Single-atom engineering of directional charge transfer channels and active sites for photocatalytic hydrogen evolution, Adv. Funct. Mater. 28 (2018) 1802169.
[50] L. Kong, Y. Dong, P. Jiang, G. Wang, H. Zhang, N. Zhao, Light-assisted rapid preparation of a Ni/g-C_3N_4 magnetic composite for robust photocatalytic H_2 evolution from water, J. Mater. Chem. A 4 (2016) 9998–10007.
[51] F. Li, H. Zhou, J. Fan, Q. Xiang, Amine-functionalized graphitic carbon nitride decorated with small-sized Au nanoparticles for photocatalytic CO_2 reduction, J. Colloid Interface Sci. 570 (2020) 11–19.
[52] S. Bai, X. Wang, C. Hu, M. Xie, J. Jiang, Y. Xiong, Two-dimensional g-C(3)N(4): an ideal platform for examining facet selectivity of metal co-catalysts in photocatalysis, Chem. Commun. 50 (2014) 6094–6097.
[53] C. Wang, P. Lv, D. Xue, Y. Cai, X. Yan, L. Xu, J. Fang, Y. Yang, Zero-dimensional/two-dimensional Au25(Cys)18 nanoclusters/g-C_3N_4 nanosheets composites for enhanced photocatalytic hydrogen production under visible light, ACS Sustain. Chem. Eng. 6 (2018) 8447–8457.
[54] X. Zhao, B. Luo, R. Long, C. Wang, Y. Xiong, Composition-dependent activity of Cu–Pt alloy nanocubes for electrocatalytic CO_2 reduction, J. Mater. Chem. A 3 (2015) 4134–4138.
[55] P. Jiménez-Calvo, C. Marchal, T. Cottineau, V. Caps, V. Keller, Influence of the gas atmosphere during the synthesis of g-C_3N_4 for enhanced photocatalytic H_2 production from water on Au/g-C_3N_4 composites, J. Mater. Chem. A 7 (2019) 14849–14863.
[56] J. Zhang, G. Zhang, X. Chen, S. Lin, L. Mohlmann, G. Dolega, G. Lipner, M. Antonietti, S. Blechert, X. Wang, Co-monomer control of carbon nitride semiconductors to optimize hydrogen evolution with visible light, Angew. Chem. 51 (2012) 3183–3187.
[57] M. Zhang, X. Wang, Two dimensional conjugated polymers with enhanced optical absorption and charge separation for photocatalytic hydrogen evolution, Energy Environ. Sci. 7 (2014) 1902.
[58] J. Zhang, X. Chen, K. Takanabe, K. Maeda, K. Domen, J.D. Epping, X. Fu, M. Antonietti, X. Wang, Synthesis of a carbon nitride structure for visible-light catalysis by copolymerization, Angew. Chem. 49 (2010) 441–444.
[59] J. Zhang, M. Zhang, S. Lin, X. Fu, X. Wang, Molecular doping of carbon nitride photocatalysts with tunable bandgap and enhanced activity, J. Catal. 310 (2014) 24–30.
[60] Z. Pan, P. Niu, M. Liu, G. Zhang, Z. Zhu, X. Wang, Molecular junctions on polymeric carbon nitrides with enhanced photocatalytic performance, ChemSusChem 13 (2020) 888–892.
[61] R. Kuriki, H. Matsunaga, T. Nakashima, K. Wada, A. Yamakata, O. Ishitani, K. Maeda, Nature-inspired, highly durable CO_2 reduction system consisting of a binuclear ruthenium(II) complex and an organic semiconductor using visible light, J. Am. Chem. Soc. 138 (2016) 5159–5170.
[62] K. Maeda, R. Kuriki, O. Ishitani, Photocatalytic activity of carbon nitride modified with a ruthenium(II) complex having carboxylic- or phosphonic acid anchoring groups for visible-light CO_2 reduction, Chem. Lett. 45 (2016) 182–184.
[63] R. Kuriki, K. Sekizawa, O. Ishitani, K. Maeda, Visible-light-driven CO_2 reduction with carbon nitride: enhancing the activity of ruthenium catalysts, Angew. Chem. 54 (2015) 2406–2409.
[64] F. Dong, Z. Zhao, T. Xiong, Z. Ni, W. Zhang, Y. Sun, W.K. Ho, In situ construction of g-C_3N_4/g-C_3N_4 metal-free heterojunction for enhanced visible-light photocatalysis, ACS Appl. Mater. Interfaces 5 (2013) 11392–11401.
[65] J. Zhang, M. Zhang, R.Q. Sun, X. Wang, A facile band alignment of polymeric carbon nitride semiconductors to construct isotype heterojunctions, Angew. Chem. 51 (2012) 10145–10149.
[66] A. Crake, K.C. Christoforidis, R. Godin, B. Moss, A. Kafizas, S. Zafeiratos, J.R. Durrant, C. Petit, Titanium dioxide/carbon nitride nanosheet nanocomposites for gas phase CO_2 photoreduction under UV-visible irradiation, Appl. Catal. B Environ. 242 (2019) 369–378.
[67] Z. Tong, D. Yang, T. Xiao, Y. Tian, Z. Jiang, Biomimetic fabrication of g-C_3N_4/TiO_2 nanosheets with enhanced photocatalytic activity toward organic pollutant degradation, Chem. Eng. J. 260 (2015) 117–125.

[68] X. Fan, T. Wang, B. Gao, H. Gong, H. Xue, H. Guo, L. Song, W. Xia, X. Huang, J. He, Preparation of the TiO_2/graphic carbon nitride core-shell array as a photoanode for efficient photoelectrochemical water splitting, Langmuir 32 (2016) 13322–13332.
[69] L. Chen, X. Zhou, B. Jin, J. Luo, X. Xu, L. Zhang, Y. Hong, Heterojunctions in g-C_3N_4/B-TiO_2 nanosheets with exposed {001} plane and enhanced visible-light photocatalytic activities, Int. J. Hydrog. Energy 41 (2016) 7292–7300.
[70] M. Reli, P. Huo, M. Sihor, N. Ambrozova, I. Troppova, L. Matejova, J. Lang, L. Svoboda, P. Kustrowski, M. Ritz, P. Praus, K. Koci, Novel TiO_2/C_3N_4 photocatalysts for photocatalytic reduction of CO_2 and for photocatalytic decomposition of N_2O, J. Phys. Chem. A 120 (2016) 8564–8573.
[71] K.C. Christoforidis, 2D materials for solar fuels production, in: S. Zafeiratos (Ed.), 2D Nanomaterials for Energy Applications Graphene and Beyond Micro and Nano Technologies, Elsevier, 2020.
[72] J. Li, B. Huang, Q. Guo, S. Guo, Z. Peng, J. Liu, Q. Tian, Y. Yang, Q. Xu, Z. Liu, B. Liu, Van der Waals heterojunction for selective visible-light-driven photocatalytic CO_2 reduction, Appl. Catal. B Environ. 284 (2021), 119733.
[73] S. Guan, L. An, S. Ashraf, L. Zhang, B. Liu, Y. Fan, B. Li, Oxygen vacancy excites Co_3O_4 nanocrystals embedded into carbon nitride for accelerated hydrogen generation, Appl. Catal. B Environ. 269 (2020), 118775.
[74] J. Chen, S. Shen, P. Guo, M. Wang, P. Wu, X. Wang, L. Guo, In-situ reduction synthesis of nano-sized Cu_2O particles modifying g-C_3N_4 for enhanced photocatalytic hydrogen production, Appl. Catal. B Environ. 152–153 (2014) 335–341.
[75] X. Jiang, Z. Zhang, M. Sun, W. Liu, J. Huang, H. Xu, Self-assembly of highly-dispersed phosphotungstic acid clusters onto graphitic carbon nitride nanosheets as fascinating molecular-scale Z-scheme heterojunctions for photocatalytic solar-to-fuels conversion, Appl. Catal. B Environ. 281 (2021), 119473.
[76] D. Zheng, G. Zhang, Y. Hou, X. Wang, Layering MoS_2 on soft hollow g-C_3N_4 nanostructures for photocatalytic hydrogen evolution, Appl. Catal. A Gen. 521 (2016) 2–8.
[77] C. Zhu, Y. Wang, Z. Jiang, F. Xu, Q. Xian, C. Sun, Q. Tong, W. Zou, X. Duan, S. Wang, CeO_2 nanocrystal-modified layered MoS_2/g-C_3N_4 as 0D/2D ternary composite for visible-light photocatalytic hydrogen evolution: interfacial consecutive multi-step electron transfer and enhanced H_2O reactant adsorption, Appl. Catal. B Environ. 259 (2019), 118072.
[78] P. Madhusudan, R. Shi, S. Xiang, M. Jin, B.N. Chandrashekar, J. Wang, W. Wang, O. Peng, A. Amini, C. Cheng, Construction of highly efficient Z-scheme $Zn_xCd_{1-x}S$/Au@g-C_3N_4 ternary heterojunction composite for visible-light-driven photocatalytic reduction of CO_2 to solar fuel, Appl. Catal. B Environ. 282 (2021), 119600.
[79] H. Hou, F. Gao, L. Wang, M. Shang, Z. Yang, J. Zheng, W. Yang, Superior thoroughly mesoporous ternary hybrid photocatalysts of TiO_2/WO_3/g-C_3N_4 nanofibers for visible-light-driven hydrogen evolution, J. Mater. Chem. A 4 (2016) 6276–6281.
[80] F. Cheng, H. Yin, Q. Xiang, Low-temperature solid-state preparation of ternary CdS/g-C_3N_4/CuS nanocomposites for enhanced visible-light photocatalytic H_2-production activity, Appl. Surf. Sci. 391 (2017) 432–439.
[81] J.-P. Zou, L.-C. Wang, J. Luo, Y.-C. Nie, Q.-J. Xing, X.-B. Luo, H.-M. Du, S.-L. Luo, S.L. Suib, Synthesis and efficient visible light photocatalytic H_2 evolution of a metal-free g-C_3N_4/graphene quantum dots hybrid photocatalyst, Appl. Catal. B Environ. 193 (2016) 103–109.
[82] J. Duan, S. Chen, M. Jaroniec, S.Z. Qiao, Porous C_3N_4 nanolayers@N-graphene films as catalyst electrodes for highly efficient hydrogen evolution, ACS Nano 9 (2015) 931–940.
[83] L. Xu, W.-Q. Huang, L.-L. Wang, Z.-A. Tian, W. Hu, Y. Ma, X. Wang, A. Pan, G.-F. Huang, Insights into enhanced visible-light photocatalytic hydrogen evolution of g-C_3N_4 and highly reduced graphene oxide composite: the role of oxygen, Chem. Mater. 27 (2015) 1612–1621.

CHAPTER 10

Carbon nitride-based optical sensors for metal ion detection

Ekta Sharma[a], Ashish Guleria[b], Kulvinder Singh[c], Ritu Malik[d], and Vijay K. Tomer[d]
[a]Department of Chemistry, School of Basic and Applied Sciences, Maharaja Agrasen University, Baddi, Himachal Pradesh, India
[b]Department of Applied Sciences, WIT Dehradun, Dehradun, Uttarakhand, India
[c]Department of Chemistry, DAV College, Chandigarh, India
[d]Department of Mechanical Engineering, University of California, Berkeley, CA, United States

Contents

1. Introduction

In recent times, significant attention has been given to storage of energy and global preservation of environment [1–4]. Modern civilization, rapid industrialization and extreme use of natural assets leads to various environmental problems, such as groundwater contamination, air pollution, and many others [5–9]. These pollutants, particularly heavy metal ions, are harmful not only to the environment but also to the living beings [10]. The heavy metal ions include transition metals, metalloids, and some f-block elements. These heavy metal ions can cause a crucial menace to human health, animals, and to ecosystem [11,12]. In order to detect or remove these heavy metal ions, there are various conventional techniques, such as electrochemical, coagulation, precipitation, adsorption, and ion exchange method [13–19]. However, they have some practical inapplicability due to their low binding abilities, testing procedure, and nanotoxicity. Hence, there is a need of suitable materials with high metal loading capacity, facile synthesis, and good biocompatability [20]. Among all the detection methods available based on the usage of fluorescent materials, quantum dots (QDs) have gained considerable interest because of their magnificent optical and chemical properties and have excellent applications in drug delivery, bioimaging, and sensing [20–26]. As semiconductor-based QDs have some toxicity issues, carbon dots (CDs) have emerged as a better alternative because of their outstanding applications [27,28]. The CDs are highly resistant to photobleaching, have low toxicity and good biocompatibility along with marvelous applications in the field of biological labeling, biosensors, drug/gene delivery, biomedicine, biological

Nanostructured Carbon Nitrides for Sustainable Energy and Environmental Applications
https://doi.org/10.1016/B978-0-12-823961-2.00005-7

sensing, high accuracy, and essential simplicity [29–32]. CDs were first discovered occasionally during the separation and purification of single-walled carbon nanotubes by arc discharge method in 2004 [33]. Therein, graphitic carbon nitride-based quantum dots (g-CN QDs), a N-rich carbonaceous material with a prototypical two-dimensional (2D) graphitic structure, based on triazine or tris-triazine units as their building blocks, have emerged [34,35]. In practical application, they are most stable with band gap of 2.7 eV [36]. These are emerging as a new attractive metal-free catalyst in photocatalytic applications and other energy conversion processes, such as hydrogen evolution, pollutant removal, and CO_2 reduction reaction. They also exhibit interesting electronic properties, promising catalytic activities, high in-plane nitrogen content, and are enriched with environmentally friendly features. These have attracted numerous research interests because of their simple synthesis method, biocompatibility, easy functionalization, high water stability, high quantum yield, chemical stability, and high photoluminescence [37]. Due to these properties, they are extensively used in sensing applications, such as ion sensor, gas sensor, humidity sensor, and biosensor [38–45]. Fig. 10.1 depicts the pictorial representation of properties and applications of g-CN QDs [46].

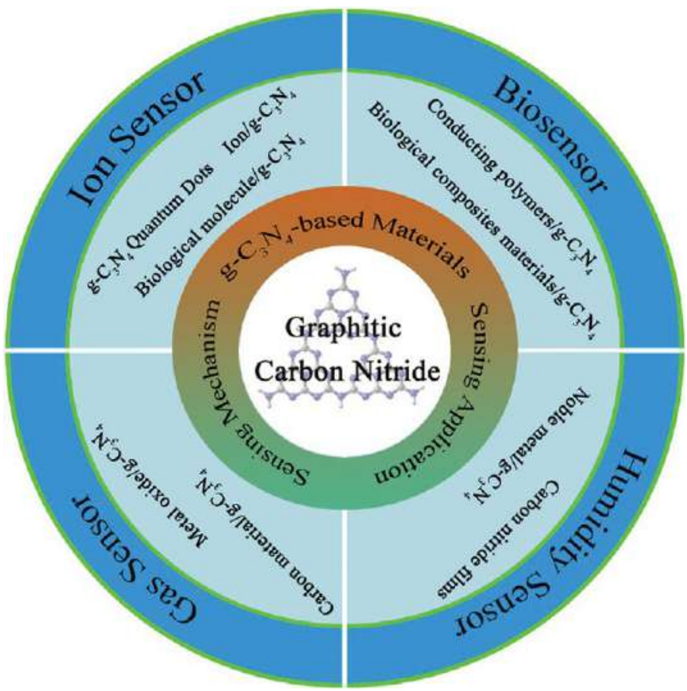

Fig. 10.1 Schematic of sensing applications of g-CN. *(From Y. Wang, R. Zhang, Z. Zhang, J. Cao, T. Ma, Host–guest recognition on 2D graphitic carbon nitride for nanosensing, Adv. Mater. Interfaces 6(23) (2019), https://doi.org/10.1002/admi.201901429.)*

Generally, g-CN QDs have a framework of π-conjugated of C–N graphitic layers over GQDs and CDs, which contain C–C and C–O layers. In particular, there is sp^2 hybridization between N and C, which gives rise to π-conjugated graphitic planes [47,48]. Further the modifications of the g-CNQDs using various dopants can generate recognition probes for specific target analytes, which help in designing of the nanosensors. Recently, fluorescent graphitic carbon nitride quantum dots are gaining interest due to their graphene-like structure and also have van der Walls forces that join the covalently bonded C–N layers [49]. Due to the presence of elements like C, N, and O, they are most prominent in practical applications and are environment friendly [45]. These g-CN QDs have splendid optical properties due to which they are used in various applications in drug delivery, catalysis, bioimaging, pollutant degradation, and in sensing. There are numerous reports in literature on sensing properties of pristine g-CN QDs [50–52]. These reports explained that pristine g-CN QDs works best for sensing of Hg^{2+} ions but to further explore their sensing properties toward other ions or to improve their selectivity pristine g-CN QDs must be modified by doping. Doping enhances their sensing properties toward other ions.

2. Graphitic carbon nitride quantum dots as an optical sensor for Hg^{2+} ions

Based on the unique properties of g-CN QDs, they have a strong response toward sensing of mercury ions. Pristine g-CN QDs have advantage in detecting Hg^{2+} ions. This mechanism has been explained by Singh et al. [53]. They synthesized g-CN QDs with water stable carboxyl and cofunctionalized with amine *via* microwave assisted solvothermal method. These prepared g-CN QDs were used in the detection and removal of mercury ions in micro-cartridge method. They also have done density functional theory (DFT) calculation and exposed mercury atom interaction. These DFT calculations explained mercury atom embedded on the surface of g-CN leads to the distortion in structure, band gap reduction and dielectric response alteration. Fig. 10.2 represents the schematic representation of g-CN QDs and their conjugation with NHS activated agarose to trap mercury ion present in contaminated water.

Fig. 10.3A shows the X-ray diffraction (XRD) spectrum and the inset of XRD shows the high-resolution transmission electron microscopy (HRTEM) image of g-CN QDs. In the XRD spectrum, there are two peaks. The small peak is at 11.690 degrees which is due to nitrogen linked plane structure of elementary triazine moiety and an intense peak (002) at 27.130 degrees which is due to crystalline nature of g-CN QDs. From HRTEM it is confirmed that the size of QDs is below 10 nm which is the characteristic size of g-CN QDs. The Fourier-transform infrared (FTIR) spectrum shows various peaks and band, confirming the presence of C=N bond stretching, C=O vibrations, N–H, O–H bond vibration and presence of triazine ring (Fig. 10.3B).

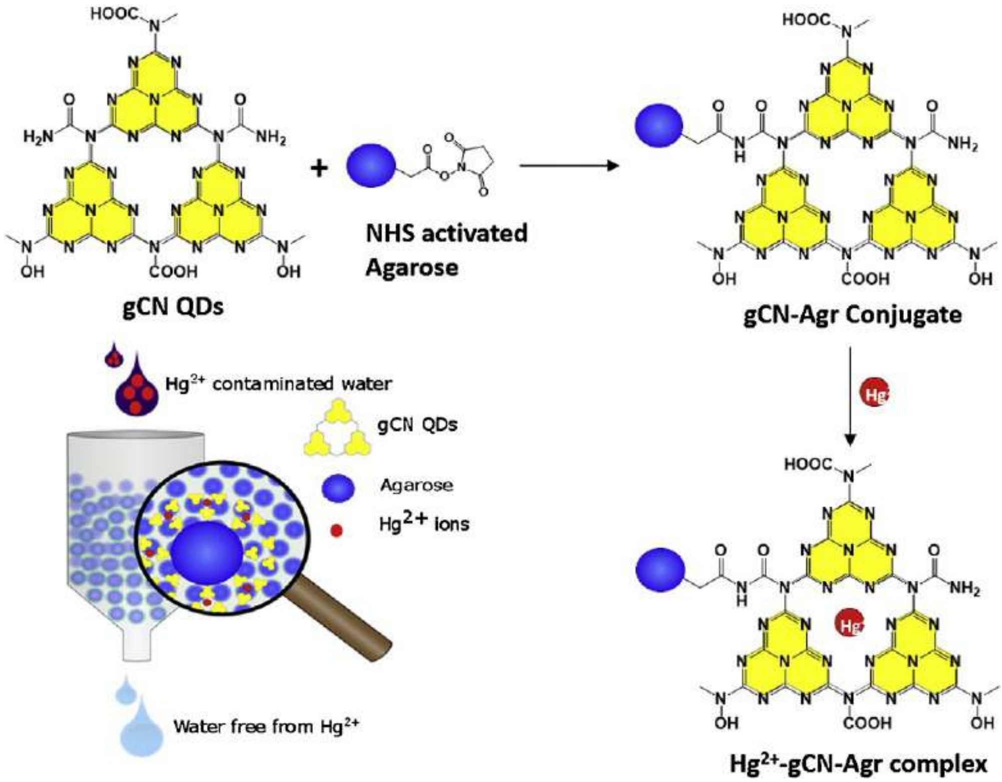

Fig. 10.2 Schematic representation of synthesizing g-CN QDs and subsequent bioconjugation with functionalized agarose matrix packed in microcartridge for trapping Hg^{2+} ions present in contaminated water. *(From M. Shorie, H. Kaur, G. Chadha, K. Singh, P. Sabherwal, Graphitic carbon nitride QDs impregnated biocompatible agarose cartridge for removal of heavy metals from contaminated water samples, J. Hazard. Mater. 367 (2019) 629–638, https://doi.org/10.1016/j.jhazmat.2018.12.115.)*

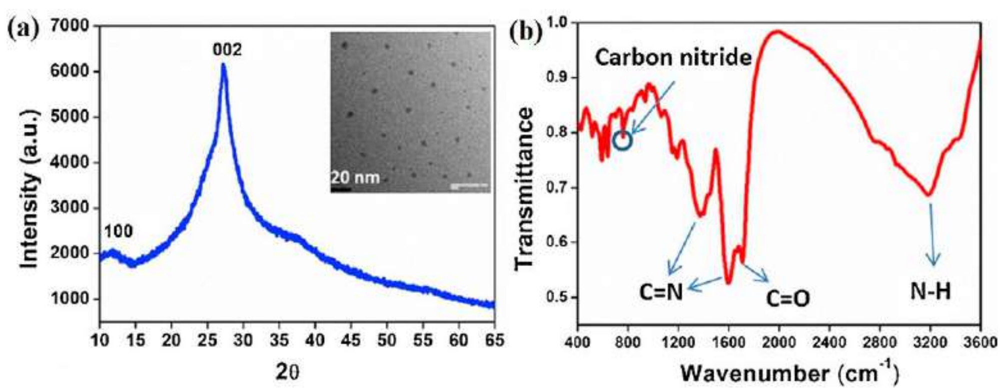

Fig. 10.3 (A) XRD spectrum, inset shows HRTEM image of g-CN QDs, (B) FTIR spectrum of g-CN QDs. *(From M. Shorie, H. Kaur, G. Chadha, K. Singh, P. Sabherwal, Graphitic carbon nitride QDs impregnated biocompatible agarose cartridge for removal of heavy metals from contaminated water samples, J. Hazard. Mater. 367 (2019) 629–638, https://doi.org/10.1016/j.jhazmat.2018.12.115.)*

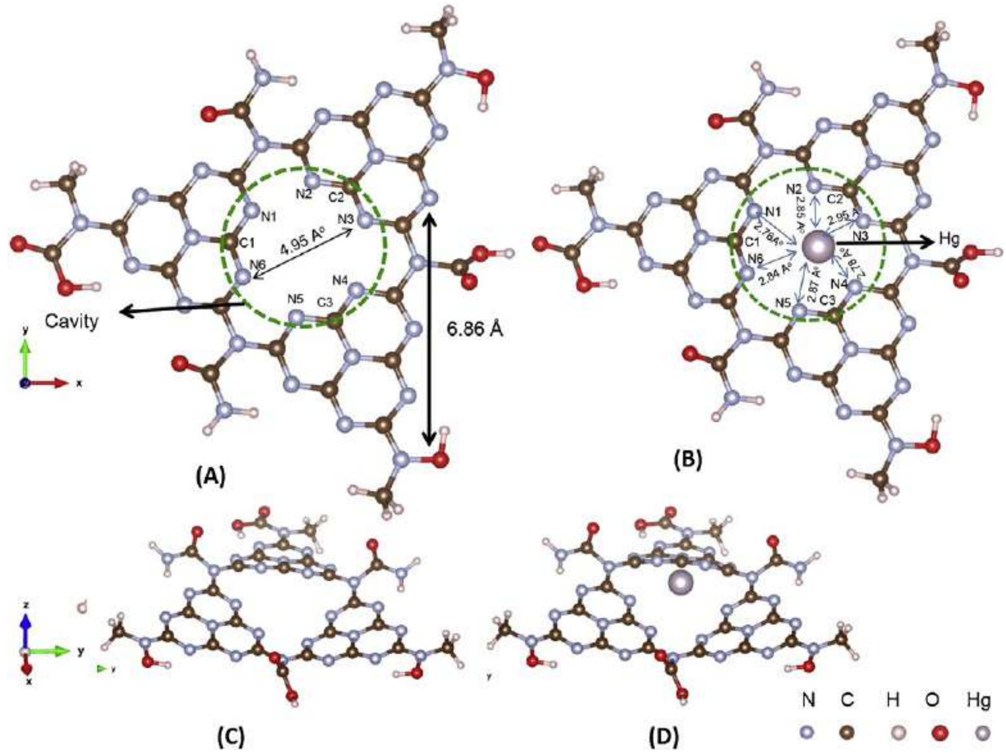

Fig. 10.4 Optimized structure (A) top view of bare sheet g-CN, circled area shows view of electron rich cavity where Hg atom get trapped, (B) top view of g-CN-Hg geometric structure, (C) side view of g-CN sheets, (D) side view of g-CN-Hg geometric structure. Balls in *blue* (*light gray* in print version), *brown* (*dark gray* in print version), *red* (*dark gray* in print version), *white*, and *gray* are nitrogen, carbon, oxygen, hydrogen, and mercury atoms, respectively. *(From M. Shorie, H. Kaur, G. Chadha, K. Singh, P. Sabherwal, Graphitic carbon nitride QDs impregnated biocompatible agarose cartridge for removal of heavy metals from contaminated water samples, J. Hazard. Mater. 367 (2019) 629–638, https://doi.org/10.1016/j.jhazmat.2018.12.115.)*

Further computational studies were carried out, the sheets of graphitic heptazine is periodic along *x*–*y* plane consists of 79 atoms (Fig. 10.4).

Functional groups such as carboxyl, amino, and hydrogen atom passivated along the ends. Along *x*, *y* directions, dimensions were taken to be 18.43 and 19.04 Å, respectively. In 2D sheets, the artificial interactions are avoided by simulating the system with 20 A of vacuum perpendicular to the sheets direction. Fig. 10.4A shows the cavity which is designated by dotted lines in the optimized structure of g-CN. In g-CN unit cell, there are three units of heptazine, and g-CN in which Hg is embedded referred as g-CN-Hg. Further, the dielectric response was calculated by first-order time-dependent perturbation theory for g-CN and g-CN-Hg. Kohn-Sham (KS) formalism was used for computing transition matrix element in between employed and nonemployed single electron

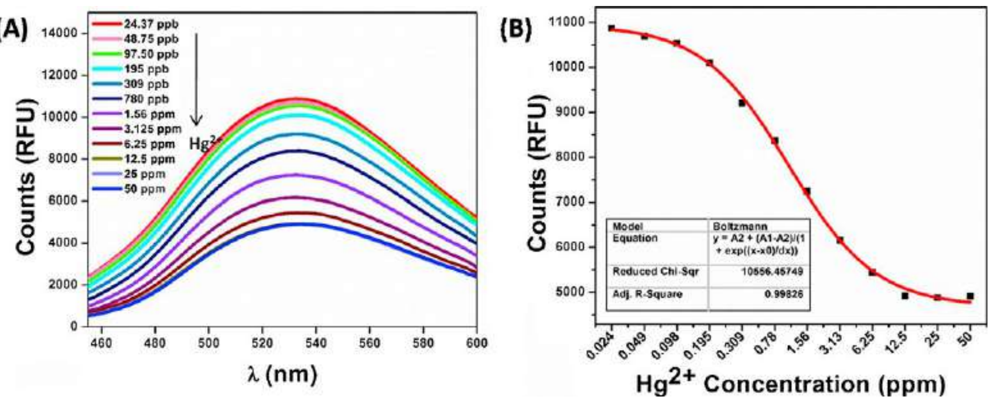

Fig. 10.5 (A) Effect of mercury (II) ions on fluorescence intensity of g-CN QDs, (B) fitted data of peak intensities. *(From D. Vashisht, E. Sharma, M. Kaur, A. Vashisht, S.K. Mehta, K. Singh, Solvothermal assisted phosphate functionalized graphitic carbon nitride quantum dots for optical sensing of Fe ions and its thermodynamic aspects, Spectrochim. Acta Part A Mol. Biomol. Spectrosc. 228 (2020) 117773, https://doi.org/10.1016/j.saa.2019.117773.)*

[54]. For vertical polarization electric field's direction is perpendicular to the g-CN sheets while in case of parallel polarization the electric field is plane with g-CN sheets. The decrease in photo luminescent properties on addition of Hg^{2+} is concentration dependent in the range of 50 ppb to 50 ppm (Fig. 10.5A and B).

To test the binding affinity of Hg^{2+} with g-CN QDs in water, a sample of microcartridge packed g-CN-Agarose conjugate were taken. This sample show bright blue fluorescence in the presence of UV light. The conjugate was further analyzed to confirm the binding by scanning electron microscopy (SEM) and FTIR with agarose microbeads. The optical spectroscopy is used to measure the residual Hg^{2+} when the solution is passed through the column. The concentration range is higher than that allowed by WHO [55], to check authentic ability of column in short span of time with heavy amount of mercury. Ag NPs were used to check the unbound amount of Hg^{2+} leaching from the column [56,57]. The reduction potential of Hg^{2+} and Ag^{+} are 0.855 and 0.799 V [58]. This shows that if both the ions are present in a solution, then Hg^{0} will change to Hg^{2+} and Ag^{+} will change to Ag^{0}. When AgNPs are added a standard curve is generated there. This standard curve is used to detect the amount of Hg^{2+} ions by adding the flow through with AgNPs by observing the loss of surface plasmon in AgNPs, which is due to the presence of Hg^{2+} ions as shown in Table 10.1.

For checking the binding of mercury, the column was tested with three runs and each time thoroughly washed for regaining the mercury binding ability and to calculate the capacity of binding. It was observed that there is no mercury loss during the column washing, which is due to the high interaction degree. It was found that from 10 mL sample volume, the column was capable of binding 90.71% of mercuric ions. To check the

Table 10.1 Analysis of mercuric ion binding ability of Agr-g-CN column successive runs of highly contaminated water samples and validation with mercuric ions spiked in real water sample collected from various sources [53].

Water source	Hg^{2+} added (ppm)	Hg^{2+} absorbed (ppm)	Hg^{2+} recovered (ppm)	% absorption
Run 1	2700	2454.84	245.16	90.92
Run 2	2700	2489.4	210.6	92.20
Run 3	2700	2403	297	89.00
Sewage	2700	2605.5	94.5 ± 7.56	96.50
Tap	2700	2670.3	29.7 ± 3.78	98.90
Rain	2700	2664.09	35.91 ± 12.96	98.67

practical capability of capturing Hg^{2+} ions by microcartridge, the water samples were taken from different resources such as sewage, tap, and rain water and centrifuged at 3000 rpm for separating solid contaminants from water. These samples were incubated with 2700 ppm of Hg^{2+} ion concentration and these samples were observed with Ag NPs. It was analyzed that the column was able to capture mercuric ions in natural water samples and also have very high number of interfering particles. This shows that pristine g-CNQDs show sensing behavior toward mercury ions.

3. Graphitic carbon nitride quantum dots as an optical sensor for Fe^{2+} and Fe^{3+} ions

g-CN QDs have also been used in sensing of heavy metal ions wherein the selectivity of material has been enhanced either by induction of metal ion binding functionality on the surface or by doping or both by functionalization and doping. Ngo et al. synthesized g-CN QDs functionalized with Phenyl Boric Acid by hydrothermal method for selective detection of glucose with detection limit of 16 nM [59]. Li et al. have synthesized functionalized g-CN QDs with conjugated polyene by calcination process. These have less PL intensity, great fluorescence lifetime in comparison to pristine g-CN QDs which helps to lower the rate of recombination of photogenerated electrons and holes [60]. Singh et al. have synthesized phosphate functionalized graphitic carbon nitride with solvothermal method where oleic acid was used as a solvent [45]. The morphology of these g-CN QDs was studied by XRD, FTIR, and TEM. XRD spectrum shows two peaks, one at $2\theta = 12.5°$ which is due to the repeating melem units and the second peak is an intense peak which is at 27° corresponding to 002 plane and arises due to interplanar stacking of g-CN structure (Fig. 10.6A). The FTIR studies show various characteristic peaks which corresponds to different functionalities such as peaks at 3430 and 3220 cm^{-1} is due to O–H and N–H, 1715 cm^{-1} is due to C=O, at 1660 and 768 cm^{-1} is due to triazine moiety. Triazine moiety is the basic building block of g-CN structure. The peaks

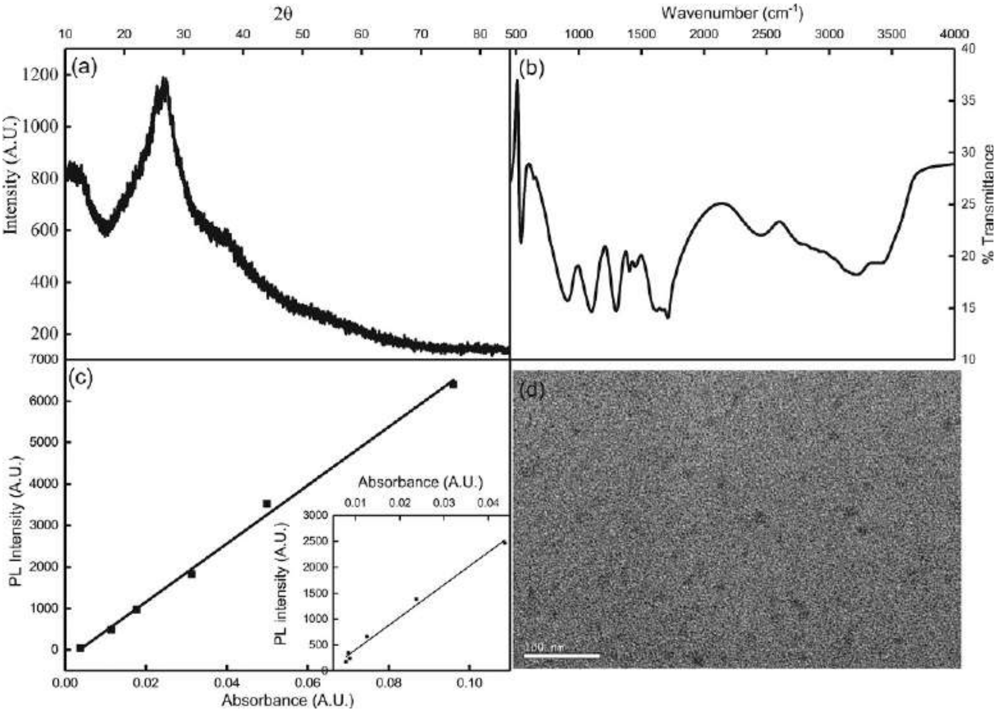

Fig. 10.6 (A) XRD pattern of Ph-g-CNQDs, (B) FTIR spectrum of Ph-g-CNQDs, (C) plot of PL intensity vs absorbance at particular concentration of Ph-g-CNQDs (inset of panel (C) depicts the PL intensity vs absorbance of quinine sulfate as reference), (D) TEM image of Ph-g-CNQDs. *(From D. Vashisht, E. Sharma, M. Kaur, A. Vashisht, S.K. Mehta, K. Singh, Solvothermal assisted phosphate functionalized graphitic carbon nitride quantum dots for optical sensing of Fe ions and its thermodynamic aspects, Spectrochim. Acta Part A Mol. Biomol. Spectrosc. 228 (2020) 117773, https://doi.org/10.1016/j.saa.2019.117773.)*

at 1620 and 1415 cm^{-1} is due to C–P, at 1403, 1296, 1099 cm^{-1} is due to P–O and 908, 541 cm^{-1} is due to P–OH and P–C functionalities (Fig. 10.6B). Fig. 10.6C reveals the dependence of absorbance and photoluminescence on respective concentration. Inset of Fig. 10.6C shows the relationship of absorbance and photoluminescence at respective concentration of reference, i.e., quinine sulfate. Quantum yield was calculated using the relationship given below [61].

$$Q = Q_r \frac{m \times n^2}{m_r} \times n_r^2$$

where Q_r is quantum yield of reference, Q is quantum yield of quantum dots, m is the slope of sample in absorbance vs photoluminescence emission graph, and m_r is slope of absorbance vs photoluminescence emission of reference. The quantum yield of synthesized quantum dots comes out to be 60.54% using this equation. The TEM image show particles are well dispersed, spherical in shape and the size of these phosphate functionalized g-CN QDs are below 10 nm. This study reveals that their size is in the quantum dot regime of size (Fig. 10.6D).

To further explore these Ph-g-CNQDs they have done optical studies which include UV and fluorescence studies. From UV studies they found out that there are two shoulders and a sharp peak. The shoulder at 265 nm and a peak at 330 nm belongs to $\pi \rightarrow \pi^*$ and $n \rightarrow \pi^*$ transition which are due to melem moiety. There is a shoulder at 368 nm which arises due to the defective surface sites (Fig. 10.7A). They also studied PL emission of Ph-g-CNQDs by exposing them at different wavelengths from 320 to 500 nm. The intensity increases with increase in excitation wavelength up to 350 nm after that intensity starts decreasing. Therefore, the excitation wavelength is fixed to 350 nm and emission wavelength at 450 nm (Fig. 10.7B). Emission spectrum is excitation dependent as increase in excitation wavelength also causes increase in emission wavelength (Fig. 10.7C). CQDs exhibit PL due to trapping of energy by defective surface sites

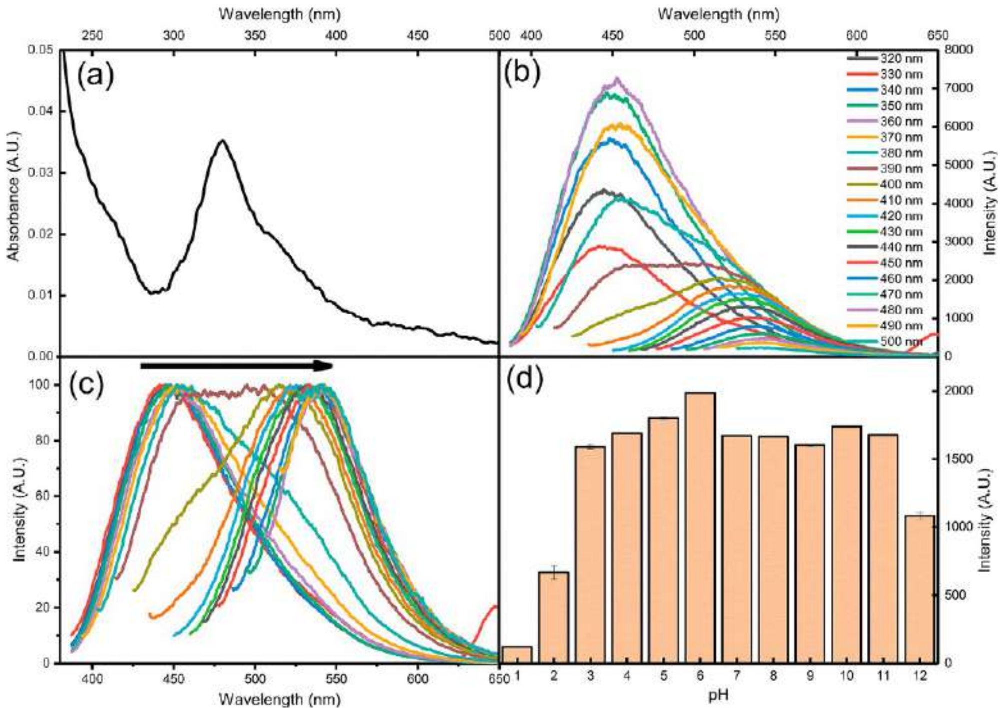

Fig. 10.7 (A) UV-vis spectrum of Ph-g-CNQDs, (B) effect of excitation on emission of Ph-g-CNQDs, (C) normalized graph of emission at different excitations, and (D) effect of pH on emission of Ph-g-CNQDs. *(From D. Vashisht, E. Sharma, M. Kaur, A. Vashisht, S.K.Mehta, K. Singh, Solvothermal assisted phosphate functionalized graphitic carbon nitride quantum dots for optical sensing of Fe ions and its thermodynamic aspects, Spectrochim. Acta Part A Mol. Biomol. Spectrosc. 228 (2020) 117773, https://doi.org/10.1016/j.saa.2019.117773.)*

due to surface passivation [62]. The nature of PL emission is nonemissive due to absence of UV-vis chromophores. This shows that these quantum dots itself generate bright blue emission [63]. These Ph-g-CNQDs show brilliant emission in the pH range 3.0–12.0. This confirms that there is no interference due to pH (Fig. 10.7D).

To detect the selectivity of Ph-g-CNQDs, these are exposed to different metal ion solutions such as Zn^{2+}, Pb^{2+}, Ni^{2+}, Na^{+}, Mg^{2+}, Ce^{3+}, K^{+}, Al^{3+}, Cr^{2+}, Ca^{2+}, Fe^{2+}, Cu^{2+}, Cd^{2+}, Ba^{2+}, Co^{2+}, and Fe^{3+}. Ph-g-CNQDs show higher sensing response toward Fe^{2+} and Fe^{3+} and except for these two ions Ph-g-CNQDs do not show any noticeable quenching toward any other ion. 0.25 mM of Fe^{2+} and Fe^{3+} quench the PL intensity of Ph-g-CNQDs to 33.66% and 65.80% (Fig. 10.8).

This behavior is due to the difference in paramagnetism of both the ions. Fe^{3+} ions are more paramagnetic than Fe^{2+}. All electrons in Fe^{2+} ion pair up and gives rise to low spin state due to strong ligand effect of N, O, K. Due to this reason, diamagnetic effect dominates and paramagnetic quenching is less in case of Fe^{2+} in comparison to Fe^{3+}. To further confirm the selectivity studies effect of concentration of these two ions on the PL intensity of Ph-g-CNQDs were also studied and as we increase the concentration the PL intensity of Ph-g-CNQDs started decreasing (Fig. 10.9A and B). Fig. 10.9C and D shows the PL intensity versus concentration plot for Fe^{2+} and Fe^{3+} ions. In case of ferrous ions, as we increase the concentration, the trend of quenching is linear up to 600 μM but after 600 μM, it becomes nonlinear. In the same way, ferric ions show linear behavior up to 300 μM and after that it becomes nonlinear. This linear behavior disappears after

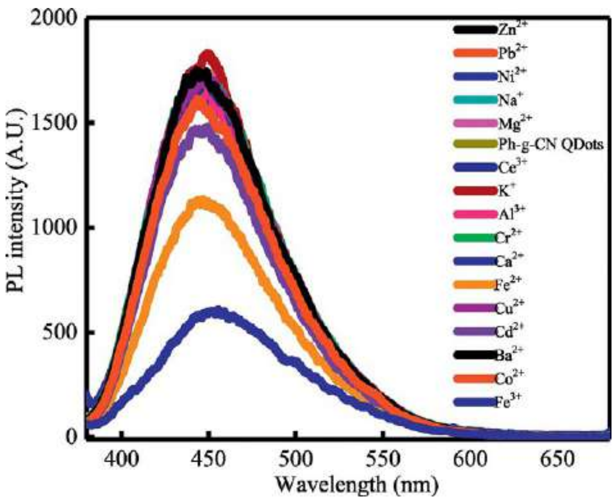

Fig. 10.8 Selectivity studies of Ph-g-CNQDs. *(From D. Vashisht, E. Sharma, M. Kaur, A. Vashisht, S.K. Mehta, K. Singh, Solvothermal assisted phosphate functionalized graphitic carbon nitride quantum dots for optical sensing of Fe ions and its thermodynamic aspects, Spectrochim. Acta Part A Mol. Biomol. Spectrosc. 228 (2020) 117773, https://doi.org/10.1016/j.saa.2019.117773.)*

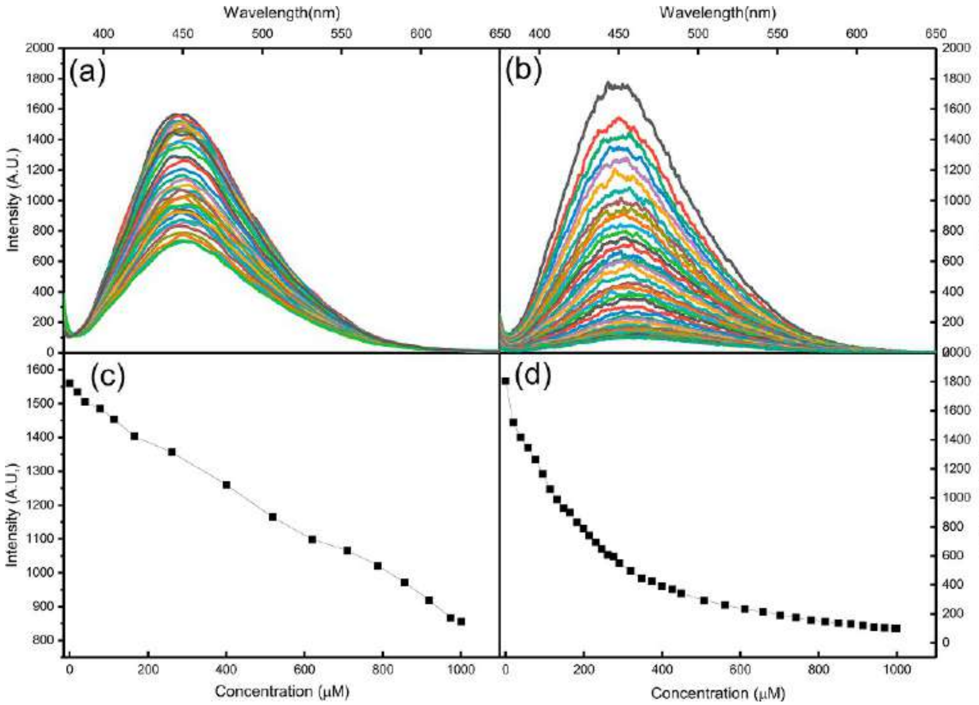

Fig. 10.9 (A) Effect of concentration of Fe(II) ions on emission of Ph-g-CNQDs, (B) effect of concentration of Fe(III) ions on emission of Ph-g-CNQDs, (C) PL intensity vs concentration plot of Fe(II), and (D) PL intensity vs concentration plot of Fe(III). *(From D. Vashisht, E. Sharma, M. Kaur, A. Vashisht, S.K. Mehta, K. Singh, Solvothermal assisted phosphate functionalized graphitic carbon nitride quantum dots for optical sensing of Fe ions and its thermodynamic aspects, Spectrochim. Acta Part A Mol. Biomol. Spectrosc. 228 (2020) 117773, https://doi.org/10.1016/j.saa.2019.117773.)*

sometime because number of binding sites decreases and later on increasing the concentration both dynamic and static quenching was observed.

4. Conclusion

In recent years, g-CN QDs have gained a lot of pace in diverse field especially in optical sensing due to its high-water stability, excellent photoluminescence, photo/chemical resistant, and most important is the ease of functionalization. In this chapter, we have discussed facile synthesis of pristine graphitic carbon nitride. Optical results reveal the synthesis of pristine g-CN with quantum dot regime having excellent optical properties. The synthesized QDs have been successfully utilized for the optical detection of Hg ions with the wide concentration range (50 ppb to 50 ppm). DFT studies have been utilized for the support of the hypothesis of metal ion binding with g-CN QDs. Further, to enhance an applicability of the present work, a microcartridge has been developed using agarose bind g-CN QDs for the removal of Hg ions from water system. To further enhance the selectivity of g-CN QDs, another work has been discussed in detail, i.e., phosphate-functionalized g-CN QDs for the detection of the Fe (II/III) ions. In this section, solvothermal technique has been implemented for the synthesis of Ph-g-CNQDs. XRD confirms melem unit and graphitic nature of g-CN QDs. FTIR results reveals the triazine molecules as well as surface functionalization of g-CN QDs with phosphate group. Quantum yield calculation comes out to 60.54% revealing the excellent photoluminescence nature of Ph-g-CNQDs. Phosphate functionalities have also been confirmed by using XPS studies. pH studies reveal that the Ph-g-CNQDs have broad workability in wide pH range from 2.0 to 12.0. In application part Ph-g-CNQDs have shown the selectivity toward both Fe (II) and Fe (III) ions via surface catalyzed energy transfer from QDs to metal ions. Out of the two Fe ions, Fe (III) shows better binding affinity toward Ph-g-CNQDs due to its higher charge density and is fully supported by the K_{sv} values. It has been observed that the review of data in this explains the facile and ease fabrication of both pristine and functionalized g-CN QDs with excellent photoluminescence enhances the energy transfer from QDs to Hg (II), Fe (II)/(III) ions, respectively. These types of functionalization of QDs could not only enhance the selectivity but also improve the quantum yield of QDs.

References

[1] K. Singh, Nanosensors for food safety and environmental monitoring, in: Nanotechnology for Food, Agriculture, and Environment, Springer, Cham, 2020, pp. 63–84, https://doi.org/10.1007/978-3-030-31938-0_4.

[2] K. Singh, S. Kumar, K. Agarwal, K. Soni, V. Ramana Gedela, K. Ghosh, Three-dimensional graphene with MoS_2 nanohybrid as potential energy storage/transfer device, Sci. Rep. 7 (1) (2017), https://doi.org/10.1038/s41598-017-09266-2.

[3] K. Singh, S.K. Mehta, Electrochemical determination of hydrazine using ZnO nanoellipsoids modified gold electrode, Sens. Lett. 14 (6) (2016) 577–582, https://doi.org/10.1166/sl.2016.3678.

[4] S.K. Mehta, S. Gupta, Khushboo, K. Singh, G.R. Chaudhary, Multicomponent gold hybrid structures: synthesis and applications, Rev. Adv. Sci. Eng. 1 (2012) 103–118, https://doi.org/10.1166/rase.2012.1008.

[5] R. Malik, V.K. Tomer, Y.K. Mishra, L. Lin, Functional gas sensing nanomaterials: a panoramic view, Appl. Phys. Rev. 7 (2) (2020), https://doi.org/10.1063/1.5123479.

[6] A. Rani, K. Singh, A.S. Patel, A. Chakraborti, S. Kumar, K. Ghosh, P. Sharma, Visible light driven photocatalysis of organic dyes using SnO_2 decorated MoS_2 nanocomposites, Chem. Phys. Lett. 738 (2020), https://doi.org/10.1016/j.cplett.2019.136874.

[7] R. Malik, V.K. Tomer, N. Joshi, V. Chaudhary, L. Lin, Nanosensors for monitoring indoor pollution in smart cities, in: P.K.S.B. Han, V.K. Tomer, T.A. Nguyen, A. Farmani (Eds.), Nanosensors for Smart Cities, Elsevier, 2020, pp. 251–266, https://doi.org/10.1016/b978-0-12-819870-4.00014-1.

[8] K. Singh, S.K. Mehta, Utilization of ZnO nanoflowers as efficient electrochemical catalyst for the oxidation of hydrazine, Sens. Lett. 13 (11) (2015) 1002–1006, https://doi.org/10.1166/sl.2015.3574.

[9] V.K. Tomer, K. Singh, H. Kaur, M. Shorie, P. Sabherwal, Rapid acetone detection using indium loaded WO_3/SnO_2 nanohybrid sensor, Sensors Actuators B Chem. 253 (2017) 703–713, https://doi.org/10.1016/j.snb.2017.06.179.

[10] S. Sangar, S. Sharma, V.K. Vats, S.K. Mehta, K. Singh, Biosynthesis of silver nanocrystals, their kinetic profile from nucleation to growth and optical sensing of mercuric ions, J. Clean. Prod. 228 (2019) 294–302, https://doi.org/10.1016/j.jclepro.2019.04.238.
[11] M.A. Seid, K. Anil, G. Reeta, Heavy Metal Pollution: Source, Impact, and Remedies, Springer Science and Business Media LLC, 2011, pp. 1–28, https://doi.org/10.1007/978-94-007-1914-9_1.
[12] P.B. Tchounwou, C.G. Yedjou, A.K. Patlolla, D.J. Sutton, Heavy metal toxicity and the environment, EXS 101 (2012) 133–164, https://doi.org/10.1007/978-3-7643-8340-4_6.
[13] A. Umar, K. Singh, S.K. Mehta, H. Fouad, O.Y. Alothman, Highly sensitive enzyme-less glucose biosensor based on α-Fe_2O_3 nanoparticles, Nanosci. Nanotechnol. Lett. (2018) 429–434, https://doi.org/10.1166/nnl.2018.2668.
[14] R. Malik, N. Joshi, V.K. Tomer, Advances in designs and mechanisms of MoO3 nanostructures for gas sensors: a holistic review, Mater. Adv. 2 (2021) 4197–4227.
[15] A. Da̧browski, Z. Hubicki, P. Podkościelny, E. Robens, Selective removal of the heavy metal ions from waters and industrial wastewaters by ion-exchange method, Chemosphere 56 (2) (2004) 91–106, https://doi.org/10.1016/j.chemosphere.2004.03.006.
[16] P.D. Johnson, P. Girinathannair, K.N. Ohlinger, S. Ritchie, L. Teuber, J. Kirby, Enhanced removal of heavy metals in primary treatment using coagulation and flocculation, Water Environ. Res. 80 (5) (2008) 472–479, https://doi.org/10.2175/106143007X221490.
[17] T. Vaishali, S. Ekta, G. Ashish, S. Sugandha, S. Kulvinder, Modification and management of lignocellulosic waste as an ecofriendly biosorbent for the application of heavy metal ions sorption, Mater. Today: Proc. (2020), https://doi.org/10.1016/j.matpr.2020.02.756.
[18] Y. Al-Hadeethi, A. Umar, K. Singh, A.A. Ibrahim, S.H. Al-Heniti, B.M. Raffah, Ytterbium-doped ZnO flowers based phenyl hydrazine chemical sensor, J. Nanosci. Nanotechnol. (2019) 4199–4204, https://doi.org/10.1166/jnn.2019.16283.
[19] Y. Al-Hadeethi, A. Umar, K. Singh, A.A. Ibrahim, S.H. Al-Heniti, B.M. Raffah, A. Cochis, Highly sensitive picric acid chemical sensor based on samarium (Sm) doped ZnO nanorods, J. Nanosci. Nanotechnol. (2019) 3637–3642, https://doi.org/10.1166/jnn.2019.16105.
[20] E. Sharma, D. Vashisht, A. Vashisht, V.K. Vats, S.K. Mehta, K. Singh, Facile synthesis of sulfur and nitrogen codoped graphene quantum dots for optical sensing of Hg and Ag ions, Chem. Phys. Lett. 730 (2019) 436–444, https://doi.org/10.1016/j.cplett.2019.06.040.
[21] V.K. Tomer, S. Duhan, Ordered mesoporous Ag-doped TiO_2/SnO_2 nanocomposite based highly sensitive and selective VOC sensors, J. Mater. Chem. A 4 (2016) 1033–1043.
[22] L. Liu, H. Jiang, J. Dong, W. Zhang, G. Dang, M. Yang, Y. Li, H. Chen, H. Ji, L. Dong, PEGylated MoS_2 quantum dots for traceable and pH-responsive chemotherapeutic drug delivery, Colloids Surf. B: Biointerfaces 185 (2020), https://doi.org/10.1016/j.colsurfb.2019.110590.
[23] Z. Qu, L. Liu, T. Sun, J. Hou, Y. Sun, M. Yu, Y. Diao, S. Lu, W. Zhao, L. Wang, Synthesis of bifunctional carbon quantum dots for bioimaging and anti-inflammation, Nanotechnology 31 (17) (2020), https://doi.org/10.1088/1361-6528/ab6b9d.
[24] K. Singh, G.R. Chaudhary, S. Singh, S.K. Mehta, Synthesis of highly luminescent water stable ZnO quantum dots as photoluminescent sensor for picric acid, J. Lumin. 154 (2014) 148–154, https://doi.org/10.1016/j.jlumin.2014.03.054.
[25] K. Singh, S.K. Mehta, Luminescent ZnO quantum dots as an efficient sensor for free chlorine detection in water, Analyst 141 (8) (2016) 2487–2492, https://doi.org/10.1039/c5an02599k.
[26] W. Su, R. Guo, F. Yuan, Y. Li, X. Li, Y. Zhang, S. Zhou, L. Fan, Red-emissive carbon quantum dots for nuclear drug delivery in cancer stem cells, J. Phys. Chem. Lett. 11 (4) (2020) 1357–1363, https://doi.org/10.1021/acs.jpclett.9b03891.
[27] M.J. Molaei, A review on nanostructured carbon quantum dots and their applications in biotechnology, sensors, and chemiluminescence, Talanta 196 (2019) 456–478, https://doi.org/10.1016/j.talanta.2018.12.042.
[28] A. Valizadeh, H. Mikaeili, M. Samiei, S.M. Farkhani, N. Zarghami, M. Kouhi, A. Akbarzadeh, S. Davaran, Quantum dots: synthesis, bioapplications, and toxicity, Nanoscale Res. Lett. 7 (2012), https://doi.org/10.1186/1556-276X-7-480.
[29] R. Das, R. Bandyopadhyay, P. Pramanik, Carbon quantum dots from natural resource: a review, Mater. Today Chem. 8 (2018) 96–109, https://doi.org/10.1016/j.mtchem.2018.03.003.

[30] P. Namdari, B. Negahdari, A. Eatemadi, Synthesis, properties and biomedical applications of carbon-based quantum dots: an updated review, Biomed. Pharmacother. 87 (2017) 209–222, https://doi.org/10.1016/j.biopha.2016.12.108.

[31] A. Sanati, M. Jalali, K. Raeissi, F. Karimzadeh, M. Kharaziha, S.S. Mahshid, S. Mahshid, A review on recent advancements in electrochemical biosensing using carbonaceous nanomaterials, Microchim. Acta 186 (12) (2019), https://doi.org/10.1007/s00604-019-3854-2.

[32] J. Zhang, J. Ge, M.D. Shultz, E. Chung, G. Singh, C. Shu, P.P. Fatouros, S.C. Henderson, F.D. Corwin, D.B. Geohegan, A.A. Puretzky, C.M. Rouleau, K. More, C. Rylander, M.N. Rylander, H.-W. Gibson, H.C. Dorn, In vitro and in vivo studies of single-walled carbon nanohorns with encapsulated metallofullerenes and exohedrally functionalized quantum dots, Nano Lett. 10 (8) (2010) 2843–2848, https://doi.org/10.1021/nl1008635.

[33] J. Shi, G. Ni, J. Tu, X. Jin, J. Peng, Green synthesis of fluorescent carbon dots for sensitive detection of Fe^{2+} and hydrogen peroxide, J. Nanopart. Res. 19 (6) (2017), https://doi.org/10.1007/s11051-017-3888-5.

[34] X. Fan, Y. Feng, Y. Su, L. Zhang, Y. Lv, A green solid-phase method for preparation of carbon nitride quantum dots and their applications in chemiluminescent dopamine sensing, RSC Adv. 5 (68) (2015) 55158–55164, https://doi.org/10.1039/c5ra05397h.

[35] Y. Tang, Y. Su, N. Yang, L. Zhang, Y. Lv, Carbon nitride quantum dots: a novel chemiluminescence system for selective detection of free chlorine in water, Anal. Chem. 86 (9) (2014) 4528–4535, https://doi.org/10.1021/ac5005162.

[36] V.K. Tomer, R. Malik, V. Chaudhary, Y.K. Mishra, L. Kienle, R. Ahuja, L. Lin, Superior visible light photocatalysis and low-operating temperature VOCs sensor using cubic Ag(0)-MoS_2 loaded g-CN 3D porous hybrid, Appl. Mater. Today 16 (2019) 193–203, https://doi.org/10.1016/j.apmt.2019.05.010.

[37] R. Malik, V.K. Tomer, State-of-the-art review of morphological advancements in graphitic carbon nitride (g-CN) for sustainable hydrogen production, Renew. Sustain. Energy Rev. 135 (2021), https://doi.org/10.1016/j.rser.2020.110235.

[38] R. Malik, V.K. Tomer, V. Chaudhary, M.S. Dahiya, S.P. Nehra, S. Duhan, K. Kailasam, A low temperature, highly sensitive and fast response toluene gas sensor based on In(III)-SnO_2 loaded cubic mesoporous graphitic carbon nitride, Sensors Actuators B Chem. 255 (2018) 3564–3575, https://doi.org/10.1016/j.snb.2017.09.193.

[39] R. Malik, V.K. Tomer, V. Chaudhary, M.S. Dahiya, A. Sharma, S.P. Nehra, S. Duhan, K. Kailasam, An excellent humidity sensor based on In-SnO_2 loaded mesoporous graphitic carbon nitride, J. Mater. Chem. A 5 (27) (2017) 14134–14143, https://doi.org/10.1039/c7ta02860a.

[40] R. Malik, V.K. Tomer, T. Dankwort, Y.K. Mishra, L. Kienle, Cubic mesoporous Pd-WO_3 loaded graphitic carbon nitride (g-CN) nanohybrids: highly sensitive and temperature dependent VOC sensors, J. Mater. Chem. A 6 (23) (2018) 10718–10730, https://doi.org/10.1039/c8ta02702a.

[41] R. Malik, V.K. Tomer, N. Joshi, T. Dankwort, L. Lin, L. Kienle, Au-TiO_2-loaded cubic g-C_3N_4 nanohybrids for photocatalytic and volatile organic amine sensing applications, ACS Appl. Mater. Interfaces 10 (40) (2018) 34087–34097, https://doi.org/10.1021/acsami.8b08091.

[42] H. Singh, V.K. Tomer, N. Jena, I. Bala, N. Sharma, D. Nepak, A.D Sarkar, K. Kailasam, S.K. Pal, A porous, crystalline truxene-based covalent organic frameworks and its applications in humidity sensing, J. Mater. Chem. A 5 (8) (2017) 21820–21827.

[43] V.K. Tomer, R. Malik, K. Kailasam, Near-room-temperature ethanol detection using Ag-loaded mesoporous carbon nitrides, ACS Omega 2 (7) (2017) 3658–3668, https://doi.org/10.1021/acsomega.7b00479.

[44] V.K. Tomer, N. Thangaraj, S. Gahlot, K. Kailasam, Cubic mesoporous Ag@CN: a high performance humidity sensor, Nanoscale 8 (47) (2016) 19794–19803, https://doi.org/10.1039/c6nr08039a.

[45] D. Vashisht, E. Sharma, M. Kaur, A. Vashisht, S.K. Mehta, K. Singh, Solvothermal assisted phosphate functionalized graphitic carbon nitride quantum dots for optical sensing of Fe ions and its thermodynamic aspects, Spectrochim. Acta Part A Mol. Biomol. Spectrosc. 228 (2020) 117773, https://doi.org/10.1016/j.saa.2019.117773.

[46] Y. Wang, R. Zhang, Z. Zhang, J. Cao, T. Ma, Host–guest recognition on 2D graphitic carbon nitride for nanosensing, Adv. Mater. Interfaces 6 (23) (2019), https://doi.org/10.1002/admi.201901429.

[47] P. Mishra, M. Ritu, V.K. Tomer, N Joshi, Hybridized graphitic carbon nitride (g-CN) as high performance VOCs sensor, Functional Nanomaterials: Advances in Gas Sensing Technologies, Springer, 2020, pp. 285–302.
[48] D. Nepak, V.K. Tomer, K. Kailasam, Chapter 3: Carbon nitrides (g-C_3N_4) and covalent triazine frameworks (CTFs), RSC Catal. Ser. 2018 (31) (2018) 67–101. Royal Society of Chemistry https://doi.org/10.1039/9781788013116-00067.
[49] R. Malik, V.K. Tomer, V. Chaudhary, Hybridized graphene for chemical sensing, in: Functionalized Graphene Nanocomposites and Their Derivatives, Elsevier, 2019, pp. 323–338, https://doi.org/10.1016/b978-0-12-814548-7.00016-7.
[50] S. Barman, M. Sadhukhan, Facile bulk production of highly blue fluorescent graphitic carbon nitride quantum dots and their application as highly selective and sensitive sensors for the detection of mercuric and iodide ions in aqueous media, J. Mater. Chem. 22 (41) (2012) 21832–21837, https://doi.org/10.1039/c2jm35501a.
[51] M. Sadhukhan, S. Barman, Bottom-up fabrication of two-dimensional carbon nitride and highly sensitive electrochemical sensors for mercuric ions, J. Mater. Chem. A 1 (8) (2013) 2752–2756, https://doi.org/10.1039/c3ta01523h.
[52] Y. Xu, X. Niu, H. Zhang, L. Xu, S. Zhao, H. Chen, X. Chen, Switch-on fluorescence sensing of glutathione in food samples based on a graphitic carbon nitride quantum dot (g-CNQD)-Hg^{2+} chemosensor, J. Agric. Food Chem. 63 (6) (2015) 1747–1755, https://doi.org/10.1021/jf505759z.
[53] M. Shorie, H. Kaur, G. Chadha, K. Singh, P. Sabherwal, Graphitic carbon nitride QDs impregnated biocompatible agarose cartridge for removal of heavy metals from contaminated water samples, J. Hazard. Mater. 367 (2019) 629–638, https://doi.org/10.1016/j.jhazmat.2018.12.115.
[54] X. Wang, X. Chen, A. Thomas, X. Fu, M. Antonietti, Metal-containing carbon nitride compounds: a new functional organic-metal hybrid material, Adv. Mater. 21 (16) (2009) 1609–1612, https://doi.org/10.1002/adma.200802627.
[55] F.R. Spellman, J.E. Drinan, The Drinking Water Handbook, CRC Press, 2012, https://doi.org/10.1201/b12305.
[56] M.L. Firdaus, I. Fitriani, S. Wyantuti, Y.W. Hartati, R. Khaydarov, J.A. Mcalister, H. Obata, T. Gamo, Colorimetric detection of mercury (II) ion in aqueous solution using silver nanoparticles, Anal. Sci. 33 (7) (2017) 831–837, https://doi.org/10.2116/analsci.33.831.
[57] A. Jeevika, D.R. Shankaran, Functionalized silver nanoparticles probe for visual colorimetric sensing of mercury, Mater. Res. Bull. 83 (2016) 48–55, https://doi.org/10.1016/j.materresbull.2016.05.029.
[58] P. Vasileva, T. Alexandrova, I. Karadjova, Application of starch-stabilized silver nanoparticles as a colorimetric sensor for mercury(II) in 0.005 mol/L nitric acid, Journal of Chemistry 2017 (2017), https://doi.org/10.1155/2017/6897960.
[59] Y.L.T. Ngo, W.M. Choi, J.S. Chung, S.H. Hur, Highly biocompatible phenylboronic acid-functionalized graphitic carbon nitride quantum dots for the selective glucose sensor, Sensors Actuators B Chem. 282 (2019) 36–44, https://doi.org/10.1016/j.snb.2018.11.031.
[60] H. Li, H.Y. Lee, G.S. Park, B.J. Lee, J.D. Park, C.H. Shin, W. Hou, J.S. Yu, Conjugated polyene-functionalized graphitic carbon nitride with enhanced photocatalytic water-splitting efficiency, Carbon 129 (2018) 637–645, https://doi.org/10.1016/j.carbon.2017.12.048.
[61] A. Jaiswal, S. Sankar Ghosh, A. Chattopadhyay, One step synthesis of C-dots by microwave mediated caramelization of poly(ethylene glycol), Chem. Commun. 48 (3) (2012) 407–409, https://doi.org/10.1039/c1cc15988g.
[62] H. Xie, Y. Fu, Q. Zhang, K. Yan, R. Yang, K. Mao, P.K. Chu, L. Liu, X. Wu, Selective and high-sensitive label-free detection of ascorbic acid by carbon nitride quantum dots with intense fluorescence from lone pair states, Talanta 196 (2019) 530–536, https://doi.org/10.1016/j.talanta.2019.01.003.
[63] L. Shen, L. Zhang, M. Chen, X. Chen, J. Wang, The production of pH-sensitive photoluminescent carbon nanoparticles by the carbonization of polyethylenimine and their use for bioimaging, Carbon 55 (2013) 343–349, https://doi.org/10.1016/j.carbon.2012.12.074.

Index

Note: Page numbers followed by *f* indicate figures, and *t* indicate tables.

H

I

K

M

S

T

U

V

W

X

Z

NANOSTRUCTURED CARBON NITRIDES FOR SUSTAINABLE ENERGY AND ENVIRONMENTAL APPLICATIONS

Edited by Shamik Chowdhury and Mu Naushad

Key Features

- Provides insights into various aspects of carbon nitride materials from multidisciplinary perspectives
- Discusses how nanostructured carbon nitrides can tackle global energy and environmental challenges in a sustainable manner
- Explores the design and fabrication of carbon nitride-based materials with optimized structures, controlled morphologies, and tailored properties for practical implementation

In recent years, carbon nitride, a new type of two-dimensional (2D) material, has attracted great interest, in terms of fundamental scientific investigation and potential practical applications, for a range of energy and environmental technologies. This can be largely attributed to its optoelectronic and physicochemical properties, including moderate band gap, adjustable energy band configuration, tailor-made surface functionalities, low cost, metal-free nature, remarkable thermochemical stability, and environmentally benign manufacturing protocol.

Nanostructured Carbon Nitrides for Sustainable Energy and Environmental Applications offers a comprehensive, authoritative, and critical account of the recent progress in the development and application of multifunctional carbon nitride materials and their hybrid heterostructures. There are two major objectives of this book: first, to provide a systematic overview of the key design principles toward the fabrication of high-performance carbon nitride–based nanostructures; and second, to provide insights into a range of clean energy technologies and environmental remediation methods that build on these nanoengineered carbon nitrides.

This book serves as an important reference source for materials scientists and engineers who are interested in developing their understanding of how carbon-based nanomaterials are being used for sustainable energy and environmental applications.

About the Editors

Dr. Shamik Chowdhury is Assistant Professor in the School of Environmental Science and Engineering, Indian Institute of Technology Kharagpur, West Bengal, India.

Dr. Mu. Naushad is a Full Professor in the Department of Chemistry, College of Science, King Saud University, Riyadh, Saudi Arabia.

ISBN 978-0-12-823961-2

9 780128 239612

ELSEVIER elsevier.com/books-and-journals